National Aeronautics and Space Administration

NASA-ISRO SAR (NISAR) Mission Science Users' Handbook

Second Edition

Launch Date:
July 30, 2025

Document Date:
October 2025, Second Edition, v01

Dear Colleagues,

As the Earth Science Director at NASA, it is a truly great pleasure to introduce the second edition of the NISAR Science Users' Handbook.

On July 30, shortly after 8:00 AM Eastern time, I witnessed a major milestone for NASA Earth science, and for the United States: the launch of NISAR, short for NASA-ISRO Synthetic Aperture Radar.

This satellite is among our agency's most ambitious science satellite missions. Launched from Satish Dhawan Space Centre on India's southeastern coast, NISAR is carrying an innovative dual synthetic aperture radar system – two bands collecting information that will be processed into extraordinarily detailed and comprehensive measurements of Earth's surface. This is something that can only be accomplished from the vantage point of space.

Why is this mission important? We know the Earth's surface is in constant and meaningful motion. Even subtle, seemingly minor shifts in the land and ice surface can signal important change. The science from NISAR will advance our understanding of and help us better prepare for landslides, earthquakes, volcanoes, and other disasters. It will help us measure and understand the processes driving glacier melt, the depth of mountain snowpack, and changes in the ice sheets of Greenland and Antarctica.

Thanks to our Early Adopters program and Earth Action portfolio, NISAR's actionable science will be put to use immediately, informing decisions around land-use planning, the development of critical infrastructure, agriculture and water management practices, and disaster preparedness and response.

The discovery and the use are the "why" of NISAR's importance. But "how" we built and launched NISAR, and how we will operate this mission over its lifetime, are also important. NISAR's data, science, and observations will be open and accessible. NISAR was built in cooperation with a strategic international partner in India, allowing us to share both mission costs and mission rewards.

In short, NISAR is a model for the next-generation of NASA Earth-observing missions – driven by tech innovation, developed jointly with a strategic partner for cost efficiency, and focused on delivering actionable science to help people and organizations make more informed decisions every day. Join me in recognizing this great achievement. Go NISAR!

Sincerely,

Karen St. Germain
Director NASA Earth Science

Foreword to the Second Edition

NISAR has advanced from Phase C (final design and fabrication) through Phase D, in which assembly, integration, and testing were completed; the launch was successfully conducted; and the commissioning period has nearly concluded since the first publication of the NASA ISRO SAR (NISAR) Science Users' Handbook. The mission is now poised to enter its science operations (Phase E), systematically collecting near global land and ice L-band and regional S-band synthetic aperture radar data at unprecedented spatio-temporal scales that will enable a new suite of Earth science research and applications.

The first edition of the NISAR Science Users' Handbook introduced the mission to the science and applications communities, providing descriptions of its science focus areas, mission requirements, Level-3 data algorithms, and calibration and validation efforts. This second edition updates the material to reflect the maturation of all aspects of the mission, including revised mission characteristics, new material on the global soil moisture product, links to the Level-3 Algorithm Theoretical Basis Documents (ATBDs) and/or Jupyter Notebooks for each science discipline, and expanded descriptions of the numerous science and applications NISAR will enable in the cryosphere, hydrosphere, biosphere, and geosphere disciplines, as well as natural disasters, hazards, and coastal/ocean monitoring.

We gratefully acknowledge the material content and feedback provided by the NISAR Science Team and Project Science Team, which has directly shaped the improvements in this edition. We also recognize the essential contributions and support of our partners at ISRO centers, including Space Applications Centre, UR Rao Satellite Center, National Remote Sensing Center, and the Indian Institute for Remote Sensing, as well as NASA Headquarters.

This Second Edition supersedes previous versions.

Paul Rosen
NISAR Project Scientist, NASA/JPL

Gerald Bawden
NISAR Program Scientist, NASA/HQ

Brandi Downs
Second Edition Editor-in-Chief, NASA/JPL

Suggested Citation: NISAR (2025, version 1). NASA-ISRO SAR (NISAR) mission science users' handbook, second edition. NASA Jet Propulsion Laboratory. 246 pp. https://doi.org/10.48577/jpl.UD4HV3

Contents

Contents

List of Authors

Falk Amelung
University of Miami

Karen An
Jet Propulsion Laboratory,
California Institute of Technology

Edward Armstrong
Jet Propulsion Laboratory,
California Institute of Technology

Gerald Bawden
NASA Headquarters

Rajat Bindlish
NASA Goddard Space Flight Center

Adrian Borsa
Scripps Institution of Oceanography,
University of California, San Diego

Sean Buckley
Jet Propulsion Laboratory,
California Institute of Technology

Susan Callery
Jet Propulsion Laboratory,
California Institute of Technology

Manab Chakraborty
Space Applications Centre,
Indian Space Research Organisation

Steven Chan
Jet Propulsion Laboratory,
California Institute of Technology

Bruce Chapman
Jet Propulsion Laboratory,
California Institute of Technology

Anup Das
Space Applications Centre,
Indian Space Research Organisation

Narendra Das
Michigan State University

Andrea Donnellan
Purdue University

Brandi Downs
Jet Propulsion Laboratory,
California Institute of Technology

Ralph Dubayah
University of Maryland

Heresh Fattahi
Jet Propulsion Laboratory,
California Institute of Technology

Kurt Feigl
University of Wisconsin

Eric Fielding
Jet Propulsion Laboratory,
California Institute of Technology

Richard Forster
University of Utah

Alex Gardner
Jet Propulsion Laboratory,
California Institute of Technology

Margaret Glasscoe
Jet Propulsion Laboratory,
California Institute of Technology

Bradford Hager
Massachusetts Institute of Technology

Scott Hensley
Jet Propulsion Laboratory,
California Institute of Technology

Benjamin Holt
Jet Propulsion Laboratory,
California Institute of Technology

Xiaodong Huang
Jet Propulsion Laboratory,
California Institute of Technology

Cathleen Jones
Jet Propulsion Laboratory,
California Institute of Technology

Ian Joughin
Applied Physics Laboratory,
University of Washington

Josef Kellndorfer
Earth Big Data, LLC.

Seungbum Kim
Jet Propulsion Laboratory,
California Institute of Technology

Raj Kumar
Space Applications Centre,
Indian Space Research Organisation

Marco Lavalle
Jet Propulsion Laboratory,
California Institute of Technology

Rowena Lohman
Cornell University

Zhong Lu
Southern Methodist University

Jessica Martinez
University of Massachusetts, Amherst

Kyle McDonald
City College of New York

Franz Meyer
University of Alaska, Fairbanks

Tapan Misra
Space Applications Centre,
Indian Space Research Organisation

Frank Monaldo
National Oceanic and Atmospheric
Administration

Sandip Oza
Space Applications Centre,
Indian Space Research Organisation

Matthew Pritchard
Cornell University

Eric Rignot
University of California, Irvine

Paul Rosen
Jet Propulsion Laboratory,
California Institute of Technology

Sassan Saatchi
Jet Propulsion Laboratory,
California Institute of Technology

Priyanka Sharma
Jet Propulsion Laboratory,
California Institute of Technology

Marc Simard
Jet Propulsion Laboratory,
California Institute of Technology

Mark Simons
Jet Propulsion Laboratory,
California Institute of Technology

Paul Siqueira
University of Massachusetts, Amherst

Ekaterina Tymofyeyeva
Jet Propulsion Laboratory,
California Institute of Technology

Howard Zebker
Stanford University

Simon Zwieback
University of Alaska, Fairbanks

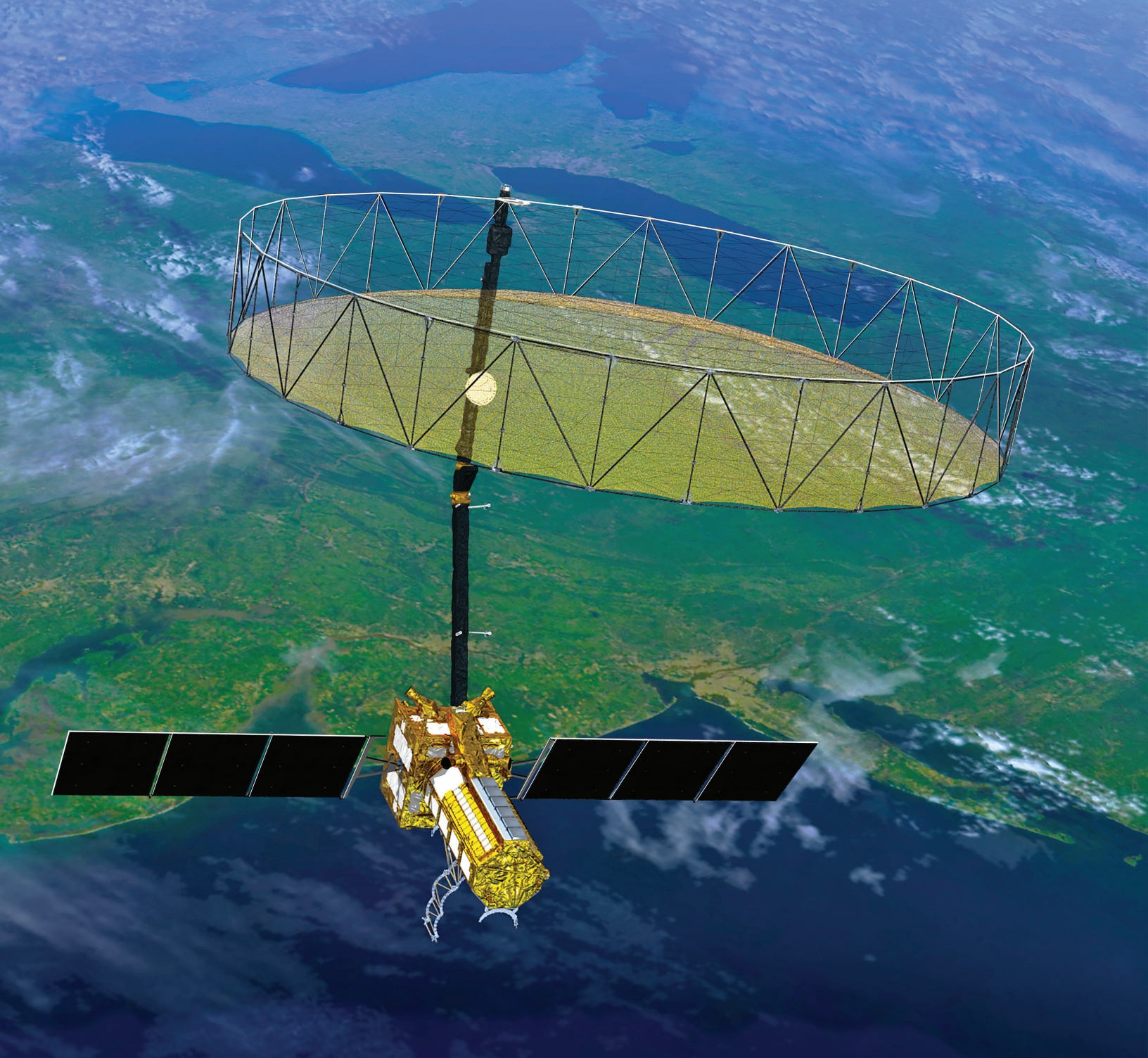

FIGURE 1-1

Artist's concept of NASA-ISRO Synthetic Aperture Radar (NISAR) in orbit. The mission will produce L-band (24-cm wavelength) polarimetric radar images and interferometric data globally, and comparable S-band (9.4-cm wavelength) data over India and targeted areas around the world. Credit: NASA/JPL-Caltech.

1 INTRODUCTION

NISAR PROVIDES A MEANS OF DISENTANGLING AND CLARIFYING SPATIALLY AND TEMPORALLY COMPLEX PHENOMENA, RANGING FROM ECOSYSTEM DISTURBANCES TO ICE SHEET COLLAPSE AND NATURAL HAZARDS INCLUDING EARTHQUAKES, TSUNAMIS, VOLCANOES, AND LANDSLIDES.

The NASA-ISRO Synthetic Aperture Radar (NISAR, Figure 1-1) mission is a partnership between the National Aeronautics and Space Administration (NASA) and the Indian Space Research Organization (ISRO). NISAR's Earth-orbiting radar will make global measurements of Earth surface change in support of multiple scientific disciplines. NISAR observations will provide new insights into critical phenomena including ecosystem health, ice sheet melt, and natural disasters such as earthquakes, volcanoes, and landslides. The purpose of this handbook is to prepare scientists and algorithm developers to make full use of NISAR data. It provides a foundational overview of the mission, its design, and its data products.

Following the 2007 National Academy of Science Decadal Survey report, "Earth Science and Applications from Space: National Imperatives for the Next Decade and Beyond," NASA began studying concepts for a Synthetic Aperture Radar (SAR) mission to determine Earth change in three disciplines: ecosystems (vegetation and the carbon cycle), solid Earth sciences (land surface deformation), and cryospheric sciences (primarily ice sheet and glacier motion related to climatic drivers and effects on sea level). These early studies laid the groundwork for an international partnership with ISRO, which led to a joint spaceborne mission incorporating both L-band and S-band SAR systems. The 2018 Decadal Survey, "Thriving on Our Changing Planet: A Decadal Strategy for Earth Observation from Space," reaffirmed the importance of the NISAR mission and supported continued international collaboration between NASA and ISRO.

The Earth Science Division (ESD) of NASA's Science Mission Directorate (SMD) directed the Jet Propulsion Laboratory (JPL) to manage the United States component of the NISAR project. ESD assigned the Earth Science Mission Program Office (ESMPO), located at Goddard Space Flight Center (GSFC), responsibility for overall program management.

NISAR builds on the legacy of the Deformation, Ecosystem Structure and Dynamics of Ice (DESDynI) radar mission concept, one of the four Tier 1 missions recommended in the 2007 Decadal Survey. To meet the needs of three distinct global scientific communities and support a wide range of applications that benefit society, NISAR was engineered to exceed the capabilities of currently operating SAR satellites. NISAR's design includes a dual-frequency, fully polarimetric radar, with a nominal imaging swath of 240 km, enabling nearly complete global coverage every 12 days. The lidar component of the original DESDynI concept is being fulfilled

NISAR WILL BE THE FIRST NASA RADAR MISSION TO SYSTEMATICALLY AND GLOBALLY STUDY SOLID EARTH, ICE MASSES, AND ECOSYSTEMS.

by the Ice, Cloud, and land Elevation Satellite-2 (ICESat-2) and the Global Ecosystem Dynamics Investigation (GEDI) lidar missions, operating contemporaneously with NISAR.

NISAR launched July 30, 2025 with a 90-day commissioning period. The mission will conduct a minimum of three full years of science operations with the L-band SAR in a near-polar, dawn-dusk, fixed, sun-synchronous orbit to satisfy NASA's requirements. ISRO's requirements specify five years of operation with the S-band SAR. If the system does not deplete its fuel reserves during the nominal mission period, it will be possible to extend mission operations for either instrument.

NISAR's science objectives are based on priorities identified in the 2007 Decadal Survey and further articulated in the 2010 report on NASA's Climate-Centric Architecture. NISAR is the first NASA radar mission to systematically and globally study the solid Earth, land ice, sea ice, and ecosystems. NISAR will measure glacier and land-surface motions and changes with full interferometric capability, and will monitor crop growth, ecosystem disturbances, and biomass with polarimetric SAR, elucidating underlying processes and improving fundamental scientific understanding. The measurements will improve forecasts and assessment of ecosystem and land use change, ice sheet evolution, and natural hazards.

NASA also supports the use of NISAR data for a broad range of societal applications, including global disaster response, agricultural monitoring, and soil moisture assessment. ISRO has identified additional applications of relevance to India, such as monitoring of agricultural biomass, assessing local and regional natural disasters, studying snow and glaciers in the Himalayas, and observing Indian coastlines and near-shore ocean dynamics.

All NISAR science data (both L-band and S-band) will be freely and openly available to the public, consistent with the long-standing NASA Earth Science open data policy, via the Alaska Satellite Facility (https://asf.alaska.edu). With its global acquisition strategy, cloud-penetrating capability, high spatial resolution, and 12-day repeat sampling, NISAR will provide reliable, spatially dense time series of radar data offering a unique resource for exploring Earth change (Table 1-1).

Over the course of the mission, NISAR is expected to deliver:

- Comprehensive assessment of tectonic motion across on-land plate boundaries, identifying areas of high strain and capturing the deformation signatures of several hundred earthquakes, as well as the periods of time before and after these seismic events, significantly contributing to our understanding of fault systems and the global earthquake cycle;
- Comprehensive inventories of global volcanoes, detecting changes in their state of activity, and contributing to their associated risk assessment;
- Comprehensive global assessments of ecosystem disturbance, agricultural change, and wetlands dynamics to inform carbon flux models at the most critical spatial and temporal scales;
- Comprehensive global biomass inventory, in combination with ICESat-2, GEDI, and other missions, to set the decadal boundary conditions for carbon flux models, with coverage of areas with low to moderate biomass, where ecosystem dynamics are greatest;
- Monthly velocity and grounding line assessments of the Greenland and

Antarctica ice sheets as a key boundary condition for ice sheet models;

- Regular monitoring of the world's glaciers and ice caps;
- Comprehensive mapping of sea ice motion and inferred deformation, improving our understanding of ocean-atmosphere interaction at the poles;
- Fast, reliable, and regular sampling of land and ice, benefitting applications, including infrastructure monitoring, agriculture and forestry, disaster response, aquifer utilization, and marine navigation.
- Systematic soil moisture products enabled by the U.S. Satellite Needs Working Group will track near global variability supporting a wide range of science and applications observational needs.

TABLE 1-1. NISAR CHARACTERISTICS

NISAR Characteristic:	Enables:
L-band (24 cm wavelength)	Foliage penetration and interferometric coherence
S-band (9.4 cm wavelength)	Sensitivity to light vegetation
SweepSAR[1] technique with imaging swath > 240 km	Global-scale data collection at full resolution
Polarimetry (single/dual/quad)	Surface characterization and biomass estimation
12-day exact repeat orbit	Rapid sampling and time-series analysis
3–10 meters mode-dependent SAR resolution	Small-scale feature detection
3 years science operations (5 years consumables)	Long-term monitoring and temporal changes analysis
Pointing control < 273 arcseconds	Deformation interferometry
Orbit control < 350 meters	Deformation interferometry
Observation duty cycle >50% L-band and >10% S-band	Comprehensive land and ice coverage
Nominal mission pointing left only	Consistent time series and data continuity

[1] SweepSAR is a technique to achieve wide swath at full resolution. See Section 4.7 for a more detailed description.

FIGURE 1-2

NISAR will image Earth's dynamic surface over time, providing information on changes in ice sheets and glaciers, the evolution of natural and managed ecosystems, earthquake and volcano deformation, subsidence from groundwater and oil pumping, and the human impact of these and other phenomena (all images are open source).

Credit: Jesse Kelpszas/Shutterstock.

2 SCIENCE FOCUS AREAS

IN RESPONSE TO INTERIOR FORCES, PLATE TECTONICS DEFORM EARTH'S SURFACE, CAUSING EARTHQUAKES, SPAWNING VOLCANOES, BUILDING MOUNTAINS, AND DRIVING EROSION.

Earth's land and ice surface is constantly changing and interacting with Earth's interior, oceans, and atmosphere. In response to interior forces, plate tectonics deform Earth's surface, building mountains, driving erosion, and triggering earthquakes and volcanic eruptions. Human and natural forces are rapidly modifying the global distribution and structure of terrestrial ecosystems on which life depends, causing steep reductions in species diversity, endangering sustainability, altering the global carbon cycle, and affecting climate. Dramatic changes in ice sheets, sea ice, and glaciers are key indicators of these climate effects. For instance, increasing mass loss from glaciers and ice sheets contributes to accelerated rates of sea level rise.

NISAR addresses the needs of Solid Earth, Ecosystems, Cryospheric, and Soil Moisture science disciplines, with a specific focus on the following key scientific objectives to:

1. Determine the likelihood of earthquakes, volcanic eruptions, landslides, and land subsidence;
2. Understand the dynamics of carbon storage and uptake in wooded, agricultural, wetland, and permafrost systems;
3. Understand the response of ice sheets to variations in the climate, the interaction of sea ice and climate, and impacts on sea level rise worldwide;
4. Constrain global patterns of soil moisture and their temporal variability, across a wide range of land cover types and climate regimes.

NISAR also provides data for many science applications, enabling users to:

1. Understand the dynamics of groundwater, hydrocarbon, and sequestered CO2 reservoirs in the context of natural resource management;
2. Provide agricultural monitoring capability to support food security objectives;
3. Apply NISAR's unique data set to hazard identification and mitigation;
4. Provide information to support disaster response and recovery;
5. Provide observations of land ice flow and land subsidence to constrain rates of regional relative sea level rise.

NISAR will provide systematic global measurements to characterize processes, frequent measurements to understand temporal changes, and a minimum three-year duration to estimate long-term trends and determine subtle rates and rate changes. NISAR will serve the objectives of a number of major science disciplines and will meet the needs of a broad science community with numerous applications, including earthquakes, volcanoes, landslides, ice sheets, sea ice, snow and glaciers, coastal processes, ocean and land parameter retrieval, and ecosystems. In addition, NISAR will play a role in the response to and

recovery from natural disasters such as floods, wildfires, and earthquakes.

NISAR observations will address several science and applications areas in which the 2018 Decadal Survey recommends progress:

- Determining the extent to which the shrinking of glaciers and ice sheets – and their contributions to sea-level rise – are accelerating, decelerating, or remaining unchanged;
- Quantifying trends in water stored on land (e.g., in aquifers) and the implications for issues such as water availability for human consumption and irrigation;
- Understanding alterations to surface characteristics and landscapes (e.g., snow cover, snow melt, landslides, earthquakes, eruptions, urbanization, land-cover, and land use) and their implications for risk and resource management;
- Assessing the evolving characteristics and health of terrestrial vegetation and aquatic ecosystems, which is important for understanding key consequences such as crop yields, carbon uptake, and biodiversity;
- Observing the rate of motion of ice sheet and glacier surfaces to help estimate their contributions to sea-level rise;
- Identifying and quantifying where coastal land subsidence or uplift will compound or decrease the effects of relative sea level rise;
- Examining movement of land surfaces and changes in strain rates to provide critical insights into the processes that govern earthquakes, volcanic eruptions, landslides, and tectonic plate deformation.

2.1 SOLID EARTH PROCESSES: EARTHQUAKES, VOLCANOES, AND LANDSLIDES

Society's exposure to natural hazards is increasing. Earthquakes threaten densely populated regions like the west coast of the USA – home to about 50 million citizens and costly infrastructure. Volcanic eruptions endanger populations in many areas of the globe and can disrupt air travel. Localized changes in the land surface can precipitate catastrophic events such as landslides. Properly preparing for, mitigating, and responding to nature's disasters require detecting, measuring, and understanding the

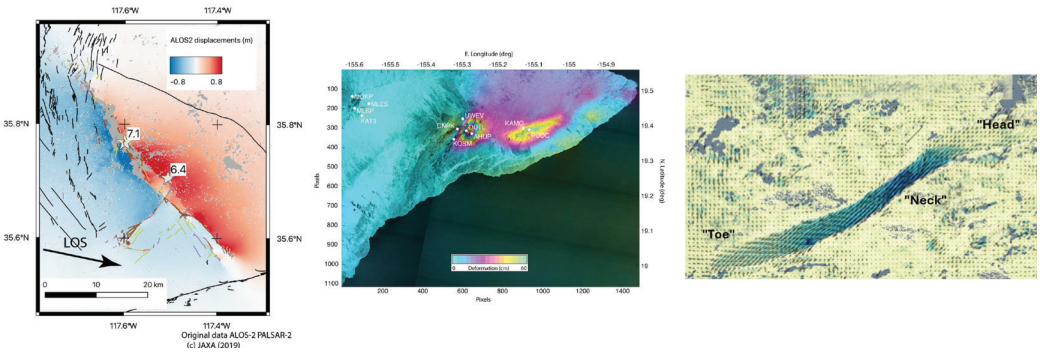

FIGURE 2-1

NISAR will measure surface deformation to determine the likelihood of earthquakes, volcanic eruptions, and landslides. (Left) 2019 M_w 7.1 and M_w 6.4 Ridgecrest earthquakes shown in L-band ALOS-2 displacement map (Fielding et al., 2020). (Middle) Observed cumulative deformation at Kilauea and Chain of Craters on island of Hawaii, Spring 2018; data from Sentinel-1 (Zebker, 2021). (Right) Slumgullion landslide inversion of L-band UAVSAR from four images in April 2012 (Delbridge et al., 2016).

slow-moving processes that often foreshadow or even trigger natural disasters.

NISAR's ability to observe subtle land surface deformation over time provides an opportunity to monitor, mitigate, and respond to natural hazards such as earthquakes, volcanoes, and landslides (Figure 2-1). The magnitude and dynamics of these surface changes also provide information about the underlying Earth processes at work. NISAR will uniquely address several questions posed in NASA's Challenges and Opportunities for Earth Surface and Interior report (Davis et al, 2016):

1. What is the nature of deformation associated with plate boundaries, and what are the implications for earthquakes, tsunamis, and other related natural hazards?
2. How do tectonic processes and climate variability interact to shape Earth's surface and create natural hazards?
3. How do magmatic systems evolve, under what conditions do volcanoes erupt, and how do eruptions and volcano hazards develop?
4. What are the dynamics of Earth's deep interior, and how does Earth's surface respond?

NISAR will also address to varying degrees several questions posed in the 2018 Decadal Survey by the Earth Surface and Interior Panel:

1. How can large-scale geological hazards be accurately forecast in a socially relevant timeframe?
2. How do geological disasters directly impact the Earth system and society following an event?
3. How will local sea level change along coastlines around the world in the next decade to century?
4. What processes and interactions determine the rates of landscape change?
5. How much water is traveling deep underground, and how does it affect geological processes and water supplies?

Measuring the ***coseismic*** displacements associated with earthquakes is essential for describing which parts of a fault have ruptured, which parts may have been brought closer to failure, and for constraining the distribution of fault slip at depth and potentially partitioned across multiple faults. Seismic data provide the best estimates of the speed of rupture propagation and the timing of slip on individual fault patches, but the overall distribution of subsurface fault slip is best constrained by combining coseismic displacements, such as those from NISAR, with seismic data (e.g., Pritchard et al., 2006; 2007; Simons et al., 2011; Duputel et al., 2015). These estimates of fault slip parameters then provide key input into mechanical models of faults and the surrounding crust and upper mantle, estimates of stress change on neighboring faults, and inform our basic understanding of regional seismic hazards.

Measurements of ***secular*** velocities, the motion between earthquakes, in tectonic plate boundary regions place constraints on models of fault physics, contributing to estimates of long-term seismic hazard. NISAR will enable imaging of Earth's plate boundary zones at depth, sampling the range of different tectonic styles, capturing plate boundaries at different stages of the earthquake cycle, and informing regional assessments of seismic hazard (e.g., Jolivet et al., 2015).

Detecting and quantifying ***transient*** deformation play an essential role in improving our understanding of fundamental processes associated with tectonics, subsurface movement of magma and volcanic eruptions, landslides, response to changing surface loads, and a wide variety of anthropogenic phenomena. Aseismic and post-seismic fault slip transients, volcanic and landslide deformation, and local subsidence and uplift due to migration of crustal fluids occur globally over temporal and spatial scales ranging from sub-daily to multi-year, and tens of meters

to hundreds of kilometers. Many eruptions are preceded by surface deformation induced by moving magma in the subsurface. However, periods of magma movement do not always result in an eruption. Systematic measurement of deformation over volcanoes should help clarify why and will provide a better understanding of when a volcano may erupt. Similarly, many landslides move intermittently and may have periods of increased rates of slow-sliding before catastrophic runout. NISAR will enable detection and inventory of slow-moving and deep-seated landslides, enabling better understanding of variations in movement and how mass movement is triggered.

2.2 ECOSYSTEMS: BIOMASS, DISTURBANCE, INUNDATION, AND AGRICULTURE

In recent decades, the world has been experiencing unprecedented environmental changes that are manifested through intensifying events such as floods, droughts, wildfires, hurricanes, tornadoes, and insect infestations. Due to an increase of population density, especially in vulnerable regions such as coastal zones and the tropics, the effect of these changes have significant human and economic costs that are important to assess in near real-time while the events are occurring. Through a changing population, these impacts are also putting pressure on our landscapes and ecosystems that generate food, energy, and living spaces. For these reasons it is important to quantify such events and their impacts over both the short- and long-term (Figure 2-2).

Because of its ability to collect data at both night and day, and under most weather conditions, NISAR radar data will be a critical tool for addressing the problems mentioned above as well as other ecosystems-related priorities such as better quantifying the structure of forests, their condition and extent, their functioning as carbon sources and sinks, and to characterize and quantify changes resulting from disturbance and recovery, to name a few.

For the disciplines that study ecosystems, and the broader scientific community, NISAR will help address questions as diverse as:

- How do land use and environmental changes in forests, wetlands, and agricultural regions affect the carbon cycle and species habitats?
- How are forest-held Biomass and Carbon stocks spatially distributed throughout the globe?
- How are changes in the growing season affecting patterns of vegetation biomass, both spatially and temporally, across boreal ecosystems?
- How are the disturbance effects of fire, flooding, and deforestation affecting the functions of ecosystems, their services to human populations, the biome, and biodiversity?
- Are the frequency and severity of ecosystem disturbances changing over time?
- For inland and coastal wetlands, what are the seasonality and geographic extent of their hydrologic cycles and how are these changing with time?
- What is the portion and location of land surfaces that are being used to generate agricultural crops, and how are these changing as a function of weather, drought/floods, and farming practices?

Through NISAR's dual-polarized and radiometrically terrain-corrected (RTC) products that will cover the majority of the Earth's land surfaces at least two times every twelve days (once on ascending and once on descending passes of the satellite's orbit), the mission is uniquely able to image the landscape through its use of radio waves that penetrate into the forest canopy and scatter from large woody components (stems and branches). This will provide new and complementary information about forest structure compared to those typically derived from optical

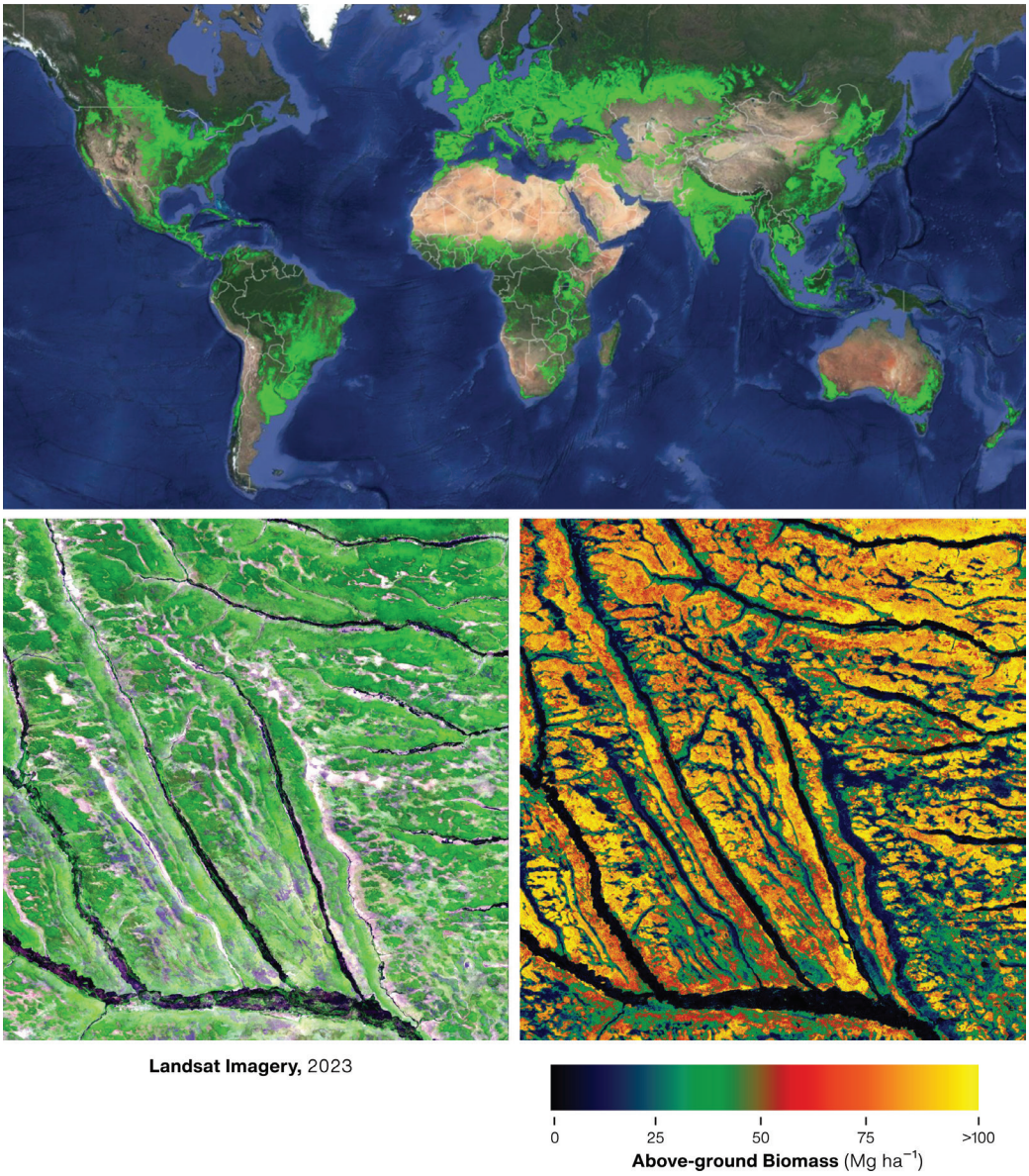

FIGURE 2-2

(Top) Global crop area estimate (in green) from 2017 in a nominal 30 m resolution primarily from Landsat imagery. Sourced from USGS. (Bottom) Spatial variation of vegetation cover and above-ground biomass (AGB) in Miombo Woodlands of Central Angola, Africa. The left panel shows Landsat imagery, whereas the right panel illustrates estimated above-ground biomass derived from the Japanese Aerospace Exploration Agency's (JAXA's) ALOS/PALSAR satellite in 2023. ALOS/PALSAR was used here to simulate similar imagery as will be made available on a regular basis from NISAR.

satellite imagery. These woody components constitute the bulk of the dry biomass of forests and where carbon is stored from the canopy's exchange of oxygen for carbon dioxide with the atmosphere.

Through its frequent revisits and reliability of observations through most weather conditions, NISAR will assess vegetation biomass over low to moderate levels; will monitor and identify changes of forest structure and biomass from disturbances such as fire, logging, or deforestation; and will characterize the recovery of these resources after disturbances.

Such changes and degradation of terrestrial ecosystems are leading to steep reductions in biodiversity. Additionally, quantitative understanding of the role of terrestrial ecosystems in atmospheric carbon dioxide absorption is limited by large uncertainties in two areas:

- estimates of current carbon storage in above-ground forest biomass, and

- large uncertainties in the quantity of biomass change over time.

From 1990 to 2000, the global area of temperate forest increased by almost 3 million hectares per year, while deforestation in the tropics occurred at an average rate exceeding 12 million hectares per year. Uncertainty in the change of biomass is greatest in the tropics and considered more uncertain than changes in forested areas (Millennium Ecosystem Assessment Synthesis Report, 2005). The distinction between biomass and forested area is important because biomass tends to be more indicative of essential forest characteristics such as their age and their ability to support diverse habitats for flora and fauna. Examples, such as shown in bottom half of Figure 2-2, illustrate the complementary information derived from SAR, which can better estimate the quantity of biomass stored in forest ecosystems.

In addition to the topics of forest and forest disturbance, wetland ecosystems exert major impacts on global biogeochemistry, hydrology, and biological diversity. The extent and variation of seasonally inundated wetland areas play key roles in ecosystem dynamics. Wetlands contribute approximately one-fourth of the total methane annually emitted to the atmosphere and are identified as the primary contributor to interannual variations in the growth rate of atmospheric methane concentrations. NISAR will make it possible to map such wetlands and to capture their dynamics through the season, even penetrating through the forest canopy and mapping those areas where the forest and soils have adapted to the presence of standing water. Through these observations, NISAR will contribute to our understanding of the extent and duration of such flooding and hence better quantify the amount and timing of methane production in these natural regions.

Changes in climatic patterns are projected to have a pronounced effect on global wetlands through alterations in hydrologic regimes. In turn, climate-driven and anthropogenic alterations to tropical and boreal peatlands have the potential to create significant feedback to the climate through the release of large pools of soil carbon and effects on the generation of methane. With its ability to penetrate through clouds and tree canopies, NISAR data will be able to resolve the inundation extent and dynamics of wetlands globally with high temporal and spatial resolution and hence be able to better characterize these peatlands and how they are evolving over time. Such observations will be important for identifying these regions and provide policymakers information needed for protecting their vital role in ecosystem function.

Lastly, agricultural regions, known as managed ecosystems, will benefit from the NISAR mission. Environmental and ecological changes over time will affect agricultural supplies, practices, and food security that support a global population of more than 8 billion.

As a matter of policy, national and international organizations work to monitor trends and conditions of agriculture on a timely basis to better guide policy and decision-making and address food supply issues that may threaten large populations. Because of the variable nature of planting, water supplies, and harvesting practices, such efforts are work-power intensive and time-consuming. NISAR's high resolution, frequent revisit, and robustness to weather conditions will complement these approaches and provide geospatial information that will enhance accuracy and provide means for improving the global food supply.

Although it is difficult to predict all of the ways in which the science community will incorporate NISAR data into enhancing our understanding of natural environments, these are just a few examples of how the mission will serve the ecosystems community. This will be made possible in part by NISAR's ability to provide dependable observations throughout the year, at repeat periods and spatial resolutions that are on par with those characteristics that drive biomass, disturbance, agriculture, inundation, and other foundational components of ecosystems.

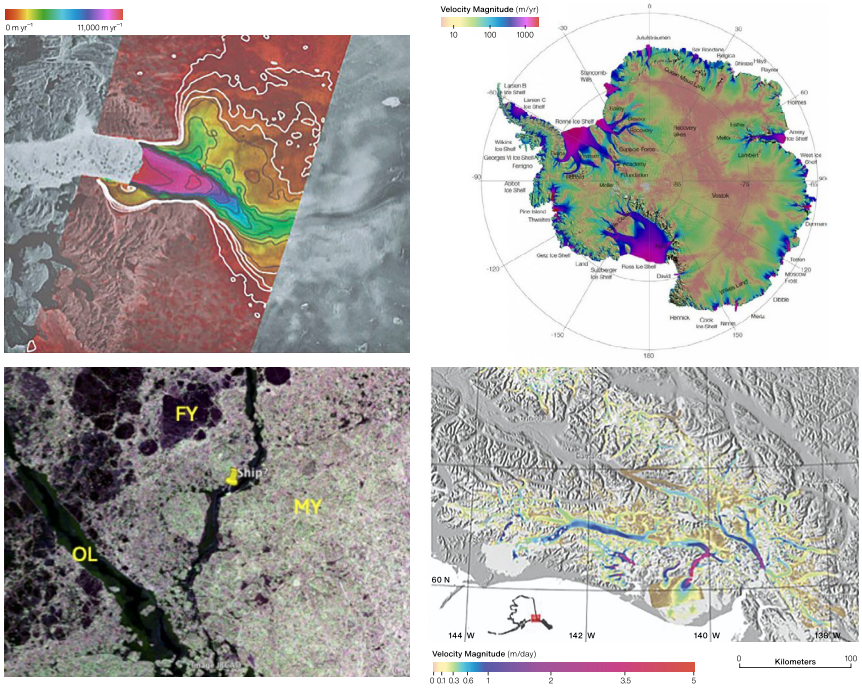

FIGURE 2-3

NISAR will measure changes in glacier and ice sheet motion, sea ice, and mountain glaciers to determine how global climate and ice masses interrelate and how melting of land ice raises sea level. (Top left) Canadian RADARSAT mission shows the rapid speedup of Jakobshavn Isbrae in Greenland between February 1992 and October 2000 (Joughin et al. 2004a). (Top right) Ice flow of the Antarctic ice sheet from ALOS PALSAR, Envisat ASAR, RADARSAT-2, and ERS-1/2 satellite radar interferometry (Rignot et al. 2011a). (Bottom left) UAVSAR L-band sea ice image, which includes old ice (MY), first year ice (FY), and an open lead (OL). (Bottom right) Surface velocity map for the Wrangell-St. Elias Mountains, the Chugach Mountains / Kenai Peninsula, the Alaska Range, and the Tordrillo Range using L-band radar (Burgess et al. 2013).

2.3 DYNAMICS OF ICE: ICE SHEETS, GLACIERS, AND SEA ICE

NISAR will address how glaciers and ice sheets interrelate with global climate and sea level (Figure 2-3). Ice sheets and glaciers are the largest contributors to sea level rise with a potential to raise sea level by several tens of centimeters to more than a meter in the coming century. Over the satellite period of observations, Arctic sea ice has thinned, shifted from a predominately perennial to seasonal ice cover, and reduced in extent at the end of summer by nearly 30 percent. In the Antarctic, the sea ice cover has been reduced by a similar 30%, primarily in recent years. Collectively, these effects mean that despite their remote location, changes in ice have global economic and health implications in a changing climate. The 2018 Decadal Survey prioritizes observations in "understanding glacier and ice sheet contributions to rates of sea-level rise and how likely they are to impact sea-level rise in the future." It asks, "How much will sea level rise, globally and regionally, over the next decade and beyond, and what will be the role of ice sheets and ocean heat storage?" NISAR will address the following related questions:

- Will there be catastrophic collapse of the major ice sheets, including Greenland and West Antarctic and, if so, how rapidly will this change occur?
- What will be the resulting time patterns of sea-level rise at the global and regional level?
- How are mountain glaciers and ice caps worldwide changing in relation to climate, and what is their impact on sea level now and in the future?
- How is the sea ice motion and deformation changing in a warming polar environment?

- How rapidly will the sea ice cover in Antarctica continue to decrease or will it recover?
- How are the sea ice dynamics changing with time?

Flow rates of outlet glaciers around many parts of Greenland and Antarctica have increased significantly, more than doubling in some cases. These accelerations and increased melt rates have caused glacier and ice sheet margins to thin by up to tens of meters per year as ice is lost to the sea. Much of this ice (e.g., floating ice shelves) acts as a buttress holding back interior ice. Loss of this buttressing introduces instability of these ice sheets, which will likely lead to a more rapid rise in sea level. NISAR will provide temporally and geographically comprehensive observations to characterize and understand ice sheet and glacier dynamics. NISAR will measure velocities of the Greenland and Antarctic ice sheets through time, determine the time-varying position of the grounding line around Antarctica, and monitor the extent and stability of buttressing ice shelves.

Sea ice is another component of the Earth cryosphere system that is changing rapidly and in ways that can affect climate worldwide. Comprehensive observations of sea ice extent, motion, concentration, and thickness, derived from multiple satellite observations, including NISAR, will improve our understanding of the interactions between the ice, ocean, and atmosphere, and their future behavior. NISAR observations of ice motion over both the Arctic and Antarctic will enable a unique, comprehensive examination of the significantly different responses to climate forcing that are occurring between the two polar regions.

Mountain glaciers and ice caps are among the most important indicators of environmental change, provide freshwater resources, and contribute as much to present-day sea level rise as either ice sheet. The Himalayas is the largest and highest mountain range in the world and plays a significant role in the regional hydrological cycle and climate in central and south Asia. The Himalayan region has a unique mass-energy exchange regime that may have a serious impact on climate change. Systematic observations of snow-ice extent, surface condition, and flow will improve our understanding of the underlying processes acting on them. The NISAR radar, with its greater penetration depth, large swath, and frequently repeated observations, will enable the study of snow and the global distribution of glaciers at much improved spatio-temporal scales.

Earth is continuously readjusting to redistribution of water and ice associated with the retreat of the Pleistocene ice sheets and ongoing melting of remaining glaciers, ice caps, and ice sheets. The readjustment, also known as Gravity, Earth Rotation and viscoelastic solid-Earth Deformation (GRD), includes Glacial Isostatic Adjustment (GIA) and viscoelastic response to modern surface mass change. The resulting surface deformation has important implications for our ability to predict relative sea level rise, which captures not just sea level rise but also land elevation change occurring in response to changes in surface loading. Accurate sea level rise predictions are also tied to our understanding of the rheological structure of the mantle, with different structural models predicting different patterns of surface deformation.

2.4 APPLICATIONS

With frequent, repeated observations over hazard-prone areas, NISAR will add an extensive new dataset of surface change observations to serve the many applications that use Earth observation data (see Appendix E, Section E.4). All NISAR data products will be publicly and freely available through an easy-to-navigate web portal and NASA's standard programmatic interfaces, ensuring that the nation's investment in NISAR can be fully leveraged by a variety of agencies and individuals.

NISAR observations will deliver actionable science data products and capabilities to support a wide

range of users and decision-makers. The mission will help address critical questions such as:

- Are there any active landslides or sinkholes near critical infrastructure such as railways, pipelines, bridges, dams, roads, or buildings? If so, how fast are they moving?
- What buildings and infrastructure were damaged following a major disaster such as a hurricane, earthquake, fire, debris flow, or tornado?
- How does land subsidence or uplift, driven by groundwater withdrawal or hydrocarbon production, affect community resilience and infrastructure stability in coastal regions?
- What homes, buildings, infrastructure, and land are under water associated with floods, storm surge, or dam failures, especially when there are clouds?
- What is the extent and thickness of marine oil spills?
- How many acres of crops are present in a region, what are their soil moisture conditions, and how might these affect crop growth and seasonal production forecasts?
- What are the pre-fire conditions, such as fuel load, soil moisture, and vegetation moisture? After a fire, what is the burned area, burn severity, and risk of post-fire debris flows?
- How much biomass is contained in a forest, and how is it changing over time due to forest management, habitat shifts, pests, urban expansion, or disasters like wildfires?
- Where are sea ice patches and icebergs located, especially during the winter months?

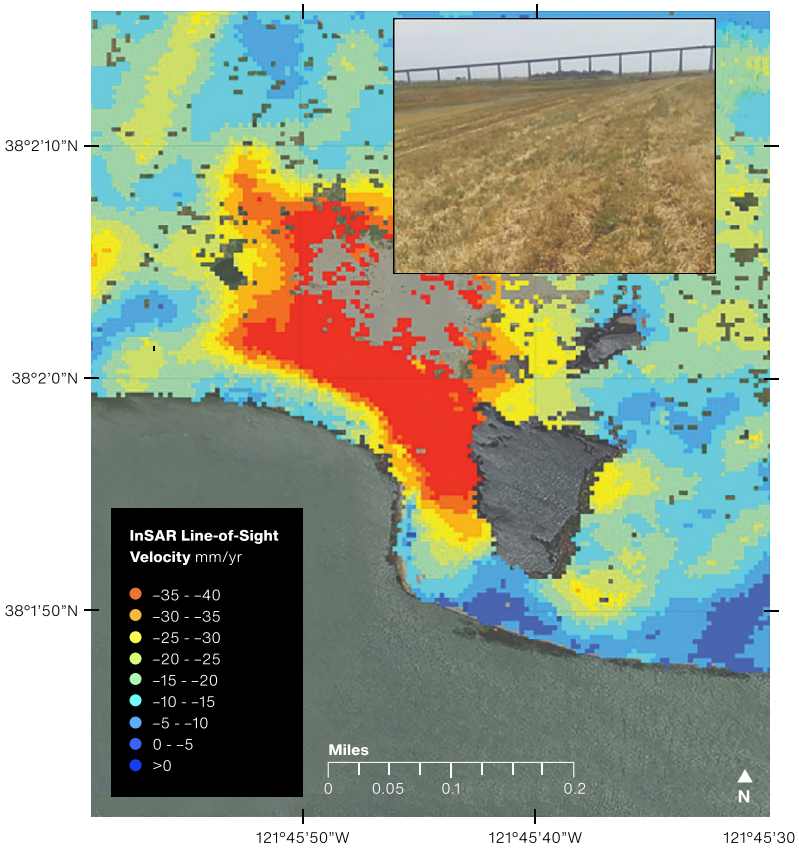

FIGURE 2-4

NISAR will measure surface changes that impact infrastructure. Shown here is ground movement along one of the levees that prevents flooding of an island in the Sacramento-San Joaquin Delta. Inset photo shows a view looking east towards the area of rapid deformation (red/orange color). The deformation signal is not obvious to the naked eye on the ground, but ground-based inspection revealed cracks in the levee. (Source: Deverel, 2016)

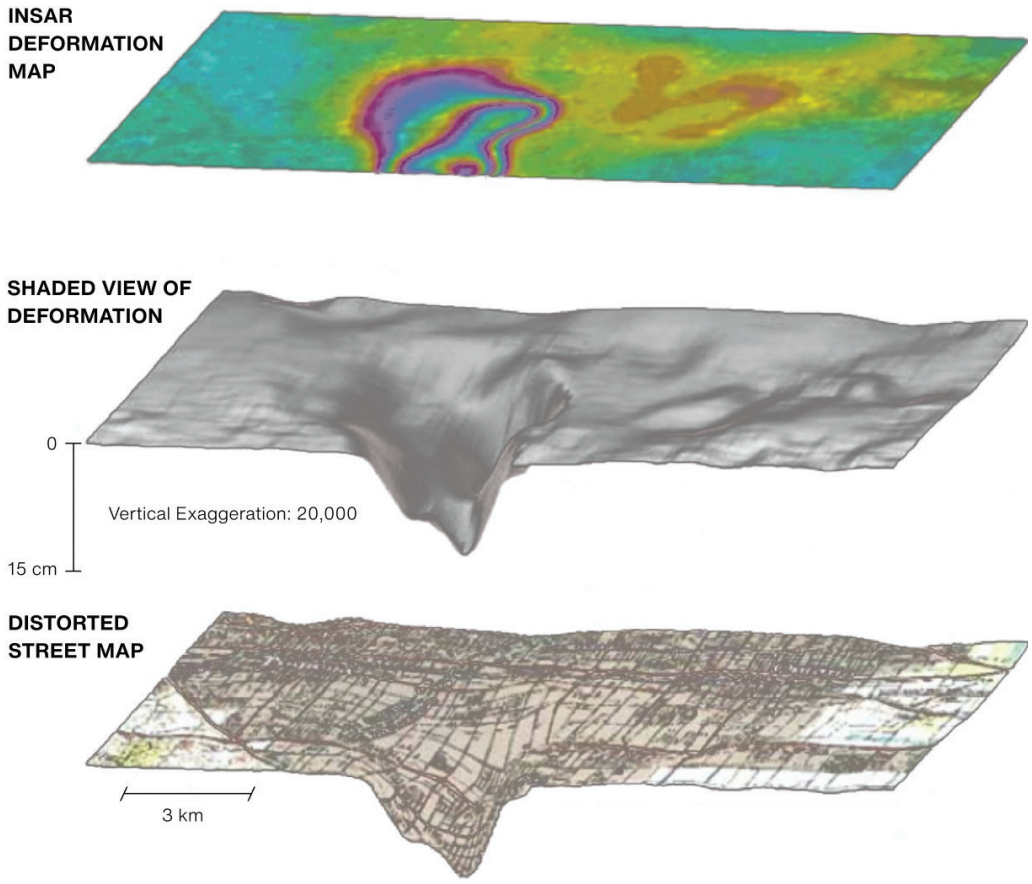

FIGURE 2-5

NISAR will measure changes in reservoirs. Shown here is subsidence due to ground water measured with the C-band ERS-1 SAR satellite northeast of Los Angeles (image created by Gilles Peltzer, JPL/UCLA).

Section E.4 provides further detail on these and other applied science topics.

NISAR will support applications across five main areas: (1) critical infrastructure monitoring (Figure 2-4); (2) assessment of anthropogenic and natural hazards such as earthquakes, volcanoes, landslides, floods, fires, and sinkholes; (3) maritime and coastal waters situational awareness (e.g., oil spills, ice detection, waves, and underwater slips — see Section 2.6); (4) ecosystem services (Appendix E); and (5) underground water, oil, and gas reservoir management (Figure 2-5; Appendix E). A major contribution of NISAR will be in urgent response, which is described in more detail in Section 2.5. NISAR will produce several low-latency data products designed to support targeted data collection during and after disasters or other impactful events, aiding response and recovery communities when timely information is critical. For less time-sensitive applications, NISAR standard products may directly meet observational needs or serve as a foundation for generating customized products. These derived products are particularly valuable for applications such as ecosystem services or hazard monitoring and mitigation efforts where latency is less critical (e.g., drought monitoring).

Over the course of the mission, NISAR will serve as a reliable source of information for monitoring surface conditions and supporting proactive planning for resource and disaster management. NISAR will be effective for detecting and tracking slow-onset disasters such as droughts and widespread crop failures, leveraging its frequent, repeated observations to detect changes over long time periods. Even subtle changes, such as slow-moving landslides or land subsidence

indicated by deformation in large structures, can become apparent in long time series. These regular observations will help establish the normal variability of surface conditions and disentangle long-term impact, e.g., from ground subsidence or slow movement associated with landslides or faults, from seasonal changes and episodic, event-induced changes (e.g., an earthquake). Knowledge of the spatial scale of change combined with information about the timescale on which the changes are occurring can provide information about the processes driving change, e.g., whether land subsidence is due to groundwater, hydrocarbon production, or natural processes that changes in resource management cannot reverse.

Surface deformation measurements relevant to solid Earth science (see Section 2.1) will be valuable for agencies monitoring geological hazards including landslides, faults, volcanoes, and sinkholes. Monitoring ground movement in hazard-prone areas can improve risk management by identifying event precursors – for example, accumulating elastic strain along a seismogenic fault, accelerated landslide motion after rainfall, or ground uplift linked to expanding magma chambers. This information is also critical for assessing movement affecting buildings, transportation networks, flood control, and water infrastructure. Critical infrastructure monitoring will be revolutionized by access to NISAR data to inform short and long term planning. The stresses induced during natural disasters can lead to failure of already-compromised structures, and a significant part of risk management involves predicting and mitigating likely structural failures during extreme events, e.g., avoiding overtopping of sea walls during king tides or earthquake-induced levee failure, by proactive maintenance, which can be guided by NISAR measurements of trends. Through the long and consistent collection of data, NISAR will be used to monitor the development of conditions/tipping points that could lead to infrastructure failure. For instance, NISAR can be used to monitor levees (Figure 2-4), dams, and aquifers that are under stress from groundwater over-utilization, and areas where fluid injection into and withdrawal from the subsurface are potentially affecting water quality or local roads and other structures.

Small surface deformation signals, such as subsidence, require long time series to accurately measure vertical land movement. Measurements sensitive to change from geologic, anthropogenic, or climate-related causes require adequate sampling to resolve temporal variation of displacements with seasonal or finer resolution. Annual cycles result from water withdrawal and recharge in aquifer systems (Figure 2-5), or from natural patterns, such as the freezing and thawing of the active layer overlying permafrost in the Arctic and sub-Arctic regions. Human-induced deformations from activities like oil and gas extraction or infrastructure degradation can occur on various timescales, demanding high temporal and vertical resolution for differentiation. Human-induced deformations, such as those caused by oil and gas mining or degradation of transportation infrastructure, can occur over many different time scales, and their identification and differentiation require resolving processes at much better than the annual time scale. A key example is the measurement of surface displacement above hydrologic aquifers, where it is necessary to separate the inelastic subsidence that permanently reduces the storage capacity of an aquifer from the annual subsidence and inflation due to water use patterns. Since proper management of the aquifer system depends on maintaining the long-term storage of the system, NISAR must be able to distinguish among these components. A similar statement applies to permafrost-induced degradation of roads or other structures, where long-term subsidence trends relating to permafrost decay need to be separated from quasi-seasonal deformation signals caused by the freeze-thaw cycle of the overlying active layer (Liu et al. 2010, 2012). In both examples, the measurements are similar to those needed to determine secular velocities along tectonic boundaries, except that the horizontal component of displacement is

small and therefore the emphasis needs to be on accurate determination of the vertical component with sufficiently high resolution to pinpoint critical areas most heavily impacted in order to allocate resources for targeted remediation.

The NISAR program has developed a Utilization Plan outlining how the mission will engage with the end user community to advance the use of its data for practical applications (https://nisar.jpl.nasa.gov/system/documents/files/31_NISAR_Utilization_Plan.pdf). There are also a series of white papers highlighting individual applications (https://nisar.jpl.nasa.gov/applications/societal-benefit/). Those topics, among others, are included in Appendix E, Section E.4.

2.5 DISASTER RESPONSE

Natural disasters, like floods and earthquakes, cause thousands of fatalities and cost billions annually. Nearly ten percent of the world's population lives in low-lying coastal areas subject to flooding. Large earthquakes can cause damage hundreds of kilometers from their epicenter, impacting a wide area. Volcanic eruptions destroy cities and towns, eject ash clouds that disrupt air travel, and impact regional agriculture. Today, the economic and human impacts are growing as population pressure drives development in high-risk areas and as climate change increases the intensity and frequency of severe weather events.

NISAR's systematic collection of SAR data over nearly all land and ice regions globally ensures that data will be available to support urgent response, recovery, and research efforts for most disasters. NISAR acquires dual polarization L-band data over nearly all land surfaces across the globe, supplemented with S-band data over India's areas of interest and several sites globally intended for multi-frequency studies. In addition, L-band images are acquired routinely over the Gulf Coast, Caribbean Sea, and most coastal U.S. waters to approximately 665 km offshore of CONUS and Hawaii. These acquisitions, combined with specific requests for data in other areas not regularly imaged, will support emergency response, meeting a mission goal of NISAR. In this way, the mission provides tangible support to society beyond the science value provided by better understanding of the processes involved, which can also lead to better forecasting and risk assessment.

NISAR has a requirement to deliver data for urgent response on a best effort basis. Following a disaster or in anticipation of a forecasted event, NISAR can be tasked for high priority data acquisition, downlink, and processing to provide low latency information to support urgent response. All new acquisitions that are tagged as needed for disaster response are processed with low latency and delivered to a special archive where they can be easily accessed and downlinked. There is the unavoidable delay between when a disaster occurs and the next imaging opportunity, so NISAR will add to the set of Earth observing instruments in space that can respond to disasters, shortening overall the time to data delivery. Appendix E, Section E.4, provides information on the many types of disasters to which NISAR can contribute significant response information. Nearly the full range of disasters can be addressed, from floods to fires to earthquakes, volcanos, landslides, and even oil spills and dam collapse.

Disasters like floods, forest fires, and coastal and oceanic oil spills can be monitored using radar images that are provided by NISAR. Other disasters result directly in ground movement, such as ground rupture during an earthquake. In these cases, deformation measurements of the disaster area can dramatically improve determination of the scope of the event, leading to better assessment for targeting response assets and more efficient recovery. Furthermore, the same data used to monitor ground deformation in disaster-prone regions can be used to detect large-scale surface disruption, which can be used to develop synoptic high-resolution damage proxy maps. In addition to identifying ground and structures disruption, damage proxy maps can identify flood extent. These maps aid emergency natural disaster

response throughout the globe regardless of the level of local infrastructure, so that the response coordinators can determine from afar where to send responders within the disaster zone.

2.6 OCEAN STUDIES AND COASTAL PROCESSES

As mentioned in Section 2.5, NISAR acquires L-band data over extensive areas of U.S. coastal waters including Hawaii and extending into the Caribbean Sea. In addition, both L-SAR and S-SAR acquire data over areas of interest to India, primarily in and around India and in the Arctic and Antarctic. The NISAR L-band and S-band radar suite will be sensitive to the ocean roughness with wide dynamic range, enabling studies of air-sea interaction including winds, both surface and internal waves, and circulation features including current fronts, eddies, and upwelling zones. Also, NISAR at L-band will image most water at the land-sea coastal interface globally because the radar will be turned on prior to reaching land. These nearshore coastal areas are of key interest for studies of marine pollution and water quality including river discharge, coastal shipping, shallow bathymetry, and coastline impact including from storms and flooding. Repeated and regular measurement of surface wind speed will enable mapping of wind speed patterns over time, an important factor in the siting of offshore wind power turbines. In addition, the high target-to-background contrast at L-band will help identify oil slicks and ships in the open as well as coastal ocean.

One of the focus areas for NISAR data will be the study of coastal processes, made possible by coastal ocean data acquired along many coastlines globally and the extensive data collected of waters in proximity to the USA and India. A large percentage of the world's population resides near the coasts and derives their livelihood from the coastal regions, and this is particularly true in India and southeast Asia. Coastal regions, being at the confluence of land, sea, and atmosphere, are subjected to various natural forces and processes resulting in erosion of and deposition at the coasts. To understand the nature and magnitude of coastal processes, periodic mapping and monitoring of coastal erosional and depositional landform features, shoreline changes, and coastal habitats are required. SAR has been proven to be a useful tool for mapping and monitoring of coastal areas due to its sensitivity to landform structures, moisture content, and high land-water contrast. NISAR will provide a unique opportunity to study coastal

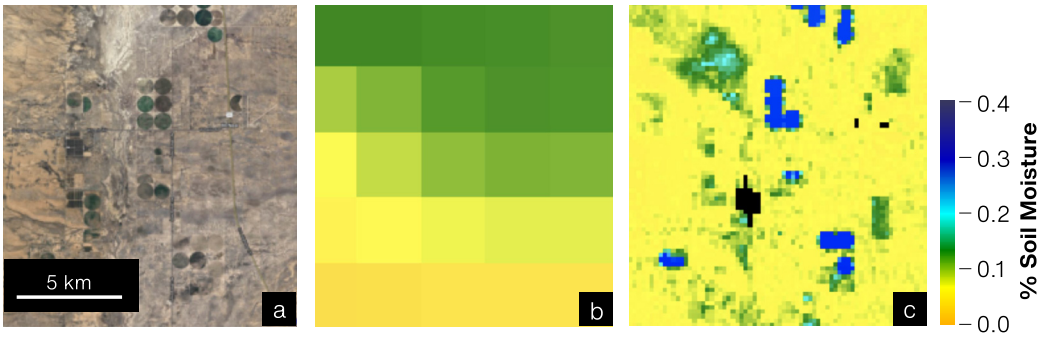

FIGURE 2-6

NISAR soil moisture product example based on NISAR-simulated data derived from ALOS-2 PALSAR-2 data acquired on July 13, 2022, over a region in southeastern Arizona. (a) Optical imagery, (b) interpolated ECMWF soil moisture model, and (c) NISAR retrieval example over same spatial extent.

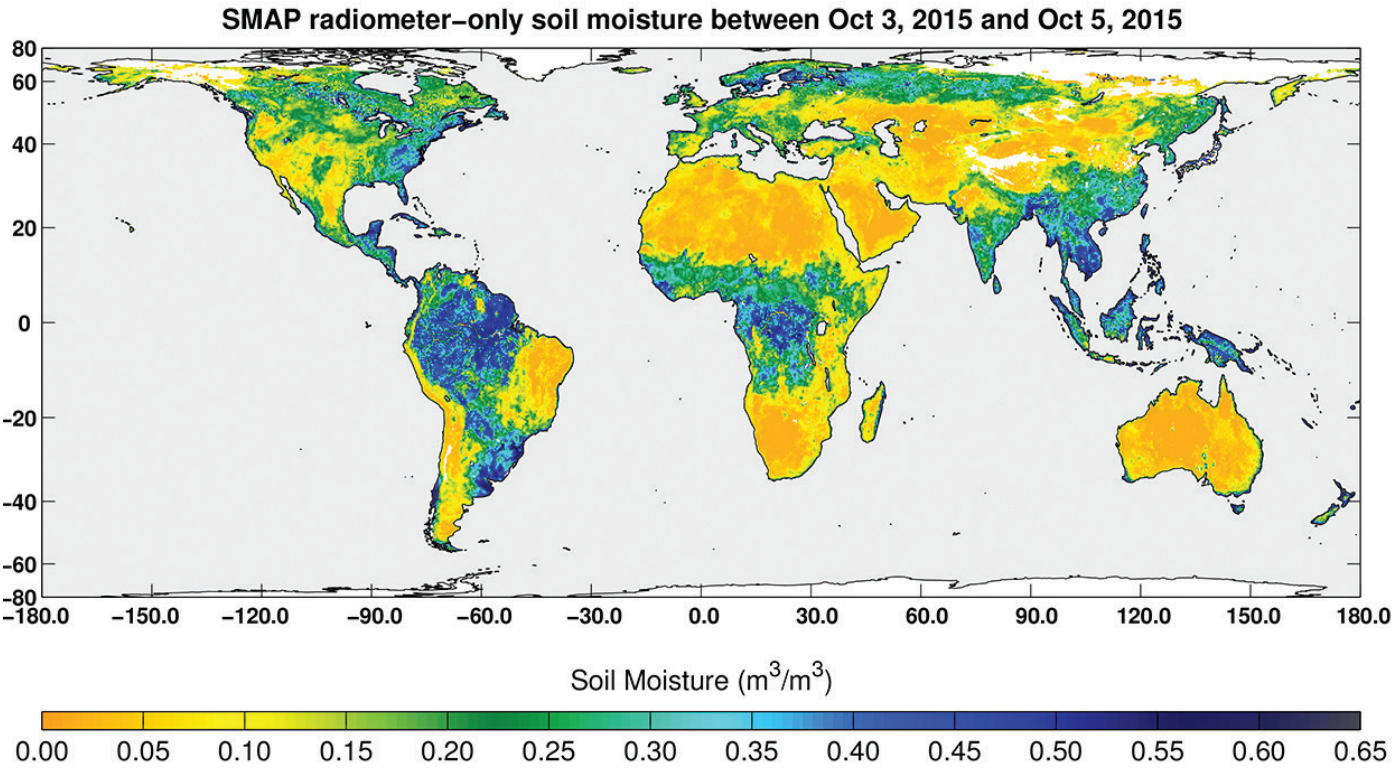

features and map shoreline changes through high repeat cycle, synoptic coverage of coastal areas. The Indian data are important for ISRO to address the following specific questions:

- How are Indian coastlines changing?
- What is the shallow bathymetry around India?
- What is the variation of winds in India's coastal waters?

2.7 SOIL MOISTURE

The distribution of soil moisture across the Earth drives a wide range of processes, including variations in the availability of water in agricultural regions, inputs to fluvial systems, and the exchange of water and heat energy between the land surface and the atmosphere. Information about soil moisture information is an important input for reservoir management, drought prediction, decisions about irrigation, and forecasting of crop yields.

NISAR will provide soil moisture estimates over all land areas not covered in ice, snow, or urban development, with a target unbiased root mean squared error (ubRMSE) of 6%, except for in regions characterized by high relief or dense vegetation (e.g., forests). The NISAR soil moisture product (Figure 2-6) will be generated with a 200-m resolution over most areas (400-m in the Sahara), which is a significantly finer resolution than is available from most other satellite-based soil moisture retrievals, such as from NASA's Soil Moisture Active Passive (SMAP) mission (Figure 2-7). This higher resolution will allow for more meaningful interpretation of soil moisture dynamics in areas with heterogeneous land cover and land use, where soil moisture can vary substantially over the scale of individual agricultural fields.

FIGURE 2-7

Global map of surface soil moisture estimated by the L-band radiometer onboard NASA's SMAP satellite for October 3–5, 2015. NISAR will produce a similar soil moisture product but at enhanced spatial resolution to allow soil moisture mapping at field-scale. Credit: NASA/JPL.

Credit: zlikovec/Shutterstock.

3 MISSION MEASUREMENTS AND REQUIREMENTS

NISAR will utilize the techniques of synthetic aperture radar interferometry and radar polarimetry to measure surface deformation and change of the solid Earth, cryosphere, and ecosystems. For a brief introduction to basic radar concepts, including radar imaging (SAR), polarimetry, and interferometry, refer to Appendix C. There are also a wide variety of resources available to learn more about the technology and techniques of NISAR. Here are some examples:

- https://appliedsciences.nasa.gov/what-we-do/capacity-building/arset
- https://eo-college.org/
- https://www.earthscope.org/education/skill-building-learning/courses/
- https://asf.alaska.edu/training-resources/

3.1 MEASUREMENTS OF SURFACE DEFORMATION AND CHANGE

The technique of Interferometric Synthetic Aperture Radar (InSAR) uses coherent processing of radar signals collected over the same scene at two different times to derive surface deformation from the change in the relative phase of the two returns (Figure 3-1; Rosen et al., 2000; Hanssen, 2001). The radar instruments on NISAR will

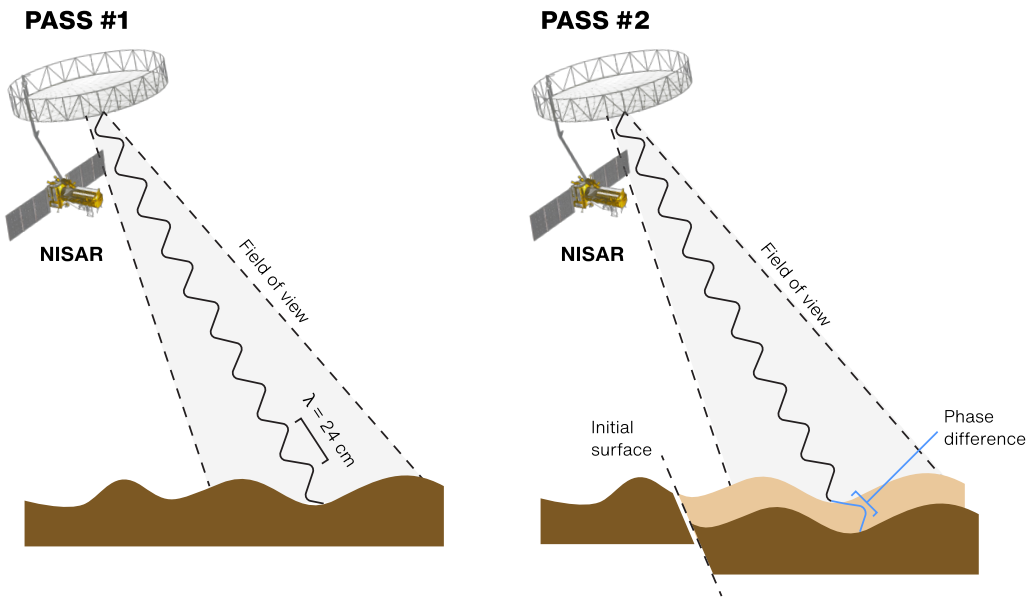

FIGURE 3-1

InSAR measures surface deformation by measuring the difference in the phase of the radar wave between the two passes if a point on the ground moves and the spacecraft is in the same position for both passes (zero baseline). InSAR deformation geometry is demonstrated in these figures. On Pass #1 (left), a surface of interest is imaged and the radar satellite measures the phase $\phi 1$ (x,y) between the satellite and the ground along the line-of-sight (LOS) direction. Later at Pass #2 (right), the satellite makes another measurement $\phi 2$ (x,y) between the satellite and the ground. If the ground moves between passes, the phase difference $\Delta\phi$ (x,y) is proportional to the ground deformation between passes along the LOS direction.

operate as repeat-pass InSAR to measure surface deformation of land and ice-covered surfaces. An InSAR satellite passing over a location before and after an event, such as an earthquake, tectonic deformation, volcanic inflation or ice sheet motion, at exactly the same point in inertial space (zero baseline), measures how the ground shifts between passes, via a radar interferogram. This is the product of the first image with the complex conjugate of the second. The interferogram measures the difference in phase of the radar wave between two passes, which is sensitive to ground motion directed along the radar line of sight (LOS). An InSAR image of the point-by-point phase difference of the wave on the surface is used to create a map of the movement of the surface over time. In this way, ground deformation along the LOS direction on the scale of a fraction of the radar wavelength can be resolved as long as the phase coherence between the signals is maintained (Zebker and Goldstein, 1986; Gabriel et al., 1989). The radar instrument can take observations through cloud cover, without sunlight, and can measure sub-centimeter changes.

3.2 LAND COVER AND FOREST CHARACTERIZATION WITH L-BAND SAR

NISAR will serve to estimate above-ground biomass, identify croplands and inundated extent, and detect forest disturbances. The overall ecosystem science community will greatly benefit from the mission, which is characterized by high frequency revisit time of 12 days and L-band capabilities. By their fundamental nature, ecosystems are driven by hydrologic and seasonal cycles, and hence undergo dynamic changes throughout the year. When combined with the need for monitoring changes in these systems, through fire, drought, encroachment, deforestation, or otherwise, it is important to detect and demarcate these regions in order to provide quantitative measures of inventory and change that affect the many services that ecosystems offer to populations worldwide. NISAR's dynamic observations and compilation of a new historical record will provide an important resource throughout the mission's lifetime and beyond.

Among the important features of the mission characteristics are its wide swath, high resolution, 12-day repeat orbit cycle and dual-frequency (L- and S-band) capability. These features will allow the mission to provide meaningful observations for a broad diversity of ecosystems with a timely revisit period. With a resource such as NISAR, and distributed under NASA's open data policy, the NISAR mission will support improved management of resources and understanding of ecosystem processes.

Changes in forest structure observed by NISAR, whether due to natural cycles, or human or natural disturbances, will provide critical measurements for assessing the role of forests and their feedback within the global carbon cycle. The NISAR mission will resolve the severity and timing of disturbances at a spatial resolution of 1 hectare and a temporal resolution of 12 days. This rapid revisit capability will also enable timely monitoring of cropland status, soil moisture conditions, and the extent of flooding and inundation.

In addition to the basic resource of measuring radar reflectivity, the NISAR mission has a number of other capabilities that will be useful for the ecosystems discipline. Among these features are the capabilities of performing repeat-pass interferometry and collecting polarimetric data. While the core capability of the payload is the L-band SAR used to meet all of NASA science requirements, a secondary S-band SAR, built by ISRO, will provide opportunities in collecting dual-frequency observations over key sites in India and others that are distributed globally. The mission itself includes a large diameter (12 m) deployable reflector and a dual frequency antenna feed to implement the SweepSAR wide-swath mapping system, which is the enabling technology to allow for global mapping, fast revisit, frequent temporal sampling, and full resolution. The polarimetric capability of the NISAR system provides dual-

polarized (dual-pol) global observations for every cycle and the potential for quad-pol observations in India and the U.S. The dual-pol system is based on transmitting horizontally or vertically polarized waveforms and receiving signals in both polarizations. Over land surfaces, the transmit polarization will principally be horizontally polarized, and receive will be over both vertical and horizontal polarizations, resulting in polarization combinations known as HH and HV to describe the configuration.

NISAR polarization configurations will enable accurate estimation of vegetation above-ground biomass up to 100 t/ha. In polarimetric backscatter measurements, forest components (stems, branches, and leaves) are scatterers within the footprint of the radar beam that interact with the incoming waves. The size (volume), dielectric constant (moisture or wood density), and orientation and morphology of the scatterers determine the magnitude and polarization of the reflected waves. As a result, the backscatter radar energy at linear polarizations is a function of the forest volume and biomass. The shape of this function depends on the wavelength, polarization, forest type, and moisture conditions. The relationship varies with vegetation type and environmental conditions (e.g., soil moisture and roughness), but with multiple polarizations and repeated measurements, the biomass can be determined with high accuracy.

For a limited set of targets, the NISAR mission will make fully polarimetric measurements (i.e., quad-pol) by alternating between transmitting H-, and V-polarized waveforms and receiving both H and V (giving HH, HV, VH, VV imagery). Polarization combinations, such as dual- and quad-pol, allow for a fuller characterization of ground-targets' responses to the SAR. Variations in the polarimetric responses of targets to different combinations of polarization can be related to the physical characteristics of the target reflecting energy back to the radar, and hence can be used for classifying target type and performing quantitative estimates of the target state.

3.3 REQUIREMENTS AND SCIENCE TRACEABILITY

NASA and ISRO have developed a joint set of requirements for NISAR. These agency-level requirements are known as "Level 1" (L1) requirements and control the implementation of the mission: The NISAR mission must fulfill these requirements to be successful.[1] ISRO places additional requirements on the L-band system to acquire data over science areas of interest to India that are above and beyond the NASA requirements, including coastal bathymetry and ocean winds, geology of India, and coastal shoreline studies (Table 3-1). Unlike the NASA requirements, the quantitative values associated with these measurements are characterized as goals; it is the collection of the data toward these goals that drives the ISRO requirements. There are no explicit requirements on science measurements at S-band, just a statement identifying the impact such measurements can make, leaving open a range of options for exploring its potentials.

Table 3-1 shows an overview of the L1 baseline requirements for the mission. Baseline requirements represent the full complement of science requested by NASA of the NISAR Mission. The NISAR project teams at JPL and ISRO use the L1 requirements to develop a detailed set of Level 2 (L2) project requirements, which govern the implementation in such a way that by meeting the L2/L1 requirements, the requirements will be met. The L2 science requirements are described in Appendix D. NASA and ISRO have jointly coordinated all requirements at Level 1 and Level 2. Lower level requirements are generated by the NASA and ISRO project teams independently. The teams coordinate hardware and activities through interface documents.

[1] There is also a set of threshold requirements, which define the minimum complement of science considered to be worth the investment. Baseline requirements can be relaxed toward thresholds when implementation issues lead to loss of performance.

TABLE 3-1. LEVEL 1 BASELINE REQUIREMENTS

ATTRIBUTE	2-D Solid Earth Displacement	2-D Ice Sheet & Glacier Displacement	Sea Ice Velocity	Biomass	Disturbance	Cropland, Inundation Area
Duration	3 years	3 years	3 years	3 years	3 years	3 years
Resolution	100 m	100 m	5 km grid	100 m (1 ha)	100 m (1 ha)	100 m (1 ha)
Accuracy	3.5 $(1+L^{1/2})$ mm or better, 0.1 km < L <50 km, over 70% of areas interest	100 mm or better over 70% of fundamental sampling intervals	100 m/day or better over 70% of areas	20 Mg/ha for areas of biomass < 100 Mg/ha	80% for areas losing > 50% canopy cover	80% classification accuracy
Sampling	12 days or better, over 80% of all intervals, < 60-day gap over mission	12 days or better	3 days or better	Annual	Annual	12 days or better
Coverage	Land areas predicted to move faster than 1 mm/yr, volcanoes, reservoirs, glacial rebound, landslides	Global ice sheets and glaciers	Arctic and Antarctic sea ice	Global areas of woody biomass cover	Global areas of woody biomass cover	Global areas of crops and wetlands
Urgent	24-hour tasking 5-hour data delivery (24/5.) Best-effort basis	24/5. Best-effort basis	24/5. Best-effort basis	24/5. Best-effort basis	24/5. Best-effort basis	24/5. Best-effort basis

TABLE 3-2. ISRO S-BAND BASELINE GOALS

ATTRIBUTE	Coastal Wind Velocity	Bathymetry	Coastal Shoreline Position	Geological Features	Sea Ice Characteristics
Duration	3 years	3 years	3 years	3 years	3 years
Resolution	1 km grid	100 m grid	10 m	10 m	10 m
Accuracy	2 m/s over at least 80% of areas of interest	20 cm over at least 80% of areas of interest	5 m over at least 80% of areas of interest	N/A	N/A
Sampling	6 days or better	Every 6 months	12 days or better	90 days or better, with at least two viewing geometries	12 days or better
Coverage	Oceans within 200 km of India's coast	India's coast to an offshore distance where the depth of the ocean is 20 m or less	India's coastal shoreline	Selected regions including paleochannels in Rajasthan, lineaments and structural studies in Himalayas and in Deccan plateau	Seas surrounding India's Arctic and Antarctic polar stations

The requirement on 2-D solid Earth and ice sheet displacement covers a range of lower level requirements on the ability to measure deformation of land. The science described above for deformation relies on a time series of data acquired regularly and with fast sampling. This range of science can be specified as individual requirements on velocities or strain rates, but that would lead to a large number of L1 requirements. This requirement is written with the foreknowledge of flow-down to repeat-pass interferometry and specifies the sampling and accuracy understood to be achievable. The accuracy is controlled largely by the noise introduced by the atmosphere, which the project cannot control. The intent of this requirement is to design a system that reliably delivers regularly sampled, interferometrically viable data on ascending and descending orbit passes as needed to achieve the science at a particular target. As such, the L2 requirements may improve one aspect of the L1 requirements at the expense of another (e.g., resolution vs. accuracy).

The requirement on 2-D ice sheet and glacier displacement covers a range of lower level requirements on the ability to measure deformation of ice. It is a similar geodetic measurement as for the solid Earth requirement above, but the environment has a different influence on the ice-covered regions than land, so the L1 requirement is specified with different resolution and accuracy requirements. As with land deformation, the intent of this requirement is to design a system that reliably delivers regularly sampled interferometrically viable data on ascending and descending orbit passes as needed to achieve the science at a particular target. As with solid Earth requirements, the L1 capability as defined allows for a flow-down to a set of L2 requirements that meet the ice-sheet science objectives.

The requirement on sea ice velocity is also a deformation requirement but is called out separately because it relies on different kinds of measurements with different sampling and accuracy requirements. In this case, the intent of the requirement is to observe the poles regularly and track sea ice features in sequential radar imagery as the features move over relatively short time scales. This is a proven technique and has been shown to provide best results with frequent repeated acquisitions obtained every 2–4 days or better. To date, this type of sampling has only been obtained for the Arctic sea ice cover. NISAR will obtain this sampling for the Antarctic sea ice cover for the first time.

The requirement on biomass and disturbance states that the mission measure global biomass and its disturbance and recovery, but only specifies an accuracy for the low-density woody biomass. The global requirement on biomass and disturbance/recovery allows a specification of the details of disturbance and recovery at L2 but requires global observations at L1. Thus, in regions of high-density woody biomass, where there are no explicit accuracy requirements, measurements must be made to ensure the capture of disturbance and recovery. The requirement on cropland and inundation area is an overall classification requirement of ecosystems of particular interest to the science community. The classifications are binary (e.g., agriculture/non-agriculture, inundated/non-inundated) and are distinct from the biomass disturbance and recovery classifications in the previous requirement.

The urgent response requirement for NISAR is written to ensure that the mission has some capability for disaster response built into it, but one that does not drive the costs for development or operations. NISAR is primarily a science mission, but radar imaging systems are among the most useful space remote sensing assets for understanding disasters because they can deliver reliable imagery day or night, rain or shine, that are not obscured by smoke or fire. ISRO has identified a number of science goals that do not fall in the joint Baseline requirements as summarized in Table 3-2 and articulated above. The measurement metrics in the table are specified as goals because it is difficult to quantify how well they can be met. NISAR will collect S-band SAR data needed to support these goals.

TABLE 3-3. SCIENCE TRACEABILITY MATRIX

Science Objectives	Science Measurement Requirements		Instrument Requirements		Projected Performance	Mission Requirements (Top Level)
	Physical Parameters (Spatial and Temporal)	Observables				
Determine the contribution of Earth's biomass to the global carbon budget	Annual biomass at 100 m resolution and 20% accuracy for biomass less than 100 Mg/ha	Radar reflectivity radiometrically accurate to 0.5 dB	Frequency	L-band	1215–1300 MHz	Seasonal global coverage per science target mask 6 samples per season Ascending/descending Maximum incidence angle diversity 3-year mission
			Polarization	Dual-pol	Quad-pol	
			Resolution	5 m range	3-m range 8-m azimuth	
			Geolocation accuracy	1 m	0.5 m	
			Swath-Averaged Co-pol Radiometric Accuracy	0.9dB	0.07 dB	
	Annual disturbance/ recovery at 100 m resolution		Swath-Averaged Co-pol Radiometric Accuracy	1.2 dB	1.2 dB	
			Range ambiguities	–15 dB	–18 dB	
			Azimuth ambiguities	–15 dB	–20 dB dual-pol	
			ISLR	–15 dB	–20 dB dual-pol	
			Noise equivalent σ^0	–23 dB	–23 dB	
			Access	Global	Global	
Determine the causes and consequences of changes of Earth's surface and interior **Determine how climate and ice masses interrelate and raise sea level**	Surface displacements to 20 mm over 12 days	Radar group and phase delay differences on 12 day centers	Frequency	L-band	1215–1300 MHz	Every cycle sampling Ascending/descending Global coverage per science target mask Non-tidal cycle repeat Reconfigurable Left/viewing for Antarctic/ Arctic coverage Orbit repeatability to <500
			Polarization	Single-pol	Quad-pol	
			Resolution	4-m range 10-m azimuth	3-m range 8-m azimuth	
			Repeat interval (d)	12 days or less	12 days	
			Swath width	238 km	240 km	
			Incidence angle range	33–46 degrees for d=12	32–47 degrees	
			Pointing control	273 arcsec	273 arcsec	
	Surface displacements to 100 m over 3 days	Radar group delay differences on 3-day centers	Repeat interval (d)	12 days or less	12 days	Every opportunity sampling Complete sea-ice coverage
			Swath width	240 km	242 km	
Respond to hazards	Hazard-dependent imaging	Radar imagery	Any of above			Re-target hazard area to previously acquired mode within 24 hours Deliver data after acquisition within 5 hours

TABLE 3-4. OVERVIEW OF KEY AND DRIVING REQUIREMENTS

Key & Driving Requirement	Why Is It Challenging?	Why Is It Needed?
Interferometry capability between any two repeated acquisitions	Interferometry requires that the spacecraft be (a) controlled in its orbit to better than 350 m positioning throughout the mission and (b) controlled in its pointing to a small fraction of a degree	Interferometry is needed to obtain geodetic measurements at the required spatial sampling
Fast sampling (6 days) and interferometric revisit (12 days) over all Earth's land surfaces	Implies that the accessible field-of-regard of the instrument covers the > 240-km ground track spacing	Fast sampling is required to observe Earth's most dynamic and poorly understood processes without aliasing. The repeat period chosen for NISAR is a balance between covering interesting and practical regions (from an observation planning point of view)
Frequent sampling over most of Earth's surface	Given the multiplicity of disciplines, the only way to acquire sufficient data to meet coverage and accuracy requirements is for the radar to have a field of view equal to its field of regard (> 240 km). This requires specialized hardware to create an extra-wide swath at full resolution SweepSAR	In addition to fast sampling, many samples are needed throughout the mission to defeat the noise sources that limit accuracy. To first order, more data are needed to average errors down to an acceptable level
Polarimetry	Polarimetry requires additional hardware, mass, and power resources, adding to complexity and cost	Classification of surfaces and estimation of biomass cannot be done at the required accuracies without a polarimetric capability
Signal-to-noise ratio	The mission must be designed with sufficient power and antenna gain to observe dim targets adequately	Many of Earth's surface types are poor reflectors. When reflection is low, the noise dominates the measurement and leads to less accurate results
Radiometric predictability over time	Knowledge of the signal level enables quantitative associations to be made between radar signals and geophysical parameters. This drives design of structure stiffness and electrical tolerances in the radar	Knowing the signal level is important to the absolute radar cross-section measurements used to derive biomass and classifications

3.4 SCIENCE TRACEABILITY TO MISSION REQUIREMENTS

The Science Traceability Matrix (STM) connects the science requirements to instrument and mission requirements (Table 3-3). Due to the breadth of the science goals for NISAR, and the interplay between instrument and mission operations scenarios to meet the science goals as just described, it is difficult to capture traceability in a way that the sensitivities of science requirements to mission capabilities, and vice versa, is transparent.

All disciplines – solid Earth, cryosphere, and ecosystems – require long wavelengths. For ecosystems, long wavelengths are needed to maximize the sensitivity to biomass variability. For solid Earth and cryospheric deformation, long wavelengths are preferred to minimize the effects of temporal change of the surface; it takes a larger change of the surface to create significant decorrelation when the wavelength is long.

All disciplines benefit from polarimetry – while ecosystems demand polarimetry to meet their objectives, deformation science can

take advantage of polarimetry to characterize environmental effects, like soil moisture variations, and potentially optimize correlation in vegetated regions.

All disciplines are interested in mapping dynamic processes – ones that can change from week to week, or instantaneously, such as when a storm front hits, a glacier surges, or an earthquake strikes. In that sense, all disciplines are interested in regular sampling with the fastest revisit time achievable given the constraints of the project.

All disciplines also require global reach so that entire systems can be characterized, e.g., all of Amazonia, all of Greenland and Antarctica, or all of the "ring of fire." For global access and fast revisit, a wide-swath or steerable mapping system is required.

All disciplines also require many samples in time (i.e., every cycle) to reduce noise sources associated with environmental variability (e.g., soil moisture changes) so a solely steerable mapping system generally will not suffice. A wide-swath mapping system such as ScanSAR (Moore et al., 1981) or SweepSAR (Freeman et al., 2009) is required for global access, fast revisit, and frequent temporal sampling.

All disciplines require spatial averaging of intrinsic resolution SAR or InSAR data (looks) to reduce speckle and other local noise effects. To meet the demanding accuracy requirements described here, the system must have fine resolution in both image dimensions to create sufficient looks to average. A ScanSAR system that has reduced resolution in the along-track dimension will not suffice, particularly given the limited allowable range resolution at L-band. Therefore, a SweepSAR wide-swath mapping system, which allows wide swath while maintaining resolution in the alongtrack dimension, is required for global access, fast revisit, frequent temporal sampling, and full resolution. SweepSAR is explained in greater detail in Section 4.7.

At this highest level, the system described in the next section is necessary to meet the objectives of all disciplines. The general observational characteristics – wide swath, fast repeat, fine resolution, and multiple polarizations – represent the most basic flow-down from science requirements to mission and instrument requirements. Table 3-4 summarizes the key and driving requirements on the mission system to satisfy the science requirements.

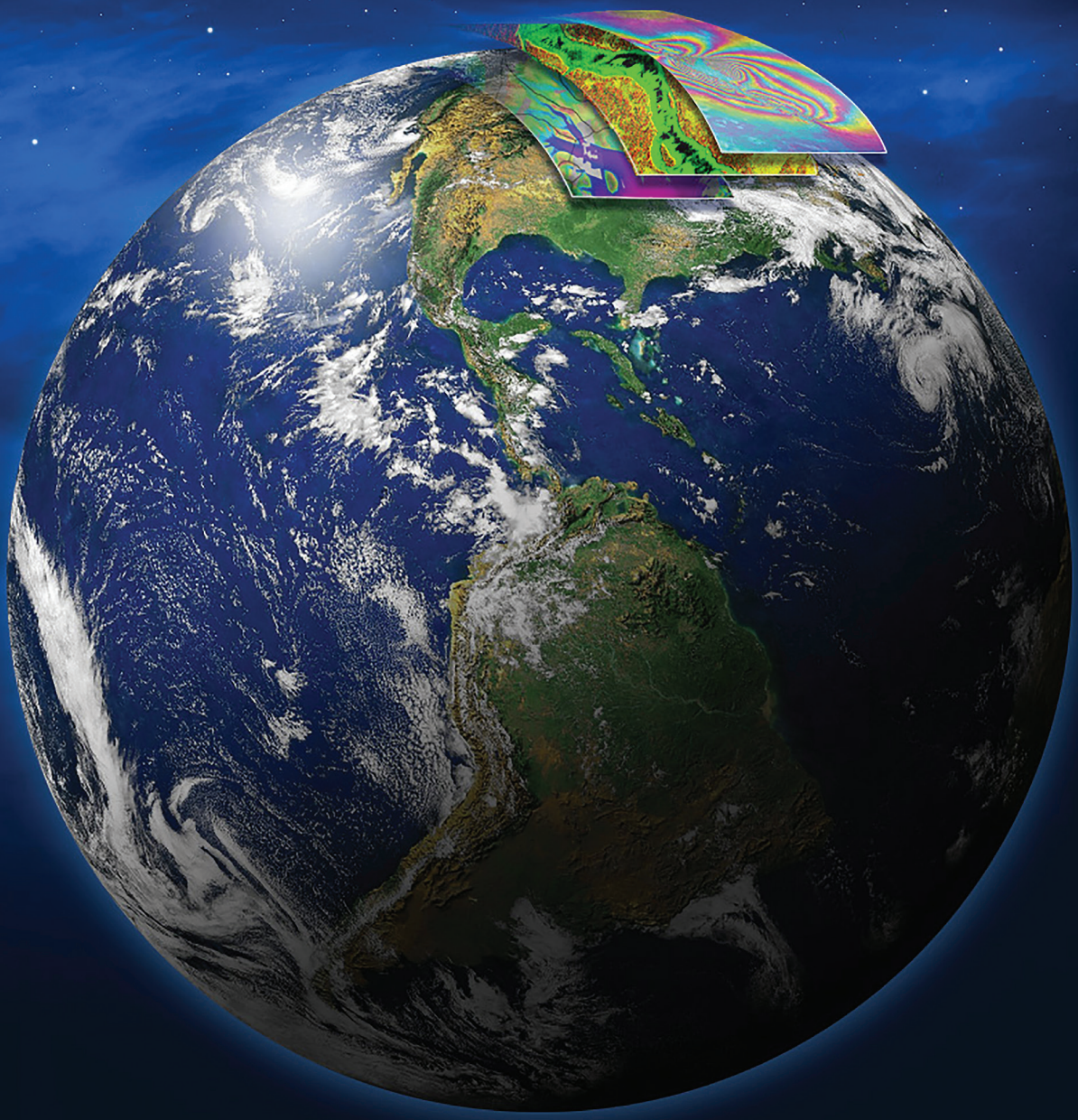

Credit: Caltech/JPL.

4 MISSION CHARACTERISTICS

THE LAUNCH VEHICLE FOR THE NISAR OBSERVATORY IS AN ISRO GEOSYNCHRONOUS SATELLITE LAUNCH VEHICLE (GSLV) MARK II. THE GSLV LAUNCHES FROM SATISH DHAWAN SPACE CENTRE IN SRIHARIKOTA, INDIA.

This section describes NISAR mission attributes that are important to the use and interpretation of the data. The observing strategy attributes include areas of acquisition, mode of operation, frequency of coverage, the orbit, and the radar observational capabilities. The mission operations design and constraints, which can influence science acquisition planning and execution, are also described. This design includes NASA and ISRO's plans to respond to urgent events.

4.1 OBSERVING STRATEGY

The NISAR mission aims to achieve global coverage of all vegetated land, full coverage of land ice and sea ice in both polar regions and in mountains, and frequent coverage of land areas that are deforming rapidly. The regular global coverage of land prepares the mission to respond to events that are unusual, such as mid-plate earthquakes. Regular observations of coastal waters around the US and India are also planned. Global coverage requirements for NISAR science are specified in the L1 requirements (Figure 4-1). Each of the L2 science requirements (listed in Appendix D) specifies a measurement objective, an accuracy of that measurement, and the area of interest or target area over which the measurement must be made.

Science targets are proposed by each of the three NISAR scientific discipline teams (solid Earth, ecosystems, and cryosphere), in the form of geographical polygons and nominal radar modes (see Appendix F for NISAR target maps by each discipline). With these targets and the L2 measurement accuracy requirements stated in Appendix D in mind, an observing strategy can be devised that takes into account the desired number and frequency of acquisitions needed in any given time interval, radar modes to be used, the season (if relevant), and whether to observe on the ascending or descending pass or both.

All NASA requirements can be met exclusively with the NASA-provided L-band radar system. In addition to the NASA science requirements, ISRO scientists have specified targets of interest in India and its surrounding coastal waters. These areas have similar attributes as those defined by the NASA Science Definition Team (SDT) for global targets. The ISRO requirements combine L-band and S-band observations. Operating the L- and S-band radars simultaneously will provide unique data and also minimize mode conflicts over India. However, the programmatic guideline is to not require simultaneous operation, but to make it an implementation goal.

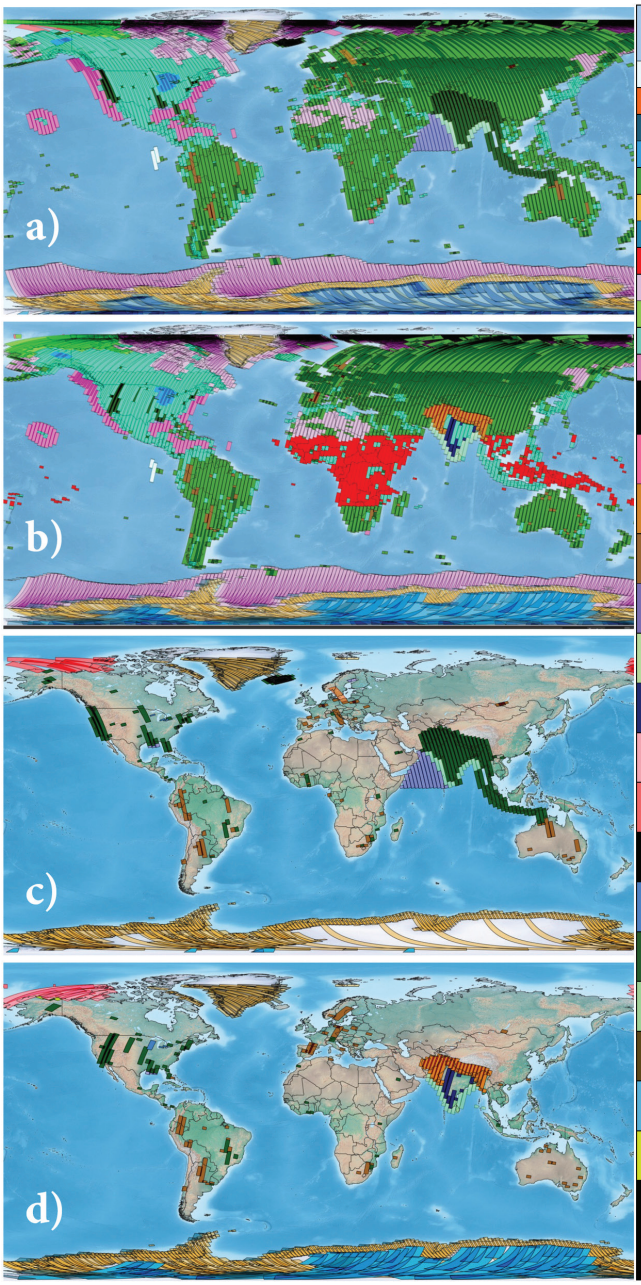

Mode Number	Mnemonic	Primary Science Target
001	L:ENG:NO:77M+---:FS:B4:F04	Noise only collection H+V, 4-bit BFPQ
068	S:DB-:DH:37W----:--:B4:D03	New mode
076	S:DB-:SH:37W----:--:B4:D03	ISRO land ice
130	L:SCI:QP:20M+05N:FS:B4:F28	US agriculture / India agriculture low res
148	L:SCI:DH:20M+05N:FS:B4:D01	Background land
150	L:SCI:SH:77M+---:HS:B4:D02	Land ice
151	L:SCI:SH:40M+05N:FS:B4:D02	Land ice low res
152	L:SCI:SH:20M+05N:FS:B4:D01	Low data rate study mode single-pol
153	L:SCI:SV:05W+---:FS:B4:D01	Sea ice dynamics
154	L:SCI:QD:05W+---:FS:B4:D01	Open ocean
156	L:SCI:DH:40M+05N:FS:B4:D02	L-only background land
161	L:SCI:DV:05W+---:FS:B4:D01	ISRO ice / Sea ice
190	L:PST:CP:77M+---:FS:B4:F04	4-bit post-take
191	L:PRE:NO:77M+---:FS:B4:F04	4-bit pre-take
196	L:SCI:DV:20M+05N:FS:B4:F04 S:DB-:CP:25W----:--:B4:---	Sea ice types
201	L:SCI:QP:20M+05N:FS:B4:F05 S:DB-:CP:25N----:--:B4:---	India agriculture / Himalayas / Image cal/val
212	L:SCI:DH:20M+05N:FS:B4:D01 S:DB-:DH:37W----:--:B4:---	Systematic coverage & deformation
214	L:SCI:SV:05W+---:FS:B4:D01 S:DB-:DV:10W----:--:B4:---	Ocean
215	L:SCI:DV:20M+05N:FS:B4:D01 S:DB-:CP:25W----:--:B4:---	Sea ice types / Coastal sea
217	L:SCI:DH:40M+05N:FS:B4:D02 S:DB-:SH:75W----:--:B4:---	High-res deformation (urban / landslide)
231	L:SCI:QD:05W+---:FS:B4:D01 S:DB-:DV:10W----:--:B4:---	Beaufort Sea
233	L:SCI:QD:05W+---:FS:B4:D01 S:DB-:CP:25W----:--:B4:---	Beaufort Sea / Antarctica stations
234	L:SCI:DH:20M+05N:FS:B4:D01 S:DB-:CP:37W----:--:B4:---	ISRO background
237	L:SCI:QP:20M+05N:FS:B4:F05 S:DB-:DH:37N----:--:B4:---	ISRO cal/val
238	L:SCI:DH:40M+05N:FS:B4:D02 S:DB-:DH:37W----:--:B4:---	ISRO background land and global science cal/val targets
242	L:SCI:DH:40M+05N:FS:B4:D02 S:---:DH:25W----:--:B4:---	Urban areas and ES sites
246	L:SCI:SH:77M+---:HS:B4:D02 S:---:SH:37W----:--:B4:---	Land ice - Greenland
247	L:SCI:SH:40M+05N:FS:B4:D02 S:---:SH:37W----:--:B4:---	Land ice - Antarctica
248	L:SCI:DH:40M+05N:FS:B4:D02 S:DB-:DV:10W----:--:B4:---	ISRO Bohai Bay and NASA urban area
254	L:PST:CP:77M+---:FS:B4:F04 S:---:DX:75W----:--:B8:---	4-bit joint post-take
255	L:PRE:NO:77M+---:FS:B4:F04 S:---:DX:75W----:--:B8:---	4-bit joint pre-take

FIGURE 4-1

NISAR Reference Observation Plan coverage maps for global ascending (a) and descending (b) passes, and joint L-band and S-band ascending (c), and descending (d) data takes. This plan will be in place for the initial six months of the mission. The project plans to review and adjust the plan every six months, depending on science team input, available resources, and other programmatic factors. The legend describes the modes that will be employed. There are some variations in coverage seasonally, for example over the poles as sea ice comes and goes, but largely the acquisition plan is intended to be static geographically to allow generation of consistent time series over the life of the mission. The mnemonics for the modes follow the scheme given in Table 4-1. For S-band, the mnemonic scheme is similar: S:XX:MM:BBP:WW:DD:FFF. Here, the beam forming mode XX for the S-band instrument is added (DB = beamform; DR = raw channels of the beamformer; NR = no beamforming). For joint modes, the PRF scheme is left off the mnemonic because it is the same as for L-band.

TABLE 4-1. L-BAND MODE MNEMONIC SCHEME

L:CCC:MM:BB_lP_l+BB_UP_U:WW:DD:FFF	
Attribute	**Meaning**
L	L-band
CCC	Mode category (ENG = engineering mode, SCI = science mode, PST = post-take, PRE = pre-take)
MM	Mode name (QP = quad pol; DH = dual pol HH/HV; SH = single pol HH; QD = HH in lower band, VV in upper band; QQ = HH/HV in lower band, VV/VH in upper band)
BB_l	Bandwidth of lower band
P_l	Pulse width of lower band (W = wide, M = medium, N = narrow)
BB_U	Bandwidth of upper band
P_U	Pulse width of upper band
WW	Swath width (FS = full swath 240 km, HS = half swath)
DD	Bit depth (B4 = 4 bit quantization, B3 = 3 bit quantization)
FFF	Pulse repetition frequency scheme (e.g., F28 is fixed PRF scheme, D01, is a variable PRF scheme)

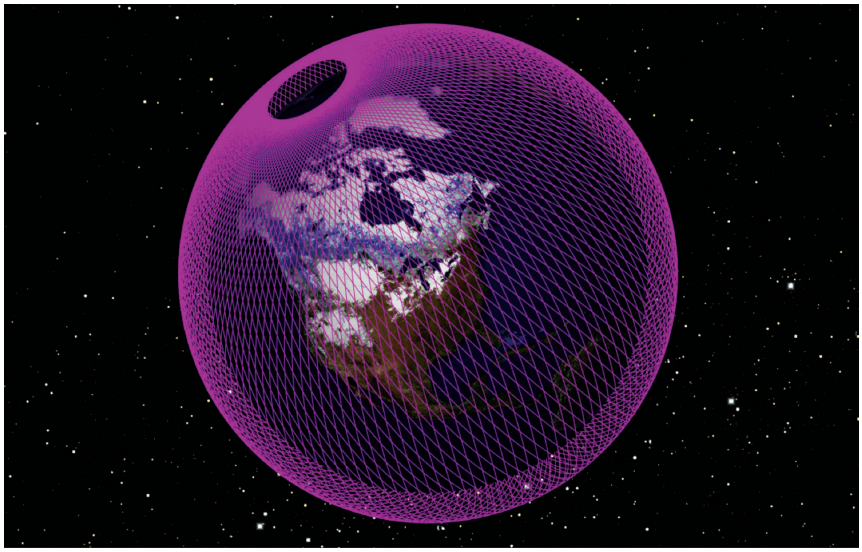

FIGURE 4-2

NISAR orbit tracks for a full twelve-day cycle. NISAR will execute 173 orbits in twelve days, roughly 100 minutes per orbit. While the orbit tracks are symmetric with respect to north and south, the swath coverage is asymmetric due to the side-looking orientation of the radar instruments. NISAR will point leftward relative to the satellite velocity vector, creating a larger loss in coverage over the Arctic. The orbital elements are given in Table 4-2.

4.2 REFERENCE SCIENCE ORBIT

The NISAR observatory launched July 30, 2025, on an ISRO Geosynchronous Satellite Launch Vehicle (GSLV) Mark II from Satish Dhawan Space Centre (SDSC) in Sriharikota, India. Launch services were provided by ISRO. The baseline orbit was selected to satisfy scientific and programmatic requirements. NISAR's 747-km altitude orbit, consisting of 173 orbits/cycle, will allow for global coverage every 12 days, as shown in Figure 4-2 and Table 4-2.

During science operations, NISAR will fly within a diamond-shaped orbital corridor defined for each of the repeat cycle's 173 orbits and tied to the rotating Earth (Figure 4-3). This corridor is defined to enable accurate correlation of science observations from pass-to-pass and cycle-to-cycle, supporting assessment of changes in the science targets. The dimensions of the diamond were calculated as an upper bound on acceptable error produced by a non-zero baseline between

TABLE 4-2. ORBITAL ELEMENTS AT THE FIRST ASCENDING EQUATOR CROSSING FOR THE NISAR REFERENCE SCIENCE ORBIT; NISAR WILL ORBIT THE EARTH IN A NEAR-POLAR, SUN-SYNCHRONOUS ORBIT

ORBITAL ELEMENT	VALUE (osculating)	VALUE (mean)
Semi-Major Axis (SMA), (km)	7134.573	7125.486
Eccentricity	0.00125	0.001165
Inclination (deg)	98.39851	98.40537
Longitude of Node (deg)	–172.817	–172.818
Argument of Periapsis (deg)	68.93757	90.09422
True Anomaly (deg)	–68.9375	–90.0982

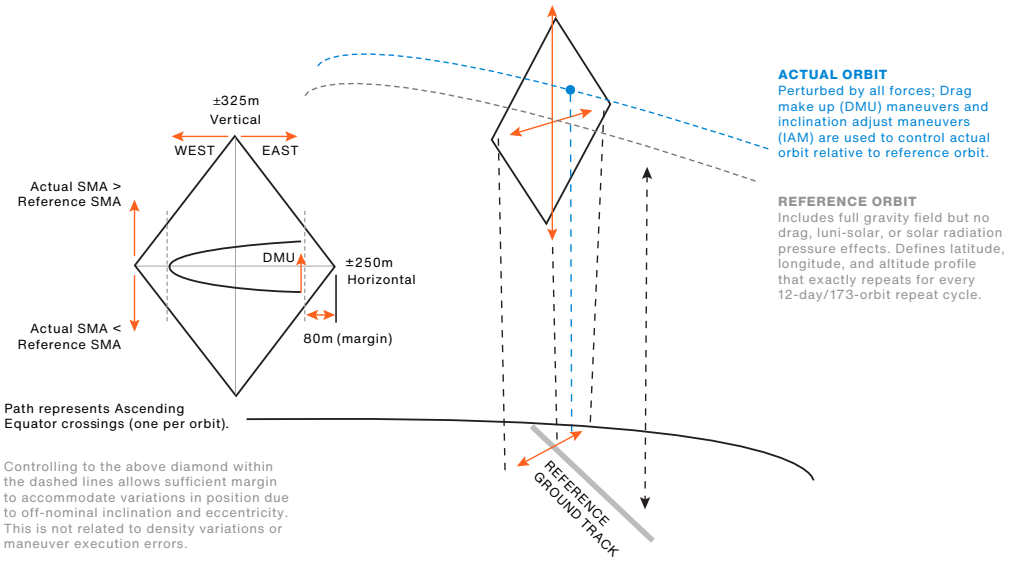

FIGURE 4-3

During science operations, NISAR will fly within a diamond-shaped orbital corridor defined for each of the repeat cycle's 173 orbits and tied to the rotating Earth.

passes/cycles among three primary factors (Rosen et al., 2000) of phase unwrapping error, geometric decorrelation, and topographic leakage, but ultimately dominated by the former (phase unwrapping error, i.e., high fringe rate in regions of large topographic relief).

The center of the diamond is defined by the 173-orbit reference trajectory (referred to as the reference science orbit), which is fixed to the Earth's surface and is exactly repeated every 12 days. The diamond can be thought of as a fixed altitude, longitude, and latitude profile that spans the entire repeat cycle; a conceptual representation of this corridor is shown in Figure 4-4. To maintain the diamond, the JPL Navigation team plans on executing maneuvers over the long ocean passes (Atlantic and Pacific) as much as possible not to impact science data collection.

The NISAR spacecraft will accommodate two fully capable synthetic aperture radar instruments (24-cm wavelength L-SAR and 10-cm wavelength S-SAR), each designed as array-fed reflectors to work as SweepSAR scan-on-receive wide swath mapping systems. The spacecraft launched on an ISRO GSLV-II

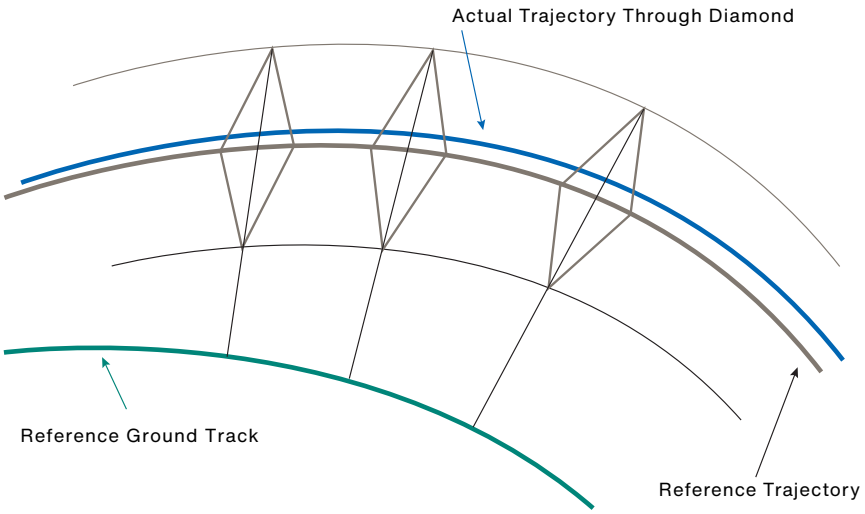

FIGURE 4-4

Actual versus reference trajectory for NISAR as maintained within the diamond.

launch vehicle into a polar sun-synchronous dawn dusk orbit. The mapping scenario calls for frequent sampling over broad areas to create time series and allow for noise reduction through stacking methods. Thus, a high-rate instrument and data downlink system are required. The average capacity of the envisioned data downlink is on the order of 26 Tbits per day, supporting the instruments that can produce at L-band from 72 Mbps in its lowest bandwidth mode to over 1500 Mbps in the most demanding high-bandwidth, multi-polarization mode. Tables 4-3 and 4-4 summarize the overall mission characteristics.

TABLE 4-3. OVERVIEW OF NISAR MISSION CHARACTERISTICS

ELEMENT	DESCRIPTION
Launch Date	July 30, 2025
Orbit	12-day exact repeat, sun-synchronous, dawn-dusk, polar, 747 km altitude
Mission Duration	3 years nominal, with extended mission fuel reserve
Science Data Downlink Approach	• 30–45 minutes of data downlink per orbit at 3.5 Gbps data rate through polar ground stations • 2.2 Gbps direct downlink to India over Indian ground stations
Observation Approach	• L-band multi-mode global radar imaging • S-band multi-mode targeted radar imaging • Dual-frequency capable • ~240 km swath for all modes • Full pol, multiple bandwidths up to 80 MHz • Near-zero Doppler pointing, fixed boresight • Left-looking for the entire mission, relying on the international SAR constellation to fill in coverage around the Arctic pole
Mapping Approach	Current approach defines a reference mission with fixed modes over broad target areas.

TABLE 4-4. MAJOR MISSION AND INSTRUMENT CHARACTERISTICS FOR NISAR

PARAMETERS	S-BAND	L-BAND
Orbit	747 km with 98° inclination	
Repeat Cycle	12 days	
Time of Nodal Crossing	6 AM/6 PM	
Frequency	3.2 GHz ± 37.5 MHz	1.257 GHz ± 40 MHz
Available Polarimetric Modes	Single Pol (SP): HH or VV Dual Pol (DP): HH/HV or VV/VH Compact Pol (CP): RH/RV Experimental Quad (QP): HH/HV/VH/VV	SP: HH or VV DP: HH/HV or VV/VH CP: RH/RV Quad Pol (QP): HH/HV/VH/VV
Available Range Bandwidths	10 MHZ, 25 MHz, 37.5 MHz, 75 MHz	5 MHZ, 20 MHz, 40 MHz, 80 MHz (Additional 5 MHz iono band for 20 & 40 MHz modes at other end of pass-band)
Swath Width	>240 km (except for QP)	>240 km (except for 80 MHz BW)
Spatial Resolution	7m (Az); 3m–24m (Slant-Ra)	7m (Az); 3m–48m (Slant-Ra)
Incidence Angle Range	34–47 deg	34–47 deg
Noise Equivalent σ^o	-25 dB (baseline) -20 dB (threshold)	-25 dB (for required full-swath modes)
Ambiguities	< -20 dB for all modes except QP	< -23 dB swath average in SP or DP modes < -17 dB swath average in QP modes
Data and Product Access	Free and Open	

NASA contributions include the L-band SAR instrument, including the 12-m diameter deployable mesh reflector and 9-m deployable boom and the entire octagonal instrument structure. In addition, NASA is providing a high-capacity solid-state recorder (approximately 9 Tbits at end of life), GPS, 3.5 Gbps Ka-band telecom system, and an engineering payload to coordinate command and data handling with the ISRO spacecraft control systems. ISRO is providing the spacecraft and launch vehicle, as well as the S-band SAR electronics to be mounted on the instrument structure. The coordination of technical interfaces among subsystems is a major focus area in the partnership.

NASA and ISRO will share science and engineering data captured at their respective downlink stations, and each organization will maintain their own ground processing and product distribution system. The science teams and algorithm development teams at NASA and ISRO will work jointly to create a common set of product types and software. The project will deliver NISAR data to NASA and ISRO for archive and distribution. NASA and ISRO have agreed to a free and open data policy for these data.

4.3 MISSION PHASES AND TIMELINE

Figure 4-5 provides a high-level overview of the NISAR mission timeline, and Table 4-5 provides more details on the different phases of the mission.

LAUNCH PHASE

The NISAR Observatory will be launched from ISRO's Satish Dhawan Space Centre (SDSC), also referred to as Sriharikota High Altitude Range (SHAR), located in Sriharikota on the southeast coast of the Indian peninsula, on the GSLV Mark-II expendable launch vehicle contributed by ISRO. The launch sequence encompasses the time interval that takes the observatory from the ground, encapsulated in the launch vehicle fairing, to after separation, and ends with the completion of solar array deployment and the observatory in an Earth-pointed attitude and in two-way communication with the ground. The launch sequence is a critical event.

COMMISSIONING PHASE

The first 90 days after launch will be dedicated to commissioning, or in-orbit checkout (IOC), the objective of which is to prepare the observatory for science operations. Commissioning is divided into sub-phases of initial checkout (ISRO engineering systems and JPL engineering payload checkout), deployments, spacecraft checkout, and instrument checkout. Philosophically, the sub-phases are designed as a step-by-step buildup in capability to full observatory operations, beginning with the physical deployment of all deployable parts (notably the boom and radar antenna, but not including the solar arrays, which are deployed during launch phase), checking out the engineering systems, turning on the radars and testing them independently, and then conducting joint tests with both radars operating.

SCIENCE OPERATIONS PHASE

The science operations phase begins at the end of commissioning and contains all data collection required to achieve the L1 science objectives. The science operations phase comprises three years of the primary science operations required by NASA, followed by extended operations phases required by ISRO or extended through the NASA Senior Review process. During this phase, the science orbit will be maintained via regular maneuvers, scheduled to avoid or minimize conflicts with science observations. Extensive calibration and validation (Cal/Val) activities will take place throughout the first 5 months, with yearly updates of 1-month duration.

The observation plan for both L- and S-band instruments, along with engineering activities

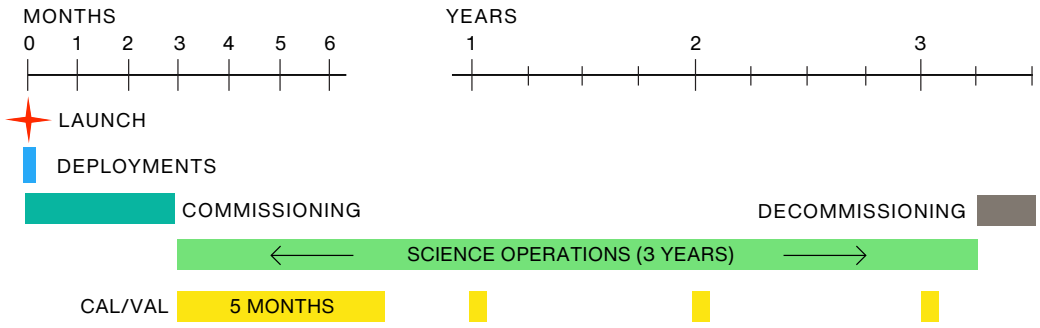

FIGURE 4-5

Mission timeline and phases for NISAR. The mission timeline for NISAR will be divided into launch, a 90-day commissioning or in-orbit checkout period, followed by 3 years of nominal science operations, and 90 days of decommissioning.

TABLE 4-5. NISAR MISSION PHASES

MISSION PHASE	START DATE	DURATION	BOUNDARY END STATE
Launch (L)	Mid-2025 (L - 24 hours)	1 day + ~40 minutes	Spacecraft in target orbit, power positive, in two-way communication
Commissioning	L + ~40 minutes	90 days	All systems ready to begin science data collection
Science Operations	L + 90 days	3 years	Mission objectives are complete
Decommissioning	L + 3.25 years	90 days	Spacecraft in disposal orbit and passivated

(e.g., maneuvers, parameter updates, etc.), will be generated pre-launch via frequent coordination between JPL and ISRO. This plan is called the reference mission; the science observations alone within that reference mission are called the reference observation plan (ROP). The schedule of science observations will be driven by a variety of inputs, including L- and S-band target maps, radar mode tables, and spacecraft and ground-station constraints and capabilities. This schedule will be determined by JPL's mission planning team, and the project will endeavor to fly the reference mission, which includes these science observations exactly as planned pre-launch (accommodating for small timing changes based on the actual orbit). Periodic updates are possible post-launch, which will lead to a new reference mission.

Routine operations of NISAR are dominated by orbit maintenance maneuvers, science observations, and data-downlink. Additional activities will include continuous pointing of the solar array to maximize power and continuous zero-doppler steering of the spacecraft.

DECOMMISSIONING PHASE

The 90-day decommissioning phase begins after the science phase operations conclude. NASA deorbit and debris requirements are not applicable for NISAR, however the project must comply with ISRO's guidelines to end the mission safely. ISRO adheres to the IADC Space Debris Mitigation Guidelines, IADC-02- 01, Revision 1, September 2007.

4.4 GROUND SEGMENT OVERVIEW

The NISAR ground segment consists of the Ground Data System (GDS), Science Data System (SDS), and Mission Planning & Operations System. The GDS and SDS manage the end-to-end flow of data from raw data to fully processed science data products.

GROUND DATA SYSTEM

The GDS includes the tracking stations, data capture services, communications network, and end party services (Figure 4-6). The stations, services, and communications are NASA multi-mission capabilities managed by the Goddard Space Flight Center (GSFC). The GDS will send the raw science data to the SDS, which converts

the downlinked raw data into Level 0a and Level 0b data that are the starting point for the science data processing.

SCIENCE DATA SYSTEM

The SDS converts the Level 0b data into L1/L2 science data products that the NISAR mission provides to the science community for research and applications. The SDS facility is designed to process data efficiently and distribute data products in a timely manner to the community as required to meet mission objectives. The facility includes computer hardware dedicated to operational data production. In addition, the SDS facility is planned as a cloud-based hybrid SDS, with all elements cloud-enabled. This allows for some processing to be done at JPL and some to be distributed to the external cloud. The science and algorithm development teams will have access to cloud instances separate from the production instances to enhance algorithmic accuracy and performance.

The SDS is controlled through a cloud-based production management system at the Jet Propulsion Laboratory (JPL) in Pasadena, California. JPL is responsible for implementation of software to generate Level 1 radar instrument data products and Level 2 products. The science team is responsible for generating Level 3 geophysical data products for calibration and validation purposes. As funds permit, software for Level 3 products may be migrated to the production system to generate larger areas of Level 3 products.

To facilitate the software development process, the SDS will establish a mechanism for developmental instances of the SDS to be made available to the algorithm development and science teams. These developmental instances will be logically separate from the production system but will allow development and testing of the software that will be used to automatically generate the science data products once NISAR is in orbit.

NASA NEAR-SPACE NETWORK (NSN)

NISAR will downlink both to ISRO ground stations (see above) and to NASA Near-Space Network (NSN) stations. For the NASA stations, Ka-band antennas will be used at one or more complexes. The specific antenna complexes currently identified are Alaska, United States; Svalbard, Norway; Punta Arenas, Chile; and Troll, Antarctica.

JPL MISSION OPERATIONS CENTER (MOC)

JPL will perform mission operations from multiple buildings at JPL in Pasadena, California, all of which are considered to make up the MOC. The existing multi-mission Earth Orbiting Missions Operation Center (EOMOC) will provide operations teams with consoles, workstations, and voice and video displays. Navigation and GPS operations will be conducted from other JPL locations.

JPL SCIENCE DATA PROCESSING FACILITY

JPL science data processing will be done using the JPL SDS. SDS software and storage will be hosted by cloud services, Amazon Web Services (AWS) in Oregon.

NASA DISTRIBUTED ACTIVE ARCHIVE CENTERS (DAACS)

NASA's Earth Observing System (EOS) operates DAACs around the United States and has been interoperating with foreign sites. For NISAR, the Alaska Satellite Facility (ASF) DAAC has been selected. The DAAC will utilize AWS cloud services for processing, storage, and distribution.

ISRO TELEMETRY, TRACKING, AND COMMAND NETWORK (ISTRAC)

The ISRO ISTRAC facility in Bangalore will be used for spacecraft operations and to schedule and operate a set of S-band Telemetry, Tracking and Commanding (TTC) stations.

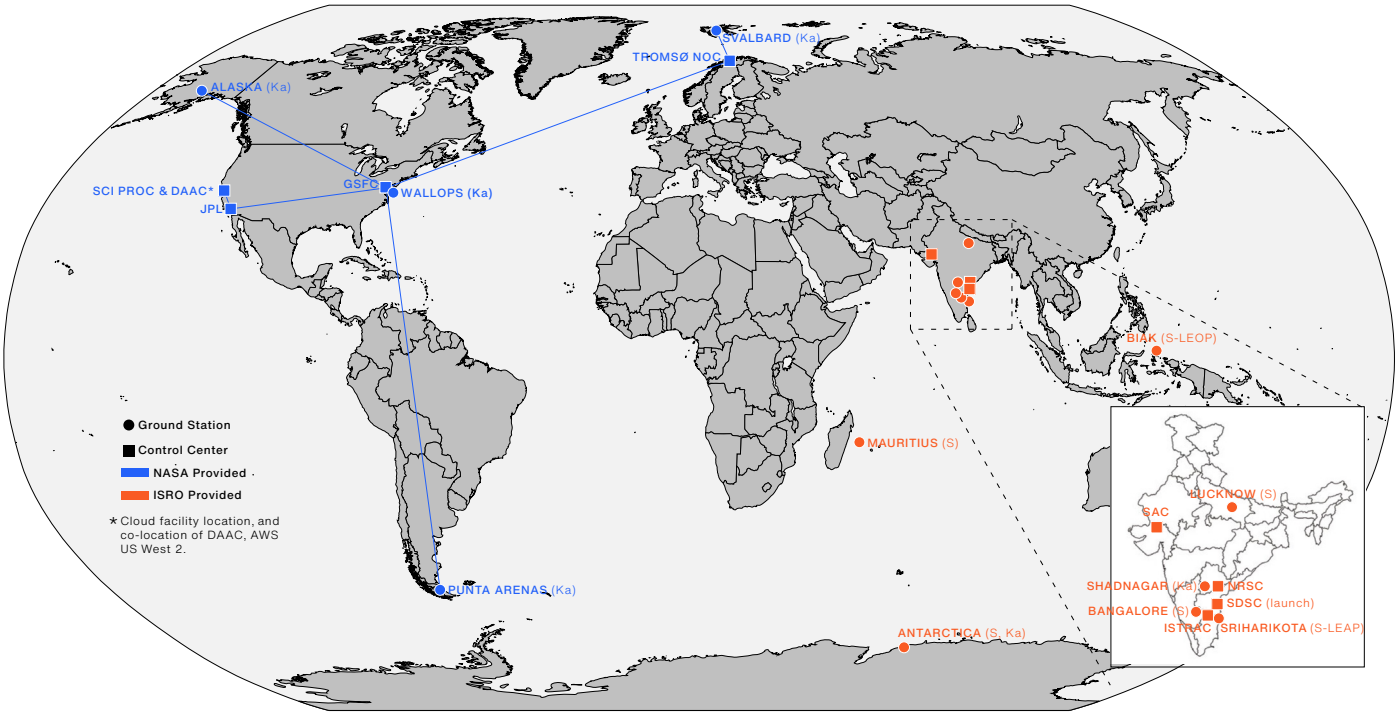

NATIONAL REMOTE SENSING CENTRE (NRSC)

The ISRO NRSC operates an Earth science acquisition, processing, and dissemination center in Hyderabad, India. For NISAR, this center operates two Ka-band stations as part of their Integrated Multi-Mission Ground segment for Earth Observation Satellites (IMGEOS), one near NRSC in Shadnagar, India, and another remote station in Antarctica. The station in Shadnagar is also referred to as the Shadnagar Acquisition Network, or SAN.

SATISH DHAWAN SPACE CENTRE (SDSC), SHRIHARIKOTA RANGE (SHAR)

SDSC SHAR, with two launch pads, is the main launch center of ISRO, located 100 km north of Chennai. SDSC SHAR has the necessary infrastructure for launching satellites into low Earth orbit, polar orbit, and geostationary transfer orbit. The launch complexes provide complete support for vehicle assembly, fueling, checkout, and launch operations.

WIDE AREA NETWORKS (WANS)

WANs will be used for long-distance exchanges among NISAR facilities. All WANs will consist of circuits carrying TCP/IP-based traffic.

4.5 TELECOMMUNICATIONS

The NISAR observatory's telecommunications system provides one uplink path and three downlink paths. The uplink path is from ISRO's command center at ISTRAC through the observatory's S-band antenna mounted on the ISRO spacecraft bus. The three downlink paths are as follows: tracking and engineering telemetry, from the same S-band antenna back down to ISRO's spacecraft operations center at ISTRAC; instrument data from both L- and S-band systems, through the shared spacecraft Ka-band antenna (provided by ISRO) to ISRO's NRSC facilities near Hyderabad via ISRO's Ka-band ground stations at Shadnagar and Antarctica; and the same instrument data and engineering telemetry through the shared

FIGURE 4-6

NISAR ground stations (including the NASA Near-Earth Network stations in Alaska, Svalbard, and Punta Arenas; ISRO stations in Antarctica, Shadnagar, Bangalore, Lucknow, Mauritius, Biak), control center, and launch location at SDSC in Sriharikota, India.

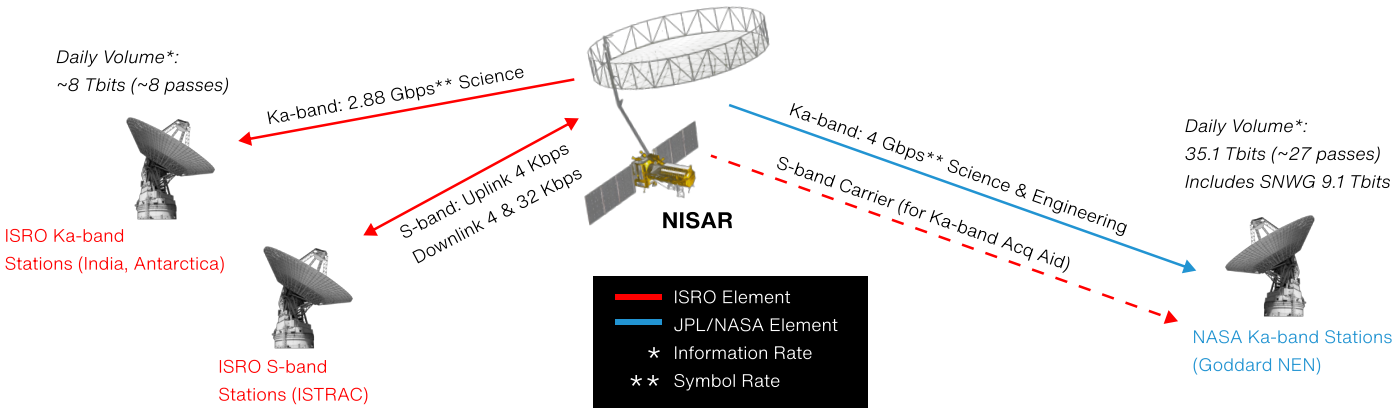

FIGURE 4-7

NISAR telecommunications links include Ka-band downlink to NASA and ISRO stations at 4 Gbps and 2.88 Gbps, respectively, and S-band uplink and downlink from and to ISRO ground stations.

spacecraft Ka-band antenna to NASA NSN stations (Figure 4-7).

ISRO's 2.88 Gbps Ka-band system provides for science data downlink to Indian ground stations with an effective information rate of 2.2 Gbps. Ka-band downlink to NASA ground stations will be at 4.0 Gbps with an information rate of 3.45 Gbps via a JPL provided transmitter. ISRO supplies the Ka-band electronics and a 0.7m High Gain Antenna (HGA) mounted on the spacecraft's nadir surface to be used by both ISRO and JPL Ka-band transmitters, through a JPL provided and controlled switch. The antenna gimbal and control of the gimbal will be provided by ISRO. There will be 15 to 20 downlink sessions per day, with average session duration of less than 10 minutes. Note that there are separate Ka-band telecom transmitters, but they share the same Ka-band antenna. This system is fully redundant and cross-strapped except for the antenna and Ka-band gimbal.

KA-BAND COMMUNICATIONS

ISRO's NRSC facility operates an Earth science downlink and processing center in Shadnagar, India, near Hyderabad. This facility is the primary

TABLE 4-6. NISAR KA-BAND GROUND STATIONS

NASA/ ISRO	STATION	ID	USAGE PLAN	LATITUDE (°)	LONGITUDE (°)	ALTITUDE (M)
NASA	Alaska	AS4	Primary Site: Maximum Utilization	64.795 °N	147.538 °W	162
NASA	Svalbard	SG2	Primary Site: Maximum Utilization	78.230 °N	15.398 °E	499
NASA	Punta Arenas	PA	Backup/Secondary Site – As Needed	52.938 °S	70.857 °W	17
NASA	Wallops	WG5	NASA Primary Site: High Utilization	37.925 °N	284.523 °E	0
ISRO	Shadnagar	SAN	Primary Site	17.028 °N	78.188 °E	625
ISRO	Antarctica	ANT	Primary Site	69.394 °S	76.173 °E	0

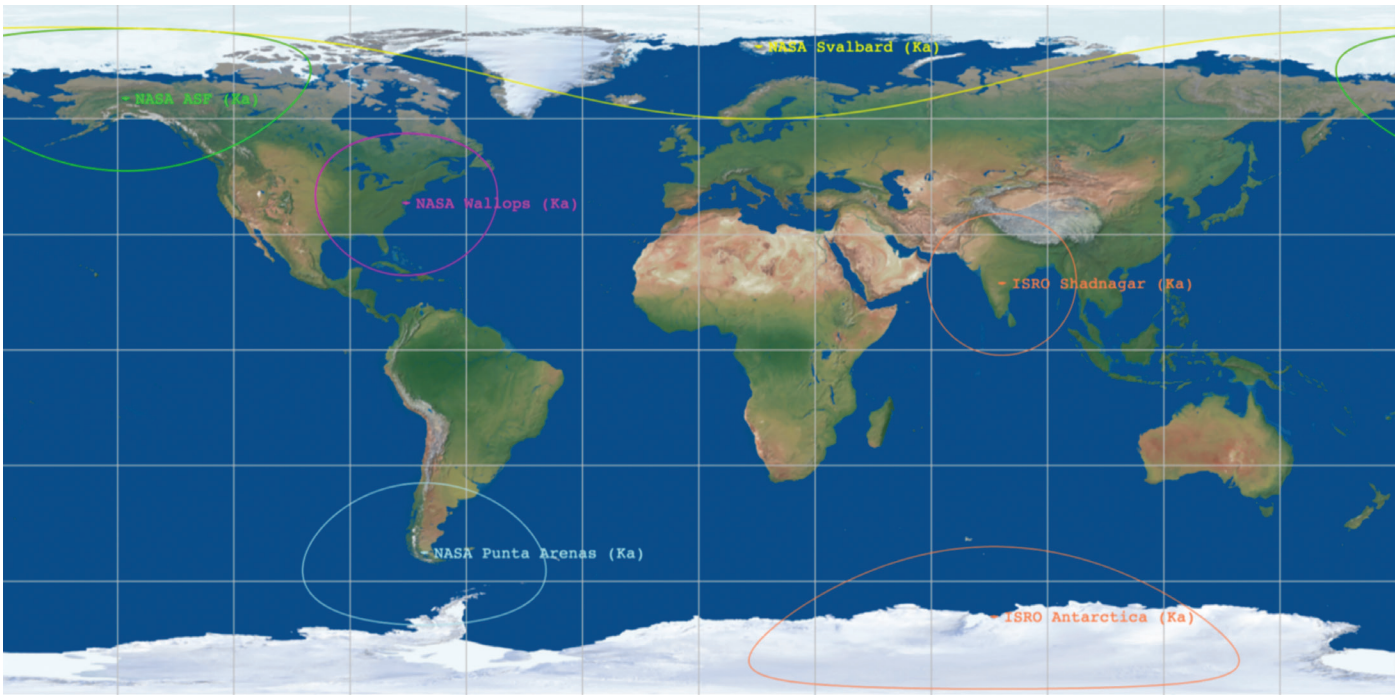

FIGURE 4-8

Locations of NISAR Ka-band ground stations (NASA stations in Alaska, Svalbard and Punta Arenas, and ISRO stations in Shadnagar and Antarctica are shown).

center for ISRO Ka-band communications from the observatory during nominal science operations. NRSC plans to place a Ka-band reception antenna here within the existing Integrated Multi-Mission Ground segment for Earth Observation Satellites (IMGEOS) facility at SAN. ISRO also plans to use another Ka-band ground station (Bharati in Antarctica) for science data downlinks. Primary playback of science data, however, will utilize NASA stations of the NSN at the ASF and Svalbard (Norway). These stations are shown in Table 4-6 and Figure 4-8. The current science data downlink strategy calls for all S-band radar data to be downlinked to the ISRO ground stations, and all L-band radar data to be downlinked to the NSN stations.

4.6 MISSION PLANNING AND OPERATIONS

Since nearly all objectives are best satisfied with regular repeated observations of any given science target, the NASA-ISRO Joint Science Team will create an overall science observation strategy that establishes a nominal repetitive observing baseline prior to launch. It is anticipated that the Joint Science Team will alter the nominal observation plan during the course of the mission. Applications and other government users may also request plan changes. The project team will strive toward accommodating these within the project constraints. These post-launch updates to the Reference Observation Plan will be applied on a quarterly or semi-annual frequency basis, with accommodation of urgent response requests in response to natural hazards and other emergencies (Figure 4-9). The Joint Science Team will rely on Mission Operations and the Project Science Team to understand the implications of any changes to the observation plan. Changes will be specified through target/mode/attributes as is currently done. The Mission Operations Team will then rerun the mission scenario simulation to examine resource (power, thermal, data downlink, cost) constraint violations. The Project Science Team will apply the updated Candidate Observation Plan through the science performance models to see if there are any impacts to L1/L2 science requirements.

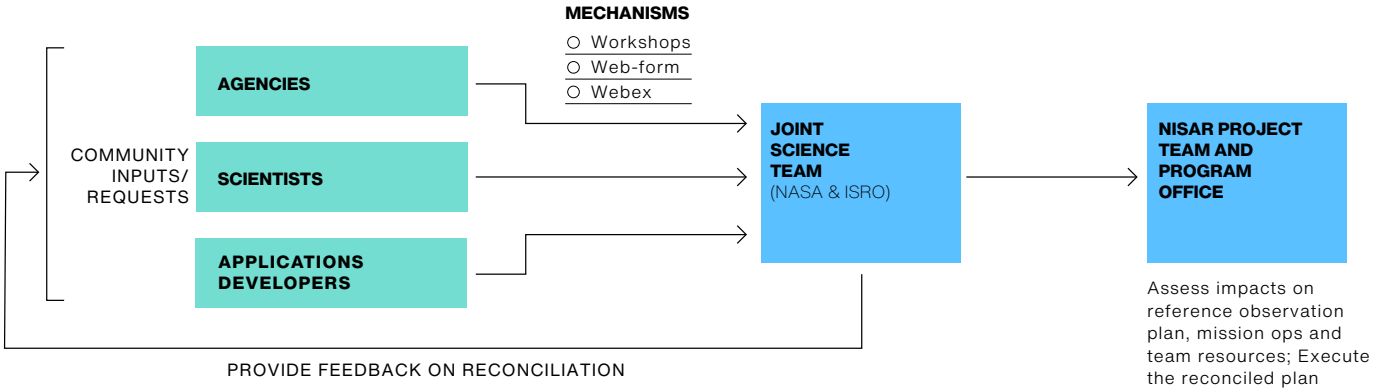

FIGURE 4-9

Flowchart showing steps to be followed for long-term re-planning of the Reference Observation Plan. This process will be followed periodically (roughly every 6 months) for updating the plan during operations.

If resource violations or performance impacts are identified, iteration will be required.

JPL will develop the coordinated observation plan that takes into account spacecraft power, maneuvers, data throughput sizing, and availability of downlink channels. That plan will be sent to ISRO for uplink to, and execution on, the observatory. JPL manages all L-band SAR instrument operations, with the ISRO uplink station serving as a pass-through for L-band instrument commands. ISRO manages all S-band SAR operations. All instrument operations are guided by the coordinated observation plan, with specific commands/sequences to implement the plan developed by the respective organizations. Navigation is led by JPL, with maneuver design provided from JPL to ISRO to implement the maneuvers. Maneuver implementation is fed back to JPL as input for the next maneuver planning process. In the same vein, JPL provides the telecom sequence for the NASA-provided Ka-band telecom subsystem used for all science data downlink, while ISRO feeds back to JPL the ISRO-provided Ka-band telecom subsystem downlink contacts. JPL is responsible for producing the required science data specified by NASA and delivering them to NASA DAAC(s). The ISRO NRSC will process and distribute the required science data specified by ISRO.

Mission operations will be a joint JPL-ISRO effort. Day-to-day observatory operations will be conducted at the ISRO Telemetry Tracking and Command Network (ISTRAC) center in Bangalore. ISTRAC monitors and controls the spacecraft, downlinking spacecraft telemetry to a local archive from where JPL can pull data as needed. All science data is downlinked via the JPL Ka-band telecom, initially processed, and archived first in the JPL Science Data System, and then in the ASF DAAC, from where ISRO can pull the data as-needed. In addition, a subset of L-band and S-band data (specified by SAC) will be downlinked directly to India (NRSC ground station) via the spacecraft Ka-band telecom.

4.7 INSTRUMENT DESIGN

The L-band Synthetic Aperture Radar (L-SAR) instrument is the focus of the NASA-chartered science goals for NISAR. To meet these goals, it will be heavily utilized during the mission. Current mission scenarios have the instrument on and collecting data for 45–50% per orbit on average, with peaks as high as 70%.

The L-SAR is a side-looking, fully polarimetric, interferometric synthetic aperture radar operating at a wavelength of 24 cm (Rosen et al., 2015). The L-SAR is capable of 242-km swaths, 7-m resolution along track, 2–8 m resolution cross-track (depending on mode) and can operate in various modes including quad-polarimetric modes, i.e., transmitting in both vertical and horizontal polarizations, and receiving in both the same polarizations transmitted, and cross-polarizations. A cross

polarization mode, for example, receives the horizontally polarized component of the return signal when vertically polarized pulses were transmitted, and vice versa. From the NISAR science orbit, the instrument's pointing accuracy is such that the L-SAR data can be used to produce repeat-pass interferograms sensitive to large-scale land deformation rates as small as 4 mm/year.

To meet the requirements of all science disciplines, the L-SAR radar instrument is designed to deliver fast sampling, global access and coverage, at full resolution and with polarimetric diversity. The technological innovation that allows this performance is the scan-on-receive "SweepSAR" design, conceived and refined jointly with engineering colleagues at the German Space Agency (DLR) under the DESDynI study phase.

SweepSAR (Figure 4-10) requires the ability to receive the echoed signal on each element independently, such that localized echoes from the ground can be tracked as they propagate at the speed of light across the swath. As an echo moves from receive element to receive element, the signals from neighboring elements must be combined to form a continuous record of the echo. Given the width of the swath (~244 km), returns from two or more echoes must be processed simultaneously. This operation is best performed using digital combining techniques, so the received echo is digitized immediately upon reception, filtered, decimated, and then sent to a signal combiner.

On transmit, the entire radar feed aperture is illuminated, which creates a narrow strip of radiated energy on the 12-m reflector that illuminates the full 242 km swath on the ground. On receive, the echo illuminates the entire reflector, and that energy is focused down to a particular location on the radar feed aperture depending on the timing of the return. The narrowness of the receive beam on the ground (due to the wide reflector illumination) minimizes ambiguity noise so that individual pulses can be tracked separately as they sweep across the feed.

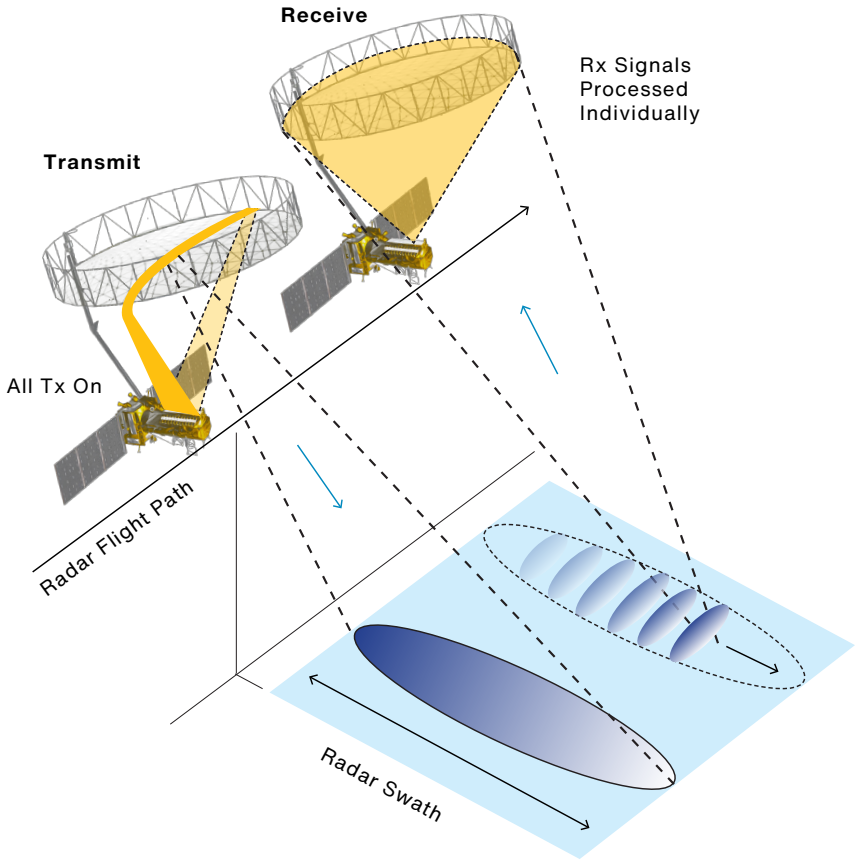

FIGURE 4-10

SweepSAR technique, which allows full-resolution, multi-polarimetric observations across an extended swath (> 240 km). By transmitting energy across the full feed aperture, a wide swath is illuminated on the ground. Each patch element on the feed can receive independently, allowing localization in time, hence space, of the return echo scattered from the ground. Note: Transmit and scanning receive events overlap in time and space. Alongtrack offset shown is for clarity of presentation only.

The SweepSAR L-band and S-band radars are designed to work independently or together. The L-band hardware is built at JPL, and the S-band electronics portion at ISRO. The feed apertures at L- and S-band are also built by JPL and ISRO, respectively, phase-matched to their respective electronics and cabling. In this sense, each radar is a self-contained instrument up to the radiated energy from the feed aperture. Thereafter, both share the same reflector, with a nearly identical optical prescription (F/D=0.75). Because a distributed feed on a reflector-feed antenna has a single focus, much of the radiated and received energy is not at the focus. Since S-band wavelength is 2.5 times shorter than L-band, but the feed is the same length to achieve identical swath coverage, the S-band system has greater deviations from the focus. Thus,

the design has been iterated to derive the best offset, tilt, and phasing of each radar to balance the performance across the two systems. This analysis has been done independently by the JPL and ISRO teams, then cross-compared to validate.

For the radars to operate together as a dual-frequency system, it is necessary to share oscillator and timing information to lock their pulse repetition frequency together, which is done with simple interfaces. Another concern is the coupling between the feed apertures. In the current design, the two apertures are mechanically and electrically separated to keep the coupling manageable.

Filtering, decimation, calibration estimation, and combining are done in a set of field programmable gate arrays (FPGAs) or application-specific integrated circuits (ASICs) on each radar. This complication exists for both L-band and S-band and leads to a multiplicity of parallel processing efforts in the spaceborne electronics. The SweepSAR technique was demonstrated in an airborne configuration to show its efficacy (Hensley et al., 2010).

With SweepSAR, the entire incidence angle range is imaged at once as a single strip-map swath, at full resolution depending on the mode, and with full polarization capability if required for a given area of the interest. Azimuth resolution is determined by the 12-m reflector diameter and is on the order of 8 m.

Because the radar cannot receive echoes during transmit events, there are one or more gaps in the swath if the radar's pulse rate is fixed. NISAR has the ability to vary the pulse rate in order to move the gaps around over time. The data can then be processed to gapless imagery by interpolating across the gaps.

Over most of the world, the instruments will be operated independently. The requirements for range resolution, polarization, and radar modes supported by the instrument are science target dependent. The instrument supports a fixed set of polarizations and bandwidth combinations of those listed in Table 4-7. The physical layout of the payload is depicted in Figure 4-11.

During data collection, the observatory performs near zero Doppler steering to compensate for the Earth's rotation during observations. The mission will be conducted in a left-only mode of operation to better optimize science return, with the expectation that other sensors can achieve science in the high Arctic regions.

FIGURE 4-11

NISAR system and instrument physical layout.

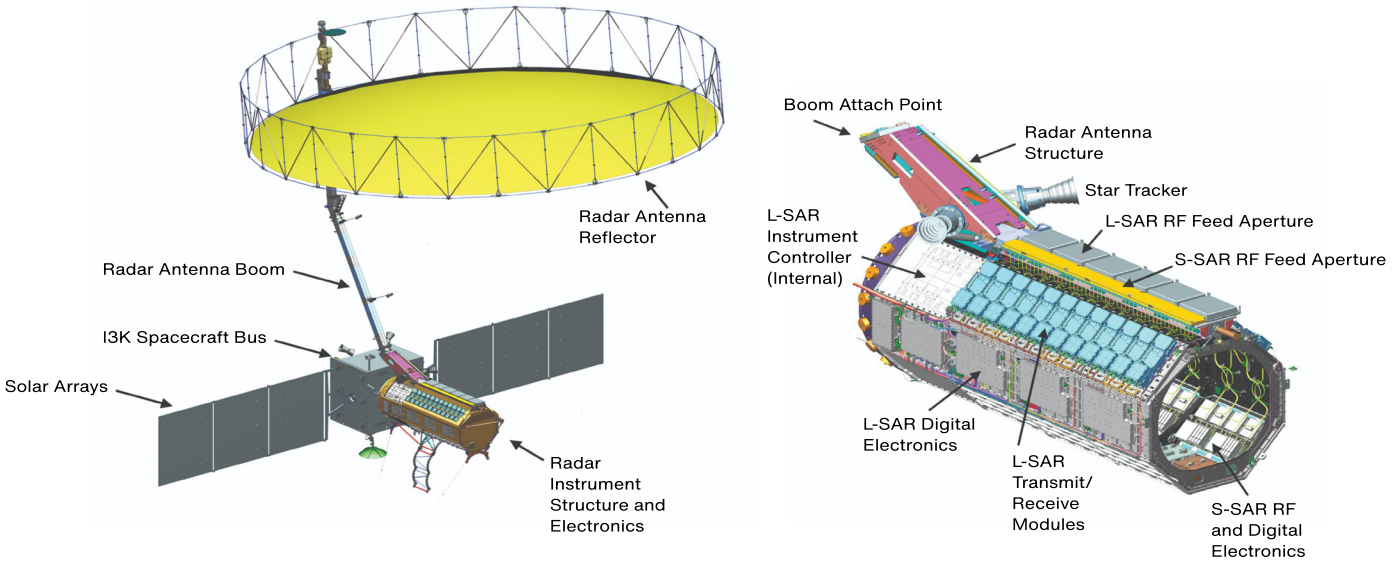

TABLE 4-7. SUPPORTED POLARIZATIONS AND BANDWIDTH COMBINATIONS

ELEMENT	DESCRIPTION
Operational Implementation	SweepSAR scan-on-receive
Configuration	• 12-m diameter mesh reflector used for both L- and S-band • S-band 2 x 24 / L-band 2 x 12 patch array, one TR module per patch-pair subarray per polarization • Independent S- and L-band electronics with timing synchronization for simultaneous operations • Digitization at each receive array element followed by real-time combining
Radar Center Frequency	S-band 3200 MHz; L-band 1260 MHz; simultaneous operations possible
Realizable Bandwidths	• 5 MHz (L) • 10 MHz (S) • 25 MHz (S); 20+5, 40+5 MHz split spectrum (L) • 37.5 MHz (S); 40 MHz (L) • > 75 MHz (S); 80 MHz (L)
Realizable Polarizations	Single-pol through quad-pol, including compact-pol and split-band dual-pol
Incidence Angle Range	~34–48 degrees
Performance	• < –23 dB NES0 depending on mode • < –15 to –20 dB ambiguities variable across swath • 3–50 m range resolution depending on mode, sub-pixel geolocation; ~7 m azimuth resolution

The radar is designed to operate in a variety of modes to satisfy the various science objectives; these may include single polarization (horizontal or vertical only) modes, dual polarization (e.g., transmit in horizontal polarization and receive in both horizontal and vertical polarization) modes, quad polarization (transmit in both and receive in both) modes, circular polarization modes, and combinations of any of the above (one for L-band, and a different one for S-band). The L-band radar has been designed to operate in a "split-spectrum" mode, whereby two distinct radar pulses are transmitted sequentially in time, each with its own center frequency and pulse frequency modulation rate. Having widely separated bands enables the estimation of the ionospheric phase variability to greater accuracy than would be possible with a single narrower band. This is discussed in greater detail in Section 7.2.

Table G-1 in Appendix G shows the available modes for the L-SAR and S-SAR instruments. For each of the observation targets, there is a single mode (polarization, bandwidth, radar band combination) that is used over that area. For overlapping targets, such as background land and U.S. agriculture, the more capable mode is a superset of capability of the other mode. Transition between these modes is seamless at L-band, which nearly eliminates data loss. While the global measurements largely will be at L-band, there will also be regular acquisitions at S-band made jointly with L-band over India and other targeted areas around the world. Mode transitions at S-band will incur a gap in acquisition as the instrument reconfigures on the order of a few seconds. The mission plan attempts to minimize such transitions to the extent possible. As the mission evolves, insights into the most beneficial uses of S-band in place

of L-band or as a dual-frequency system will be gained, with the observation plan modified accordingly.

The Shuttle Imaging Radar-C was the first orbiting multi-frequency, multi-polarization SAR around Earth and demonstrated the value of having multiple wavelengths. Possible benefits include:

- Use of S-band in polar regions can reduce the impact of the ionosphere, since the S-band signal will be five times less sensitive than L-band to ionospheric perturbations.
- Use of L-band and S-band jointly will allow a good estimate of the ionosphere using dual-band mitigation techniques (Rosen et al., 2010).
- Use of L-band and S-band jointly to extend the range of sensitivity for biomass estimation and surface deformation, and aid in estimating soil moisture.
- Use of L-band and S-band jointly to study differential surface roughness and volume scattering effects, improving classification of natural surfaces.
- Use of L-band and S-band jointly or separately to study decorrelation rates of natural surfaces, improving the utility of interferometry for change detection and change classification.

These capabilities will provide researchers with a fundamentally new global (at L-band) and globally distributed (at S-band) data set for research. It is important to note that the system downlink is at present fully tasked, so opportunities for dual-band collection must be balanced against alterations to the nominal observation plan.

4.8 FLIGHT SYSTEMS/SPACECRAFT

The NISAR flight system design, development, integration, testing, and operations are a joint venture, with equivalent-scale contributions from both JPL and ISRO. The suite of flight systems consists of the launch vehicle and free-flying observatory. The NISAR observatory is designed around the core payloads of L- and S-band SAR instruments, designed to collect near-global radar data over land and ice to satisfy the L1 science goals. In addition to the two radar instruments, the NISAR payload includes a global positioning system (GPS) receiver for precision orbit determination and onboard timing references, a solid-state recorder, and a high-rate data downlink subsystem to enable transmission of the high-volume science data to the ground. Figure 4-11 shows the fully integrated and deployed observatory system. The 12-meter Radar Antenna Reflector (RAR) is at top, supported by the Radar Antenna Boom (RAB). The boom is attached to the radar instrument structure (RIS), which is itself attached to the ISRO I3K spacecraft bus. Extending on either side of the bus are two solar arrays each with three panels that together supply approximately 4,000 W of power when illuminated (i.e., at all times when not in eclipse or off Sun-pointing). The radar payload integration (L-band and S-band integration) occurred at JPL, and the overall observatory integration occurred at ISRO Satellite Center (ISAC) in Bangalore, India. The main elements of the system are illustrated in Figures 4-11 and 4-12.

ISRO provides the spacecraft bus, which includes all systems required for central command and data handling, uplink and downlink, propulsion, attitude control, solar arrays, the S-band radar electronics, and a Ka-band telecom system and gimbaled High Gain Antenna (HGA) dish. ISRO also provides the launch vehicle. NASA/JPL provides the L-band radar electronics, the deployed boom and radar reflector, a high capacity/high-speed Solid State Recorder (SSR), the GPS, high-rate Ka-band Payload Communication Subsystem (PCS), the pyro firing system for boom and antenna deployments, and a Payload Data System (PDS) that monitors and controls the JPL systems and handles communications between all of the JPL systems and the ISRO spacecraft bus.

The NISAR science requirements levy special functional requirements on the heritage ISRO spacecraft and its associated mission operations.

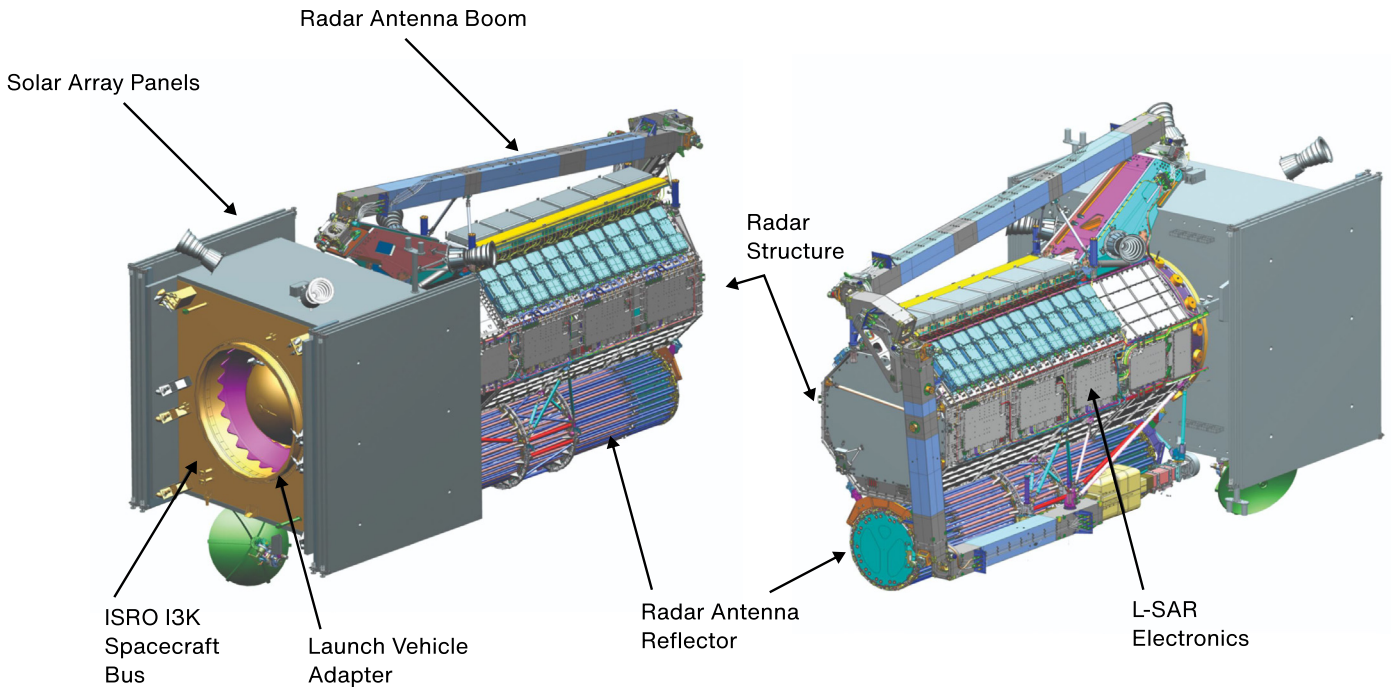

FIGURE 4-12

Spacecraft in stowed configuration.

Both L-band and S-band radar payloads require substantial average power for operation on-orbit, which leads to a spacecraft design with large deployable solar arrays. The baseline science observation plan calls for up to 35 Terabits (Tb) per day of L-band and 6 Tb per day of S-band radar data collection, downlink, and processing. This plan drives the spacecraft design to include a Ka-band telecom system to accommodate the high bandwidth requirements. The spacecraft Attitude and Orbit Control Subsystem (AOCS) is designed to address several critical science-enabling functions: 1) it must fly along the same orbit to within narrow tolerances (500 m) over the life of the mission; 2) it must be able to control the attitude of the observatory as a whole to point at a fixed angular location relative to an ideal orbit track and nadir at any given point on orbit; 3) it must be able to slew and hold attitude to observe Earth from both sides of the orbit plane. For orbit control, there is sufficient fuel to accommodate at least 5 years of operations at the chosen altitude. The propulsion system is agile enough to perform the necessary small orbit control maneuvers every few days that are required to maintain the strict orbital tube requirements. JPL augments the ISRO spacecraft capability with GPS receivers, providing GPS time message and a 1 pulse per second (pps) signal to the spacecraft and radar instruments.

The spacecraft design has been optimized to accommodate all key and driving requirements, and refined technical analyses show that predicted performance meets science needs. The solar arrays have the required capability, plus an extra string of cells for contingency. The NASA Ka-telecom system and ground network is sized to handle the throughput baseline up to 35 Tb per day, although the margins are tight for many of the elements of the data system, many of which are part of the ground system. The ISRO system is sized to handle up to 8 Tb per day. For pointing control, rigid-body analysis shows that the system is controllable to the required accuracy.

Credit: trekandshoot/Shutterstock.

5 MISSION DATA PRODUCTS

THE NISAR DATA PRODUCT LEVELS HAVE BEEN DEFINED IN ACCORDANCE WITH THE NASA EARTH OBSERVATION SYSTEM DATA AND INFORMATION SYSTEM (EOSDIS) CRITERIA FOR SCIENCE PRODUCT PROCESSING LEVEL CLASSIFICATION.

NISAR data products are organized by product level, with Level 0 being a raw form of data and Level 3 being a geocoded derived science product in physical units. The NISAR L0A product is the received raw data with metadata added to support storage at the DAAC. The NISAR L0B product is a refined version of the radar signal data with transmission artifacts removed. NISAR L1 products include all products in radar (range-Doppler) coordinates, including the range-Doppler single look complex (SLC), range-Doppler wrapped nearest-time interferograms (RIFG), range-Doppler unwrapped (RUNW), and range-Doppler pixel offsets (ROFF). The NISAR L2 products are provided in geocoded map grids and include geocoded single look complex (GSLC), geocoded polarimetric covariance matrix (GCOV), geocoded unwrapped (GUNW), and geocoded pixel offsets (GOFF) products. The NISAR Science Data System (SDS) team is responsible for generating the L-band L0–L2 products (Table 5-1), and the NISAR Project Science and Science Teams generate the L3 products at selected calibration/validation sites distributed globally. In addition to L0–L2 products, the NISAR SDS will generate L3 soil moisture products at a near-global scale over all land masses excluding Antarctica and Greenland.

The products principally designed for solid Earth deformation and ice sheet cryospheric science include RSLC, RIFG, RUNW, ROFF, GSLC, and GUNW. Sea ice velocity L3 products will be derived using GCOV products.

The products principally designed for ecosystems science include GSLC and GCOV. The L2 GSLC product, generated from the L1 RSLC product, enables users to perform amplitude as well as interferometric analysis directly on a geocoded grid. Depending on the polarimetric acquisition mode (single, dual, or quad), the GSLC product can have 1, 2, or 4 complex-valued layers for each of the possible main and side bands. Based on the polarimetric acquisition mode and processing option (symmetrized or non-symmetrized cross-polarimetric channel), the polarimetric covariance matrix can have 1, 3, or 6 complex-valued layers. These products primarily support the NISAR ecosystem requirements of biomass estimation, disturbance detection, inundation mapping, and crop area delineation, as well as additional ecosystem and land-cover applications that may be developed during the NISAR mission. Ancillary data needed to create these products, such as orbits and calibration files, are included in the metadata layers of these products. For interferometry, the dense field of range and azimuth offsets, suitable for local resampling to account for substantial motion between scenes, are also included as metadata at L1 and L2. The data layer descriptions are included in the latest version of the NASA SDS Product Description Document, available at the ASF DAAC (https://nisar.asf.earthdatacloud.nasa.gov/NISAR-SAMPLE-DATA/DOCS/NISAR_D-95672A_NASA_SDS_Product_

Description_20250523_w-sigs.pdf), and the individual NASA SDS Product Specification documents, available on the NISAR website (https://nisar.jpl.nasa.gov/data/sample-data/).

The NISAR L0-L2 products consist of two major components: (1) science products comprising self-describing binary data and metadata, and (2) quality assurance (QA) products. The science data product is based on the HDF5 specification (https://support.hdfgroup.org/documentation/hdf5/latest/_s_p_e_c.html) that has the following advantages:

- Open, self-describing format
- Supports hierarchical tree data arrangement
- Supported by GIS and database software
- Provides flexibility to support any binary data format making it scalable to support all levels of NISAR products
- Widely used for a range of NASA EOS missions (e.g., MODIS, AIRS, TRMM, CERES, MISR, GSSTF, and Aquarius)

In general, each L0–L2 product is distributed as a single HDF5 granule. The NISAR QA products include human and machine readable reports on the quality metrics of the products as well as a high-level summary of the QA checks, plots, and

TABLE 5-1. NISAR L-BAND MISSION PRODUCTS

PRODUCT LEVEL	PRODUCT NAME	SCOPE	DESCRIPTIONS
L0	Incoming Data (Raw)	Global	Raw downlinked data delivered to SDS with metadata added for archiving.
	Radar Signal Data (RSD)	Global	Corrected, aligned, and time-ordered radar pulse data derived from RAW products and used for further processing
L1	Range-Doppler Single Look Complex (RSLC)	Global	Standard L1 product that will be used to generate all higher level products.
	Nearest-Time Interferogram (RIFG)	Antarctica and Greenland. Nearest pair in time and co-pol channels only.	Multi-looked flattened (WGS84 ellipsoid) interferogram with topographic fringes in range-Doppler coordinates.
	Nearest-Time Unwrapped Interferogram (RUNW)	Global except Antarctica and Greenland. Nearest pair in time and co-pol channels only.	Multi-looked, unwrapped differential Interferogram in range-Doppler coordinates.
	Range-Doppler Pixel Offsets (ROFF)	Antarctica and Greenland. Nearest pair in time and co-pol channels only.	Pixel offsets obtained from cross correlation of RSLC images in radar coordinates.
L2	Geocoded SLC (GSLC)	Global and all channels.	Geocoded L1 SLC product using the MOE state vectors and a Digital Elevation Model (DEM).
	Geocoded Nearest- Time Unwrapped Interferogram (GUNW)	Global except Antarctica and Greenland. Nearest pair in time and co-pol channels only.	Geocoded multi-looked unwrapped differential interferogram. Same as UNW but resampled onto a UTM grid.
	Geocoded Polarimetric Covariance Matrix (GCOV)	Global and all channels. Single/dual/quad pol.	Geocoded polarimetric covariance matrix (1, 3, or 6 layers) using the MOE state vectors and a DEM.
L3	Geocoded Soil Moisture (GSM)	Global except Antarctica and Greenland.	Soil moisture derived from radar backscatter on a 200m grid except in the Sahara, which is on a 400m grid.

FIGURE 5-1

Data Product Levels. Products through Level 2 will be produced for the entire mission data set. Products at higher levels will be produced by the science team for calibration and validation purposes.

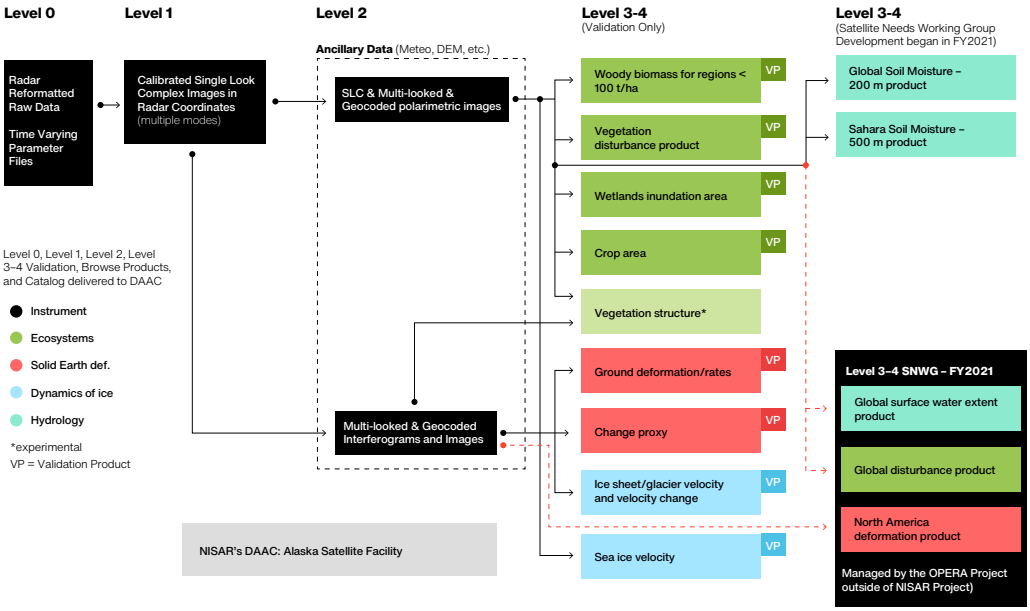

low resolution browse image for each product.

Other than the soil moisture product, Level 3–4 processing will be conducted by the NISAR science team. Measurements will include biomass, disturbance/recovery maps, ice and land displacements, and velocity fields, all in geocoded coordinates. These products will also be delivered to the NASA DAAC; however, they will be generated only over selected regions of the world for calibration and validation purposes. Figure 5-1 shows the overall data products that will be generated by the project and delivered to the NASA DAAC.

5.1 L0 DATA PRODUCTS

The NISAR SDS will produce two types of Level 0 data. The L0A product is the received raw data with metadata added to support storage at the DAAC. Although the L0A dataset will be publicly available, this downlinked raw data will not be directly usable by the scientific community. The L0B product is a refined version of the radar signal data with transmission artifacts removed. The project will process all L- and S-band data acquired over the NASA downlink network to L0B, which is a reformatted, organized, and regularized version of the instrument science data coming down in the science telemetry. L0B data are a basic input to a SAR image formation processor and is typically the starting point for many SAR scientists.

INCOMING RAW DATA (L0A)

The L0A data product represents a collection of time-tagged raw data packets and telemetry information downlinked to the GDS, and typically do not have any overlap. The data are ordered in time, but not all communication artifacts, missing data, and synchronization errors are necessarily corrected. The raw signal data from the primary imaging band and the auxiliary 5 MHz sub-band are interleaved in this product and are not yet decomposed into corresponding I/Q channels. A multi-polarization L0A product will contain layers corresponding to each polarization (for both the primary and auxiliary band). Data are compressed by the radar using a block floating point quantization algorithm and the L0A product will maintain this compressed state.

Each L0A raw data product will be reduced to a

L0B product for use in further processing by the SDS. Each radar pulse will be tagged with its own metadata (e.g., receive time and pulse repitition frequency [PRF]). The data are arranged on an increasing azimuth time and increasing slant range grid. The downlinked data are packaged into L0A products on reception. L0A data are primarily for archive purposes; it is anticipated that users who want to focus the raw data to SAR imagery will start with L0B.

RADAR SIGNAL DATA (L0B)

The L0B product consists of aligned and filled raw radar signal data that are used to derive higher level science products. The block floating point quantized samples from L0A raw data product are decoded and packed into complete range lines in the L0B product. Sampling Window Start Time (SWST) shifts for the radar pulses are aligned and each pulse is annotated with mode and PRF changes as well as missing data information. The following metadata are added at this stage to assist in further processing into L1/L2 products:

- Nominal pulse/chirp characteristics and actual replicas of transmitted chirps
- Doppler centroid estimate
- Orbit and attitude data
- Geographic coordinate boundaries
- I/Q bias estimates
- Calibration antenna patterns and related information
- Calibration noise records
- Channel delay calibration estimates
- Polarimetric compensation matrix

The L0A-to-L0B processor aligns or rearranges the raw radar signal data to ease further processing and does not modify the actual signal data (i.e., operations like radio frequency interference [RFI] removal are not applied at this stage). Raw signal data and metadata corresponding to the main imaging band and the auxiliary 5 MHz sub-band are stored in separate data groups within the HDF5 product granule. A multi-polarization L0B product will contain layers corresponding to each polarization (for both the primary and auxiliary band). Each radar pulse will be tagged with its own metadata (e.g., receive time and PRF). The data are arranged on an increasing azimuth time and increasing slant range grid. The L0B product is the primary input for L1 product generation.

5.2 L1 DATA PRODUCTS

There are multiple L1 products to support the NISAR science disciplines. The L1 RSLC data product is the output of a SAR image formation processor. It is calibrated for time and phase delays in the radar and propagation path (using a static troposphere model) and for antenna pattern effects and measured pointing offsets. Each science target may require a different resolution and set of polarizations, hence the product will accommodate multiple modes. This product is created at the fullest resolution possible, given the range bandwidth of the mode and the size of the antenna. Other L1 data products, including interferograms and pixel offsets, will be derived from the SLC product. The interferograms and correlation maps will be formed from nearest-in-time pairs of data sets. Given N interferometrically viable data sets, one can produce N(N-1)/2 unique interferograms, an impractically large number of interferograms to produce and store given that not all are typically used in scientific analysis. Forming nearest-in-time pairs yields only N-1 interferograms, each of which is typically used in further analysis. The open source NISAR processing software can be used to augment the nearest-neighbor interferograms to form a more redundant network. The SLC product contains look up tables for radiometric ellipsoid correction. The project plans to use the Medium-fidelity Orbit Ephemeris (MOE) product, available within one day of acquisition for L1 and L2 processing, as it is nearly as accurate as the final orbit product and reduces processing latency.

RANGE-DOPPLER SINGLE LOOK COMPLEX (RSLC)

This product refers to the standard range-Doppler geometry SLC imagery that are operationally delivered by SAR sensors around the world. The L1 RSLC product (Figure 5-2) will be distributed in the zero-Doppler radar geometry convention. The L0B-to-L1 processor will handle PRF changes within a data granule and the output imagery will be on a grid characterized by a fixed set of starting slant range, starting azimuth time, azimuth time interval, and slant range spacing values. All the primary image layers for a multi-polarization or multi-frequency product will be generated on a common azimuth time-slant range grid. For many NISAR L-band science acquisition modes with a 5 MHz side-band the dimension of the RSLC in azimuth direction is identical between the main and side bands. The dimension of the 5 MHz in range direction is 1/4th of the 20 MHz data and 1/8th of 40 MHz data.

The L1 RSLC is used to derive other L1 and L2 products. This product will contain individual binary raster layers representing complex signal return for each polarization layer. The RSLC data corresponding to the auxiliary 5 MHz sub-band is stored in a similar format but in a separate data group within the HDF5 product granule. The RSLC product is also packed with input, instrument, and processing facility information; processing, calibration, and noise parameters; geolocation grid; and data quality flags. The RSLC product complex floating point backscatter is Beta-0 (β^0) with secondary layer LUTs provided to convert to Sigma-0 (σ^0) and Gamma-0 (γ^0).

NEAREST-TIME RANGE-DOPPLER INTERFEROGRAM (RIFG)

The L1 RIFG product represents the ellipsoid height corrected, wrapped interferogram generated from two L1 range-Doppler RSLCs in the range-Doppler geometry of the earlier acquisition and flattened for ellipsoid and topographic phase. The data are arranged on a uniformly spaced, increasing zero-Doppler azimuth time and increasing slant range grid. The RIFG product is primarily meant for detecting grounding lines and is only generated for acquisitions over Antarctica, Greenland, and selected mountain glaciers. The products are multi-looked to a posting of 30 meters on the ground.

The L1 RIFG product contains individual binary rasters for the coherence and the complex interferogram for each co-pol channel. The RIFG products are produced from a pair of RSLCs coregistered using a Digital Elevation Model (DEM) and the best available orbit ephemeris. This coregistration is further refined by using incoherent cross-correlation on the pair of coarsely coregistered RSLCs. The RIFG product includes the slant range and along-track sub-pixel offsets obtained from incoherent cross-correlation.

NEAREST-TIME RANGE-DOPPLER UNWRAPPED INTERFEROGRAM (RUNW)

The L1 RUNW product represents the unwrapped, multilooked differential interferogram generated from two L1 range-Doppler RSLCs in the range-Doppler geometry of the earlier acquisition. The data are arranged on a uniformly spaced, increasing zero-Doppler azimuth time and increasing slant range grid. For every ingested L1 RSLC product, an archived L1 RSLC product corresponding to the same imaging geometry and nearest in time is identified and a RUNW processing job is launched. The RUNW product is generated between co-pol channels over cryosphere regions including Greenland, Antarctica, and selected mountain glaciers. DEMs will be used for producing these data products, which are multi-looked to a posting of 80 meters on the ground.

The L1 RUNW product will contain individual binary raster layers representing single precision floating point unwrapped phase for each co-pol channel. In addition, byte layers with quantized coherence, geometry masks and connected component information, and floating-point layers

corresponding to the amplitudes of reference and secondary acquisitions are included in the HDF5 granule. In addition to the metadata of the original L1 SLC granules, lookup tables for parallel and perpendicular baseline components, range, and azimuth offsets are also included. Additional metadata will include lookup tables for various phase corrections (e.g., solid Earth tides, European Centre for Medium-Range Weather Forecasts [ECMWF] tropostatic dry delay and ECMWF tropostatic wet delay, ionospheric phase screen). These phase corrections are not applied to the data but are available to users for application in post-processing workflows.

NEAREST-TIME RANGE-DOPPLER PIXEL OFFSETS (ROFF)

The ROFF product contains a collection of dense pixel offsets layers obtained from incoherent speckle tracking on pairs of coregistered RSLC products in the Range Doppler geometry of the earlier (i.e., "reference") RSLC product. The RSLC products used to produce ROFF are aligned with geometrical coregistration using the orbit ephemerides and a DEM. The ROFF products contain 3 layers of pixel offsets in range and azimuth direction obtained with different cross correlation configurations to capture the motion at different resolutions. Since the geometrical separation between the reference and secondary RSLCs are compensated during the coregistration process, the estimated pixel offsets mostly represent movements of targets on ground between the acquisition times of the reference and secondary images. The offsets products are especially of great interest when the large movements of ground targets decorrelate the interferometric signal and make it challenging to estimate reliable displacement with interferometric phase. Moreover, while interferometric phase is only sensitive to movements in slant range direction, the pixel offsets allow for the estimation of large movement in azimuth direction. The ROFF product is primarily meant for cryosphere applications, and it is generated for LSAR acquisitions over Antarctica, Greenland, and pre-identified mountain glaciers.

5.3 L2 DATA PRODUCTS

Level 2 products are geocoded and include GSLC, GCOV, GUNW, and GOFF. The GSLC product contains look-up tables for radiometric ellipsoid correction. The GCOV product contains radiometric terrain corrected SAR backscatter and includes a conversion layer to convert between Gamma-0 and Sigma-0. All L2 geocoded products contain three-dimensional metadata cubes to represent imaging geometry parameters at low spatial resolution as a function of height. This allows users to interpolate the three-dimensional cube using a DEM to obtain a two-dimensional geometry layer at the posting of the product.

All geocoded products are precisely geolocated on a map coordinate system by accounting for tropospheric delay, ionospheric delay, and solid Earth. The tropospheric delay is compensated using a static tropospheric model during focusing of the raw data. The ionospheric Total Electrons Content (TEC) between NISAR and targets on the ground are estimated using Global Navigation Satellite System (GNSS) receivers on ground and the dual frequency GPS receiver on the NISAR platform. The GNSS receivers on the ground estimate total TEC between GNSS satellites and ground while the GPS receiver on NISAR estimates above orbit TEC between the NISAR altitude and GPS satellites. The difference of the two TEC estimates gives below-orbit TEC, which is required to estimate ionospheric delay for precise geocoding.

GEOCODED SINGLE LOOK COMPLEX (GSLC)

The L2 GSLC product (Figure 5-3) is derived from the L1 range-Doppler SLC product and projected onto a geocoded map grid. The data are arranged on a uniformly spaced, north-south and west-east aligned UTM/WGS84 grid at mid latitudes and a polar stereographic system at high latitudes. The

spacing of the GSLC product in east and north directions will be comparable to the full resolution original L1 RSLC product. The GSLC product can be directly overlaid on a map or combined with other similar GSLC products to derive interferograms and change maps, for example.

The L2 GSLC product will contain individual binary raster layers representing complex signal return for each polarization layer. The GSLC product will be produced globally.

GEOCODED NEAREST-TIME UNWRAPPED INTERFEROGRAM (GUNW)

The L2 GUNW product (Figure 5-4) is derived from the L2 RUNW product by projecting it onto a geocoded grid at 80 meter posting. The data are arranged on a uniformly spaced, north-south and west-east aligned UTM/WGS84 grid at mid latitudes. Similar to other L2 products, the GUNW at polar regions is produced on a polar stereographic projection system.

GEOCODED POLARIMETRIC COVARIANCE MATRIX (GCOV)

The L2 GCOV product (Figure 5-5) is derived from the L1 RSLC product providing terrain-corrected polarimetric covariance projected onto a predefined Universal Transverse Mercator (UTM) or polar stereographic projection system grid. The GCOV product is distributed in a lexicographic polarimetric basis. The layer representing terrain-corrected backscatter distributed with the GCOV product is γ^0.

GEOCODED PIXEL OFFSETS (GOFF)

The GOFF product is derived from the ROFF product by projecting the range-Doppler pixel offsets layers into the UTM/Polar Stereographic projection system.

The GOFF product contains individual binary raster layers representing the sub-pixel offset shifts between a pair of coregistered RSLC products. Pixel offsets layers within a GOFF granule share the same starting pixel and are referenced to geographic coordinates. Pixel offset layers are distributed without performing any conventional post-processing operation, i.e., layers might contain offsets outliers and are not low pass filtered to reduce noise in the data.

The GOFF product is primarily meant for cryosphere applications and is only generated for L-SAR acquisitions over Antarctica, Greenland, and pre-selected mountain glaciers.

METADATA CUBES

All L1 and L2 NISAR L-band products store slowly spatially varying ancillary data in a metadata cube to reduce the size of products. Metadata cubes are represented as three-dimensional arrays in the NISAR product HDF5. The axes of the array are interpreted as (height, increasing azimuth time, and increasing slant range) in case of radar geometry products and as (height, decreasing northing, and increasing easting) in case of geocoded products. The data are organized with height as the first axis. Each height layer is the same size. Metadata cubes have fixed coarse grid spacing (e.g., 1 km spacing, which is significantly coarser than the product spacing) and allow for easy merging when multiple products along the same imaging track are to be concatenated. The metadata cube also spans a field slightly larger than the original image product to allow users to interpolate data without introducing edge effects. The components of the radar Line Of Sight (LOS) vector, such as unit vector in east and north direction, incidence angle, and elevation angle, and components of the interferometric baseline including parallel and perpendicular baseline, are provided as metadata cubes.

5.4 L3 SOIL MOISTURE PRODUCT

The Level 3 Soil Moisture product will be produced globally on a best effort basis, over all land areas except for those covered by permanent ice cover or urban areas. Soil moisture retrievals will be performed in regions with

vegetation water content > 5 kg/m2, areas with high topographic relief, and during time periods of snow cover or precipitation, but such results will be flagged. The accuracy goal for the soil moisture retrievals is 0.06 m3/m3 for unflagged data. The soil moisture products will be made available on the 200-meter EASE-Grid 2.0, except for in the Sahara, where the resolution will be 400-meters, and will involve three retrieval layers generated using three independent algorithms. The products are accompanied by layers containing ancillary data used in each retrieval, including the aggregated version of the Level 2 polarimetric GCOV product and information necessary for reprojecting the soil moisture products onto coordinate systems.

5.5 DATA PRODUCT DELIVERY / HOW TO ACCESS NISAR DATA

One Earth Science Data Center (ESDC) has been designated by NASA's Earth Science Division to archive and distribute NISAR science data: the Alaska Satellite Facility (ASF). ASF Distributed Active Archive Center (ASF DAAC) will receive validated NISAR science data products from the NISAR SDS, along with algorithm source code and ancillary data used in deriving the products and provide long-term archiving and distribution services for the general public.

NISAR is required to begin delivering calibrated and validated L1–L2 science products to ASF DAAC within eight months after the end of the Commissioning. A beta release of L1–L2 data products will be delivered to ASF DAAC within 2 months after Commissioning. Validated L3 science products are required to be available for delivery to ASF DAAC within 6 months after Commissioning for displacement related products, and 12 months for ecosystems related products. The beta release of L3 data products will be delivered within 3 months after Commissioning for displacement related products, and 6 months for ecosystems related products. At the end of the L1–L2 and L3 Cal/Val activities, the data products will be reprocessed as needed using enhanced calibrated/validated algorithms, so that they become part of a consistently processed total mission data set.

ASF DAAC is responsible for permanent archiving and public distribution of the NISAR data products. The specialized data sets used to perform the Cal/Val of the L1–L3 science data products, and Cal/Val reports documenting the data quality and accuracy assessments resulting from the Cal/Val activities, will be delivered to ASF along with the validated L1–L3 science data products.

FIGURE 5-2

A NISAR sample RSLC product, focused from ALOS-1 raw data.

Fig. 5-2

FIGURE 5-3

NISAR sample GSLC product generated from the ALOS-1-derived RSLC sample product.

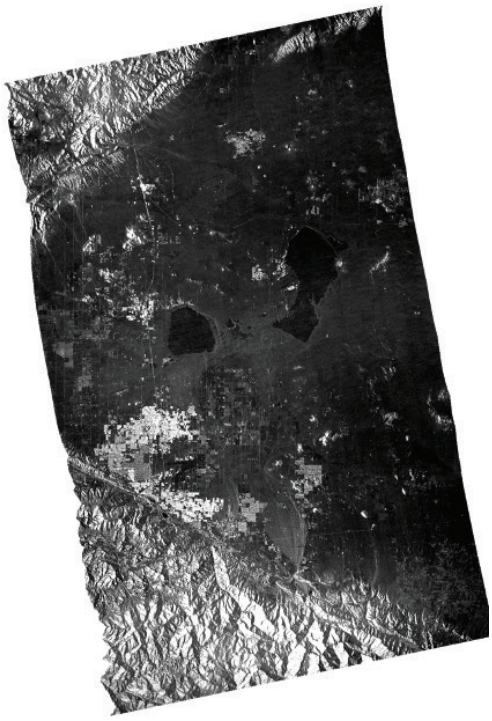

Fig. 5-3

FIGURE 5-4

NISAR sample GUNW product generated from the ALOS-1-derived RSLC sample product.

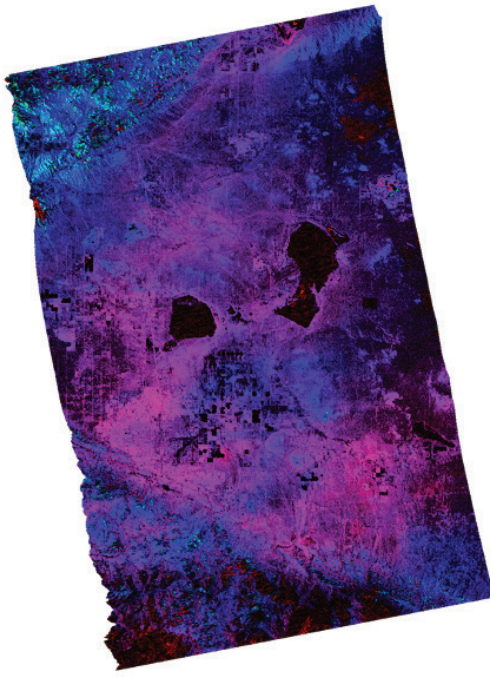

Fig. 5-4

FIGURE 5-5

NISAR sample GCOV product generated from the ALOS-1-derived RSLC sample product.

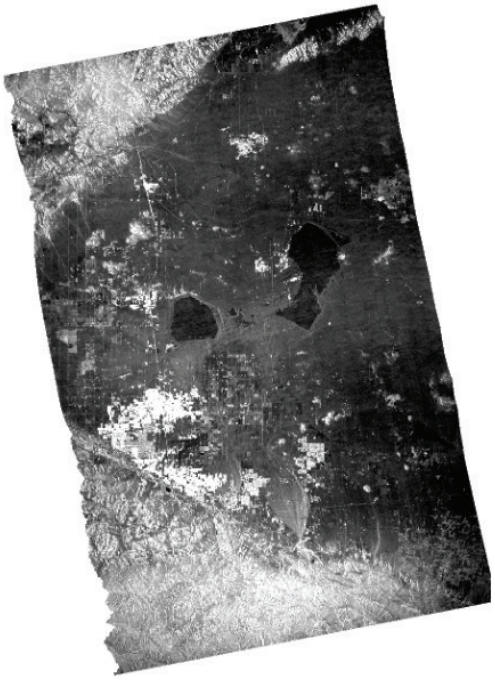

Fig. 5-5

Credit: trekandshoot/Shutterstock..

6 SCIENCE REQUIREMENTS VALIDATION: THEORY AND METHODS

THE SCIENCE TEAM USES LEVEL 3/4 SCIENCE DATA PRODUCTS TO VALIDATE LEVEL 2 SCIENCE REQUIREMENTS.

This section describes the theoretical basis of the algorithms and associated data products that will be used to validate NISAR's Level 2 (L2) science requirements enumerated in Appendix D. Each science discipline (solid Earth, ecosystems, cryosphere, and soil moisture) has a different set of L2 requirements and is treated separately. Validation activities use a combination of standard Level 0-2 data products produced by the NISAR project, along with Level 3-4 data products generated by the science team for specific calibration and validation (Cal/Val) regions (Chapter 8). The Level 3 Algorithm Theoretical Basis Documents (ATBDs) and/or Jupyter Notebooks for each science discipline can be found on the NISAR website at https://science.nasa.gov/mission/nisar/.

6.1 SOLID EARTH SCIENCE

This section describes how the NISAR project will validate the Solid Earth Science Level 2 science requirements for secular deformation rates (Requirement 658), coseismic deformation (Requirement 660), transient deformation (Requirement 663), and permafrost deformation (Requirement 671). Since all four requirements specify a minimum standard for global coverage, their validation relies on demonstrating required measurement accuracy across Cal/Val regions that span a range of vegetation types, topographic relief, and deformation characteristics (see Chapter 8).

6.1.1 THEORETICAL BASIS OF ALGORITHM

APPROACH TO VALIDATING SOLID EARTH L2 REQUIREMENTS

Two different approaches will be used by the NISAR Science Team for validating the Solid Earth L2 requirements—depending on the availability of reference observations from GNSS stations or field surveys. Both approaches require separate validation on ascending and descending tracks to ensure that at least two components of motion are validated.

In the first approach (Method #1), InSAR-derived surface displacements will be compared with observations of surface motion from collocated continuous GNSS stations, or, in the case of permafrost validation, with direct field measurements from surveying techniques. Since all requirements are written in terms of relative displacements, this comparison is done using differences of differences (i.e., double differences) of InSAR and GNSS/field observables between GNSS/field station locations. For a GNSS/field station network of N stations, this will yield N(N-1)/2 distinct observations, distributed across a range of baseline distances. As discussed below, the methodology differs slightly if the comparison is performed using single interferograms (Requirement 663) versus using basis functions that are fit to time series derived from many interferograms (Requirements 658/660/671). In both cases, the underlying premise is that GNSS/field observations

provide much higher quality (i.e., lower noise) deformation estimates than does InSAR, albeit at a limited number of locations.

The second approach (Method #2) can be done without comparison to GNSS-observed displacements, but it is only appropriate for negligibly deforming regions. Here, the autocorrelation of noise in NISAR interferograms will be examined under the assumption that surface deformation is zero at all relevant spatial scales. Method #2 involves differencing InSAR displacement observations between a large number of randomly chosen pixel pairs and confirming that the estimates are statistically consistent with no deformation within the scene.

L2 REQUIREMENT 658 – SECULAR DEFORMATION RATE

Validation of secular deformation rates (or velocities) begins with an InSAR line-of-sight (LOS) displacement time series, from which an LOS velocity will be estimated for each pixel in the InSAR scene. Although the requirement specifies that the validation spans 3 years of data, the validation can be performed for periods shorter than 3 years if annual effects are mitigated by using data that span multiples of 1 year, or by explicitly modeling and removing seasonal displacements.

The relative InSAR LOS velocity between any two pixels in the InSAR scene is simply the difference in velocities at those pixels. Validation Method #1 uses relative InSAR vector velocities between pixels collocated with GNSS stations <50 km apart. The accompanying relative GNSS LOS velocities are generated by taking the 3-component GNSS position time series, projecting them into the InSAR LOS direction, estimating the GNSS LOS velocities, and differencing the GNSS LOS velocities between the same station pairs. To validate NISAR's 2 mm/yr velocity target, InSAR and GNSS relative velocity estimates for all station pairs are differenced to form a set of residuals, and the residuals are checked to see if 68.2% (i.e., 1 standard deviation about the mean) fall within ±2 mm/yr.

Validation Method #2 is identical to Method #1 except that the relative velocities are determined for random pairs of InSAR pixels within a scene, and the InSAR LOS velocity differences are used directly for the validation.

L2 REQUIREMENT 660 – COSEISMIC DISPLACEMENTS

To validate NISAR's ability to recover relative coseismic displacements of 100 mm or larger, surface displacement offsets will be estimated from InSAR and GNSS time series spanning significant earthquakes. InSAR (LOS) displacements are used directly in this analysis, and GNSS 3-component displacements are projected into the LOS direction to be geometrically consistent. InSAR and GNSS displacement time series are then modeled using a set of standard basis functions, which includes a velocity term, Heaviside step functions centered at the time of any earthquakes, and optional postseismic and seasonal terms. Coseismic displacements are assumed to be captured entirely by the Heaviside term, and the amplitude of the step is used as the displacement offset.

The relative InSAR coseismic displacement between any two pixels in the InSAR scene is simply the difference in the Heaviside step amplitude at those pixels for the earthquake being analyzed. Validation Method #1 uses relative InSAR coseismic displacements between pixels collocated with GNSS stations <50 km apart. The accompanying relative GNSS coseismic displacements are the Heaviside amplitude difference between the same station pairs.

To validate NISAR's fulfillment of the coseismic requirement, the InSAR and GNSS relative coseismic displacements for all station pairs are differenced to form a set of residuals, the baseline distance L between stations is calculated, and the residuals are binned in 5 km baseline increments out to 50 km. The validation

target is hit if 68.2% of the residual values fall within $\pm 4(1 + L^{1/2})$ mm over 0.1 km < L < 50 km (e.g., within ±5 mm at 0.1 km and within ±32 mm at 50 km). Validation approach #2 is similar to approach #1 except that the relative coseismic displacements are determined for random pairs of InSAR pixels within a scene that does not include a significant earthquake, and the statistics are calculated directly from the InSAR differences.

L2 REQUIREMENT 663 – TRANSIENT DISPLACEMENTS

Validation of NISAR's L2 requirements for transient displacement will use operational 12-day unwrapped interferograms to provide (LOS) displacement estimates across target Cal/Val regions. Method #1 will generate relative InSAR displacements by differencing 12-day displacement values between pixels collocated with GNSS stations < 50 km apart. The accompanying relative GNSS LOS displacements will be generated by taking the 3-component GNSS position time series at those station locations, projecting them into the InSAR LOS direction, estimating the GNSS offset across the 12-day span of the interferogram, and differencing the GNSS LOS positions between the same station pairs. The validation will be the same as described for the coseismic requirement, except that the accuracy specification is $\pm 3(1 + L^{1/2})$ mm over 0.1 km < L < 50 km.

To validate the noise in individual interferograms in Method #2, interferograms over a set of non-deforming sites will be utilized. In practice, characterization of transient deformation will usually be improved by examining longer time series of displacement. The approach described here validates the requirement that short-timescale or temporally complex transients can be characterized using a single interferogram.

L2 REQUIREMENT 671 – PERMAFROST DISPLACEMENT

Validation of NISAR's L2 requirement for permafrost displacement will use comparison of time series of snow-free 12-day interferograms and field observations of surface displacement at specific sites. The permafrost requirement states that NISAR will measure surface deformation in permafrost areas during snow-free months, with a target of 80% of measurements achieving an accuracy of or better than $4(1 + L^{1/2})$ mm for any 90-day interval, over length scales of 0.1 km < L < 50 km. In practice, snow-free images are often only available during summer months for many permafrost areas.

On permafrost terrain, these summer displacements (primarily subsidence) can vary by centimeters across the 100 m spatial scale of NISAR pixels. Therefore, the strategy for evaluating the Method #1 accuracy of surface displacement on permafrost relies on increasing the quantity of measurements at a single site far beyond what a continuous GNSS station could provide. Four sites have been established in the North Slope of Alaska along the Dalton Highway. At each of these sites, surface elevations relative to a fixed benchmark are measured at the start and end of every summer, spanning approximately 90 days. Each site contains three 100 m transects, spaced 50 m apart, and sampled every 2 m along each transect, for a grand total of 153 sample points within the 100×100 m^2 site. Surface elevations are measured by a field team using both differential GNSS as well as a digital levelling technique. For the Method #1 validation, the time series of InSAR displacements is fit to a continuous function using a permafrost focused spline-fitting algorithm (Zwieback and Meyer, 2021b), and then the difference of InSAR displacements between each field site is compared to the difference measured during the field surveys. Validation Method #2 is also performed for a 90-day time series in this scene, with pixel pairs randomly drawn from within the scene.

6.1.2 IMPLEMENTATION APPROACH FOR ALGORITHM

GENERALIZED TIME SERIES ANALYSIS

The InSAR and GNSS/field data comparisons described above for Requirements 658, 660, and 671 (but not for Requirement 663, which uses single interferograms) will be performed in the framework of generalized time series analysis, whereby information in each time series is characterized by one or more underlying basis functions. The problem is cast as an overdetermined least squares (LSQ) estimation problem, from which parameters can be inferred for the simultaneous fit of various components to the time series, on a station-by-station or pixel-by-pixel basis.

These components – which include secular velocities, seasonal sinusoids, temporal offsets, spline-fits, and post-seismic exponential decay – represent much of the non-stochastic variance in the time series and are well-suited to the specific validation targets. For instance, for Requirements 658 (secular deformation) and 671 (permafrost displacement), the velocity component of these fits will be used, while for Requirement 660 (coseismic deformation) the velocity, Heaviside (instantaneous step), and exponential/logarithmic components will be used. To perform the validations, estimates of the fit parameters for these functions, rather than the raw time series themselves, will be used for the statistical comparisons of InSAR and GNSS/field observations.

The time series analysis will be performed using Miami INsar Time-series software in Python (MintPy; Yunjun et al., 2019), which is openly

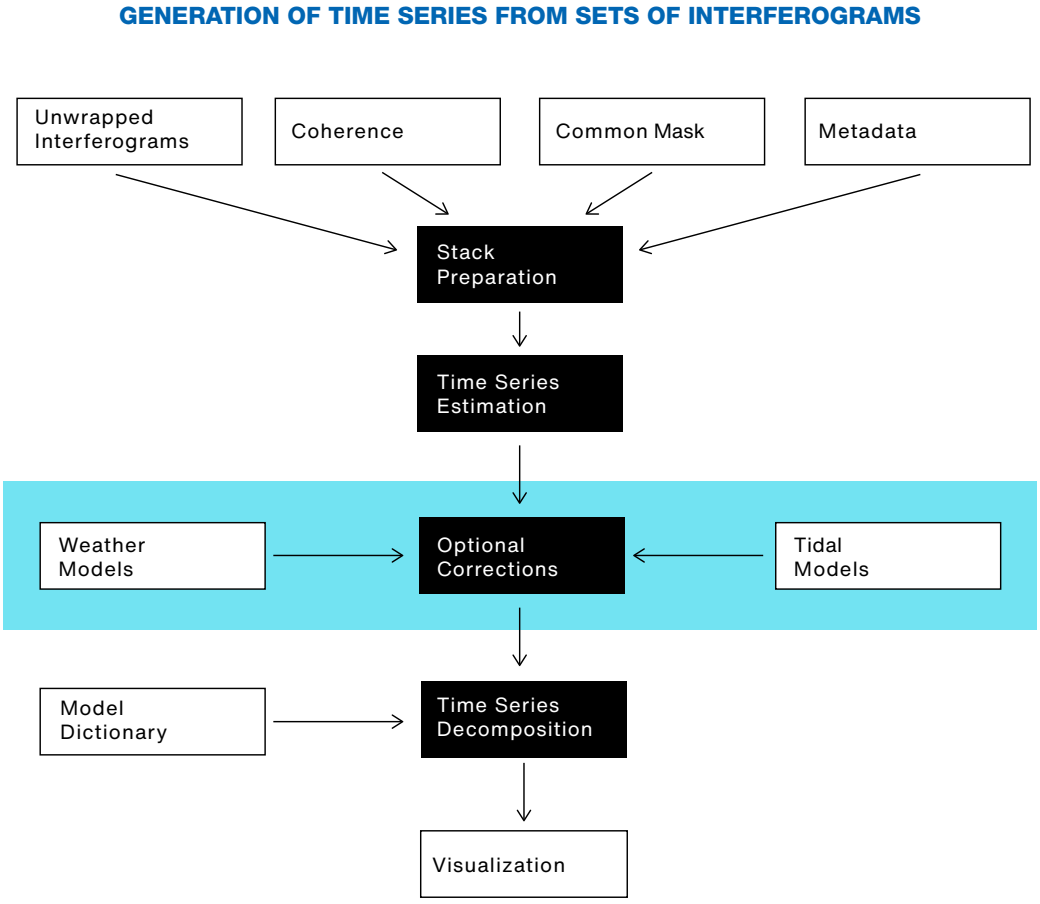

FIGURE 6-1

NISAR L3 product generation workflow for solid Earth.

available via GitHub. The L3 product generation workflow (Fig. 6-1) includes the four steps below, currently implemented as a set of Jupyter Notebooks publicly available on GitHub (https://github.com/nisar-solid/ATBD).

INSAR STACK PREPARATION

In the initial processing step, L2 unwrapped interferograms within the validation period are gathered, organized, and reduced to a common grid for analysis. These interferograms can include a range of temporal baselines, but at a minimum all nearest-neighbor (i.e., 12-day) interferograms are included. For operational NISAR processing, the following are used in the preparation of this interferogram "stack":

- Geocoded unwrapped interferograms (GUNWs)
- Corresponding coherence layers
- Corresponding ionospheric phase correction layers
- Perpendicular baseline associated with the interferograms
- A radar simulation file containing the pixel elevations
- Radar incidence and azimuth angles
- Shadow, layover, and land/water mask layers corresponding to the interferograms

In the current concept, L2 data will be provided as coregistered stacks of unwrapped interferograms. Hence, no separate coregistration is planned during stack preparation. The output of the stack preparation step is a self-contained HDF5 product that is used in the remainder of the processing workflow.

TIME SERIES ESTIMATION AND PARAMETERIZATION

The time series (i.e., the unfiltered displacement of each pixel vs. time) is estimated from the processed stack using a small-baseline subset (SBAS; Bernardino et al., 2002) approach. Since we expect high-quality orbital control for NISAR and anticipate that the set of interferograms will typically include all nearest-neighbor (i.e., ~12-day) and skip-1 (i.e., ~24-day) interferograms, the SBAS step should be somewhat trivial. The ionospheric phase corrections can be applied to the individual interferograms before the SBAS inversion, or a second SBAS inversion can be applied to the pair-estimated ionospheric phase corrections to obtain and apply the corrections to the dates of the displacement time series. We expect that ionospheric phase corrections will be necessary to meet the science requirements for the L-band NISAR data (see Chapter 7).

OPTIONAL CORRECTIONS

Phase distortions related to solid Earth and ocean tidal effects, orbital errors, and temporal variations in the vertical stratification of the atmosphere can be mitigated using various approaches. MintPy provides functionality for phase deramping and the removal of solid Earth tides and tropospheric delay, but it is expected that these corrections will not be needed to validate the mission requirements. All but the solid Earth tide correction are already included as options in the Jupyter Notebook implementations of the solid Earth requirement validation, so they can be easily applied if needed.

6.1-1
$$U(t) = a + vt + c_1 \cos(\omega_1 t - \phi_1) + c_2 \cos(\omega_2 t - \phi_2) + \sum_{j=1}^{N_{\text{eq}}} (h_j + f_j F_j(t - t_j)) H(t - t_j) + \frac{B_\perp(t)}{R \sin\theta} \Delta z + \text{residual}$$

DECOMPOSITION OF INSAR TIME SERIES INTO BASIS FUNCTIONS

Given a time series of InSAR LOS displacements, the observations for a given pixel, U(t), can be parameterized as:

which includes a constant offset (*a*), velocity (*v*), and the amplitudes (*c*) and phases (φ) of annual (ω_1) and semiannual (ω_2) sinusoidal terms. Where needed, we include additional complexity, such as coseismic and postseismic processes parameterized by Heaviside (step) functions *H* and postseismic functions F (the latter typically exponential and/or logarithmic) or spline parametrizations to describe seasonal permafrost displacement (Zwieback & Meyer; 2021b). $B_{\perp}(t)$, *R*, θ, and Δz are, respectively, the perpendicular component of the interferometric baseline relative to the first date, slant range distance, incidence angle, and topography error correction (e.g., Fattahi and Amelung, 2013) for the given pixel.

This parameterization of ground deformation has a long heritage in geodesy, originally in the analysis of GNSS time series and more recently with InSAR data (e.g., Blewitt, 2007, Hetland et al., 2012, Agram et al., 2013). For validation purposes, we perform the same parameterization on GNSS/field data time series used in the analysis, after projecting the GNSS/field observations into the InSAR line of sight.

For both the InSAR and GNSS time series parameterizations, we can write the problem as

$$Gm = d \qquad \textbf{6.1-2}$$

where G is the design matrix constructed from the functional terms in Equation 6.1-1 evaluated at the SAR image dates, m is the vector of model parameters (the coefficients in Equation 6.1-1), and d is the vector of SBAS displacements. For GNSS position time series, G, d, and m are evaluated daily, while for field data, they are evaluated when field data are acquired. Equation 6.1-2 can be solved using a least squares minimization of the L2-norm of the weighted misfit (e.g., Aster et al., 2018):

$$\operatorname{argmin}\ \phi(m) = (d - Gm)^T C_d^{-1} (d - Gm) \qquad \textbf{6.1-3}$$

Here, the data covariance matrix, C_d, is constructed using the empirical estimate of correlation from each contributing interferogram over the appropriate subset of pixels (i.e., masking out water bodies and regions that are decorrelated, such as agricultural fields) and superscript T denotes matrix transpose. Only pixels that are coherent in most interferograms are used as input to the construction of C_d. The solution for this overdetermined minimization problem can be written as

$$m_{\text{est}} = G^{-g} d \qquad \textbf{6.1-4}$$

where

$$G^{-g} = [G^T C_d^{-1} G]^{-1} G^T C_d^{-1} \qquad \textbf{6.1-5}$$

The full covariance on the estimated parameters, C_m, can be estimated from

$$C_m = G^{-g} C_d G^{-gT} \qquad \textbf{6.1-6}$$

With this formulation, we can obtain GPS/field-measured and InSAR velocity estimates and their formal uncertainties (including in areas where the expected answer is zero).

6.1.3 VALIDATION PRODUCTS

NISAR L3 Solid Earth products will include:

- Maps of locations where the InSAR and GNSS/field-observed data are being compared
- LOS displacement vs. time plots, showing:
  - InSAR time series using a standard SBAS approach (Berardino et al., 2002, Hooper, 2006)
  - The parameterized LSQ solution to the InSAR data
  - The corresponding time series of the LOS component of the GNSS/field time series

- The corresponding LSQ solution to the LOS component of the GNSS time/field series

- Tables and/or figures of comparisons showing LSQ solutions and error estimates of velocities and offsets as a function of baseline length from both InSAR and GNSS/field observations.

6.2 ECOSYSTEMS SCIENCE – BIOMASS

The NISAR L2 science requirement for aboveground biomass (AGB) is expressed as:

The NISAR project shall measure aboveground woody vegetation biomass annually at the hectare scale (1 ha) to an RMS accuracy of 20 Mg/ha for 80% of areas of biomass less than 100 Mg/ha.

AGB is a fundamental parameter for characterizing the spatial distribution of carbon in the biosphere. Biomass is defined as the total mass of living matter within a given unit of environmental area and is of interest for several applications. It is the raw material of food, fiber, and fuelwood. It is important for soil, fire, and water management. It is also related to the vegetation structure, which, in turn, influences the biological diversity of the planet (Bergen et al., 2009; Saatchi et al., 2007; Frolking et al., 2009). Biomass density (the quantity of biomass per unit area, or Mg, 106 grams of dry weight per ha) is used to determine the amount of carbon released to the atmosphere (as CO_2, CO, and CH_4 through burning and decay) when ecosystems are disturbed and is a strong indicator of the ecosystem function in terms of carbon sequestration through photosynthesis and primary production. Aboveground carbon density of woody vegetation is approximately 50% of the biomass with small variations depending on forest type and composition (IPCC, 2006). The current knowledge of the distribution and magnitude of terrestrial biomass is based almost entirely on ground measurements over an extremely small, and possibly biased, sample with almost no measurements in the southern hemisphere and equatorial regions (Schimel et al., 2015).

The NISAR mission's observing strategy is designed to provide sufficient coverage to estimate aboveground woody vegetation biomass at a spatial resolution of 100 m (1 ha), over the lifetime of the mission. This will provide fine-grain products of carbon stocks and changes required for understanding and quantifying the global carbon cycle. An upper threshold of 100 Mg/ha is set to reflect the sensitivity of L-band backscatter measurements to biomass and allows coverage of more than 50% of the global forests and the entire area of other woody vegetation (FRA, 2010). This sensitivity will allow NISAR to quantify the carbon stocks and changes of the most dynamic and variable component of global vegetation and to provide significant contribution to the global carbon cycle and climate science (Houghton et al., 2009; Saatchi et al., 2011; Harris et al., 2012).

6.2.1 THEORETICAL BASIS OF ALGORITHM

Because of its sensitivity to volume scattering and dielectric contrast, SAR backscatter measurements are sensitive to vegetation AGB. SAR observations from a spaceborne platform can thus be used for mapping and monitoring AGB on a global scale. However, the SAR backscatter sensitivity to AGB varies depending on the wavelength and geometry of the radar measurements, and is influenced by the surface topography, structure of vegetation, and environmental conditions such as soil moisture and vegetation phenology or moisture. The NISAR algorithm will make use of high-resolution and time series backscatter observations at dual-polarizations (HH and HV) to estimate AGB by compensating for the effects of environmental changes (soil and vegetation moisture and phenology) and structure (vegetation and surface topography).

Radar observations from vegetation have been studied for more than four decades both

theoretically and experimentally (Ulaby et al., 1984; Tsang et al., 1985; Ulaby and Dobson, 1989; Cloude, 2012). At L-band frequencies, these studies have shown that the radar measurements at different polarizations depend strongly on the AGB, but the relationship may vary depending on the structure and dielectric properties of vegetation components and underlying soil surface (Saatchi et al., 1994; Saatchi and McDonald,1997; Ulaby et al., 1990). The soil is most commonly described as a homogeneous medium having a complex dielectric constant, ε, that is a function of the volumetric soil moisture, mv, as well as the soil texture, temperature, and bulk density; several empirical models exist for this relationship (Dobson and Ulaby, 1986; Hallikainen et al., 1985; Mironov et al., 2004; Peplinski et al., 1995). Studies of soil surface scattering and soil moisture remote sensing at L-band have shown that the surface scattering can be expressed in terms of soil dielectric constant at the top 5 cm and the surface roughness characteristics in terms of root mean square (RMS) roughness height and spatial correlation length (Fung et al., 1992). In most SAR-related models for the remote sensing of soil surfaces, it is assumed that the effect of the spatial correlation is reduced significantly during the SAR azimuthal processing and multi-looking, and that the sensitivity of the radar signature to soil surface RMS height variation remains as the dominant surface structure influencing the surface scattering (Oh et al., 1992; Shi et al., 1997; Dubois et al., 1995; Bagdadi et al., 2002; Bryant et al., 2007). Other landscape features such as directional row or tillage may impact radar cross sections at 100 m spatial resolution but are assumed irrelevant in natural vegetation such as forests and shrublands.

A variety of approaches exist for describing vegetation media, including characterization of vegetation structure such as stalks, trunks, and leaves in terms of canonical cylindrical or disk shapes with specified size and orientation distributions in a set of vegetation layers, and with dielectric constants similar to live wood of trees and leaf material (Saatchi et al., 1994; Saatchi and McDonald, 1997; Saatchi and Moghaddam, 2000; Yueh et al., 1992; Lang et al., 1983; Karam et al. ,1992; Ulaby et al., 1990). The total L-band backscatter from vegetation arises from a combination of scattering and attenuation of individual canopy components (trunk, branch, and leaf) that can be represented as a sparse scattering medium (Lang, 1981; Chauhan et al., 1994). This approach requires knowledge of tree structure (size, orientation, and density; or equivalently species and biome), dielectric constant, and ground characteristics (RMS height, correlation length, and dielectric constant).

Simpler approaches only use the vegetation water content (VWC) to provide analytical forms for attenuation and scattering effects. The most common model used in microwave frequencies is the water cloud model that includes two scattering components from the vegetation volume and its underlying ground but ignores the volume-ground interaction (Attema and Ulaby, 1978). Such models are mainly applicable for higher frequency (C-band and above) characterization of the vegetation backscatter (Matzler, 1994; Ulaby and El-rayes, 1987). In this work, and for the fuller scattering model, the backscattering coefficient is expressed as the combination of three scattering components (Fig. 6-2). These are: 1) volume (vol) scattering, 2) volume and surface interaction (vol-surf), and 3) surface scattering (surf):

$$\sigma^0_{\mathrm{pq}} = \sigma^0_{\mathrm{pq\text{-}vol}} + \sigma^0_{\mathrm{pq\text{-}vol\text{-}surf}} + \sigma^0_{\mathrm{pq\text{-}surf}} \quad \textbf{6.2-1}$$

whre p and q denote polarization of transmitted and received radar signals, respectively. These can be either vertical (v) or horizontal (h) in a linear polarization radar system. The three dominant scattering terms are derived from basic electromagnetic theory by solving Maxwell's equations in a discrete random media (Saatchi and Lang, 1989; Lang, 1981; Tsang et al., 1985; Saatchi and McDonald, 1997; Chauhan et al., 1991).

FIGURE 6-2

Dominant scattering mechanisms of L-band SAR measurements of forest ecosystems contributing to NISAR dual-pol backscatter observations.

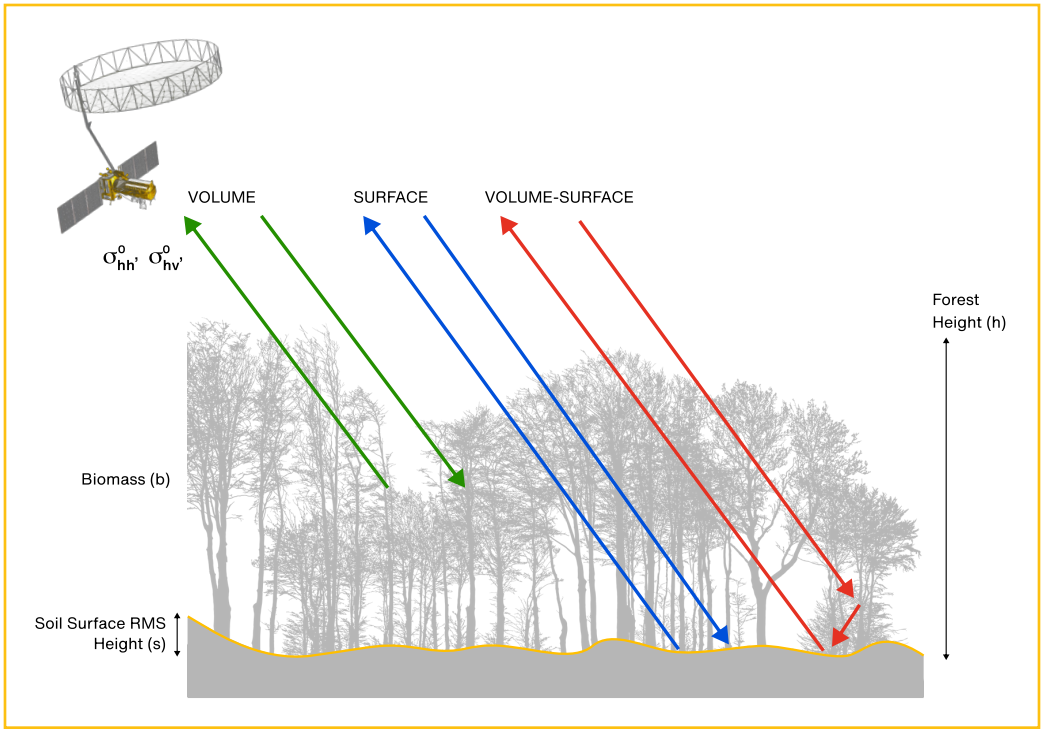

These terms can be expressed in a closed and semi-empirical form as:

$$\sigma^0_{\text{pq-vol}} = A_{\text{pq}} b^{\alpha_{\text{pq}}} \cos\theta \left[1 - \exp\left(-\frac{B_{\text{pq}} b^{\beta_{\text{pq}}}}{\cos\theta}\right)\right] \quad \textbf{6.2-2}$$

$$\sigma^0_{\text{pq-vol-surf}} = C_{\text{pq}} \Gamma_{\text{pq}}(\varepsilon, s) b^{\gamma_{\text{pq}}} \exp\left(-\frac{B_{\text{pq}} b^{\beta_{\text{pq}}}}{\cos\theta}\right) \quad \textbf{6.2-3}$$

$$\sigma^0_{\text{pq-surf}} = S_{\text{pq}}(\varepsilon, s) \exp\left(-\frac{B_{\text{pq}} b^{\beta_{\text{pq}}}}{\cos\theta}\right) \quad \textbf{6.2-4}$$

where $S_{pq}(\varepsilon,s)$ is the scattering from rough soil surface and can be represented by the semi-empirical model of Oh et al. (1992). The surface reflectivity $\Gamma_{pq}(\varepsilon,s)$ in the vol-surf backscatter is given by:

$$\Gamma_{\text{pq}} = \left|R_{\text{p}}(\varepsilon) R^*_{\text{q}}(\varepsilon)\right| \exp\left(-k^2 s^2 \cos^2\theta\right) \quad \textbf{6.2-5}$$

where $R_p(\varepsilon)$ is the Fresnel reflection coefficient of semi-infinite soil medium at polarization *p* with the dielectric constant of ε and exp ($-k^2s^2 \cos^2\theta$) represents the Kirchhoff's damping factor associated with the RMS height (*s*) of the surface (Fung et al., 1981), *k* is the wavenumber, θ is the local incidence angle, and *b* is the aboveground biomass density in the unit of Mg ha^{-1}. The Fresnel reflection coefficients in terms of complex dielectric constant (ε) are:

$$R_{\text{H}} = \frac{\cos\theta - \sqrt{\varepsilon - \sin^2\theta}}{\cos\theta + \sqrt{\varepsilon - \sin^2\theta}}$$

$$R_{\text{V}} = \frac{\varepsilon\cos\theta - \sqrt{\varepsilon - \sin^2\theta}}{\varepsilon\cos\theta + \sqrt{\varepsilon - \sin^2\theta}} \quad \textbf{6.2-6}$$

For the scattering from the rough soil surface $S_{pq}(\varepsilon,s)$, there are several models that can be adopted at the L-band frequency. The semi-empirical model developed by Oh et al. (1992) is used in the NISAR algorithm. This model is derived from a set of radar polarimetric measurements at multiple frequencies (L-, C-, and X-bands) and incidence angles (10°–70°) over rough soil surface with a variety of moisture (dielectric constants) and roughness (RMS height). The model provides good agreements with radar backscatter measurements in the field at L-band frequency and can be summarized as:

$$S_{\text{HH}} = g\sqrt{v}\cos^3\theta\left(\left|R_{\text{H}}\right|^2 + \left|R_{\text{V}}\right|^2\right)$$

$$S_{\text{VV}} = \frac{g}{\sqrt{v}}\cos^3\theta\left(\left|R_{\text{H}}\right|^2 + \left|R_{\text{V}}\right|^2\right)$$

$$S_{\text{HV}} = uS_{\text{VV}} \quad \textbf{6.2-7}$$

where

$$g = 0.7\left[1 - \exp(-0.65(ks))^{1.8}\right] \quad \textbf{6.2-7a}$$

$$u = 0.23\sqrt{\Gamma_0}\left[1 - \exp(-ks)\right] \quad \textbf{6.2-7b}$$

$$v = 1 - \left(\frac{2\theta}{\pi}\right)^{\frac{1}{3\Gamma_0}} \exp(-ks) \quad \textbf{6.2-7c}$$

and,

$$\Gamma_0 = \left|\frac{1-\sqrt{\varepsilon}}{1+\sqrt{\varepsilon}}\right|^2 \quad \textbf{6.2-7d}$$

is the Fresnel reflectivity of the surface at nadir.

The above model is used because it provides a simple expression as a function of soil dielectric constant and the surface RMS height. Other rough surface scattering models can also be used. Some examples are the Integral Equation Method (IEM) model, small perturbation method, and Kirchhoff approximation. These models have been compared and tested over study sites with detailed ground measurements to suggest that 1) the contribution from rough surface scattering is comparatively smaller than the volume and volume-surface contributions, particularly in the forested environments (therefore, the residual effects of the uncertainty of surface scattering characterization is small), 2) the Oh et al. (1992) model is preferred over other models because of its simplicity (based only on two parameters) and its direct link to backscattering coefficients of the soil dielectric constant instead of soil moisture, and 3) other models such as the small perturbation method have no cross polarized (HV) term and underestimate the measurements of radar backscatter over bare soil surfaces.

This model above is characterized by a set of coefficients (A_{pq}, B_{pq}, C_{pq}, and α_{pq}, β_{pq}, δ_{γ}) that depend on the polarization of the observation but are independent of the vegetation aboveground biomass (b), soil dielectric constant (ε), and surface roughness (s). These coefficients represent weighting factors for scattering and attenuation of vegetation through its various components (trunks, branches, leaves) that depend on their orientation and configurations (arrangements) within the forest canopy. The semi-empirical model separates the ground and vegetation parameters. The vegetation parameters are all combined into aboveground biomass (b) and ground parameters represented by surface dielectric constant (soil moisture) and roughness.

As discussed earlier, the algorithm model coefficients α_{pq}, β_{pq}, and δ_{γ} are considered the allometric or structure-related parameters and depend on only the orientation or arrangement of scatterers in the vegetation but are independent of biomass. Similarly, A_{pq}, B_{pq}, and C_{pq} are considered the radiometric coefficients of the algorithm that depend on the radiometric correction of radar due to the terrain correction and heterogeneity of vegetation structure.

In the volume term, $A_{\mathrm{pq}}b^{\alpha_{\mathrm{pq}}}$ and $B_{\mathrm{pq}}b^{\beta_{\mathrm{pq}}}$ control the relationship between biomass and the backscatter power of and the attenuation respectively. These terms are represented in the form of a power-law derived from a series of allometric models combining size, growth rate, and their metabolic characteristics (Sarabandi and Lin, 2000; Enquist et al., 2009; Smith and Heath, 2002). The model parameters α_{pq} and β_{pq} are independent of vegetation biomass and depend on the geometry of tree canopies in terms of size and orientation of trunks, branches, and leaves and may vary depending on the vegetation type. The volume surface interaction term $C_{\mathrm{pq}}b^{\gamma_{\mathrm{pq}}}$ represents the strength of the specular reflection and includes the scattering from both trunk and crown layers reflected from ground surface. Similarly, the coefficients A_{pq}, B_{pq}, C_{pq} also depend on the forest structure and the SAR backscatter radiometric calibration (e.g., terrain correction) but are independent of aboveground biomass. The model therefore, has three unknown biophysical variables (b, ε, s) and six polarization dependent coefficients (A_{pq}, B_{pq}, C_{pq}, and α_{pq}, β_{pq}, δ_{γ}) that must be determined for different forest types.

The overall sensitivity of the model at the L-band frequency is shown in terms of the biomass by using data from SAR measurements from the ALOS PALSAR satellite and model simulations (Fig. 6-3). The sensitivity of backscatter measurements to AGB depends

FIGURE 6-3

Sensitivity of L-band HV backscatter to vegetation biomass. Both ALOS PALSAR satellite L-band observations (left) and model simulations (right) show the effect of vegetation attenuation on the radar saturation level.

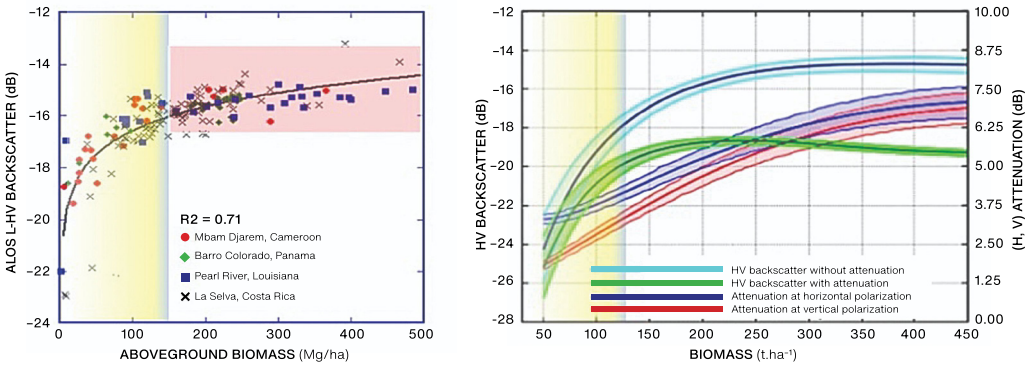

on the wavelength, with longer wavelengths allowing better penetration of the microwave signal into the canopy and scattering from the tree trunks that contain most of the tree biomass. At shorter wavelengths, the attenuation of the signal limits the penetration and reduces the effect of the scattering from tree components, causing a loss of sensitivity to biomass at some threshold AGB. At the NISAR L-band frequency (~24-cm wavelength), the biomass sensitivity threshold also depends on the vegetation structure (configuration and size of scattering elements), the dielectric constant (water content in the vegetation components), soil moisture, topography, and surface roughness. It has been established that the upper limit of L-band radar sensitivity to biomass is approximately 100 Mg/ha (Mitchard et al., 2009; Robinson et al., 2013; Saatchi et al., 2007; Saatchi et al., 2011; Mermoz et al., 2015). In regions where forest biomass exceeds 100 Mg/ha, it is recommended to use interferometric temporal decorrelation measurements (Lavalle et al., 2012; Lavalle et al., 2023), other sensors such as the ESA's P-band SAR mission BIOMASS (Le Toan et al., 2011), and/or a combination of long-baseline

FIGURE 6-4

Global distribution of above-ground biomass. Map is stratified in categories to demonstrate areas in green and yellow where NISAR above-ground biomass products will be of low uncertainty.

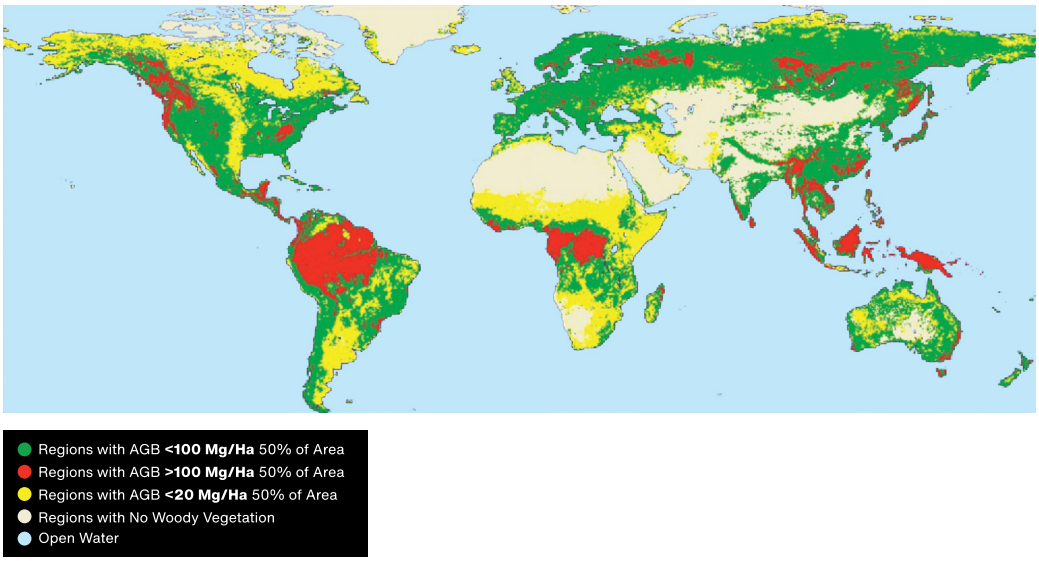

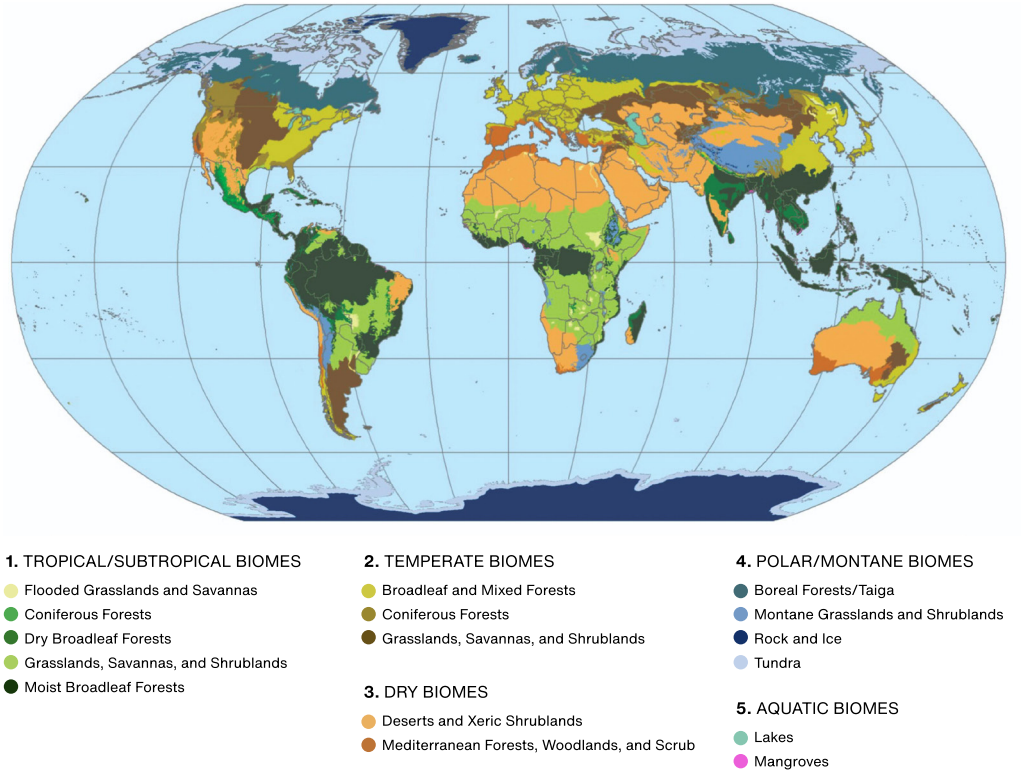

FIGURE 6-5

Distribution of global ecoregions and biomes for the development of the vegetation biomass algorithm. The ecoregions are derived from a combination of climate, topography, soil, and vegetation data (Olson et al., 2001). The focus of the Cal/Val plan and algorithm development would be on biomes that have distinct differences in the model.

SAR interferometry and backscatter at L-band, and lidar sensors, such as those available from the NASA's GEDI mission (Saatchi et al., 2011; Shugart et al., 2011; Hall et al., 2011).

Based on the empirical/theoretical experience outlined above, NISAR will generate biomass estimates of woody vegetation up to 100 Mg/ha using high-resolution multi-temporal NISAR L-band SAR backscatter imagery, and the above semi-empirical algorithmic model (Saatchi and Moghaddam, 2000; Hensley et al., 2014). The target area of the NISAR biomass product will be all forests and shrublands across different ecoregions, distributed globally (Fig. 6-4). Even in regions where forest biomass is larger than 100 Mg/ha, there are significant areas with degraded or naturally heterogeneous vegetation that the biomass may remain below the NISAR sensitivity limit. The low biomass regions are considered among the most dynamic regions due to various management and human land use activities, or frequency of natural disturbance such as drought, fire, and storms.

The semi-empirical algorithm has several advantages over fully empirical regression models. These advantages are:

1. The model is physically based and captures the behavior of radar measurements over complex vegetation structures.
2. The model includes surface moisture variables as the key variable impacting the temporal observations of radar backscatter.
3. The model has a simple analytical formulation allowing sensitivity analysis and error propagation (Hensley et al., 2010).

All vegetation and biome (i.e., coniferous, deciduous, mixed, tropical evergreen, and shrubland savanna as shown in Fig. 6-5) specific

structural and calibration coefficients of the model will be derived for the NISAR mission.

To use the semi-empirical model as an algorithm to estimate the forest or vegetation AGB requires a priori quantification of the model coefficients for different forest types and the number of observations to account for the soil moisture (ε) and surface roughness (s) variations. To meet this challenge, the model must be developed through a process of Cal/Val approaches over different forest types or ecoregions before the launch of the NISAR. The model coefficients are quantified over a series of study sites (Cal/Val sites) that includes ground measurements of vegetation structure, and airborne or satellite L-band observations that can simulate the NISAR observations (see Chapter 8 for ecosystem Cal/Val plan).

6.2.2 IMPLEMENTATION APPROACH FOR ALGORITHM

During the pre-launch Cal/Val activities, the science team determines the initialization of the algorithm and evaluates its performance to meet the science requirements. The algorithm depends on several model coefficients that are expected to vary as a function of biome and be subjected to a natural variability of observed radar backscatter with changes in soil moisture and season. The following describes the approach that is used for determining these model parameters.

QUANTIFICATION OF MODEL COEFFICIENTS α_{pq}, β_{pq}, AND δ_{γ}

The model coefficients related to vegetation structure can be determined in four steps:

1. A three-dimensional forward scattering model (Saatchi and McDonald, 1997; Saatchi and Moghaddam, 2000) has been used over the key Cal/Val study sites with ground measurements of tree structure to fit a power law function to the scattering and attenuation terms of the scattering model to vegetation biomass. The coefficients are the exponents of the model fits and are used as initial conditions in retrieving these coefficients over Cal/Val study sites in step 2.
2. It is assumed that the structural parameters of the algorithm will remain fixed and will not change spatially or temporally within each ecoregion and during the NISAR time series observation. To determine α_{pq}, β_{pq}, and δ_{γ} for different ecoregions and for two polarizations of HH and HV, the Cal/Val study sites within each ecoregion will be used. At these sites, multi-temporal (3 to 5 images capturing seasonal variations) radar backscatter measurements, ground vegetation biomass, soil moisture, and surface roughness measurements are available or estimated from radar measurements directly over bare surfaces within the study site. The coefficients are determined using the Levenberg-Marquardt Approach (LMA) for nonlinear least square estimation (Marquardt, 2009). The method is used in many software applications for solving generic curve-fitting problems and has already been applied in several SAR estimation approaches (Troung-Loi et al., 2015).
3. If the soil moisture and roughness data are not available from ground measurements in the Cal/Val study area, these variables are estimated from areas of low vegetation or bare fields within the study area or the SAR image scene. A crude low vegetation or non-forest mask is generated for the time series data stack. This mask is obtained by thresholding the HV SAR image scene available over the Cal/Val site. A threshold of –13 dB has been used to generate such a forest mask on ALOS-1 and -2 data sets by JAXA. By assuming σ^0hv > forest_threshold, the non-forest or low-vegetation areas are separated. A similar approach is used in the NISAR algorithm for disturbance and will be the same for both algorithms. Once the mask is developed, the soil dielectric constant and RMS height of the surface

roughness are determined by inverting the Oh et al., (1992) model described above in Equation 6.2-7. These values are used as the initial condition of the estimation of the structural variables for all areas considered forest or vegetation using a nearest neighbor interpolation approach (Troung-Loi et al., 2015)

4. For cases where α_{pq}, β_{pq}, and γ_{pq} cannot be estimated unambiguously using the LMA curve-fitting or estimation approach, the theoretical values derived from the forward model simulations and power-law model fits will be used. Estimates of coefficients related to vegetation structure will also include uncertainty associated with the LMA least-squares approach. The uncertainty can be used within a Bayesian approach to account for uncertainty in the algorithm and estimation of the biomass.

QUANTIFICATION OF MODEL COEFFICIENTS A_{pq}, B_{pq}, C_{pq}

The radiometric coefficients of the algorithm can be determined simultaneously with those related to vegetation structure. The estimation of these coefficients is based on the following assumptions:

1. Coefficients A_{pq}, B_{pq}, and C_{pq} are assumed to vary temporally due to changes in vegetation water content and phenology. This assumption can be verified over different ecoregions to relax the temporal variations to monthly or seasonal.
2. The radiometric coefficients are assumed to remain constant spatially within a local moving window (3×3 or larger) to allow for spatial stability of the algorithm. This assumption depends on the spatial heterogeneity of vegetation structure (e.g., canopy gaps) that influences the magnitude of volume and volume-surface interactions.
3. The coefficients can be determined over Cal/Val study sites where biomass, soil moisture, and roughness are available or determined as discussed in 6.2.1 to allow for testing the validity of moving window size for each vegetation type or ecoregion. Using a minimum of 3×3 moving window will allow the algorithm to have different coefficients for each local area. The alternative approach is to use A_{pq}, B_{pq}, C_{pq} derived over the Cal/Val sites within each ecoregion as the fixed coefficients for the entire ecoregion as shown in Table 6-2 for the five dominant ecoregions globally.

PRE-LAUNCH CALIBRATION OF MODEL COEFFICIENTS

The pre-launch calibration of the algorithm model applies to the structural coefficients, α_{pq}, β_{pq}, and γ_{pq}, that remain constant for each ecoregion globally throughout the NISAR mission. ALOS PALSAR or UAVSAR data that simulate the NISAR observations can be used to estimate these coefficients. The requirement for pre-launch calibration is the selection of the study sites that represent the variability in the structure of the dominant vegetation types.

POST-LAUNCH CALIBRATION OF MODEL COEFFICIENTS

The post-launch calibration is mainly focused on assessing the assumption of spatial heterogeneity as observed by NISAR large incidence angle variations and therefore larger topographical variations.

APPLICATION OF THE BIOMASS ALGORITHM TO THE NISAR TIME SERIES IMAGE STACK

The AGB (b), soil dielectric constant (ε), and roughness (s) are estimated from dual-pol (σ^0_{HH} and σ^0_{HV}) measurements. The algorithm, shown in Fig. 6-6, uses a Bayesian approach to estimate AGB. The estimation approach enables the use of multi-temporal backscatter measurements

FIGURE 6-6

Flowchart showing the implementation of the NISAR algorithm for AGB estimation globally.

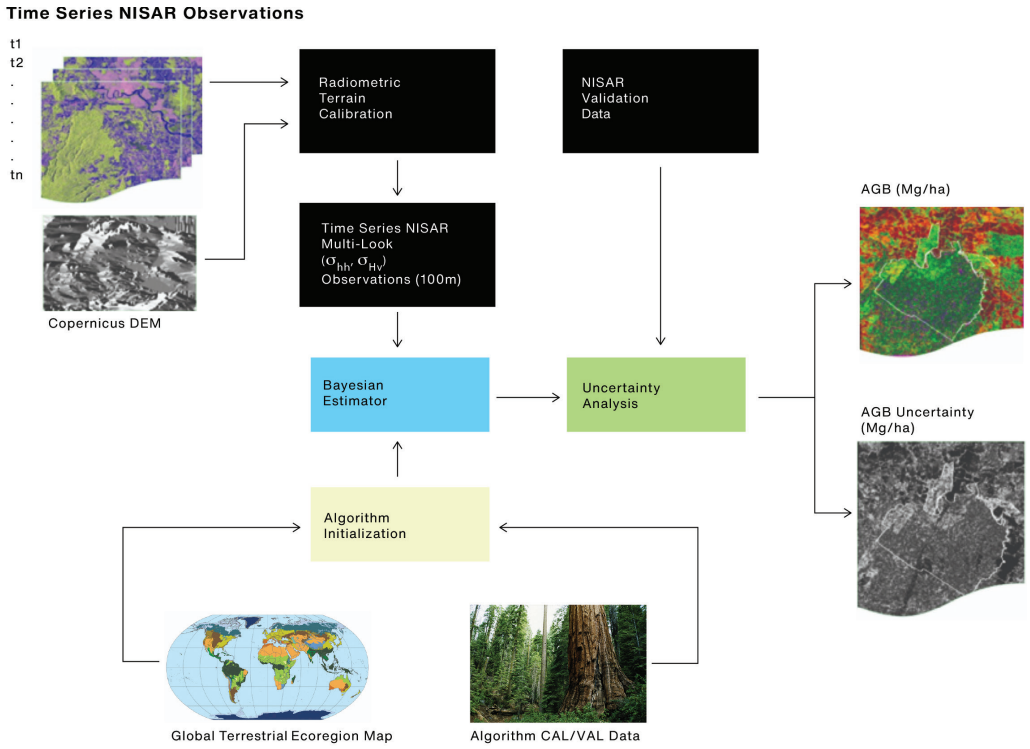

to quantify all variables while accounting for measurement uncertainty.

The implementation includes the following steps:

1. The time series (t_1, t_2, … t_n) of radiometric terrain corrected (RTC) HH and HV polarized images are fed into the algorithm as they become available from the NISAR processor. NISAR dual-pol observations are collected for NISAR ecosystem science in the background land mode every 12 days on ascending and descending orbits for most of the world's vegetated surfaces. To save on downlink data rate, in the tropical regions (+/- 23.5 degrees latitude) the cross-polarized data are collected on all descending orbits, but only on alternating ascending orbits. There are approximately 45 dual-pol observations per year in the tropical regions and 60 dual-pol observations everywhere else.
2. Use t_1 data at HV polarization and a simple threshold to develop a mask of forest/non-forest over the entire NISAR image scene. This threshold is initially set to -13 dB (as derived from ALOS PALSAR data). It will be adjusted, as necessary, when NISAR data becomes available.
3. Use the Oh et al. (1992) model to estimate soil dielectric constant and roughness for all non-forest pixels identified by the mask. Use the estimates of (ε_0,s_0) as the initial conditions for all pixels in the NISAR image by using a nearest neighbor interpolation of a simple Kriging approach. The interpolation provides initial conditions and bounds for all pixels with forests or vegetation cover that will be used in the NISAR biomass retrieval algorithm.
4. Use a simple model based on HH and HV polarization, derived from ALOS PALSAR data, and adjusted with local incidence angle (Yu and Saatchi, 2016) to estimate

forest biomass (b_0) for all forest and non-forest pixels in the NISAR image scene. Use b_0 and its distribution as the initial condition and the bounds for the biomass for the retrieval algorithm.

5. Include the NISAR HH, HV as the measurements data and the initial conditions (b_0, ε_0, s_0), and the joint probability distributions as the a priori information in the NISAR Bayesian-based retrieval algorithm.
6. For ecosystems with a strong phenological signature in the L-band RCS, the algorithm uses a global land cover or ecoregion map to set the geographically and temporally appropriate coefficients for the inversion algorithm.
7. The algorithm will provide the first estimates of the biophysical variables (b_1, ε_1, s_1) from the first NISAR image along with the uncertainty of the estimates.
8. When the NISAR image t_2 becomes available, repeat step 2 to develop a new forest/non-forest mask. Compare the mask derived from t_1 with the mask from t_2. Develop a new mask to update the forest/non-forest mask by adding the non-forest pixels.
9. Repeat steps 3 and 4 for all new non-forest pixels.
10. Update (b_1, ε_1, s_1) maps with the all-new forest/non-forest pixels.
11. Repeat steps 5 and 6 by using the updated values for (b_1, ε_1, s_1) as the new a priori information in the NISAR retrieval algorithm and produce (b_2, ε_2, s_2) and the uncertainty.
12. If no more NISAR imagery is available, iterate steps 9 and 10 by using the average of b_1 and b_2 as the new a priori information for b and the average of s_1 and s_2 as the new a priori information for s. This step is designed to make sure that the biomass and roughness remain constant for the NISAR observations, while the soil dielectric constant is updated. The iteration will continue to provide stable values of (b_2, ε_2, s_2) and improved estimates of the uncertainty.
13. If more NISAR imagery is available, repeat steps 7 to 11.
14. If a disturbance has been detected using the disturbance algorithm during the time series analysis, reset all three variables for the pixel by repeating steps 2 to 4.
15. Forest biomass growth can be detected during the algorithm retrieval from the time series NISAR data if a significant trend is observed in biomass estimation after implementing step 10. The time series estimates of the biomass, b, can be used to study or report the trend in biomass from the first NISAR imagery.
16. Annually, the updated biomass values will be reported as a map with 100 m × 100 m (1 ha) spatial grid cells globally. However, the algorithm will provide estimates of all three variables, and the uncertainty, every time the RTC NISAR images become available throughout the year.
17. The algorithm assumes that during a one-year period of multi-temporal observations, the soil dielectric constant will vary, while AGB and roughness, s, are treated as constant except in cases of land cover change (e.g., deforestation or disturbance; see forest disturbance product description).
18. The algorithm performance using the Bayesian approach is evaluated at 100-m spatial resolution products for all areas with AGB > 0. All areas with AGB > 100 Mg/ha will be identified and aggregated into one class, and areas with AGB = 0 will be another class.

By following this method, the algorithmic model is used to estimate AGB from radar backscatter observations. The effects of other variables associated with soil moisture and surface roughness on the radar backscatter

TABLE 6-1. STUDY SITES USED TO DEVELOP REPRESENTATIVE MODELS FOR GLOBAL ESTIMATION OF BIOMASS

FOREST TYPE	RADAR OBSERVATION	LOCATION	DATE	IN SITU DATA	REFERENCE
Needleleaf	AIRSAR	Boreal Forest of Canada	1993-1996	18 Sites, 64 plots	Saatchi and Moghaddam, 2000
Broadleaf Deciduous	UAVSAR	Howland Forest, Maine, USA	2009–2010	32 1-ha plots lidar data	Robinson et al., 2013
Mixed Broadleaf/ Needle Leaf	AIRSAR/UAVSAR	Maine, Duke, Harvard, etc.	2004/2009	78 plots/lidar data	Robinson et al., 2013
Broadleaf Evergreen	AIRSAR/UAVSAR/ALOS PALSAR	Sites distributed in Costa Rica, Peru, Gabon	2004–2015	Combined plots/lidar data	Saatchi et al., 2011
Savanna/Dry Forest	ALOS/PALSAR	Uganda/ Cameroon/ Mozambique/ Gabon	2007–Present	160 plots 0.4–1.0 ha	Mitchard et al., 2009

TABLE 6-2. MODEL PARAMETERS DERIVED FOR DIFFERENT VEGETATION TYPES DURING THE NISAR PHASE A STUDY OVER EXISTING CAL/VAL SITES

MODEL PARAMETERS	BROADLEAF EVERGREEN	BROADLEAF DECIDUOUS	NEEDLELEAF	MIXED BROADLEAF & NEEDLELEAF	DRY FOREST WOODLAND SAVANNA
A_{HH}	0.229	0.241	0.189	0.211	0.11
A_{HV}	0.0867	0.0683	0.013	0.0365	0.03
B_{HH}	0.0108	0.0944	0.00211	0.0789	0.00908
B_{HV}	0.0148	0.0165	0.00195	0.0855	0.012
C_{HH}	0.005	0.008	0.0076	0.0083	0.009
C_{HV}	0.002	0.0062	0.0047	0.0053	0.007
α_{HH}	1.1	1.1	0.19	0.96	0.20
α_{HV}	0.2	0.3	0.11	0.27	0.18
β_{HH}	1.1	1.1	0.89	0.96	1.0
β_{HV}	1.1	1.0	0.9	0.89	1.0
γ_{HH}	1.1	1.1	0.89	0.96	1.3
γ_{HV}	0.5	0.9	0.23	0.27	1.1

measurements are also considered. Currently, the algorithm is calibrated over different ecoregions using the Cal/Val data. Locations of forests used to derive parameters used by the algorithm, as developed over five key forest and woodland biomes, is given in Table 6-1. Parameters are given in Table 6-2. A general flowchart, describing the current algorithm implementation is shown in Fig. 6-6. The number of ecoregions that require separate algorithms will be finalized later after performing the algorithm Cal/Val activities across the global ecoregions.

IDENTIFICATION OF BIOMASS DISTURBANCE

The implementation of the biomass algorithm using the time series stack of dual-pol NISAR imagery requires the detection of disturbance to reset the biomass values at the pixel level. The detection of disturbance can be the simple band threshold as determined for the forest/non-forest mask or the use of the disturbance algorithm. Here, a similar approach as in the disturbance algorithm will be implemented to report the vegetation biomass before the disturbance and

detection of the post-disturbance accumulation of the biomass.

6.2.3 VALIDATION PRODUCTS

The L2 aboveground biomass product is a raster image at 100-m spatial resolution produced over the Cal/Val sites. The raster product is in one-byte format with pixel values representing AGB as an integer number from 0 to 100 Mg/ha, and a fixed value for biomass greater than 100 Mg/ha. The product will be generated every year using observations collected during the year. The input product is multi-look L2, 20 m, radiometrically terrain-corrected imagery. Also required for generating the biomass products are ancillary data of a global land ecoregion map to select the algorithm coefficients, surface digital elevation model to improve the inversion model with local incidence angle, a soil moisture map (derived from SMAP or SMOS), and in situ and lidar data for calibration and validation of the model. The Bayesian methodology will also provide uncertainty estimates at the pixel level. Initial values for surface roughness, s, are obtained for the Cal/Val sites during pre-launch activities and determined post-launch by the closest Cal/Val site within the same ecoregion.

6.3 ECOSYSTEMS SCIENCE – DISTURBANCE

The NISAR L2 science requirement for forest disturbance is expressed as:

The NISAR project shall measure global areas of vegetation disturbance at 1 hectare resolution annually for areas losing at least 50% canopy cover with a minimum classification accuracy of 80%.

Accurate annual measurements of the global area of forest disturbance from NISAR will be a significant contribution to the global accounting of carbon emissions from land cover change (van der Werf et al., 2009). The NISAR disturbance product complements the NISAR biomass, inundation, and active agricultural area products to jointly improve our understanding of carbon emissions from land cover change and the success of mitigation strategies like avoided deforestation or zero-deforestation commitments. As such, the disturbance product from NISAR will constitute an invaluable contribution to the accounting needs for the United Nations negotiated policy mechanism for Reducing Emissions from Deforestation and Forest Degradation (REDD) as well as emerging bi- and multilateral carbon treaties involving forest carbon accounting (Romijn et al., 2012; Baker et al., 2010). To date, forest carbon accounting with remote sensing methods has made significant progress, and international efforts by the Committee on Earth Observing Systems (CEOS) and the GEO Global Forest Observing Initiative (GFOI) strive to improve national efforts on forest carbon Monitoring, Reporting and Verification (MRV, GFOI, 2013). As cloud cover is a major impediment to reliably acquiring high-spatial resolution annual data sets with optical sensors over tropical, sub-tropical, and boreal regions, SAR observations have emerged as a critical complement (Kellndorfer, 2014; Kellndorfer, 2019; Reiche, 2016; Reiche, 2018; Walker, 2010; Watanabe, 2018; Ygorra, 2021). Achieving reliable and timely accounting of forest disturbance globally at consistent annual or even sub-annual intervals will improve our scientific understanding of global carbon emission dynamics from forests, both from natural and anthropogenic disturbances.

6.3.1 THEORETICAL BASIS OF ALGORITHM

The NISAR disturbance detection algorithm is based on time series analysis techniques of observed NISAR L-band calibrated backscatter measurements, foremost using cross-polarized observations (L-HV). At its core, the algorithm is analyzing backscatter from two time series of observations with change point detection. Time series may be temporally segmented (e.g., freeze/thaw, wet/dry season observations only). The segmentation is determined spatially based on the observational data to account for ecosystem

Credit:
Mark Prytherch/Shutterstock

specific seasonality (see Fig. 6-5). A simple, yet robust approach for detecting disturbance in these time series of backscatter images is based on change point detection with cumulative sums analysis, which have been employed in many sectors such as statistical control, financial trends, and meteorological analysis (Kellndorfer, 2019; Ruiz-Ramos, 2020; Ygorra, 2021). During the NISAR mission, time series–based cumulative sums are calculated for each 20 m pixel, either from the full year observation period, or from seasonally segmented subsets, which is adequate in complex biomes like the boreal region with strong seasonality.

The corresponding cumulative sum curves from a full or partial year of data initialize the algorithm. Subsequent observations will be classified based on change points identified through cumulative sum analysis, indicating the timing of detected changes. If within a 100 x 100 m resolution cell, 5 or more pixels are flagged as disturbed, either from the entire time series or seasonal subsets of the time series, the entire cell is flagged as disturbed.

The NISAR measurement metric for disturbance determination relies on the measurement of cross-polarized L-band backscatter change with forest fractional canopy cover loss of 50% or more as observed and compared over annual timeframes. At its core, L-band cross-polarized backscatter exhibits a significant variation (several dB), depending on the initial state of canopy density and forest structure, when forest fractional canopy cover is reduced by 50% or more.

To provide a more theoretical foundation for the use of time series analysis of backscatter change based on the target scattering physics, a theoretical scattering model has been developed and described (Cartus et al., 2018). This model includes the scattering model and an observational error model, to show the separation between simulated natural and disturbed forest canopies. A summary of this simple observational model tailored for disturbance (i.e., ignoring double bounce) using cross-polarized observations is given here.

In a relationship between radar observation and classification accuracy, an error model is needed for the observations and those components that contribute to the target radar cross section (RCS). The observational error model that relates the observed RCS, for each polarization *pq*, written here as σ_{obs} for simplicity, to the observation

error sources, $\sigma^0_{\text{obs-error}}$ and the RCS of a forest canopy, σ^0_{forest} is

$$\sigma^\circ_{\text{obs}} = \sigma^\circ_{\text{obs-error}} + \sigma^\circ_{\text{forest}} \quad \textbf{6.3-1}$$

The observational errors consist of instrumental effects, such as calibration and quantization errors, observational ambiguities, and speckle noise. With these factors considered, the RCS of the forest can be written as

$$\sigma^\circ_{\text{forest}} = (1-\eta)\sigma^\circ_{\text{ground}} + \eta\left[\sigma^\circ_{\text{ground}} e^{-\alpha h} + \sigma^\circ_{\text{veg}}\left(1 - e^{-\alpha h}\right)\right] \quad \textbf{6.3-2}$$

which is an "infinite resolution" model borrowed from optical techniques, where the contribution of the ground surface σ^0_{ground} is combined with the average return from a layer of vegetation, σ^0_{veg}, weighted by the fraction of vegetation canopy cover, η. In the above, the two-way loss of signal energy as it passes through the canopy is accounted for by α, the extinction, and a vegetation height (h) estimate. α is normally given in units of dB/m.

The above equation can be rearranged to separate the ground and the vegetation scattering returns, as in

$$\sigma^\circ_{\text{forest}} = \sigma^\circ_{\text{ground}}\left[1 - \eta\left(1 - e^{-\alpha h}\right)\right] + \sigma^\circ_{\text{veg}}\left[\eta\left(1 - e^{-\alpha h}\right)\right] \quad \textbf{6.3-3}$$

When multiple observations are made, (6.3-1) through (6.3-3) can be combined to relate the vector of observations to the spatially varying values and the set of constants that describe the mean RCS of the ground and vegetation, as in

$$\begin{bmatrix} \sigma^\circ_{\text{obs-1}} \\ \sigma^\circ_{\text{obs-2}} \\ \vdots \\ \sigma^\circ_{\text{obs-}N} \end{bmatrix} = \begin{bmatrix} 1-\eta_1(1-e^{-\alpha h}) & \eta_1(1-e^{-\alpha h}) \\ 1-\eta_2(1-e^{-\alpha h}) & \eta_2(1-e^{-\alpha h}) \\ \vdots & \vdots \\ 1-\eta_N(1-e^{-\alpha h}) & \eta_N(1-e^{-\alpha h}) \end{bmatrix} \begin{bmatrix} \sigma^\circ_{\text{ground}} \\ \sigma^\circ_{\text{veg}} \end{bmatrix} \quad \textbf{6.3-4}$$

which, for a given number of observations, N, can be inverted to estimate the RCS of the ground and vegetation returns. Through simulations with real ALOS-1 L-band measurements with estimates for h and η from ancillary data sources, the validity of backscatter-based change detection of 50% canopy density loss was demonstrated for the project in a memorandum by Siqueira and others in 2014. Time series analysis allows for the minimization of error sources from soil and vegetation moisture as well as speckle noise variations.

6.3.2 IMPLEMENTATION APPROACH FOR ALGORITHM

Prerequisites for the disturbance detection algorithm are fully calibrated, radiometrically terrain corrected (RTC) backscatter time series where pq=HV. Co-polarized data (pq=HH) are useful for identifying potential ambiguities and unsupervised clustering and are employed to mask non-forest areas such as wetlands and agricultural areas. The time series RTC products are subjected to multi-temporal speckle noise reduction according to Quegan et al., 2001. A diagram giving the processing flow for the disturbance algorithm is shown in Fig. 6-7 (next page).

SEASONAL SUB-SETTING OF TIME SERIES DATA STACK

For many biomes, seasonal stratification of time series will improve detection of disturbance events, e.g., where freeze/thaw or dry/wet season conditions introduce significant backscatter changes.

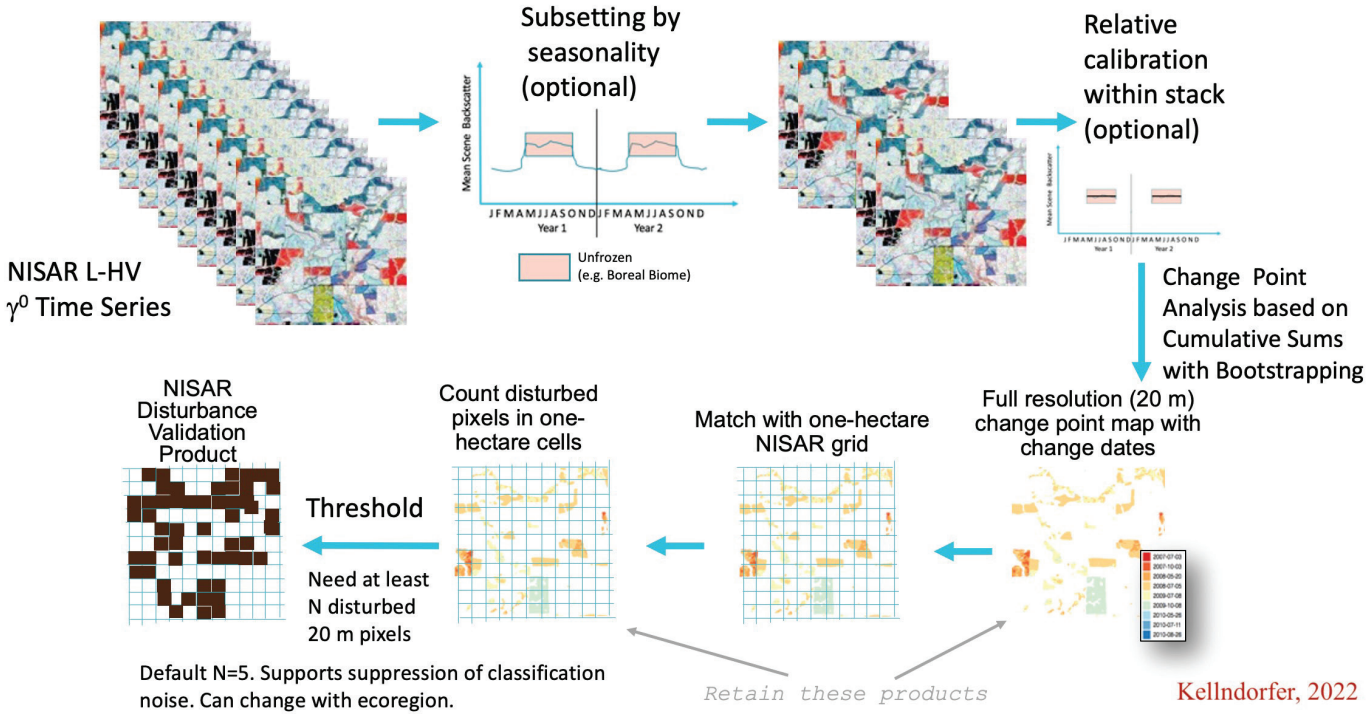

FIGURE 6-7

Algorithmic flow of disturbance detection with NISAR time series data based on change point analysis.

Thus, the first step in the disturbance detection algorithm is the sub-setting of time series data stacks and selection of scenes to minimize gross environmental effects on backscatter levels. Selection of the scenes can be performed with a global scene means comparison and threshold approach as follows:

1. A crude forest/non-forest mask is generated for a time series data stack. This mask can be obtained from ancillary existing land cover classifications (e.g., from Landsat, ALOS-1), or by thresholding an early HV SAR image from typical seasons of interest (e.g., non-frozen, dry season). A threshold of -13 dB has been used to generate such a forest mask on ALOS-1 and 2 data sets by JAXA.
2. For all pixels t_i under the mask, the mean (on the power scaled data) at each time step i = 1, n is generated to produce a time series of means as:

$$\tau_{\text{mean}} = \left\{\overline{t_1}, \overline{t_2}, \overline{t_3}, ..., \overline{t_n}\right\}$$

3. Here, τ_{mean} is a collection of mean values, where $\overline{t_i}$ indicates the mean pixel value for the forested pixels in the image. This is a large-scale assessment of the seasonal effects within the image.
4. τ_{mean} is sorted from low to high values.
5. The gradient for the sorted τ_{mean} is computed as $\nabla\tau_{\text{mean}}$.
6. A threshold for significant major backscatter change is applied to the gradient of the sorted time series means such that $\text{subset}(\nabla\tau_{\text{mean}}) = \nabla\tau_{\text{mean}} > \text{change\_threshold}$
7. NISAR images that correspond to time steps in the subset from step 5 (or the complement of subsets) are selected to form the time series for change detection analysis.

Both the forest mask and change threshold can be estimated per ecosystem from statistical analysis with canopy density masks. During the NISAR mission, we will generate a lookup table for biomes and ecoregions for these thresholds.

RELATIVE CALIBRATION OF SUBSETTED DATA STACK

For improved results, the time series stacks are calibrated relative to each other to a higher precision than perhaps required through routine standard calibration of the NISAR imagery. This calibration step examines distributed targets that are expected to be unchanged or minimally changed in brightness over a set time span of images. With NISAR's 240 km swath width, it is reasonably assumed that a statistically large area, A_{ni}, will not be disturbed (or otherwise changing) during any of the observations in the subsetted time series observations. These areas will be identified partly through the use of the threshold-based forest mask from one scene and applied again through all images.

The calibration correction for image n, f_n, for each polarization channel pq, is

$$f_{\mathrm{pq}}^{n} = \frac{\overline{(\sigma_{\mathrm{pq}}(A_{\mathrm{ni}}))_t}}{(\sigma_{n,\mathrm{pq}}(A_{\mathrm{ni}}))} \qquad \textbf{6.3-5}$$

where $\overline{(\sigma_{\mathrm{pq}}(A_{\mathrm{ni}}))_t}$ is the average σ over the area A_{ni} for all images over the timespan t corresponding to the selected images according to the procedure above, and $\overline{(\sigma_{n,\mathrm{pq}}(A_{\mathrm{ni}}))}$ is the average σ over the area A_{ni} for the image n. Image values for the refined calibration of image n for each polarization channel will be given by $\sigma^{c}_{n,pq,}$

$$\sigma_{n,\mathrm{pq}}^{c} = f_{\mathrm{pq}}^{n}\sigma_{n,\mathrm{pq}} \qquad \textbf{6.3-6}$$

CHANGE POINT DETECTION WITH CUMULATIVE SUM ANALYSIS

Disturbance detection for each calibrated pixel x, y (or segment, k) of the image for disturbed forests for image, n, will then be the result of the cumulative sum analysis performed for each pixel.

Cumulative sum analysis of time series is the basis for classical change point detection that investigates the change in mean before and after a change in a time series (Schweder et al., 1976). It is a distribution-free approach, applicable to short, irregular time series for detecting gradual and sudden changes. A graphical example of this process is shown in Fig. 6-8.

Let **X** be the time series of the subset of n selected scenes as

$$X = (X_1, X_2, ..., X_n) \qquad \textbf{6.3-7}$$

The residuals of the time series are computed (in power units) as

$$R = (X_1 - \chi), (X_2 - \chi), ..., (X_n - \chi) = (R_1, R_2, ..., R_n) \qquad \textbf{6.3-8}$$

where

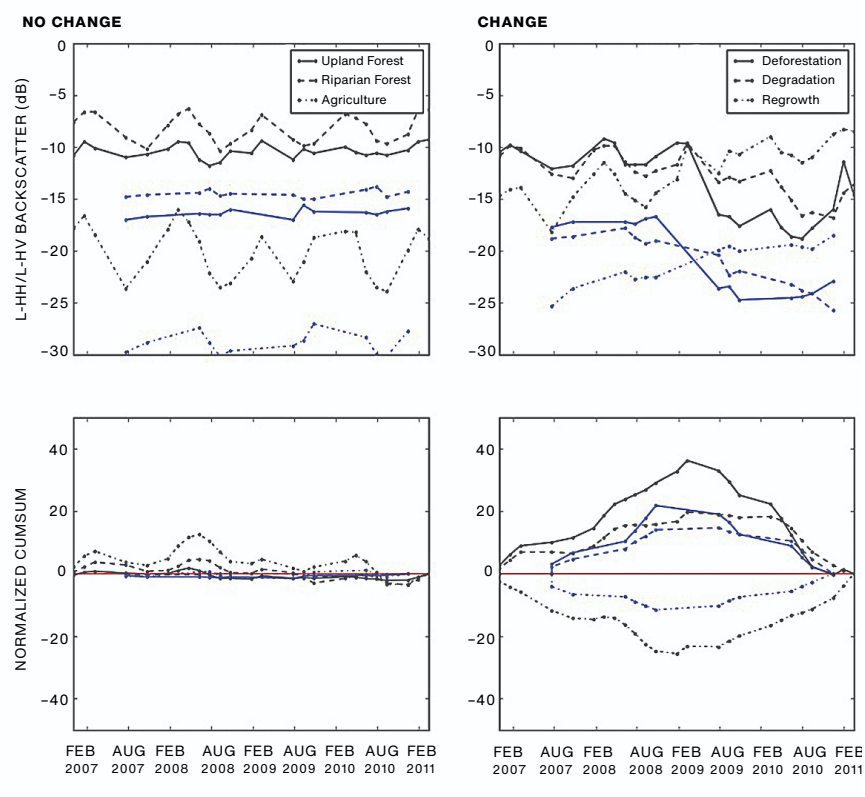

FIGURE 6-8

Example of ALOS-1 time series (top) for various unchanged (left) and changed (right) land cover types. Bottom figures show the corresponding cumulative sum curves. Black lines=L-HH, blue lines=L-HV backscatter/ cumulative sum curves.

$$\chi = \frac{\max(X) - \min(X)}{2} \quad \textbf{6.3-8a}$$

is the half-range of the time series.

The cumulative sums, S_i, are defined as the sum of the residuals, R_i, at each time step such that

$$S_i = S_{i-1} + R_i \quad \textbf{6.3-9}$$

with i = 1, …, n and $S_0 = 0$.

In the cumulative sum, the slope of S is indicative of change in a time series:

- Upward slope: Values are above global mean
- Downward slope: Values are below global mean
- Change in slope direction: Indication of change point location

The magnitude of change is calculated as

$$S_{\mathrm{DIFF}} = \max(S) - \min(S) \quad \textbf{6.3-10}$$

Larger S_{DIFF} values are indicative of greater change. A change point can be defined with two criteria:

a) A clear change in slope is detected in the cumulative sum curve, with upward and downward slopes exceeding a gradient threshold.

b) S_{DIFF} exceeds a threshold for change labeling.

Criteria a) and b) are values to be determined empirically from calibration activities as they can be expected to be different for different forest structural types and environments with varying soil moisture conditions.

Also cross-checking will be performed to determine whether all observations shall be part of the cumulative sum calculation, i.e., whether scene subsetting was indeed appropriate or if further pruning might be necessary. Once a threshold value is determined from calibration efforts, change can be flagged based on the cumulative sum values.

A candidate change point is identified from the S curve at the time where S_{MAX} is found: $T_{CPbefore} = T(S_i = S_{MAX})$ with

- $T_{CPbefore}$, timestamp of the last observation before change
- Si, cumulative sum of R with i = 1, ... n
- n, number of observations in the time series

The first observation after change occurred ($T_{CPafter}$) is then found as the first observation in the time series following $T_{CPbefore}$.

A possible method to define $\mathrm{threshold}_{S_{\mathrm{DIFF}}}$ is based on a standard deviation of all S_{DIFF} observations in the image stack. A suitable value can be found from experimental ALOS-1.

This threshold will also vary with ecosystem and forest structural types.

For assessment of the robustness of detected change points, CUMSUM change point detection can be combined with bootstrapping (random reordering of the observation dates in the time series) to measure confidence in marking a change point.

First, a confidence interval is computed from the number of times a bootstrapped S_{DIFF} is less than the original SDIFF. High count corresponds to higher confidence in a change point. Count can be expressed as a percentage confidence level (CL):

$$\mathrm{CL} = \mathrm{count}(S_{\mathrm{DIFF\text{-}Bootstrapped}} < S_{\mathrm{DIFF}})/\mathrm{N} \quad \textbf{6.3-11}$$

with N = number of bootstrapped samples.

The latter computation also makes change point detection in time series somewhat robust against outliers in a time series as their importance in a bootstrapped analysis decreases.

After applying a confidence level filter to further clean out spurious single 20-m pixels, a 2×2 sieve filter is applied to the raster data set where

change points are identified. This is not necessary if the analysis was performed on image segments (to be tested).

The resulting image is vectorized to a fixed one-hectare grid, and all polygons containing disturbance flagged pixels are retained for a final output product. If in any one-hectare cell, five or more 20-m pixels are labeled disturbed, the 1-ha cell is flagged as disturbed. Retaining only one-hectare cells as vector layers with attributes for number of detected disturbed pixels, error metrics, and trends (retaining values of subsequent years) will result in a vast reduction of the image raster layers as only 3%–5% of any given area on average can be expected to be disturbed. To monitor disturbance trends, it is suggested that two intermediary products are retained: (1) 20 m resolution change point detection with change date, (2) 1-hectare cells with count of disturbed 20 m pixels. The NISAR final product is a thresholded binary image based on the pixel count.

6.3.3 VALIDATION PRODUCTS

The NISAR mission L2 science requirement for disturbance detection defines disturbance as "50% or more fractional forest canopy cover lost in a one-hectare (100×100 m2) resolution cell." The mission shall measure disturbance annually with an error rate of less than 20% globally. The first NISAR disturbance product will be issued for the second year of the mission. The algorithm specified in this document is designed to produce products meeting this mission requirement by quantifying annually disturbed forested areas. The disturbance product will be issued as a 20-m binary base product with pixels flagged as disturbed (1) or not (0), and a 100-m raster product with numbers from 0 to 16 for the count of marked disturbed pixels. Error metrics for detection will also be made available for the 20-m and 1-ha products.

6.4 ECOSYSTEMS SCIENCE – INUNDATION

The NISAR L2 science requirement for wetlands inundation is expressed as:

The NISAR project shall measure inundation extent within inland and coastal wetlands areas at a resolution of 1 hectare every 12 days with a classification accuracy of 80%.

A review of publications quantifying the accuracy of mapping wetlands with L-band SAR was completed in October 2014. The review concluded the wetlands accuracy requirement could be achieved by NISAR. Methods to classify radar images ranged from utilizing simple thresholds to machine learning approaches, sometimes in combination with image segmentation. Inundated vegetation can be observed by L-band SAR when woody vegetation vertically emerges from the water surface, enhancing the double bounce scattering mechanism that is especially apparent in the HH channel. Wetlands are often adjacent to open water or senesce into open water surfaces that provide a significant contrast to these landscapes, facilitating detection and mapping of inundation regions using the NISAR mission.

The baseline NISAR algorithm uses a simple method to identify surface water extent: detection thresholds applied to the SAR backscatter. The objective of this algorithm, described, for example, in Chapman et al, 2015, is not necessarily to produce the best possible wetland inundation product, but rather to quantify the sensitivity of the NISAR dual polarization (HH and HV) data to inundation classes. This allows validation of the wetland inundation requirement. Once quantified at a variety of wetlands and wetland conditions, the optimum approach for any given wetland may be developed. An example case study given in Downs et al. 2023 demonstrates this threshold classification approach over the Sudd wetlands in South Sudan.

For open water areas, the detection threshold will be a maximum backscatter value below which we

can presume is the result of surface scattering of the incident radiation away from the sensor to a degree not normally found in dry, naturally occurring, smooth surfaces. On occasion, wind roughening can increase the backscatter to levels higher than this threshold, and some smooth, dry surfaces can indeed have backscatter values comparable to open water. However, in general, this type of threshold is effective at identifying open water areas. This threshold is somewhat dependent on the incidence angle.

Where there is inundated vegetation, it is found that the incoming radiation scatters off the water surface and off the vertically emergent vegetation (especially woody vegetation) directly back to the radar antenna - a double bounce reflection. In this case, we set a minimum threshold on the HH backscatter (as double bounce reflections do not tend to modify the polarization), but HV can be helpful in excluding areas of high-volume scattering.

For classification of open water, the backscatter is generally significantly lower than non-inundated landscapes with three possible exceptions: 1) depending on the noise equivalent σ^0 of NISAR, distinguishing open water from other low backscatter targets such as bare ground or mudflats may be difficult; 2) at steep incidence angles, wind roughening can make open water brighter than typical open water values; and 3) open water with floating vegetation may be difficult to separately categorize. In the first case, since open water does not generally change quickly or to a large degree compared to the extent of inundated vegetation, averaging the data over time or over area can be helpful for reducing the noise over bare ground areas, which are generally brighter than the expected noise equivalent σ^0. In the second case, we will make use of images taken with different viewing geometry and times to identify open water surfaces. Indeed, observing the response of open water and land surfaces from different look angles could be obtained through comparison of imagery from ascending and descending orbits. Another method to distinguish open water from bare ground is through examination of the interferometric coherence. The observed repeat-pass coherence over bare ground is typically higher than that of open water. For the third case, a subcategory of floating vegetation may be difficult to discern from open water (depending on the characteristics of the emergent vegetation), but these areas may alternatively be identifiable as open surface water and therefore meet the objectives of the requirement.

As a preliminary step, a baseline classification will be generated from the multi-temporal radar backscatter average of an image sequence to represent the initial inundation state representative of the time period of the images. The wetland classification generated for each orbit cycle could be improved through change detection of the images within this orbit cycle relative to this baseline. The accuracy of the subsequent classifications generated for each orbit cycle could potentially be improved through comparison with an additional but shorter multi-temporal average. This would improve the robustness of the classification by increasing the effective number of looks within 1 ha pixels at the expense of temporal resolution. If multi-temporal averaging were required to meet classification accuracy requirements, the multi-temporal averaging would be accomplished as a separate pre-processing step and implemented as rolling averages to maintain the 12-day interval for the output of classification results. As such, pixels transitioning between different inundation states during the temporal averaging period could still be captured.

6.4.1 IMPLEMENTATION APPROACH FOR ALGORITHM

The classification of wetland inundation in NISAR images follows the processing flow shown in Fig. 6-9 and is described here. Execution of this classification scheme is detailed in the ATBD Jupyter Notebook provided by the NISAR Project. First, the images of the multi-temporal sequence can be radiometrically calibrated relative to each other to a higher precision than perhaps

required through routine standard calibration of the NISAR imagery. This calibration step examines distributed targets that are expected to be unchanged or minimally changed in brightness over a set timespan of the set. Given n images before and after each image to be classified, it is reasonably assumed that a statistically large area, A_{ni}, will not be inundated (or otherwise changing) during any of the 2n observations surrounding the image to be calibrated and classified. These areas will be identified through use of an a priori wetlands mask and partly through image segmentation or other methods over the 2n images.

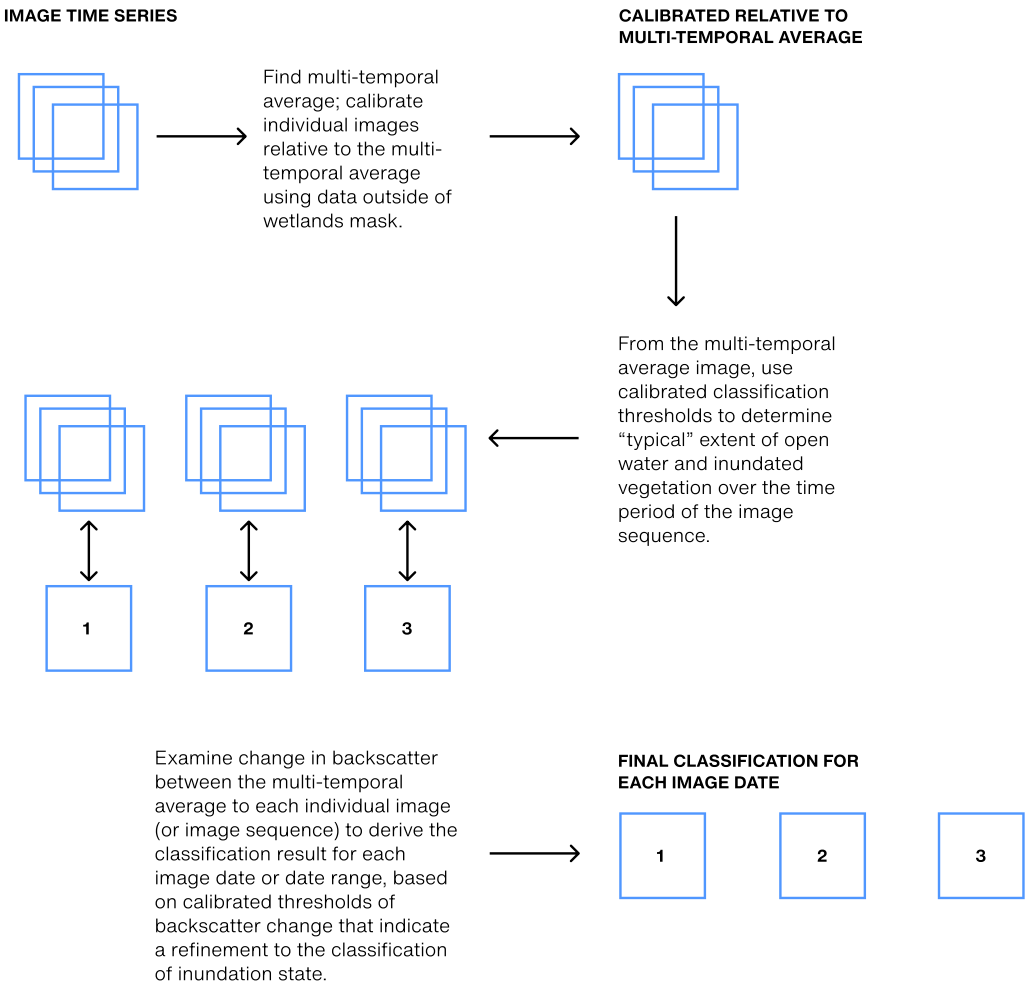

FIGURE 6-9

Algorithm flow for an example multi-temporal sequence of three images for inundation.

Four classes will be identified from a multitemporal average of a subset of images:

1. IV: Inundated vegetation (dominated by double bounce scatter in HH channel)
2. OW: Open water (low specular scattering in both channels)
3. NI: Not inundated (brighter specular scatter, volume scattering)
4. NC: Not classified (pixels do not align with the scattering model)

In addition, this same multi-temporal image sequence allows the algorithm to include a sensitive change detection component for improved robustness. Change detection will allow for refinement within the multitemporal image sequence for change of class during the image sequence that may be more robust than simply classifying the image backscatter and backscatter ratio values. The four refined image classes are:

- N_2IV: Not inundated to inundated vegetation (increase in double bounce scattering component)
- IV_2N: Inundated vegetation to not inundated (decrease in double bounce scattering component)
- N_2O: Not inundated to open water (decrease in scattering to only low specular scattering)
- O_2N: Open water to not inundated (increase in specular or volume scattering)

Given the calibration correction and the image values from Equations 6.3-5 and 6.3-6, the multi-temporal average of the 2n images is $\overline{\sigma_{\mathrm{pq}}}$.

INUNDATED VEGETATION

Classification C for each calibrated pixel *x, y* (or segment *k*) is:

$$\mathrm{C}_{x,y} = \mathrm{IV} \quad \text{or} \quad \mathrm{C}_k = \mathrm{IV} \quad \text{if} \quad \begin{cases} \dfrac{\overline{\sigma_{\mathrm{HH}}}}{\overline{\sigma_{\mathrm{HV}}}} > \sigma_{\mathrm{T}}^{\mathrm{r_{iv}}} & \text{and} \\ \overline{\sigma_{\mathrm{HH}}} > \sigma_{\mathrm{T}}^{\mathrm{HH_{iv}}} \end{cases} \qquad \textbf{6.4-1}$$

where the thresholds $\sigma_{\mathrm{T}}^{\mathrm{r_{iv}}}$ and $\sigma_{\mathrm{T}}^{\mathrm{HH_{iv}}}$ may be a function of the incidence angle, θ_{inc}, and are determined through a pre-launch and post-launch calibration process. $\sigma_{\mathrm{T}}^{r_{\mathrm{iv}}}$ is the threshold value for classification of inundated vegetation ("IV") from the ratio of the polarization channels HH and HV, $\frac{\overline{\sigma_{\mathrm{HH}}}}{\overline{\sigma_{\mathrm{HV}}}}$, and $\sigma_{\mathrm{T}}^{\mathrm{HH_{iv}}}$ is the threshold value for classification of inundated vegetation from the HH backscatter given by $\overline{\sigma_{\mathrm{HH}}}$. The backscatter, including the multitemporal average, is also a function of incidence angle.

OPEN WATER

Classification C for each pixel *x, y* (or segment *k*) of the image for open water ("OW") for the multi-temporal average image is:

$$\mathrm{C}_{x,y} = \mathrm{OW} \quad \text{or} \quad \mathrm{C}_k = \mathrm{OW} \quad \text{if} \quad \begin{cases} \dfrac{\overline{\sigma_{\mathrm{HH}}}}{\overline{\sigma_{\mathrm{HV}}}} > \sigma_{\mathrm{T}}^{\mathrm{r_{ow}}} & \text{and} \\ \overline{\sigma_{\mathrm{HH}}} < \sigma_{\mathrm{T}}^{\mathrm{HH_{ow}}} \end{cases} \qquad \textbf{6.4-2}$$

where the thresholds $\sigma_{\mathrm{T}}^{r_{\mathrm{ow}}}$ and $\sigma_{\mathrm{T}}^{\mathrm{HH_{ow}}}$ may be a function of the incidence angle, θ_{inc}, and are determined through a pre-launch and post-launch calibration process. $\sigma_{\mathrm{T}}^{r_{\mathrm{ow}}}$ is the threshold value for classification of open water from the ratio of the polarization channels HH and HV, $\frac{\overline{\sigma_{\mathrm{HH}}}}{\overline{\sigma_{\mathrm{HV}}}}$, and $\sigma_{\mathrm{T}}^{\mathrm{HH_{ow}}}$ is the threshold value for classification of open water from HH backscatter given by $\overline{\sigma_{\mathrm{HH}}}$.

NOT INUNDATED

All other image pixels have $C_{x,y}$=NI or C_k=NI. This generally encompasses areas outside the wetlands mask and may include areas within the wetlands mask, such as those areas determined as not inundated ("NI") by exclusion from the open water and inundated vegetation classes.

NOT CLASSIFIED

There may be a small number of pixels where the classification is indeterminate ("NC"). For example, at the given incidence angle, it is not possible to conclusively classify the data. For those cases, the classification would be $C_{x,y}$=4 or C_k=4.

$$\mathrm{C}_{x,y} = \mathrm{NC} \quad \text{or} \quad \mathrm{C}_k = \mathrm{NC} \quad \text{if} \quad \begin{cases} \sigma_{\mathrm{T}}^{\mathrm{r_{in}}} > \dfrac{\overline{\sigma_{\mathrm{HH}}}}{\overline{\sigma_{\mathrm{HV}}}} > \sigma_{\mathrm{T}}^{\mathrm{r_{ow}}} & \text{and} \\ \sigma_{\mathrm{T}}^{\mathrm{HH_{in}}} > \overline{\sigma_{\mathrm{HH}}} > \sigma_{\mathrm{T}}^{\mathrm{HH_{ow}}} \end{cases} \qquad \textbf{6.4-3}$$

TRANSITION FROM NOT INUNDATED TO INUNDATED VEGETATION

Examining the change in backscatter from the multi-temporal "typical" inundation state would refine the classification of transition regions C' within C. If the change in backscatter meets calibrated thresholds for a transition from not inundated vegetation

to inundated vegetation ("N_2IV"):

$$C'_{x,y} = N_2IV \quad \text{or} \quad C'_k = N_2IV \quad \text{if} \quad \begin{cases} C = NI \quad \text{and} \\ \sigma^{c}_{n,HH} > \sigma^{HH_{veg}}_{T} \quad \text{and} \\ \dfrac{\sigma^{c}_{n,HH}}{\overline{\sigma_{HH}}} > \sigma^{tr_{min\text{-}iv}}_{T} \quad \text{and} \\ \dfrac{\sigma^{c}_{n,HV}}{\overline{\sigma_{HV}}} < \sigma^{tr_{HVmax}}_{T} \end{cases} \tag{6.4-4}$$

where $\sigma^{HH_{veg}}_{T}$ is the minimum HH threshold backscatter value for vegetation covered terrain; $\sigma^{tr_{min\text{-}iv}}_{T}$ is the minimum change threshold ratio relative to the previous observation for HH backscatter indicating a transition from non-inundated to inundated vegetation; and $\sigma^{tr_{HVmax}}_{T}$ is the maximum HV change threshold ratio relative to the previous observation indicating that the vegetation characteristics did not otherwise change.

TRANSITION FROM INUNDATED VEGETATION TO NOT INUNDATED

Looking for areas that may be decreasing in inundation extent from inundated vegetation to not-inundated ("IV_2N"):

$$C'_{x,y} = IV_2N \quad \text{or} \quad C'_k = IV_2N \quad \text{if} \quad \begin{cases} C = IV \quad \text{and} \\ \sigma^{c}_{n,HH} > \sigma^{HH_{veg}}_{T} \quad \text{and} \\ \dfrac{\sigma^{c}_{n,HH}}{\overline{\sigma_{HH}}} < \sigma^{tr_{max\text{-}iv}}_{T} \quad \text{and} \\ \dfrac{\sigma^{c}_{n,HV}}{\overline{\sigma_{HV}}} > \sigma^{tr_{HVmin}}_{T} \end{cases} \tag{6.4-5}$$

where $\sigma^{tr_{max\text{-}iv}}_{T}$ is the maximum change threshold ratio relative to the multi-temporal average observation for HH backscatter, indicating a transition from inundated to non-inundated vegetation; and $\sigma^{tr_{HVmin}}_{T}$ is the minimum HV change threshold ratio relative to the multi-temporal average, indicating that the vegetation characteristics did not otherwise change.

TRANSITION FROM NOT INUNDATED TO OPEN WATER

Similarly, for open water we may examine cases where open water extent is increasing ("N_2O"):

$$C'_{x,y} = N_2O \quad \text{or} \quad C'_k = N_2O \quad \text{if} \quad \begin{cases} C = NI \quad \text{and} \\ \sigma^{c}_{n,HH} < \sigma^{HH_{veg}}_{T} \quad \text{and} \\ \dfrac{\sigma^{c}_{n,HH}}{\overline{\sigma_{HH}}} < \sigma^{tr_{max\text{-}ow}}_{T} \end{cases} \tag{6.4-6}$$

where $\sigma^{tr_{max\text{-}ow}}_{T}$ is the maximum change threshold ratio relative to the multi-temporal average for HH backscatter, indicating a transition from non-inundated terrain without vegetation to open water.

TRANSITION FROM OPEN WATER TO NOT INUNDATED

Looking for areas that may be decreasing in open water extent ("O_2N"):

$$C'_{x,y} = O_2N \quad \text{or} \quad C'_k = O_2N \quad \text{if} \quad \begin{cases} C = OW \quad \text{and} \\ \sigma^{c}_{n,HH} < \sigma^{HH_{veg}}_{T} \quad \text{and} \\ \dfrac{\sigma^{c}_{n,HH}}{\overline{\sigma_{HH}}} > \sigma^{tr_{min\text{-}ow}}_{T} \end{cases} \tag{6.4-7}$$

where $\sigma^{tr_{min\text{-}ow}}_{T}$ is the minimum change threshold ratio relative to the multi-temporal average for HH backscatter, indicating a transition from open water to non-inundated terrain without vegetation.

Similar tests for indeterminate areas where C=4 for Equations 6.4-4 and 6.4-6 would be made. For all pixels or regions where C′ is nonzero, C is replaced with C′.

An error layer will be generated utilizing the observed probability distribution function of inundated vegetation, open water, and non-inundated backscatter values compared with the calibrated threshold values.

6.4.2 VALIDATION PRODUCTS

The specified product for validation of the L2 requirement to measure inundation extent is a raster classification of inundated extent at a spatial resolution of 1 hectare. The classification has the following primary values: 1) inundated vegetation; 2) open water; 3) not inundated; 4) indeterminate. Categories 1, 2, 3, and 4 may have subcategories for pixels in transition. The product can be generated every 12 days after the first 6 (approximate) months of observations are completed and assumes that 20 or 40 MHz dual polarization HH, HV data are acquired every 12 days for both ascending and descending orbit directions. The input data are the L2, 10-20 m, radiometric and terrain corrected, multi-looked imagery. The incidence angle for each image pixel should also be provided as input data.

Also required for generating the classification product is an a priori wetlands mask where inundation could occur and excluding confounding landscape types such as urban areas and agricultural areas, as well as terrain slopes, volcanic terrains, and deserts. For the selected Cal/Val sites, these masks can be easily generated

from ancillary information such as land cover classifications like the National Land Cover Database (NLCD) generated from Landsat data. The value of each 1-ha cell will be either through direct classification of the average of the input 10-20-m SAR data product or by majority vote among the classes of the 16 input pixels and the direct classification of the 1 ha SAR.

An error probability layer for the classification will be provided, based on a statistical analysis of the observed backscatter distributions versus the backscatter thresholds used in the classification.

6.5 ECOSYSTEMS SCIENCE – CROP MONITORING

The NISAR L2 science requirement for agricultural crop area is expressed as:

The NISAR project shall measure crop area at 1 hectare resolution every 3 months with a classification accuracy of 80%.

To feed a growing population of more than 8 billion, food production and supply occur on a global basis. To better guide policy and decision making, national and international organizations work to transparently monitor trends and conditions of agriculture on a timely basis. Because of the variable nature of planting and harvesting practices, efforts such as this are manpower intensive and time-consuming tasks.

Organizations such as the U.S. Department of Agriculture (USDA), World Bank, and Food and Agriculture Organization of the United Nations (FAO) publish statistics on crop area, type, and yield on a regular basis. Much of these data are derived from in-country surveys, augmented by what are, to date, limited remote sensing components. The community continues to be solicited for inputs regarding crop area, type, and yield as well.

While current remote sensing inputs for crop-area identification methods rely primarily on reflectance spectra from optical data, radar has the potential for making a great impact because of its sensitivity to the structure of groundcover and its insensitivity to cloud cover and lighting conditions (Huang, X. et al. 2020). Through its global observing strategy and 12-day revisit period, the NISAR mission has the capacity for collecting data that are relevant to the societally important applications of monitoring and measuring global food production. This is reflected in the mission's crop area requirement.

6.5.1 THEORETICAL BASIS OF ALGORITHM

The crop area algorithm is based on the coefficient of variation (CV), which is the ratio of the standard deviation over the mean for a time series of orthorectified radar cross-section data (Whelen and Siqueira, 2018). Here, the coefficient of variation is computed for both the co- and cross-polarized data (HH and HV) averaged to a hectare-scale, and where the time series are collected quarterly. These time periods cover typical growing seasons of crops and make best use of the background (i.e., HH ± HV) land observations planned by NISAR.

There are two principal advantages that are offered by NISAR over existing technical approaches for crop area estimation. These are: 1) an effectively all-weather observing strategy that will provide observations of a given area every 12 days (or two times every 12 days if we include ascending and descending passes), and 2) the measure of radar cross section, which is dependent on contributions of volume and surface scattering, which are likely to change dramatically for actively managed agricultural landscapes. Measures of radar cross section are more robust than interferometric measures of change, such as through the decorrelation signature, which may be an appealing alternative or augmentation to the base algorithm that is described here and will be used for estimating active crop area.

There are two types of error that can affect the active crop area estimates: those associated with the instrument and those related to the region being observed. For sources of error related to the instrument, measurement stability and cross-track variability in the signal to noise ratio (SNR) will be the dominant factors. Simulations and ALOS-1 observations for India have shown that the coefficient of variation will be robust for relative calibration errors up to 1 dB (ALOS-1 is quoted to have a calibration accuracy of some 10ths of a dB).

Variation in the SNR will occur as a function of the target brightness and the incidence angle. Normalization of the RCS standard deviation by the RCS mean will remove much of this variability. Regions with very low SNR, close to the noise floor of NISAR, will be removed through a simple threshold classifier based on the brightness of the mean RCS.

Sources of error in active crop area that are associated with the target can be principally assigned to three sources. These are: 1) weather-induced changes to the radar cross section, 2)

disturbance events mistaken for crop regions, and 3) misclassification of regions as potentially belonging to agricultural landscapes (e.g., urban areas and open water).

Errors that are related to weather-induced changes in the RCS will manifest themselves as short-term variations in the trajectory of the RCS as the agricultural region changes from barren land, emergent plants, full grown crops to harvested land. As the plants above the soil grow and mature, changes in the soil moisture will have less of an effect on the overall signature, even for regions that are left fallow, and hence classified as non-active crop regions. The changes in the radar cross section for barren ground is only on the order of a few dB or less, much smaller when compared to the many dB that the RCS undergoes throughout the growing season.

Errors induced by a disturbance event as opposed to actively managed land may result in a degree of misclassification for agricultural area. This effect is expected to be small however, especially when comparing regions from one year to the next. For this reason, estimates of active agricultural crop area are not planned to meet the full requirement accuracy of 80% until after the first year of NISAR observations.

Lastly, misclassified regions such as open water and urban regions included in the mask for NISAR assessment of agricultural area are a potential source of error. Use of a simple threshold classifier on the RCS mean, however, has shown to be an effective method for removing open water regions and those with low SNR; while urban regions with a bright RCS and proportionally small variation in the RCS as a function of time, have been shown thus far to be correctly identified by the CV-based classifier of crop area used here. Kraatz et al. (2023) demonstrate the ability of the CV approach to accurately classify crop and non-crop area over complex landscapes, with the analysis extending over built-up regions, forest, and agricultural fields in Maryland, USA. To date, the CV-based classifier also appears to be more successful, detailed, and accurate than those classifiers that depend on optical data alone.

The NISAR measurement metric for crop area determination relies on the CV, which is a measure of the degree of change (normalized with respect to the mean backscatter) as a function of time. This metric makes use of the fact that agricultural landscapes are heavily managed, and hence, the scattering physics of agricultural crops change more than other land cover types. Such a metric has been shown to be robust over varied landscapes and geographic regions, with a published example demonstrated over the continental US (Rose et al., 2021). The CV method described here has been tested under NISAR-like observing conditions, such as those that are related to a specialized staggered pulse repetition frequency (PRF) processing approach being implemented by NISAR (Kraatz et al., 2022), and over regions where repeat-observations from NASA's UAVSAR L-band platform were made over agricultural growing regions in the southeastern US (Kraatz et al., 2021). It should be noted too, that a time-series analysis of SAR data has proven to be useful for classification of crop types as well (Whelen and Siqueira, 2017; 2018).

A full treatment and analysis using the CV for crop area determination using L-band ALOS-2 PALSAR-3 NISAR simulated data, C-Band Sentinel-1A data, and Planet-Scope optical data can be found in Anconitano et al. (2024). To provide a more theoretical foundation for the use of the CV based on the target scattering physics, a theoretical scattering model and observational error model were developed in Cartus et al., 2018. This model helps show the ability of repeated SAR observations to detect the separation between simulated natural and actively managed landscapes. A summary of this model is given here.

A relationship between radar observation and classification accuracy is needed for the observations and those components that contribute to the target RCS. The observational

error model is the same model as used by the forest disturbance algorithm (Cartus et al., 2018). It relates the observed radar cross section for each polarization pq, written here as σ^o_{obs} for simplicity, to the observation error sources, $\sigma^o_{obs\text{-}error}$, and the radar cross section of an agricultural field, σ^o_{field} :

$$\sigma^o_{\text{obs}} = \sigma^o_{\text{obs-error}} + \sigma^o_{\text{field}} \qquad \textbf{6.5-1}$$

It can be shown that the radar cross section of the field can be broken down into components of the return from the ground, σ^o_{ground}, volume, σ^o_{vol}, and double bounce, σ^o_{db}, returns from the vegetation components. Additional parameters that govern the model are the fractional canopy cover, η, the attenuation of the signal as it passes through the vegetation layer, α, and the height of the vegetation layer, *h*. The net model, which is based on (Dobson and Ulaby, 1986; Askne et al., 1997) is given as

$$\sigma^o_{\text{field}} = \sigma^o_{\text{ground}}[1-\eta(1-e^{-\alpha h})] + \sigma^o_{\text{vol}}[\eta(1-e^{-\alpha h})] + \sigma^o_{\text{db}}\eta h e^{-\alpha h} \qquad \textbf{6.5-2}$$

By creating a time series model for the inputs of Equation 6.5-2 (e.g., in terms of how η, h, and α are changing over the growing season), it is possible to create a time series for the radar cross section observed for a field. A similar time series is created for a land cover type that is not changing over time (e.g., given values for the RCS of ground, volume, and double bounce). With these two simulated time series, the observing period of NISAR is included to determine the season during which the two target types are being observed, and a time series of NISAR observations simulated and the CV computed. Once done, a threshold classifier is employed based on the CV and a hypothesis test applied to the resulting classification. Given that the CV probability density functions (pdfs) have thus been determined for the two different land cover types (managed versus unmanaged), the hypothesis test and probabilities of correct and incorrect classification are determined as a function of the choice of threshold.

6.5.2 IMPLEMENTATION APPROACH FOR ALGORITHM

The algorithm flow is presented in Fig. 6-10. Time series are assembled every 3 months after the first year of data collection, and from that, the CV is computed for each available polarization. Minimally, this would be HH and HV polarized fields; however, in the US and in India, it is expected that fully polarimetric data will be available.

For each of the computed coefficients of variation, a determination will be made via a predetermined threshold, on a per hectare basis, if the CV indicates that the area is actively being managed or not. Results for each polarization will be compared with the other polarization results, as well as combined with ancillary data that may be available from ESA's Climate Change Initiative (CCI; esa-landcover-cci.org) and the Shuttle Radar Topography Mission (SRTM) (or better) topographic map.

Based on the limited set of inputs, and comparison to the previous quarter's results, a determination is made for which of the four classes that each 1-ha region should be classified: 1) active crop area, 2) newly active crop area, 3) inactive crop area, and 4) not crop. The observing strategy for the determination of crop area is broken down into two time periods: 1) during the first year of observations, there is no planned delivery of crop area determination from NISAR, and 2) during successive years, a 1 ha-resolution raster image of the crop area classification will be generated every three months.

The first year of NISAR observations are used for the determination of baseline thresholds for crop area classification based on the CV metric determined for both HH and HV polarizations (CV_{HH} and CV_{HV}), computed separately for the ascending and descending passes of NISAR. These thresholds are determined through the NISAR post-launch calibration period, where

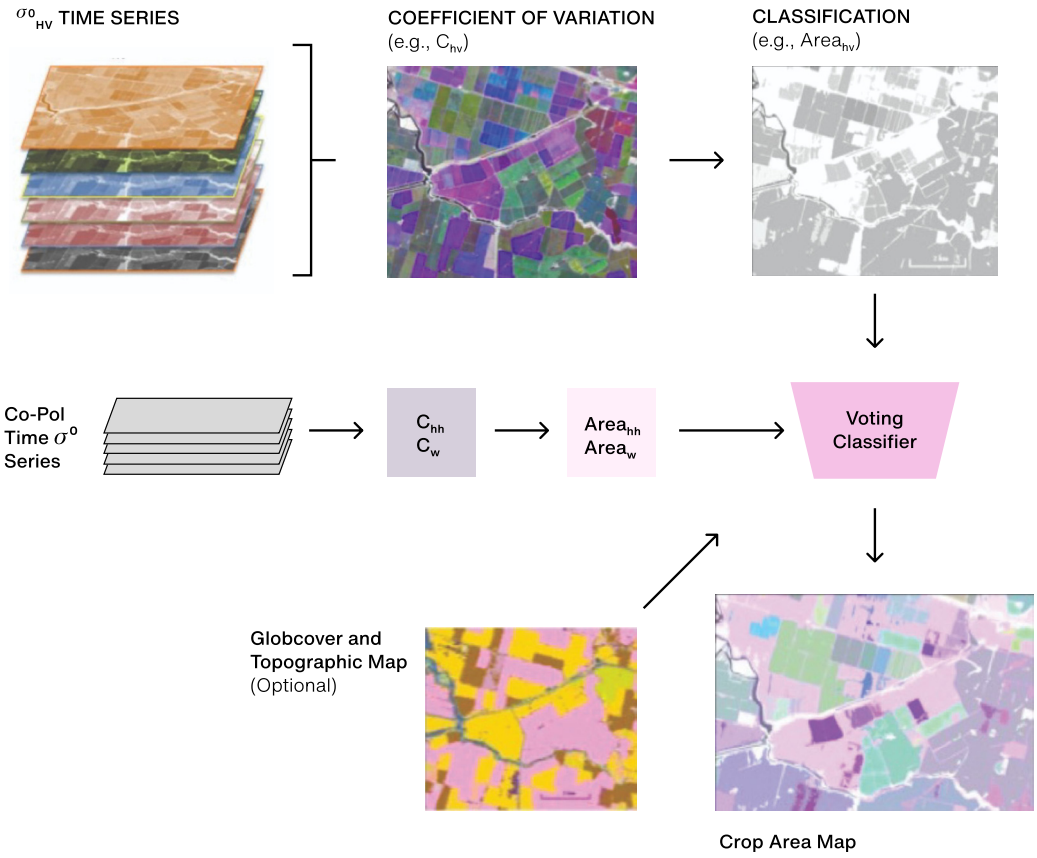

FIGURE 6-10

Data and algorithm flow diagram for active crop area classification.

histograms of CV_{HH} and CV_{HV} for the ascending and descending passes are created for crop and non-crop regions using predetermined validation resources from ESA's CCI and USDA's CropScape data layers. Values of CV_{HH} and CV_{HV} are determined for each 3-month period, post launch, bracketed by the dates: December 1 – February 28, March 1 – May 31, June 1 – August 31, and September 1 – November 30, as well as for the entire one-year period.

The CV for each polarization is determined by the standard deviation of the radar cross section divided by the mean of the radar cross section, collected as a function of time (e.g., the 3-month period), at the 20-m resolution of the input data product. Units of the input radar cross sections should be in m^2/m^2 and not dB. That is:

$$\mathrm{CV}_{\mathrm{pq}} = \frac{\mathrm{stddev}(\sigma^o_{\mathrm{pq}}(t))}{\mathrm{mean}(\sigma^o_{\mathrm{pq}}(t))} \qquad \textbf{6.5-3}$$

where

$$\mathrm{mean}(\sigma^o_{\mathrm{pq}}(t)) = \overline{\sigma^o_{\mathrm{pq}}} = \frac{1}{N}\sum_{n=1}^{N}\sigma^o_{\mathrm{pq}}(n\Delta t) \qquad \textbf{6.5-4}$$

and

$$\mathrm{stddev}(\sigma^o_{\mathrm{pq}}(t)) = \sqrt{\frac{1}{N-1}\sum_{n=1}^{N}\left(\sigma^o_{\mathrm{pq}}(n\Delta t) - \overline{\sigma^o_{\mathrm{pq}}}\right)^2} \qquad \textbf{6.5-5}$$

In the above, N is the total number of observations in the observing period, and Δt is the time between NISAR passes (expected to be 12 days). Calculations of the CV are made on a per-pixel (20 m) basis and aggregated after computation into 1-hectare pixels where both the mean and standard deviation of the CV determination are kept at the 1 ha-resolution for each polarization and orbital direction of the satellite. Hence, each 1 ha-resolution element will

consist of eight values, four for the mean of the CV, and four for the standard deviations, as in:

$$\mathrm{CV}_{\text{HH-asc}},\ \mathrm{CV}_{\text{HV-asc}},\ \mathrm{CV}_{\text{HH-desc}},\ \mathrm{CV}_{\text{HV-desc}},$$
$$\mathrm{stddev}(\mathrm{CV}_{\text{HH-asc}}),\ \mathrm{stddev}(\mathrm{CV}_{\text{HV-asc}}),\ \mathrm{stddev}(\mathrm{CV}_{\text{HH-desc}}),\ \mathrm{stddev}(\mathrm{CV}_{\text{HV-desc}}) \quad \textbf{6.5-6}$$

Of the group of four estimates of CV, the estimate with the highest standard deviation will be eliminated and the remaining three will be used in a threshold classification whose value of threshold is determined through the NISAR calibration phase. An additional threshold will be used for detecting water bodies, which, because of their small values for radar cross section, will also display large values for CV. In the last step, a voting classifier is used to determine if the region is an active crop region or not.

Determination of which pixels change classes over time can be determined by comparing one time period classification versus a previous, thus providing useful information about planting and harvesting periods. More accurate determination of the start of the planting and harvesting seasons can be determined on a per-pixel basis by going back to the original radar cross-section data and using a running window to determine when the CV statistics changed.

6.5.3 VALIDATION PRODUCTS

The specified product for validation of the L2 requirement to measure crop area is a raster classification. The pixel values based on prior and current determination of active crop area are given in Table 6-3: 1) not a crop; 2) newly active crop area; 3) inactive crop area (fallow); 4) active crop area; and 5) not evaluated (class 0). The resolution of the product will be 1 ha. The product is intended to be generated every 3 months after the first year of observations are completed, and assumes that 20-MHz dual polarization HH, HV data are acquired every 12 days for both ascending and descending orbit directions.

The input product is the L2, 20-m, radiometric and terrain corrected, calibrated multi-look imagery for each of the polarizations, for each period of data collection. Mosaics of the data are not desired. To make the co-registration and geolocation of images a trivial process, pixel locations should be quantized onto a predetermined geographic grid.

Also required for generating the classification product is a land cover mask that indicates those regions where agricultural monitoring is intended to be performed. Additional layers would prove useful in increasing the accuracy of the agricultural area classification and are being investigated as part of the NISAR phase C efforts. These are as follows:

1. An up-to-date version of ESA's CCI land cover map (esa-landcover-cci.org). These data are useful for defining limits of urban areas, inside of which formal agricultural practices are excluded from the analysis.
2. Topographic and look angle maps that are co-registered to the NISAR data grid.

TABLE 6-3. PIXEL CLASSES FOR ACTIVE CROP AREA BASED ON PRIOR AND CURRENT DETERMINATION

		PRIOR DETERMINATION	
		0	1
Current Determination	0	Not a crop (class 1)	Fallow (class 2)
	1	Newly active (class 3)	Active (class 4)

Such maps need only be supplied once using the expected viewing geometry of the sensor.

6.6 CRYOSPHERE SCIENCE – ICE SHEETS

A major objective for NISAR is to collect data to measure velocity over the Greenland and Antarctic ice sheets through time. These same data will be used to determine the time-varying position of the grounding line around Antarctica and on floating ice tongues in Greenland. The ice sheet related science requirements call for measurements of ice sheet velocity derived using a combination of interferometric phase data and offsets from speckle tracking. Near ice sheet grounding lines, time series of interferometric phase will be differenced to estimate relative tidal displacement, which helps grounding line position. This section describes the algorithms needed to generate these products.

6.6.1 THEORETICAL BASIS OF ALGORITHM

For slow-moving areas (<50 m/yr) and some fast-moving areas where the data are conducive to such measurement, horizontal velocity will be measured using radar LOS determined from the interferometric phase from at least two crossing orbit tracks (i.e., ascending/descending) under the assumption that flow is parallel to the known surface (Joughin et al., 1998). An advantage of this technique is that the data are relatively high-resolution (<100 m) and the phase noise is low (<~2 cm). A major disadvantage is that for fast moving areas it is difficult or impossible to unwrap the phase. Another issue is related to regions where there is significant ionospheric activity such that the spatially variable path delay introduces large interferometric phase errors (several m/yr errors). For NISAR, these errors will largely be removed using split-spectrum processing applied to the 80-MHz-bandwidth data.

In areas where the motion is too fast for interferometric phase measurements, velocity will be determined using the azimuth and range offsets derived by cross-correlating patches from pairs of images to determine displacements between image acquisitions (Gray et al., 1998; Michel and Rignot, 1999). Although image features can improve correlation, this technique works best when the speckle patterns are well correlated; hence, this technique is often called speckle tracking. Advantages to this method are that velocity estimates can be derived from a pair of images collected along a single orbit track (i.e., ascending or descending only orbits) and it can be used to measure extreme motion (>10 km/yr). Because the technique uses image chips several 10s of pixels in dimension, the spatial resolution is much poorer (>~200 m) than phase estimates. Since displacement is resolved to within a fraction (i.e., ~1/20 of a several-meter pixel) of a range or azimuth pixel, accuracy also is much less than phase estimates, which resolve motion to a fraction of a wavelength.

In polar regions, ionospheric distortion can be severe, particularly for the azimuth offsets. This distortion can produce errors of more than 100 m/yr in some locations. This problem can be mitigated by using range-only offsets from crossing orbits as described below.

The requirements for fast and slow motion reflect the fact that lower resolution speckle tracking is best suited to measuring fast-flowing outlet glaciers, while interferometric phase is ideal for the slow-flowing interior. Although the 50 m/yr distinction between slow and fast flow in the requirements is aimed at separating the areas where each technique should work the best, in many cases, interferometric phase will still work in considerably faster-flowing areas (up to about 500 m/yr for NISAR). Thus, no single velocity threshold can cleanly separate the regions where phase fails and speckle-tracking must be used. For example, the RADARSAT phase can sometimes be unwrapped on smooth flowing ice shelves at speeds approaching 1000 m/yr. By contrast, for some regions on the ice sheets where the speeds are less than 100 m/yr, there are strong phase gradients where ice flows over

bumps that make phase unwrapping difficult or impossible. As a result, for all the velocity-related requirements, at each point on the ice sheet, the corresponding requirement will be met using the best available combination of interferometric phase and speckle-tracked offsets. The different temporal and spatial resolutions specified in the requirements reflect the amount of spatial and temporal averaging necessary to meet each requirement.

The basic algorithmic approach will follow earlier approaches (Joughin, 2002). Specifically, at each point in the output grid, the algorithm will cycle through the various options:

1. Range-azimuth offsets from a single orbit track,
2. Unwrapped phase (for range) with azimuth offsets from a single orbit track,
3. Range-range offsets from crossing orbit tracks, and
4. Unwrapped phase-phase data from crossing orbits.

At each point in the output, all the viable combinations will be calculated. Estimated errors for each type of velocity estimate will be used to weight the results to produce an optimal inverse-error weighted average for the horizontal components of velocity. All of these combinations have been widely used (Joughin et al., 2010a; Rignot et al., 2011a; Mouginot et al., 2017), with recent work demonstrating the range-range offsets combination (Joughin et al., 2018). This latter combination is more attractive for NISAR because a) the 80-MHz mode provides considerably finer range (~2.5 m) than azimuth (~7 m) resolution, b) there will be ample ascending/descending coverage, and c) relative to azimuth offsets, the range offsets are less affected by ionospheric distortion. Hence, the range-range offsets combination likely will be the dominant contributor to velocity estimates in regions of fast flow. All of the above methods will be implemented, but any of them can be selectively turned off (e.g., methods 1 and 2 where azimuth offsets add no improvement to the derived estimates).

All ice-sheet velocity maps will be produced on polar stereographic grids at a posting of 100 m (actual resolution in faster-moving regions will be 250 m or better). Consistent with the existing products, the Greenland map-projection will use a standard latitude of 70°N and a central meridian of 45°E, and the Antarctica projection will use a standard latitude of 71°S and a central meridian of 0°. Glacier products outside of Greenland and Antarctica will use region-dependent projection (e.g., UTM).

TIDAL DISPLACEMENT

Differential tidal displacement products will be produced by differencing pairs of interferograms over the ice shelves and grounding lines. This differencing approach cancels the horizontal motion (assumed constant) common to both interferograms, leaving only the double-differenced, time-varying, vertical tidal displacement, which indicates the location of the grounding line/zone, i.e., the place where ice detaches from the bed and starts becoming afloat in the ocean waters (Rignot et al., 2011b; Scheuchl et al., 2016). Although this technique is generally applied to phase-only data, in the presence of very high strain rates, it is possible to apply the technique on range offsets with a reduced level of precision in determining the grounding line position and in detecting vertical displacements (Joughin et al., 2016).

GLACIER ESTIMATES

The mission will collect an unprecedented volume of data to measure glacier velocities in regions outside of Greenland and Antarctica. The steep terrain where many of these glaciers exist, however, present challenges (e.g., glaciers lying in radar-shadowed regions) that make it difficult to quantify what fraction of glaciers can be successfully mapped; prior measurements indicate a relatively high likelihood of success for many regions (Burgess et al., 2013). As a result, glaciers are a mission goal rather than a requirement, requiring no formal validation. Thus, the focus of this document is on producing ice-sheet velocity measurements. These algorithms, however, are

directly applicable to mapping glaciers. Actual implementations of production processors might require some modification for specific projections and other region-dependent data. Hence, throughout the remainder of the document where ice-sheet velocity mapping is referred to, it is with the understanding that the text is equally applicable to glaciers; any place where this might not be the case will be so noted.

6.6.2 IMPLEMENTATION APPROACH FOR ALGORITHM

The implementation approach for estimating ice velocities uses speckle tracking and interferometric phase to compute the velocities.

QUANTITIES USED IN VELOCITY ESTIMATION AND GROUNDING-LINE ESTIMATION

Velocity estimates are derived using either interferometric phase or speckle-tracked matches as described below. Here we define the notation used for the quantities that go into the velocity estimation equations.

RAW SPECKLE-TRACKED OFFSETS

At a given set of range-azimuth coordinates, (ρ_1,s_1), in the reference SLC (first image acquired), cross correlation is used to locate the same point, (ρ_2,s_2), in the second SLC, which is in non-integer values. The raw range and azimuth offsets, (δ_ρ, δ_S), are given by

$$\delta_\rho = \rho_2 - \rho_1 \text{ and } \delta_s = s_2 - s_1 \qquad \textbf{6.6-1}$$

RAW INTERFEROMETRIC PHASE

Given two co-registered SLCs, I_1 and I_2, the phase of the interferogram is given by

$$\phi_w = \mathrm{Arg}(I_1 I_2^*) \qquad \textbf{6.6-2}$$

which is only known modulo 2π. Thus, a phase unwrapping algorithm is applied to determine the unwrapped phase, f.

CALIBRATED OFFSETS AND PHASE

The interferograms and range offsets also contain information about the topography, with sensitivity determined by the baseline. The imaging geometry will introduce additional displacements unrelated to surface motion. These differences can be corrected using the orbit and timing information. Here we encapsulate this information (i.e., state vectors, range delays, and any other ancillary information) into vectors, $\mathbf{o}_1$ and $\mathbf{o}_2$, for the first and second images, respectively. With this information, signals other than those related to surface motion can be removed to produce the surface-displacement only component of the range offset as

$$\widetilde{\delta}_\rho = \delta_\rho - f_\rho(\boldsymbol{o_1}, \boldsymbol{o_2}, z) \qquad \textbf{6.6-3}$$

Note here we assume the offsets have been scaled from pixels to meters. As our purpose here is to define terms rather than to provide the details of the corrections, which are provided elsewhere, we have bundled the geometry, baseline, and elevation dependent corrections in a scalar function, f_ρ. Similarly, we can correct the azimuth displacements as

$$\widetilde{\delta}_s = \delta_s - f_s(\boldsymbol{o_1}, \boldsymbol{o_2}) \qquad \textbf{6.6-4}$$

The unwrapped interferometric phase, f, requires similar correction such that

$$\widetilde{\phi} = \phi - f_\phi(\boldsymbol{o_1}, \boldsymbol{o_2}, z) \qquad \textbf{6.6-5}$$

Note this correction for phase assumes that at least one point of known speed is used as a control point to determine the unknown 2π ambiguity associated with phase unwrapping. Such control points are routinely used in ice-sheet velocity mapping (Joughin et al., 2010b; Rignot et al., 2011a).

VELOCITY ESTIMATES AT A POINT

The following subsection describes how velocity is estimated at each point. Note all equations are computed assuming the look vector lies in a plane orthogonal to the satellite track (e.g., small squint). These equations have been

widely used with data from a variety of sensors, with no issues thus far. The imaging geometry for NISAR has low squint, so these equations should be similarly valid. As synthetic products become available, we will examine the validity of this assumption given the more rigorous NISAR error requirements (< 1 m/yr). Should this assumption not hold, then a transformation to a squinted coordinate system will be applied to the equations below. Such a transformation, however, does not change any of the underlying principles described below, nor have an impact on the viability of the algorithms, which are all well tested.

ICE VELOCITY DERIVED FROM SPECKLE TRACKING ALONG A SINGLE ORBIT TRACK

Speckle tracking provides two components of the three-component velocity vector: the along-track horizontal component and the line-of-sight component, which mixes vertical and horizontal motion (Fig. 6-11). Although there is a component of the vertical velocity directed toward or away from the ice-sheet surface, this motion generally is small enough (<1 m/yr) that it can be ignored or estimated independently. Instead, much of the vertical motion is assumed to be due to surface-parallel flow (i.e., a particle on the surface flowing along the surface gradient; Joughin et al., 1996). If the slope is known and surface-parallel flow can be assumed, the line-of-sight component can be resolved into horizontal and vertical components.

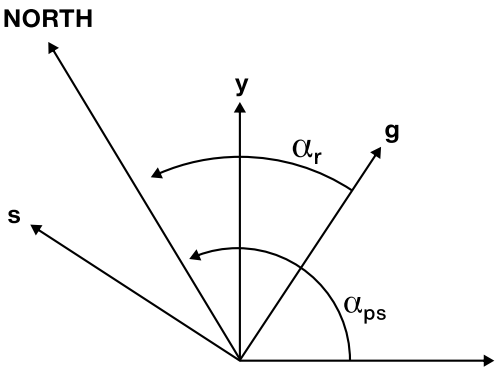

FIGURE 6-11

Radar- and projection-determined coordinate systems and their rotation angles relative to north.

The line-of-sight displacement is given by

$$\widetilde{\delta}_\rho = \Delta g \sin(\psi) - \Delta z \cos(\psi) \quad \textbf{6.6-6}$$

where Ψ is the local incidence angle (with respect to an ellipsoidal Earth), and Δz and Δg are the vertical and ground-range displacements, respectively. Solving for the horizontal displacement yields the following expression:

$$\Delta g = \frac{\widetilde{\delta}_\rho}{\sin(\psi)} + \Delta z \cot(\psi) \quad \textbf{6.6-7}$$

Assuming surface parallel flow, the vertical displacement is given by

$$\Delta z = \widetilde{\delta}_s \frac{\partial z}{\partial s} + \Delta g \frac{\partial z}{\partial g} \quad \textbf{6.6-8}$$

Combining these two equations yields

$$\Delta g = \frac{\frac{\widetilde{\delta}_\rho}{\sin(\psi)} + \widetilde{\delta}_s \cot(\psi)\frac{\partial z}{\partial s}}{1 - \cot(\psi)\frac{\partial z}{\partial g}} \quad \textbf{6.6-9}$$

Using this equation and the azimuth-offset estimate, the velocities in the radar-determined horizontal coordinates are given by

$$v_g = \frac{\Delta g}{\Delta T} \text{ and } v_s = \frac{\widetilde{\delta}_s}{\Delta T} \quad \textbf{6.6-10}$$

Equation 6.6-10 gives the horizontal ice velocity in the radar-determined coordinates, but the final estimate is produced in the projection-determined xy-coordinate system (Fig. 6-11).

The rotation angle of the radar coordinates with respect to north is given by

$$\alpha_r = \begin{cases} \text{atan2}\left(\frac{\partial s}{\partial \text{lat}}, \frac{\partial g}{\partial \text{lat}}\right) & \text{Right Looking} \\ \text{atan2}\left(\frac{\partial s}{\partial \text{lat}}, \frac{-\partial g}{\partial \text{lat}}\right) & \text{Left Looking} \end{cases} \quad \textbf{6.6-11}$$

In this equation, the quantities δ_s, δ_g are the distances in the along-track and ground-range coordinates, respectively, corresponding to an incremental northward displacement, δ_{lat}. The

rotation angle relative to north for a point (x_{PS},y_{PS}) in polar stereographic coordinates is given by

$$\alpha_{\mathrm{PS}} = \begin{cases} \operatorname{atan2}(-y_{\mathrm{PS}}, -y_{\mathrm{PS}}) & \text{Northern Hemisphere} \\ \operatorname{atan2}(y_{\mathrm{PS}}, y_{\mathrm{PS}}) & \text{Southern Hemisphere} \end{cases} \quad \textbf{6.6-12}$$

Note this angle is unique to each position in the output grid.

Horizontal velocities are then determined by rotating to the polar stereographic system as

$$\begin{bmatrix} v_x \\ v_y \end{bmatrix} = \begin{bmatrix} \cos(\alpha_{\mathrm{PS}} - \alpha_r) & \sin(\alpha_{\mathrm{PS}} - \alpha_r) \\ -\sin(\alpha_{\mathrm{PS}} - \alpha_r) & \cos(\alpha_{\mathrm{PS}} - \alpha_r) \end{bmatrix} \begin{bmatrix} v_g \\ v_s \end{bmatrix} \quad \textbf{6.6-13}$$

Note the polar-stereographic coordinate system preserves angles but has a latitude-dependent scale distortion. While locations are posted in polar-stereographic coordinates, which are subject to this distortion, velocity vectors are posted in meters/year with no scale distortion.

ICE VELOCITY DERIVED FROM SPECKLE TRACKING AND INTERFEROMETRY ALONG SINGLE ORBIT TRACK

In areas where interferometric fringes are noisy or aliased so they cannot be unwrapped, speckle tracking provides a reasonable estimate. If data are available only along a single orbit track and the phase can be unwrapped, then a hybrid estimate can be derived (Fig. 6-12). In this case, substituting the range displacement given by the offsets $(\widetilde{\delta}_\rho * \nabla_\rho)$ for the equivalent displacement in phase $(\lambda\widetilde{\phi}/4\pi)$ in Equation 6.6-9 yields the surface-parallel-flow approximated ground range displacement as

$$\Delta g = \frac{\frac{\lambda\widetilde{\phi}}{4\pi\sin(\psi)} + \widetilde{\delta}_s \Delta_s \cot(\psi)\frac{\partial z}{\partial s}}{1 - \cot(\psi)\frac{\partial z}{\partial g}} \quad \textbf{6.6-14}$$

Substituting this quantity into Equations 6.6-10 and 6.6-13 yields the horizontal velocity vector in polar stereographic coordinates.

ICE VELOCITY DERIVED FROM INTERFEROMETRY FROM CROSSING ORBITS WITH SURFACE-PARALLEL FLOW

When data from crossing ascending/descending orbits are available, the surface-parallel flow assumption can be used to estimate horizontal components of velocity (Joughin et al., 1998; Mohr et al., 1998). Geometrically, this makes this 3-D problem a 2-D problem by assuming the velocity vector lies in a tangent-plane to the ice surface. In this case, using phase from ascending and descending passes, the horizontal components of the velocity vector are given by

$$\begin{bmatrix} v_x \\ v_y \end{bmatrix} = (\boldsymbol{I} - \boldsymbol{ABC})^{-1}\boldsymbol{AB} \begin{bmatrix} \frac{\lambda_a \widetilde{\phi}_a}{4\pi\Delta T_a \sin(\psi_a)} \\ \frac{\lambda_d \widetilde{\phi}_d}{4\pi\Delta T_d \sin(\psi_d)} \end{bmatrix} \quad \textbf{6.6-15}$$

where

$$\boldsymbol{A} = \begin{bmatrix} \cos\beta & \cos(\alpha+\beta) \\ \sin\beta & \sin(\alpha+\beta) \end{bmatrix} \quad \textbf{6.6-16}$$

$$\boldsymbol{B} = \left(\frac{1}{\sin\alpha}\right)^2 \begin{bmatrix} 1 & -\cos\alpha \\ -\cos\alpha & 1 \end{bmatrix} \quad \textbf{6.6-17}$$

$$\boldsymbol{C} = \begin{bmatrix} \frac{\partial z}{\partial x}\cot(\psi_a) & \frac{\partial z}{\partial y}\cot(\psi_a) \\ \frac{\partial z}{\partial x}\cot(\psi_d) & \frac{\partial z}{\partial y}\cot(\psi_d) \end{bmatrix} \quad \textbf{6.6-18}$$

In the equations, quantities are as defined above with subscripts $_a$ and $_d$ to indicate whether they are from an ascending or descending pass, respectively. The angles α and β are defined in Fig. 6-12. The incidence angles Ψ_a are Ψ_d are defined relative to an ellipsoidal Earth. A detailed derivation of these equations is given by Joughin et al. (1998).

ICE VELOCITY DERIVED FROM SPECKLE TRACKING FROM CROSSING ORBITS WITH SURFACE-PARALLEL FLOW

As described above, the ionosphere may introduce unacceptably large errors in some azimuth offset estimates. Range offsets are much less sensitive to ionospheric errors, so

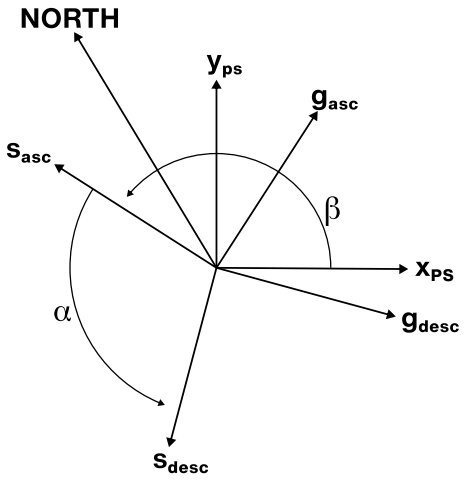

FIGURE 6-12

Definition of angles used in the computation of horizontal velocities from ascending and descending orbits. The angle between the polar stereographic x-axis and the local along-track direction for the ascending orbit is denoted by β and the angle between the ascending and descending along-track directions by α.

when range offsets are combined from crossing orbits, they can produce far less noisy velocity estimates. Such horizontal velocity estimates can be determined from range-offsets with the same methods as for interferometric phase. This measurement is made by replacing $(\lambda_a \widetilde{\phi}_a / 4\pi)$ and $(\lambda_d \widetilde{\phi}_d / 4\pi)$ in Equation 6.6-15 with , $\widetilde{\delta}_{\rho,a}$ and $\widetilde{\delta}_{\rho,d}$, where the $_a$ and $_d$ subscripts indicate the offsets for the ascending and descending orbits, respectively.

ICE VELOCITY MOSAICKING

The sections above describe how to measure velocity at a point given the relevant phase or offset data. Rather than point measurements, continental-scale mosaics stitched together from data derived from hundreds to thousands of SAR image pairs are required for ice sheets. Such algorithms are relatively mature, and ice-sheet wide mosaics have already been produced from earlier sensors (e.g., Fig. 6-13; Joughin et al., 2010a; Rignot et al., 2011a). While providing a major leap forward in our understanding of ice sheet behavior, products from existing sensors are limited in accuracy by insufficient data collection from instruments not optimized for this type of mapping. Temporal resolution of these products is also limited by a dearth of data (i.e., it took 20 years of the data from several SARs to produce a gap-free Greenland mosaic). Thus, by routinely imaging the ice sheets, NISAR will greatly improve the coverage, accuracy, and spatiotemporal resolution of ice velocity estimates to help improve our understanding of how the ice sheets will contribute to sea level change.

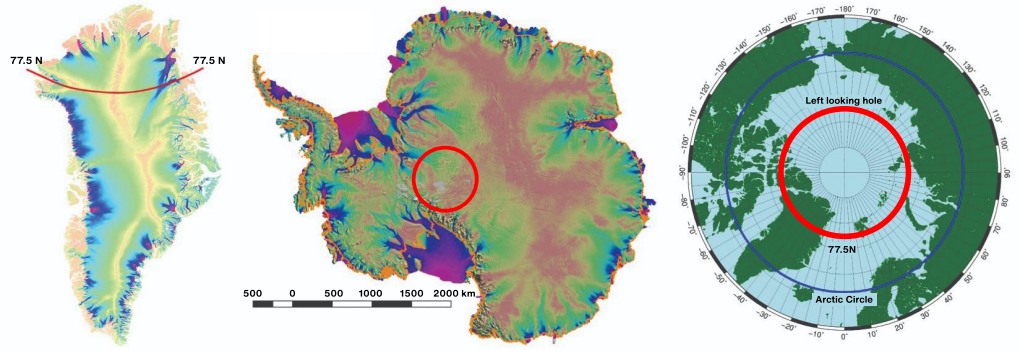

FIGURE 6-13

Example of the types of Level 3 products that will be produced for the cryosphere using the algorithms described in this document. (Left) Greenland example with slow-moving interior velocity and fast-moving glaciers derived from ALOS PALSAR and RADARSAT-1 tracks. (Middle) Antarctic with ice sheet interior and fast ice streams example from RADARSAT-2, ALOS PALSAR, Envisat ASAR, and ERS-1/2 tracks using speckle tracking and phase. Errors in these maps do not meet NISAR requirements. With 30+ acquisitions a year along each track and phase data, NISAR will meet its stated requirements. (Right) Coverage at the north pole. Because NISAR will be left-looking, areas north of 77.5 will not be imaged (i.e., area inside red circle). The hole is much smaller at the South Pole (red circle Antarctica map) with standard coverage and the mission will attempt to fill it in with off-pointing campaign coverage.

COMBINED ESTIMATE

As described above, there are multiple methods for determining velocity at each point using phase or offsets from single or crossing orbit tracks. To apply these methods, a mosaicking algorithm is needed to produce a large-scale mosaic, using the best data available at each point. Here we describe an approach to mosaicking the data based on a specific implementation of a processor, which implements all the algorithms described above to produce a mosaic (Joughin, 2002). Variations on this approach exist (Mouginot et al., 2017).

In producing such a mosaic, the algorithm proceeds by looping over the images to be mosaicked. If an estimate is being derived using data from along a single track (i.e., azimuth offsets are used), the algorithm next identifies where the corresponding region in the output grid lies, and loops over the corresponding points in the output grid. It then interpolates the relevant offset or phase data from the source image, which is in radar coordinates. Where this interpolation is successful and there is valid data, the velocity components, v_x and v_y, are determined using Equations 6.6-10, 6.6-13, and 6.6-14. At each point, the algorithm uses phase data if available for the range component, and if not, then range-offset data. After looping through all points in the sub-region of the output grid, the algorithm proceeds to the next image.

Where crossing orbits are used, the algorithm cycles through all the descending (arbitrarily decided; ascending first will work just as well) images. For each of these descending images, the program then loops over all the ascending images to determine if there is overlap. If there is overlap, then the code identifies where the region of overlap falls in the output grid. Next, the algorithm loops over these output points and computes the surface-parallel-flow approximated velocities using Equation 6.6-15, using either phase or range-offset data. In the above discussion, we have assumed that where phase data are available, they are available for both ascending and descending passes and, if not, then range-offset data are available for both passes. There can be cases, however, where range-offset data only are available from one track direction and phase data from the other. In this case, there is nothing to preclude using Equation 6.6-15 with range-offset from one track direction and phase data from the other.

As just described, for each pair or crossing pair, the algorithm estimates v_x and v_y at each point in the output grid. For coastal velocities, there may only be a single estimate for most points in the output grid. By contrast, for annual velocities, thirty or more independent estimates may be averaged for each point in the final output. Thus, as each point estimate is derived using image pairs, the individual estimates are weighted by w_x and w_y, summed in an output buffer. The final velocity estimate in the x-direction is derived from N individual estimates given by

$$v_x = \sum_{i=1}^{N} f_i w_{x,i} v_{x,i} \qquad \textbf{6.6-19}$$

and a similar expression applies for v_y. Note f_i is an additional feathering weight as described below. If we assume the errors are unbiased (zero mean), then the weights must sum to one. In this case and assuming the individual estimates are independent, the minimum error (σ_x^2) is given by f_i=1 and weights

$$w_{x,i} = \frac{1}{\sigma_{x,i}^2}\left(\sum_{i=1}^{N}\frac{1}{\sigma_{x,i}^2}\right)^{-1} \qquad \textbf{6.6-20}$$

If feathering (see below) is applied ($f_i \neq 1$), then

$$f_i w_{x,i} = \frac{f_i}{\sigma_{x,i}^2}\left(\sum_{i=1}^{N}\frac{f_i}{\sigma_{x,i}^2}\right)^{-1} \qquad \textbf{6.6-21}$$

In practice, the mosaicking algorithm does not know how many estimates are available at any given point in the output grid. As a result, it weights each estimate $f_i/\sigma_{x,i}^2$ and sums the result in the output buffer. At the same time, a separate buffer is maintained and the weights are summed $\left(\sum_{i=1}^{N}\frac{f_i}{\sigma_{x,i}^2}\right)$. When all data are included in the mosaic, the weighted average is completed

by normalizing the final result by the summed weights.

Assuming errors are independent, then the error estimate for the weighted average is given by

$$\begin{aligned}\sigma_x^2 &= \sum_{i=1}^{N} (f_i w_{x,i})^2 \sigma_{x,i}^2 \\ &= \left(\sum_{i=1}^{N} \frac{f_i}{\sigma_{x,i}^2}\right)^{-2} \sum_{i=1}^{N} \frac{f_i^2}{\sigma_{x,i}^4} \sigma_{x,i}^2 \\ &= \left(\sum_{i=1}^{N} \frac{f_i}{\sigma_{x,i}^2}\right)^{-2} \sum_{i=1}^{N} \frac{f_i^2}{\sigma_{x,i}^2}\end{aligned} \quad \textbf{6.6-22}$$

As a result, error estimates are cumulated by summing $f_i^2/\sigma_{x,i}^2$ in error buffer, and the results are normalized as indicated in Equation 6.6-22.

FEATHERING

While the weighting method described above is designed to achieve a minimum variance estimate, it may be sub-optimal with respect to other factors. In particular, a discontinuity at a data-take boundary is a non-physical result and can lead to problems when attempting model inversions. As a result, additional weighting is employed to "feather" the data and redistribute local errors over a wider range. This additional weighting function is used to apply a linear taper from the edge of the data to some distance from the edge. This is accomplished by applying a distance transform that gives the distance, d, at any point in the interior to the nearest point on the image edge. The feathering function is then given by

$$f(d) = \begin{cases} \dfrac{d}{f_l} & 0 \le f_l \le 1 \\ 1 & f_l \ge 1 \end{cases} \quad \textbf{6.6-23}$$

This is similar to the feathering scheme used for the SRTM mosaicking. Note the distance transform is applied to the source data, so the feather length, f_l, is in radar coordinates. This function is applied as indicated by Equation 6.6-19.

As an example, if the feather length is 20, then pixels on the edge are weighted by 0, pixels within 20 pixels of the edge are weighted linearly with distance from the edge over a range from 0 to 1, and interior pixels by 1. The feathering weights are used to update the initial weights in the temporary buffers, and the results are added to the weight buffers as indicated in Equation 6.6-19. Tidal displacement is determined by double differencing phases ($\widetilde{\phi}$ from Equation 6.6-5) from two interferograms (Rignot et al., 2011b).

TIDAL DISPLACEMENT AT GROUNDING LINES

From one interferogram between images 1 and 2 acquired over a time interval ΔT, where Ψ is the incidence angle, Δg is the horizontal displacement, and Δz is the vertical displacement, we get a line-of-sight displacement,

$$\widetilde{\delta}_{\rho_{12}} = \Delta g \sin(\psi_{12}) - \Delta z_{12} \cos(\psi_{12}) \quad \textbf{6.6-24}$$

From a second interferogram spanning the same time interval ΔT between images 2 and 3, we get a second line-of-sight displacement:

$$\widetilde{\delta}_{\rho_{23}} = \Delta g \sin(\psi_{23}) - \Delta z_{23} \cos(\psi_{23}) \quad \textbf{6.6-25}$$

As the radar imaging geometry is exactly repeated, we have $\Psi_{12} \sim \Psi_{23}$. Assuming that the horizontal displacement does not change with time, differentiation of the two interferograms leads to:

$$\Delta z_{23} - \Delta z_{12} = \left(\widetilde{\delta}_{\rho_{12}} - \widetilde{\delta}_{\rho_{23}}\right) / \cos(\psi) \quad \textbf{6.6-26}$$

The vertical signal, $\Delta z_{23} - \Delta z_{12}$ reflects changes in elevation of the ice surface due to changes in sea water height over floating glacier ice driven by changes in oceanic tide, atmospheric pressure, or ocean dynamics. Over grounded ice, the vertical motion reflects subsidence or uplift of ice caused by the migration of basal water pockets beneath the glacier that either push the ice surface down (water evacuated from a cavity) or pushes it up (water incursion in a cavity). In the case of floating ice, the zone of flexing of the glacier, where the glacier slowly adjusts to flotation, is several kilometers wide (Fig. 6.14). The region where the glacier detaches from the bed the first time, i.e., $\Delta z_{23} - \Delta z_{12} \sim 0$, define the "grounding line." As the grounding line migrates by hundreds of meters or even kilometers with

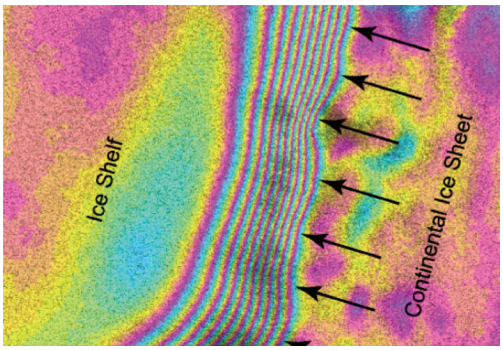

FIGURE 6-14

Example transition region between grounded glacier ice (right) and floating glacier ice (left) in a differential SAR interferogram, with interferometric fringes at the transition boundary caused by the visco-elastic flexing of ice as it adjusts to hydrostatic equilibrium. Ice flow is from right to left. With its left-looking geometry, NISAR will map tidal flexing and grounding line positions over the entire periphery of Antarctica, repeatedly, every 12 days.

changes in oceanic tide, the region of transition eventually defines a "grounding zone." With NISAR, we will map tidal flexing and grounding lines over extensive areas along the periphery of ice sheets.

6.6.3 VALIDATION PRODUCTS

The Science Team shall produce the following ice-sheet demonstration/validation products:

- Ice sheet velocity products at time scales of 12 days to a year for validation purposes. Examples of such products are velocity maps covering the GPS validation sites, areas that overlap with coverage provided by other sensors, and regions of ice-free stationary areas (e.g., bedrock outcrops).
- Differential tidal displacement maps to validate grounding line requirements.
- Velocity estimates to validate the mountain glacier measurement goals.
- A limited set of demonstration products within budgetary limitations.

These products are designed to validate the L2 requirements, but not to completely fulfill them. While data will be collected to meet the requirements throughout the mission, the bulk of the processing to fully meet the requirements will be carried out by the scientific community at large, with funding external to the project.

6.7 CRYOSPHERE SCIENCE – SEA ICE

Another cryosphere science objective of NISAR is to measure the motion or velocity of sea ice, a major type of ice in the polar regions that forms when salty ocean water freezes. The fine resolution of SAR along with frequency, polarization, and short temporal repeat sampling enable the observation of multiple ages and forms of sea ice needed to measure the detailed motion of sea ice over time with considerable accuracy. With NISAR's left-looking SAR configuration, sea ice imagery will be obtained in the Southern Ocean surrounding Antarctica and in the Arctic region up to 77.5°N, with higher latitudes to be augmented by ongoing C-band missions including the Sentinel-1 series and the Radarsat Constellation Mission (RCM). The former is expected to be the most complete coverage of sea ice obtained to date in the southern hemisphere. In this section, we describe a fundamental concept of sea ice parameters that explains the role of sea ice motion and deformation from SAR.

6.7.1 THEORETICAL BASIS OF ALGORITHM

The basic concepts of sea ice motion are position, displacement, and velocity. Displacement is the difference in position over time of an ice feature. Velocity is derived from displacement during the measured time interval. Sea ice moves with the general ocean circulation forced by winds and currents but also at the smaller scales of individual floes, aggregates of floes, and the formation of leads (or open water). Ice motion controls the abundance of thin ice and surface exchange processes including heat flux between the ocean and atmosphere and ice production.

Sea ice is materially considered to be a brittle solid with some plasticity, and its motion is spatially discontinuous, forced by winds and currents, which results in both lead formation where new ice is formed and deformation that produces ridges and complex motions including rotation, shear, and vorticity.

SEA ICE THICKNESS DISTRIBUTION

The sea ice thickness distribution is probably the single most important parameter of sea ice and its role in the global climate system. Sea ice thickness is the integrated result of both ocean and atmosphere forcing and interactions. Cooler conditions result in thicker ice and warmer conditions thinner ice. Taken as a whole, the thickness distribution includes both dynamic and thermodynamic sea ice processes. Over both small and large scales, several types of sea ice may be present as an aggregate containing a range of thickness due to varying stages of growth and mechanical deformation. Thorndike et al. (1975) conceived of the temporal development of ice thickness distribution, $\delta g/\delta t$, which can be written as:

$$\delta g/\delta t = -\delta(fg)/\delta h + \mathrm{div}(vg) + \Phi \qquad \textbf{6.7-1}$$

As summarized by Haas (2010), the three terms that contribute to the thickness distribution are as follows: $f(h, x, t) = \delta h/\delta t$ is the thermodynamic growth or melt rate of ice of thickness h at a location x and time t, v is the ice drift velocity vector, and Φ is the so-called redistribution function. In general, the thinner and thicker components of the thickness distribution arise from dynamics and the median values from thermodynamics (Fig. 6-15, upper panel). Thermodynamic growth is faster for thin ice than thick due to steeper temperature gradients between the ocean and atmosphere (Fig. 6-15 [lower left]). The presence of snow slows ice growth and pressure ridges (keels) may exceed a depth that will lead to melt if the depth extends down into the warmer ocean layers.

The second term in the equation above represents divergence and advection due to ice motion, as forced by winds and currents. Away from the coast or at the margins of the central ice pack itself, ice will drift freely, and drift direction and speed are closely related to geostrophic wind (outlined below). Divergence generates cracks, leads, or polynyas in all areas of open water where new ice will form. Divergence changes the sea ice fraction of an area or grid cell, removing

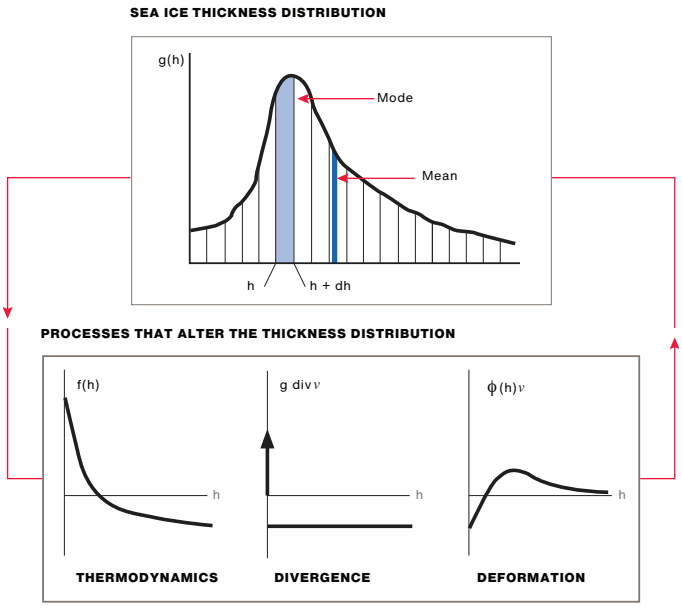

FIGURE 6-15

Illustration of the contribution of the different terms and processes in the equation above to the ice thickness distribution. (After Haas [2010] and Thorndike et al. [1975].)

ice of finite thickness and causing a delta signal at zero thickness in the thickness distribution (Fig. 6-15 bottom center).

The last term in the above equation is the redistribution function describing how thin ice is deformed and transformed into thicker ice classes from both convergence and deformation. It is the most critical term to understand the temporal development of the thickness distribution and also the most unknown, since it depends on fracture mechanics and other factors including small-scale ice properties, friction between ice blocks, snow and ice interfaces, and deformation energy and length scales. Thinner ice will deform more readily than thicker ice (Fig. 6-15, lower right). Within the redistribution term, ice strength and rheology are of great importance. Models were derived that consider ice rheology as a plastic or viscous-plastic (Hibler, 1979; Coon, 1980). The rheology describes a viscous flow of an ice field, with plastic deformation once ice concentration and internal ice forces exceed a certain threshold, driven by winds and currents. Contemporary models include coupled atmosphere-ice-ocean conditions (e.g., Zhang et al., 2000; Holland et al., 2006).

ICE MOTION AND OBSERVATIONAL BASIS

Sea ice moves in response to wind and ocean currents. Large-scale circulation of sea ice (Fig. 6-16) determines the advective part of the ice balance (i.e., the regional exchange of sea ice and export to lower-latitude oceans). This knowledge provides a velocity boundary condition on the ocean surface, while the small-scale motion describes the interaction of individual floes, aggregation of floes, and the formation of leads (areas of open water) and ridges.

The mechanical response of the ice cover to large-scale atmospheric and oceanic forcing is concentrated along fractures up to kilometers in widths, and lengths that can span hundreds of kilometers. Rather than deforming continuously throughout the ice cover, sea ice moves and deforms due to fractures/cracks created by brittle failure (see Fig. 6-16). When openings

FIGURE 6-16

Illustration of the processes that dynamically (by divergent or convergent ice motion and deformation) modify the ice thickness distribution. (After Haas, 2010.)

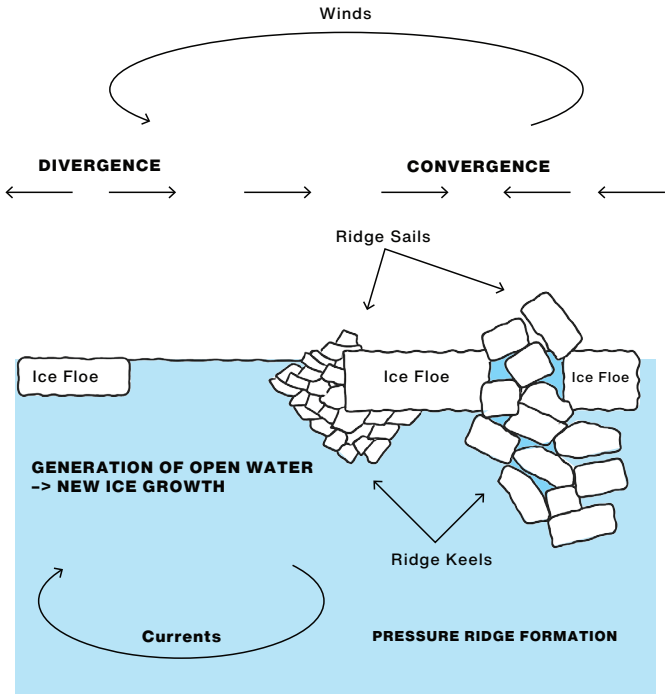

along these cracks expose the relatively warm underlying ocean to the frigid winter atmosphere, heat exchanges are large, and new ice forms that releases salt as concentrated brine, which gradually sinks into deeper waters. Convergence or closing of pack ice forces thinner ice to raft or pile up into pressure ridges and to be forced down into keels, increasing the ice-ocean and ice-atmosphere drag. Typically, a distribution of openings and closings is formed when collections of ice floes with irregular boundaries are sheared relative to one another. Over time, the redistribution of ice associated with deformation alters the volume of sea ice and heat that can be stored within a given area of an ice-covered ocean. Together with thermodynamic growth, these dynamic processes shape the unique character of the ice cover's thickness distribution and profoundly impact the strength of the ice and its thermal properties over a wide range of temporal and spatial scales. Accurate quantification and simulation of the relative contributions of thermodynamics and dynamics to ice thickness distribution are thus crucial for understanding the behavior and the vulnerability of the sea ice cover in both polar regions in a warming climate.

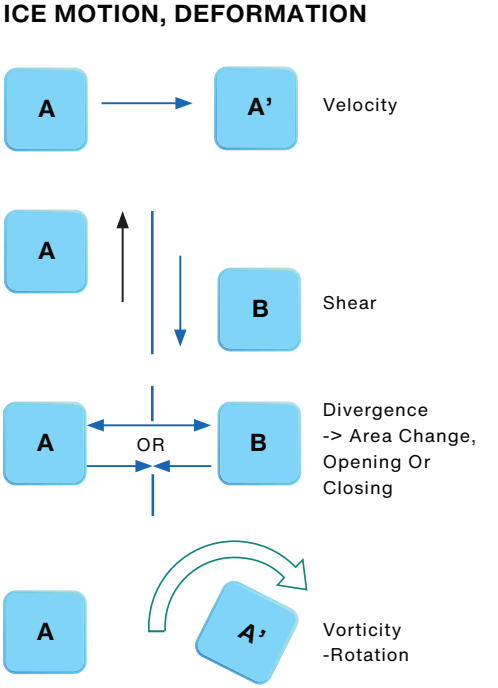

FIGURE 6-17

Illustration of basic forms of ice motion over time of a single ice floe (velocity, vorticity) and deformation of a floe or adjoining floes that undergo shear or divergence (results in opening or closing).

SEA ICE DEFORMATION

Summarizing from Kwok (2001) and Holt et al. (1992), the multiple forces that act on sea ice include the Coriolis force, water drag, air drag, gradients due to the tilt of the sea surface, and the ice stress gradients resulting from floe-to-floe interactions and stress variations within individual floes. In the Arctic Ocean, where sea ice motion is constrained by continental boundaries, strong interactions between ice floes take place and influence the basin-wide circulation and deformation/convergence of the ice cover. In contrast, ice motion around Antarctica is mostly divergent (Kottmeier et al., 1992), with a northerly drift component toward lower latitudes and the surrounding open ocean.

Mechanical deformation results in divergence, convergence, and shear of the ice pack. The relative motion of floes creates areas of open water and significantly affects air-ice-ocean interaction. In winter, newly opened leads are the source of new ice growth, brine rejection to the ocean, and rapid heat transfer from the ocean to the atmosphere. Areas of open water and thin ice dominate the net heat flux into the atmosphere and brine flux into the ocean. The stresses by which ice floes resist motion are related to the strain rate, the spatial variation in ice velocity. Closings of the ice cover cause ice to raft and to pile up into pressure ridges and forced down into keels, increasing the ice-atmosphere and ice-ocean drag.

These spatial differences in relative motion exist on small floe-floe scales but also may extend over considerable distances, at both linear and nonlinear scales. This complex interplay of thermodynamics, deformation, and motion is typically included in aggregate form in sea ice dynamics models. An accurate ice dynamics model must reflect the appropriate portions of these processes as well as their beginning and end states. Each of these processes alters the

sea ice thickness distribution in a unique manner. SAR-derived ice motion and deformation have been fundamental in providing measurements of spatial distribution and temporal development of these processes. After Kwok (2001), the basic forms of sea ice deformation are divergence, vorticity, and shear, as below:

$$\nabla \cdot u = \frac{1}{2}(u_x + v_y) \qquad \textbf{6.7-2}$$

$$\zeta = \frac{1}{2}(v_x - u_y) \qquad \textbf{6.7-3}$$

$$e = \left[(u_x - v_y)^2 + (u_y + v_x)^2\right]^{\frac{1}{2}} \qquad \textbf{6.7-4}$$

u_x, u_y, v_x, v_y are the spatial gradients in ice motion computed using a contour integral around the boundary of an area of ice, or in terms of SAR, a grid cell (~10 km on a side). The boundaries are defined by the line segments connecting the four vertices of a cell.

Divergence, $\nabla \cdot u$, is a measure of area change. Vorticity, ζ, is the principal measure of rotation. Shear, e, is the scalar magnitude of shear. Fig. 6-17 is a schematic of motion and deformation concepts from a sequential image pair.

When combined with thermodynamics, i.e., ice growth and melt, how do measurements of dynamics contribute to the sea ice thickness distribution? Motion or velocity, distance traveled over time, simply indicates that ice is forced by wind and currents and is not stationary in space. When two pieces of ice move apart from each other, an opening or lead is formed, exposing the ocean directly to the atmosphere. In winter, ice grows rapidly within the lead as heat is lost from the relatively warmer ocean to the colder atmosphere. In summer, the open water will be warmed preferentially to the ice by solar radiation, enhancing ice melt. This can occur within a defined area or cell or between adjacent cells and is defined as a fractional increase in area. When two pieces of ice are forced together, this represents a loss in area within a cell or between adjacent cells. This generally represents a ridging process, where the thinnest components of sea ice will preferentially break up and be piled up into pieces, which stack up both on top and below the remaining ice floe. Shear and vorticity represent other components of deformation and have less effect on the overall sea ice thickness distribution but may be closely related to adjacent divergence.

Measurement of small-scale sea ice motion is challenging because of the spatial and temporal scales spanned by the processes responsible for producing its variability. The relative motion between ice floes along narrow (meters to kilometers) fractures requires imaging sensors with not only high spatial resolution but also short sampling intervals. Ice deformation at sub-daily time scales associated with tidal forcing or inertial effects becomes more prominent as the ice cover thins. Presently, basin-scale fields of sea ice motion at different spatial resolutions can be derived from tracking common ice features in a variety of satellite imagery. Of particular interest are those from satellite SAR imagery. SAR is uniquely suited for small-scale observations of sea ice cover and change detection because of its spatial resolution (tens of meters), day/night coverage, and ability to see through clouds. Temporal sampling, however, remains an issue because orbiting satellites are limited in their ability to cover the same area repeatedly. Deriving sea ice motion from pairs of SAR images is best obtained using temporal repeat sampling of a few days or less to capture the more complete range of ice dynamics.

EULERIAN AND LAGRANGIAN ICE MOTION

There are two general ways of sampling a sea ice motion field: Eulerian and Lagrangian. In the Eulerian specification, the motion field is sampled using specific grids or individual ice particles in the space through which the ice moves as time passes between pairs of observations and then is repeated by resetting the grid or individual ice particles in the next pair of observations. The Eulerian approach provides velocity and deformation over a single pair of observations. With the Lagrangian specification, in contrast, the motion field is sampled and followed over time starting with an initial grid or individual ice particles through multiple observation pairs, producing an array of trajectories as the particles move through space and time. This particle array has the advantage of being able to provide sampling of the motion field as well as a time record of the deformation of material elements within the ice cover (Kwok et al., 1995; Stern et al., 1995). Since sea ice is a brittle solid, it does not deform continuously throughout the ice cover; rather, sea ice moves and deforms due to fractures and cracks created by brittle failure. As local ice strength is determined by weaknesses in the fracture patterns that advect with the ice cover, the Lagrangian approach is more appropriate where details of ice kinematics and the openings and closings of the ice cover, for understanding ice mechanics and surface heat balance, are of interest. However, this observational requirement adds complexity to the ice-motion tracking process and quality checking. In addition to recording the location history of the array at each time-step, the connectivity of the particles that define the material elements must be maintained. Both Eulerian and Lagrangian type products have been generated previously at the Alaska Satellite Facility using Radarsat-1 and Envisat ASAR for the Arctic and limited portions and times of the Southern Ocean sea ice cover. For NISAR, the focus for development and post-mission validation will be on the use of Eulerian tracking.

For a given overlapping image pair, grid cells with initial dimensions of 5 or 10 km on a side are determined within each image and are used to derive the detailed motion and deformation that occurred over the time interval between each image. Past results show that basin-scale deformation of the divergence, vorticity, and shear of the ice cover may extend across a significant distance of the sea ice cover. The deformation fields indicate linear kinematic features (LKFs) that characterize the opening, closing, and shear of the ice cover. The high-resolution ice motion vectors derived from this approach have a data quality comparable to that from buoy drifts (~0.1 cm/s) and have provided an unprecedented level of spatial and temporal detail of deformational features. On a routine basis, the location, coverage, and seasonal development of leads and ridges can be provided. Narrow fracture zones (up to kilometers wide) are long linear features that can extend for hundreds of kilometers, and these fracture patterns appear as oriented rather than random patterns from the kilometer scale to the scale of the Arctic basin. Deriving complete maps of the Arctic Ocean as well as new motion/deformation mapping of the dynamic sea ice cover surrounding Antarctica will provide complete information on the motion and deformation of the detectable sea ice cover of both major sea-ice covered oceans for the first time.

6.7.2 IMPLEMENTATION APPROACH FOR ALGORITHM

The derivation of sea ice motion and deformation employs the use of feature tracking using cross correlation. Basin-wide seasonal sea ice motion fields are optimally obtained using multiple pairs of images with each image pair obtained over a sampling interval of a few days or less.

BASIC SEA ICE MOTION CONCEPT

Following Holt et al. (1992), the fundamental concepts of ice motion are position, displacement, and velocity. Consider ice at a position x at time t = 0; at some later time, the ice has moved to a new position $x(t_i+1)$. A displacement is the

difference in the positions of an ice particle at two different times

$$u = \left[x(t_i + 1) - x(t_i)\right] \quad \textbf{6.7-5}$$

The average velocity over the intervening time interval $T = t_i{+}1 - t_i$, is

$$\boldsymbol{V} = \frac{u}{\boldsymbol{T}} \quad \textbf{6.7-6}$$

As described in Kwok et al. (1990) and Holt et al. (1992), the linear model of ice motion relates the mean ice velocity v of an ice field to the geostrophic wind (Thorndike and Colony, 1992; Colony and Thorndike, 1986),

$$\boldsymbol{v} = \boldsymbol{AG} \quad \textbf{6.7-7}$$

where **v**, the ice velocity, and **G**, the geostrophic wind, are vectors and consequently treated as complex numbers. The term **A** is a complex multiplier, giving the ratio of ice speed to wind speed and an ageostrophic drift angle θ (positive counterclockwise) from the wind vector to the ice vector. Typical values for the Arctic of (A, θ) range from (0.011, –18°) in summer to (0.008, –5°) in winter in relation to the mean wind speed (Thorndike and Colony, 1992). For the Weddell Sea, these numbers are 0.016 and 10° to 15°, respectively (Kottmeier et al., 1992). While the physical processes are many, on the time scales of days, more than 70% of the variance of the ice motion is explained by the geostrophic wind alone. As will be described in a later section, this relationship of ice motion and geostrophic wind can be used in the ice motion algorithm to do the initial identification of the second of the image pair to be used for tracking, guided by weather data.

GEOLOCATION ERRORS

Following Holt et al. (1992) and Kwok and Cunningham (2002), the two primary sources of error in measuring ice motion with satellite imagery are absolute geographic position (e_g) of each image pixel and a tracking error (e_f), which is the uncertainty in identifying common features from one image to the next. The position error applies independently to each position in each image, i.e., a position is the true position plus an error of $x + e_g$. The tracking error e_f applies to a displacement observed between two images. If it is assumed that e_g and e_f are each normally distributed with zero bias, have standard deviations σ_g and σ_f, and are uncorrelated between two time-separated images A and B, the two errors can be treated separately. Including errors, an estimate of the displacement of an ice feature is given by

$$u = (x_b + e_{gB}) - (x_a + e_{gA}) + e_f \quad \textbf{6.7-8}$$

The standard error in u has a zero mean and a variance of

$$\sigma_u^2 = 2\sigma_g^2 + \sigma_f^2 \quad \textbf{6.7-9}$$

where σ_g and σ_f are uncertainties in the geolocation of the image data and the tracking of sea ice features from one image to the next. The error in velocity is σ_u divided by the time interval of displacement. Errors in the time interval are usually negligible.

Given two images, if the locations of an ice feature found in each image are close together, the geolocation errors between the two images are assumed to be correlated. The spatial differences between the two points are not dependent on geolocation error, so the error in displacement tends to $2\sigma_f^2$. When SAR displacement is compared to that of a drift buoy, buoy location errors must be also considered. In previous efforts, displacement errors between SAR and ice drift buoys were found to be on the order of 0.2 – 0.3 km, derived from sensor geolocation errors of 0.1 km, tracking errors from 0.1 – 0.3 km, and pixel resolutions from 0.05 – 0.1 km, not including error offsets in drift buoy locations. Currently, most sea ice drift buoys include the use of GPS, which significantly reduces location errors. The NISAR geolocation errors are also significantly improved from the previous sensors, so it is anticipated the errors in SAR-derived sea ice motion and deformation will be significantly improved compared to previous results.

NISAR SEA ICE MOTION RETRIEVAL ALGORITHM

The NISAR science team requirement is to produce Eulerian sea ice motion products due to their expediency in production, which requires a minimum of operator quality assurance and correction. It is expected at some point that Lagrangian products will also be produced supported by additional funding, such as from NASA Making Earth System Data Records for Use in Research Environments (MEaSUREs) opportunities. The Lagrangian products are fundamentally equivalent in terms of the ice displacements but because these are generated based on observing and maintaining the original grid area and vertices over time even when the ice undergoes deformation, additional valuable products are generated.

There are several fundamentally key components of the NISAR mission that make it particularly valuable for deriving sea ice motion and deformation, that will lead to the derivation of uniquely valuable sea ice products. First, the longer frequency of L-band has been shown to highlight deformed ice preferentially compared to the long and extensive C-band SAR record. This is expected to provide similar winter records as C-band and improved and more accurate sea ice feature tracking in spring and, importantly, longer into the summer months, where ice surface features on C-band become less distinct due to surface melt. Next, the synoptic coverage of the Arctic and Southern Ocean sea ice covers during the entire duration of the mission will provide unprecedented SAR coverage of both polar regions that can be used for ice motion. Radarsat-1 provided annual ice motion mappings of much of the western Arctic but never complete and continuous coverage for multiple years over the entire Arctic. Ice motion of Antarctic sea ice from SAR was also previously limited to only 1-2 mappings for periods of a few months from the Ross or Weddell Seas. The sea ice motion mapping of the Southern Ocean from NISAR will be unprecedented and will enable a thorough derivation of the different ice dynamics from both polar oceans.

The algorithm to be used has been described in multiple publications based on the use of ERS-1 and primarily Radarsat-1 SAR imagery (Kwok et al., 1990; Holt et al., 1992; Kwok et al., 1995; Kwok and Baltzer, 1995; Kwok and Cunningham, 2002). The algorithm is transferred from Fortran to Python-based scripts to be made publicly available, and is modified to incorporate the NISAR image format and metadata as well as Sentinel-1 imagery. To summarize, the design includes comprehensive steps to locate image pairs using an ice motion estimator, for tracking ice in both the central pack and marginal ice zones using areal correlation and feature matching and displaying ice motion fields based on a grid system mapping to a polar stereographic projection. The algorithm uses a combination of different filters at several stages of the tracking process to remove spurious or low quality vectors, based on correlation statistics. Clustering of the motion vectors is used to identify dominant modes of motion in the sampled field, whereupon the filtering process discards erroneous vectors by examining cluster centroids that are inconsistent with the dominant modes. Also, a smoothness constraint is applied to ensure the spatial consistency of the displacement field. The filtering process in the algorithm attempts to optimize the ratio of good to bad vectors so that 95% of the motion vectors are accurate to the determined displacement error.

6.7.3 VALIDATION PRODUCTS

NISAR will produce sea ice motion products for the Arctic and Southern Oceans. It will also produce demonstration products of seasonal maps of sea-ice motion for the Arctic Ocean and Weddell Sea and export for the Arctic Ocean. The validation products will be a comparison of SAR-derived ice motion with coincident sea ice drift buoys.

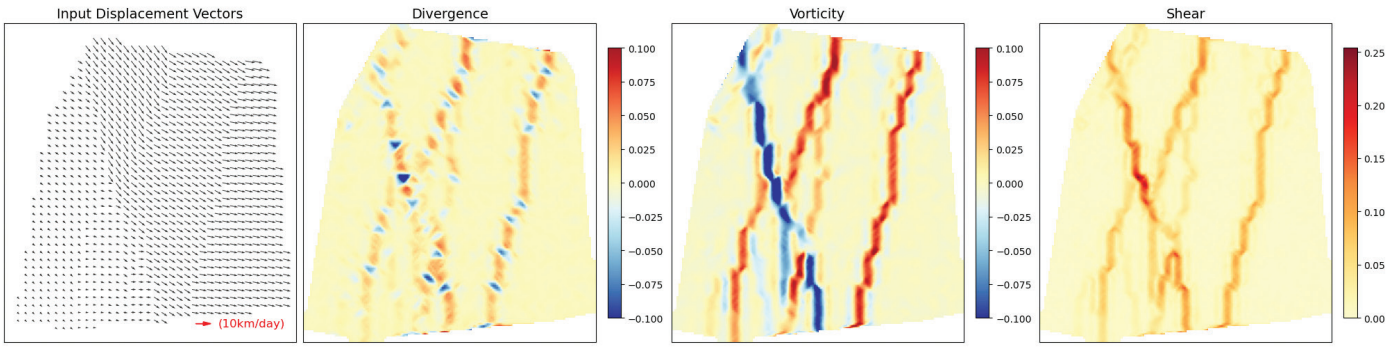

FIGURE 6-18

Sample products of sea ice motion, divergence, vorticity, and shear, derived from a pair of Sentinel-1 SAR (interferometric mode) images in the Arctic Ocean, illustrate fracture patterns between different fields of sea ice composited together and moving as "rigid plates" against each other.

EULERIAN ICE MOTION PRODUCTS

a. Displacement (x, y, km)

b. Ice motion vector (direction, deg)

c. Deformation (spatial variation of velocity): shear, divergence, vorticity

A seasonal examination of the Arctic region where there is a large density of sea ice drift buoys will be done each year for validation. This will also be performed over a region of Antarctic sea ice cover where sea ice drift buoys are present. A representative product derived using the updated sea ice motion algorithm is shown in Fig. 6-18.

DEMONSTRATION PRODUCTS

a. First product (Year1-Year2). Map of one full season of sea ice motion for the sea ice covers at Weddell Sea and Beaufort-Chukchi Seas

b. Second product (Year2-Year3): Map of one full season of sea ice motion for the Southern Ocean and map of one full season of sea ice motion and export from the Arctic Ocean.

6.8 SOIL MOISTURE SCIENCE

Soil moisture is a key variable in the Earth system that governs the exchange of water and heat energy between the land surface and the atmosphere, as well as the availability of water to plants and within fluvial systems. Evaporation and plant transpiration play important roles in the development of weather patterns and the production of precipitation. Large-scale dry or wet surface regions can impart positive feedbacks on subsequent precipitation patterns, and simulations with numerical weather prediction models have shown that improved characterization of surface soil moisture, vegetation, and temperature can lead to significant forecast improvements. Soil moisture also strongly affects the amount of precipitation that runs off into nearby streams and rivers. Soil moisture information can be used for reservoir management, early warning of droughts, irrigation scheduling, and crop yield forecasting. Soil moisture data have the potential to significantly improve the accuracy of short-term weather forecasts and reduce the uncertainty of long-term projections of how climate change will impact Earth's water cycle (Entekhabi et al., 2010).

Satellite remote sensing of soil moisture has advanced significantly over the last decade due to the success of the Soil Moisture/Ocean Salinity (SMOS) (Kerr et al. 2010) and Soil Moisture Active/Passive (SMAP) (Entekhabi et al., 2010) missions, both of which provide global soil moisture retrievals at approximate 3-day repeat intervals at an accuracy of approximately 0.04 m^3/m^3. A key limiting factor of SMAP and SMOS soil moisture measurements is their coarse spatial resolution of ~10 km or more, which limits their utility for "field-scale" (i.e., ~1 km spatial resolution or smaller) agricultural monitoring. Although SMAP was also intended to produce soil

moisture retrievals at a 3 km resolution using its L-band multi-polarization radar (Entekhabi et al., 2010), the failure of the radar after 3 months of operation limited the results that could be achieved (Kim et al. 2017).

The NISAR mission will provide global observations of Earth land surface dynamics that are critical to multiple Earth Science disciplines, including observations of ecosystem carbon and water cycles. The unique capabilities of the NISAR mission have motivated the production of a field-scale land surface soil moisture product, particularly given the fact that no other mission explicitly focused on soil moisture remote sensing is currently planned for launch during the NISAR operational period. NISAR also presents an opportunity for development of soil moisture retrieval approaches that can fully take advantage of its ground-breaking capabilities. Therefore, three independent retrieval approaches will be used (described below), and each of the three products will be included in the Level 3 NISAR soil moisture product. The calibration/validation effort will include the comparison of all three retrieval approaches against in situ data in a range of land cover types and climatic zones. The three approaches differ greatly in terms of their dependence on independent ancillary data (e.g., vegetation water content or independent coarse soil moisture estimates), their computational expense, and their temporal resolution (i.e., whether they depend on the SAR backscatter on a single date or if they employ a form of change detection approach that relies on multiple dates).

While the data from the calibration/validation period will be used to determine which of the three approaches demonstrates optimal performance in those settings, individual users may find that their specific application is better served by a different product. For instance, the product that is associated with the lowest unbiased root-mean-squared error (ubRMSE) when averaged over the entire time series at a location may not also be the one that is best able to capture the effect of isolated, extreme events. The free and open NISAR calibration/validation database will empower users to explore these factors and determine which product best suits their needs.

6.8.1 THEORETICAL BASIS OF ALGORITHM

PHYSICAL MODEL INVERSION ALGORITHM

The physical model inversion (PMI) algorithm was the baseline algorithm for SMAP (Kim et al. 2017) and has been adapted for NISAR. The scattering models for 9 vegetation types (forest, shrub, savanna, grass, corn, soybean, canola, wheat, and bare soil) are simplified by focusing on three independent variables that co- or cross-pol backscattering is most sensitive to at L-band. These are root-mean-squared (rms) height (s), the real part of dielectric constant (r), and vegetation water content (VWC). Furthermore, because it is computationally intensive to compute the scattering model, to allow near-real-time estimates, the retrieval algorithm leverages

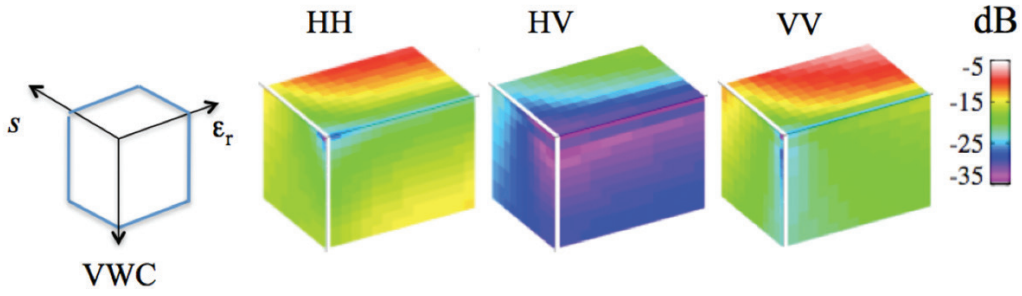

FIGURE 6-19

L-band data cubes for a given incidence angle, illustrating how the scattering model predicts co- and cross-pol backscatter (σ^0) will vary with surface roughness (s), dielectric constant (ε_r), and vegetation water content (VWC). From (Kim et al., 2014).

a precomputed lookup table representation of the physical forward models (Kim et al., 2014). Since there are three dimensions, the lookup table is referred to as a "data cube" (Fig. 6-19). The data cube also allows the user to replace and update a forward model while retaining the same retrieval formulae and product generation system. The data cubes were generated at every few degrees over a range of incidence angles and are interpolated to the incidence angle of interest.

The algorithm searches for a soil moisture solution such that the difference between computed and observed backscatter is minimized in a least squares sense (Kim et al., 2012). The algorithm estimates s (soil roughness) first and then retrieves r (soil dielectric constant) using the estimated s. Vegetation effects are corrected by selecting the forward model's σ^0 at the VWC level given by an ancillary source or NISAR HV measurements, which is implemented by slicing the 2-dimensional lookup table (LUT) in the VWC-soil moisture space at the given VWC level. The key components of the algorithm are (1) inverting the physical forward model and (2) reducing retrieval ambiguity using a time-series of backscatter observations. The end-to-end flow of the retrieval is shown in Fig. 6-20. Equation 6.8-1 formulates the cost function, $C(s, \mathrm{VWC}, \varepsilon_{r1}, \varepsilon_{r2}, ..., \varepsilon_{rN})$, to minimize when both HH and VV are available (VV contribution to the cost vanishes when only HH is available) at a range of times 1, 2, ... , N:

$$\begin{aligned} C(s, \mathrm{VWC}, \varepsilon_{r1}, \varepsilon_{r2}, \ldots, \varepsilon_{rN}) = {} & w_{1,\mathrm{HH}}(\sigma^0_{\mathrm{HH}}(t_1) - \sigma^0_{\mathrm{HH,fwd}}(s, \mathrm{VWC}, \varepsilon_{r1}))^2 \\ & + w_{1,\mathrm{VV}}(\sigma^0_{\mathrm{VV}}(t_1) - \sigma^0_{\mathrm{VV,fwd}}(s, \mathrm{VWC}, \varepsilon_{r1}))^2 \\ & + w_{2,\mathrm{HH}}(\sigma^0_{\mathrm{HH}}(t_2) - \sigma^0_{\mathrm{HH,fwd}}(s, \mathrm{VWC}, \varepsilon_{r2}))^2 \\ & + w_{2,\mathrm{VV}}(\sigma^0_{\mathrm{VV}}(t_2) - \sigma^0_{\mathrm{VV,fwd}}(s, \mathrm{VWC}, \varepsilon_{r2}))^2 \\ & + \ldots \\ & + w_{N,\mathrm{HH}}(\sigma^0_{\mathrm{HH}}(t_N) - \sigma^0_{\mathrm{HH,fwd}}(s, \mathrm{VWC}, \varepsilon_{rN}))^2 \\ & + w_{N,\mathrm{VV}}(\sigma^0_{\mathrm{VV}}(t_N) - \sigma^0_{\mathrm{VV,fwd}}(s, \mathrm{VWC}, \varepsilon_{rN}))^2 \end{aligned} \qquad \textbf{6.8-1}$$

where values from observations and from the forward model are denoted as σ^0 and σ^0_{fwd} (both in dB), respectively, and the $W_{N,HH}$ values refer to weights applied to the fit to the different dates and polarizations. Note that this formulation can accommodate temporal changes in VWC, because σ^0_{fwd} depends on the VWC value available at each time. σ^0 varies monotonically with respect to variations in both *s* and ε_r (Fig. 6-19), so the minimums of C are unique for a given set of input parameters.

TIME SERIES RATIO ALGORITHM

The "time-series ratio" (TSR) approach for retrieving soil moisture from radar backscatter time series measurements attempts to eliminate the confounding influences of vegetation and surface roughness through a "ratio method" (Ouellette et al., 2017; Mattia et al., 2009; Mattia et al., 2018; He et al., 2017; Park et al., 2021; Park et al., 2022; Horton et al., 2022; Horten et al., 2024). The method is developed for terrain classes in which vegetation volume scattering can be neglected and either the soil-vegetation interaction term or vegetation attenuated surface backscatter dominate the measurement. Under this assumption, we can use the first-order small-perturbation model (SPM) to express the surface backscattered normalized radar cross section (NRCS), σ^0, as:

$$\sigma^0_{\mathrm{PP}} = 4\pi k^4 s^2 \theta \left|\alpha_{\mathrm{PP}}\right|^2 W(2k\sin\theta, 0) \qquad \textbf{6.8-2}$$

where $k = 2\pi/\lambda$ is the wavenumber, θ is the incidence angle, s is the soil roughness, $W(\zeta_x,\zeta_y)$ is the 2D normalized surface roughness spectrum, and *PP* indicates polarization (e.g., HH, VV). The alpha coefficient (α_{PP}) includes the surface electrical properties for each polarization (either HH or VV), which is a function of the dielectric constants of the soil and the incidence angle. For HH polarization, the $|\alpha(\varepsilon)|$ function is, in fact, identical for both surface backscatter and soil-vegetation interaction terms (and equal to the Fresnel reflection coefficient amplitude), so that the dependence on permittivity is identical when either term or their combination dominates. In VV polarization, however, the $|\alpha(\varepsilon)|$ functions differ for the two terms so that performance may degrade in cases where soil-vegetation interaction dominates.

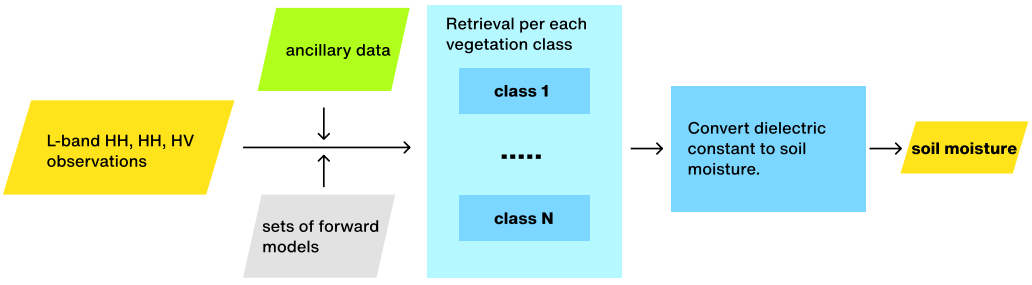

FIGURE 6-20

Overall flow of the physical model inversion algorithm.

In summary, the backscattered NRCS for a vegetated soil layer is in general a function of parameters related to soil, vegetation, and roughness, making the inverse problem of solving for soil moisture more difficult. However, over short timescales, changes due to the confounding roughness and vegetation factors may be negligible. The TSR algorithm assumes that the surface roughness and vegetation properties remain almost constant over two consecutive measurements (separated by 12 days for NISAR for identical viewing geometries). If the roughness parameters and incidence angle remain unchanged, the ratio of consecutively measured NRCS values at time t_1 and t_2 can be approximated as:

$$\frac{\sigma^0_{\mathrm{PP}}(t_2)}{\sigma^0_{\mathrm{PP}}(t_1)} \approx \left| \frac{\alpha_{\mathrm{PP}}(t_2,\varepsilon,\theta)}{\alpha_{\mathrm{PP}}(t_1,\varepsilon,\theta)} \right|^2 \qquad \textbf{6.8-3}$$

With a time-series of N NRCS observations, N-1 ratio values are obtainable, and a matrix can be constructed as:

$$\begin{bmatrix} 1 & -\sqrt{\frac{\sigma^0_{\mathrm{PP}}(t_1)}{\sigma^0_{\mathrm{PP}}(t_2)}} & \dots & 0 & 0 \\ 0 & 1 & \dots & 0 & 0 \\ \vdots & \vdots & \ddots & \vdots & \vdots \\ 0 & 0 & \dots & 1 & -\sqrt{\frac{\sigma^0_{\mathrm{PP}}(t_{N-1})}{\sigma^0_{\mathrm{PP}}(t_N)}} \\ 0 & 0 & \dots & 0 & 1 \end{bmatrix} \begin{bmatrix} |\alpha_{\mathrm{PP}}(t_1)| \\ |\alpha_{\mathrm{PP}}(t_2)| \\ \vdots \\ |\alpha_{\mathrm{PP}}(t_N)| \end{bmatrix} = \begin{bmatrix} 0 \\ 0 \\ \vdots \\ 0 \end{bmatrix} \qquad \textbf{6.8-4}$$

where PP can be either HH or VV polarization. The resulting N-1 by N matrix is underdetermined and therefore requires additional ancillary information to complete its solution. The required ancillary information can take a variety of forms, but in the current operational implementation involves maximum and minimum bounds on the alpha coefficients over the time series. Given these bounds, a bounded least-squares solution of (Eqn. 6.8-4) can be performed to obtain the alpha coefficients. The matrix in Equation 6.8-4 can be extended when both HH and VV co-pol observations are available or when multi-frequency data are available. The final soil moisture outputs are inverted from the alpha coefficients (a known function of incidence angle, polarization, and relative permittivity) using the Mironov relative permittivity model and ancillary soil clay fraction information (e.g., Mironov et al., 2004).

MULTI-SCALE RETRIEVAL ALGORITHM

The soil moisture multi-scale disaggregation (DSG) algorithm (Lal et al., 2023) leverages a combination of well-validated, precise, coarse resolution (~9 km) soil moisture products with high-resolution L-band SAR observations (~10 m) that carry a distinct signature of soil moisture variations at finer spatial scales (Fig. 6-21).

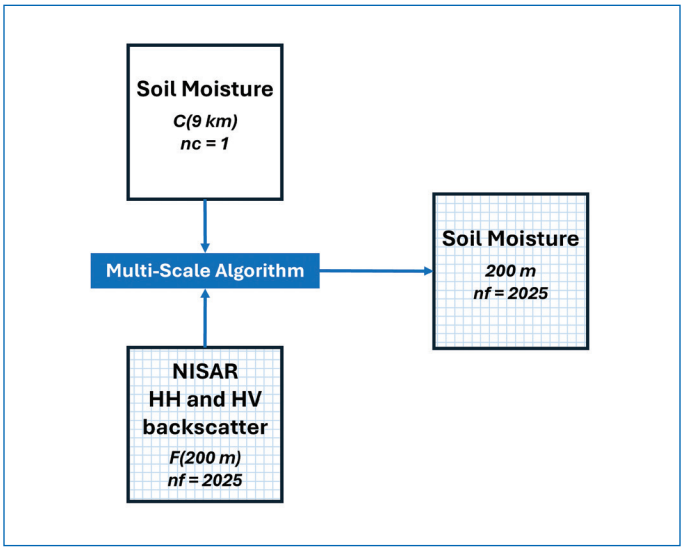

FIGURE 6-21

EASE2-Grid 2.0 topology to be used in the DSG NISAR soil moisture algorithm. "C" refers to coarse-resolution (~9 km) grid cells, and "f" refers to fine-resolution (~200 m) grid cells. nf refers to the number of fine-resolution cells (nf=45x45=2025) that are perfectly nested within one coarse-resolution cell within the EASE-Grid 2.0 projection used for the aggregation step.

The relationship between SAR co-pol backscatter (σ_{HH} at L-band) and volumetric soil moisture was reported on by Kim and van Zyl (2009), who found a nearly linear relationship between the two during the Washita 92 field experiment. Another study by Piles et al. (2009) also reported a similar observation, i.e., a linear relationship between σ_{HH} of L-band and volumetric soil moisture during the SMEX02 campaign. The formulation of the NISAR soil moisture multi-scale algorithm is based on this observed linear relationship between SAR backscatter and volumetric soil moisture.

Based on the above correlations, we hypothesize that the volumetric soil moisture and co-polarized SAR backscatter (σ_{HH}) are linearly correlated through an equation of the form:

$$\mathrm{SM}(t) = \alpha + \beta\left[\sigma_{\mathrm{HH}}(t)\right] \qquad \textbf{6.8-5}$$

where $\sigma_{HH}(t)$ is given in dB. At a given scale (coarse or fine), the α and β parameters in Equation 6.8-5 depend on the land use, vegetation cover types, surface roughness, and incidence angle, and can both also vary seasonally, particularly β.

The α and β parameters at the coarse scale are related to spatial averages of $\sigma_{HH}(t)$ over each coarse-resolution grid cell, C, and a

known soil moisture estimate, *SM(C, t*).

$$\mathrm{SM}(C,t) = \alpha(C) + \beta(C)\langle\sigma_{\mathrm{HH}}(F_n,t)\rangle \qquad \textbf{6.8-6}$$

where $\langle\sigma_{\mathrm{HH}}(F_n,t)\rangle$ is the spatial average of $\sigma_{\mathrm{HH}}(F_n,t)$ in dB over all the fine-resolution grid cells, F_n, within the coarse-resolution grid cell, *C*. The parameters α*(C)* and β*(C)* can be obtained by time-series regression of *SM(C, t)* and $\langle\sigma_{\mathrm{HH}}(F_n,t)\rangle$. In the current implementation, the β*(C)* values have been determined a priori and depend on the dominant land cover class within each coarse-resolution pixel.

NISAR can also provide high-resolution cross-polarization radar backscatter measurement, which will be highly sensitive to vegetation and surface characteristics such as surface roughness, sensitivity to moisture, and topography change. The relationship between co-polarization and cross-polarization within a coarse-resolution cell can be defined using a heterogeneity parameter, Γ, defined here as the slope of a regression between the values of co-polarization and cross-polarization within that coarse-resolution cell.

The fine-resolution soil moisture retrieval for the DSG algorithm is:

(see Equation 6.8-7 at bottom of page) **6.8-7**

where σ_{HH}*(C, t)* and σ_{HV}*(C, t)* are the spatial averages of the fine-resolution backscatter values within each coarse-resolution cell, $\langle\sigma_{\mathrm{HH}}(F_n,t)\rangle$ and $\langle\sigma_{\mathrm{HV}}(F_n,t)\rangle$. More details about the derivation of Equation 6.8-7 are given in (Das et al., 2019).

6.8.2 IMPLEMENTATION APPROACH FOR ALGORITHM

All three algorithms ingest SAR observations (e.g., σ_{HH}, σ_{HV}) that have first been aggregated to ~200 m resolution using a hybrid filter and the EASE-Grid 2.0 projection (Das et al., 2019). This aggregation step reduces the effect of speckle noise by nearly ~20 times.

The source of coarse resolution ancillary data, including soil moisture, precipitation, and soil temperature, is the European Centre for Medium-range Weather Forecasts (ECMWF, native resolution 0.1°, gridded to 9 km global EASE-Grid 2.0 projection). The soil moisture product for ECMWF has previously been shown to have an ubRMSE of about ~0.05 m^3/m^3 and a wet bias of about 0.05 m^3/m^3 to 0.1 m^3/m^3 (Lal et al., 2022). VWC used in the PMI algorithm are specific to each day of year and are based on a decade of VWC values inferred from the Moderate Resolution Imaging Spectroradiometer (MODIS). The minimum and maximum soil moisture values used in the TSR algorithm are based on ten years of SMAP observations.

PRE-LAUNCH CALIBRATION/VALIDATION OF SOIL MOISTURE RETRIEVALS

During the pre-launch interval, testing and calibration/validation of the retrieval algorithms was performed using simulated NISAR data based on UAVSAR observations and ALOS PALSAR/PALSAR2 data. The SMAP Validation Experiment in 2012 (SMAPVEX12) (e.g., McNairn et al., 2012) provided data at 55 agricultural and 4 forested sites, covering 9 separate land cover classes with between 6 and 13 observation dates where both in situ and remote sensing soil moisture retrievals are available. PALSAR2 data over sites in Arizona, Iowa, and Georgia were also used, with between 30–50 observations between 2021 and 2024, but without access to a dedicated Cal/Val campaign on the ground. These pre-launch results are associated with ubRMSE below the 0.06 m^3/m^3 threshold for at least one algorithm at locations where there were sufficient in situ observations available for assessment. A limitation of the pre-launch data is that there were not in situ observations at a location that experienced a large dynamic range of soil moisture – this will be addressed in the post-launch campaigns.

POST-LAUNCH CALIBRATION/VALIDATION OF SOIL MOISTURE RETRIEVALS

The post-launch validation effort will primarily focus on two types of in situ observations: "Super Sites," which are characterized by locations where in situ soil moisture measurements are taken at more than one location within a single pixel, and "Sparse Network Sites," where only one observation location is present within a pixel. At Super Sites, other information will also be gathered on vegetation characteristics, surface roughness, etc. There are also a number of independent partners who have agreed to contribute data at locations under the same conditions as the Super Sites. Sparse Network Sites that will be utilized include the USDA Soil

6.8-7

$$\mathrm{SM}(F_n,t) = \mathrm{SM}(C,t) + \beta(C)\left\{\left[\sigma_{\mathrm{HH}}(F_n,t) - \sigma_{\mathrm{HH}}(C,t)\right] + \Gamma\left[\sigma_{\mathrm{HV}}(C,t) - \sigma_{\mathrm{HV}}(F_n,t)\right]\right\}$$

Climate Analysis Network (SCAN/SNOTEL), NSF National Ecological Observatory Network (NEON), US Climate Reference Network (USCRN), and the USC Soil Moisture Sensing Controller And oPtimal Estimator Project (SoilSCAPE), which also contains some locations that meet the Super Site criteria.

Data and results from post-launch Cal/Val efforts will be free and openly available to the public. These results will guide selection and/or weighting of the three retrieval approaches in the top-level combination soil moisture layer within the product. This combination will initially be the arithmetic mean of all valid retrievals at a given time and location.

6.8.3 VALIDATION PRODUCTS

NISAR backscatter observations will be used to estimate a near-global level 3 high resolution soil moisture product (200 m in most areas, 400 m in the Sahara). This product will be provided on average twice every 12 days. The NISAR soil moisture product is expected to have a data latency of 72 hours (3 days), driven in part by the 48-hour data latency of the NISAR Level 2 backscatter product. The NISAR soil moisture product will have an accuracy goal of 0.06 m^3/m^3 over areas with vegetation water content below 5 kg/m^2. Soil moisture estimates in urban areas, regions with dense vegetation or permanent snow or ice, or at times of excessive precipitation, frozen ground or snow cover, will be flagged during the retrieval process.

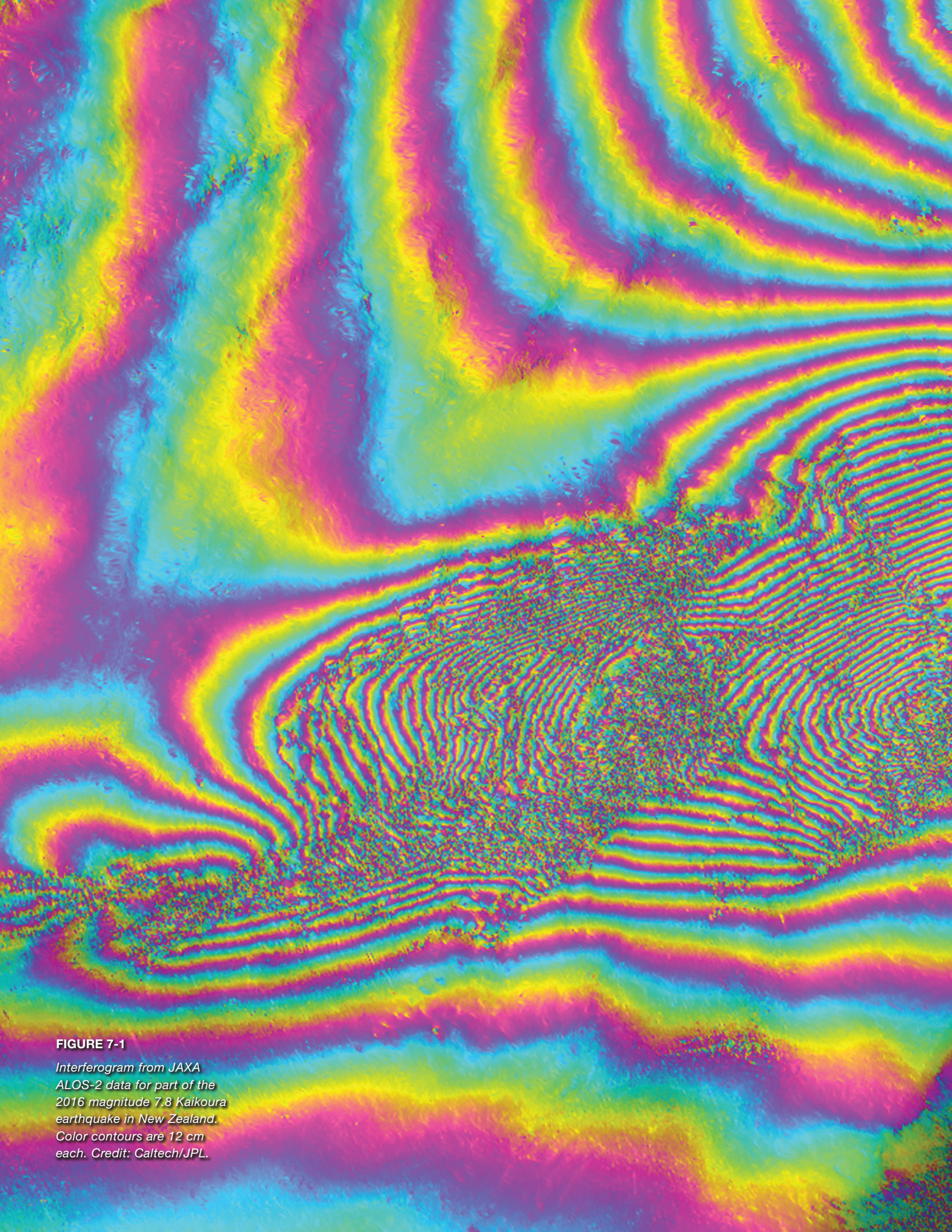

FIGURE 7-1

Interferogram from JAXA ALOS-2 data for part of the 2016 magnitude 7.8 Kaikoura earthquake in New Zealand. Color contours are 12 cm each. Credit: Caltech/JPL.

7 COMPONENTS AND UNCERTAINTIES OF THE RADAR SIGNAL

This section describes the key sources of error in the radar measurements that can affect science performance. Understanding these error sources is essential for correctly interpreting NISAR data. These errors may arise from instrument noise, geometric factors, scattering behavior, or propagation effects, among others.

7.1 POLARIMETRIC SIGNALS AND ERROR SOURCES

The radar-observed radiometric properties of a surface, represented by the polarimetric backscatter, amplitude, and phase, are characterized through the radar backscattering cross section. The amount of energy scattered back to the radar depends on the detailed arrangements of scatterers within a resolution element and their electrical properties; therefore, the cross section generally varies with the observation angle and environmental conditions. Since radar images are coherent, they exhibit "speckle" properties: even in a region with multiple distributed scatterers with uniformly constant radar cross section, each resolution element will exhibit significant amplitude and phase fluctuations, such that the images appear to be spatially random from element to element. This natural variance, coupled with random noise sources originating in the radar system, requires describing radar cross section as a statistical process, using the covariances of the observed quantities.

Element-to-element errors in radar measurements include additive thermal noise and various sources of multiplicative noise, such as quantization effects, like- and cross-polarized channel signal leakage, and ambiguities, which are artifacts caused by echoes from different times or locations being misinterpreted as part of the scene under analysis. Multiplicative noise is signal-dependent and therefore can be correlated with the target response, complicating its separation from the signal of interest.

In radar polarimetry, the full scattering behavior is captured by estimating the covariance matrix from combinations of like- and cross-polarization channels and using these to infer properties of the surface. Accurate estimation requires spatial averaging over a local region – an operation commonly referred to as multi-looking – to reduce the inherent variance due to speckle. This introduces a trade-off between radiometric accuracy and desired spatial resolution. The number of independent resolution elements averaged, referred to as the effective number of looks, impacts the precision of the surface parameters derived from the data.

Systematic errors in polarimetric and radiometric measurements can stem from variations in antenna gain patterns, channel imbalances, cross-talk between polarization channels, and inaccuracies in the calibration of amplitude and phase that can vary over the image and potentially over time. These system-level error sources introduce biases in the polarimetric radar observables, which can mislead image interpretation unless properly corrected. Accurate radiometric and polarimetric calibration, typically achieved using well-characterized reference targets (e.g., corner reflectors), is essential to reduce the impact of systematic error sources for robust surface characterization.

Derivation of the radar cross section requires knowledge of the total "link budget," including transmitted power, antenna gain, propagation losses, and receiver sensitivity according to the radar equation. Errors in any of these components, including uncertainties in the digital elevation model (DEM), can introduce spatially varying biases in the backscatter coefficient (σ^0). To meet science requirements for absolute and relative radiometric accuracy, the end-to-end radar system must remain stable and well-characterized over time and across the swath.

Overall, the error in polarimetric backscatter measurements, $\Delta\sigma_{pq}$ (where pq = hh, hv, vv indicates the polarimetric channel), is a function of speckle, thermal noise, temporal variability, calibration uncertainties, and area projection correction terms. An expression for this error, in terms of system and measurement parameters, is given by Hensley et al. (2014) as:

7.2 INTERFEROMETRIC SIGNALS AND ERROR SOURCES

As with polarimetry, random resolution element-to-element noise is introduced from speckle, thermal effects, and multiplicative noise sources. These are quantified by the interferometric correlation, which is the amplitude-normalized cross covariance of the interferometric observations. As with polarimetry, local averaging reduces this noise component.

The broader systematic effects on the phase difference are important in interferometry. Since it is a differential measurement, if the system is stable and the pointing is perfect over time, phase due to system delays or antenna pattern will cancel in the phase difference. In practice, the system will not be perfectly pointed, or the antenna patterns and system phases will vary over time. These

SPECKLE NOISE | THERMAL NOISE | BACKSCATTER TEMPORAL VARIABILITY | CALIBRATION ERRORS | AREA PROJECTION ERRORS

$$\Delta\sigma_{\mathrm{pq}} = \left[\left(\frac{1}{\sqrt{N}}\frac{1}{\sqrt{N_{\mathrm{os}}}} + \frac{1}{\sqrt{N}}\frac{1}{\sqrt{N_{\mathrm{ot}}}}\frac{1}{\mathrm{SNR}}\right)\sigma_{\mathrm{pq}} + \frac{1}{\sqrt{N_{\mathrm{ot}}}}\Delta\sigma_{\mathrm{pq}_t}(b) + \frac{1}{\sqrt{N_{\mathrm{ot}}}}\Delta\sigma_c + \sqrt{\frac{A_{\mathrm{dem}}}{A_{\mathrm{pix}}}}\frac{1}{\sqrt{N}}\frac{1}{\sqrt{N_{\mathrm{os}}}}\Delta\sigma_a\right] \quad \text{7.1-1}$$

where Table 7-1 defines the symbols.

TABLE 7-1. BACKSCATTER ERROR MODEL DEFINITIONS

Symbol	Definition
N	Number of spatial looks per observation
N_{ot}	Total number of observations over time, both speckle identical and speckle diverse, $N_{ot} = N_o s + N_{oi}$
N_{os}	Observations with non-correlated (diverse) speckle
N_{oi}	Observations with correlated (identical) speckle
SNR	Signal-to-noise ratio
$\Delta\sigma_{pqt}$	Backscatter temporal variability
$\Delta\sigma_c$	Backscatter calibration error
$\Delta\sigma_a$	Backscatter area projection error
A_{dem}	Area of a pixel in DEM used for slope computations
A_{pix}	Area in a radar pixel

differential phase effects typically have a different nature from those due to ground motions and are tied to the geometry of the spacecraft orbit, so they can often be mitigated in scientific data reduction.

Another effect of importance is the phase delay experienced by the electromagnetic wave propagating through the ionosphere and the neutral atmosphere. The state of these media changes rapidly over time, so every time an observation is made (i.e., every 12 days from a given vantage point), the phase delay across the image will be different. These introduce a spatially correlated but temporarily random component to the differential signal that is one of the chief limiting noise sources. The wide bandwidth of the radar data can be exploited to estimate signal dispersion due to the ionosphere such that this dispersion can be mitigated (Meyer et al., 2011).

IMPACT OF TOPOGRAPHY

NISAR products are derived using a DEM of the Earth to remove propagational phase terms resulting from topography. In the event that the DEM does not accurately reflect the surface elevation at the time of the acquisition, topography-related phase terms would appear in NISAR products. This effect could be significant

wherever there is a large surface height change, such as a caldera collapse in a volcano, meter-scale glacier motion, large earthquake displacements, or any event in which the surface elevations differ by more than a meter or two. Default NISAR products are referenced to the ESA Copernicus DEM, which was last updated in the 2019 time frame, and are planned to remain unrefined until at least 2026. Surfaces that have evolved since then may not be properly accounted for in NISAR products, although in many cases the distortions will be minor, perhaps less than 1 cm in most cases. The DEM used for NISAR data processing will be included either in each data product or in static layers available for each data frame location. The on-demand segment of the NISAR processing system is planned to allow use of arbitrary DEMs, and users may choose to use these alternative DEMs rather than the default Copernicus DEM.

IMPACT OF THE TROPOSPHERE

We can mitigate the effects of atmosphere propagation noise through a combination of modeling using an independent estimate of the state of the atmosphere and through an averaging or filtering process that assumes a spatially correlated but temporally uncorrelated random process, as distinct from the ground motion, which is generally both spatially and temporally correlated.

$$\begin{aligned}\Delta\phi &= \Delta\phi_{\mathrm{def}} + \Delta\phi_{\mathrm{err}} \\ &= \Delta\phi_{\mathrm{def}} + \Delta\phi_{\mathrm{atmos}} + \Delta\phi_{\mathrm{orb}} + \Delta\phi_{\mathrm{topo}} + \Delta\phi_{\mathrm{n}}\end{aligned} \qquad \textbf{7.2-1}$$

where $\Delta\varphi_{def}$ is the phase due to the true ground deformation in the LOS direction, $\Delta\varphi_{atmos}$ is the phase due to the tropospheric and ionospheric delays, $\Delta\varphi_{orb}$ is the phase due to satellite orbit errors, $\Delta\varphi_{topo}$ is the phase due to error in the surface topography, and $\Delta\varphi_{n}$ is a residual noise term that includes scattering variability and thermal noise. All the noise terms contribute to the signal quality, as quantified by correlation, at various spatial scales. The correlation can be expressed as:

$$\gamma_{\mathrm{e}} = \gamma_{\mathrm{SNR}}\gamma_{\mathrm{B}}\gamma_{\mathrm{V}}\gamma_{\phi}\gamma_{\mathrm{T}} \qquad \textbf{7.2-2}$$

where the correlation terms are defined in Table 7-2. The table provides formulas illustrating the dependency of the various correlation terms with regard to system parameters.

The displacement noise corresponding to this correlation is given by

$$\sigma_d = \frac{\lambda}{4\pi}\frac{1}{\sqrt{2N}}\sqrt{\frac{1-\gamma_e^2}{\gamma_e^2}} \qquad \textbf{7.2-3}$$

When the correlation is low, the displacement noise is high and vice versa. N is the number of pixels that can be averaged to reduce the noise level.

Interferometric performance depends critically on how well the total interferometric phase difference φ_{int} can be measured, which in turn depends on the SNR. We can relate SNR to the phase-difference measurement uncertainty $\sigma_{\varphi int}$. The variance of the measured phase difference, $\sigma^2_{\varphi int}$, is due to the random phase component introduced by the noise accompanying the signal, and it

TABLE 7-2. ELEMENTS OF THE INTERFEROMETRIC CORRELATION

Correlation Term	Expression	System Dependence
Total SNR	$\gamma_{\mathrm{e}} = \gamma_{\mathrm{SNR}}\gamma_{\mathrm{B}}\gamma_{\mathrm{V}}\gamma_{\phi}\gamma_{\mathrm{T}}$	Signal-to-noise ratio
Geometric Baseline	from $\gamma_{\mathrm{SNR}} = \frac{\mathrm{SNR}}{\mathrm{SNR}+1}$, $\gamma_{\mathrm{B}} = 1 - \frac{2B\cos^2(\theta_{\mathrm{l}})\delta_{\mathrm{g}}}{\lambda\rho}$	Short baseline *B*, fine resolution δ_g, and long wavelength λ maximize correlation. Look angle θ_l and range ρ are relatively fixed in useful orbits with low drag (above ~ 600 km).
Geometric Volume	from $\gamma_{\mathrm{V}} = \mathrm{sinc}\left(\frac{k_{\mathrm{z}}h_{\mathrm{c}}}{2}\right)$, $k_{\mathrm{z}} = 4\pi\left(\frac{B}{\lambda\rho\sin(\theta_{\mathrm{l}})}\right)$	Short baseline *B* and long wavelength λ maximize correlation. Look angle θ_l and range ρ are relatively fixed in useful orbits with low drag (above ~ 600 km).
Geometric Rotation	from $\gamma_{\phi} = 1 - \frac{2\sin(\theta_{\mathrm{l}})\phi_{\mathrm{rot}}\delta_{\mathrm{az}}}{\lambda}$	Small pointing rotation φ_{rot}, fine along-track resolution δ_{az}, and long wavelength λ maximize correlation. Look angle θ_l and range ρ are relatively fixed in useful orbits with low drag (above ~ 600 km).
Temporal	$\gamma_{\mathrm{T}} = e^{-\left(\frac{4\pi}{\lambda}\right)^2\sigma^2_{\mathrm{los}}}$	Depends on natural targets. Longer wavelengths decorrelate less for a given surface change, proportional to wavelength squared in general.

is approximately proportional to the inverse of the SNR,

$$\sigma^2_{\phi\text{int}} \approx \frac{1}{\text{SNR}} \quad \textbf{7.2-4}$$

So, for example, to secure the single-look value $\sigma^2_{\phi\text{int}}$ = 0.1 rad, it is necessary that SNR = 100, or, equivalently, 20 dB.

Phase artifacts in InSAR images are often attributed to neutral tropospheric delays (Zebker et al., 1997; Hanssen et al., 1998). Because the Earth's troposphere is non-dispersive at appropriate frequencies, radar signals that operate at different frequencies are subject to the same tropospheric delays. For a typical X-band interferogram (such as TerraSAR-X), a phase cycle of 2π in the interferogram corresponds to λ/2 = 1.55 cm deformation, where λ is the radar signal wavelength. In a typical radar scene, tropospheric noise occurs with variation on the order of centimeters or even greater across the interferogram. As a result, any expected centimeter-level crustal deformation signature is obscured by tropospheric noise.

To obtain accurate InSAR deformation measurements, some effort is needed to handle or suppress the atmospheric noise signature. Onn and Zebker (2006) introduced a method to correct for atmospheric phase artifacts in a radar interferogram using spatially interpolated zenith wet delay data obtained from a network of GNSS receivers in the region imaged by the radar. Li et al. (2006a, 2006b) used Medium Resolution Imaging Spectrometer (MERIS), Moderate Resolution Imaging Spectroradiometer (MODIS), and GPS data to estimate the water vapor field in order to correct interferograms that are corrupted by atmospheric artifacts. Foster et al. (2006) employed a high-resolution weather model to predict tropospheric delays for the acquisition times of SAR images. However, estimating tropospheric delays using auxiliary data such as GNSS, MERIS/MODIS, or weather model usually produces a tropospheric noise model with resolution much coarser than InSAR image resolution, and the model uncertainty can be relatively large for studying centimeter-level crustal deformations.

Many have proposed algorithms to estimate tropospheric delays during SAR data acquisition times directly from InSAR data. Emardson et al. (2003) mitigated tropospheric effects by averaging N independent interferograms because the wet component of the neutral atmosphere is uncorrelated at time scales longer than 1 day. This stacking approach is limited by the number of interferograms that are available over the time of interest. Lin et al. (2010), Lauknes (2011), and Hooper et al. (2012) assumed that tropospheric delays in InSAR data are topographically correlated and can be partially removed by knowledge of the local elevation changes. However, the assumption that tropospheric delay is proportional to surface elevation may not be valid for turbulent tropospheric processes. Use of globally available weather reanalysis models (e.g., ECMWF and North American Regional Reanalysis [NARR]) has also shown considerable ability to mitigate topographically correlated phase errors – with the advantage of not absorbing potential geophysical signals into empirical corrections (e.g., Jolivet et al., 2014a).

Since many of the problems proposed by the science team for this mission require correction at the mm to cm level, a more complex approach will be required. A variety of InSAR time series algorithms now exist including SBAS, NSBAS, MInTS, and various permutations of these approaches. These algorithms can filter out tropospheric delays in InSAR data assuming that errors in InSAR deformation estimates are primarily due to tropospheric noise that are uncorrelated in time. These methods require many observations at frequencies much greater than the expected time scale of deformation. Such algorithms to mitigate tropospheric noise have been shown to be very effective, even in reducing the very short wavelength TerraSAR-X data. Thus, with long and dense time series, we can address many state-of-the-art problems and applications.

IMPACT OF THE IONOSPHERE

Ionospheric distortions are an important error source in L-band NISAR data and can cause degradation of amplitude, phase, and polarization information in certain geographic locations and under certain ionospheric conditions (Meyer, 2011).

For a linearly polarized SAR of frequency *f*, the impacts of the ionosphere can be derived from the Appelton–Hartree equation (see, e.g., Meyer and Nicoll, 2008), and are largely composed of an induced phase shift $\Psi_{iono}(f)$ and a rotation of the polarization orientation $\Omega(f)$, a phenomenon known as Faraday rotation.

The phase shift experienced by a SAR with look angle Ψ can be obtained by integrating the ionospheric refractivity N_{iono} along the (two-way) ray path s to the ground, resulting in

$$\Psi_{\text{iono}}(f_0) = -2\frac{2\pi f_0}{10^6}\int \frac{N_{\text{iono}}(f_0, s)}{c} ds \approx 4\pi\frac{\kappa}{c f_0}\cdot \sec(\varphi)\cdot \text{TEC} \quad \textbf{7.2-5}$$

where *TEC* is the ionospheric total electron content integrated along the vertical, f_0 is the center frequency of a specific microwave signal, c is the vacuum speed of light, and $\kappa = \frac{1}{2}\cdot\frac{e}{(4\pi^2 m\varepsilon_0)} = 40.28\left[\frac{m^3}{s^2}\right]$. Equation 7.2-5 shows that $\Psi_{iono}(f_0)$ is inversely proportional to f_0, such that phase shifts increase for lower signal frequencies such as L-band.

Uncompensated phase shifts can affect SAR image geometry and focus and can reduce the fidelity of the interferometric phase (Meyer, 2010). While the first two of these impacts are rare, ionospheric distortions in repeat-pass InSAR data are more likely to occur. From Equation 7.2-5 we can derive these ionospheric impacts Ψ_{iono} on the (repeat-pass) interferometric phase according to:

$$\phi_{\text{iono}} = 4\pi \frac{\kappa}{c f_0} \sec(\varphi) \cdot \Delta_t \ \text{TEC} \qquad \textbf{7.2-6}$$

Equations 7.2-5 and 7.2-6 show that ionospheric phase delay is dispersive as the effect scales with frequency. NISAR uses this dispersive nature to perform ionospheric phase delay correction. Similar to approaches used by the GNSS community, NISAR correction technology extracts sub-bands from the SAR range frequency spectrum and estimates ionospheric phase delays by comparing the phase information in these sub-bands (Fattahi et al., 2017; Gomba et al., 2016).

Faraday rotation is caused by different propagation velocities of left-handed and right-handed signals in the ionosphere, causing a phase difference between these polarizations (Xu et al., 2004). The magnitude of Faraday rotation for a wave of frequency f_0 that has traveled at a look angle Ψ two-way through the ionosphere is given by (Meyer and Nicoll, 2008)

$$\Omega(f_0) = \frac{\kappa}{f_0^2} B \cos(\theta) \sec(\varphi) \ \text{TEC} \qquad \textbf{7.2-7}$$

with the angle between magnetic field and signal propagation Θ, and local geomagnetic field B. Equation 7.2-7 also shows that Faraday rotation increases at low frequencies. At L-band, uncompensated Faraday rotation can have moderate impacts on the polarimetric and interferometric signal quality (Zwieback and Meyer, 2021a). While no algorithms exist to compensate NISAR's dual-pol data for Faraday rotation effects, simulations show that the impact on NISAR science requirements are negligible.

SIGNAL COMPONENTS FROM MULTIPLE SCATTERERS: PHASE CLOSURE OBSERVABLES

In many, if not most, cases the phase of an interferometric radar signal is interpreted as a difference in propagation path from the sensor to the pixel under study. A primary assumption is that the echo results from the backscatter of a single effective phase center, such that it is possible to derive a surface deformation time series from a sequence of repeated radar observations. Recent works (e.g., De Zan et al., 2015; Michaelides et al., 2019, Ansari et al., 2021) present small but evident inconsistencies in these time series when they are examined in phase closure analyses. The magnitude of the inconsistencies is relatively small, often mm-scale, but this can be significant for very precise InSAR measurements.

Phase closure methods have been used for many years to analyze measurements from multi-element interferometer systems. Computing phase closure involves summing the returns from three elements circularly in pairs, and for many signals the sum obtained this way is nearly zero if the system is working properly. In the radar case, we can sum three radar interferograms and display a phase closure image of the surface. The phase closure operation cancels out any deformation signal components, and the resulting nonzero phase pixels are often spatially correlated with changes in surface terrain.

The systematic nature of the residual closure phase can be viewed as corrupting the desired deformation signal, and it can be reduced or eliminated using methods similar to SBAS analysis (Michaelides et al., 2019). This and other work view the closure phase as noise, and depending on its magnitude, it can be removed to improve the sensitivity of the InSAR measurements. More recent research (Wig et al., 2022, 2024; Zheng et al., 2022) has shown that the closure phase signal can instead be exploited as a fingerprint of detailed changes within the surface, especially in regard to changes in water content.

This work demonstrates that nonzero closure phase results from the interference of multiple echoes within a radar pixel, for example as happens when radar signals reflect from the top and bottom of a vegetation canopy, or from the surface and a subsurface layer in a soil. If the water content of either of these changes over time, the way that the multiple echoes combine depends on the change in dielectric properties of the medium. Zheng's model shows a similar interference if multiple pixels in a larger multilook pixel behave differently, and in this case, simple different deformations at each location can produce nonzero closure phase.

NISAR work will investigate these effects and their effectiveness at measuring soil moisture or canopy moisture, extending work done to date using Sentinel-1 and other radar systems. We expect that the effects will be greater when observed with NISAR, because its longer L-band wavelength can more easily penetrate volumes and surfaces and enhance the interference effect.

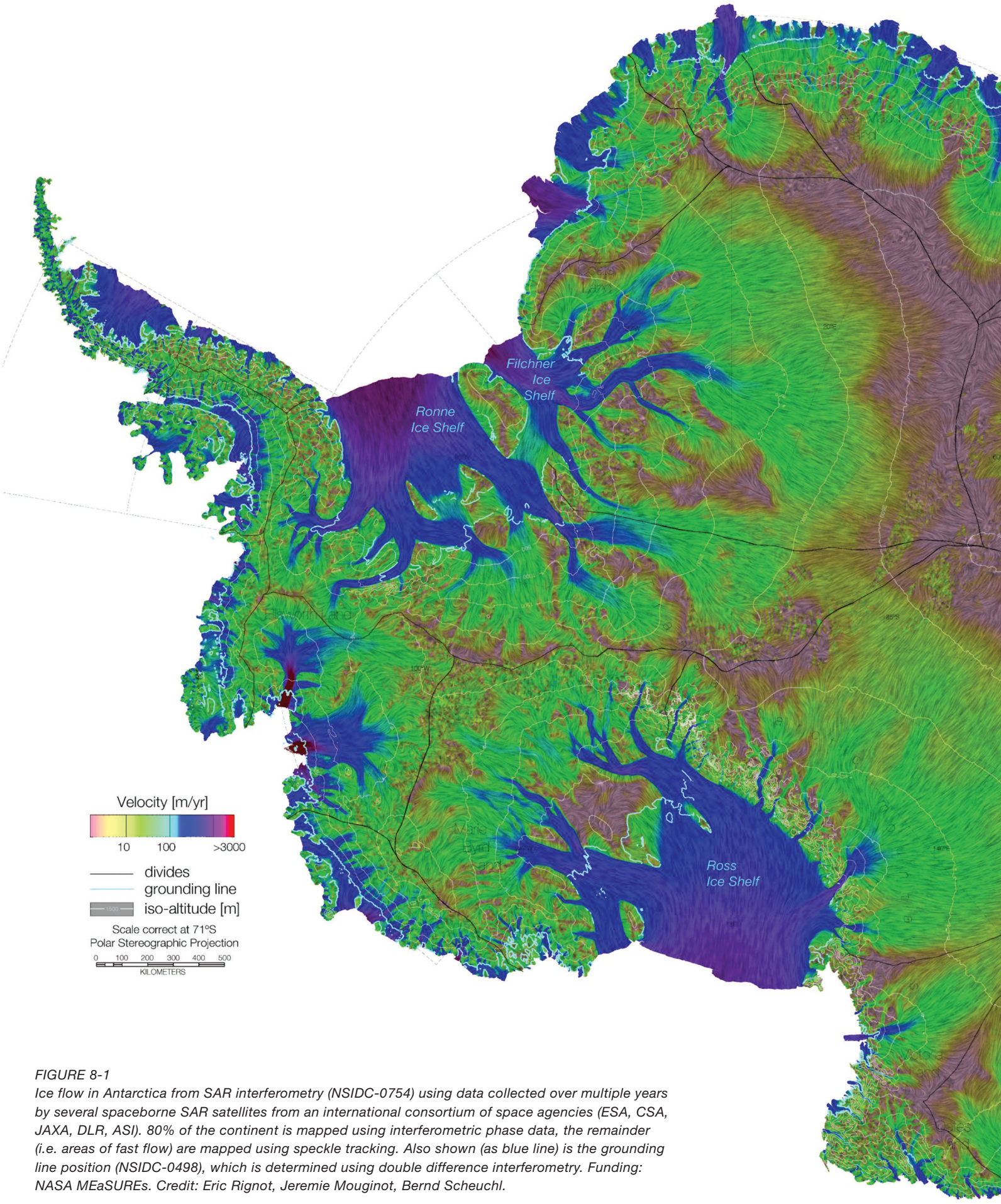

FIGURE 8-1
Ice flow in Antarctica from SAR interferometry (NSIDC-0754) using data collected over multiple years by several spaceborne SAR satellites from an international consortium of space agencies (ESA, CSA, JAXA, DLR, ASI). 80% of the continent is mapped using interferometric phase data, the remainder (i.e. areas of fast flow) are mapped using speckle tracking. Also shown (as blue line) is the grounding line position (NSIDC-0498), which is determined using double difference interferometry. Funding: NASA MEaSUREs. Credit: Eric Rignot, Jeremie Mouginot, Bernd Scheuchl.

8 CALIBRATION AND VALIDATION ACTIVITIES

Calibration and Validation (Cal/Val) for NISAR comprises instrument calibration, image calibration, calibration of algorithms used to derive higher level science products such as biomass or glacier velocities, as well as demonstration (validation) that the data acquired, when flowed through the science processing algorithms, create products that meet the mission's science requirements. Instrument calibration is generally addressed in the pre-launch period through measurements made in a relevant simulated space-like environment. This section addresses the other elements of Cal/Val mentioned above.

8.1 BACKGROUND

In developing the Calibration/Validation plan for NISAR, there are precedents and experiences that can be utilized. The Committee on Earth Observation Satellites (CEOS) Working Group on Calibration and Validation (WGCV; https://ceos.org/ourwork/workinggroups/wgcv/) has established standards that may be used as a starting point for NISAR. The Land Products Sub-Group (http://lpvs.gsfc.nasa.gov/) has expressed the perspective that "A common approach to validation would encourage widespread use of validation data and thus help toward standardized approaches to global product validation. With the high cost of in-situ data collection, the potential benefits from international cooperation are considerable and obvious."

Cal/Val has become synonymous in the context of remote sensing with verifying the suite of processing algorithms that convert raw data into accurate and useful geophysical or biophysical quantities. This can include vicarious calibration efforts, which refers to techniques that make use of natural or artificial sites on the surface of the Earth for the post-launch calibration of sensors, which is typically called "image calibration" for SAR systems.

A useful reference in developing a validation plan is the CEOS Hierarchy of Validation:

- Stage 1: Product accuracy has been estimated using a small number of independent measurements obtained from selected locations and time periods and ground-truth/field program effort.
- Stage 2: Product accuracy has been assessed over a widely distributed set of locations and time periods via several ground-truth and validation efforts.
- Stage 3: Product accuracy has been assessed and the uncertainties in the product well-established via independent measurements made in a systematic and statistically robust way that represents global conditions.

A validation program would be expected to transition through these stages over the mission life span. The NISAR mission may collaborate with the NASA Global Ecosystem Dynamics Investigation Lidar (GEDI) mission and the ESA BIOMASS mission due to complementary science requirements for measuring above-ground biomass. It is likely that science operations for all three missions will partly overlap in time. Therefore, joint validation of biomass requirements may be possible and desirable.

DEFINITIONS

For the Calibration/Validation Plan to effectively address the achievement of mission requirements, a unified definition base must be developed. The NISAR Cal/Val Plan uses the same source of terms and definitions as the NISAR Level 1 and Level 2 requirements.

NISAR Calibration and Validation are defined as follows:

- Calibration: The set of operations that establish, under specified conditions, the relationship between sets of values of quantities indicated by a measuring instrument or measuring system and the corresponding values realized by standards.
- Validation: The process of assessing by independent means the quality of the data products derived from the system outputs.

8.2 CALIBRATION AND VALIDATION ACTIVITIES

Calibration and validation are divided into pre- and post-launch activities. Pre-launch activities focus on deployment of targets and in situ sensors. Post-launch calibration and validation activities focus on data retrievals and production of validation products.

PRE-LAUNCH

During the pre-launch period, there have been a variety of activities that fall under calibration and validation. These mainly involved on-ground instrument calibration, algorithm development and evaluation, and establishment of the infrastructure and methodologies for post-launch validation. Requirements for Cal/Val related to specific NISAR data products were identified by the respective science algorithm teams in their Algorithm Theoretical Basis Documents (ATBDs). The production processing algorithms in the ATBDs have been coded and tested. Calibration procedures and algorithms for the NISAR radar (L1 products), higher level image products (L2) (incorporating such characteristics as geocoding and/or multilooking), and the L3 products (which will be used to validate the NISAR science requirements) will be developed.

Pre-launch instrument calibration included modeling, analysis, simulations, and laboratory and test-facility measurements. Algorithm development for all products included testbed simulations, laboratory and test-facility data, field campaigns, exploitation of existing in-situ and satellite data, and utilization of instrument and geophysical models.

The science team identified calibration and validation sites and resources needed for post-launch calibration. For calibration of radar-specific parameters, the Project deployed calibration targets, similar to those found at the array at Rosamond Dry Lake on Edwards Air Force Base, currently used for calibration of NASA's airborne L-band radar instrument Uninhabited Aerial Vehicle Synthetic Aperture Radar (UAVSAR). These targets will be used early in the post-launch phase to evaluate the instrument calibration, radiometric calibration of the imagery, and image performance; and also during the mission science operations to ensure that image calibration is stable over time. For some science requirements, ground instrumentation was deployed prior to launch to Cal/Val sites and verified with contemporary data sources. Repeated field observations will also be conducted at some validation sites. Contemporary and historical data sets, especially L-band SAR and time series data from Sentinel-1, were compiled for Cal/Val sites; demonstration products were developed for algorithm testing and verification.

POST-LAUNCH

In the post-launch period, the calibration and validation activities will directly address the measurement requirements for the L1–L3 data products. Each data product has quantifiable performance specifications to be met over the

mission lifetime, with calibration and validation requirements addressed in their respective ATBDs.

Post-launch calibration and validation activities are divided into three main parts after launch:

1. Three-month instrument checkout phase, after which delivery of validated L1 products to the public archive will begin.
2. Five-month Science Cal/Val phase, after which delivery of validated L3 products to the public archive will begin.
3. Periodic Cal/Val performed annually. During this period, additional algorithm upgrades and reprocessing of data products can be implemented if found necessary (e.g., as a result of drifts or anomalies discovered during analysis of the science products), as well as validation of those science requirements that require a year's worth of data or more.

The main objectives of post-launch calibration/validation activities are two-fold: 1) Monitoring the stability of instrument calibration and 2) Validation of higher-level data products (L3) with ground truth at selected validation sites. Instrument calibration stability is verified by continuing to collect calibration data over sites used during instrument checkout, using the same radar modes as in nominal science operations (this is different from instrument checkout, when multiple modes are used for various calibrations). Table 8-1 lists the instrument parameters that will be calibrated post-launch by the instrument and science team.

The objective of science data product validation is to validate that global data yielded by NISAR will meet the Project's L2 science requirements. L3 products will be generated by the science team at the selected validation sites. Validation of the L3 science products will be carried out by a combination of fieldwork and analysis.

For solid Earth deformation, there are a number of suitable pre-instrumented validation sites in the world that can be used: GNSS networked arrays exist throughout western North America and in other parts of the world. GNSS sites and arrays have been used for several years for

TABLE 8-1. POST-LAUNCH CALIBRATION PARAMETERS AND METHODS

PARAMETERS	METHODS
Antenna Pattern and Beamforming	Use undisturbed Amazon rainforest to compare residual brightness variations relative to ideal
Impulse Response	Measure 3-dB resolution, ISLR, PLSR of corner reflector arrays
Multiplicative Noise Characterization	Use a target to measure total MNR plus thermal noise
Thermal Noise Characterization	Use sniffer pulses to measure thermal noise levels
Common Time Delay	Compare range measurement on surveyed corner reflectors
Differential Time Delay	Cross-correlate data between polarimetric channels to measure channel misregistration
Time Tag	Compare along-track position measurement on surveyed corner reflectors
Pointing Angle Biases	Use bright homogeneous backscatter region to compare measured Doppler centroid to expected Doppler centroid and measure angle biases
Polarimetric Balance	Use combination of calibration targets and distributed targets to estimate polarimetric calibration

this purpose. The density of GNSS stations is on the order of one per 20–50 km, which will allow validation of the upper end of the accuracy length scale. At some validation sites (e.g., those related to the validation of science requirement 671), this pre-instrumented GNSS data record will be augmented with field observations in the form of GNSS or levelling campaigns to facilitate validation efforts. At shorter scales, measurement requirements will be validated by analysis – examining areas known to be stable over a period of time and comparing the expected noise performance to that measured. The NASA fully polarimetric airborne SAR, UAVSAR, will also collect interferometric data for validation of surface deformation rates at smaller spatial scales. Since the errors tend to be dominated by environmental effects like water vapor and surface decorrelation, what is most important is to validate that the contributions of instrument noise are within acceptable values allowing the overall accuracies to be met.

For ice sheets and glaciers, the higher-level products will be validated in the relevant environment of Greenland and Antarctica. The Project deployed arrays of GNSS ground stations on a divide-to-coast flow line, through a variety of ice types to which the ice velocity products will be compared.

For sea-ice, the Project will exploit buoy data deployed by other agencies and countries in the Arctic and Antarctic oceans, comparing the measured buoy velocities to measured ice velocity vectors from the data.

For validation of the forest biomass measurement requirement, there is a worldwide network of managed and measured forests and fields that provide a natural in situ data set against which to validate biomass products. The Project has supported fieldwork and airborne lidar data collections at some of these sites to acquire biomass validation data sets from diverse forest types.

For permafrost deformation, forest disturbance, wetland inundation, and crop area requirements, the science team will compare NISAR products to those derived from a combination of proven remote sensing techniques using other data sets, such as optical imagery, and through the collection of field measurements.

For soil moisture, a combination of focused field campaigns and semi-permanent networks of soil moisture sensors, with more than one sensor per pixel, will be used to evaluate the NISAR soil moisture retrievals, as well as global networks of soil moisture sensors, as available.

Table 8-2 shows the nominal list of global sites at which L3 data products for all science disciplines will be generated and validated.

Several teams will be performing various functions during the calibration/validation sub-phase.

- The joint science team, which will be composed of the NISAR science team, the Project science team at JPL, and the ISRO science team, will plan and organize field campaign support (e.g., corner reflectors, GNSS stations, in situ campaigns).
- The necessary NISAR observations for Cal/Val activities will be planned by the NISAR Mission Systems team.
- The instrument health and performance will be evaluated with auxiliary measurements on the spacecraft and instrument by the NISAR Radar Instrument team.
- The SAR image data will be processed by the Science Data System (SDS) team.
- All image calibration parameters will be evaluated and validated by the algorithm development team.
- Algorithm parameters needed for generating L3 data products (e.g., biomass algorithm parameters, inundation threshold values, etc.) are to be calibrated

TABLE 8-2. SUMMARY OF NISAR CAL/VAL VALIDATION SITES

MEASUREMENT	VALIDATION SITE	COMMENT
Instrument calibration	Corner reflector arrays deployed in Oklahoma, Alaska, and the Rosamond dry lakebed in Southern California	Absolute radiometric calibration, relative calibration, instrument performance, geolocation, beam formation
Instrument calibration	Distributed targets in non-flooded, non-deforested tropical forest locations in South America and Africa	Crosstalk calibration, antenna pattern, channel imbalance, relative calibration
2-D and 3-D velocity time series of ice sheet	10 GNSS receivers along a divide-to-coast flow line in Greenland. 6 GNSS devices on Antarctic Ice Shelf. ISRO and independently funded investigators may have GNSS devices at additional locations	Could use wider area data such as Ice Bridge contemporaneous data sets, should they exist
Sea-ice velocities	West Arctic, Southern Ocean	Using available buoy data from the International Arctic Buoy Program (IABP) and International Programme for Antarctic Buoys (IPAB)
2-D deformation time series of solid Earth	Multiple Cal/Val sites around the world with extensive GNSS receiver instrumentation augmented by field-surveyed sites in northern Alaska	Other similar size and scale geodetic ground networks may be available as well
Permafrost	Surveyed sites in northern Alaska	These natural target sites will be precisely surveyed in the spring and fall to measure their seasonal surface deformation
Biomass	Five canonical biomes distributed across 15 climatic zones, with field measurements of biomass: Needleleaf, Broadleaf Deciduous, Mixed Broadleaf/Needleleaf, Broadleaf Evergreen, Savanna/Dry Forest	Use existing and heritage Cal/Val locations (roughly 30 sites distributed globally); collaboration with BIOMASS and GEDI validation campaigns
Disturbance	Known areas of forest management (e.g. southeastern U.S.), fire databases, known disturbance areas, and targets of opportunity (determined after disturbance events)	Forest management plans for clear cutting and selective logging, use of high-resolution optical data to determine canopy fraction change, use of active fire databases
Crop area	U.S. and India agricultural areas imaged with quad pol mode and selected JECAM sites	Local assessment surveys, cropscape, high-resolution optical time series, and JECAM data
Inundation area	Wetland sites with NASA funded studies such as in Alaska (ABoVe); South America (Pacaya-Samiria); Florida Everglades; Louisiana Delta; Mississippi River floodplain; coastal lagoon sites in India	Other international sites as well if field data are available; five types of validation data may be used depending on location
Soil moisture	Intensive observations (more than one sensor per pixel) at 10+ locations within the United States, sampling a range of crop types and climates	Other available soil moisture networks (including international) will be used, with lower priority for sites with one measurement location per pixel

and updated by the joint science team as validation data becomes available. Frequency of updates depends on the sensitivity of the algorithm and the timing of the field campaigns.

- The L2 science requirements will be validated by the joint science team.

A variety of field experiments/campaigns to validate the L3 science products that will be used to validate the L2 science requirements will be organized by the joint science team during this sub-phase. Possible campaigns include, but are not limited to:

- Deployment, inspection, and maintenance of trihedral corner reflectors in Oklahoma (in partnership with Oklahoma State University) and Alaska (in partnership with the Alaska Satellite Facility at the University of Alaska, Fairbanks).
  - Used for instrument calibration and performance
  - Reflectors were deployed prior to launch, and will be inspected and maintained during the Cal/Val phase and during science operations thereafter
- Biomass estimated from airborne and/or field measurements for globally representative forest areas
  - Used for calibration of biomass algorithm parameters and validation of science requirement
- Field validation of inundation extent for boreal, temperate, and tropical wetlands
  - Used for calibration of inundation threshold values and validation of inundation science requirement
- Field validation of active crop area
  - Used for calibration of crop area threshold values and validation of the active crop area science requirement
- Field evaluation of soil moisture
  - Used for evaluation of the soil moisture target of 6% unbiased RMSE
- Field validation of surface deformation in permafrost areas
  - Used for validation of the permafrost deformation science requirement
- Installation of 10 GNSS receivers along a divide-to-coast flow line in Greenland and 6 GNSS receivers on an ice shelf in Antarctica
  - GNSS receivers were deployed in 2024 in Greenland and Antarctica
  - Used for validating observations for all snow types and melt states of glacier velocities

Members of the joint science team will also utilize data from various resource networks

TABLE 8-3. EXISTING OR NEAR-TERM AIRCRAFT-BASED SENSORS

AIRBORNE SYSTEMS	SENSOR
NASA UAVSAR	L-band quad-pol repeat pass InSAR, P-band quad-pol SAR, Ka-band single pass InSAR
DLR FSAR	X-band through P-band quad pol repeat pass InSAR
JAXA Pi-SAR	L-band quad-pol SAR
LVIS	Scanning laser altimeter
G-LiHt	Scanning lidar, profiling lidar, VNIR imaging spectrometer, thermal imager
ISRO L/S airborne radar	S-band and L-band SAR
UAS	Lidar, thermal IR, and/or multispectral instruments

for validating the L3 data products, e.g., NASA Arctic-Boreal Vulnerability Experiment (ABoVe), National Science Foundation (NSF) National Ecological Observatory Network (NEON), Network of the Americas (NOTA), corner reflector arrays, and GNSS station networks that are distributed globally.

The exit criteria/final conditions to be satisfied for ending the calibration/validation sub-phase are:

- L-SAR and S-SAR instrument calibration stability has been demonstrated and verified. Appropriate adjustments have

TABLE 8-4. POSSIBLE FIELD EXPERIMENTS FOR NISAR CAL/VAL

FIELD EXPERIMENTS / AIRBORNE DATA / SATELLITE OBSERVATIONS	OBJECTIVES	NUMBER OF PLANNED EXPERIMENTS					
		PRE-LAUNCH	OBSERV. CHECKOUT	CAL/VAL PHASE	SCIENCE OPERATIONS YEAR 1	SCIENCE OPERATIONS YEAR 2	SCIENCE OPERATIONS YEAR 3
Deployment of 20+ corner reflectors (CR)	Instrument calibration	1					
Inspection and maintenance of 20+ CRs	Instrument calibration				1	1	1
Deployment of one passive receiver	Validation of antenna pattern and digital beamforming parameters		1-3				
Biomass from field measurements / airborne lidar	Calibration of biomass algorithm parameters, and validation of science requirement	10		6	6	6	
Field validation of inundation extent for boreal, temperate, and tropical wetlands	Calibration of inundation threshold values and validation of inundation science requirement	3		2	2	2	2
Field validation of crop area	Calibration of crop area threshold values and validation of inundation science requirement	2		2	2	2	2
Field evaluation of soil moisture	Evaluate soil moisture	2		4			
Field validation of permafrost deformation	Validate surface deformation in permafrost areas	2		2	2	2	2
10 GNSS receivers in Greenland	Velocity measurements for all snow facies and melt states	1	1				
Maintain 10 GNSS receivers in Greenland	Validate observations for all snow facies and melt states				1	1	1
6 GNSS receivers on ice shelf in Antarctica	Validate velocity measurements	1	1				
Maintain 6 GNSS receivers on ice shelf in Antarctica	Validate velocity measurements	1	1		1	1	1

been proposed, verified, and processed (revisions resulting from Cal/Val could affect mission timeline, radar modes, Cal/Val process, SDS processing and data analysis, ground systems, mission operations, and ground field campaigns and supporting infrastructure including corner reflectors, GNSS stations, etc.).

- L3 data products over Cal/Val sites have been validated via a mix of ground truth and remote sensing data (this only refers to the initial validation; these products will be validated periodically over the course of the mission).
- The flight systems (spacecraft, engineering payload, RBA), payloads (L-SAR and S-SAR instruments), and ground systems (GDS, SDS, MOS) biases are well characterized, so that calibrations can be routinely applied and incorporated to adjust or remove biases to generate calibrated L1/L2 data products.
- The algorithms and retrieval of geophysical parameters (L3 data products) from L1/L2 products are validated, and any biases can be sufficiently characterized and removed.

Some validation campaigns will involve comparisons with datasets from airborne sensors (e.g., NASA UAVSAR, lidar; see Table 8-3) and other contemporary spaceborne sensors (e.g., NASA GEDI, ICESat-2, ESA Biomass, the PlanetScope constellation, Landsat 8/9, Sentinel-1, Sentinel 2). Possible field campaigns are noted in Table 8-4.

8.3 CALIBRATION/VALIDATION ROLES AND RESPONSIBILITIES

The NISAR joint science team (consisting of scientists selected by NASA and ISRO), along with the supporting Project Science Team (PST), will plan and organize field campaign support (e.g., corner reflectors, GNSS stations, in situ campaigns). The SDS will nominally collect and process the radar data. The NISAR SDS and radar instrument team will work together to regularly update instrument calibration parameters for generating L1 and L2 products. The instrument team will work with the mission planning team to ensure appropriate calibration data are acquired. The joint science team will analyze and evaluate imagery data processed by the SDS, interpret results, and generate L3 data products over selected science validation sites. They will calibrate and update algorithm parameters (e.g., biomass algorithm parameters, inundation threshold values, etc.) regularly in their calculations of L3 products. They will also verify the end-to-end acquisition, calibration, and processing of the imagery. Lastly, the joint science team will validate that the science requirements have been achieved by the mission.

The NISAR Cal/Val Plan is developed and implemented by the NISAR Cal/Val team, which includes members of the joint science team, the ISRO Cal/Val team, and members of the Project science and science data system staff at JPL. The NISAR Cal/Val Plan was developed by taking into consideration a broad range of inputs and contributions from the U.S. and international communities, including Cal/Val plans of other Synthetic Aperture Radar (SAR) missions related to the NISAR science disciplines. Detailed roles and responsibilities for specific tasks are shown in Table 8-5.

COMMUNITY INVOLVEMENT

The NISAR Project welcomes high-quality in situ data that can be used for calibrating or validating NISAR images, algorithms, and products.

TABLE 8-5. CAL/VAL POINTS OF CONTACT

	PROJECT SCIENCE TEAM	JOINT SCIENCE TEAM	SCIENCE DATA SYSTEMS TEAM	RADAR INSTRUMENT TEAM
Validation algorithms		X		
L0a-L0b			X	X
L0-L1			X	X
L1-L2	X	X	X	
L2-L3	X	X		
Calibration algorithms		X		
Point target analysis			X	X
Doppler analysis			X	X
GNSS network comparisons	X	X		
Tropospheric phase calibration	X	X		
Ionosphere (absolute delay / relative split spectrum delay)	X	X		
Soil moisture	X	X		
Calibration activities				
Work associated with calibration algorithms	X	X	X	X
Coding of algorithms (Phase C/D)	X	X	X	
Acquisition of test data - scoped by each discipline	X	X		
Testing of calibration tools			X	
Field work - scoped by each discipline	X	X		
Validation activities				
Validation field work	X	X		
Processing test data	X	X	X	
Processing mission data		X	X	
Comparison of results to requirements	X	X	X	

Credit: Taras Vyshnya/Shutterstock.

9 CONCLUSIONS

NISAR WORKSHOPS, CONFERENCE SESSIONS, AND TECHNICAL TRAINING FOSTER THE INTEGRATION OF NISAR DATA INTO EARTH SCIENCE STUDIES BY CURRENT AND FUTURE GENERATIONS OF SCIENTISTS AND ENGINEERS.

Earth's surface and vegetation cover are constantly changing. By measuring these changes globally and continuously, NISAR will enable breakthrough science while supporting informed decision making across a wide range of societally relevant applications. With its broad and aspirational set of science objectives, NISAR is poised to be the first Decadal Survey mission to fulfill NASA's aspiration to remain at the forefront of scientific discovery while enabling applications for societal benefit.

One of the goals of the NISAR project is to expand community engagement across both the science and applications communities. To this end, NISAR will continue to convene workshops, conference sessions, and technical training to foster the integration of NISAR data into Earth science studies by current and future generations of scientists, geologists, and engineers.

The synergistic potential with observations from other satellite radar missions is also exciting. Europe's Sentinel-1 satellites, Canada's RADARSAT constellation, and Japan's ALOS missions all provide complementary observations at various radar bands. Additionally, NASA's Global Ecosystem Dynamics Investigation (GEDI) lidar on the International Space Station and the European Space Agency's fully polarimetric BIOMASS radar mission provide biomass and vegetation structure measurements relevant to NISAR. Studies combining observations from these various sources will not only assist in cross-verification and validation but will also yield new insights into Earth surface processes.

Over two decades in the making, NISAR represents the aspirations of a generation of scientists. The NISAR science team comprises many scientists who have exploited SAR data from many sources, some from as early as SEASAT in 1978. These scientists have tremendous depth of experience in what SAR can and cannot do. They are of like mind in both frustration with the lack of available science-grade SAR data available to the research community, and excitement about the opportunities NISAR will provide to scientists around the world. Many of the techniques developed with SEASAT and SIR-C, both short-lived missions flown decades ago, are as relevant today as they were then. The international SAR sensors that blossomed after these U.S. missions have indeed led to new and exciting discoveries. The examples shown in this document drawn from these missions can only hint at the anticipated major improvement in our understanding of Earth that the NISAR mission will contribute.

10 ACKNOWLEDGMENTS

This document was produced at Jet Propulsion Laboratory, California Institute of Technology, under a contract with the National Aeronautics and Space Administration. The first edition was published in 2019 during the development phase of the mission. This second edition captures the NISAR mission status at the time of launch.

The NASA and ISRO project management and engineering teams have dedicated countless hours to developing a first-of-a-kind radar mission with unprecedented capabilities. The principal contributors to this document are listed below. Science Team members are listed by name in the document itself.

Cost estimates stated herein are as of publication and do not necessarily represent cost at final mission.

EDITORS

Priyanka Sharma, JPL, Editor-in-chief of unpublished edition, prior to 2016
Andrea Donnellan, JPL, Editor-in-chief, first edition
Brandi Downs, JPL, Editor-in-chief, second edition
Margaret Glasscoe, JPL, Associate editor, first edition
Ekaterina Tymofyeyeva, JPL, Associate editor, second edition

CONTRIBUTORS

2012-2016 NASA Science Definition Team
2016-2019 NASA Science Team
2019-2022 NASA Science Team
2022-2025 NASA Science Team
2012-2025 ISRO Science Team
Gerald Bawden, NASA
Sean Buckley, JPL
Susan Callery, JPL
Joshua Doubleday, JPL
Sara Hatch, JPL
Scott Hensley, JPL
Paul Rosen, JPL
Scott Shaffer, JPL
Peter Xaypraseuth, JPL

Credit: NASA/JPL.

APPENDIX A:
HISTORICAL BACKGROUND FOR NISAR

SEASAT LED TO A SERIES OF NASA SPACE SHUTTLE–BASED RADAR MISSIONS AND INSPIRED THE DEVELOPMENT OF SPACEBORNE SAR SYSTEMS WORLDWIDE.

The first civilian SAR satellite in history, called SEASAT, was launched by NASA in 1978. SEASAT's L-band (24 cm wavelength) SAR operated for three months before the failure of the spacecraft's power system. SEASAT led to a series of NASA space shuttle–based radar missions and inspired the development of spaceborne SAR systems worldwide. Launching another free-flying scientific SAR in the U.S. has proven elusive, despite strong demand from the science and applications community.

In 2007, the National Research Council Committee on Earth Science and Applications from Space recommended a mission to measure changes in land, ice, and vegetation structure, called DESDynI (Deformation, Ecosystem Structure, and Dynamics of Ice) as one of the first in a series of Decadal Survey missions to carry forward the nations spaceborne observation program. The objective for DESDynI was to address the critical needs of three major science disciplines - Solid Earth, Ecosystems, and Cryospheric sciences - plus provide data important for many applications. The primary mission objectives for DESDynI were to: 1) determine the likelihood of earthquakes, volcanic eruptions, and landslides through surface deformation monitoring; 2) characterize the global distribution and changes of vegetation aboveground biomass and ecosystem structure related to the global carbon cycle, climate, and biodiversity; and 3) project the response of ice masses to climate change and impact on sea level. In addition, NISAR will provide observations that will greatly improve our monitoring of groundwater, hydrocarbon, and sequestered CO2 reservoirs. The Decadal Survey noted that these surface processes can be characterized and monitored from space using SAR and light detection and ranging (lidar). Initial designs of DESDynI consisted of an L-band polarimetric SAR designed to operate as a repeat-pass interferometric SAR (InSAR) and a multibeam lidar.

In 2008, NASA appointed a DESDynI Science Study Group (DSSG) to articulate specific science requirements for the DESDynI mission and established a pre-formulation project team at the Jet Propulsion Laboratory (JPL) and Goddard Space Flight Center (GSFC) to flow these requirements down to a specific mission implementation. JPL was overall project lead and responsible for the SAR project element; GSFC was responsible for the lidar project element. The DSSG wrote a Science Definition Document (SDD) describing in great detail the science behind the mission and developed a set of Level 1 and Level 2 requirements and preliminary science targets, including observing attributes such as radar mode, sampling strategy, pointing diversity, etc., which guided the project work.

A complete mission concept was developed for DESDynI. The pre-formulation team successfully conducted a Mission Concept Review (MCR) in January 2011. After the MCR, NASA received direction from the US Administration (Office of Management and Budget) to reformulate the

concept to reduce its scope. The lidar was to be removed as a component of the DESDynI program, and the cost of the radar project element was to be reduced significantly.

In May 2012, NASA competed and selected a DESDynI radar (DESDynI-R) Science Definition Team (SDT) to redefine DESDynI science to flow to an affordable, radar-only NASA mission. Past and current SDT members are listed in Tables B-1 and B-2 in Appendix B. At the same time, the JPL project team studied a number of options to reduce cost and/or scope including partnerships with other space agencies.

Through discussions between NASA and ISRO on the possibility of a joint radar mission, it became clear that the goals originally identified for DESDynI-R were of great interest to the ISRO science community. In January 2012, ISRO identified targeted science and applications that were complementary to the primary mission objectives, agricultural monitoring and characterization, landslide studies, Himalayan glacier studies, soil moisture, coastal processes, coastal winds, and monitoring hazards. For many of these objectives, the addition of an S-band polarimetric capability will add considerably to the measurement, extending the measurement sensitivity at L-band to lower values while decreasing sensitivity to ionospheric and soil moisture effects.

Since January 2012 when the initial L- and S-band SAR mission concept was put forward as a partnership, JPL and ISRO teams have been attempting to refine the science plan and its implications for the mission. In September 2013, ISRO received initial approval from the Government of India for jointly developing with NASA the L- and S-band SAR mission. A Technical Assistance Agreement (TAA) between ISRO and California Institute of Technology / JPL was enacted on September 30, 2013. NASA Administrator Charles Bolden and K. Radhakrishnan, Chairman of ISRO, signed the NISAR Implementing Arrangement (IA) on September 30, 2014.

APPENDIX B:
NISAR SCIENCE TEAM

The NISAR Science Team members are drawn from the science disciplines related to the mission. The Science Team is renewed at three-year intervals and the makeup of the Team evolves to fit the NISAR science and mission needs. An ISRO Science Team addresses the ISRO objectives. JPL also has an internal Project Science Team to coordinate technical activities.

B.1 NAA SCIENCE DEFINITION TEAM

NASA selected a Science Definition Team (SDT) known as the "DESDynI-R SDT" in May 2012. The expertise of the members spans the science disciplines identified in the 2007 National Research Council (NRC) Decadal Survey of Earth Science and Applications for the DESDynI mission concept.

"DESDynI-R" refers to the radar component of the DESDynI concept. In addition to discipline scientists, the Team comprises applications and radar phenomenology experts. Table B-1 lists the 2012–2015 SDT members, their affiliations and areas of interest. A solicitation was issued in 2015 to recompete the SDT. Selections were

TABLE B-1. NASA SAR MISSION SCIENCE DEFINITION TEAM (2012-2015)

SDT Member	Institutional Affiliation	Areas of Interest
Bradford Hager Deformation Lead	Massachusetts Institute of Technology	Solid Earth
Ralph Dubayah Ecosystems Lead	University of Maryland	Ecosystems
Ian Joughin Cryosphere Lead	University of Washington Applied Physics Lab	Cryosphere
Gerald Bawden*	US Geological Survey/NASA HQ	Hazards, hydrology, applications
Kurt Feigl	University of Wisconsin	Solid Earth
Benjamin Holt	Jet Propulsion Laboratory	Sea ice
Josef Kellndorfer	Woods Hole Research Center	Ecosystems, carbon policy
Zhong Lu	Southern Methodist University	Volcanoes
Franz Meyer	University of Alaska, Fairbanks	Applications, techniques, deformation
Matthew Pritchard	Cornell University	Solid Earth, cryosphere
Eric Rignot	University of California, Irvine	Cryosphere
Sassan Saatchi	Jet Propulsion Laboratory	Ecosystems
Paul Siqueira	University of Massachusetts, Amherst	Ecosystems, techniques
Mark Simons	California Institute of Technology	Solid Earth, hazards, cryosphere
Howard Zebker	Stanford University	Solid Earth, applications, techniques

**Transitioned from SDT member to NASA HQ after selection*

made in April 2016, and the new team was in place by May 2016. The new team has 11 returning members and 9 new team members. Table B-2 lists the recompeted and selected Science Definition Team. This Team was formally recognized as the Science Team in 2018. The current Science Team is listed in Table B-3.

TABLE B-2. NASA SAR MISSION SCIENCE DEFINITION TEAM (2016-2019)

SDT Member	Institutional Affiliation	Areas of Interest
Mark Simons Deformation Lead	California Institute of Technology	Solid Earth, hazards
Paul Siqueira Ecosystems Lead	University of Massachusetts, Amherst	Ecosystems, techniques
Ian Joughin Cryosphere Lead	University of Washington Applied Physics Lab	Cryosphere
Cathleen Jones Applications Lead	Jet Propulsion Laboratory	Applications
Falk Amelung	University of Miami	Solid Earth, atmospheres
Adrian Borsa	Scripps Institution of Oceanography	Solid Earth
Bruce Chapman	Jet Propulsion Laboratory	Wetlands
Eric Fielding	Jet Propulsion Laboratory	Solid Earth
Richard Forster	University of Utah	Cryosphere
Bradford Hager	Massachusetts Institute of Technology	Solid Earth
Benjamin Holt	Jet Propulsion Laboratory	Sea ice
Josef Kellndorfer	Earth Big Data, LLC.	Ecosystems, carbon policy
Rowena Lohman	Cornell University	Solid Earth, cryosphere
Zhong Lu	Southern Methodist University	Volcanoes
Franz Meyer	University of Alaska, Fairbanks	Applications, techniques, deformation
Frank Monaldo	National Oceanic and Atmospheric Administration	Oceans, sea ice
Eric Rignot	University of California, Irvine	Cryosphere
Sassan Saatchi	Jet Propulsion Laboratory	Ecosystems
Marc Simard	Jet Propulsion Laboratory	Ecosystems, techniques
Howard Zebker	Stanford University	Solid Earth, applications, techniques

TABLE B-3. NISAR SCIENCE TEAM (2019-PRESENT)

SDT Member	Institutional Affiliation	Areas of Interest
Mark Simons Deformation Lead	California Institute of Technology	Solid Earth, hazards
Paul Siqueira Ecosystems Lead	University of Massachusetts, Amherst	Ecosystems, techniques
Ian Joughin Cryosphere Lead	University of Washington Applied Physics Lab	Cryosphere
Cathleen Jones Applications Lead	Jet Propulsion Laboratory	Applications
Rowena Lohman Soil Moisture Lead	Cornell University	Soil moisture, solid Earth
Rajat Bindlish	Goddard Space Flight Center	Soil moisture
Adrian Borsa	Scripps Institution of Oceanography	Solid Earth
Bruce Chapman	Jet Propulsion Laboratory	Wetlands
Narendra Das	Michigan State University	Soil moisture
Ralph Dubayah	University of Maryland	Ecosystems
Richard Forster	University of Utah	Cryosphere
Alex Gardner	Jet Propulsion Laboratory	Cryosphere
Sean Helfrich	National Oceanic and Atmospheric Administration	Oceans, sea ice
Benjamin Holt	Jet Propulsion Laboratory	Sea ice
Josef Kellndorfer	Earth Big Data, LLC.	Ecosystems, carbon policy
Seungbum Kim	Jet Propulsion Laboratory	Soil moisture
Zhong Lu	Southern Methodist University	Volcanoes
Kyle McDonald	City College of New York	Ecosystems
Franz Meyer	University of Alaska, Fairbanks	Applications, techniques, deformation
Eric Rignot	University of California, Irvine	Cryosphere
Sassan Saatchi	Jet Propulsion Laboratory	Ecosystems
Howard Zebker	Stanford University	Solid Earth, applications, techniques

B.2 ISRO SCIENCE TEAM

ISRO forms a science team once a project is approved, which is the equivalent of entering formulation. The ISRO scientists involved in defining the ISRO-specific science requirements through KDB-B are given in Table B-4. ISRO Science Team Principal Investigators are given in Table B-5.

TABLE B-4. ISRO PRE-FORMULATION SCIENCE TEAM (PRIOR TO KDP-B)

SDT Member	Institutional Affiliation	Areas of Interest
Tapan Misra*	Space Applications Centre, Ahmedabad	Radar phenomenology, lead prior to KDP-B
Manab Chakraborty** Raj Kumar (after KDP-B)	Space Applications Centre, Ahmedabad	Agriculture Oceans, lead after KDP-B
Anup Das	Space Applications Centre, Ahmedabad	Ecosystems
Sandip Oza	Space Applications Centre, Ahmedabad	Cryosphere

**Became SAC director in April 2016*

***Retired in April 2016*

TABLE B-5. ISRO SCIENCE TEAM PRINCIPAL INVESTIGATORS

Science Team Leadership		
Rashmi Sharma (SAC, Lead)	Deepak Putrevu (SAC, Co-Lead)	P. Venkat Raju (NRSC, Co-Lead)
Anup Kumar Das (SAC, Co-Lead)	John Mathew (ISRO HQ, Programmatic Interface and Coordination)	Raj Kumar (SAC, Previous Lead)
Ecosystems – Forestry and Agriculture		
C. Patnaik (SAC, Lead)	Hitendra Padalia (IIRS)	Lele Nikhil Vinayak (SAC)
Saroj Maity (SAC)	Dipanwita Haldar (IIRS)	Suraj Reddy Rodda (NRSC)
Mukesh Kumar (SAC)	Ayan Das (SAC)	Sujata Ghosh (ADRIN)
Srikanth P. (NRSC)	Anand S.S. (SAC)	
Ecosystems – Hydrology and Soil Moisture		
Praveen Kumar Gupta (SAC, Lead)	Ashwin Gujrati (SAC)	Dharmendra K. Pandey (SAC)
Saksham Joshi (NRSC)	Annie Maria Issac (NRSC)	Hari Shankar Srivastava (IIRS)
Cryosphere Sciences		
Sushil Kumar Singh (SAC, Lead)	Praveen K. Thakur (IIRS)	Naveen Kumar Tripathi (SAC)
Purvee Joshi (SAC)	Vaibhav Garg (IIRS)	Sai Krishna C (NRSC)
Sandip R. Oza (SAC)		
Solid Earth and Geosciences		
K.M. Sreejith (SAC, Lead)	Ritesh Agrawal (SAC)	R.S. Chatterjee (IIRS)
Priyam Roy (NRSC)	Swati Singh (NRSC)	Hari Shankar (IIRS)
Gopal Sharma (NESAC)	Tathagata Chakraborty (SAC)	
Coastal and Ocean Applications		
Neeraj Agrawal (SAC, Lead)	Abhisek Chakraborty (SAC)	Ratheesh Ramakrishnan (SAC)
Anup K. Mandal (SAC)	Suchandra Aich Bhowmick (SAC)	Rajesh Sikhakolli (NRSC)
Disaster Response Services		
Durga Rao KHV (NRSC, Lead)	Tapas Ranjan Martha (NRSC)	Arijit Roy (IIRS)
Kuntala Bhushan (NESAC)	Venkata Ramani A (NRSC)	
Science Data Products		
V. Manavala Ramanujam (SAC, Lead)	Usha Sundari Ryali HSV (NRSC)	Krishna Murari Agrawal (SAC)
Raghav Mehra (SAC)	Samneet Thakur (SAC)	
Data Calibration		
Shweta Sharma (SAC, Lead)	Maneesha Gupta (SAC)	Bhaskar Dube (SAC)
Santhisree B. (NRSC)	Shashi Kumar (IIRS)	Jayasri P. V. (NRSC)
Applications Tools		
Jayaprasad P. (SAC, Lead)	Sanid C. (SAC)	Tarun S. Maganti (SAC)
Rosly Boy Lyngdoh (NESAC)	Shivani Tyagi (SAC)	Samvram Sahu (NRSC)
K. Radha Krishna (NRSC)	Ashish Joshi (IIRS)	Nidhi Chaubey (ADRIN)

SAC – Space Applications Centre
NRSC – National Remote Sensing Centre
ISRO HQ – Indian Space Research Organisation Headquarters
IIRS – Indian Institute of Remote Sensing
NESAC – North Eastern Space Applications Centre
ADRIN – Advanced Data Processing Research Institute

B.3 PROJECT SCIENCE TEAM

JPL maintains a Project Science Team (PST) distinct from the SDT, headed by a project scientist, currently Paul Rosen. The project scientist works side-by-side with the project manager to coordinate the science and technical developments and calls on JPL staff scientists to perform analyses in support of the science team activities.

The project scientist conducts weekly coordination teleconferences with the Science Team leads and the full Science Team to maintain information flow and coordinate analysis, requirements definition, and documentation. In addition to the PST, the Project Applied Sciences Team, Algorithm Development Team (ADT), Science Data Systems (SDS) Team, and Mission Systems Team, all contribute collaboratively to advance the objectives of the science plan. Members of each team are listed in Table B-6.

TABLE B-6. NISAR PROJECT SCIENCE TEAM (PST)

PST Leadership		
Paul Rosen Project Scientist	Marco Lavalle Deputy Project Scientist	Susan Owen Former Deputy Project Scientist
PST - Calibration and Validation (Cal/Val)		
Bruce Chapman Cal/Val Lead	Ronald Muellerschoen	Naiara Pinto
Brandi Downs	Annemarie Peacock	Katherine "KC" Cushman
Christopher Mulverhill		
PST Science Validation Coordination		
Ekaterina Tymofyeyeva Solid Earth Lead	Alexandra Christensen Ecosystems Lead	Catalina Taglialatela Cryosphere Lead
Eric Fielding	Seongsu Jeong	Emre Havazli
Robert Zinke	Michael Aivazis	Edward Armstrong
PST - Performance		
Ekaterina Tymofyeyeva	Shadi Oveisgharan	Leif Harcke
PST - Interdisciplinary		
Charles Elachi	Eric Gurrola	Scott Hensley
Sang-Ho Yun		
Project Applied Sciences Team		
Shanna McClain NASA Program Applications Lead	Elodie Macorps Mission Applications Lead	Karen An Mission Applications Lead
Batuhan Osmanoglu	Susan Owen	Natasha Stavros
Tim Stout	Ekaterina Tymofyeyeva	Erika Podest
Algorithm Development Team (ADT)		
Heresh Fattahi ADT Lead	Sean Buckley Former ADT Lead	Brian Hawkins
Virginia Brancato	Gustavo H. X. Shiroma	Hirad Ghaemi
Geoffrey Gunter	Samantha Niemoeller	Xiaodong Huang
Bo Huang	Jungkyo Jung	Tyler Hudson
Seongsu Jeong	Ryan Burns	Joanne Shimada
Piyush Agram		
Science Data Systems (SDS) Team		
Cecilia Cheng SDS Manager	Hook Hua SDS Architect	Laura Jewell Former SDS Deputy Manager
Susan Neely	Jeffrey Pon	Helen Mortensen
Michael Joyce	Gerald Manipon	Michael Cayanan
Namrata Malarout	Max Zhan	Alex Torres
Mariyetta Madatyan	Alice Stanboli	Lan Dang
Cathy To	Diego Garay	Lela Rodriguez
Hoan Luu	Jimmie Young	
NISAR Missions Systems Team		
Ana Maria Guerrero Mission Systems Manager	Maher Hanna Deputy Mission System Manager	Josh Doubleday Mission Planning Lead
Francois Rogez	Priyanka Sharma	Thomas Moline
Ian Roundhill	Naresh Kumar (ISRO)	

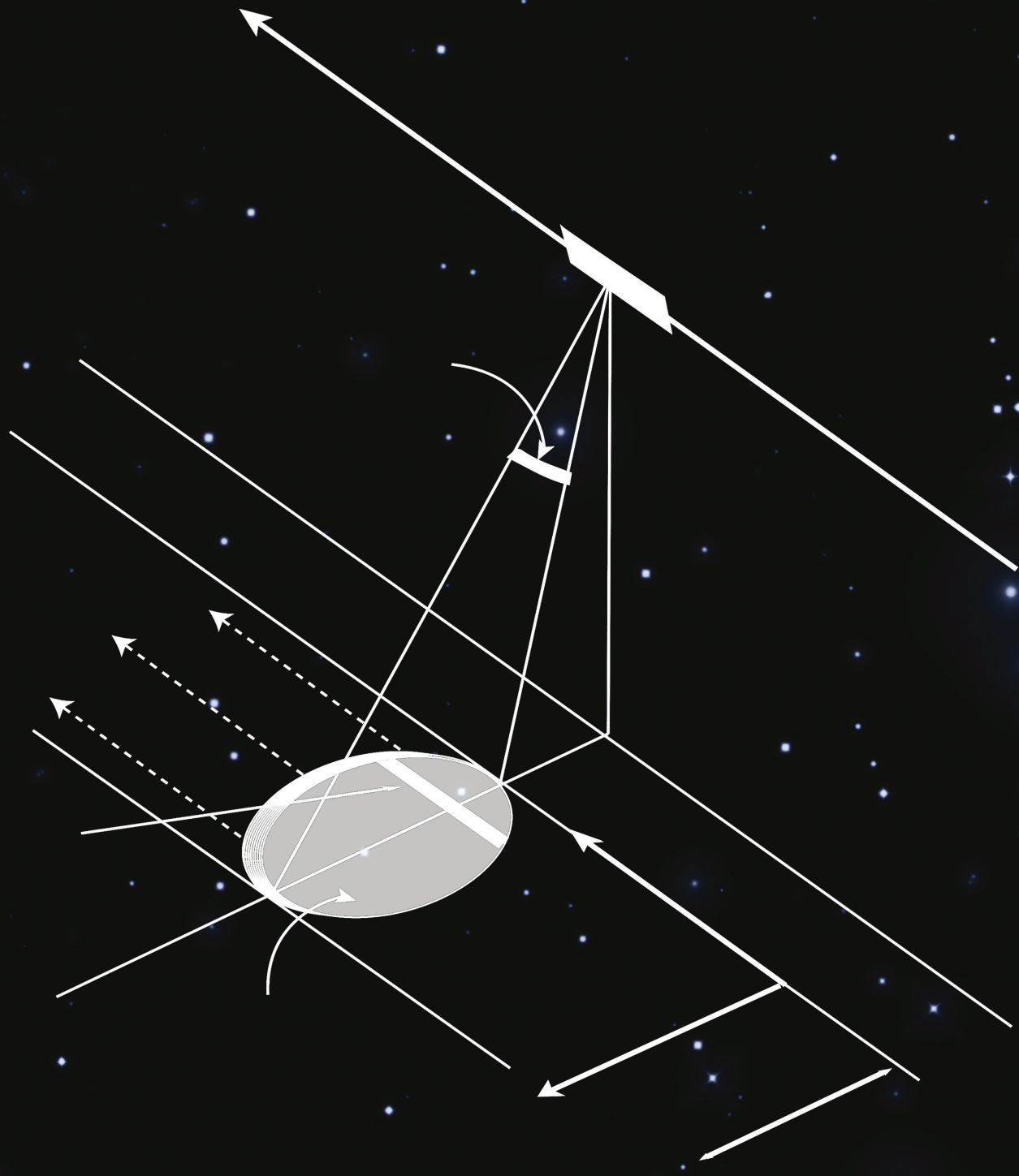

APPENDIX C: KEY CONCEPTS

This appendix covers the key concepts for the NISAR radar mission. The key concepts include an overview of the radar imaging and the basic related science products that the mission will produce.

C.1 BASIC RADAR CONCEPTS: RADAR IMAGING, POLARIMETRY, AND INTERFEROMETRY

For those unfamiliar with the NISAR mission, this section gives a brief introduction to key concepts and terms that are central to NISAR science and measurements. These include radar imaging, polarimetry, and interferometry concepts. There are a number of excellent introductory books (Richards, 2009; van Zyl and Kim, 2011; Hanssen, 2001) and book chapters (Simons and Rosen, 2007; Burgmann et al., 2000) on these subjects.

C.1.1 SYNTHETIC APERTURE RADAR (SAR)

Synthetic aperture radar (SAR) refers to a technique for producing fine resolution images from an intrinsically resolution-limited radar system. The wavelengths, λ, that are used for radar remote sensing of Earth's surface are typically in the range of a few to tens of centimeters. At these wavelengths, the energy radiated from a radar antenna of dimension D fans out over an angular range that is equivalent to the beam width λ/D of the antenna. For a typical spaceborne SAR configuration with wavelengths of ~10 cm and an antenna of 10 m size, this beam width is 1/100 radians, or about 0.6 degrees. For a radar in space observing Earth 1000 km below, the beam size on the ground is then 1000 λ/D = 10 km. This intrinsic resolution of the radar system is insufficient for many applications, and practical solutions for improving the resolution needed to be found.

SAR techniques exploit the motion of the radar in orbit to synthesize an aperture (antenna), which typically will be about 10-km long in the flight direction. This principle is illustrated in Figure C-1. While the radar is traveling along its path, it is sweeping the antenna's footprint across the ground while it is continuously transmitting and receiving radar pulses. In this scenario, every given point in the radar swath is imaged many times by the moving radar platform under constantly changing yet predictable observation geometries. In SAR systems, this change in observation geometry, resulting in a constant change of the distance from the radar to the point on the ground, is precisely encoded in the phase of the observed radar response. The phase history for any point on the ground located at a constant distance parallel to the flight track is unique to that point. By compensating the phase history of each pulse that is affecting a particular point on the ground, it is possible to focus the energy across the 10 km synthetic aperture and create an image of vastly improved resolution. The theoretically achievable synthetic aperture resolution can be calculated from D/2, is independent of the range or wavelength, and corresponds to D/2=5 m for the previously outlined spaceborne scenario.

Through the outlined principles, SAR defeats the intrinsic resolution limits of radar antennas in the along-track direction. In the cross-track or range direction, orthogonal to the satellite path, the resolution is not defined by the antenna beam width, but rather the width of the transmitted pulse. Referring to Figure C-1, this is because the transmitted pulse intersects the imaged surface as it propagates in the beam. After a two-way trip of a transmitted pulse from sensor to the ground and back, two objects can be distinguished if they are spatially separated by more than half the pulse width. Hence, range resolution is controlled

by the transmitted waveform that is generated by the radar and not the size of the antenna footprint on the ground. Wider bandwidth signals generate finer resolution images in range.

For most purposes, the transmitted signal can be thought of as a single frequency sinusoid with a well-defined amplitude and phase. Thus, the image constructed from the SAR processing is a complex image – each resolution element, or pixel, has an amplitude and phase associated with it. Once calibrated, the amplitude is proportional to the reflectance of the surface. The phase is proportional to the distance the wave traveled between the radar and the ground, any propagation phase delays due to the atmosphere or ionosphere, and any phase contribution imparted by the reflectance from the surface.

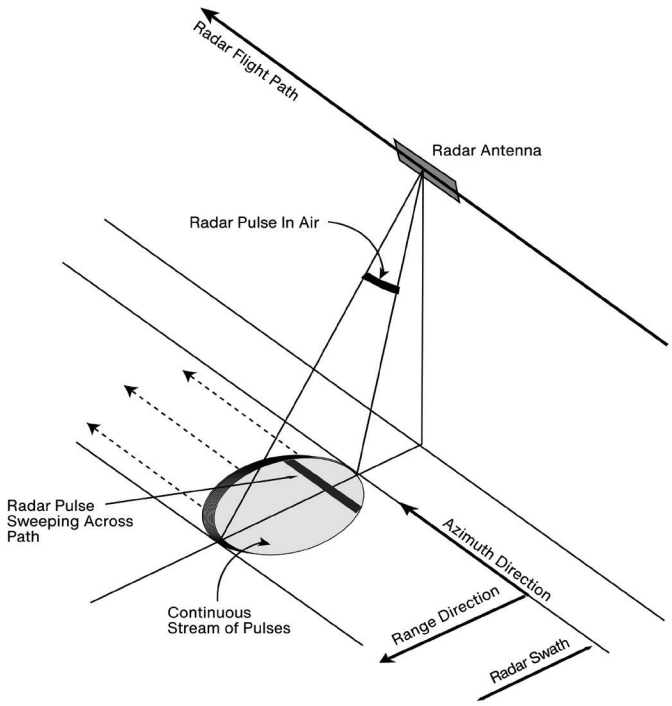

FIGURE C-1

Configuration of a radar in motion to enable synthetic aperture radar imaging. Radar antenna illuminates an area on the ground determined by its wavelength and antenna dimension. Pulses are sent and received continuously such that any point on the ground is sampled often. The range/phase history of each point is compensated to focus energy acquired over the synthetic aperture time to fine resolution. In range, resolution is achieved by coding the pulse with a wide bandwidth signal waveform.

C.1.2 POLARIMETRY

A radar antenna can be designed to transmit and receive electromagnetic waves with a well-defined polarization, which is defined as the orientation of the electric field vector in the plane orthogonal to the wave propagation direction. By varying the polarization of the transmitted signal, SAR systems can provide information on the polarimetric properties of the observed surface. These polarimetric properties are indicative of the structure of the surface elements within a resolution element. Oriented structures such as buildings or naturally aligned features (e.g., sand ripples) respond preferentially to similarly oriented polarizations and tend to preserve polarimetric coherence, whereas randomly oriented structures lead to depolarization of the scattered signals.

A polarimetric radar can be designed to operate as a single-pol system, where there is a single polarization transmitted and a single polarization received. A typical single-pol system will transmit horizontally or vertically polarized waveforms and receive the same (giving HH or VV imagery). A dual-pol system might transmit a horizontally or vertically polarized waveform and measure signals in both polarizations in receive (resulting in HH and HV imagery). A quad-pol or full-pol system will alternate between transmitting H- and V-polarized waveforms and receive both H and V (giving HH, HV, VH, VV imagery). Operating in quad-pol mode requires a pulsing of the radar at twice the rate of a single- or dual-pol system since the transmit polarization has to be alternated between H and V in a pulse-by-pulse manner to enable coherent full-polarized data acquisitions. Since this type of operation can cause interference between the received echoes, a variant of quad-pol known as quasi-quad-pol can be used, whereby two dual-pol modes are operated simultaneously: an HH/HV mode is placed in the lower portion of the allowable transmit frequency band and a VH/VV mode is operated in the upper portion. Being disjoint in frequency, the modes do not interfere with each other. However, the observed HH/HV and VH/VV data are mutually incoherent.

While most spaceborne systems are linearly polarized, it is also possible to create a circularly polarized signal on transmit, whereby the tip of the electric field vector is rotating in a circle as it propagates. This is typically implemented by simultaneously transmitting equal amplitude H and V signals that are phase shifted by 90 degrees. Various combinations of right-circular and left-circular polarization configurations on transmit and receive allow synthesizing single-, dual-, and quad-pol mode data from circular-polarized observations. Circular polarization is relevant to NISAR as recent work has emphasized the benefits of hybrid polarization, where a circularly polarized wave is transmitted and H and V

signals are received. The dual-pol instance of this mode is known as compact-pol. Compact-pol captures many of the desirable scattering properties of a dual-pol system, e.g., discriminating between oriented and random surfaces, while better balancing the power between the receive channels.

Classical radar polarimetry focuses on relating the complex backscatter observed in various polarimetric combinations to the electrical and geometric properties of the observed surfaces in order to extract meaningful information. Observation-based empirical work, as well as theoretical modeling, helps establish these relationships. For example, over soils, surface roughness and moisture both contribute to the backscattered amplitude, but it can be shown that HH and VV images have similar responses to roughness, such that the ratio HH/ VV is primarily an indicator of moisture content. As another example, bare surfaces have a weak depolarizing effect, while vegetation canopies generally are highly depolarizing. So, a joint examination of the dual-pol channels HH and HV can distinguish these surface types.

For this mission, quantifying biomass is an important measurement objective. Empirical relationships have been developed that allow mapping of radar backscatter amplitude to the amount of biomass present in an image resolution cell. The relationship varies with vegetation type and environmental conditions (e.g., soil moisture and roughness), but with multiple polarizations and repeated measurements, the biomass can be determined with sufficient accuracy.

C.1.3 INTERFEROMETRIC SYNTHETIC APERTURE RADAR (INSAR)

As noted above, each resolution element encodes the phase related to the propagation distance from the radar to the ground as well as the intrinsic phase of the backscattering process. The resolution element comprises an arrangement of scatterers – trees, buildings, people, etc. – that is spatially random from element to element and leads to a spatially random pattern of backscatter phase in an image. As such, since we can only measure the phase in an image within one cycle (i.e., we do not measure the absolute phase), it is not possible to observe the deterministic propagation component directly.

Interferometric synthetic aperture radar (InSAR) (Rosen et al., 2000; Hanssen, 2001) techniques use two or more SAR images over the same region to obtain surface topography or surface motion. In this section, we explain how an InSAR phase measurement relates to actual ground deformation (see Massonnet et al., 1993; a tutorial summary is found in Chen, 2014a).

Figure C-2 illustrates InSAR imaging geometry. At time t_1, a radar satellite emits a pulse at S_1, then receives an echo reflected from a ground pixel, A, and measures the phase ϕ_1 of the received echo. All scatterers within the associated ground resolution element contribute to ϕ_1. As a result, the phase ϕ_1 is a statistical quantity that is uniformly distributed over interval $(0, 2\pi)$ so that we cannot directly use ϕ_1 to infer the distance r_1 between S_1 and A. Later at time t_2, the satellite emits another pulse at S_2 and makes a phase measurement ϕ_2. If the scattering property of the ground resolution element has not changed since t_1, all scatterers within the resolution element contribute to ϕ_2 the same way as they contribute to ϕ_1. Under the assumption that $|r_1 - r_2| << |r_1|$ (the parallel-ray approximation), the phase difference between ϕ_1 and ϕ_2 can be used to infer the topographic height z of the pixel A (Hanssen, 2001, Section 3.2).

If we know the topographic height z, we can further measure any small ground deformation occurring at pixel A between t_1 and t_2. Figure C-3 illustrates the InSAR imaging geometry in this case. At time t_1, a radar satellite measures the phase ϕ_1 between the satellite and a ground pixel A along the LOS direction. Later at time t_2, the ground pixel A moves to A' and the satellite makes another phase measurement ϕ_2 between the satellite and the ground pixel,

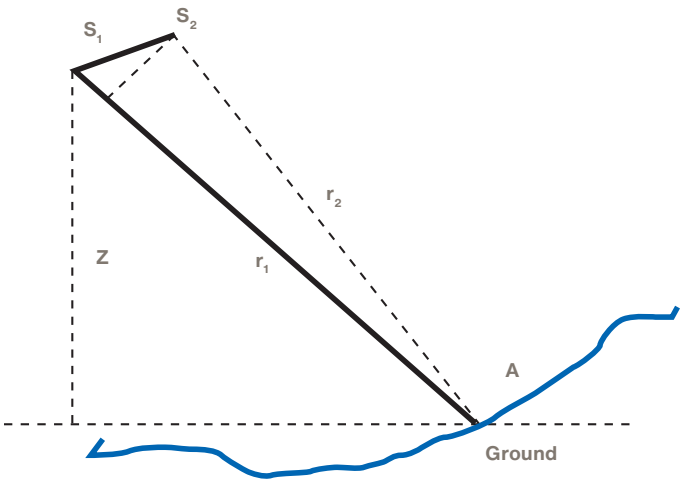

FIGURE C-2

Illustration of InSAR imaging geometry. The distance between the satellite at S_1 and a ground pixel A is r_1 and the distance between the satellite at S_2 and the ground pixel A is r_2. The topographic height of the pixel A is z. Here we assume $|r_1 - r_2| << |r_1|$ (the parallel-ray approximation) and no ground deformation occurs at pixel A between the two SAR data acquisition times.

Chen (2014b). After removing the known phase ϕ' due to the surface topography, the unwrapped (module 2π) InSAR phase $\Delta\phi = \phi_2 - \phi_1 - \phi'$ is proportional to the ground deformation Δd between t_1 and t_2 along the satellite LOS ground direction as

$$\Delta\varphi = \varphi_2 - \varphi_1 - \varphi' = \frac{4\pi\Delta d}{\lambda} \quad \text{C.1-1}$$

where λ is the radar wavelength. In this equation, we assume that there is no error in the InSAR phase measurement. Below we discuss in depth various error sources in InSAR deformation measurements and their impact on InSAR image quality.

Note that InSAR techniques only measure one-dimensional LOS motion. However, deformation is better characterized in three dimensions: east, north, and up. Given an LOS direction unit vector $e = [e_1, e_2, e_3]$, we can project the deformation in east, north, and up coordinates along the LOS direction as:

$$\Delta d = e_1\Delta d_{\text{east}} + e_2\Delta d_{\text{north}} + e_3\Delta d_{\text{up}} \quad \text{C.1-2}$$

Because radar satellites are usually polar orbiting, the north component of the LOS unit vector e_2 is often negligible relative to the east and vertical components. When InSAR measurements along two or more LOS directions are available, we can combine multiple LOS deformation measurements over the same region to separate the east and vertical ground motions, given that the term $e_2\,\Delta d_{\text{north}}$ is negligible.

For this mission, interferometric observations of any given point on the ground are acquired every 12 days. Ground motion can be measured for a gradually changing surface that is not disrupted between images.

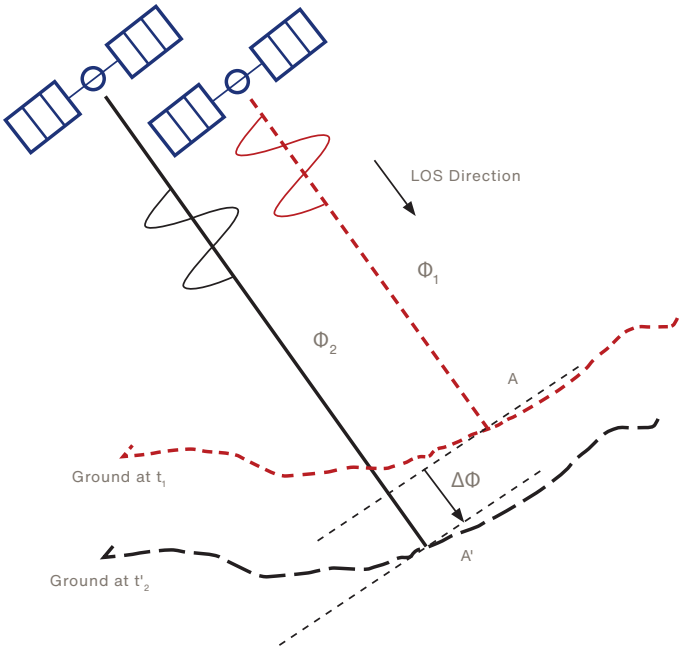

FIGURE C-3

InSAR deformation geometry. At time t_1, a ground pixel of interest is at point A and a radar satellite measures the phase ϕ_1 between the satellite and the ground pixel along the LOS direction. Later at time t_2, the ground pixel moves to A′ and the satellite makes another measurement ϕ_2 between the satellite and the ground pixel. The phase difference Δϕ is proportional to the ground deformation between t_1 and t_2 along the LOS direction.

C.2 DEFORMATION-RELATED TERMINOLOGY

The Earth's crust and cryosphere deform due to different forces acting on them. Deformation may be linear, episodic, or transient.

C.2.1 DEFORMATION AND DISPLACEMENT

In general, the term deformation refers to the change in shape of a solid or quasi-solid object. In the context of this mission, surface deformation refers to the change in shape as observed on the Earth's free surface, i.e., the interface separating the atmosphere from the uppermost layer of solid Earth, whether rock, soil, ice, or a combination thereof.

Displacement **u** is a vector quantity defined as the change in a particle's position **X** between one instant in time (epoch) t_1 and a later epoch t_2, such that $\mathbf{u} = \mathbf{X}(t_2) - \mathbf{X}(t_1)$. Typically, displacement is calculated with respect to the particle's initial, fixed position $\mathbf{X}(t_0)$ at some reference time t_0.

The *change in range* Δρ is a scalar quantity equal to the change in the (1-way) distance from the radar sensor to the target pixel on the ground. Range change is a particular component of the displacement vector. To calculate the range change, we project the displacement vector **u** onto the line of sight using the scalar ("dot") product such that $\Delta\rho = -\mathbf{u} \bullet \mathbf{s}$, where **s** is a unit vector pointing from the target on the ground toward the radar sensor in orbit. If the target moves toward the sensor, then the distance between them decreases and the range decreases such that $\Delta\rho < 0$.

Line-of-sight (LOS) displacement u_{LOS} is a scalar quantity that is equal in absolute value to the range change Δρ. Most, but not all, authors reckon upward motion of the target (toward the sensor) to be a positive value of LOS displacement, such that $u_{LOS} > 0$.

Velocity **v** is a vector quantity defined as the derivative of displacement with respect to time t such that $\mathbf{v} = d\mathbf{u}/dt$. In

discussing velocity fields, it is important to define the reference frame. The relative velocity of a particle j with respect to particle i is $\mathbf{v}_{j,i} = \mathbf{v}_j - \mathbf{v}_i$. A so-called absolute velocity is taken with respect to a fixed origin located at position $\mathbf{X}_0$ that is assumed to be stationary, such that $\mathbf{v}_0 = \mathbf{0}$.

To quantify deformation using radar, the mission offers at least two approaches:

1. Degrees or cycles. One fringe in an interferogram corresponds to one cycle (2π radians) of phase change or half a wavelength in range change. Phase is ambiguous because it is defined as an angle on the unit circle such that $-\pi \leq \Delta\phi \leq \pi$. Since the phase change is known only to within an integer number of cycles (i.e., modulo 2π), it is called "wrapped." Converting ambiguous, wrapped phase change $\Delta\phi$ in radians to range change $\Delta\rho$ in millimeters requires unwrapping algorithms (e.g., Chen and Zebker, 2002; Hooper and Zebker, 2007).
2. The techniques called speckle tracking and feature tracking estimate the shift of an image patch relative to its neighbors by cross-correlating the amplitudes or complex values of two images covering the same location at two different times (e.g., Vesecky et al., 1988). To do so, the technique generates "normalized cross-correlation" of image patches of complex or detected real-valued SAR images. The location of the peak of the two-dimensional cross-correlation function yields the image offset (displacement).

The successful estimation of the local image offsets depends on having correlated speckle patterns (speckle tracking) and/or the presence of nearly identical features (feature tracking) in the two SAR images at the scale of the employed patches. If speckle correlation is retained and/or there are well-defined features, the tracking with image patches of tens to hundreds of meters in size can be performed to a tenth-of-a-pixel or better accuracy with improved accuracy at the expense of resolution by averaging adjacent estimates (Gray et al., 1998; Michel and Rignot, 1999; Strozzi et al., 2008). The result yields two horizontal components of the displacement vector. Of these, the component that is parallel to the ground track of the satellite is also called an azimuth offset. The other effectively measures the same range displacement as the interferometric phase, albeit with more noise and poorer resolution. Where available, the less noisy phase data can be combined with the azimuth offsets to produce a less noisy vector estimate of displacement (Joughin, 2002).

C.2.2 STRAIN, GRADIENTS, AND ROTATION

For a one-dimensional element, the strain ε is expressed as the dimensionless ratio of its change length ΔL to its original length L, such that $\varepsilon = \Delta L/L$. If one end of the element is held fixed, then the change in length is equal to the displacement of the other end, such that $\Delta L = u$. For small strains, we can think of the strain as the gradient of the displacement, i.e., the partial derivative of displacement u with respect to the position coordinate x. Generalizing to three dimensions yields a second-order tensor called the deformation gradient tensor $F_{ij} = \partial_{ui} / \partial_{xj}$ (Malvern, 1969). The deformation tensor can be decomposed into a symmetric part, called the strain tensor, and an anti-symmetric part called a rotation or spin. The temporal derivatives of these quantities are called the velocity gradient tensor L_{ij}, the strain rate tensor E_{ij}, and the spin rate tensor Ω_{ij}, respectively (Malvern, 1969).

SAR interferometry is especially sensitive to gradients of the displacement field. For example, if a rock outcrop 10 meters in width stretches by 10 mm, then the strain will be $\varepsilon = 0.001$. Similarly, if the same outcrop tilts by 10 mm (about a horizontal axis) or spins (about a vertical axis), then the angle of rotation will be approximately 1 milliradian. Such behavior was observed in interferograms of the deformation field produced by the Landers earthquake in California (Peltzer et al., 1994).

To quantify the deformation gradient tensor F_{ij}, we can differentiate the wrapped phase in an interferogram to find the range gradient ψ. Following Sandwell and Price (1996), Ali and Feigl (2012) take the discrete derivative of range change $\Delta\rho$ with respect to a horizontal coordinate in position X to define the observable quantity for the k^{th} pixel as:

$$\Psi^k = \frac{\Delta\rho^{(k+1)} - \Delta\rho^{(k-1)}}{X^{(k+1)} - X^{(k-1)}} \qquad \text{C.2-1}$$

For example, a difference of 0.1 cycles in phase or 2.8 mm in range change over the 100 m distance between adjacent pixels in a C-band interferogram corresponds to a range gradient of $\psi \sim 2.8 \times 10^{-5}$. While range change is one component of the displacement vector (measured in millimeters), its (dimensionless) gradient is one component of the "deformation gradient" tensor F_{ij} (Malvern, 1969). Unlike wrapped phase change, the range change gradient is continuous and differentiable (Sandwell and Price, 1996), offering a number of advantages for streamlining data analysis.

C.2.3 STRESS AND RHEOLOGY

Stress is the force applied to a body per unit area. It also can imply the resistance a solid body offers to an applied force. In

mechanics, constitutive relationships describe how stress and strain depend on each other. The study of constitutive relationships and the relevant material properties is called rheology. For example, during an earthquake, Earth's crust deforms with an elastic rheology according to Hooke's Law. Understanding Earth's rheology is one of the primary goals of the mission.

C.3 ECOSYSTEMS-RELATED TERMINOLOGY

NISAR addresses the amount of living material in ecosystems as well as the disturbance and recovery of ecosystems.

C.3.1 BIOMASS

Biomass is defined as the total mass of living matter within a given unit of environmental area, usually measured as mass or mass per unit area of dry weight. Biomass is a fundamental parameter characterizing the spatial distribution of carbon in the biosphere. It is related to forest structure and hence also important for modeling animal habitats and tracking biodiversity. The NISAR mission will focus on the above-ground biomass of woody plants and forests, comprising about 80% of terrestrial total biomass in vegetation (Houghton, 2005a; Cairns et al., 1997). Half of all biomass in woody vegetation is carbon equivalent to approximately 3.67 units of CO_2 that directly links biomass to the terrestrial carbon cycle and climate change (Penman et al., 2003).

C.3.2 DISTURBANCE

Disturbance is defined as a discrete event that involves the removal of biomass, mortality, or change in the structure and is considered the major agent in determining the heterogeneity of forest ecosystems across a broad range of scales in space and time. Forest disturbance can be abrupt (e.g., hurricanes) or chronic (e.g., acid rain); stand-replacing (e.g., clear-cut logging) or not (e.g., selective logging); complete (e.g., landslides) or incomplete (e.g., insect defoliation); natural (e.g., tornados) or anthropogenic (e.g., land conversion); widespread (e.g., fire) or geographically restricted (e.g., avalanches); temporary (e.g., blow downs) or permanent (deforestation and land use conversion) (Frolking et al., 2009; Chambers et al., 2013). We focus on disturbances as abrupt events that cause changes in forest biomass and are at the scale detectable by spaceborne remote sensing (> 100 m). Disturbance is measured as the area and/or the intensity of biomass changes in units of area/year or mass/area/year.

C.3.3 RECOVERY

Recovery of forests and woody vegetation refers to the reestablishment or redevelopment of above ground biomass and structure characteristics after the impact of a particular disturbance. The nature and rate of recovery depend on the size and severity of disturbance and the pre-disturbance state of the ecosystem (Frokling et al., 2009; Chazdon et al., 2001). Recovery can follow a prescribed trajectory to meet certain production goals in managed ecosystems and/or a natural trajectory depending on environmental conditions in the case of unmanaged ecosystems. We focus on recovery as a process or trajectory defined by the area of the post-disturbance growth of biomass at scales of disturbance (> 100 m) and measured in the units of area/year or mass/area/year.

C.3.4 INUNDATION

Inundation is defined as vegetated or non-vegetated areas that are flooded seasonally by freshwater or tidal water, whether shallow or deep. Inland waters (rivers, lakes, reservoirs) within about 100m of the shoreline are thus included in the definition. Offshore areas (coral reefs, seagrass beds) are not included. Wetlands characterized by saturated soil with the water table below ground level are not included except as inclusions within inundated wetlands, e.g., higher points of microtopography. The 12-day repeat orbit observing cadence of NISAR will create a time history of flooding and inundation that will be useful for the mapping of plant and animal habitats as well as providing a means for understanding its impact on the environment.

C.3.5 CLASSIFICATION

In the remote sensing of the Earth's land surfaces, classification refers to the process of differentiating between different landcover types. For example, this can involve binary distinctions of disturbed vs. not disturbed, inundated vs. not inundated, or actively managed vs. unmanaged lands. More nuanced types of landcover classification can create multiple categories to determine plant species, degrees of flooding, or even crop types. For the purpose of mission planning, many of the types of classification that are implemented as part of the mission science requirements are kept relatively simple so that errors can be predicted and tracked based on the instrument characteristics, observing strategy, and confounding sources that can cause the natural world to defy categorization. In the case of NISAR Ecosystems, the basic classification tasks are related to the detection of biomass, disturbance (e.g., deforestation, degradation), inundation status (inundated wetlands), and active crop area. During NISAR's post-launch period, it is expected that the larger user community will be innovative in using its time series and consistent coverage to develop new algorithms for exploring this rich dataset (e.g., Whelen and Siqueira, 2018).

Credit: demamiel/Shutterstock.

APPENDIX D:
BASELINE LEVEL 2 REQUIREMENTS

The Level 1 requirements (Table 3-1) capture the essential elements of the measurements by discipline and expand to greater detail at Level 2. The baseline L2 requirements capture the specific measurements that will be validated by research area and product type. The following sections list the baseline L2 requirements by discipline. Figure D-1 shows the high-level mapping from L1 to L2. The colors codify the relationships at Levels 1 and 2. The tabs on the corners of the requirements boxes indicate the radar technique used to make the measurements. It should be clear that there are a limited number of techniques used to support a multiplicity of requirements, which should help reduce the amount of validation required.

D.1 LEVEL 2 SOLID EARTH

Table D-1 itemizes the solid Earth L2 requirements, which comprise interseismic, coseismic, and post-seismic deformation, and a set of additional deforming sites on land that include volcanoes, landslide-prone areas, aquifers, permafrost, and areas of increasing relevance such as hydrocarbon reservoirs and sequestration sites.

The requirements for deformation are specified in terms of accuracy over relevant relative length scales, and at a particular resolution, and vary depending on the style of deformation and its expected temporal variability. For instance, interseismic deformation is specified in terms of a relative velocity over a given length

FIGURE D-1

High-level mapping from L1 to L2 requirements by discipline.

TABLE D-1. LEVEL 2 REQUIREMENTS FOR SOLID EARTH

Attribute	Secular Deformation (658)	Coseismic Deformation (660)	Transient Deformation (663)	Permafrost Deformation (671)
Measurement	Spatially averaged relative velocities in two dimensions	Point-to-point relative displacements in two dimensions	Point-to-point relative displacements in two dimensions	Point-to-point relative displacements in two dimensions
Method	Interferometry, speckle tracking	Interferometry, speckle tracking	Interferometry, speckle tracking	Interferometry
Duration	3 years	3 years	Episodic over mission, depending on science target	3 years
Product Resolution	100 m; smoothed according to distance scale L	100 m	100 m	100 m
Accuracy	2 mm/yr or better, 0.1 km < L < 50 km, over > 70% of coverage areas	4 (1+ $L^{1/2}$) mm or better, 0.1 km < L < 50 km, over > 70% of coverage areas (L in km)	3 (1+$L^{1/2}$) mm or better, 0.1 km < L < 50 km, over > 70% of ~ 2,000 targeted sites	4 (1+$L^{1/2}$) mm or better, 0.1 km < L < 50 km at 80% of selected regions
Sampling	One estimate over 3 years, two directions	4 times per year to guarantee capture of any earthquake on land before surface changes too greatly	Every 12 days, two directions	Every 12 days in snow-free months
Coverage	Land areas predicated to move faster than 1 mm/yr	All land, as earthquake locations are known a priori	Post-seismic events, volcanoes, ground-water, gas, hydrocarbon reservoirs, landslide-prone	Targeted permafrost tundra landscapes in northern Alaska
Response Latency	N/A	24-hour tasking, 5-hour data delivery (24/5). Best effort basis on event	24/5. Best effort basis on event	N/A

scale. Interseismic deformation is slow, on the order of cm/yr. To adequately model this deformation, accuracies far better, on the order of mm/yr, are required. To achieve good accuracy, often many measurements are needed over time to reduce noise via averaging. Coseismic deformation is extremely rapid, on the order of seconds, with postseismic deformation occurring thereafter, and generally larger in magnitude, so frequent, less accurate measurements preceding and soon after the event are needed.

Resolutions vary depending on science focus. Interseismic deformation is generally broad except at aseismically creeping faults, so low resolution is adequate. For deformation associated with earthquakes, volcanoes, permafrost subsidence, and landslides, the spatial patterns of deformation are finer, so finer resolution is required. The coseismic deformation requirement for large earthquakes specifies the entire land surface. Unlike the interseismic and targeted requirements, this requirement ensures that there will be observations sufficient to capture events outside of the areas that are known to be deforming rapidly.

The validation requirement is included to specify that the validation program is limited in scope to fixed areas, employing analysis to extrapolate performance to the globe.

D.2 LEVEL 2 CRYOSPHERE

Table D-2 identifies the cryosphere L2 requirements. These requirements have a very similar form to the solid Earth requirements, as they too map to geodetic imaging methods. Ice sheets and glaciers move quickly, so the faster the sampling rate

TABLE D-2. LEVEL 2 BASELINE REQUIREMENTS FOR CRYOSPHERE

Attribute	Ice Sheets & Glaciers Velocity Slow Deformation (667)	Ice Sheets & Glaciers Velocity Fast Deformation (668)	Ice Sheet Time-Varying Velocity (738)
Measurement	Point-to-point displacements in two dimensions	Point-to-point displacements in two dimensions	Point-to-point displacements in two dimensions
Method	Interferometry, speckle tracking	Interferometry, speckle tracking	Interferometry, speckle tracking
Duration	3 years	3 years	3 years
Product Resolution	100 m	250 m	500 m
Accuracy	3% of the horizontal velocity magnitude plus 1m/yr or better, over > 90% of coverage areas	3% of the horizontal velocity magnitude plus 5 m/yr or better, over > 90% of coverage areas	3% of the horizontal velocity magnitude plus 10 m/yr or better, over > 80% of coverage areas
Sampling	Each cold season, two directions	Each cold season, two directions	Each 12 days, two directions
Coverage	Areas moving slower than 50 m/yr of both poles and glaciers and ice caps	Areas moving slower than 50 m/yr of both poles	Outlet glaciers, or other areas of seasonal change
Response Latency	N/A	N/A	24/5. Best effort basis on event
Attribute	**Permafrost Displacement (671)**	**Grounding Line Vertical Displacement (445)**	**Sea Ice Velocity (670)**
Measurement	Spatially averaged in two dimensions	Point-to-point displacements in two dimensions	Point-to-point relative horizontal displacements
Method	Interferometry	Interferometry, speckle tracking	Backscatter image feature tracking
Duration	3 years	3 years	3 years
Product Resolution	100 m	100 m	Gridded at 5 km
Accuracy	$4*(1+L^{1/2})$ mm or better, over length scales 0.1 km < L < 50 km, > 80% of coverage areas	100 mm or better, over 95% of coverage areas annually, over 50% of coverage areas monthly	100 m/day, over 70% of coverage area
Sampling	In snow-free months sufficient to meet accuracy (semi-monthly)	Monthly	Every 3 days
Coverage	Targeted priority regions in Alaska and Canada	Greenland and Antarctic coastal zones	Seasonally-adjusted Arctic and Antarctic sea ice cover
Response Latency	N/A	24 hour tasking, 5 hour data delivery. Best effort on event	24/5. Best effort basis on event

for measurements, the greater the coverage of dynamic processes and the more interesting the science. Sea-ice moves even faster. Thus, the cryosphere L2 requirements are explicit in terms of the required sampling as well as regionally differentiated velocity accuracy and resolution requirements.

The permafrost requirement is explicitly a deformation requirement similar to the solid Earth requirement. It will be considered one of the targeted sites in the solid Earth L2 requirements but is included here to call out the explicit cryosphere focus. The validation requirement is included to specify that the validation program is limited in scope to fixed areas, employing analysis to extrapolate performance to the globe.

D.3 LEVEL 2 ECOSYSTEMS

Table D-3 identifies the ecosystems L2 requirements. These are parallel but give greater specificity to the L1 requirements. The

TABLE D-3. LEVEL 2 BASELINE REQUIREMENTS FOR ECOSYSTEMS

Attribute	Biomass (673)	Disturbance (675)	Inundation (677)	Crop Area (679)
Measurement	Biomass	Areal extent	Areal extent	Areal extent
Method	Polarimetric backscatter to biomass	Polarimetric backscatter temporal change	Polarimetric backscatter contrast	Polarimetric backscatter contrast and temporal change
Duration	3 years	3 years	3 years	3 years
Product Resolution	100 m	100 m	100 m	100 m
Accuracy	20 Mg/ha or better where biomass is < 100 Mg/ha, over 80% of coverage areas	80% or better classification accuracy where canopy cover changes by >50%	80% or better classification accuracy	80% or better classification accuracy
Sampling	Annual	Annual	Seasonal, sampled every 12 days to track beginning and end of flooding events	Quarterly; sampled every 12 days to track beginning and end of growing season
Coverage	Global areas of woody biomass	Global areas of woody biomass	Global inland and coastal wetlands	Global agricultural areas
Response Latency	N/A	24/5. Best effort basis on event	24/5. Best effort basis on event	N/A

woody biomass accuracy requirement is the same at Levels 1 and 2. In addition, the details of the requirement for classification are spelled out. While biomass is required to meet its accuracy requirements only where biomass is below 100 Mg/ha, the classification accuracy must be met for all biomass. The key implication of this is that the observing strategy must include sufficient global observations of biomass to enable this classification.

The requirements related to wetlands, areas of inundation and agriculture are "globally distributed", implying regional measurements, as specified in the science implementation plan target suite.

In addition to the requirements, the ecosystems subgroup has identified the goals of determining the ability of NISAR to 1) estimate vertical canopy structure, and 2) measure change in water level in vegetated environments. Current research in polarimetric interferometry shows that when temporal decorrelation is small and the interferometric baselines are large (but not too large), it is possible to retrieve canopy structure from the data. As a repeat-pass interferometer designed for two disciplines to have small baselines, NISAR is not ideally suited to this technique. However, the dense interferometric time series may lead to new innovations that allow structure estimates of value, and the team expects to explore these possibilities. It has also been shown that water level changes can be measured with some accuracy in the presence of double bounce radar reflections involving emergent vegetation from surface water (Alsdorf et al., 2000).

The validation requirement is included to specify that the validation program is limited in scope to fixed areas, employing analysis to extrapolate performance to the globe.

D.4 LEVEL 2 URGENT RESPONSE

There is no urgent response L2 science requirement. While the mission envisioned by the community – one with relatively fast revisit and a capacity for acquiring data over the globe – can serve an operational need for reliable, all-weather, day/night imaging in the event of a disaster, the project has been sensitive to the costs associated with operational systems that must deliver such data. However, demonstrating the utility of such data for urgent response for the benefit of society is important and in keeping with the recommendations of the 2007 Decadal Survey. To that end, the NISAR L1 urgent response requirement has been written with a focus on targeting and delivery latency, as previously described. The L1 urgent response requirement flows to other L2 mission requirements, but not to science directly.

U.S. Geological Survey scientists Randy Jibson and Jon Godt investigate the Seaside landslide that was triggered by the 2016 magnitude 7.8 Kaikoura, New Zealand, earthquake, along a fault that experienced significant surface offsets. Credit: USGS/Kate Allstadt.

Credit: USGS/Kate Allstadt

APPENDIX E:
NISAR SCIENCE FOCUS AREAS

This appendix provides additional background and rationale for the science objectives to be addressed by NISAR. Each section describes the 2007 Decadal Survey objectives that guided the development of the requirements for NISAR in each major science focus area, amplifying their importance through examples in the literature that were generated from existing data – something that can only loosely approximate the richness of the results that will be derived from NISAR's dense spatial and temporal data set.

E.1 SOLID EARTH

The 2007 Decadal Survey identified the following overarching science goals and related questions for solid Earth:

- Determine the likelihood of earthquakes, volcanic eruptions, landslides, and land subsidence. How can observations of surface deformation phenomena lead to more complete process models for earthquakes, volcanoes, landslides, and land subsidence and better hazard mitigation strategies?
- Understand the behavior of subsurface reservoirs.
- Observe secular and local surface deformation on active faults to model earthquakes and earthquake potential.
- Catalog and model aseismic deformation in regions of high hazard risk.
- Observe volcanic deformation to model the volcano interior and forecast eruptions.
- Map pyroclastic and lahar flows on erupting volcanoes to estimate damage and model potential future risk.
- Map fine-scale potential and extant landslides to assess and model hazard risk.
- Characterize aquifer physical and mechanical properties affecting groundwater flow, storage, and management.
- Map and model subsurface reservoirs for efficient hydrocarbon extraction and CO2 sequestration.
- Determine the changes in the near surface stress field and geometry of active fault systems over major seismically active regions in India.
- Determine land subsidence rates of major reported land subsidence areas (due to mining and/or groundwater induced) in India.
- Map major landslide-prone areas in the hilly regions of India.

These objectives require dense spatial coverage of Earth and dense temporal sampling to measure, characterize, and understand these often unpredictable and dynamic phenomena.

In situ GNSS arrays constrain the large–scale motions of Earth's surface where the arrays exist. In particular, these GNSS data can provide temporally continuous point observations that are best exploited when combined with the spatially continuous coverage provided by the InSAR imaging that NISAR will provide.

With NISAR, scientists will be able to comprehensively generate time series of Earth's deforming regions. When combined with other sources of geodetic imaging – optical satellite

imagery when daytime, cloud-free observations are available and when expected ground displacements are large; international SAR imagery when data are available and of suitable quality – an even more complete picture of Earth's 3-D motions can be constructed.

E.1.1 EARTHQUAKES AND SEISMIC HAZARDS

NISAR data will address several aspects of earthquake physics and seismic hazards, providing the ability to:

1. Determine crustal strains across the different phases of the seismic cycle. Because Earth's upper crust is elastic, interseismic deformation rates can be mapped to stressing rates, which in turn are used to guide assessments of future earthquake occurrence.
2. Derive physics-based models of faulting and crustal rheology consistent with multi-component displacement maps across all phases of the seismic cycle, complementing conventional land-based seismological and geodetic measurements. Estimates of rheological parameters are essential to understanding the transfer of stress within fault systems.
3. Assimilate vector maps of surface deformations through various stages of the earthquake cycle in large-scale simulations of interacting fault systems, currently a "data starved" discipline.

THE EARTHQUAKE CYCLE

Deformation of Earth's crust in tectonically active regions occurs on a rich variety of spatial and temporal scales. To date, the best temporal sampling is obtained from continuously operating GNSS sites. Figure E-1 shows the evolution of displacements at the GNSS site Carr Hill (CARH), near Parkfield, CA. The Mw 6.6 San Simeon earthquake of December 22, 2003, corresponds to the first discrete jump, and the Mw 6.0 Parkfield earthquake of September 27, 2004, corresponds to the discrete jump midway through the time series. The average secular motion (i.e., linear trend) has been subtracted from each component. These time series can be divided conceptually into three parts: (1) the interseismic part that occurs in the interval several years after the previous earthquake until just before the most recent earthquake; (2) the coseismic step at the time of the earthquake; and (3) the postseismic period, occurring in the days to years immediately following the earthquake, after which it merges continuously into the interseismic phase. Regions where elastic strain (i.e., the spatial gradient in displacements) is accumulating most rapidly (not shown in the figure) are those where earthquakes are most likely. Temporal changes in the elastic stressing rate such as occurred at CARH, are associated with temporal changes in the probability of earthquake occurrence.

Understanding coseismic fault slip magnitude and geometry, as well as regional local deformation signals such as triggered slip can lead to understanding of changes in surface deformation on nearby (and distant) faults. For example, CARH lurched about 15 mm to both the north and west at the time of the Mw 6.0 Parkfield earthquake. These detailed displacement measurements allow inference of the magnitude and sense of slip on the fault plane during the earthquake. Changes in deformation rates on distant faults are then

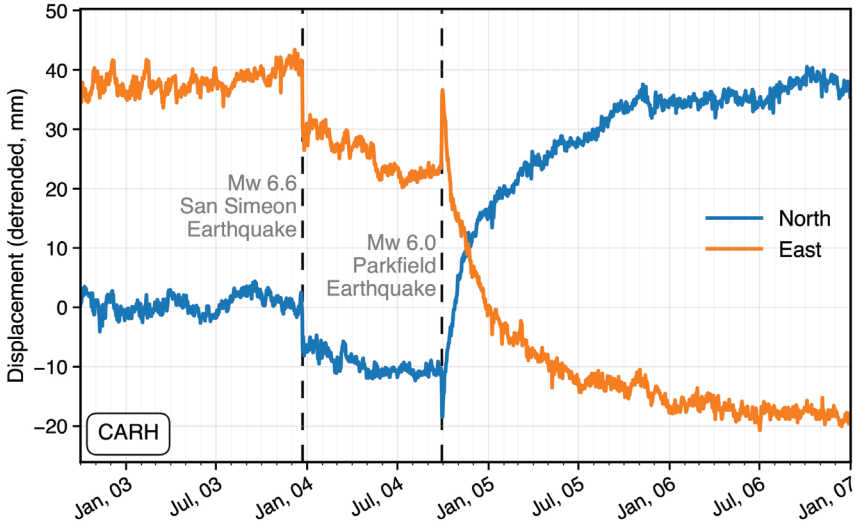

FIGURE E-1

Daily position time series at GNSS site CARH for north (blue) and east (orange) components, illustrating the coseismic offset and postseismic deformation associated with the Mw 6.6 San Simeon (December 22, 2003) and Mw 6.0 Parkfield (September 27, 2004) earthquakes (dashed lines). A linear trend has been subtracted from each component using the time period before December 2003. Data processed by University of Nevada Reno and retrieved August 27, 2025. (Figure courtesy of Yuan-Kai Liu).

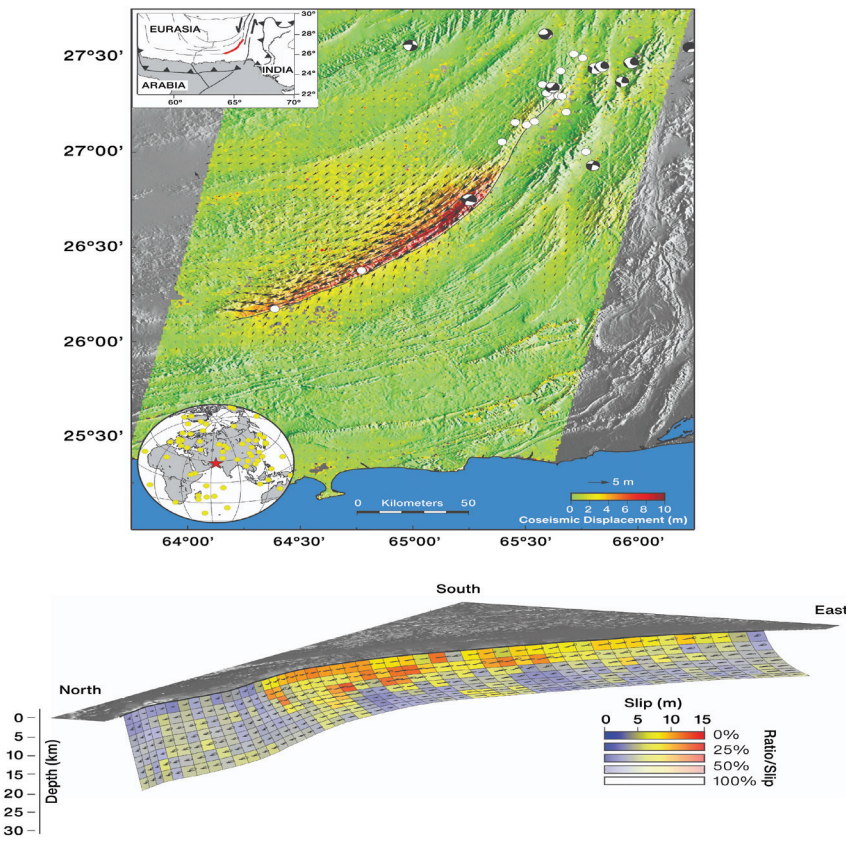

FIGURE E-2

(Top) Surface displacements and coseismic slip surface displacements for the 2013 Mw 7.7 Balochistan (Pakistan) earthquake derived from cross-correlation of Landsat 8 images (black arrows indicate the displacement direction and amplitude). (Below) Derived distribution of coseismic slip on the subsurface fault. The surface rupture of the fault, the first order subsurface geometry of the fault, and the distribution of slip are all derived using a combination of available optical and radar geodetic imaging data. Figure modified from Jolivet et al., 2014b.

monitored for evaluating any "linkages." Because of the sharp discontinuity in surface displacement and immediate postseismic deformation, a rapid repeat sampling strategy permits accurate determination of coseismic displacements, which can otherwise be obfuscated by postseismic deformation occurring between the time of the earthquake and the time of the first observation. The postseismic deformation field immediately following an earthquake can be significant, with decelerating surface displacements in the following week to months and possibly years for larger earthquakes. Such postseismic displacements as a function of time are frequently characterized by a logarithmic dependence on time consistent with a frictionally controlled fault slip process (as opposed to viscous processes). Within the time interval shown in Figure E-1, rates have not yet returned to those observed preceding the earthquake.

COSEISMIC DEFORMATION

Small earthquakes: NISAR will provide unique observations of ground displacement that will improve location accuracy of such events by an order of magnitude (e.g., Lohman et al., 2002; Lohman and Simons, 2005). Such improved locations can be used to enhance seismic tomographic models of Earth's interior structure by reducing the tradeoff between seismic wave velocities and source locations. Detailed understanding of the location and mechanism of small earthquakes is also essential to illuminate important faults. These earthquake parameters provide important ingredients when estimating the state of stress and changes in the state of stress in the crust, as well as indicators of the boundaries between creeping and non-creeping fault segments of a given fault.

Larger earthquakes: NISAR will provide maps of surface faulting complexity and will constrain first order geometric variability of the coseismic rupture at depth. Spatially continuous maps (combined with GNSS data when available) of surface displacements provide critical constraints on models of coseismic fault rupture for both small and large earthquakes. The geodetic imaging data of the kind that will be routinely provided by NISAR have already been shown to be crucial in estimating the distribution of coseismic slip on the subsurface fault and earthquake-induced changes in crustal stress. Elastic models of the lithosphere and geodetic data, combined with seismic data, reveal temporal evolution (i.e., kinematic models) of slip during an earthquake, which are in turn used to understand strong ground motions that impact the built environment. These kinematic models are among the few constraints we have on the underlying physics that shape our understanding of earthquake rupture mechanics. Such well-constrained coseismic earthquake source models are also routinely compared with inferences of earthquake magnitudes from geological field observations, providing a needed calibration of paleo-seismological inferences of historic earthquakes.

The fusion of multiple imagery sources illustrates the power of geodetic imaging (here a combination of radar and optical geodetic imaging) to constrain the complex curved surface trace of the 2013 Mw 7.7 Pakistan earthquake (Figure E-2). The geodetic data also require the dip of the fault to approximately 45 degrees from vertical, thereby documenting this event as the first example of a large strike slip event on a non-vertical fault – well outside the expectations from conventional faulting theory. Such "surprise" events that challenge conventional wisdom frequently occur outside the scope of existing ground-based geodetic networks and thus underscore the need for the global access provided by NISAR.

POSTSEISMIC DEFORMATION

Important constraints on fault behavior are also gleaned from comparisons of the distribution of coseismic fault slip with estimates of interseismic and postseismic fault slip. For instance, in Figure E-3, we see the spatially complementary distribution of coseismic and postseismic fault slip associated with the 2005 Mw 8.8 Nias earthquake, with little overlap between the two phases of fault slip. Future geodetic study will need to determine the extent to which such behavior is ubiquitous for large earthquakes and if so, raises the question of what controls seismogenic behavior. Only with data from many additional events will we be able to address this fundamental question.

Beyond seismic and postseismic fault slip, recent results document an exciting range of aseismic fault slip events (fault slip not associated with a preceding large earthquake) in both strike slip and thrust faulting environments. Such events have been documented in Mexico, Japan, Chile, the Pacific Northwest, Alaska, New Zealand, and Southern California. These events are sometimes quasi-periodic, they are frequently associated with increased seismic tremor, and remain enigmatic as to their origin. Of great interest is the extent to which such aseismic fault slip transients occur at different time scales (days, weeks, years) and the degree to which large seismic earthquakes are more or less likely in periods of these aseismic transient events. Thus far, the known events are limited to regions with pre-existing ground-based networks and we have no knowledge of the occurrence, or lack thereof, on most of the world's major faults. The global coverage, frequent repeats, and high-correlation

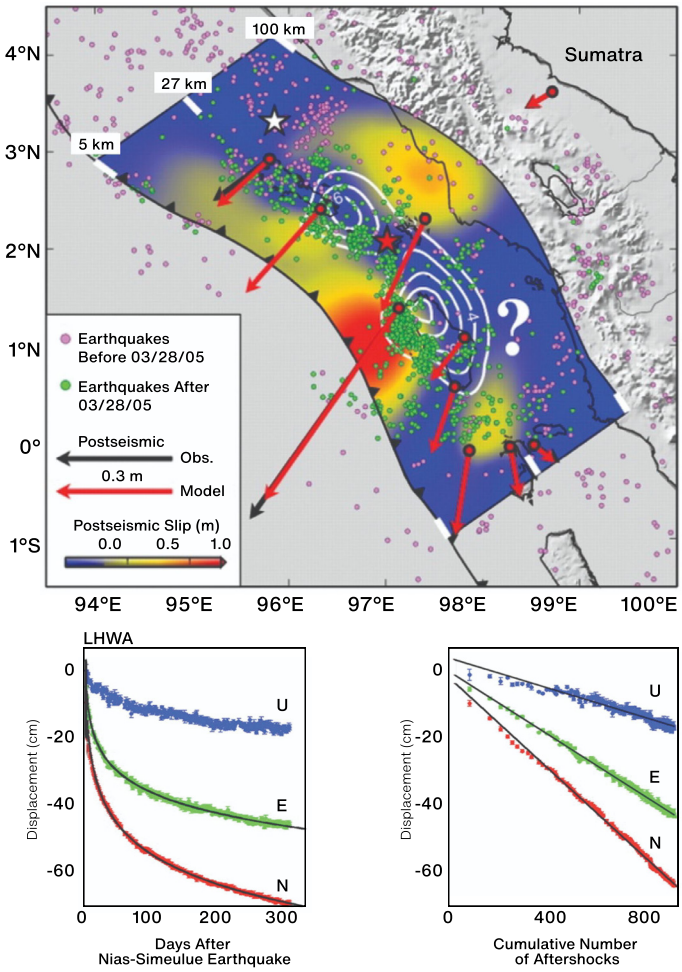

FIGURE E-3

Nias-Simeulue earthquake data. (Top) Coseismic (2-m interval white contours) and postseismic slip (color), from the 2005 Mw 8.8 aftershock of the 2004 Mw 9.1 Sumatra earthquake. Arrows indicate observed (black) and predicted (red) GNSS observations, stars show epicenters of 2004 (white) and 2005 (red) earthquakes. Dots denote earthquakes before (pink) and after (green) the 2005 event. (Bottom left) Observed and modeled postseismic displacements at one continuous GNSS site. Black solid lines are estimated from a 1D spring-slider model in which afterslip obeys a velocity-strengthening friction law. Data shown for vertical (U), east (E), and north (N) displacements. (Bottom right) The relationship between postseismic ground displacement and the cumulative number of regional aftershocks. Figure from Hsu et al (2006).

geodetic imaging provided by NISAR will enable a complete inventory of shallow aseismic fault slip and thereby allow us to begin to understand the underlying causes of these events.

Fault slip events result in a redistribution of stress in the crust and thus may be important in triggering seismic activity. Current research is elucidating the nature of earthquake-to-earthquake interactions, quantifying the statistical likelihood of linkages, and elucidating time-dependent processes (e.g., postseismic relaxation, state and rate of fault friction) that influence triggered activity. For instance, Figure E-3 compares the cumulative rate of aftershock production after the 2005 Mw 8.8 Nias earthquake with the rate of postseismic displacement observed at one of a few sparse GNSS sites. Note that seismicity represents only a few percent of the total slip required to explain the GNSS data. The observed behavior suggests that the temporal behavior of displacement and seismicity is nearly identical and that postseismic fault slip processes control the rate of earthquake production.

Existing observations of seismicity and fault slip also suggest longer-range interactions that are not fully understood. Such interactions should have detectable deformation signatures (Toda et al., 2011). Synoptic space-based imaging offers a new and promising means to identify deformation causes and effects linking regional earthquake events. Thus, NISAR will allow a systematic assessment of the relationship between seismicity and fault slip across the different phases of the seismic cycle.

Viewed from above, Earth's outer rock layers are divided into multiple tectonic plates. The slow movement of each plate results in concentrated zones of deformation in Earth's crust – zones that are frequently found at the boundaries between the plates and are the locus of large destructive seismic events on interacting systems of faults. The next leap in our understanding of earthquakes and our ability to minimize their associated hazards requires us to (1) detect regions that are undergoing slow elastic loading of seismogenic faults, (2) understand what controls the distribution of subsurface fault slip during individual large events, (3) quantify Earth's response to large earthquakes (essentially using these events as probes of the mechanical nature of faults and the surrounding crust), and (4) understand the role played by major earthquakes on changing the likelihood of future seismic events in neighboring regions.

Earthquakes are part of a cycle commonly divided into periods associated with elastic stress accumulation, release of elastic stress during an earthquake, and a period associated with rapid readjustment of the fault system and surrounding crust following a large tremor. In some faults, there are periods of very slow transient fault slip events that are so slow they do not cause significant ground shaking. Models currently used to understand the earthquake system explore the frictional properties of faults (which fault segments creep aseismically versus which segments fail in a stick-slip fashion) across all phases of the seismic cycle. These models also incorporate both elastic and inelastic behavior of the crust in which earthquake faults are embedded. The aim of these models is to rigorously simulate observations over short time scales (e.g., a single earthquake or a short period of time before and after an earthquake) in a way that is consistent with observations of longer time scale deformation as inferred from geology. There are many proposed models designed to explain existing observations of deformation in different phases of the earthquake cycle but we lack sufficient observations to test these reliably. The dedicated observing schedule of NISAR will increase the number, spatial coverage, temporal resolution, and accuracy of observations sufficiently to allow us to systematically test, reject, and/or constrain the competing models of earthquake forcing.

E.1.2 VOLCANO HAZARDS

Improving volcano hazard prediction requires determining the location, size, and composition

of magma reservoirs via geodetic, seismic, geochemical, and other observations. We must also identify the type of magmatic unrest associated with eruptions, characterize deformation prior to volcanic eruptions, and predict the type and size of impending eruptive events. High-quality geodetic observations are necessary in order to constrain timescales and mechanisms of these processes.

Volcanic hazard science flows from the same crustal deformation data used to study the seismic cycle. Deformation data allow us to:

1. Identify and monitor surface deformation at quiescent and active volcanoes: Only InSAR has the capability for monitoring virtually all of the world's potentially active volcanoes on land (approximately 1400 volcanoes).
2. Derive models of magma migration consistent with surface deformation preceding, accompanying, and following eruptions to constrain the nature of deformation sources (e.g., subsurface magma accumulation, hydrothermal-system depressurization resulting from cooling or volatile escape).
3. Monitor and characterize volcanic processes such as lava-dome growth and map the extent of eruptive products (lava and pyroclastic flows and ash deposits) from SAR backscattering and coherence imagery during an eruption, an important diagnostic of the eruption process. Similar methods can be used during or after an eruption to determine the locations of lahars or landslides.
4. Map localized deformation associated with volcanic flows that can persist for decades to understand physical property of volcanic flows, guide ground-based geodetic benchmarks, and help avoid misinterpretations caused by unrecognized deformation sources.

Deformation data are the primary observables in understanding the movement of magma within volcanoes. Although uplift from the ascent of magma into the shallow crust has been observed prior to some eruptions, particularly on basaltic shield volcanoes, the spatio-temporal character of such transient deformation is poorly known, especially at the locations of the largest explosive eruptions. Little is known about deformation on most of the world's volcanoes because only a small fraction of them are monitored. Even the incomplete surveys to date from previous satellites have discovered many newly active volcanoes (Pritchard and Simons, 2004; Fournier et al., 2010).

Detection and modeling of deformation can provide warning of impending eruptions that can reduce loss of life and mitigate impact on property. Even remote volcanoes are important to monitor as large eruptions can have a global impact through ash ejected into the stratosphere that can affect air travel (e.g., the billion-dollar impact of the 2010 Eyjafjallajokull, Iceland eruption) and climate (like the 1991 Mt. Pinatubo, Philippines eruption). In addition, InSAR data

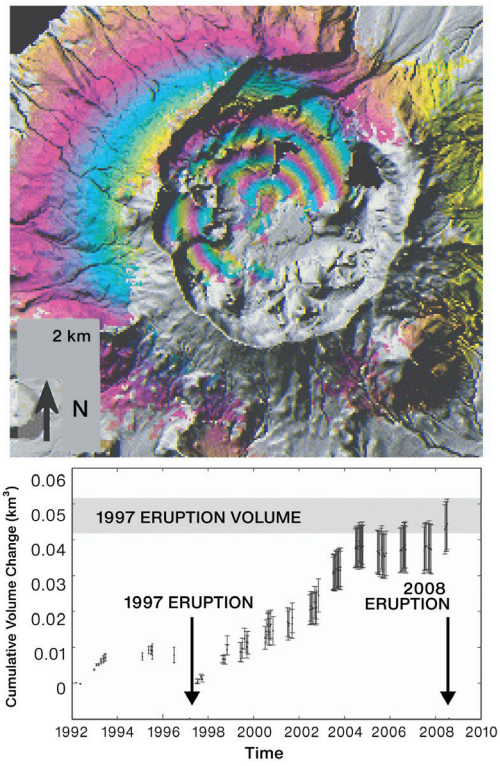

FIGURE E-4

Volcano monitoring. (Top) Average annual deformation of Mt. Okmok volcano in the Aleutian volcanic arc is related to inter-eruption magma movement from 1997 to 2008. Each fringe (full color cycle) represents 2.83-cm range change between the ground and satellite along the satellite line-of-sight direction. Areas that lack interferometric coherence are uncolored. (Bottom) Estimated volume of magma accumulation beneath Mt. Okmok as a function of time based on multi-temporal InSar (Lu et al., 2010). Error bars represent uncertainties. The shaded zone represents the source volume decrease associated with the 1997 eruption, as inferred from a co-eruption interferogram.

FIGURE E-5

High-resolution Cosmo-Skymed interferogram (top right) and backscatter SAR images (bottom) of Agung volcano, Bali, Indonesia of the 2017–2018 unrest and eruption. The interferogram shows about 15 cm of inflation within the summit crater that occurred prior to the eruptions of November 2017. The backscatter image of November 28 clearly shows the accumulation of new lava within the crater. Imagery from the Italian Space Agency (ASI) through the CEOS volcano pilot.

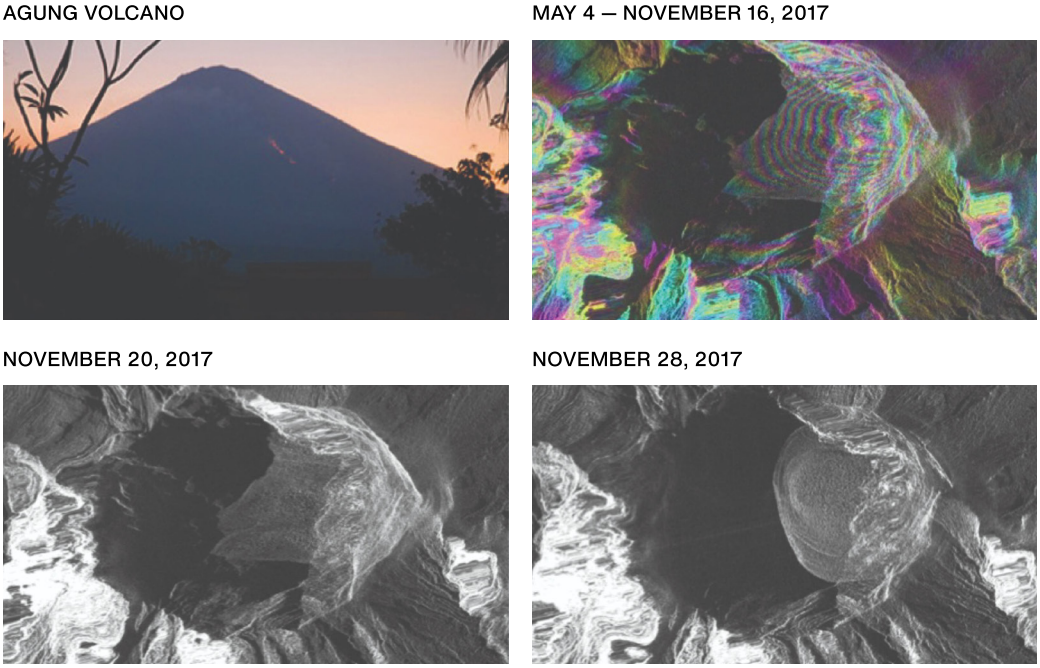

provide detailed spatial information not available from GNSS and other available geodetic data, allowing us to explore models to reveal complex geometries of intrusions and their interactions with regional crustal stress regimes. Furthermore, higher temporal resolution deformation imagery combined with other geophysical and geochemical observations will make it possible to advance volcano forecasting from empirical pattern recognition to one based on deterministic physical–chemical models of the underlying dynamics (Segall, 2013).

An example of the potential of frequent InSAR observations to monitor the temporal evolution of a volcano through an eruption cycle is illustrated (Figure E-4) by the work of Lu et al. (2010). Mt. Okmok in the Aleutian arc erupted during February–April 1997 and again during July–August 2008. The inter-eruption deformation interferograms suggest that Okmok began to reinflate soon after its 1997 eruption, but the inflation rate generally varied with time during 1997–2008. Modeling these interferograms suggests that a magma storage zone centered about 3.5 km beneath the center of the 10-km-diameter caldera floor was responsible for the observed deformation at Okmok. Multi-temporal InSAR deformation images can be used to track the accumulation of magma beneath Okmok as a function of time: the total volume of magma added to the shallow storage zone from the end of the 1997 eruption to a few days before the 2008 eruption was 85–100% of the amount that was extruded during the 1997 eruption. While the eruptive cycle from Okmok shows a pattern of deformation that may be diagnostic of impending eruption, only a fraction of the potentially active volcanoes have frequent enough observations from available GNSS or existing SAR satellites to detect such patterns. Furthermore, even from limited observations, it seems that other volcanoes show different and sometimes more complex patterns of deformation before eruption – in some cases, no deformation is observed before eruptions (Pritchard and Simons, 2004). The observations from NISAR will allow us to make dense time series observations at nearly all the world's subaerial volcanoes to better understand the relation between deformation and eruption.

Among the most important parameters needed to assess short-term volcanic hazards and better understand volcanic processes are the location,

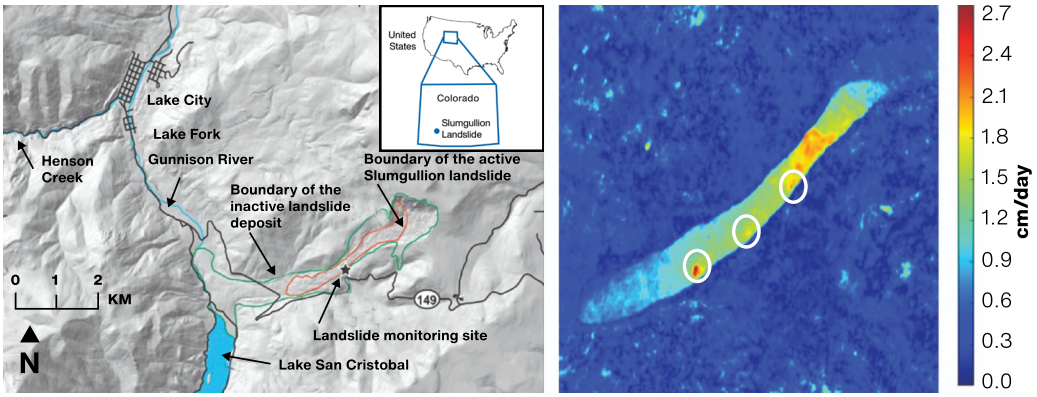

FIGURE E-6

Creeping Slumgullion landslide in southwestern Colorado (Left, at the Slumgullion Natural Laboratory). Figure on the right shows a velocity map derived from UAVSAR repeat pass observations separated by 7 days in April 2012.

volume, and composition of potentially eruptible magma (Figure E-5). Together with seismology, continuous ground deformation measurements (like GNSS), and gas geochemistry observations, the spatially dense, InSAR-derived deformation field can play a pivotal role in constraining these unknowns (Pritchard and Simons, 2002; Dzurisin, 2007; Lu and Dzurisin, 2014). InSAR data from past satellite missions have been characterized by comparatively poor coherence and temporal resolution, restricting the application of those data to simple kinematic models of magma storage and transport—especially location, geometry, and volume change. A better understanding of volcanic activity requires models that are based on the underlying physics of magma ascent and eruption. As input, such models require a variety of geochemical and geophysical data, including, critically, deformation measurements with improved spatial and temporal resolution. NISAR will provide 2-D vector deformation measurements at higher temporal resolution and better coherence than any past or present satellite InSAR sensor, making it possible to explore volcano models with complex source geometries in heterogeneous media. When combined with GNSS, seismic, gas emissions, and other measurements of volcanic activity, NISAR will facilitate the development of more realistic models that estimate, for example, absolute magma storage volume, reservoir overpressure, volatile concentrations, and other parameters. These results are critical for deterministic eruption foresting that can be updated as new data are acquired, which represents a fundamental advance over empirical forecasting that is based primarily on past experience—a common practice presently at most volcanoes worldwide (Segall, 2013).

E.1.3 LANDSLIDE HAZARDS

Landslides threaten property and life in many parts of the world. Steep slopes, rock types, and soil conditions are key underlying causes of landslides, which are typically (but not always) triggered by rainfall events, earthquakes, or thawing in arctic regions. Improved knowledge of surface composition and topography are important for characterizing landslide risk. Prediction of landslide movement is aided significantly by spatially and temporally detailed observations of downslope motion at the millimeter to centimeter level. Such observations, possible with InSAR measurements such as NISAR, can identify unstable areas. Similar to the Mt Okmok volcano, studies in areas that can be monitored with current InSAR-capable satellites have shown the potential for observations at critical times. One example is in the Berkeley Hills region in Northern California, where interferometric analysis reveals the timing, spatial distribution, and downslope motion on several landslides that had damaged homes and infrastructure (Hilley et al., 2004). A more active example, shown in Figure E-6, is the Slumgullion landslide in southwestern Colorado, which is moving at 1–3 cm per day, as determined using L-band UAVSAR observations.

IN ADDITION TO EARTHQUAKE ACTIVITY ASSOCIATED WITH THE PRODUCTION OF HYDROCARBONS, THERE IS NOW EVIDENCE THAT PRODUCTION OF WATER FROM AQUIFERS CAN TRIGGER EARTHQUAKES.

E.1.4 INDUCED SEISMICITY

Management of subsurface fluid reservoirs is an economically and environmentally important task. Obtaining observations to better manage subsurface reservoirs can have substantial benefits. In addition, the past decade has seen a substantial increase in the number of earthquakes triggered by both injection and production of subsurface fluids (Figure E-7), leading to a review by the National Research Council (2013). InSAR provides an important tool for understanding and managing the risks.

An early investigation into understanding the geomechanical response to hydrocarbon production and induced seismicity at a hydrocarbon field in Oman (Bourne et al., 2006) utilized InSAR. An oil field is overlain by a gas reservoir. InSAR and microseismic data were acquired to monitor the reservoirs' responses to changes in fluid pressure. The changes in stress associated with differential compaction resulted in fault reactivation. As hypothesized for tectonic earthquakes, there is a strong relationship between stressing rates and seismicity, with the rate of seismic activity proportional to both the rate of pressure change and the rate of surface deformation. Based on these observations, geomechanical models can be built to enable accurate prediction of the risk for well-bore failure due to fault reactivation.

Understanding the relationship between production of hydrocarbons and induced seismicity is a problem of tremendous economic importance. For example, the vast gas reservoir in Groningen province of the Netherlands provides almost 60 percent of the gas production in the Netherlands. A recent increase in earthquake activity associated with production at Groningen has caused great public concern, and in response, the Dutch government decided to cut the production cap for this reservoir in half in January 2014 (van Daalen, Wall Street Journal, 01/17/2014). The financial cost to the Dutch government in 2014 is 700 million euros ($783 million USD as of May 14, 2025). Observations such as those to be provided by NISAR will provide a comprehensive geodetic dataset that will inform such billion-dollar decisions.

FIGURE E-7

Cumulative number of earthquakes with a magnitude of 3.0 or larger in the central and eastern United States, 1970-2023. The long-term rate of approximately 29 earthquakes per year increased sharply starting around 2009. The increase has been attributed to induced seismicity. Oklahoma has decreased induced seismicity since 2016 but other areas have increased.

Source - https://en.wikipedia.org/wiki/Induced_seismicity#/media/File:Cumulative_induced_seismicity.png

This image is in the public domain in the United States because it only contains materials that originally came from the United States Geological Survey, an agency of the United States Department of the Interior. For more information, see the official USGS copyright policy.

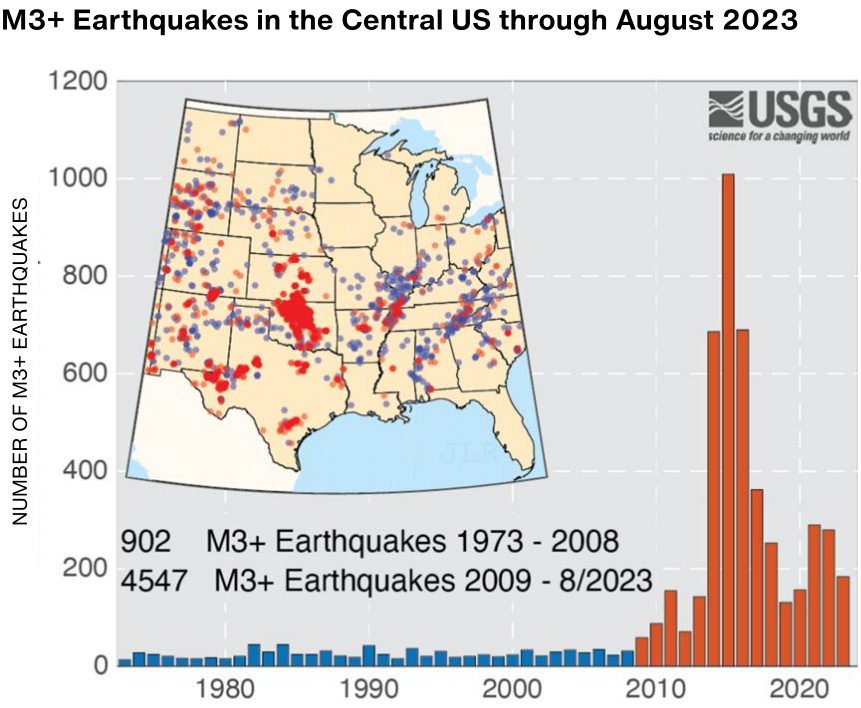

Research on the induced seismicity in Oklahoma and other areas in the central USA have shown that most of the induced earthquakes are associated with wastewater injection, where water that is extracted along with oil and gas is re-injected into another well. The injected water can cause local increases in fluid pressure and flow to nearby areas that have faults. InSAR can be used to estimate the depth of the faults that rupture in the larger induced earthquakes. For example, Fielding et al. (2017) found that the 2016 magnitude 5.8 earthquake near Pawnee, Oklahoma had the main fault slip deeper than 4.5 km (3 miles) beneath the surface. This deeper slip indicates that water from nearby wastewater injection wells likely flowed into deeper crustal layers with ancient faults that could be reactivated.

In addition to earthquake activity associated with the production of hydrocarbons, there is now evidence that production of water from aquifers can trigger earthquakes. On May 11, 2012, an Mw 5.1 earthquake struck the town of Lorca, Spain, resulting in 9 fatalities. Despite its relatively small magnitude, the quake was shallow enough that InSAR observations of surface deformation allowed inversion for the distribution of slip at depth (Gonzalez et al., 2012). Most slip occurred at a depth of 2–4 km, with a second slip patch shallower than 1 km depth – both very shallow hypocentral depths for this region. Over 250 m of water had been pumped from a shallow aquifer, with subsidence of up to 160 mm/yr observed by InSAR (Figure E-8). Gonzalez et al. (2012) hypothesize that stress changes from depletion of the aquifer triggered this unusually shallow event.

InSAR measurements of surface deformation can also provide a powerful tool for short-term risk assessment associated with production of unconventional reservoirs. For example, a recent major bitumen leak from cyclic steam injection in Alberta, Canada, in June 2013, associated with substantial precursory surface deformation would have placed valuable constraints on the physics of this unusual sequence. Unfortunately, there appears to be no existing InSAR coverage.

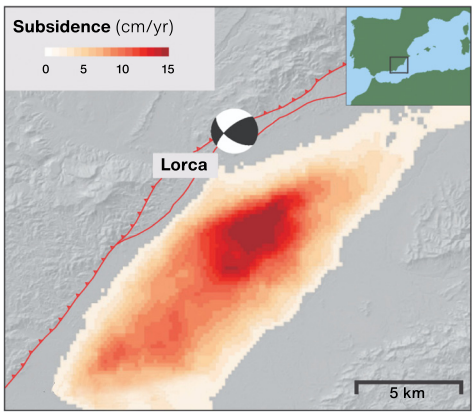

FIGURE E-8

Relationship between subsidence associated with groundwater withdrawal (red shading) and the May 11, 2012, Mw 5.1 earthquake near the city of Lorca, Spain (after Gonzalez et al., 2012).

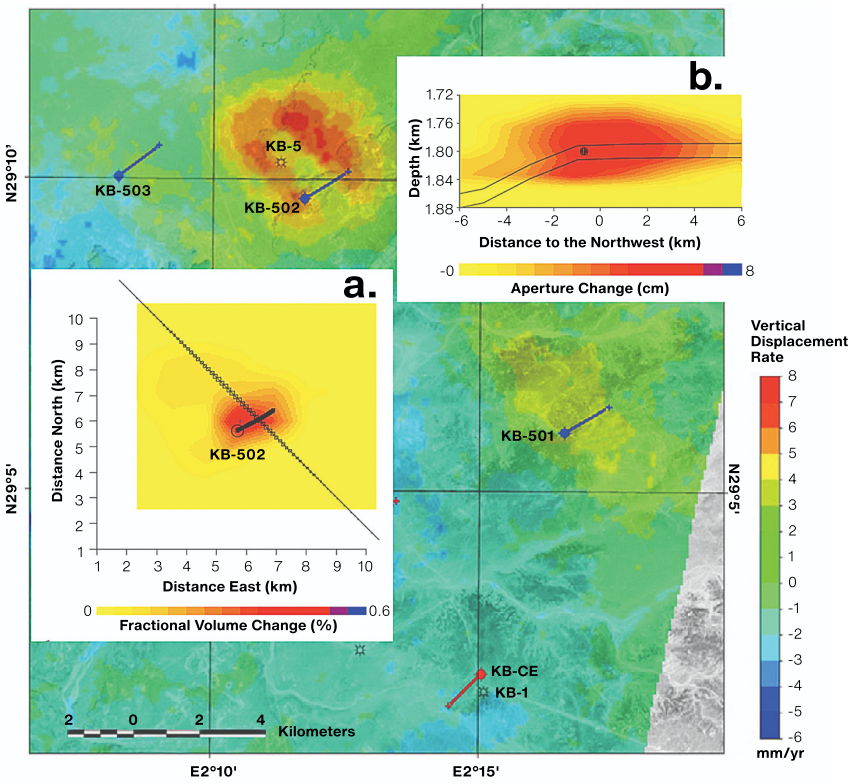

FIGURE E-9

In Salah oil field deformation. Interferogram of the In Salah oil field in Algeria, showing deformation associated with CO_2 injection over the period from March 2003 to December 2007 (Onuma & Ohkawa, 2009).

Finally, injection of CO_2 into the crust is expected to become an increasingly important means for sequestering this greenhouse gas from the atmosphere. Monitoring the surface deformation caused by fluid injection will likely become an important technique for understanding reservoir behavior and monitoring its integrity. The In Salah field in Algeria is in a favorable environment for monitoring by InSAR. ENVISAT C-band InSAR studies of deformation associated with CO_2 injection show that the field response

FIGURE E-10

U.S. subsidence areas. Areas where subsidence has been attributed to groundwater pumping (Galloway et al, 1999).

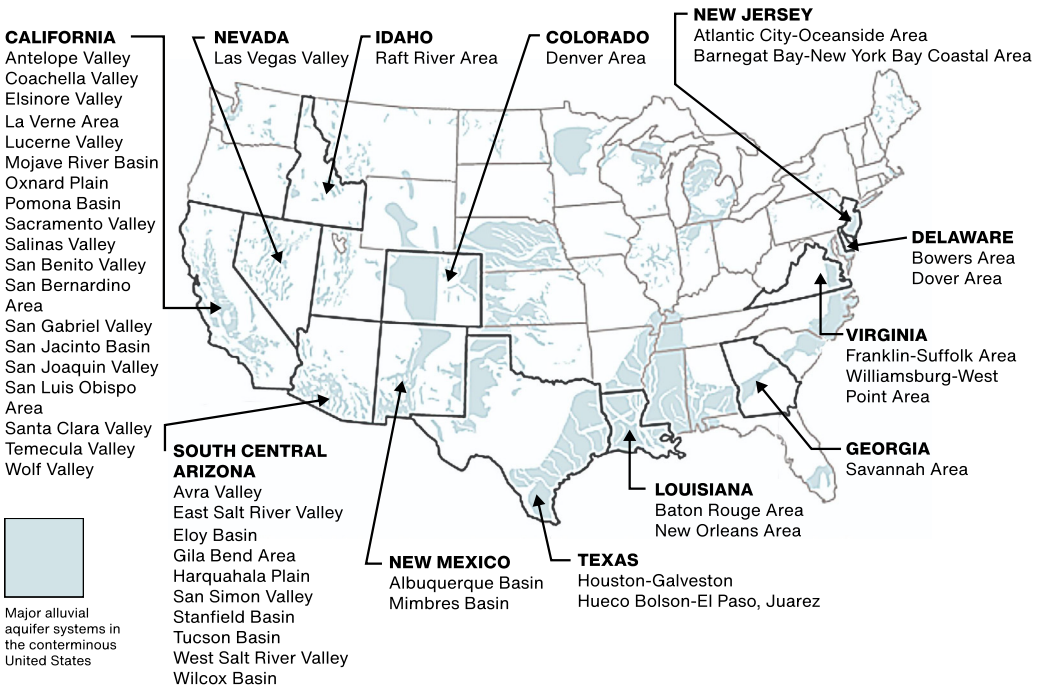

can indeed be monitored in this way (Ringrose et al., 2009). In particular, as shown in Figure E-9, the surface deformation observed by InSAR shows a two-lobed pattern near well KB-502, a horizontal well injecting CO_2 into a 20-m thick saline aquifer at 1.8 km depth. Such a two-lobed pattern indicates that, in addition to a component of isotropic volume expansion, a vertical fracture has opened, apparently extending into the caprock above the aquifer (Vasco et al., 2010). This fracture explains the early breakthrough of CO_2 into observing well KB-5 along the strike to the northwest. In response to the confirmation of the fracturing of the caprock, the injection of CO_2 at this site has been suspended.

E.1.5 AQUIFER SYSTEMS

Natural and human-induced land-surface subsidence across the United States has affected more than 44,000 square kilometers in 45 states and is estimated to cost $168 million annually in flooding and structural damage, with the actual cost significantly higher due to unquantifiable hidden costs (National Research Council, 1991). More than 80 percent of the identified subsidence in the United States is a consequence of the exploitation of underground water. The increasing development of land and water resources threaten to exacerbate existing land subsidence problems and initiate new ones (Figure E-10) (Galloway et al., 1999). Temporal and spatial changes in the surface elevation above aquifers measured with geodetic techniques provide important insights about the hydrodynamic properties of the underground reservoirs, the hydrogeologic structure of the aquifer, the potential infrastructure hazards associated with pumping, and effective ways to manage limited groundwater resources.

Groundwater extraction from aquifers with unconsolidated fine-grained sediments like clay can lead to irreversible land subsidence (Poland, 1984). A sedimentary aquifer system consists of a granular skeleton with interstices (pores) that can hold groundwater. The pore fluid pressure is maintained by the groundwater that fills the intergranular spaces (Meinzer, 1928). Under conditions of constant total stress, the pore fluid pressure decreases as groundwater is withdrawn, leading to an increase in the intergranular stress,

or effective stress, on the granular skeleton. The principle of effective stress (Terzaghi, 1925) relates changes in pore fluid pressure and compression of the aquifer system as

$$\sigma_e = \sigma_t - \rho \qquad \text{E.1-1}$$

where effective or intergranular stress (σ_e) is the difference between total stress or geostatic load (σ_t) and the pore-fluid pressure (ρ). Changes in effective stress cause deformation of the aquifer granular skeleton. Aquifer systems consisting primarily of fine-grained sediments, e.g., silt and clay, are significantly more compressible than those primarily composed of coarse-grained sediments, e.g., sand and gravel, and hence experience negligible inelastic compaction (Ireland et al., 1984; Hanson, 1998; Sneed and Galloway, 2000). Groundwater pumping can cause short- or long-term recoverable (elastic) or non-recoverable (inelastic) compaction that reduces aquifer storage capacity (Sneed et al., 2013).

Permanent (irrecoverable) compaction can occur if an aquifer is pumped below its pre-consolidation head (lowest prior pressure; Phillips et al., 2003), resulting in collapse of the skeleton, decreased pore space, and permanent loss of storage capacity. Over-development of aquifers can induce long-term elastic subsidence that lasts for decades to centuries. Depending on the thickness and the vertical hydraulic diffusivity of the fine-grained strata (aquitards) within an aquifer, the fluid-pressure change within those layers will lag behind the pressure/hydraulic head change from pumping. The pressure gradient between the pumped (usually coarse-grained) strata and the center of the fine-grained strata takes time to re-equalize. In practice, land subsidence can continue for decades or centuries after cessation of groundwater pumping, whatever time is required for balance to be restored between the pore pressure within and outside the fine-grained units (Sneed et al., 2013). The time constant of an aquitard is defined as the time following an instantaneous decrease in stress that is required for 93% of the excess pore pressure to dissipate, i.e., the time at which 93% of the maximum compaction has occurred. The time constant is directly proportional to the inverse of the vertical hydraulic diffusivity and, for a confined aquitard (draining both above and below), to the square of the half-thickness of the layer:

$$\tau = \frac{S'_s \left(\frac{b'}{2}\right)^2}{K'_v} \qquad \text{E.1-2}$$

where S'_s is the specific storage of the aquitard, b' is the aquitard thickness, K'_v is the vertical hydraulic conductivity of the aquitard, and S'_s/K'_v is the inverse of the vertical hydraulic diffusivity (Riley, 1969). Ireland et al. (1984) estimated time constants of 5-1350 years for aquifer systems at fifteen sites in the San Joaquin Valley. The scale of groundwater pumping currently underway in many areas makes this a global issue (Alley et al., 2002).

Repeat-pass interferometric SAR has become an invaluable tool for hydrologists to resolve spatially and temporally-varying aquifer properties and model parameters that are impractical to obtain with any other technology. Numerous studies have exploited InSAR imagery to assess land subsidence globally (Figure E-11). Early research in the United States focused on the deserts and major cities in the Western U.S. including the Mojave Desert (Galloway et al., 1998; Hoffman et al., 2001), Los Angeles (Bawden et al., 2001), Las Vegas (Amelung et al., 1999), and Phoenix (Casu et al., 2005). Advanced InSAR time-series analysis methods such as Persistent Scatterer InSAR (PSInSAR) and related processing approaches allow InSAR to measure subsidence in agriculture and heavily vegetated regions such as New Orleans (Dixon et al., 2006) and the California Central Valley (Sneed et al., 2013). More than 200 occurrences of land subsidence have been documented throughout the world during the past few years. Globally, InSAR has measured and tracked subsidence in areas across Europe, the Middle East, China, Japan, and Thailand. The extent of the InSAR imagery allows hydrologists to model spatially varied skeletal storage aquifer parameters as they change seasonally and annually. Before the advent of InSAR, it was not possible to know

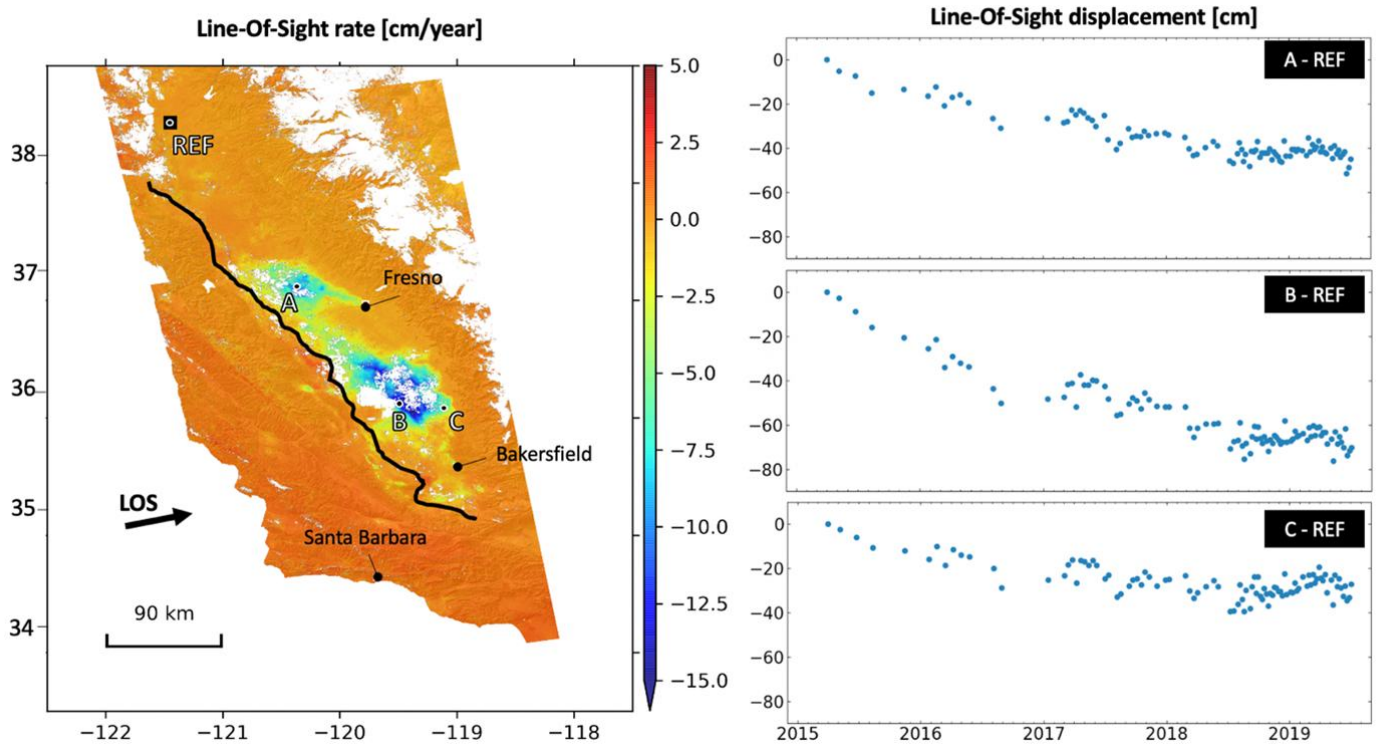

FIGURE E-11

San Joaquin Valley-wide subsidence derived from Sentinel-1 data acquired from 2015 to 2019. (Left) Black line corresponds to the location of the California aqueduct. (Right) Time series for three points showing the change in the surface as a function of time at the center (B) and edge (C) of the main subsidence feature in the valley (near Visalia, CA), and for a smaller subsidence bowl in the northern part of the San Joaquin Valley (A), all relative to a stable location to the northwest. The values plotted are the surface displacement projected onto the satellite line-of-sight (Jones et al., 2022).

the boundary conditions of a pumped aquifer; subsidence gradients are used to understand the margin locations and aquifer interactions.

InSAR's ability to measure the spatial and temporal changes associated with aquifer system compaction / land subsidence provides a direct methodology for determining the hydrologic properties that are unique to each aquifer system, thereby providing fundamental geophysical constraints needed to understand and model the extent, magnitude, and timing of subsidence. Furthermore, water agencies can take advantage of these geophysical and hydrodynamic parameters to optimize water production while minimizing subsidence and mitigating the permanent loss of aquifer storage.

One of the greatest challenges for measuring land subsidence is the loss of interferometric correlation in heavily vegetated regions and in areas with extensive agricultural production. Persistent Scatterer Interferometry (PSI) based differential InSAR techniques (e.g., Ferretti et al., 2001; Hooper et al., 2004) have greatly expanded the efficacy of C-band SAR investigations in challenging agricultural areas but are limited to the temporal sampling density of the SAR archive. Sneed et al. (2013) combined PSI C-band and differential L-band InSAR to capture the full extent of the subsidence (Figure E-11). The PSI approach, shown as contours in the figure, involved a long time series of C-band images, and resolved a maximum subsidence rate of 30 mm/yr. Only 2 ALOS L-band images spanning 2 years were available, from which a subsidence rate of 54 cm in 2 years was derived.

The improved temporal coherence achieved by L-band imagery in agriculture and heavy vegetation regions (see, e.g., Figure E-12) is one of the key motivations for India's interest in a long-wavelength radar mission, particularly coupled with more densely sampled data to reduce tropospheric noise and other effects. The C-band subsidence map in and around the city of Delhi in Figure E-12 shows coherence only in the urbanized areas (Chatterjee et al., 2006;

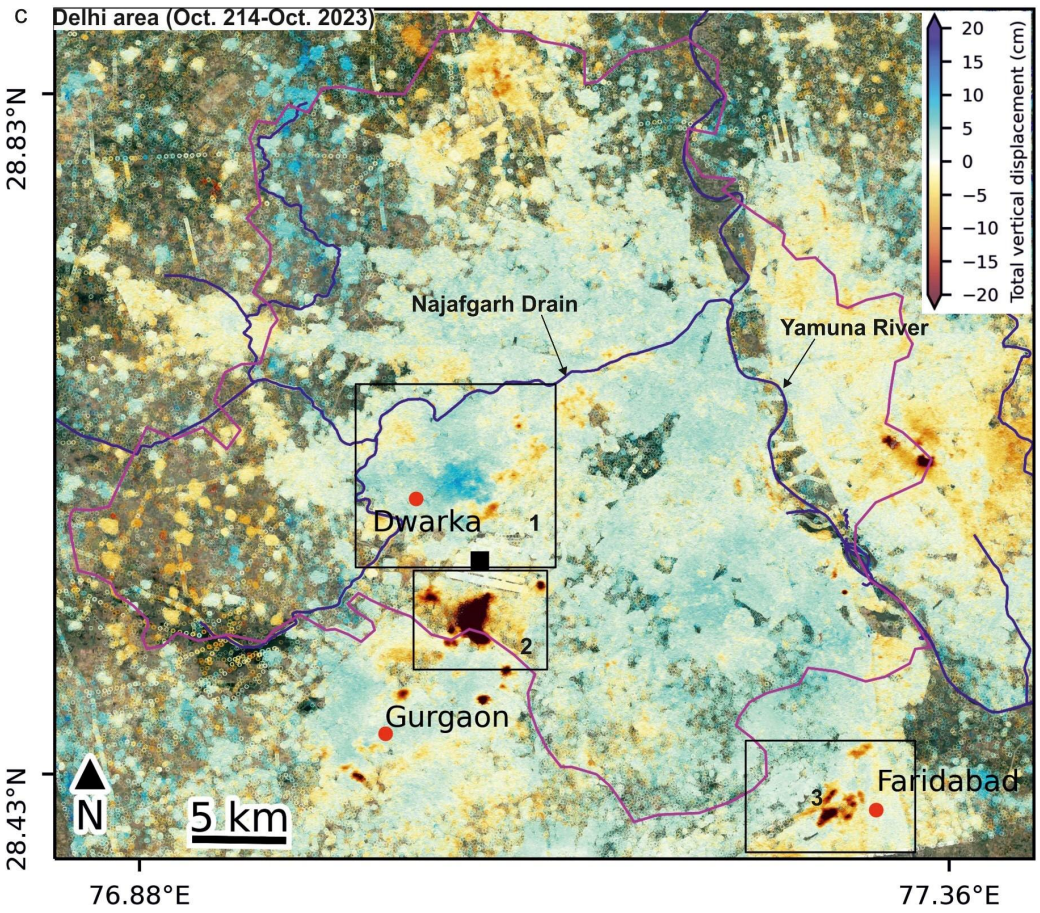

FIGURE E-12

Delhi land subsidence. Deformation maps showing average rate of land subsidence in the area of Delhi obtained from advanced time-series analysis of Copernicus Sentinel-1. The amounts of land subsidence in the urban area vary from more than 20 cm over nine years to small amounts of rebound up to 5 cm (adapted from Kumar et al., 2025). Areas of agriculture outside the cities are not well measured with this C-band data.

2007a; 2007b; Gupta et al., 2007; Kumar et al., 2025). With longer wavelength radar to improve coherence everywhere, however, subsidence measurements can be extended to much broader areas in places like India.

It can be difficult to resolve small-scale surface deformation associated with slip at depth on faults and the migration of magmatic fluids from the large ground-surface deformations caused by anthropogenic fluid withdrawal and injection. However, on their own, the large signals provide information to better understand managed groundwater, hydrocarbon, and geothermal resources, aiding in the characterization and modeling of reservoir dynamics. Pumping of unconfined aquifers can lead to elastic deformation (e.g., seasonal uplift/subsidence) if fluid extraction/recharge is well balanced; but when net fluid production is unbalanced, it can induce long-term surface deformation or permanent (inelastic) deformation. Surface change specific to fluid management is observed as horizontal and vertical deformation signals in GNSS and InSAR time series data that correlate with the production activities. The timing, location, and spatial extent of the InSAR signals are key to isolating individual processes, particularly in situations where quasi-steady state fluid pumping/injection mimics or masks tectonic/magmatic signals in GPS time series (Figure E-13).

NISAR imagery can be used to help isolate, model, and remove the effects of fluid extraction on tectonic/volcanic GNSS time series data. Future GNSS networks can be optimized to avoid anthropogenic and natural surface deformation associated with the pumping of fluids and natural groundwater recharge processes. GNSS

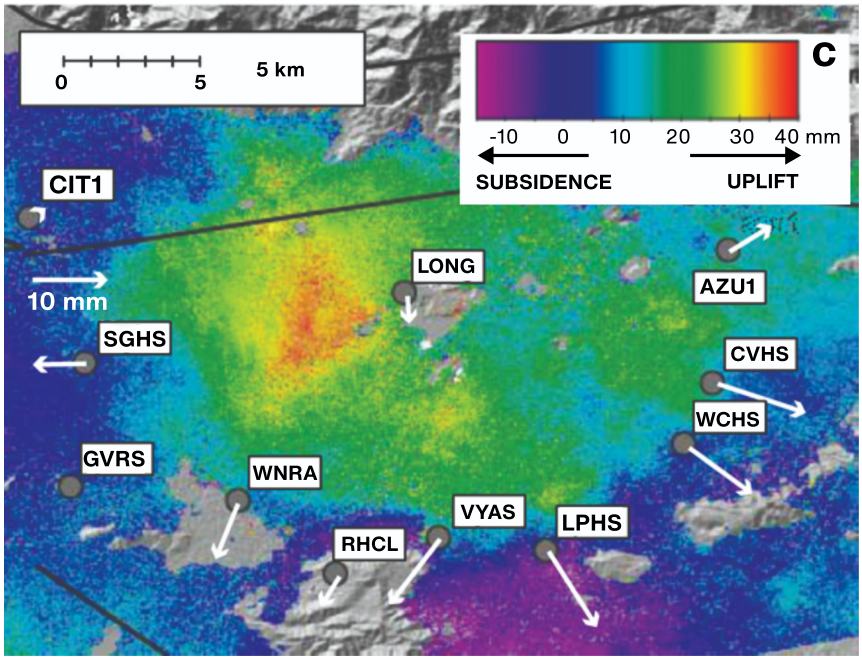

FIGURE E-13

Example of non-tectonic deformation. Unwrapped ENVISAT interferogram (January 2005 to July 2005) of the San Gabriel Valley (CA) showing surface deformation over an area 40 x 40 km associated with natural aquifer recharge during a record rainfall during the winter of 2005. The land surface uplifted 40 mm pushing GNSS sites on the margins of the basin radially outward in excess of 10 mm (labeled vectors). This groundwater hydrology transient was initially interpreted as an aseismic earthquake in an active tectonic environment; combined InSAR imagery and GNSS time series along with water levels were needed to resolve its genesis (King et al., 2007).

sites placed on the margins of active aquifer/reservoir will have horizontal motion that can mask and at times mimic the tectonic signal (Bawden et al., 2001). GNSS sites placed near the center of the subsidence will have high vertical signal with nominal horizontal displacements, therefore improving the ability to resolve tectonic deformation in an active groundwater basin.

E.1.6 GLACIAL ISOSTATIC ADJUSTMENT

In areas of present or past glaciation, surface deformation can be caused by a solid earth response to current glacier advance or retreat as well as a delayed response to changes centuries or millennia ago. The magnitude and spatial patterns of ground deformation can be used to infer changes in the ice load and the rheology of Earth's crust and upper mantle. InSAR has been used to measure the elastic response of ice mass loss in Iceland in recent decades (Zhao et al., 2014), and NISAR has the potential to make similar measurements around most of the current ice-covered areas. Furthermore, frequent L-band (high coherence) measurements with good orbital baseline control provided by NISAR will open new possibilities to measure deformation caused by ice load changes since the Little Ice Age and the Last Glacial Maximum (called Glacial Isostatic Adjustment, GIA) that can better constrain both the ice load history and the viscosity beneath areas like Canada, Alaska, Patagonia, and Scandinavia. Deformation measurements in some of these areas have been made by GNSS, but NISAR will add important spatial resolution. For example, NISAR observations can test some of the predictions of GIA made by GRACE satellite gravity observations, such as large uplift rates in northern Canada (e.g., Paulson et al., 2007) that should be detectable with NISAR.

E.1.7 PERMAFROST

Permafrost – ground that remains below freezing throughout the year – underlies approximately 15% of the Earth's terrestrial surface. Widespread changes in permafrost conditions have recently been observed, such as increasing ground temperatures and deeper seasonal thaw (Romanovsky et al., 2010; Smith et al., 2022). Permafrost is a cryospheric system, but it is categorized within the solid Earth umbrella in the NISAR project because the interferometric techniques used to measure permafrost-induced surface deformation closely resemble those of the other solid Earth disciplines.

Permafrost thaw can induce subsidence and surface instability (Streletskiy et al., 2025). A major cause for such instability is the melting of ground ice, as permafrost can contain more than 90% of ice by volume. When permafrost thaws and ground ice melts, the soils lose strength, and the surface can subside and collapse. On hillslopes, permafrost thaw can induce landslides. For instance, Bernhard et al. found a forty-fold increase in landslide activity on the Taymyr Peninsula following an extremely warm year (Bernard et al., 2022). Permafrost thaw also contributes to increasing rates of coastal and fluvial erosion, which threaten critical infrastructure and Arctic communities.

Changing permafrost conditions have major implications for the economy and the

environment. The surface instability is a major hazard to industrial installations, transportation corridors, and human settlements. The costs to maintain and repair infrastructure affected by thaw-induced soil failure and subsidence are projected to continue to increase rapidly in Alaska and across the Arctic. Changing permafrost conditions also impact water resources, ecosystem services, and the global carbon cycle (Smith et al., 2022; Streletskiy et al., 2025).

NISAR measurements of surface displacements are critical for monitoring permafrost conditions and hazards (Zwieback et al., 2024). In mountainous terrain, NISAR surface displacement measurements enable monitoring of landslides and rock glaciers. In lowlands, the surface deformation measurements can directly inform hazard assessment and planning in regions where subsidence is occurring. Thanks to their high accuracy, frequent observations, and global coverage, these NISAR observations will enhance assessment of active layer and permafrost conditions and dynamics. For instance, Liu et al. (2014) inferred permafrost thaw dynamics after a large tundra fire from InSAR. With NISAR, researchers will be able to monitor the response of permafrost to wildfires on a pan-Arctic scale. Similarly, NISAR will enhance large-scale mapping of ground ice conditions (Zwieback et al., 2025; Fig. E-14), filling a critical data need for planning in the Arctic.

In summary, NISAR will enable a spatially explicit assessment of permafrost dynamics and hazards. It will further shed light on changing hydrology, carbon cycling, and northern ecosystem character and functioning.

E.2 ECOSYSTEMS

The 2007 Decadal Survey identified that a key goal for ecosystems sciences is to characterize the effects of changing climate and land use on the terrestrial carbon cycle, atmospheric CO2 levels, and ecosystem services. Human-induced disturbances have dramatically altered the terrestrial ecosystems directly by widespread land use changes, converting old-growth and carbon-rich forests into permanent croplands and urban landscapes. Disturbances have also led to extensive losses of wetlands of up to 50 percent and increased the probability of natural disturbances such as fire, droughts, hurricanes, and storms due to fundamental shifts in the climate and atmospheric CO2 concentrations (Foley et al., 2005; Dale et al., 2001; IPCC, 2007). In recent years, the critical ecosystem services provided by mangroves have been particularly hard hit by warming ocean temperatures, rising sea levels, and population pressures. Shifts in vegetation are occurring, especially in high altitude regions where alpine tree lines are advancing.

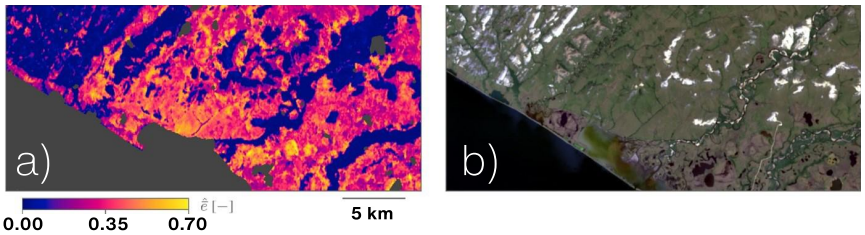

FIGURE E-14

Estimated excess ice content near the permafrost table (a) from a model-based inversion of Sentinel-1 seasonal deformation observations in Northwestern Alaska. Ice-poor locations appear in blue, largely corresponding to recent river floodplains and rocky outcrops visible in the Landsat image, and (b) ice-rich permafrost, shown in warm colors, is inferred over the vast majority of soil-covered lowlands and hillslopes. Adapted from Zwieback et al., 2025.

While these changes have important implications for the global carbon cycle and its climate feedback, there remains large uncertainty in the global extent and magnitude of these changes in the terrestrial component. The Decadal Survey highlights this shortcoming by stating that, "there are no adequate spatially resolved estimates of the planet's biomass and primary production, and it is not known how they are changing and interacting with climate variability and change."

Dynamics of global vegetation with strong impacts on global carbon cycle are identified as changes of woody biomass from deforestation, degradation, and regrowth; changes in the extent and biomass production of global crops; and the extent and inundation cycling of global wetlands (NRC, 2007). Quantifying these changes is critical for understanding, predicting, and ultimately managing the consequences of global climate change. It is the consensus of the scientific

community that systematic observations from space with the aim of monitoring ecosystem structure and dynamics are a priority to significantly reduce large remaining uncertainties in global carbon cycle and climate prediction and ecosystem models (CEOS, 2014). Therefore, a spaceborne mission meant to address the needs of the link between ecosystems and the climate will have the following scientific objectives ranked amongst the highest priority:

- Quantify and evaluate changes in Earth's carbon cycle and ecosystems and consequences for ecosystem sustainability and services.
- Determine effects of changes in climate and land use on the carbon cycle, agricultural systems, and biodiversity.
- Investigate management opportunities for minimizing disruption in the carbon cycle (ISRO).
- Determine the changes in carbon storage and uptake resulting from disturbance and subsequent regrowth of woody vegetation.
- Determine the area and crop aboveground biomass of rapidly changing agricultural systems.
- Determine the extent of wetlands and characterize the dynamics of flooded areas.
- Characterize freeze/thaw state, surface deformation, and permafrost degradation.
- Explore the effects of ecosystem structure and its dynamics on biodiversity and habitat.

E.2.1 BIOMASS

In May 2013, atmospheric CO2 concentrations passed 400 ppm, indicating an alarming rise of more than 30% over the past 50 years, caused by fossil fuel emissions (~75%) and land use change (~25%). There is strong evidence that during this period the terrestrial biosphere has acted as a net carbon sink, removing from the atmosphere approximately one third of CO2 emitted from fossil fuel combustions (Canadell et al., 2007). However, the status, dynamics, and evolution of the terrestrial biosphere are the least understood and most uncertain element of the carbon cycle (IPCC, 2007). This uncertainty spans a wide range of temporal and spatial scales. The IPCC has identified interannual variability of atmospheric CO2 being strongly controlled by the terrestrial biosphere, while the

FIGURE E-15

Major elements of the terrestrial carbon cycle: (1) Disturbance regimes; (2) Land/Atmosphere fluxes; (3) Ecosystem dynamics; (4) Terrestrial carbon pools, and; (5) Export fluxes. NISAR makes key observations in each element. (CEOS, 2014).

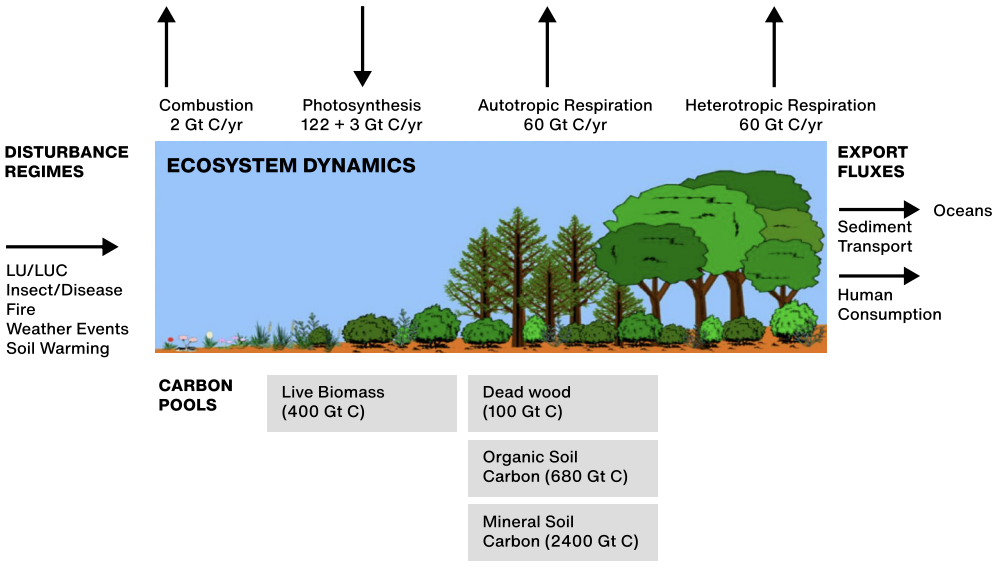

GLOBAL DISTRIBUTION OF WOODY BIOMASS

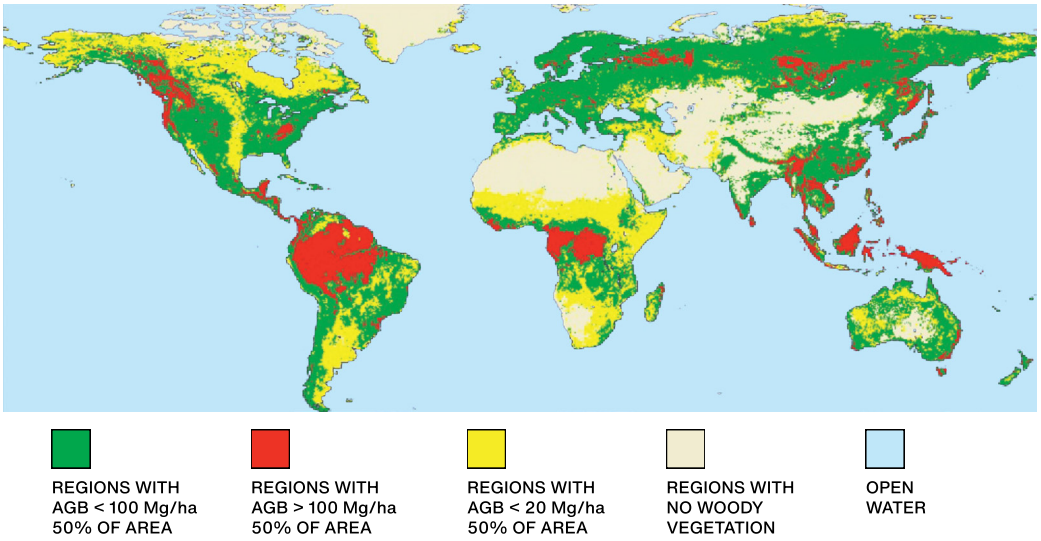

FIGURE E-16

Global distribution of woody biomass. Forest biomass density predicted from a combination of inventory data and available statistics (Kinderman, et al., 2008). Percentages refer to the percent of area for that class of biomass in each grid cell.

coupling between the terrestrial biosphere and climate was identified as one of the major areas of uncertainty in predicting climate change over decadal to century time scales. Spatially, large uncertainties exist in the distribution of carbon stocks and exchanges—in estimates of carbon emissions from forest disturbance and the uptake through forest growth.

A fundamental parameter characterizing the spatial distribution of carbon in the biosphere is biomass, which is the amount of living organic matter in a given space, usually measured as mass or mass per unit area, with half of all dry biomass being carbon (Figure E-15). Therefore, biomass represents a basic accounting unit for terrestrial carbon stock, and its temporal changes from disturbance and recovery play a major role in controlling the biosphere interaction with climate. Estimates of the amount of biomass in the world's terrestrial ecosystems range from 385 to 650 petagrams of carbon (PgC), or 10^{15} grams (Houghton et al., 2009). Forests contain more than 80 percent of the aboveground carbon stock and are thus a dominant component of the global carbon cycle (Houghton, 2005b). Because of its importance for climate, forest biomass is identified by the United Nations Framework Convention on Climate Change (UNFCCC) as an essential climate variable needed to reduce the uncertainties in our knowledge of the climate system (Global Climate Observing System GCOS, 2010).

Our current knowledge of the distribution and amount of terrestrial biomass is based almost entirely on ground measurements over an extremely small and possibly biased sample, with many regions still unmeasured. A global, detailed map of aboveground woody biomass density will halve the uncertainty of estimated carbon emissions from land use change (Houghton et al., 2009; Saatchi et al., 2013) and will increase our understanding of the carbon cycle, including better information on the magnitude, location, and mechanisms responsible for terrestrial sources and sinks of carbon. Biomass density varies spatially and temporally. Living biomass ranges over two to three orders of magnitude, from less than 5 megagrams of carbon per hectare (MgC/ha) in treeless grasslands, croplands, and deserts to more than 300 MgC/ha in some tropical forests and forests in the Pacific Northwest of North America.

Biomass density also varies considerably within ecosystem types. This variability results, in part, from limitations of the environment (for example, soil nutrients or the seasonal distribution of

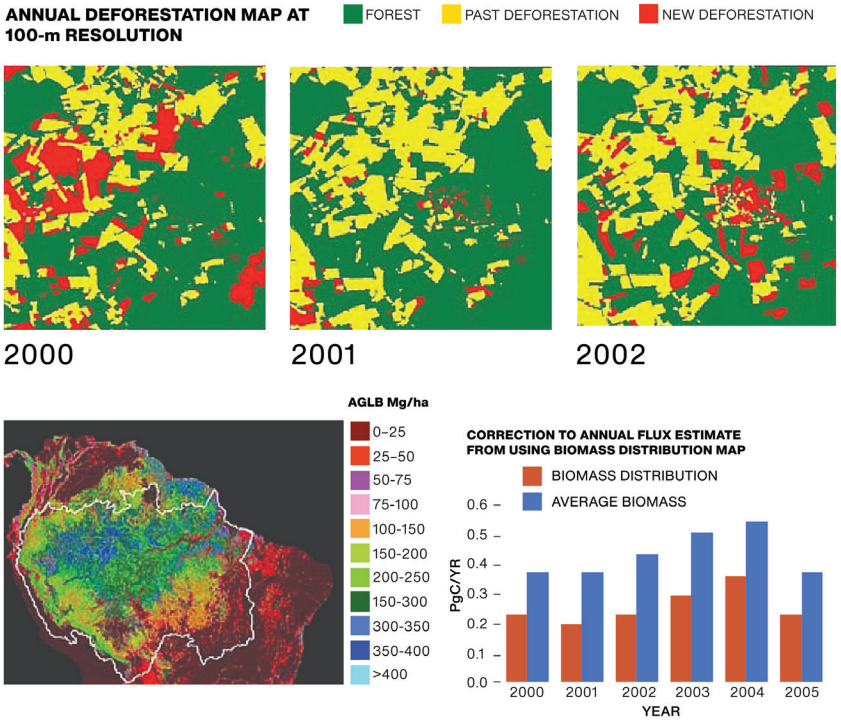

FIGURE E-17

Spatially explicit information on forest cover change and disturbance and aboveground biomass map from NISAR will significantly improve the estimates of carbon emissions from land use change to the atmosphere. Top panel shows annual deforestation of tropical forests at 1 ha grid cell simulated from Landsat based forest cover change data (Hansen et al., 2013). Bottom panel shows how by having annual biomass map of tropical forests of the Amazon basin (left image: resampled to 100 m from Saatchi et al., 2007) at the same resolution as the deforestation map can provide improved estimates of gross emissions from deforestation compared to the use of a regional mean biomass value (Harris et al., 2012).

precipitation and temperature), and in part from disturbance and recovery. The aboveground living biomass density of a recently burned forest may be nearly zero, but it increases as the forest recovers (Figure E-16). Forests do not accumulate biomass indefinitely, however, because stand-replacing disturbances keep turning old forests into young ones. However, most forest stands are in the process of recovering from natural or human-induced disturbances and, thus, are accumulating carbon, albeit generally at lower rates as they age.

Forests in temperate and boreal regions have low biomass density (< 100 Mg/ha) but are extensive in area and are subject to climate change and variability causing widespread disturbance (e.g., fire, hurricanes, droughts), and human land use change (Bonan, 2008). These forests are also considered a major carbon sink from long periods of management (Woodall et al., 2010) and increasing length of growing season from climate change (Myneni et al., 2001). Other low biomass density regions are savanna woodlands and dry forests, distributed globally in temperate and tropical regions. These regions cover more than 50 percent of the area of forest cover globally and are considered highly heterogeneous spatially and dynamic temporally.

E.2.2 BIOMASS DISTURBANCE AND RECOVERY

Perhaps more important than biomass distribution to the global carbon cycle, is the quantification of biomass change and its associated carbon flux (Houghton et al., 2009). The magnitude of the uncertainty in the global carbon flux is particularly large in the tropics. Recent calculations estimate a net positive flux from the tropics of between 0.84 and 2.15 PgC per year (Harris et al., 2012; Baccini et al., 2012; Pan et al., 2011; Le Quere et al., 2017). In the context of global climate mitigation approaches (UNFCC, 2006) and the relevant calculations of national carbon emissions, the difference between these two estimates (1.3 PgC per year) lies between the total carbon emissions of the United States (1.5 PgC per year) and China (2.5 PgC per year), the top two carbon-emitting nations (Peters et al., 2012; Global Carbon Project, 2012).

The location of the land carbon sinks and sources are unknown, as well as the reasons for their annual swings in strength that on occasion are as much as 100% (Canadell et al., 2007). To what degree are these large shifts a result of climate variability, or disturbance? Even where estimates of mean forest biomass are known with confidence, as in most developed countries, the spatial distribution of biomass is not, and the possibility that deforestation occurs in forests with biomass systematically different from the mean, suggests that this potential bias may also contribute to errors in flux estimates (Houghton et al., 2001; Houghton, 2005). To address the uncertainty in carbon fluxes and the terrestrial carbon sinks and sources, a series of accurate, annual global maps of disturbance and recovery will significantly improve estimates of emissions to the atmosphere and quantification of the large proportion of the residual terrestrial sink attributable to biomass recovery from such

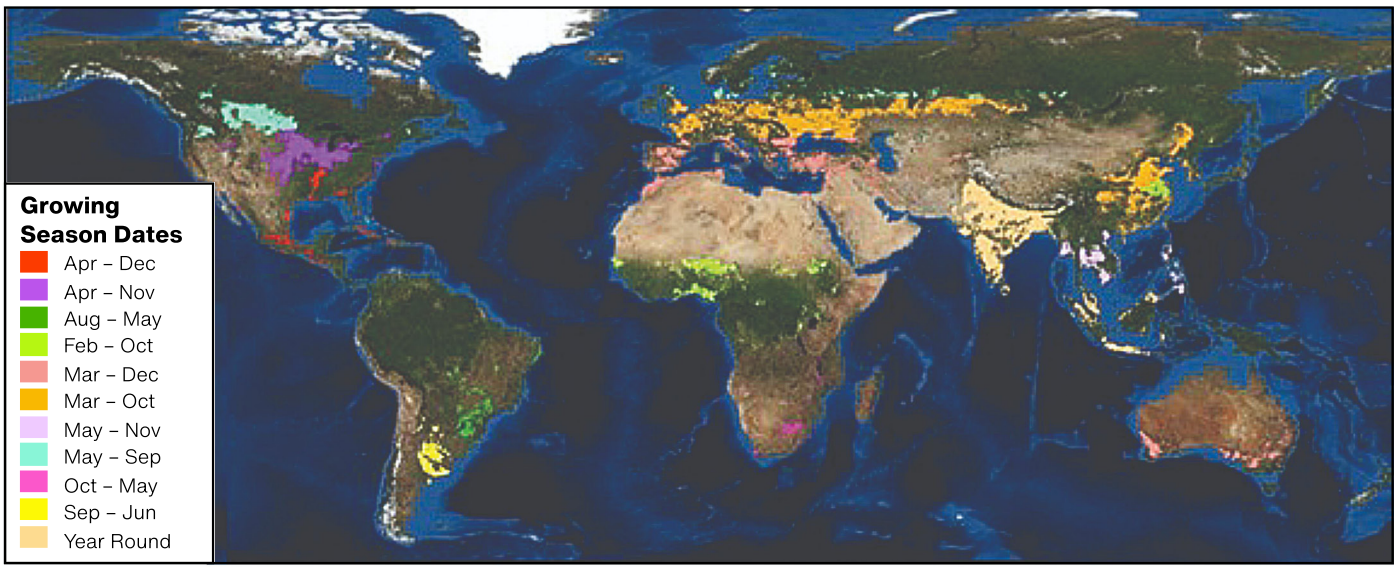

FIGURE E-18

Global image of agriculture crop areas and growing seasons. Crop types used for the assessment are based on basic grains and economically significant crops of world agriculture (e.g., rice, wheat, soybean, maize, etc.). Data source: earthstat.org.

disturbances. The spatial and temporal distribution of disturbance events, many of which occur at one hectare or below, must be observed at fine spatial resolution. Examples of such events include clear cutting, selective logging, fire, hurricanes, floods, disease, and insect infestation. Figure E-17 (previous page) shows a typical landscape mosaic of disturbance and recovery following disturbance in the Amazon basin and the emissions calculated from the use as forest biomass maps (Saatchi et al., 2007; Harris et al., 2012). By developing an annual disturbance and recovery map at the same spatial resolution as the biomass map, we can radically improve the estimates of emissions and removals (Houghton et al., 2009).

Because of various environmental and climate variables, forest ecosystems are heterogeneous in their cover, structure, and biomass distribution. The heterogeneity of ecosystems occurs at different scales and has been studied extensively in ecological theory and landscape dynamics. These studies recommend detection and classification of disturbance and recovery events at one-hectare spatial scales to reduce the uncertainty of carbon fluxes (Hurtt et al., 2010). NISAR will provide a means to reliably generate annual disturbance and recovery estimates at hectare-scale resolution for the duration of the mission and thus help reduce the uncertainties in carbon emissions and sequestration estimates.

E.2.3 AGRICULTURAL MONITORING

Since the beginning of the agricultural revolution and followed by the industrial revolution, agriculture has been a driver and early adopter of technology for the efficient production of crops. As populations have grown and moved into urban centers, governmental organizations have had an interest in food security and in assessing their availability and impact on world markets.

Crop assessment depends on multiple sources of data that are used for determining crop condition and area, often relying on inputs from the previous year's production. The various sources of inputs include satellite-based observations, weather data, ground information and economic reporting. All of these are used to inform government and commodities markets that direct the allocation of resources and predict nutrient availability.

Identified in the 2010 GEO Carbon Strategy is the monitoring and measurement of agriculture biomass and areal extent, which are important

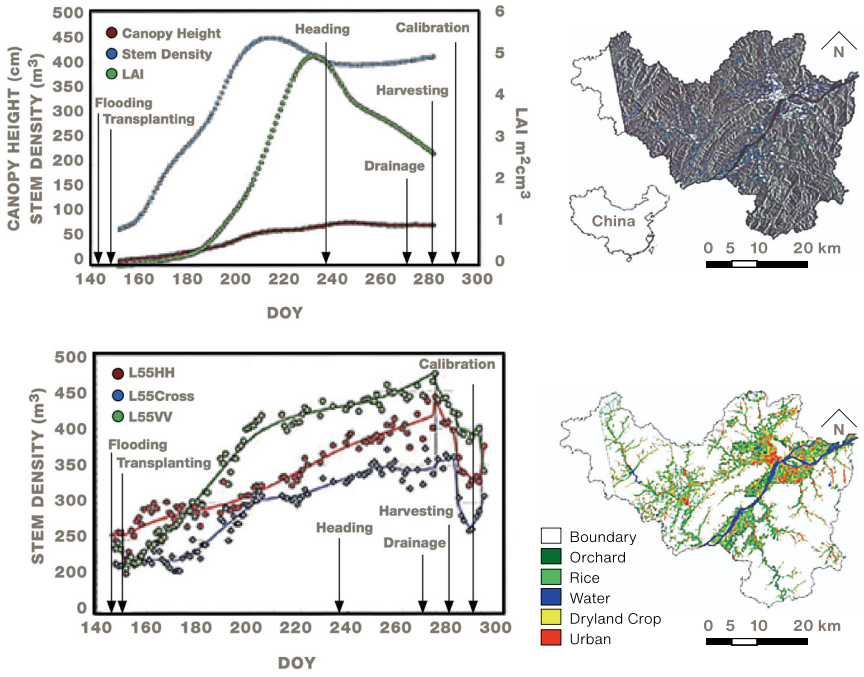

FIGURE E-19

Examples of agricultural change. (Top left) Seasonal change of plant variables determined by destructive sampling on the weekly time-cycle and interpolated on a daily time series. (Bottom left) Time course change of microwave backscattering coefficients at all combinations of polarization and incident angle for the L-band over capturing the crop yield and biomass change (Inoue et al., 2002). (Top right) The L-band ALOS PALSAR composite of three dates over Zhejiang Province in southeast China. (Bottom right) The crop classification from multi-temporal PALSAR imagery separating dry and wet crops from forests and urban areas (Zhang et al., 2014).

components of the global carbon budget and in the understanding of the effects of policy and climate on land management and crop yields. In the two-decade period from 1990–2010, large-scale clearing and conversion of forests to agriculture has resulted in an average flux of 1.3 to 1.6 gigatonnes of carbon per year (GtC/y) since the 1990s (Pan et al., 2011). While the gross distribution of growing regions worldwide is generally well known (Figure E-18), it is not at resolutions required for carbon assessment and for generating reliable, accurate, timely, and sustained crop monitoring information and yield forecasts. The role of agriculture in the GEO System of Systems (GEOSS) has given rise to the Joint Experiment for Crop Assessment and Monitoring initiative (JECAM), created by the GEO Agricultural Monitoring community, which has identified high-resolution SAR and optical remote sensing capabilities as the necessary sensor platforms for crop monitoring and agricultural risk management (GEOSS Tasks AG0703a, b; 2005).

With biomass levels in agriculture crops typically less than 50 t/ha, SAR backscatter observations provide an observational approach for the estimation of crop biomass (Figure E-19). By making short-revisit observations throughout the growing season, additional information is obtained that will help refine these biomass estimates as well as provide timely and sustained crop monitoring information that will inform yield forecasts and help evaluate agriculture management practices in response to weather and governmental policy initiatives.

Because crop yield and resource planning are dependent, in part, on soil moisture, an L-band SAR can play an important role in the planning and projecting of agricultural output. The longer wavelengths of NISAR's L- and S-band systems compared to that of C- and X-band systems (e.g., Radarsat 2, Sentinel-1, and TerraSAR-X) make it uniquely capable of assessing this component of plant growth. For example, Kraatz et al. (2021) explored dense L-band and C-band SAR time series for crop area mapping, emphasizing L-band's ability to better capture the dynamic scattering of plant growth compared to the shorter wavelengths of C-band.

The timeliness of observation for agriculture applications is also an important component. Because agricultural applications are a fundamental part of NISAR's observing strategy and NISAR's polarimetric capability, observations collected by the sensor in a consistent configuration will be collected throughout the growing season and hence provide a resource that will be of immediate use to global agricultural monitoring efforts (e.g., GEOGLAM). Furthermore, NISAR will provide a base set of observations that will be combined with yield measures, weather records, and other remote sensing resources to create predictive models that can be used from one season to the next.

E.2.4 WETLANDS AND INUNDATION

Global wetlands and their hydrologic dynamics are of major concern with respect to their impact on climate change. Wetlands are characterized by waterlogged soils and distinctive communities of plant and animal species that have evolved and adapted to the constant presence of water. Due

to this high level of water saturation as well as warming weather in low and mid-latitudes and accelerated freeze/thaw cycles in high latitudes, wetlands are one of the most significant natural sources of increased atmospheric methane. Emissions from wetlands contribute about 100–230 Tg/yr (Matthews, 2000) of methane to the atmosphere and represent 20–45% of total emissions (~ 500 Tg/yr). Thus, changes in wetland emissions can significantly impact future methane levels. Methane increases have contributed about 0.7 W/m^2 to global radiative forcing since preindustrial times (0.5 W/m^2 directly, plus an additional roughly one half the forcing from CO_2. This makes methane emissions the second most important greenhouse gas forcing (Hansen et al., 2000; Ramaswamy et al., 2001). Therefore, controlling methane emissions could mitigate global warming as much as controlling CO_2 over the next century (Kheshgi et al., 1999), and might be a more practical way to reduce near-term climate forcing, owing to methane's shorter lifetime and the collateral economic benefits of increased methane capture (Hansen et al., 2000). Projections of future emissions are typically based only on potential changes in anthropogenic emissions. It is possible, however, that natural emissions could also change substantially.

Globally, wetlands are also a critical habitat of numerous plants and animal species and play a major role in maintaining the biodiversity of the planet. Furthermore, natural wetlands and managed rice paddies are a major source of food and fiber. These regions cover 5.7 x 10^6 km^2 and 1.3 x 10^6 km^2 with an estimated net primary production of 4–9 x 10^{15} and 1.4 x 10^{15} g dry matter per year, respectively. The RAMSAR convention on wetlands has emphasized the role of remote sensing technology in obtaining inventory information and monitoring the status and activity of wetlands globally (Rosenqvist et al., 2007). A key challenge facing wetland researchers and managers is in the development of techniques for assessing and monitoring the condition of wetlands (Sahagian and Melack, 1996; Darras et al., 1998). Parameters that have been used for these purposes include the composition, location, areal extent, water status, and productivity of wetlands over time (see reviews in Finlayson et al., 1999). For wetland inventory, techniques are sought that can reliably distinguish between wet and dry land areas (regardless of vegetation cover) and the degree of soil saturation (Sahagian et al., 1997). In addition, attributes for which data can be collected through an inventory and later used to determine when change has occurred are particularly valuable as wetlands are subject both to natural change and, increasingly, to destruction and degradation associated with human activities.

Many wetlands are subject to seasonal or periodic flooding, i.e., inundation, and knowledge of the spatial and temporal characteristics of flooding patterns is crucial to understanding wetland biochemical processes, including methane production. Furthermore, river inundation represents a dominant mechanism in the lateral transport of sediments to the ocean basins, and thus is a critical factor controlling the export flux of carbon from terrestrial ecosystems (Figure E-20).

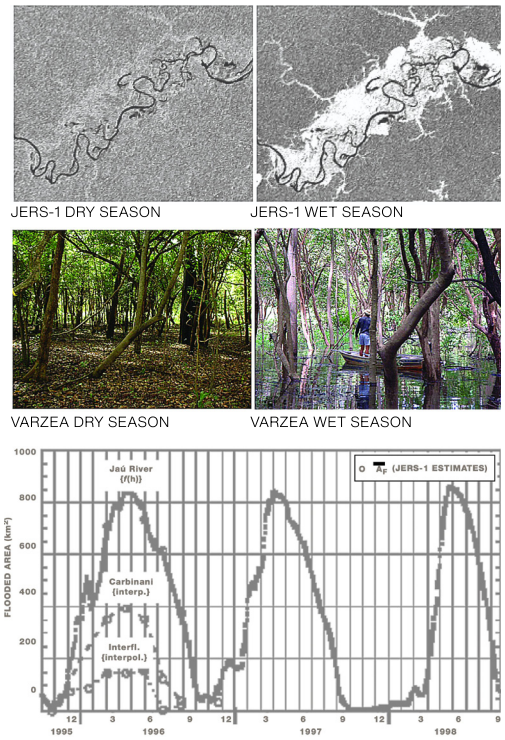

FIGURE E-20

L-band HH sensitivity in wetlands. Sensitivity of L-band radar backscatter at HH polarization for mapping the area and the cycle of inundation of the wetlands of the Amazon basin. (Rosenqvist et al., 2003).

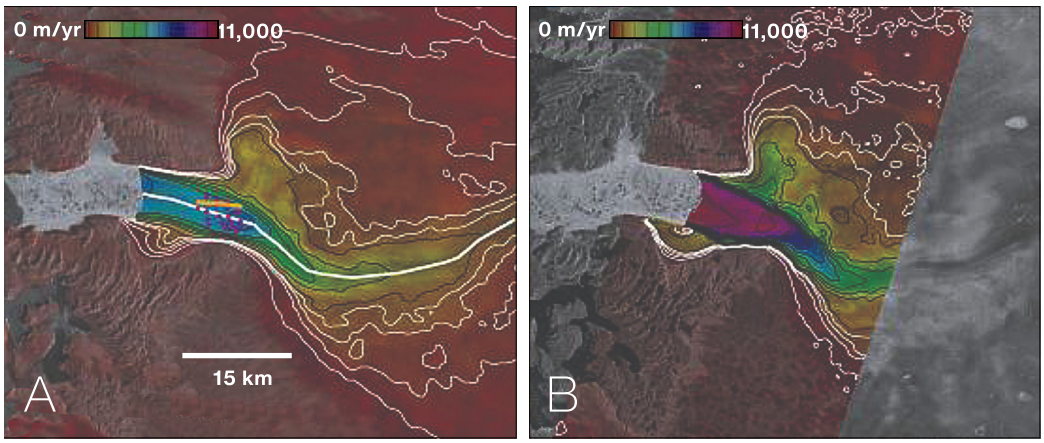

FIGURE E-21

Ice flow velocity at Jakobshavn Isbrae. Ice flow velocity determined from speckle-tracking as color over SAR amplitude imagery showing the rapid speed up of Jakobshavn Isbrae from a) February 1992 (ERS-1) to b) October 2000 (RADARSAT). In addition to color, speed is contoured with thin black lines at 1000-m/yr intervals and with thin white lines at 200, 400, 600, and 800 m/yr (Joughin et al., 2004a). Over the last few decades, glaciers in Greenland have sped up on average by more than 30% (Rignot and Kanagaratnam, 2006; Moon et al., 2012). NISAR will provide continuous observations of such speedup to provide a better understanding of the processes governing such change.

E.3 CRYOSPHERE

The cryosphere represents Earth's ice and snow-covered areas. In particular, NISAR science objectives will primarily focus on the ice sheets, glaciers, sea ice, and permafrost. Although these are the primary focus, the mission will ultimately enhance science and application studies aimed at many other elements of the cryosphere such as snow cover and lake and river ice. The Decadal Survey articulated several overarching cryosphere-related objectives. Of these, NISAR will contribute to addressing the following scientific objectives:

- Characterize and understand the processes that determine ice sheet and glacier sensitivity to climate change.
- Incorporate ice sheet and glacier displacement information into coupled ice-sheet/climate models to understand the contribution of ice sheets to sea level change.
- Understand the interaction between sea ice and climate.
- Characterize the short-term interactions between the changing polar atmosphere and changes in sea ice, snow extent, and surface melting.
- Characterize freeze/thaw state, surface deformation, and permafrost degradation.

E.3.1 ICE SHEETS

Spaceborne InSAR and altimetry observations have already made major changes to our perception of how ice sheets evolve over time (Alley et al., 2005; Bamber et al., 2007; Joughin and Alley, 2011), overturning the conventional wisdom that ice sheets respond sluggishly to climate change at centennial to millennial time scales (e.g., Paterson, 1994). Numerous observations have shown that large Greenlandic and Antarctic glaciers and ice streams can vary their flow speed dramatically over periods of seconds to years (e.g., Bindschadler et al., 2003; Joughin et al., 2004a; Rignot and Kanagaratnam, 2006; Rignot, 2011c). It was this unanticipated variability that prompted the Intergovernmental Panel on Climate Change (IPCC, 2007) to conclude:

Dynamical processes related to ice flow not included in current models but suggested by recent observations could increase the vulnerability of the ice sheets to warming, increasing future sea level rise. Understanding of these processes is limited and there is no consensus on their magnitude.

Thus, NISAR's major ice sheet goals are to provide data critically needed to remove this gap in our understanding of the fundamental processes that control ice-sheet flow. This knowledge is required to reliably model ice-sheet

response to climate change and to project the resulting contribution to sea level change over the coming decades to centuries.

Because of the highly variable dynamics of outlet glaciers and ice streams, recent observations provide only isolated snapshots of ice-sheet velocity (Figure E-21; Howat et al., 2007; Joughin et al., 2004a; Rignot and Kanagaratnam, 2006; Rignot et al., 2011a). Spaceborne altimeters designed for mapping large-scale ice changes (e.g., ICESAT-I/II) under-sample many of the narrow fast-moving glaciers with large thinning rates–up to 100 m/yr–(Howat et al., 2008). Therefore, special care must be taken in how such observations are evaluated, particularly when extrapolating to the future, since short-term spikes could yield erroneous long-term trends. In addition to indicating a trend of sustained speedup, recent results are significant in that they show flow speed and mass balance can fluctuate rapidly and unpredictably (Moon et. al., 2012). While existing sensors have revealed major changes, these observations, cobbled together from a variety of sensors, are far from systematic. Prior to 2015, there were no systematic observations by existing or future sensors with which to characterize ice-sheet flow variability and with which to develop the required modeling capability to accurately project sea level trends. While such observations began with the launch of the Copernicus Sentinel 1A/B SARs and the USGS/NASA Landsat 8 optical instrument, existing coverage does not meet community needs in terms of resolution, coverage, and accuracy. Therefore, to accurately determine ice discharge variability, to gain a firm understanding of the dynamics that drive mass balance, and to avoid aliasing these rapidly changing variables, NISAR will acquire annual-to-sub-annual observations of outlet-glacier and ice-stream variability.

Ice-sheet velocity and surface elevation are two of the most important observables for studying ice dynamics. While observations from space are largely limited to the ice sheet's surface, when used in conjunction with ice flow models, such data can be inverted to determine basal and englacial properties (Joughin et al., 2004b; Larour et al., 2005; MacAyeal, 1993; Morlighem et al., 2013). In particular, ice-flow velocity and accurate ice topography (ICESAT-II) can constrain model inversions for basal shear stress. Observations of changes in ice-sheet geometry and the associated response also provide important information. For example, inversions such as shown in Figure E-22 provide the magnitude of the shear stress, but not the form of the sliding law. Observations of the spatio-temporal response to an event such as the loss of ice-shelf buttressing can be used to derive parameters such as the exponent of a power-sliding law or may indicate another type of sliding law is needed (e.g., plastic) (Joughin et al., 2010b). Sustained and frequent sampling of rapidly changing areas by NISAR will provide the velocity observations necessary for such studies in place of the scattershot observations current systems provide, with ICESAT-II providing complementary elevation data.

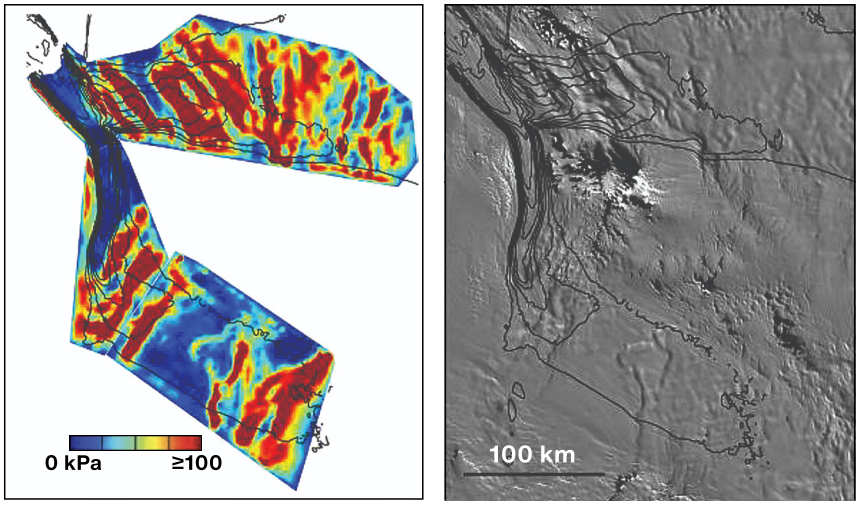

FIGURE E-22

Basal shear stress estimate for Foundation Ice Stream (left) and corresponding Mosaic of Antarctica (MOA) image (right). Flow speed is shown with 100-m/yr contours (black lines). The shear stress estimate was determined using velocity data that is similar to what NISAR will provide.

Antarctica has several large floating ice shelves that extend over the ocean from the grounded ice sheet. In contact with the ocean and at low elevation, these elements of the coupled ice-sheet/ice-shelf system are the most at risk in a warming climate (Rignot et al., 2013). While the loss of floating ice has no direct impact

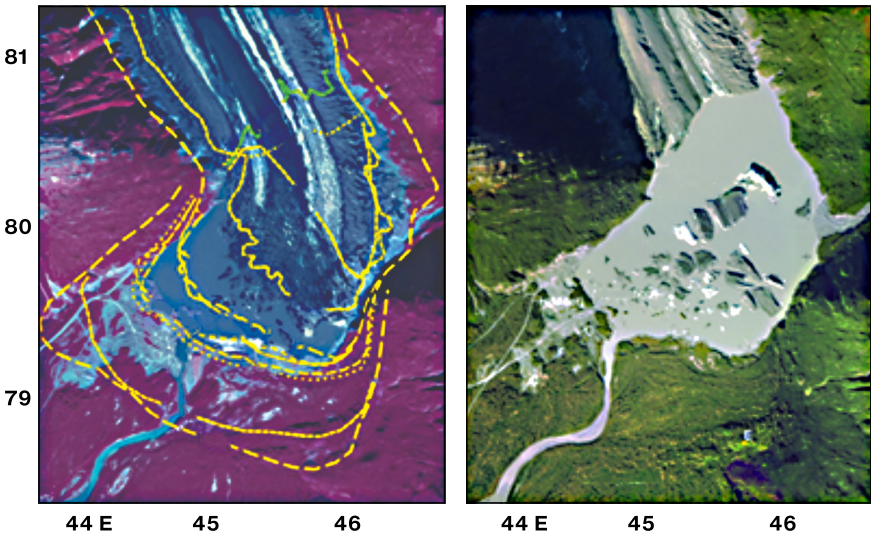

FIGURE E-23

Glacier change over time. From Kienholz (2010). Aerial imagery showing the terminus of Valdez Glacier. (left) AHAP 1978 false color orthophoto. Historical termini positions are indicated by yellow lines. The green line indicates the terminus position measured in summer 2008 using GPS. (right) True color Aero-Metric orthoimage of 2007. The rock covered terminus of the glacier can be seen at the approximate position of the green line marking the 2008 position on the left image.

on sea level, ice shelves buttress the flow of inland ice and a reduction of this buttressing as ice shelves have thinned or disintegrated is believed to be responsible for the majority of current mass loss in Antarctica (Payne et al., 2004; Rignot et al., 2004; Scambos et al., 2004; Joughin et al., 2012). Critical to studying ice shelves is accurate knowledge of velocity and thickness, which determine the mass flux distribution, the horizontal divergence of which can be used to infer basal melt rates (Jenkins and Doake, 1991; Joughin and Padman, 2003; Rignot and Jacobs, 2002). Unlike sparse spatial and temporal sampling from other missions, for the first time NISAR will provide comprehensive ice-shelf velocity data. Similarly, ICESAT-II will provide comprehensive measurements of ice shelf elevation, which can be used to determine thickness by assuming hydrostatic equilibrium. Together, these data will provide the required observations to derive time series of ice-shelf melting around Antarctica and areas of Greenland where ice shelves still exist. These observations of ice flow on floating ice will serve multiple purposes. First, along with observations of velocity for the grounded ice-sheet periphery at high temporal resolution, NISAR will provide an advanced warning system for rapid shifts in ice flow and the resulting contributions to sea level rise. Second, these observations will provide critical constraints to ocean models at the ice-ocean boundary, which are needed to evaluate the skill of these models, to improve the models through massive data assimilation, and to reduce uncertainties of sea level rise projections.

E.3.2 GLACIERS AND MOUNTAIN SNOW

Glaciers and snow-covered regions are important for many applications such as melt runoff, hydropower stations, and long-term climatic change studies. Because they are often cloud-covered, microwave remote sensing is particularly useful for studying these areas due to its all-weather capability and ability to image through darkness. Radar backscatter is influenced by material properties like surface roughness and dielectric constant and can therefore offer considerable information in relatively featureless snow-covered terrain. The potential of SAR imagery for monitoring of snow cover was discussed as early as 1980 (Goodison et al., 1981). The attenuation length of microwave radiation in cold dry snow is large and this kind of snow is transparent and therefore invisible to radar (Rott and Davis, 1993) unless the snow pack is very deep or at radar frequencies above ~10 GHz (i.e., a factor of 5–10 higher than NISAR). However, when the liquid water content of snow exceeds about 1 percent, the attenuation length is reduced to a few centimeters, and the radar backscatter is usually dominated by surface scattering (Ulaby et al., 1984). The question of whether such snow can be discriminated from snow-free terrain depends on the geometric and electromagnetic characteristics of snow cover and snow-free terrain. Various studies have shown that wet snow cover can be generally distinguished from snow-free terrain using SAR data (Baghdadi et al., 1997). Many studies have demonstrated that use of multi-polarization SAR and InSAR techniques have substantially improved snow cover mapping and detection of dry and wet snow. Periodic mapping of snow cover is important to estimate the runoff and understand the effect of climate change on mountain ecosystems.

Himalayan glaciers feed into three major river systems of India, and glaciers in many other

parts of the world are an important source of fresh water. Thus, runoff from changes in snow cover and glacier volume plays an essential role in long-term water resource management and hydropower planning activities. Glaciers have generally been in retreat during the last century, with a marked acceleration in global mass-losses in recent years (Kaser et al., 2006; Meier et al., 2007). For instance, glaciers in Alaska (see e.g., Figure E-23) are currently retreating at some of the highest rates on Earth (Arendt et al., 2002; Hock, 2005). Such rapid changes in glacier extent and volume will modify the quantity and timing of stream flow, even in basins with only minimal glacier cover (Hock and Jansson, 2006). In highly glaciated regions, at times the increases in runoff can exceed the runoff changes from other components of the water budget. Thus, in glacierized drainage basins, accurate simulation of glacier response to climate change cannot be achieved without high-resolution observations, such as those NISAR will acquire, of glacier dynamics, wastage, and retreat (Hock, 2005). In addition to influencing water resources, snow and glaciers pose hazards to nearby populations (e.g., Kaab et al., 2005). For example, glacier advance can threaten infrastructure while glacier-controlled dams (usually below the surface) can fail catastrophically causing glacial lake outburst floods (GLOFs). While NISAR observations are unlikely to be frequent enough to provide immediate warning for GLOFs, subglacial lakes can be detected and monitored by InSAR to provide some indication of the hazards they create (e.g., Capps et al., 2010).

The global distribution of glaciers, including those in Greenland and Antarctica but not connected to the ice sheets, contribute significantly to global sea-level rise and are sensitive indicators of climate change. A consensus estimate (Gardner et al., 2013) indicated that glaciers contributed 259 ± 28 Gt/yr (0.71 ± 0.08 mm Sea Level Equivalent (SLE)/yr) during the period of October 2003 to October 2009, even though they make up less than 1 percent of the Earth's global ice volume (roughly 0.5–0.6 m, SLE). Thus, glaciers contribute to present sea level rise at a rate similar to the combined rate from the Greenland and Antarctic ice sheets (289 ± 49 Gt/yr, Shepherd et al., 2012). Hence, any attempt to close the sea-level budget of the past and coming decades/centuries needs to include the contribution from glaciers as well as ice sheets. Therefore, just as for ice sheets, frequent observations of glaciers by NISAR are needed to understand glacier contributions to sea level rise.

E.3.3 SEA ICE

Within the global climate system, sea ice is an indicator of climate change, primarily due to the powerful ice-albedo feedback mechanism that enhances climate response at high latitudes. Over the satellite period of observations, Arctic sea ice has thinned, shifted from predominately perennial ice to seasonal ice, and reduced in extent at the end of summer by over 40 percent since 1979. The resulting increase in open water, subsequent reduction in surface albedo, and increased absorption of incoming radiation appears to be enhancing the strong ice-albedo feedback mechanism. The increase in open water extent has also led to an increase in ocean surface temperatures, marine productivity and shifts in the marine ecosystem composition, and an increase in wave height that further impacts the margins of the sea ice cover, essentially extending the summer melt period. In addition to a continued reduction in the summer minimum extent, the Arctic is also undergoing a significant reduction in winter ice extent, due in part to a shortened winter season. By contrast, sea ice in the Southern Ocean, largely composed of thinner seasonal ice, underwent only modest changes in extent over the decades. However, 2011–2015 was an extended period of anomalous increases in extent which have been followed since 2022 by consecutive years of the lowest levels of minimum ice extent observed in the satellite record to date.

Sea ice thickness is a time-integrated result of both thermodynamic and dynamic processes. Thus thickness is a direct response to changes in both the atmosphere and ocean, in particular

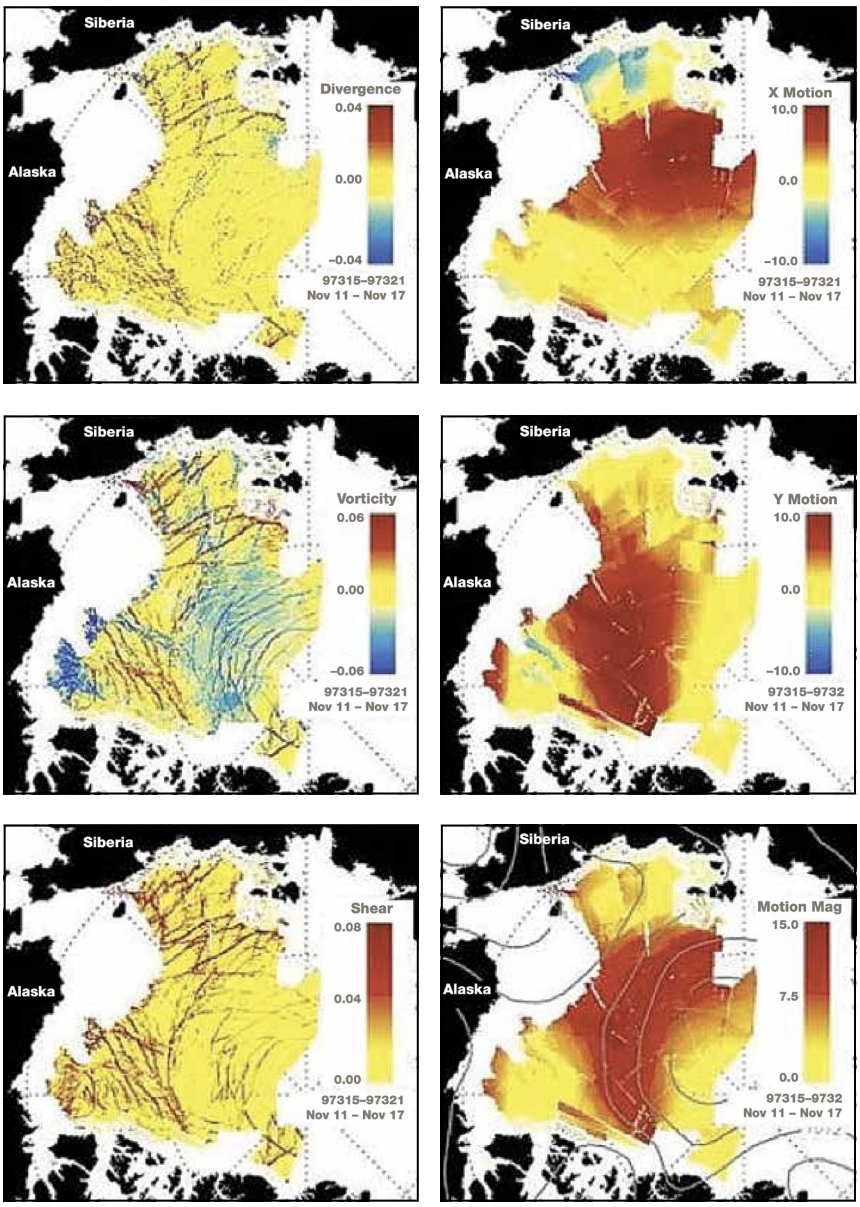

FIGURE E-24

Sea ice motion and deformation in the Arctic. Sea ice deformation (left column) and motion (right column) of the Arctic Ocean ice cover at a length scale of ~10 km derived from SAR data. (Deformation units: per day; motion units: km/day). (Kwok, 2010).

temperature as observed in the ice-albedo feedback mechanism, followed by winds and currents. As the Arctic sea ice has thinned, there has been a subsequent increase in ice motion and deformation. In comparison, there is a paucity of information on sea ice thickness, motion, and deformation for the Southern Ocean and whether any changes to these parameters are occurring. With the recent and expected continuing increases in global ocean temperatures, wind speed, and wave height, what will be the response and rate of impact on the contrasting polar sea ice regimes? Will the response influence the ice albedo-temperature feedback, for example, with enhanced changes in the ice thickness distribution and motion/deformation? Such changes in thickness and deformation are not well captured in climate models, hence extending the observational record with NISAR in both polar regions will lead to improvements in the understanding of atmosphere-ice-ocean interactions and fluxes as well as in the short-term forecasting of changes in the sea ice cover.

Away from the margins of the sea ice cover, the response of the ice cover to large-scale gradients in atmospheric and oceanic forcing is concentrated along narrow zones of failure (up to tens of kilometers in width) resulting in openings, closings, or shears. In winter, openings dominate the local brine production and heat exchange between the underlying ocean and the atmosphere. Convergence of the pack ice forces the ice to raft or pile up into pressure ridges and to be forced down into keels, increasing the ice-ocean and ice atmosphere drag. A combination of openings and closings is typical when irregular boundaries are sheared relative to one another. These processes shape the unique character of the thickness distribution of the ice cover and have profound impacts on the strength of the ice and its deformation properties over a wide range of temporal and spatial scales. A key observation for understanding the basin-scale mechanical character of the sea ice cover is how the ice moves at different length scales. These observations are of importance in quantifying and modeling sea ice behavior in a changing climate and in facilitating operational applications.

Systematic mapping of the sea ice with spaceborne SAR has proven to be the ideal method to measure small-scale detailed sea ice motion at the scales required to quantify sea ice deformation, based on the fine resolution, increased temporal sampling in the polar regions due to converging orbits, and operations independent of cloud cover and daylight. Mapping is required at regular intervals (3–6 days) with sufficient resolution (50–100 m) to be able to

identify morphological features of the sea ice cover such as ridges and the edges of floes. In the late 1980s and most of the 1990s, the availability of small volumes of ice motion data from the European SAR satellites (ERS-1, 2) allowed examination of sea ice strain rates at 5–10 km length scales and demonstrated the utility of these measurements for sea ice studies. The most significant results to date were obtained with the systematic mapping of the western Arctic Ocean obtained by RADARSAT-1, where the collaborative mission between the Canadian Space Agency and NASA enabled systematic data collections during the winter months for nearly all of the mission's lifetime, from 1996 through 2008 (Figure E-24, previous page). Using both Eulerian and Lagrangian tracking, which enables the continuous tracking of grid elements over time, ice trajectory and detailed deformation of a grid element were observed. In addition, these data were used to derive the age of newly formed ice and the loss of ice area due to ridging.

The decade-long ice-motion dataset from RADARSAT-1 has been used to quantify the various measures of opening, closing, and shear, and to estimate ice production and thickness. The data reveal that the extent of the activity, persistence, orientation, and length scale of the fracture patterns are quite remarkable. The abundance of these quasi-linear fractures is correlated to motion gradients and material strength, and they are organized into coherent patterns that persist for days. Contrast in the deformation shows that there are distinct differences in the deformation-induced ice production, and the density of these features in the seasonal and perennial ice zones. The long-time series of SAR ice motion were also used to determine the flux of ice out of the Arctic Ocean on an annual basis. These were combined with SAR-derived deformation and ice production estimates as well as independently derived sea ice thickness measurements to estimate annual changes in sea ice volume. RADARSAT observations show that deformation-induced ice production in the seasonal ice zone is greater than 1.5 times that of the perennial ice zone. The younger seasonal ice is mechanically weaker; this points to a negative feedback mechanism where higher deformation and ice production is expected as the ice cover thins. Such important information is not available in the Southern Ocean, where only limited SAR-derived ice motion maps have been generated of the Ross Sea.

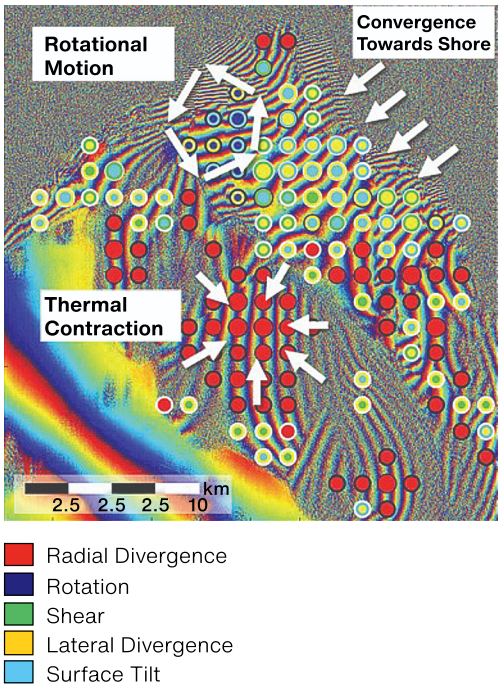

FIGURE E-25

Small-scale motion of landfast ice. Physical interpretation of small-scale motion within otherwise stationary land fast ice based on simple physical models. Hypotheses for motion regimes are indicated by white arrows and associated text boxes.

In the coastal margins of the Arctic, InSAR observations are useful for observation of landfast ice, which is sea ice that remains attached and grounded to the coastal land margin, i.e., ice that is held fast to the land. Within the moving pack ice, the ice cover is changing too rapidly to derive coherence with InSAR. However, landfast ice, by definition, remains unchanged for long periods of time. Thus, InSAR observations are useful for the automated detection of the extent of landfast ice and information on the mechanisms by which such ice attaches or detaches from the coast (Figure E-25). There is an increasing presence of human activities in the Arctic coastal margins due to ice retreat, related to oil and mineral exploration, increasing ship traffic, and the heightened need for a military presence previously not required. Along with the increasing

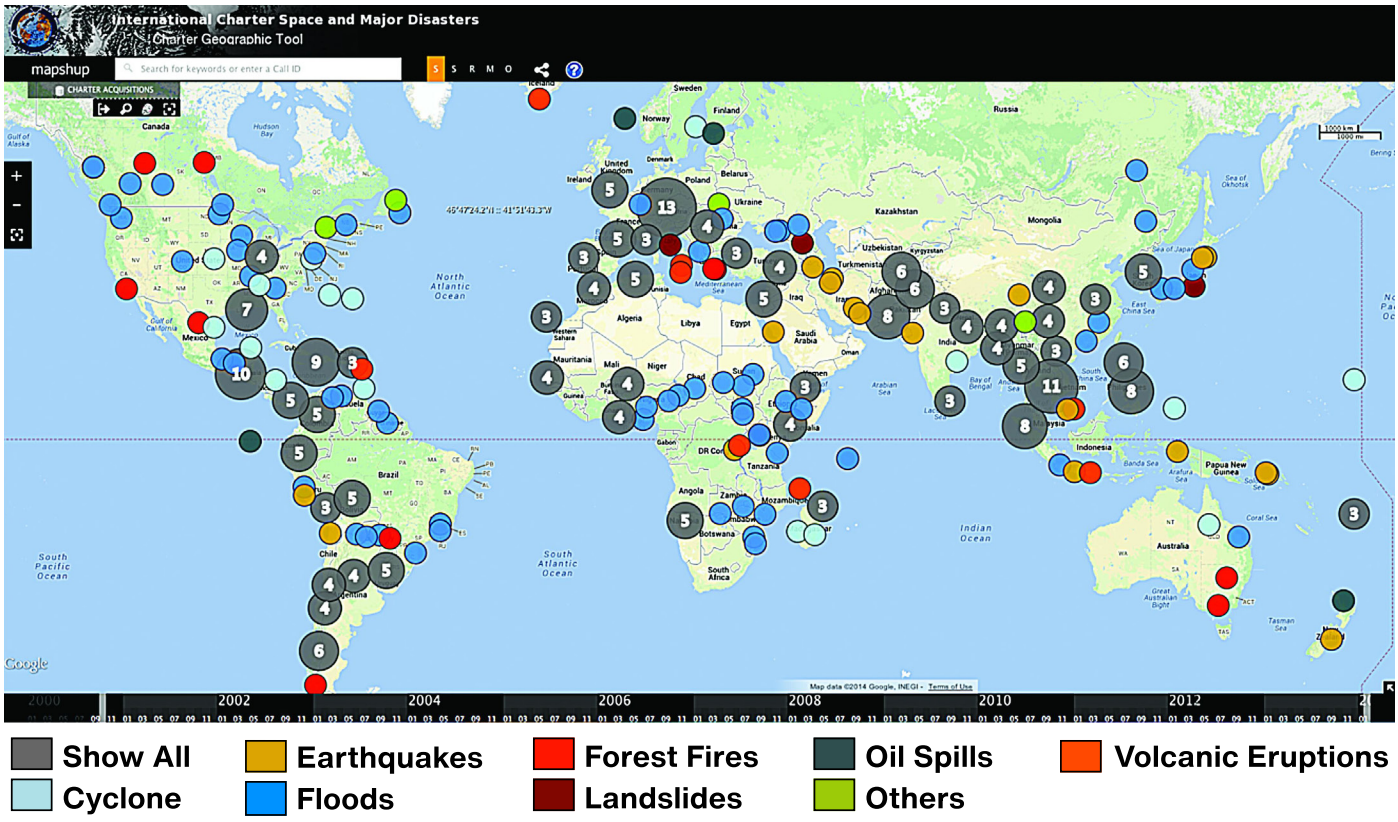

FIGURE E-26

International charter activations. Map of 474 international charter activations since the formation of the Charter in 1999 to February 2014. The color of the circle indicates the activation disaster type. Regions with multiple activations are shown as gray circles, with the number of activations in white text, and the circle sized to represent the number of activations (http://www.disasterscharter.org/).

potential of a hazardous event such as an oil spill, the need to improve the environmental understanding and monitoring of the dynamic coastal margins is clear.

The NISAR mission enables the unprecedented capability to derive ice motion and deformation for systematic mapping of both polar regions, to the extent previously not possible with international SAR missions. While RADARSAT-1 provided excellent motion products for the western Arctic, the dynamic eastern portion of the Arctic was not mapped, and essentially, neither was the Southern Ocean, so detailed observations of those regions are limited. The Southern Ocean provides a challenging mapping scenario compared to the Arctic, due to its relatively lower latitude range and that the ice motion is not constrained by land as in the Arctic. NISAR will achieve systematic and detailed mapping of the Southern Ocean sea ice cover for the first time. Mapping of the Arctic Ocean will enable continuing deformation observations of the rapidly changing and likely still thinning sea ice cover.

NISAR will enable precise motion and deformation measurements of the sea ice cover in view of the satellite, at an unprecedented level of detail and scope. These measurements will be used to improve models of the sea ice circulation and energy fluxes within the global climate system. When combined with thickness observations, such as those planned to be obtained from ICESAT-2, critical time series of sea ice thickness distribution and mass balance parameterization can be utilized within coupled climate models to improve the prediction of sea-ice changes and their role in Earth's climate system, based on both polar oceans (Kwok, 2010).

E.4 APPLICATIONS

The same data that are used by the science disciplines to improve understanding of physical and ecological processes can be used by the

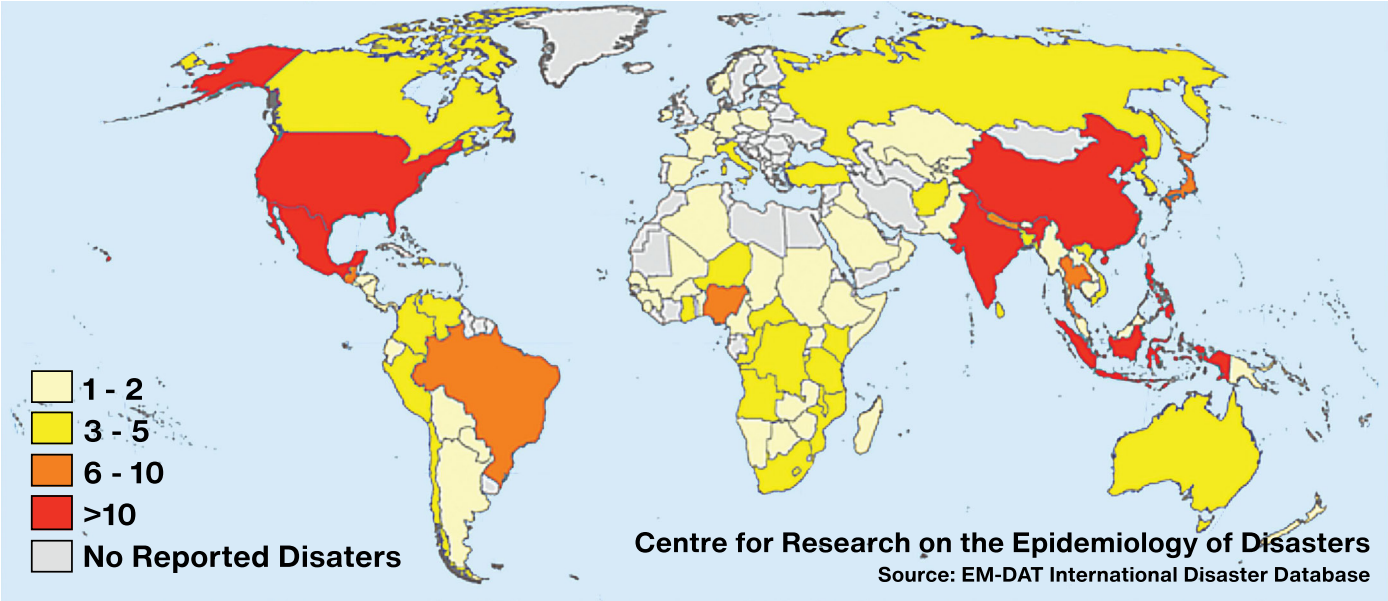

FIGURE E-27

Natural disaster occurrence statistics for 2011. The US and India have among the highest rates of natural disasters.

applications community to inform decision making, improve risk management, assess resource status, and respond to and recover from disasters. The involvement of the applications community in the development of NASA's Decadal Survey mission requirements greatly expands the societal benefit and functionality of the NISAR mission to include cross-disciplinary and applied science research; opens new collaborative opportunities between scientists, engineers, and policy makers; and significantly augments science unrelated to the primary mission goals. NISAR will contribute to the following activities relevant to applications, among others:

- Improve hazard resilience by providing the observational foundation guiding future tasking, modeling, and forecasting strategies.
- Detect early transients associated with natural, anthropogenic, and environmental and extreme hazards.
- Characterize evolving disasters in support of response and recovery efforts and better understanding of fundamental science.
- Support ecosystems applications in forestry and agriculture.
- Determine environmental factors that influence the coastal processes such as erosion/deposition and coastal land use/land cover change.
- Contribute to India's science, applications, and disaster response.

The NISAR mission, through the mission science requirements, has placed an emphasis on disaster/hazard response because of the unique value of frequent and regular observations of nearly all land across the globe. This focus acknowledges the value of the mission to both the U.S. and India (Figure E-27). In most cases, the driving requirements for response are met by the science and applications communities' needs, with the exception of rapid processing for response, which is incorporated into the mission system design.

Every year, natural and technological hazards in the United States cost an estimated $1 billion per week in the form of lives lost and public and private properties destroyed.

Between 2004 and 2013, there have been an average of 147 disaster declarations per year in the United States (http://www.fema.gov/disasters/grid/year). In 2011, both India and the United

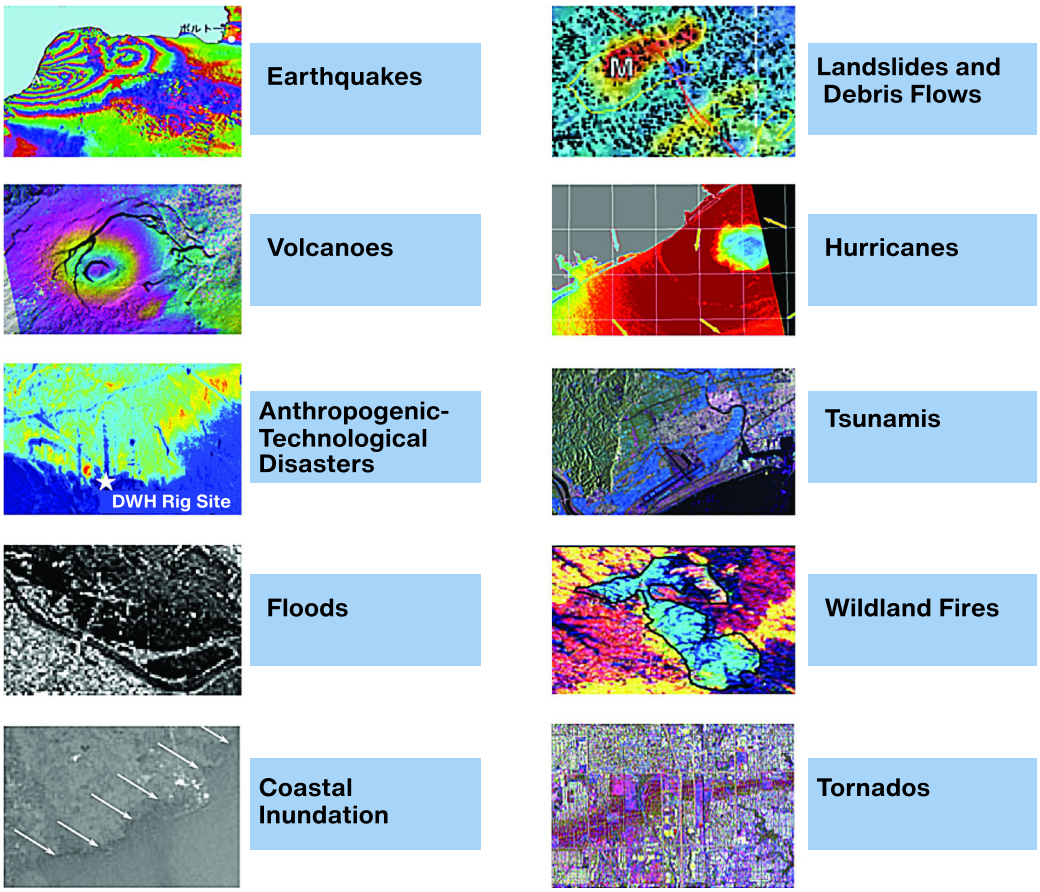

FIGURE E-28

SAR utility for disaster response. NISAR will provide response products for ten of the fifteen disasters identified by the Subcommittee on Disaster Reduction. NISAR data will directly contribute to providing information supporting all disasters shown except tsunamis, for which it will potentially support assessment of flooding and damage to land and infrastructure.

States had more than 10 major natural disasters with an economic cost >$5 billion in the U.S. alone (Figure E-27).

Historically, satellite imagery has been utilized on an ad-hoc basis for disaster response and hazard science. In 1999, the establishment of the International Charter (https://www.disasterscharter.org), an agreement that as of 2024 includes 17 of the world's space and operational agencies and satellite management organizations, significantly advanced hazard science by providing a global mechanism to collect and distribute satellite imagery in support of emergency response efforts during significant disasters with the objective to minimize the loss of life and property. As of January 2014, the International Charter has been activated 474 times since its inception, providing satellite imagery for global disasters regardless of geopolitical boundaries for a wide range of disasters, including earthquakes, floods, volcanic unrest, cyclones, fires, landslides / debris flows, and anthropogenic disasters (Figure E-26).

The Subcommittee on Disaster Reduction (SDR) identified four key factors for successful hazard mitigation and developed six Grand Challenges to provide a framework for sustained federal investment in science and technology related to disaster reduction; the SDR vision has been incorporated into the science and applications objectives of NISAR for 10 of the 15 hazards (Figure E-28) recognized by the SDR. Specifically, NISAR hazard response applications objectives are part of the traceability matrix for the mission and cover distinct areas of the hazard cycle: hazard detection, disaster characterization, societal impact, and societal integration. Hazard detection requires the systematic collection of geodetic observations to detect, characterize, and model potential hazards and disasters.

Disaster characterization requires rapid disaster assessment to develop the situational awareness of the primary hazard and the ability to recognize and characterize secondary hazards associated with the primary event. Societal impact requires rapid, damage assessment for emergency rescue efforts; system integrity assessment of lifelines, infrastructure (i.e., pipelines, levees, dams, urban corridors, factories), and environmentally sensitive regions; as well as long-term facilitation of societal/environment recovery efforts. Finally, societal integration combines hazard response and hazard science with societal needs to improve hazard mitigation efforts by enhancing hazard resilience science, providing the observational foundation guiding future tasking, modeling, and forecasting strategies.

The following sections present the range of NISAR applications, generally split among:

- Ecosystem applications
- Geologic and land hazard monitoring
- Critical infrastructure monitoring
- Maritime and coastal ocean applications
- Hydrology and underground reservoirs

The NISAR applications topics include disaster/hazard response, which cuts across all the above categories. In many cases, the difference between science and applications is one of information usage, with applications end users interested in regularly available observations or operationalizing product generation for situational awareness, resource management, decision support, and event response.

E.4.1 ECOSYSTEMS: FOOD SECURITY

To feed a growing population of more than 8 billion, food production and supply occur on a global basis. To better guide policy and decision making, national and international organizations work to transparently monitor trends and conditions of agriculture on a timely basis. Because of the variable nature of planting and harvesting practices, efforts such as these are labor intensive and time-consuming. Among the organizations that track the trends in agricultural production on a global basis is the United Nations Food and Agriculture Organization (FAO). According to FAO's 2015 statistics, over eleven percent of Earth's land surface (1.5 billion hectares) is used for farming. With an increasing population, after taking into account expected improvements in land use efficiency, the amount of land dedicated to food production is expected to grow 7 percent by 2030 to keep up with demand. This increase is equivalent to an additional 90 million hectares, roughly the size of Texas and Oklahoma combined. With the world's population critically dependent on the timely production of food and freshwater resources, the need is greater now than ever before for the application of technology to assure that population needs are met. Among the technical tools that are used to address these issues are the satellites that provide synoptic views of the globe from space. Satellite sensors are routinely used to guide decision-makers and commercial interests alike in scheduling future plantings and monitoring the effects of policy changes and a dynamic global marketplace.

The NISAR mission will provide dependable

FIGURE E-29

Two-frequency radar image of the Dnieper River growing region collected in 1994 by NASA's Spaceborne Imaging Radar-C (SIR-C). In this false color image, developing wheat fields show up as bright magenta and forests as the bright white patches that follow the river's border.

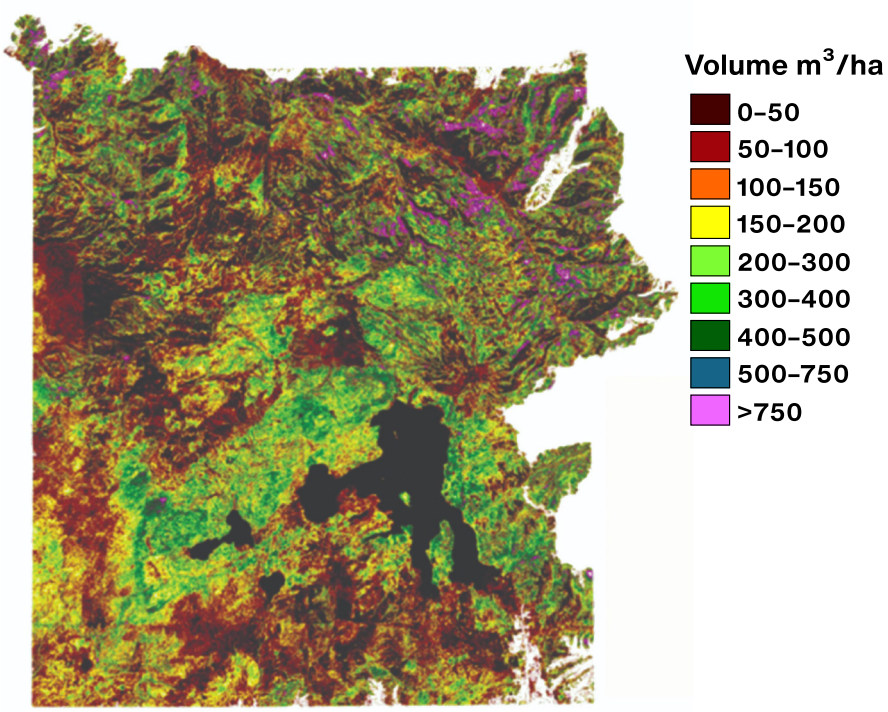

FIGURE E-30

L-band airborne radar data collected over Yellowstone National Park in 2003 was used to develop maps of forest volume and fire fuel load to help with park management and fire suppression for improving the recreational resources and revenues (Saatchi et al., 2007).

observations throughout the growing season. Radar imagery will provide near-weekly observations of almost all land areas that complement the optical data and provide independent information that is sensitive to the changing structure and moisture conditions of the crops being imaged. NISAR's data products will be available on an open access basis.

The structures of different crop and land cover types provide a rich variety of responses to the radar illumination in terms of varying polarization and frequency signatures. Because of the rapid, time-varying nature of crop rotation, growth, and harvest, frequently repeated radar observations can be used to determine both the type of crop and its stage of growth. Information like this is used to predict the health of the region's crops and the planned agricultural output. Figure E-29 shows data collected by SIR-C, a NASA mission launched on board the space shuttle in 1994. Data from areas such as the Dnieper River region of Ukraine were collected at study sites distributed throughout the globe and have been used by NISAR mission planners and other space agencies worldwide to understand how radar data can be used to improve our knowledge of the world around us. Modern day SARs, such as the Canadian Space Agency's RADARSAT and the European Commission's Sentinel satellite series, have benefited from the SIR-C mission and are being actively used today.

E.4.2 ECOSYSTEMS: FOREST RESOURCE MANAGEMENT

Forest ecosystems provide timber, fuel, and bioproducts as well as a variety of benefits by sequestering carbon from the atmosphere into the forest, purifying water and air, and maintaining wildlife habitats. One of the greatest challenges facing forest managers in the U.S. and elsewhere is to maintain the health and resilience of forest ecosystems. This requires a coordinated effort for systematic monitoring of forest cover, volume, and productivity, to develop techniques and policies for improving the stock and sustainable use of woody biomass. Optical satellite observations, such as from Landsat have played a major role in monitoring the forest cover and changes globally. But with the advent of modern radar techniques such as NISAR, frequent and uninterrupted observations of forest volume can become a reliable source of data and a tool for forest managers to assess forest status.

Forest managers and the agroforestry industry need accurate and timely data over large areas to assess forest development and prescribe actions necessary to achieve regeneration objectives. Increasing emphasis on ecosystem management, escalating silvicultural (e.g., reforestation) treatment costs, evolving computer-based decision support tools, and demands for greater accountability have produced significant demands for spatial data on forest structure and productivity at national and subnational scales globally.

In the U.S., the Forest and Rangeland Renewable Resources Planning Act of 1974 directed the Secretary of Agriculture to make and keep current a comprehensive inventory for a prospective

Renewable Resources Assessment of the forests and rangelands of the U.S. These assessments were focused on analysis of present and anticipated uses, demand for, and supply of the renewable resources, with consideration of the international resource situation and with a strong emphasis of pertinent supply, demand, and price trends. With increasing threats to forest resources from droughts, fire, and fragmentations, tracking the forest health, biomass stock, and tangible products such as timber has become a part of national security both at home and globally.

Moving toward an inclusive monitoring system, which can augment and enhance the national inventory data, requires a departure from the past remote sensing of only the forest cover. New active remote sensing techniques using both lidar and radar have the capability to measure both forest height and biomass. This high spatial resolution data on forest structure and biomass density can be readily integrated into existing forest inventory systems. The NISAR mission will observe forests weekly and collect the information needed to map global forests and shrub lands multiple times per year. Data products will be made available at intervals that are commensurate with the need of forestry organizations and industry in the U.S. and around the world. NISAR images will provide near-global information sensitive to aboveground forest structure and biomass. The measurements can help monitor forest disturbance and recovery from both natural and human sources, allowing managers to improve forest health and products.

With increased urbanization in proximity to forests, along with a growing variety of vegetation (fuel types) from changes in the landscape and management strategies, there is a pressing need for accurate, cost-efficient, large-scale maps of forest biomass, fuel loads, disturbance, and recovery. Emerging remote sensing technologies can provide exactly the kind of large-scale maps needed to more accurately predict forest biomass, fuel loads, fire risk, and fire behavior.

According to biologist Don Despain, now retired from the U.S. Geological Survey in Montana, *"The technology is now there to use radar to estimate forest fire fuel load (e.g., branch and stem biomass). And the team recognized that a much more efficient, accurate, and cost-effective approach to sensing forest structure and fuels—and then mapping them—might lie at the heart of radar remote sensing technology."* Dr. Despain was instrumental in generating the fire management plans for Yellowstone National Park. Figure E-30 shows the derived forest volume from airborne radar data (AIRSAR) data over Yellowstone National Park. NISAR will provide similar measurements from a spaceborne platform to enable monitoring changes of forest volume and fuel loads across the park weekly.

E.4.3 ECOSYSTEMS: WILDLAND FIRES

Unplanned wildland fires impact tens of millions of acres annually around the world and cost billions of dollars per year to manage and control. Although fires are crucial to many ecosystems, uncontrolled wildfires can burn homes; damage infrastructure and natural resources; kill and injure emergency responders, firefighters, and the public; impact local/regional economies; and adversely affect the global environment (http://www.sdr.gov). Categorizing fire danger, detecting fires, identifying area burned, and quantifying the severity of fires is critical for mitigating the impacts of fire.

NISAR will provide a dependable observing strategy that will collect high-resolution SAR images over 90 percent of Earth's land surfaces throughout the year. NISAR imagery can provide observations that complement optical data and independent information that is sensitive to the changing structure and moisture conditions of terrestrial (land) ecosystems. Because of the dangerous nature of fires and their sometimes remote locations, remote sensing is a widely accepted tool used by national and international organizations to detect active fires, monitor impacts from fire, and assess fire danger. For

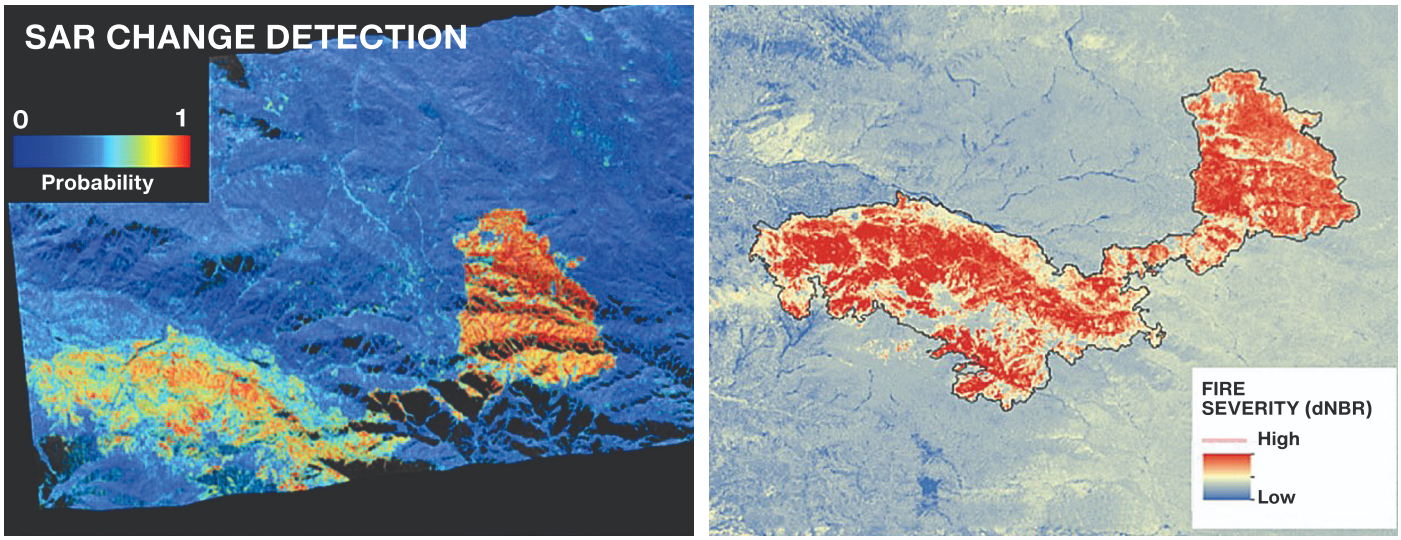

FIGURE E-31

Fire burn scar of the 2015 Lake Fire in San Bernardino National Forest, California. The left image shows probability of change derived from interferometric radar (InSAR) using 14 pre-event images and one post-fire image from an overflight on June 29, 2015, using the airborne Jet Propulsion Laboratory (JPL) Uninhabited Aerial Vehicle (UAVSAR) radar instrument. Right image is the differenced Normalized Burn Ratio (dNBR) fire severity map obtained from Landsat.

example, the National Interagency Coordination Center (NICC), the U.S. Forest Service Wildland Fire Assessment System (WFAS), the U.S. Forest Service Remote Sensing Application Center, and NASA are among the key organizations in the U.S. providing information to land and fire managers about daily and seasonal projected fire danger, active fire detections, area burnt, and fire severity. Fire danger is determined by current moisture conditions, duration of those conditions, and vegetation water content, while fire severity refers to the total environmental change caused by fire. Managers customize this information based on local expert knowledge of the total fuels available to burn to provide public service announcements and develop management strategies to mitigate potential impacts.

NISAR observations can be used for detecting vegetation and soil water content for assessing fire danger. Biomass, estimated from polarimetry data, is useful as input in fire management models for quantifying total available fuel to burn and emissions lost to the atmosphere.

The structures of different land cover types provide a rich variety of responses to radar illumination through time-varying polarization signatures. Because of rapid changes in structure and composition after disturbances like wildfire, information like this can be used to determine area burnt, even when traditional methods do not work well. NISAR polarimetry data can be used to estimate the fuel load of unburned regions, which can be used in fire management models during a wildfire to map burn area perimeters and to assess burn severity post facto (Rykhus and Lu, 2011). Maps of InSAR coherence change can be used to detect changes in the land surface associated with wildland fires, thereby mapping fire perimeters.

Time series data following a major fire can be used to track the ecosystem response and recovery and characterize secondary hazards such as debris flows and landslides. NISAR alone cannot be used to track fires: Since fires can travel tens of kilometers per day, the imaging frequency (twice in 12 days) is not sufficient to guide the hazard response community as the disaster unfolds, for which low-latency daily to sub-daily products are required. Figure E-31 shows the fire burn scar of the 2015 Lake Fire in San Bernardino National Forest, California. The radar is able to identify the more severely burned areas. Although it was possible in this particular fire to use both Landsat and InSAR data, there are many areas (e.g., Alaska) where it is frequently too dark or overcast to produce maps from optical data on a regular basis. NISAR data can improve

mapping capabilities across many areas, times of year, and weather conditions.

E.4.4 ECOSYSTEMS: FOREST DISTURBANCE

Optimal forest management requires knowledge of how forests change over time in response to natural disturbances and management activities, including invasive species; diseases; plant and animal pests; fire; changes in climate; severe weather events; pollution of the air, water, and soil; real estate development of forest lands; and timber harvest. With the world's population critically dependent on sustainably managed and utilized forest resources, the need is greater now than ever before for the application of modern technology to provide detailed and timely informational map data to the timber industry, resource managers, and forest policy makers. Satellite sensors provide synoptic views of the globe from space. This information is routinely used to guide policy for both decision-makers and commercial interests. Examples include planning forest management activities, supporting preparation of information for forest real estate transactions domestically and in foreign countries, and monitoring the effects of forest policy changes, such as logging concessions or illegal logging activities.

NISAR will provide bi-weekly observations that complement optical data and provide independent information that is sensitive to the mapping of forest disturbance, including below-canopy inundation from natural and catastrophic flooding events. Observations of Earth's land surfaces from space using active microwave sensors allows for reliable and repeated measurements to be made even under dense cloud cover. When forest canopies are disturbed, such that standing trees are partially or wholly felled or removed, or significant fractions of the upper canopy are lost, e.g., in a forest fire, the changes are reflected in a rich variety of radar signals that can be measured. The time history of changes shows when, where, and by how much the woods were altered. Figure E-32 shows data collected by the JAXA ALOS L-band SAR mission operating from 2006 to 2011. The image is a three-date color composite, where radar signatures result in color combinations that are directly related to various types of forest disturbance and regrowth.

The NISAR mission will provide data of similar quality, yet at greater observation frequency and with easy data access by the U.S. timber industry, natural resource managers, natural disaster prevention and response teams, researchers, and decision makers. The data will be a critical complement to the U.S. global land observing system by providing routine, global, cloud-free forest monitoring capacity.

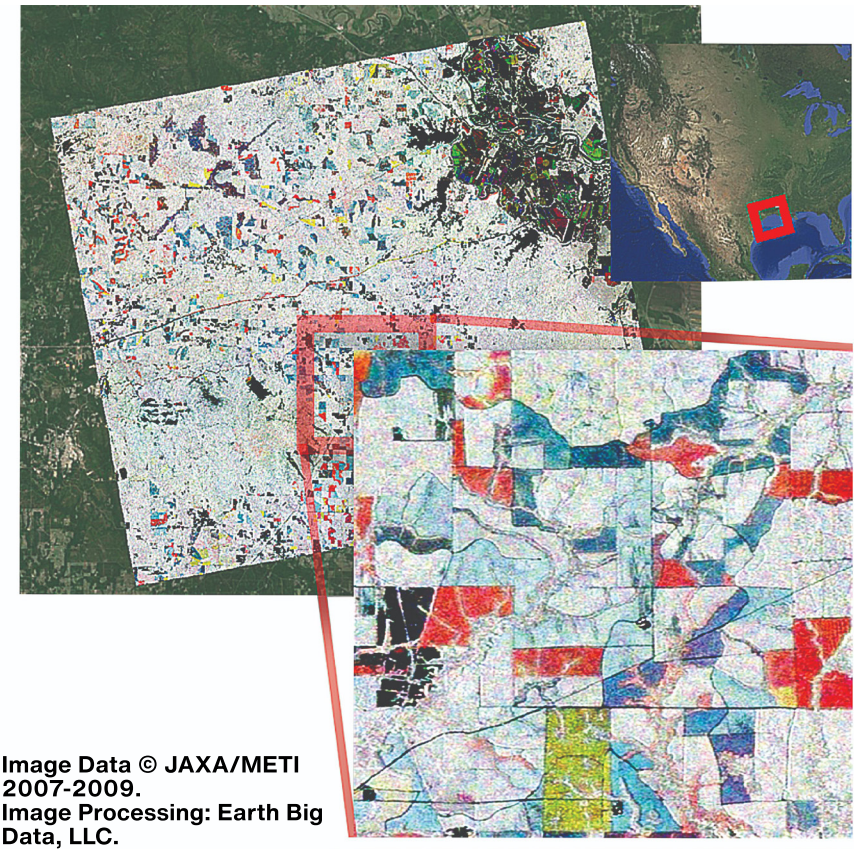

FIGURE E-32

Three-date (2007, 2008, 2009) L-Band radar image (JAXA ALOS) of timber production land in southern Louisiana, one of the most intensive timber production areas of the United States. Red and yellow colors readily show various dates and intensities of forest management activities (clear-cut and selective logging). Blue and purple colors show areas and stage of re-growing forest plantations.

E.4.5 ECOSYSTEMS: COASTAL EROSION AND SHORELINE CHANGE

Coastlines are continuously being reshaped by the interaction of strong wave action, storm surges, flooding, currents, sea-level rise, river discharge, and human activities with the local geology and mitigation efforts designed to minimize the effects of shoreline recession on coastal communities. Coastal erosion in the U.S. has increased over the past few decades and therefore represents a major coastline hazard to low-lying communities, infrastructure, and lifelines located near the coast, often in areas with high population densities. In the contiguous United States, 45 percent of the coastline is along the Atlantic or Gulf coast. The average erosion rate along the Gulf coast is nearly 2 meters a year and along the Atlantic is approaching 1 meter a year. Coastal erosion is also significant in Alaska where degradation of permafrost and reductions in coastal sea ice contribute to increased erosion rates (e.g., Eicken et al., 2011). Extreme storms, sea-level rise, land subsidence, landslides, and flooding all accelerate coastal erosion. Periodic observations of the coastline are necessary to characterize the dynamics of coastal erosion and coastal accretion processes on coastal communities and infrastructure and begin to develop models and coastal erosion/accretion scenarios for societal resiliency.

NISAR will collect systematic polarimetric SAR imagery to directly measure positional changes to the global coastline. The combined analysis of cross-polarized SAR and like-polarized images will be used to uniquely demarcate coastlines. Changes in the coastline pattern on a half-yearly interval will address the coastal dynamics scenario. Like- and cross-polarized images will be useful for monitoring the changes in the geomorphological features and land use / land cover patterns. Time-series SAR data may also be used to monitor shoreline changes. SAR data can be used to demarcate high tide lines (highest of high tides) along the coast based on manifestation of the effect of seawater on coastal landforms and landward moisture content.

E.4.6 GEOLOGIC HAZARDS: EARTHQUAKES

Earthquakes are amongst the deadliest natural hazards. There have been more than 35 earthquakes since 1900 that have killed more than 10,000 people, with seven during the period 2000-2011 (Bally, 2012) and 19 in 2020-2024 that led to activations of the International Charter to help the emergency response community directly by providing rapid imagery for the situational awareness necessary to respond to disasters. The 2004 Mw 9.1 Indonesian earthquake and tsunami, the 2010 Mw 7.0 Haiti earthquake, and the 2011 Mw 9.0 Japan earthquake and tsunami combined killed more than 450,000 people. Furthermore, through the globalization and interconnectedness of the world's economy, earthquakes can have a negative worldwide impact, e.g., the 2011 Mw 9.0 Tohoku earthquake in Japan resulted in suspension of auto manufacturing in Detroit due to a parts shortage (Wall Street Journal, 2011) and elevated insurance rates globally.

The NISAR imagery collection requirements for pure research science and earthquake applications are effectively the same – collect SAR data on every possible orbit. The key difference is that the applications community needs low-latency data to develop the situational awareness for the hazard response community. They seek to quickly understand the scope of the disaster and how to best allocate limited resources. Key questions include: What is the area affected? Where have buildings been damaged? How many? Are there secondary hazards like landslides, dam collapse, fires, etc.? Where are the safe places to evacuate people? What infrastructure and lifelines were damaged? Where was the greatest shaking or liquefaction? NISAR has the capability to automatically enable rapid processing upon downlink in response to earthquakes of significant magnitude and impact globally based on information posted by the USGS National Earthquake Information Center (NEIC). NISAR imagery will be used in a variety of ways (e.g., backscatter or coherence change), along

with integrated infrastructure and population density information and optical imagery where available to address these questions.

E.4.7 GEOLOGIC HAZARDS: VOLCANIC UNREST

Earth is home to about 1,500 volcanoes that have erupted in the past 10,000 years, and today volcanic activity affects the lives and livelihoods of a rapidly growing number of people around the globe. In the United States, more than 50 volcanoes have erupted one or more times in the past 200 years. Volcanic eruptions destroy cities and towns, eject ash clouds that disrupt air travel, and impact regional agriculture. Explosive eruptions eject ballistic rock fragments that can impact the surface up to several kilometers away from the vent. Smaller fragments are carried upward in eruption columns that sometimes reach the stratosphere, forming eruption clouds that pose a serious hazard to aircraft. Volcanic ash fall can collapse buildings, and even minor amounts can impact electrical systems and disrupt everyday life. Volcanic gases contribute to health problems and acid rain that causes corrosion and harms vegetation and livestock. Lava flows inundate property and destroy infrastructure. Volcanic mudflows have the potential to devastate entire cities even far from the source volcano. Pyroclastic flows—high-speed avalanches of hot pumice, ash, rock fragments, and gas—can move at speeds in excess of 100 km/hr and destroy everything in their path.

Worldwide, it is estimated that less than 10% of active volcanoes are monitored on an ongoing basis, meaning that about 90% of potential volcanic hazards do not have a dedicated observatory and are either monitored only occasionally or not monitored at all (Bally, 2012). As for earthquakes, the NISAR imagery collection requirements for pure research science and volcanic applications are effectively the same – collect SAR data on every possible orbit, but the applications community also needs low-latency data. NISAR has the capability to automatically enable rapid processing in response to eruptions with aviation alerts of color code Yellow or Orange based on information from the USGS Volcano Notification Service (VNS).

Many volcanic eruptions are preceded by surface deformation induced by moving magma beneath the ground. Measuring this deformation is key to understanding the potential for future eruptions. Radar observations from NISAR and other satellite missions can play a direct role in helping to monitor volcanoes and assess associated hazards, both during periods of unrest and during ensuing eruptions. Data from NISAR and other radar missions allow us to identify and monitor surface deformation at quiescent and active volcanoes through the use of radar interferometry (InSAR). Only InSAR has the capability for monitoring deformation at virtually all of the world's potentially active volcanoes on land. InSAR observations allow us to build models of subsurface magma movement preceding, accompanying, and following eruptions — information that is critically important to understand the state of activity and anticipated hazards. Radar images that allow us to monitor and characterize volcanic processes are also used to map the extent of eruptive products, like lava and ash, during an eruption. When combined with other measurements of volcanic activity, data from NISAR will facilitate the development of more realistic depictions of active volcanoes, which are critical for eruption forecasting.

E.4.8 GEOLOGIC HAZARDS: SINKHOLES AND MINE COLLAPSE

Sinkholes are formed either naturally in karst regions where carbonate rock is dissolved into groundwater or due to human activities such as oil extraction. Many sinkholes occur rapidly over a small spatial scale, so it is difficult to capture precursory deformation using remote sensing techniques. In some cases, however, there may be slow deformation before sinkholes collapse catastrophically, indicating where a future collapse is possible (e.g., Castaneda et al., 2009; Paine et al., 2012; Jones and Blom, 2014). In

addition, subsidence from mining activities and catastrophic mine collapse can be measured by NISAR (e.g., Lu and Wicks, 2010; Ismaya and Donovan, 2012).

E.4.9 GEOLOGIC HAZARDS: LANDSLIDES AND DEBRIS FLOWS

Landslides, debris flows, and other forms of ground failure affect communities in every state of the United States and result in loss of life and billions of dollars in property losses and environmental degradation every year (http://www.sdr.gov). During a two-year period between 2014 and 2016, 61 people were killed by landslides in the U.S., including 43 in the Oso landslide in Washington State (Coe, 2016). Approximately two-thirds of the United States population lives in counties where landslide susceptibility is moderate to high. Landslides are triggered by several mechanisms, including intense or long duration rainstorms, earthquakes, volcanic activity, wildland fire, coastal erosion, excavation for construction, and permafrost thaw in arctic regions. Some landslides can remain active for decades, and some of these slowly moving landslides may transition to catastrophic collapse. In areas of steep slopes, debris flows are a particularly dangerous type of landslide where slope material becomes saturated with water forming a slurry of rock and mud that moves rapidly downslope and along channels, entraining objects in its path like trees, houses, and cars, and potentially blocking bridges and tributaries. Landslide danger may continue to be high even as emergency personnel are providing rescue and recovery services.

Both L- and S-band NISAR images have the potential to significantly advance research for landslide science and provide invaluable information to the broader landslide application communities. First, NISAR's cloud penetrating imagery and coherency mapping will allow emergency responders to identify triggered landslides and assess their societal impact. For example, the 2008 Mw 7.9 Great Wenchuan earthquake in China triggered more than 60,000 landslides, blocking roads, impeding emergency response efforts, isolating and destroying villages, and damming rivers, thereby creating additional life-threatening conditions. The 1997–1998 El Niño rainstorms in the San Francisco Bay Area produced thousands of landslides and caused over $150 million in direct public and private losses (http://www.sdr.gov). Secondly, given that two-thirds of the counties in the United States have moderate to high landslide risk, NISAR will be able to identify and track motion on landslides of moderate to large size that pose a significant societal risk over wide areas. Time series analysis of these slides will detect transient changes in deformation patterns, e.g., accelerating movement, that may represent an elevated societal risk and provide early warning of catastrophic failure. Finally, time series analysis of coherence images in recent burn areas can be used to map the area of vegetation removal and then help identify and map subsequent debris flows and their spatial distribution with respect to lifelines, infrastructure, and residences. When combined with computer modeling, new debris flow hazard assessments can be made with the aim of improving societal resiliency.

E.4.10 HAZARDS: ANTHROPOGENIC TECHNOLOGICAL DISASTERS

Anthropogenic hazards, e.g., intentional attacks, industrial explosion, dam failure, etc., are broadly distributed across the globe, and events that warrant monitoring can occur with little to no prior information on the location and timing. Anthropogenic disasters can also arise in the wake of a natural disaster (e.g., nuclear reactor meltdown in Fukushima, Japan), highlighting the importance of timely generation and delivery of disaster response data after the primary event. Anthropogenic-technological disasters that impact human populations often are related to critical infrastructure, such as bridges, dams, power plants, and industrial facilities, or involve the release of material that can be distributed widely in the environment by air or water. NISAR can be tasked for rapid downlink and processing

in response to such events after a disaster occurs or in advance if it is known to be likely to occur.

E.4.11 CRITICAL INFRASTRUCTURE: LEVEES, DAMS, AND AQUEDUCTS

Water storage, conveyance, and defense structures are critical elements of a country's infrastructure that provide water and protection to businesses and communities. Levees and dams not only protect the low-lying areas but also channel water to communities and businesses where it is needed. Dams irrigate at least 10% of U.S. cropland and help protect more than 43% of the U.S. population from flooding, while satisfying 60% of the electricity demand in the Pacific Northwest (2017 NISAR Critical Infrastructure Workshop). Monitoring of levees and dams in the traditional manner through visual inspection and in situ instruments is time-consuming and personnel intensive, leading to infrequent monitoring of most areas. NISAR will increase inspections as it can image the entire U.S. several times a month regardless of cloud cover. NISAR's resolution of 6 to 12 m is a significant improvement over the Sentinel-1 resolution of 20 m, particularly for monitoring mid-size structures like levees and aqueducts.

When levees (or other water defense structures) subside, there is a high risk of catastrophic flooding. Such subsidence was observed by InSAR phase change before the Hurricane Katrina floods in New Orleans (e.g., Dixon et al., 2006). InSAR also detected motion of embankments before they failed catastrophically in Hungary, creating the worst environmental disaster in that country's history (e.g., Grenerczy and Wegmuller, 2011). Both the New Orleans and Hungary studies utilized high-resolution InSAR time series analysis methods, which will benefit from the frequent and repeated high-resolution NISAR observations. It is important to note that while these studies came after the disasters took place, with the processing of higher level products over hazard-prone areas, NISAR will allow the local, state and federal agencies to utilize remote sensing for not just disaster response, but also disaster preparation and resilience. An example of this is persistent monitoring of the California Aqueduct. Figure E-33 shows subsidence associated with groundwater withdrawal that occurred during the drought and was derived from a time series of images acquired with the UAVSAR L-band instrument from 2013 to 2017.

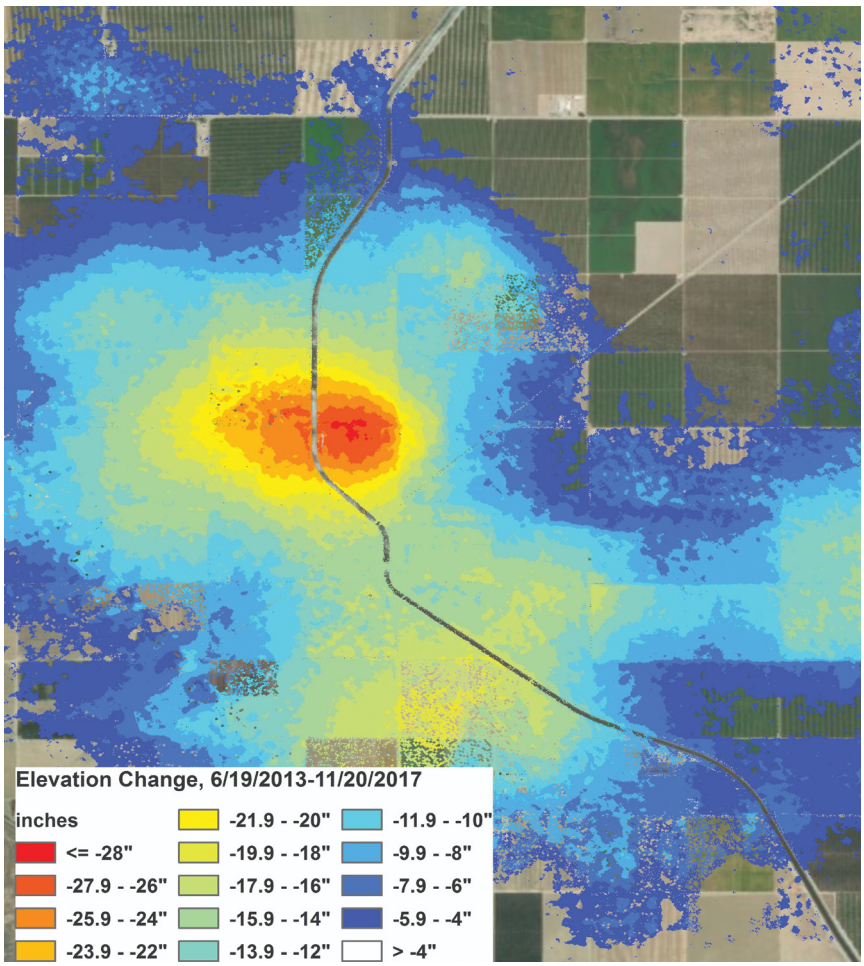

FIGURE E-33

Subsidence bowl that formed from groundwater pumping during the 2012-2016 drought in the Central Valley, California. Measurements with the L-band UAVSAR instrument were used to detect and track changes in the depth and extent of the feature during the drought. The California Aqueduct passes through the subsidence bowl, just to the west of the area having maximum subsidence.

E.4.12 CRITICAL INFRASTRUCTURE: TRANSPORTATION

Roads, bridges, railway tracks, and other transportation infrastructure or facilities require careful and continuous monitoring to maintain integrity. The regular time series of images from NISAR, analyzed to produce InSAR products, can be used to monitor the structures and the ground

nearby at scales greater than 20 m for movement that could presage damage or failure.

E.4.13 CRITICAL INFRASTRUCTURE: FACILITY SITUATIONAL AWARENESS

In many cases, critical infrastructure operators have a good understanding of their facility through instruments deployed within its confines. NISAR can augment point measurements with extended spatial coverage, and NISAR can provide information about changes happening outside the facility that could potentially impact operation or safety. NISAR can augment their knowledge by providing information in the neighborhood and regional environment in the vicinity of the facility. For example, impending or actual water intrusion into the facility could be identified during overbank flow on nearby rivers, or changes in land use identified downwind from a facility. Slow creep landslides or fault slip that cause slow degradation of performance or stress on structures could be identified.

E.4.14 CRITICAL INFRASTRUCTURE: ARCTIC DOMAIN AWARENESS

The high latitude regions of Earth are facing increased challenges related to dynamic changes of the arctic environment and modified land use patterns by polar communities and industry. In addition, as ice melts, the need to monitor northern borders for homeland security increases. SAR can provide important information to improve situational awareness and crisis response capabilities related to a range of these emerging issues including maritime security, infrastructure health, natural disaster resilience, and transportation.

The U.S. Arctic region is characterized by vast areas with limited infrastructure. Furthermore, its land and ocean areas are increasingly affected by extreme environmental conditions, threatening human lives and damaging existing infrastructure installations. On land, the annual freeze-and-thaw cycles of thick soil layers lift surfaces several tens of centimeters every winter, damaging roads and affecting the integrity of buildings and oil pipelines. An abundance of unstable slopes threatens some of the most sensitive transportation corridors in Alaska, while regular earthquakes and volcanic eruptions interfere with human life and endanger international air traffic. A recent increase in commercial activities on the opening U.S. Arctic oceans have led to rising risks of anthropogenic disasters such as oil spills and shipwrecks, which require regular large-scale remote sensing data to enable timely situational awareness.

NISAR will provide frequent, regular, and near-comprehensive coverage of Arctic land up to 77.5° N to identify and monitor surface deformation related to landslides, permafrost change, and natural hazards such as active volcanoes and earthquake zones through the use of InSAR and offset tracking. These deformations are important for the assessment of hazards affecting infrastructure and people living in the Arctic. Only InSAR has the capability of monitoring deformation across the Arctic region to provide a synoptic picture of ongoing risks. Radar images have the additional capability to detect changes in the northern coastlines, map flood extent, identify ice jams and landfast ice, monitor ship traffic (cooperative and non-cooperative) in Arctic waters, track the progression of oil spills, and identify sea ice features that may threaten infrastructure installations and ship traffic. In concert with other data, radar has shown to be an important tool in emergency response, which is important for remote areas where physical access is limited.

E.4.15 MARITIME: HURRICANES AND WIND STORMS

According to FEMA, hurricanes account for seven of the top ten most costly disasters in United States history, as of 2023. The state of Florida was struck by four major hurricanes in 2004 with losses totaling $42 billion (http://www.sdr.gov). NISAR imagery can be used to estimate wind speeds within the hurricane, show the shape and

structure of the hurricane eye, map the spatial extent of the storm surge and flooding, detect coastal erosion, and assess damage to buildings, infrastructure, and the ecosystem. NISAR includes the Gulf of Mexico, Caribbean Sea, and extensive CONUS coastal ocean in the standard acquisition plan. Combining NISAR's ascending and descending repeat orbits provides two satellite images every 12 days, which will provide the science and operations communities detailed SAR imagery and geodetic measurements. Although this temporal frequency is not sufficient to provide day-to-day imaging, NISAR will augment the global Earth observation instrument network, and it may acquire the only pre-event images in some circumstances because of its near-global land observations.

E.4.16 MARITIME: SEA ICE MONITORING

The U.S. National Ice Center (NIC) is a joint effort of the U.S. Navy, National Oceanic and Atmospheric Administration (NOAA) , and the U.S. Coast Guard. The NIC is also a part of the Northern American Ice Service (NAIS), which is jointly operated with the Canadian Ice Service. Their primary goal is to monitor sea ice extent and type, especially in the Arctic, for safety of navigation. In addition to the important cryospheric science goals of NISAR, the routine imaging of the polar regions will potentially yield important benefits for operational monitoring. One of the primary observational products is available SAR data. Since SARs provide all-weather, day-night high-resolution data, they represent the preferred means of observation. The primary limitation of SAR is coverage, which has been substantially improved with the launch of the Canadian C-band Radar Satellite Constellation.

NISAR will not only provide additional polar coverage to support operational monitoring, but L-band will augment the information available from C-band. Both frequencies are useful in delineating areas of sea-ice coverage. However, the longer wavelength of L-band permits deeper ice penetration and makes L-band more capable in discriminating sea-ice type.

For operational sea ice uses, the priorities for NISAR data acquisition in order are:

1. Polar coverage, particularly in the Arctic where there are more frequent marine operations.
2. The preferred data latency is 6 to 12 hours. After 24 hours, the data are less useful for operations.
3. The preferred polarization is dual VV and HH.
4. The next preferred polarization configuration is any like-polarization plus cross polarization.
5. The least preferred polarization configuration, but still very valuable, is any like-polarization.
6. Providing sufficiently low-latency products is the primary challenge to operational usage of NISAR data for sea ice monitoring.

E.4.17 MARITIME: COASTAL OCEAN CIRCULATION FEATURES

At the global scale, NISAR will dominantly acquire data over land and the cryosphere. To the extent that coastal regions are also imaged, which is more extensive for the U.S. and India, NISAR data can be applied to a variety of marine applications. Radar backscatter from the ocean surface is directly dependent upon the roughness of the ocean surface on scale of the radar wavelength. SAR marine applications are tied to how different ocean phenomena affect surface roughness. Although the exact mechanism for imaging waves is more complicated, to first order the slope variations of the ocean surface and the fact that surface roughness and hence radar cross section at the crests of waves is higher than in the wave troughs renders waves visible in SAR imagery. From this imagery, the two-dimensional

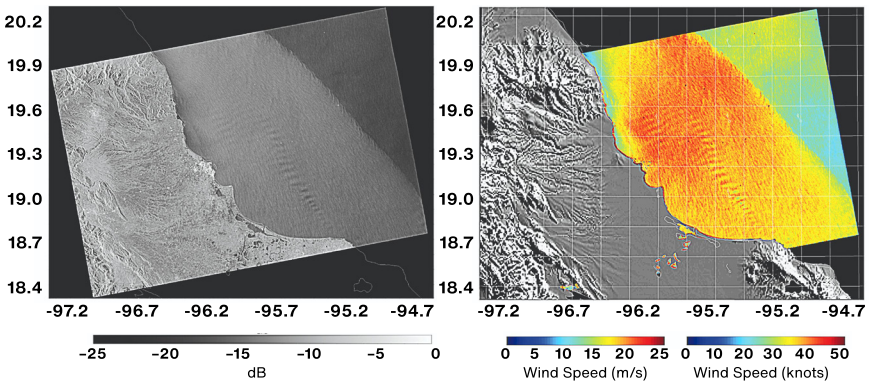

FIGURE E-34

Sentinel-1A radar cross section image (left) scaled from -25 dB to 0 dB of an area of eastern Mexico's coastal ocean acquired at 2018-01-25 00:32 UTC. Retrieved wind speed (right) scaled from 0 to 25 m/s.

ocean wave spectrum can be computed (Alpers, 1992). There are other, more advanced, marine applications of SAR that depend on taking advantage of direct velocity measurements by SAR to map ocean currents (Romeiser, 2013).

L-band or S-band radar may be more attractive for imaging of current boundaries, fronts, eddies, and internal waves since the longer (compared to C-band) wavelength is less sensitive to rapid variations in the boundary layer wind speed and will therefore be more modulated by varying surface currents. Dual-frequency measurement capabilities will allow tailoring of observations to different wind speed regimes.

Coastal upwelling processes and the formation of coastal jets and fronts result in temperature gradients, which may be detected by SAR due to reduced surface roughness over the colder water regions. Reduced sensible and latent fluxes over the colder water because of lowered air-sea temperature differences is accompanied by reduced atmospheric turbulence levels, and thus less roughness in the regions of the cooler ocean contacting the atmosphere. At VV polarization, such a pattern would appear similar to an HH-polarization image under stable air/sea conditions; however, under unstable conditions, simultaneous imagery at the two polarizations will differ significantly.

E.4.18 MARITIME: OCEAN SURFACE WIND SPEED

The most direct SAR marine application is SAR wind speed retrieval. Radar backscatter at off-nadir incidence is proportional to surface roughness near the scale of the radar wavelength. The higher the wind speed, the rougher the ocean surface, and the higher the backscattered cross section. This principle is relied upon by conventional wind speed scatterometry. Radar cross section is at maximum looking in the wind direction and at minimum in the cross-wind direction. SAR wind speed measurements generally have over an order of magnitude finer resolution than conventional scatterometers.

Figure E-34 shows a radar cross section image of the east coast of Mexico acquired by Sentinel-1 at 2018-01-25 00:32 UTC and the corresponding wind speed at resolution of 500 m. Sentinel operates at C-band (5-cm wavelength). NISAR wind speed images will be similar though less sensitive at low wind speeds (5 m/s) and more accurate at higher wind speeds (>15 m/s; Monaldo et al., 2016; Monaldo and Kerbaol, 2004; Shimada and Shimada, 2003). Not only can SAR wind speeds be used for weather forecasting, but high-resolution wind speed climatologies can be used to help select sites for offshore wind power turbines (Hasager et al., 2015). Wide swath observations, similar to those for currents in the open ocean, are preferred for the winds, with resolutions being finer than the scales of frontal systems and storm gradients at sea. These will produce even sub-kilometer scale wind estimates, which are important for coastal areas specifically related to siting, building, and monitoring wind turbines and coastal structures, shipping, and biological interactions.

E.4.19 MARITIME: ICEBERG AND SHIP DETECTION

One important marine application not directly related to ocean surface roughness is to monitor ship traffic and icebergs. At the high resolution of SARs, ships and icebergs are often visible

(Tello et al, 2005). Imaging the Atlantic shipping routes during seasons when icebergs often move into the lanes will support the NIC's mandate to provide situational awareness data on that hazard. Identifying ships near coasts can also help locate and identify illegal dumping of material in coastal water.

E.4.20 MARITIME: OIL SPILLS

Ocean surface roughness is suppressed by surfactants and mineral oil slicks. In coastal regions, NISAR has the potential to be used to monitor oil spills from ships or oil-drilling platforms (Girard-Ardhuin, 2005). Oil spills in oceans and coastal waters have widespread impact on the environment, marine life, human health/safety, society, and regional economy. The 2010 Deepwater Horizon oil spill caused a major economic disaster, spreading oil from ~50 miles off the Louisiana coast throughout much of the Gulf of Mexico and to coastal areas in all U.S. states bordering the Gulf (Figure E-35). Smaller, yet significant, spills occur regularly, mainly in coastal areas around the globe. The hazard response community and the International Charter have extensively used SAR imagery to track oil spills and help guide the mitigation efforts. A region of increasing concern regarding the potential of hazardous oil spills is the Arctic coastal zone, where the retreating and thinning sea ice cover has increased interest in transportation and petroleum exploration. A hazardous spill in the Arctic presents an extremely challenging containment and cleanup response, where NISAR may play a critical role, enhanced by the converging nature of polar observations and the ability to image throughout the extensive periods of polar winter darkness and cloud cover. Tasking of NISAR in response to such disasters may be critical and will commence after the disaster occurs.

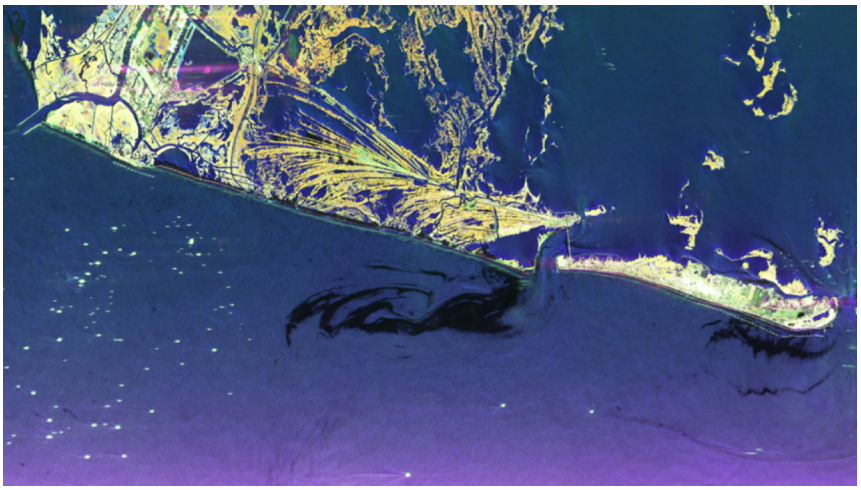

FIGURE E-35

UAVSAR image of oil from the Deepwater Horizon spill acquired over southeastern Louisiana. The oil slick shows up as a dark area in this false color image, as it dampens the capillary waves smoothing the surface, resulting in reduced backscatter energy. From Jones et al., 2011.

E.4.21 MARITIME/HYDROLOGY: FLOOD HAZARDS

Floods and other water-related hazards are among the most common and destructive natural hazards, causing extensive damage to infrastructure, public and private services, the environment, the economy, and human settlements. Recurring hydrological disaster-related losses from floods caused by tsunamis, storm surge, and precipitation have handicapped the economic advancement of both developed and developing countries (e.g., https://www.gov.uk/government/uploads/system/uploads/attachment_data/file/286966/12-1295-measuring-human-economic-impact-disasters.pdf). Most hazardous hydrologic events are local and short-lived and can happen suddenly and sometimes with little or no warning. Millions of people can be impacted by major floods. U.S. insurance claims from floods total in the billions of dollars per year. In 2015 and 2016, for example, 18 major flood events hit Texas, Louisiana, Oklahoma, and Arkansas causing extensive damage (Figure E-36). Timely evaluation of flooding conditions is crucial for effective disaster response. Saving lives and property are the initial priorities, while later assessments are needed to evaluate the extent and severity of the disaster zone.

Because satellite radar is a cloud penetrating technology, NISAR can acquire snapshots of the disaster extent regardless of atmospheric conditions to help delineate flood hazard zones; measure water level changes, primarily in wetland environments; and measure flood depth

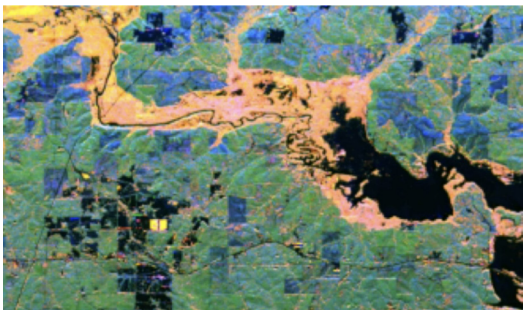

FIGURE E-36

Left: Radar false color image product near Farmerville, LA (March 13, 2016, by NASA's UAVSAR) during a devastating flood. Orange and yellow areas are flooded forests, and black areas are lakes and open floods. This type of information is invaluable for local, state, and federal agencies that provide assistance. Right: Example of the immense and costly flooding that occurred in the Farmerville region during this flood. (James Fountain, USGS)

in areas where an accurate digital elevation model (DEM) is available. NISAR can be used to map flooding events on a global basis twice every 12 days. Observations will be uninterrupted by clouds and will provide timely information for flood responders. Even flooding hidden beneath forest canopies will be visible in many areas. Multiple types of NISAR measurements will be useful for flood assessment: InSAR phase, coherence and backscatter change, including polarimetry, can be used to discern water flow direction, map inundation extent and duration, and estimate changes in water level, either based on a DEM or through double bounce scattering in flooded areas with emergent vegetation. NISAR will be capable of monitoring water level change in marsh areas, allowing for prediction of downstream flooding. Permanent stream gauges are installed and monitored specifically for that purpose, but they are sparsely distributed. NISAR data will augment these data and provide increased spatial coverage, filling in the gaps between gauges.

Among the organizations that respond to flooding disasters are state and local agencies, as well as federal agencies, such as Federal Emergency Management Agency (FEMA), the National Oceanic and Atmospheric Administration (NOAA), and the United States Geological Survey (USGS). International aid in the event of natural disasters caused by flooding often includes data sharing arrangements to help our nations respond to the humanitarian crises that flooding can cause.

Surface water hydrology hazards have similar mission requirements as the solid earth hazard applications, where they need to have an up-to-date baseline data archive, rapid tasking to ensure that the satellite is collecting data on every possible orbit in case of an event, adequate spatial coverage of the target, and data quickly delivered in a georeferenced format that is easily disseminated to the emergency responders. The addition of polarimetric SAR capabilities provides improved subcanopy imaging and characterization of the flood extent and will likely provide better estimates of the vegetative frictional contribution in the storm surge modeling (DESDynI Applications Workshop, 2008). Data frequency needs for the emergency responders are daily with sub-daily optimum for hazard response, and thus NISAR will not fully meet these needs on its own but will contribute to a suite of Earth observing instruments. Flooding, coastal inundation, and tsunami applications will greatly benefit from the higher frequency data collection to assess flood duration, inundation zones, draining, and habitat response.

E.4.22 HYDROLOGY: FLOOD FORECASTING

Flood forecasting informs downstream communities if a flood is coming and how much flooding to expect. Like a virtual stream gauge, synthetic aperture radar can measure changing water levels in standing vegetation as flood waters from heavy upriver rains head downstream.

Change in upstream water levels can be very useful for predicting downstream flooding. Permanent stream gauges are installed and monitored specifically for that purpose, but they are sparsely distributed. Not only will NISAR be capable of augmenting this network of stream gauges with continuous maps of change in water level in some areas, but NISAR will also be capable of monitoring the change in the level of floods far from the main river channel, where water can increase in level and subside at different rates. The same technology can provide information about soil moisture, another parameter needed for flood forecast models.

During natural disasters, first responders often look to NASA to provide timely and valuable information to assist their work to mitigate damage and assess destruction by these common tragic events. Many federal agencies and university researchers have difficulty evaluating the health of our waterways and wetlands due to lack of information regarding the ebb and flow of flood waters during normal and extreme seasonal flooding. The data from NISAR over wetland areas will be invaluable to management authorities, scientists, and local planning agencies. NISAR can meet these diverse needs through its dependable observing strategy that will collect high resolution data over 90 percent of Earth's land surface. NISAR will provide crucial information regarding flooding events, even in remote areas without stream gauges or other sources of ground data measuring flood conditions.

InSAR can be used to precisely measure very small changes in water level in areas with standing vegetation using repeated observations by radars like NISAR made from the same vantage point, i.e., from the same orbit. This was first demonstrated with the NASA SIR-C mission that flew on the NASA Space Shuttle in 1994. SIR-C twice imaged the Purus River, a tributary of the Amazon–Solimões River, during flooded conditions. From these images, it was possible to measure centimeter-level changes in water level during the 24 hours that had elapsed between the observations (Figure E-37).

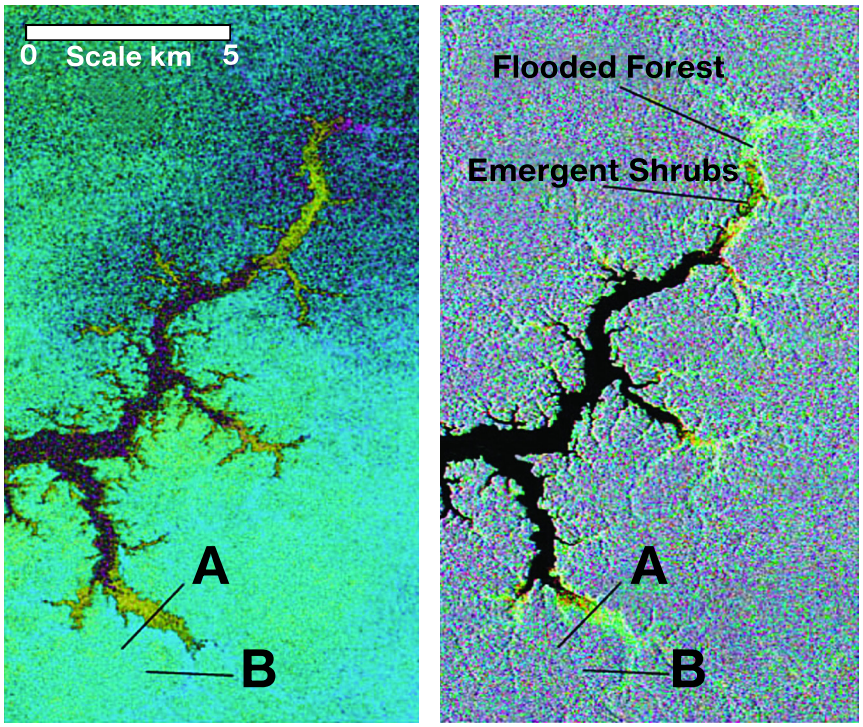

FIGURE E-37

"Change in water level" products in flooded, vegetated areas were first demonstrated by the NASA SIR-C Synthetic Aperture Radar (SAR). In this image, centimeter-level changes in water level were measured over the Purus River in Brazil from two observations acquired just 24 hours apart. (Alsdorf et al., Nature, 2000). Colors indicate how much the water level changed between the two observations. Between transects A & B was a 1-5 cm change in water level.

NISAR will function like a virtual stream gauge for flooded conditions that occur along most of the world's major rivers, capable of precisely measuring change in water level with every observation.

E.4.23 HYDROLOGY: COASTAL INUNDATION

Monitoring inundation of marshes, swamps, or other flooded areas is difficult: On the ground, inundated areas can be treacherously difficult to navigate, while from above, vegetation, clouds, and weather can make the water difficult to observe. Beyond the human impact, the extent and duration of inundation have a heavy influence on fish and other wildlife habitats, vegetation, and other parameters of ecosystem health. NISAR will allow uniquely detailed monitoring of the seasonal ebb and flow of flood waters in Earth's wetland areas, not just storm-related flooding. The NISAR all-weather and forest-penetrating radar can detect both open water areas and the flooded areas below trees (Figure E-38).

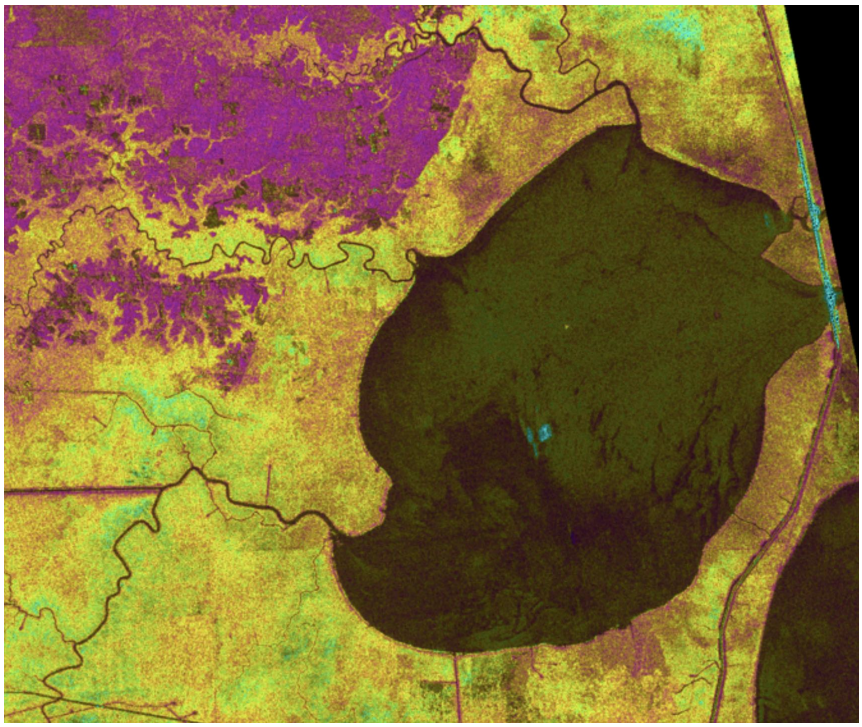

FIGURE E-38

Dual polarization radar image of the Maurepas Lake and surrounding swamp in Louisiana. This image was acquired from space by the Japanese ALOS-2 L-band radar. In this false color image, yellow areas are the flooded Cypress Tupelo swamp, pink are unflooded areas, orange areas are degraded swamp marshes, and dark areas are open water. Image © JAXA 2016.

Many federal agencies and researchers that study wetlands have difficulty evaluating their health status due to lack of information regarding the ebb and flow of flood waters during normal and extreme seasonal inundation. NISAR imagery will provide near-weekly observations that complement optical data, imaging through clouds and below the canopy. This capability makes NISAR's imaging of wetland areas valuable to management authorities, scientists, and local planning agencies. NISAR will provide invaluable new and independent information regarding flooding events in disaster scenarios, as well as data to develop unique seasonal evaluations of wetland dynamics.

E.4.24 HYDROLOGY: SOIL MOISTURE

Estimating spatial and temporal variability of soil moisture globally at sufficient resolution to help manage agriculture production, assess wildfire and landslide risks, track regional drought conditions, detect spills, and contribute to surface water routing models that estimate rainfall runoff for reservoirs, water conveyance systems, and floods will benefit a wide societal cross-section. SAR backscatter is directly related to near-surface moisture content (volumetric) that changes the reflective target properties. At microwave frequencies, the dielectric constant of dry soil is around 3, while that of water is around 80 and depends on salinity. The dielectric constant for moist soil ranges between 3 and 30. As the dielectric constant of a material increases, the Fresnel reflectivity also increases, resulting in increased backscatter. Radar wavelength determines the penetration depth. As longer wavelengths have higher penetration depth within the soil medium, they sense soil moisture from deeper layers as compared to shorter wavelengths. The impact of soil surface roughness on the backscatter intensity is also a function of the wavelength. For longer wavelengths the soil surface appears smoother, i.e., at L-band soil surface appears smoother as compared to C-band. Thus, the impact of soil moisture is more prominent in the L-band signal as compared to C-band.

Potential applications of multi-frequency SAR data in the field of soil moisture estimation were explored with the SIR-C/X-SAR mission over Bhavnagar, Gujarat. SIR-C/X-SAR operated in the L-, and C-, and X-bands. This mission clearly showed (Figure E-39) that L-band, and presumably S-band, is able to sense deeper layer soil moisture, whereas C-band and X-band are not able to sense deeper layer soil moisture due to their low penetrability within the soil medium.

A similar study conducted to understand the usefulness of L-band in soil moisture estimation over agricultural terrain used DLR-ESAR data over an agricultural area having varying surface roughness, crop cover, and soil moisture content. This study also showed that L-band can capture the signature of soil moisture better than C-band.

An advantage of co-collecting L- and S-band radar imagery will be characterizing soil moisture as a function of penetration depth and differentiating phase signatures from soil penetration variations from deformation in repeat

pass interferometry. While surface deformation is non-dispersive, one would expect the phase signature from soil moisture variations to be wavelength-dependent, so differences in S-band and L-band interferometric phase can be used to discriminate deformation from moisture changes.

NISAR has the potential to provide high-resolution soil moisture variability products that will contribute to each of the science components of the mission by characterizing and removing soil-moisture-induced noise within SAR imagery. The co-collection of L- and S-band imagery will provide depth-dependent soil moisture variability and will help isolate and remove soil moisture phase noise in targeted deformation interferograms. This combination will lower the detection threshold for resolving subtle and transient deformation in NISAR imagery. The resolution of the NISAR imagery will be at a level that can be used to manage crops, help estimate wildfire probability, constrain snowpack water content (see Section E.3.2), develop water routing and flooding numerical models, and detect spills.

E.4.25 UNDERGROUND RESERVOIRS: GROUNDWATER WITHDRAWAL

Extraction of groundwater often causes the aquifers to contract at depth that in turn causes the overlying ground surface to subside. The water in the aquifers, called groundwater, is an extremely valuable resource, like a water savings account that can be drawn on when times are hard. The water in the aquifers originally was precipitation that made its way down through the soil and rock via cracks and pores. All aquifers are not created equal: Aquifers can hold small or vast amounts of water and recharge quickly or slowly depending upon the type of rock both in and above the aquifer. Groundwater extraction often increases substantially during droughts when surface water is not available to supply demand for water. Groundwater is extracted from aquifers in every U.S. state and nearly every country around the world, so this is a widespread issue.

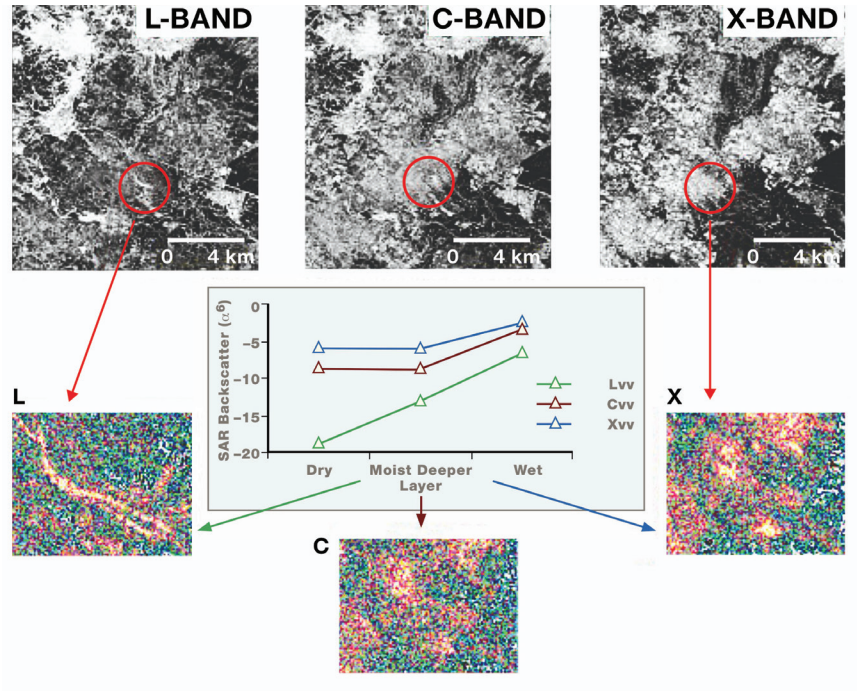

FIGURE E-39

Multi-frequency SIR-C response to deeper layer soil moisture.

Ground subsidence due to groundwater withdrawal can have many effects on infrastructure and buildings. These can be cracks in roads and bridges; reduction in freeboard on levees, canal walls, and dams; or large-scale changes in runoff, water, flow pathways, or coastal flooding. Large contractions in aquifers can also damage the water extraction wells themselves and require costly redrilling. The contraction of the aquifers when water is extracted usually includes both temporary elastic contraction that can be recovered when the water is replaced and permanent deformation that cannot be recovered. When aquifers are permanently deformed, they lose capacity to store future water.

Sustainable, low impact groundwater extraction is possible when users are given information about the aquifer and the surface changes associated with pumping. This is where imaging by satellite radars capable of measuring changes in surface elevation, like NISAR, has immediate and practical value. NISAR will image global land areas every 12 days, providing a time series of the surface

elevation change. This information shows both the long-term decline in surface elevation, which corresponds to unrecoverable loss or slow recharge of groundwater, and a seasonal cycle of uplift and subsidence that correlates to a sustainable balance between precipitation and withdrawals. Armed with this information, users can protect this valuable renewable water asset over the long term, avoiding the terrible consequences of permanent loss of water supply.

E.4.26 UNDERGROUND RESERVOIRS: OIL AND GAS PRODUCTION

Efforts to utilize subsurface resources, including water, oil, gas, and geothermal power, necessarily involve the extraction and injection of large volumes of fluid from the ground – often in areas that also host valuable infrastructure and large population centers. Groundwater effects were described in the previous section. Oil, gas, and geothermal extraction operations affect a subset of the United States and other countries around the world, but new technologies, including hydraulic fracturing, have expanded the areas where extraction occurs. Oil and gas are extracted from a wide variety of rock reservoir types and depths, using a large range of methods. Geothermal power is often extracted from the ground by pumping water out of hot rocks.

Withdrawing fluid from rocks at shallow depths without replacement will cause compaction within the reservoirs and subsidence of the overlying land surface similar to the compaction of groundwater aquifers and its associated surface subsidence. Extracting heat from geothermal reservoirs can also cause the rocks to contract and subsidence of the surface. Some advanced methods of oil and gas extraction involve the injection of water or steam into the reservoirs to stimulate extraction. If injection volumes exceed extraction, then the ground surface above may move upward. Enhanced geothermal operations may also involve greater injection than extraction, leading to uplift of the surface. In some cases, the oil and gas extracted includes a large amount of wastewater that requires disposal. In most places wastewater is reinjected into rocks at depth, which can cause induced seismicity, which is described in another section.

The NISAR satellite mission will provide high-resolution ground movement maps on a global basis with weekly sampling. Observations will be uninterrupted by weather and facilitate safe resource development by improving understanding of processes that impact regions undergoing active extraction or injection of subsurface fluids, including oil, gas, and geothermal power. The L-band radar of NISAR will enable measurements in areas of significant vegetation that have been challenging for other SAR satellites. The observations made over the lifetime of NISAR will be a giant step forward in our understanding of subsurface fluid flow and associated seismicity and will inform the next generation of methods for characterizing and managing these resources.

E.4.27 UNDERGROUND RESERVOIRS: INDUCED SEISMICITY

Earth scientists have been investigating earthquakes of tectonic origin for more than a century, developing significant insights and understanding about where they occur, how frequently they occur, their links to geologic structures and processes, their magnitude distribution, and how frequently main shocks trigger aftershocks. For the past 40 years, and particularly over the past decade, a new class of earthquakes has become increasingly important – earthquakes induced or triggered by human activities (see also Section E.1.4). Human activities hypothesized to have caused earthquakes, in decreasing order of numbers of suggested instances (e.g., www.inducedearthquakes.org) include mining, water reservoir impoundment, conventional hydrocarbon production, fluid injection including disposal of wastewater associated with hydrocarbon production, geothermal energy production (especially enhanced geothermal recovery), hydraulic fracturing, groundwater extraction, and carbon sequestration. The

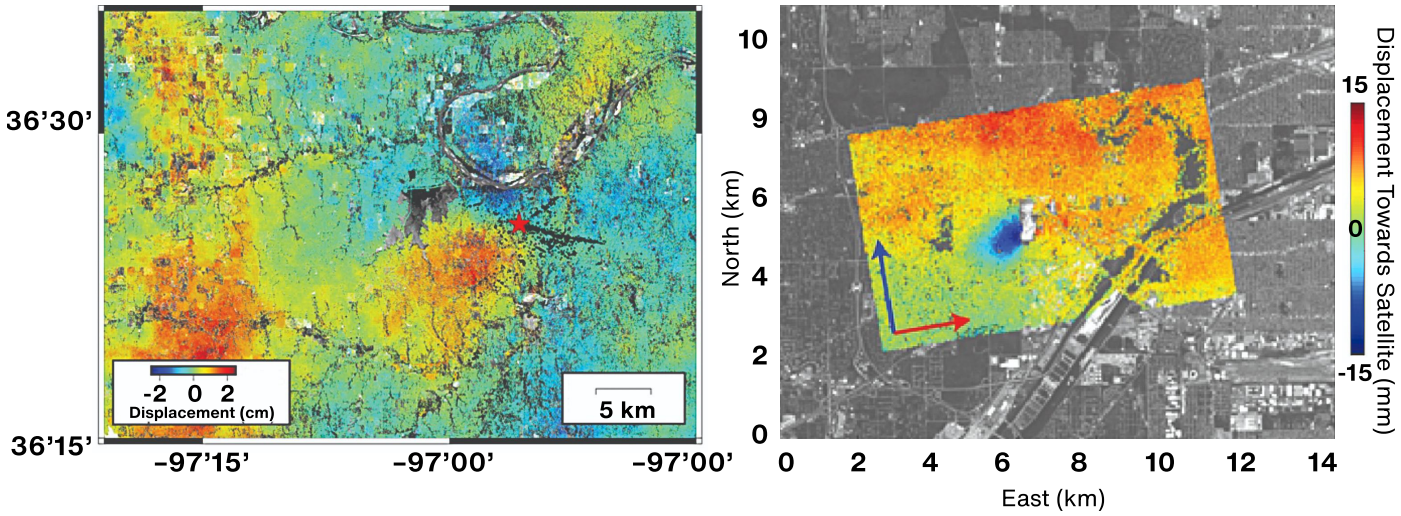

FIGURE E-40

Left: NISAR data will permit systematic mapping and monitoring of earthquakes, even in agriculturally active areas. In this example, using data from the European Space Agency's Sentinel-1a and -1b platforms, we can see several centimeters of displacement over a 10 km x 10 km region associated with the 2016 magnitude 5.8 Pawnee, Oklahoma, earthquake. The main earthquake location (red star) and aftershocks (black dots) outline a complicated pattern that provides insight into weakness in the subsurface. The red band on left is the atmospheric path delay signature of a large storm that was present during one of the image acquisitions. When many images are available, such as would be provided by NISAR, such atmospheric effects can be averaged out more effectively to determine the true ground movement. Right: Even tiny earthquakes can be imaged when enough data are available. This image uses data from the European Space Agency's TerraSAR-X platform to constrain subsidence of the ground during a 2013 magnitude 3.2 earthquake within the Chicago metropolitan area, triggered by a blast at a limestone quarry. Color indicates displacement of the ground surface towards or away from the satellite, which was traveling to the northwest in the direction of the blue arrow and aimed down towards the Earth in the direction of the red arrow. The observed displacement shown here tightly constrains the depth of this earthquake to 700 meters, much shallower than the zone where "natural" earthquakes occur.

recognition that human activity can trigger earthquakes has led to great concern among government, industry, and the public.

Some instances of earthquakes that may be triggered by human activity occur in regions that naturally experience frequent earthquakes (e. g., California, Italy, Spain, Tibet). Others, such as those in the 21st century in the central United States and the Netherlands, represent a significant change (Figure E-7). Increases in earthquake frequency are also associated with energy production at geothermal power plants and at dams that contribute hydrothermal power to the grid (Koirala et al., 2024).

The increased frequency of triggered and induced earthquakes creates new challenges, particularly since the energy and resource needs of our population are likely to continue to grow. Even forecasting the expected damage from these new types of earthquakes is not just "business as usual." Analyses of shaking reports from the central United States and the Netherlands suggest that the distribution of damage from these earthquakes, which tend to be shallower, are different from the damage expected from "traditional" earthquakes, which often occur deep underground.

Satellite-based radar imagery, when available, can be an extraordinary tool for characterizing how Earth's surface warps and deforms before, during, and after induced earthquakes. The examples of induced earthquakes in the central United States (Figure E-40) are cases where we were fortunate to have data both before and after the earthquake. Many other earthquakes in these regions have been impossible to study because of the complete lack of data before the event. This situation should change in the future: NISAR data would be acquired regularly over the

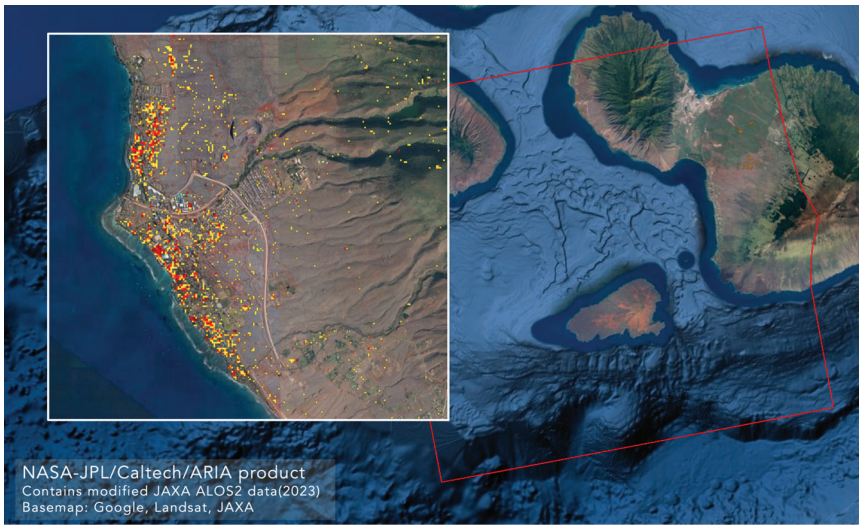

Figure E-41

Damage Proxy Map (DPM) from JAXA ALOS-2 SAR data for 2023 wildfires on Maui, Hawai'i, USA. Background from Google Earth. Red box shows image extent. Inset shows detail of damage in town of Lahaina on west coast of Maui. Yellow-orange-red color scheme shows increasing levels of likely damage.

entire United States, allowing imaging of areas like Oklahoma, Texas, and Kansas that have both active agriculture and hydrocarbon/water resource development.

E.4.28 RAPID DAMAGE ASSESSMENT

A key need after disasters with either natural or human-induced causes, is the rapid assessment of damage to buildings and other infrastructure. Frequent coverage of the land areas by imaging radar satellites, including NISAR, enables all-weather assessment of damage with measurements of coherency changes. Damage proxy maps, or change detection maps, can show areas of potential damage very quickly after the radar data are received by comparing scenes from before the disaster to those acquired just after it occurred (Yun et al., 2015; Fielding and Jung, 2024). The coherence or correlation of the phase for InSAR pairs is related to surficial change and some additional factors related to the imaging geometry (Zebker and Villasenor, 1992). Coherent change detection uses the sudden decrease of coherence after a disaster or other event to detect changes and likely damage to buildings, other infrastructure, or land surfaces and make a damage proxy map. This method has been demonstrated for a wide variety of disasters, including earthquakes, tsunamis, volcanic eruptions, hurricanes, tornadoes, and landslides (aria.jpl.nasa.gov). Flood proxy maps can be similarly derived from SAR change detection to show flood extent (Lin et al., 2019).

One example of rapid damage proxy mapping was after a magnitude 7.8 earthquake hit central Nepal on April 25, 2015. The quake killed nearly 9,000 people and induced more than 4,000 landslides in the precipitous valleys of the Himalayan Mountains. Widespread building damage was rapidly mapped using radar data acquired by Italian COSMO-SkyMed (X-band) and Japanese ALOS-2 (L-band) satellites (Yun et al., 2015). The maps were quickly released to national and international responding agencies. Field crews were dispatched to damaged sites and made ground observations guided by the maps, and a satellite operating company used these maps to target areas for imaging with ultra-high-resolution spaceborne optical sensors.

Another example of damage proxy maps from L-band SAR data is the DPM for the devastating wildfires on West Maui in Hawai'i of 8 August 2023 (Fig. E-41). The pre-event scenes were acquired on 17 July 2022 and 18 July 2023, and the post-fire scene was acquired on 13 August 2023. Because there was less than a month between the last scene before the fire and first scene after the fire, nearly all the InSAR coherence changes are due to the fire. The consistent 12-day repeat of NISAR L-band acquisitions over all land will greatly improve the accuracy of the damage proxy maps (Fielding and Jung, 2024).

E.4.29 ECOHYDROLOGY: LAND SURFACE FREEZE/THAW STATE PROCESS MONITORING

The availability of liquid water is the primary hydrological constraint to biological activity in terrestrial ecosystem processes in the northern high latitudes. These limitations present as either water deficiency or inaccessibility due to freezing. Significant amounts of water in high latitude terrestrial biomes transition between solid (frozen) and liquid (thawed) states during

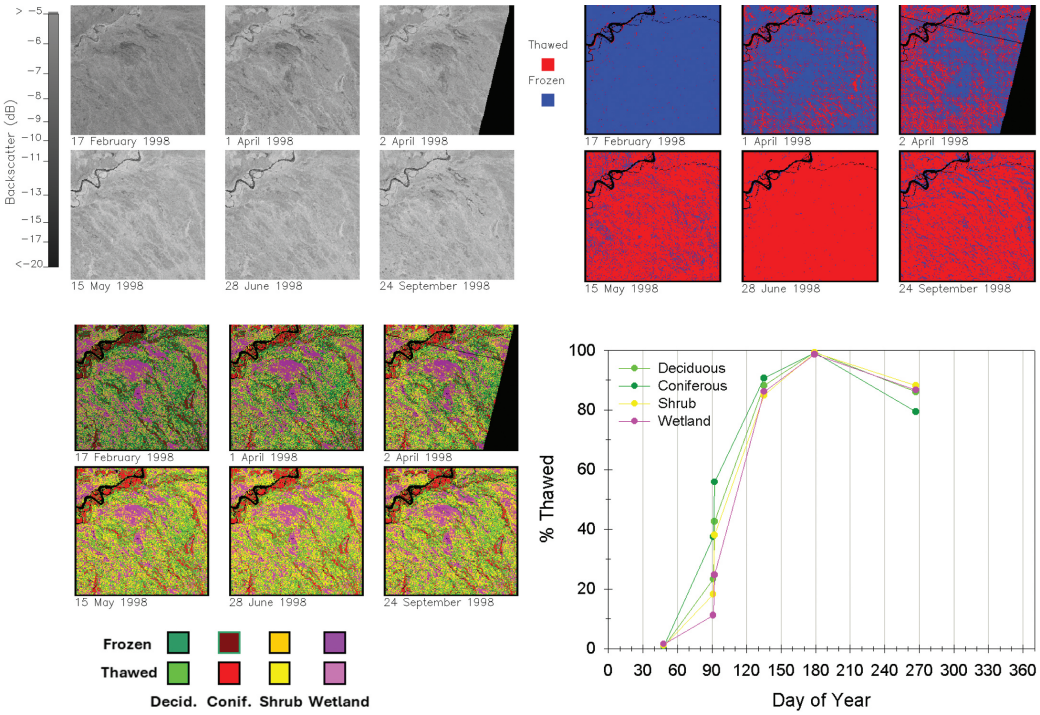

FIGURE E-42

Time-series land surface freeze/thaw (FT) state characterized by JERS-1 L-band SAR imagery over the boreal wetlands complex along the Tanana River at Bonanza Creek Experimental Forest, Alaska. (Upper left) Temporal sequence of HH-polarized L-band SAR images acquired 17 February, 1 April, 2 April, 15 May, 28 June, and 24 September 1998. Increasing backscatter (shown in dB) is indicative of transitions from frozen to thawed conditions. (Upper right) Classification of frozen (blue) and thawed (red) states across the wetlands complex, with a temporal change classifier applied to the time series SAR data. (Lower left) Merging FT state with a landcover map elucidates the heterogeneity of the FT transition with respect to four different vegetation community types, highlighting the spatial heterogeneity of landcover type and associated FT transitions that occur at fine spatiotemporal scales. (Lower right) Percent of area thawed for each landcover class across the time series.

springtime and autumn. These transitional periods impact climate, hydrological, ecological, and biogeochemical processes and associated trace gas fluxes profoundly. During the thawing season, major landscape processes closely tied to the state of water include timing and spatial dynamics of seasonal snowmelt, associated soil thaw and nutrient release in plant-available forms, runoff generation and flooding, ice breakup in large rivers and lakes, and the onset of plant growth (growing season) and soil microbial activity. In boreal forests, the switch from a small net daily loss of CO2 prior to thaw to a net gain following thaw is rapid, occurring over just a few days. During the freezing period, emissions of methane are linked to the extended "zero curtain" period, when soil temperatures are poised near 0°C for extended periods, with key linkages to liquid water prior to complete soil freeze.

SAR remote sensing techniques for identifying freeze/thaw (FT) transitions exploit the dynamic temporal response of microwave backscatter to differences in the aggregate surface dielectric constant associated with the transitioning between predominantly frozen and non-frozen conditions, related to the presence or absence of liquid water. NISAR will provide precision sampling of high latitude terrestrial ecosystems suitable for monitoring and characterizing the timing and progression of the transition of water contained in the ecosystem (i.e., snow, soil, vegetation) between solid (frozen) and liquid (thawed) phases. Characterizing these transitional processes with respect to the full progression as biomes transition through the thawing and freezing seasons provides crucial detail on the availability of liquid water and photosynthetic and heterotrophic activity that drives seasonal biological and biogeochemical processes across the terrestrial Arctic-boreal zone. Figure E-42 shows characterization of FT state progression as observed with a JERS-1 SAR backscatter time series along the Tanana River floodplain near Fairbank, Alaska. NISAR datasets will advance methodologies employing consistent high-resolution, time series data to characterize seasonal thaw and freeze processes and to disaggregate the time series signal with respect to land cover components at landscape and process relevant scales.

Credit: NASA.

APPENDIX F:
SCIENCE TARGET MAPS

Table 3-1 summarized the Level 1 requirements that NISAR must meet. The Level 1 requirements lead to Level 2 measurement accuracy, sampling, and coverage requirements for each of the scientific disciplines. The coverage requirements are globally distributed, but the areas over which requirements must be met are discipline-specific and are codified by the project in a set of science target maps comprising geographical polygons. For example, in the cryosphere the requirements specify coverage of ice sheets in Greenland and Antarctica, as well as polar sea ice, but do not specify all regions with mountain glaciers. Solid Earth deformation areas are specified in terms of fast-moving plate boundaries and selected areas with transient deformation. The figures below summarize the desired science targets for each discipline. NISAR is designed to maximize observations of these target areas.

FIGURE F-1

Solid Earth discipline target map

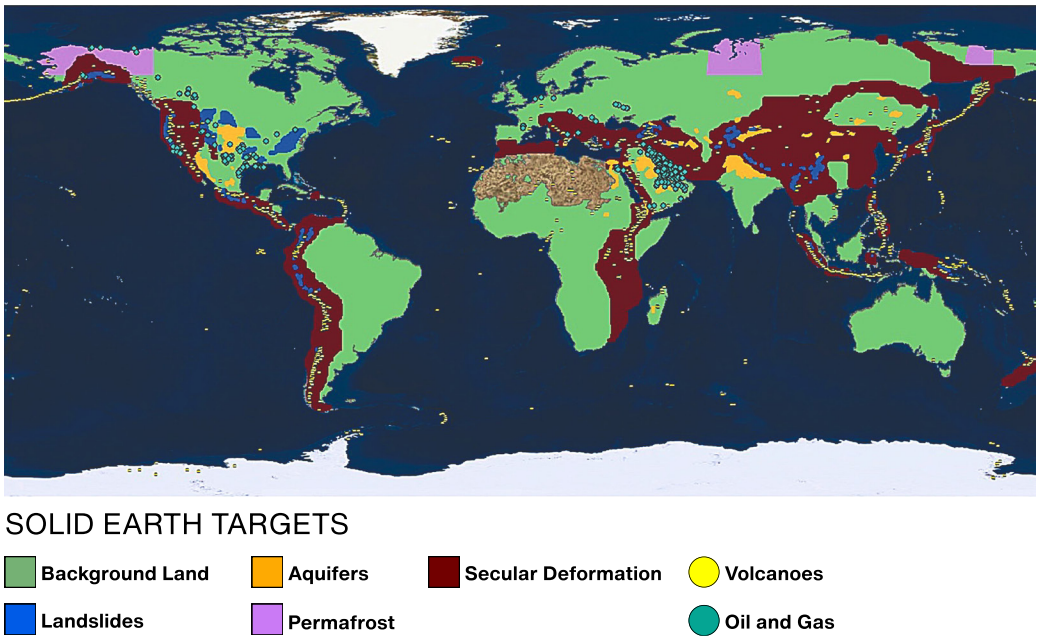

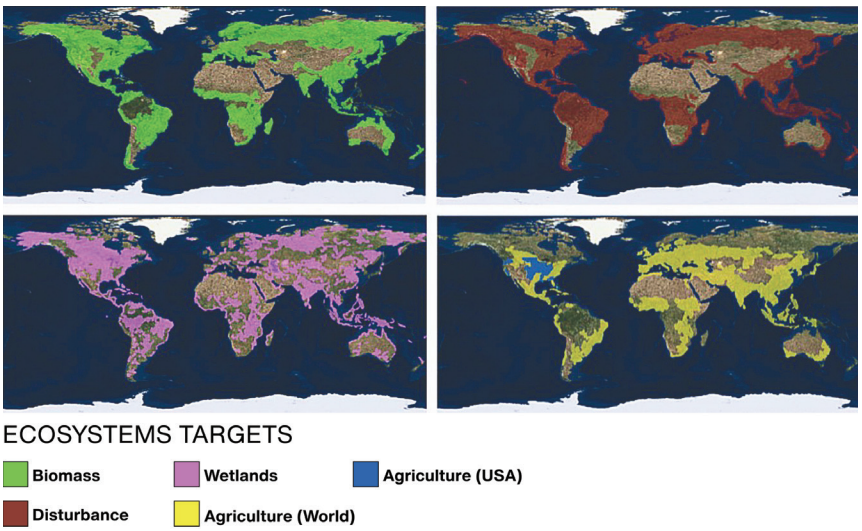

FIGURE F-2

Ecosystems discipline target map. Soil moisture targets include all land not covered in ice.

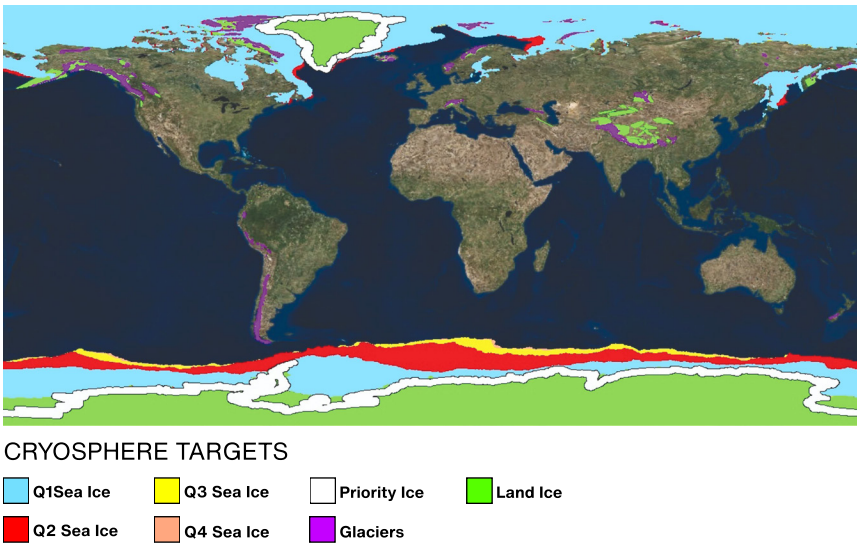

FIGURE F-3

Cryosphere discipline target map.

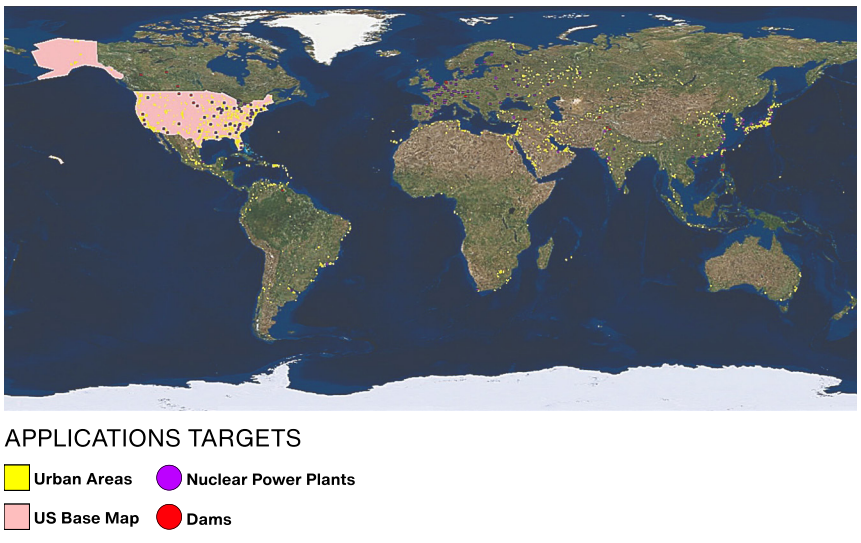

FIGURE F-4

Applications discipline target map.

APPENDIX G:
DATA PRODUCTS LAYERS

An overview of the Level-1 (L1) and Level-2 (L2) science data products generated by the NASA Science Data System (SDS) for the NISAR mission is given in Sections G.1 and G.2, respectively. For a complete and up-to-date description of the data products and associated layers, see the latest version of the NASA SDS Product Description Document, available at the ASF DAAC (https://nisar.asf.earthdatacloud.nasa.gov/NISAR-SAMPLE-DATA/DOCS/NISAR_D-95672A_NASA_SDS_Product_Description_20250523_w-sigs.pdf), and the individual NASA SDS Product Specification documents, available on the NISAR website (https://nisar.jpl.nasa.gov/data/sample-data/).

G.1 LEVEL-1 PRODUCTS

There are four L1 SAR products designed to support the NISAR NASA science disciplines (Table G-1). The data layers contained in L1 products are arranged on the slant range/Doppler grid, uniformly spaced, and with increasing zero-Doppler azimuth time and increasing slant-range distance.

TABLE G-1. L1 SCIENCE DATA PRODUCTS OVERVIEW

Product	Scope	Description	Granule Size
Range-Doppler Single Look Complex (RSLC)	Global	Used to generate all higher-level products	On pre-defined track/frame.
Range-Doppler Interferogram (RIFG)	Antarctica, Greenland, and selected mountain glaciers. Nearest pair in time and co-pol channels only.	Multi-looked flattened interferogram (topographic phase removed) in range-Doppler coordinates. Formed using high-resolution offsets.	On pre-defined track/frame
Range-Doppler Unwrapped Interferogram (RUNW)	Antarctica and Greenland. Nearest pair in time and co-pol channels only	Multi-looked, unwrapped differential Interferogram in range-Doppler coordinates. Same as RIFG, the interferogram is flattened and topographic phase is removed.	On pre-defined track/frame
Range-Doppler Pixel Offsets (ROFF)	Antarctica and Greenland. Nearest pair in time and co-pol channels only	Unfiltered and unculled layers of pixel offsets in range-Doppler coordinates with different resolutions obtained from incoherent speckle tracking	On pre-defined track/frame

G.2 LEVEL-2 PRODUCTS

There are four L2 products to address the needs of the NISAR science disciplines (Table G-2). The L2 data are arranged on a uniformly spaced, north-south and west-east aligned UTM / Polar Stereographic grid.

TABLE G-2. L2 SCIENCE DATA PRODUCTS OVERVIEW

Product	Scope	Description
Geocoded Single Look Complex (GSLC)	Global and all channels	Geocoded L1 RSLC product using the Medium-fidelity Orbit Ephemeris (MOE) state vectors and a DEM.
Geocoded Nearest-Time Unwrapped Interferogram (GUNW)	Global, nearest pair in time and co-pol channels only	Geocoded, multi-looked unwrapped differential interferogram.
Geocoded Polarimetric Covariance Matrix (GCOV)	Global and all channels	Geocoded, multi-looked polarimetric covariance matrix.
Geocoded Pixel Offsets (GOFF)	Cryosphere regions / Greenland / Antarctica	Geocoded pixel offsets, nearest pair in time and co-pol channels only

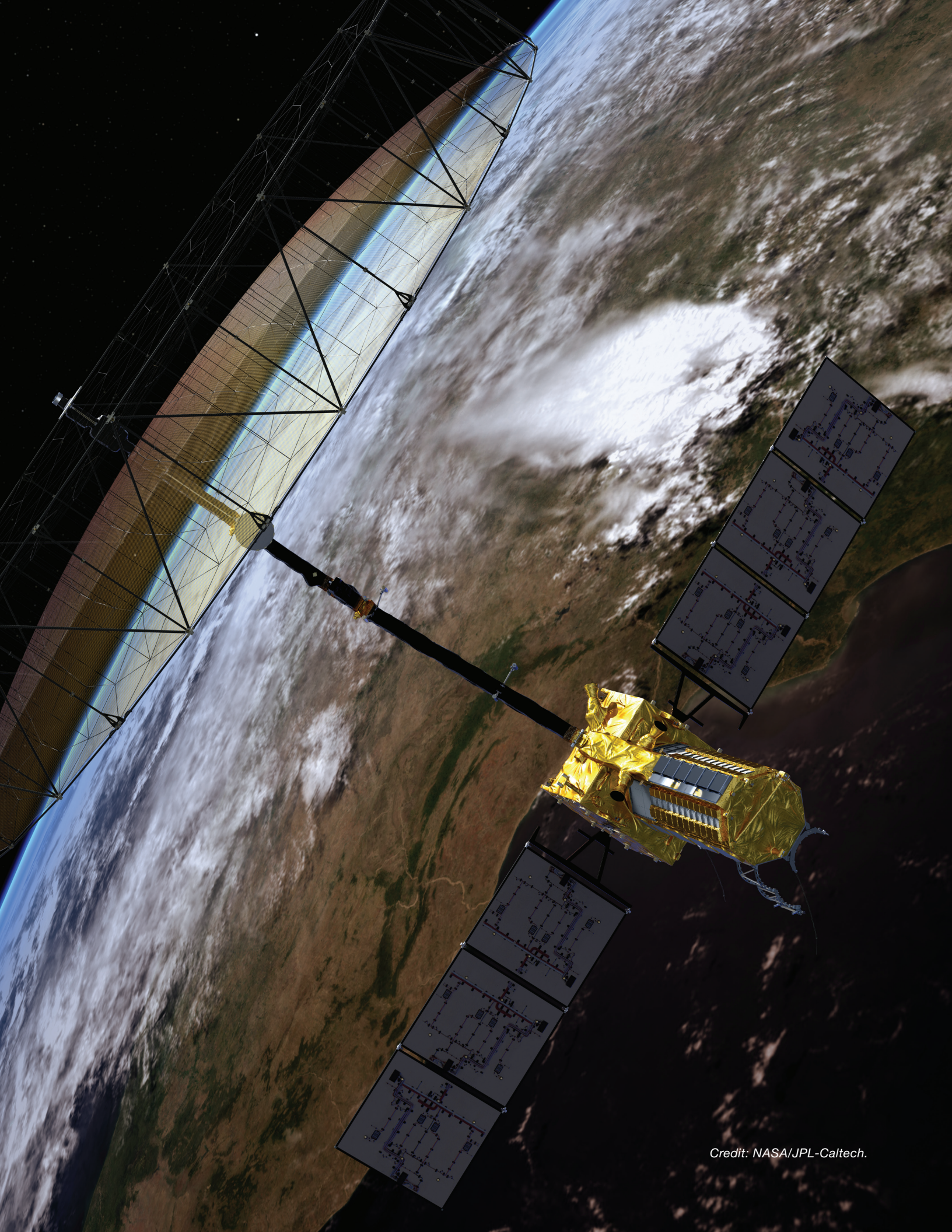

Credit: NASA/JPL-Caltech.

APPENDIX H: ACRONYMS

ACRONYM	DEFINITION
ADRIN	Advanced Data Processing Research Institute
AGB	above-ground biomass
AOCS	Attitude and Orbit Control Subsystem
AOCS	Attitude and Orbit Control System
ASF	Alaska Satellite Facility
ASI	Italian Space Agency
ASIC	application-specific integrated circuit
ATBD	Algorithm Theoretical Basis Document
AWS	Amazon Web Services
CCI	Climate Change Initiative
CEOS	Committee on Earth Observation Satellites
CEOS	Committee on Earth Observing Systems
CONUS	continental United States
CV	coefficient of variation
DAAC	Distributed Active Archive Center
DEM	digital elevation model
DESDynI	Deformation, Ecosystem Structure and Dynamics of Ice
DESDynI-R	DESDynI radar
DMU	drag make up

ACRONYM	DEFINITION
dNBR	differenced Normalized Burn Ratio
DPM	damage proxy map
DSSG	DESDynI Science Study Group
ECMWF	European Centre for Medium-range Weather Forecasts
EOMOC	Earth Orbiting Missions Operation Center
EOS	Earth Observing System (NASA)
EOSDIS	Earth Observing System Data and Information System (NASA)
ERA	European Centre for Medium-range Weather Forecasts (ECMWF) Re-Analysis
ERS	European SAR satellites
ESD	Earth Science Division (NASA)
ESDC	Earth Science Data Center
ESMPO	Earth Science Mission Program Office (NASA)
FAO	Food and Agriculture Organization of the United Nations
FEMA	Federal Emergency Management Agency
FFCC	Forest Fractional Canopy Cover
FIRMS	Fire Information for Resource Management System
FPGA	field programmable gate array
FT	freeze/thaw
GAM	Global Atmospheric Model
GCOV	Geocoded Polarimetric Covariance Matrix
GDS	Ground Data System

ACRONYM	DEFINITION
GEDI	Global Ecosystem Dynamics Investigation Lidar
GEO	Group On Earth Observations
GEOGLAM	Group on Earth Observations (GEO) Global Agricultural Monitoring
GEOSS	Group on Earth Observations (GEO) System of Systems
GFOI	Global Forest Observing Initiative
GIA	Glacial Isostatic Adjustment
GIAnT	Generic InSAR Analysis Toolbox
GLOFs	glacial lake outburst floods
GNSS	Global Navigation Satellite System
GOFF	Geocoded Pixel Offsets
GPS	global positioning system
GRD	Gravity, Earth Rotation and viscoelastic solid-Earth Deformation
GSFC	Goddard Space Flight Center
GSLC	Geocoded Single Look Complex
GSLV	Geosynchronous Satellite Launch Vehicle
GUNW	Geocoded Nearest-Time Unwrapped Interferogram
HGA	High Gain Antenna
HH	horizontal transmit and horizontal receive
HV	horizontal transmit and vertical receive
IA	Implementing Arrangement
IABP	International Arctic Buoy Program

ACRONYM	DEFINITION
ICC	Indicative Crop Classification
IEM	Integral Equation Method
IIRS	Indian Institute of Remote Sensing
IMGEOS	Integrated Multi-Mission Ground segment for Earth Observation Satellites
InSAR	Interferometric Synthetic Aperture Radar
IOC	in-orbit checkout
IPAB	International Programme for Antarctic Buoys
ISAC	ISRO Satellite Center
ISLR	Integrated Side Lobe Ratio
ISRO	Indian Space Research Organisation
ISTRAC	Indian Space Research Organisation (ISRO) Telemetry, Tracking, and Command Network
JECAM	Joint Experiment for Crop Assessment and Monitoring
JPL	Jet Propulsion Laboratory
L1	Level-1 (requirements)
L2	Level-2 (requirements)
lidar	light detection and ranging
LKF	linear kinematic feature
LMA	Levenberg-Marquardt Approach
LOS	line of sight
LSQ	least squares (estimation)
LUT	lookup table
MCR	Mission Concept Review

ACRONYM	DEFINITION
MEaSUREs	Making Earth System Data Records for Use in Research Environments
MERRA	Modern-Era Retrospective analysis for Research and Applications
MintPy	Miami INsar Time-series software in Python
MInTS	Multiscale InSAR Time-Series
MLD	Multilook Detected
MNR	multiplicative noise ratio
MOC	Mission Operations Center (JPL)
MODIS	Moderate Resolution Imaging Spectroradiometer
MOE	Medium-fidelity Orbit Ephemeris
NAIS	North American Ice Service
NAIS	Northern American Ice Service
NARR	North American Regional Reanalysis
NASA	National Aeronautics and Space Administration
NEIC	National Earthquake Information Center (United States Geological Survey)
NEON	National Ecological Observatory Network (National Science Foundation)
NESAC	North Eastern Space Applications Centre
NIC	National Ice Center (United States)
NICC	National Interagency Coordination Center
NISAR	NASA-ISRO Synthetic Aperture Radar
NLCD	National Land Cover Database
NRC	National Research Council

ACRONYM	DEFINITION
NRCS	Natural Resources Conservation Service
NRCS	normalized radar cross section
NRSC	National Remote Sensing Centre (ISRO)
NSBAS	New Small BAseline Subset
NSF	National Science Foundation
PCS	Payload Communication Subsystem
pdfs	probability density functions
PDS	Payload Data System
PgC	petagrams of carbon
PMI	physical model inversion
pps	pulse per second
PRF	pulse repetition frequency
PSI	Persistent Scatterer Interferometry
PSInSAR	Persistent Scatterer Interferometric Synthetic Aperture Radar
PSLR	Peak Side Lobe Ratio
PST	Project Science Team
QA	quality assurance
RAB	Radar Antenna Boom
RAR	Radar Antenna Reflector
RCM	Radarsat Constellation Mission
RCS	radar cross section
REDD	Reducing Emissions from Deforestation and Forest Degradation

ACRONYM	DEFINITION
RFI	radio frequency interference
RGT	reference ground track
RIFG	Range-Doppler Interferogram
RIS	radar instrument structure
RMS	root mean square
ROFF	Range-Doppler Pixel Offsets
ROP	reference observation plan
RSLC	Range-Doppler Single Look Complex
RTC	radiometrically terrain corrected
RUNW	Range-Doppler Unwrapped Interferogram
SAC	Space Applications Centre (ISRO)
SAN	Shadnagar Acquisition Network (ISRO)
SAR	Synthetic Aperture Radar
SBAS	Small BAseline Subset
SCAN	Soil Climate Analysis Network (United States Department of Agriculture)
ScanSAR	Scanning Synthetic Aperture Radar
SDD	Science Definition Document
SDR	Subcommittee on Disaster Reduction
SDS	Science Data System
SDSC	Satish Dhawan Space Centre (ISRO)
SDT	Science Definition Team
SHAR	Sriharikota High Altitude Range (ISRO)
SIR-C	Spaceborne Imaging Radar-C

ACRONYM	DEFINITION
SLC	Single Look Complex
SLE	Sea Level Equivalent
SMA	semi-major axis
SMAP	Soil Moisture Active/Passive
SMD	Science Mission Directorate (NASA)
SMOS	Soil Moisture/Ocean Salinity
SNOTEL	Snow Telemetry (Natural Resources Conservation Service)
SNR	signal to noise ratio
SoilSCAPE	Soil moisture Sensing Controller And oPtimal Estimator (University of Southern California)
SPM	small-perturbation model
SPOTL	Some Programs for Ocean-Tide Loading
SRTM	Shuttle Radar Topography Mission
SSR	Solid State Recorder
STM	Science Traceability Matrix
SweepSAR	Sweeping Synthetic Aperture Radar
SWST	Sampling Window Start Time
TAA	Technical Assistance Agreement
Tb	Terabits
TEC	Total Electrons Content
TSR	time-series ratio
TTC	Telemetry, Tracking, and Commanding (station)
UAVSAR	Uninhabited Aerial Vehicle Synthetic Aperture Radar

ACRONYM	DEFINITION
ubRMSE	unbiased root-mean-squared error
UNFCCC	United Nations Framework Convention on Climate Change
USC	University of Southern California
USCRN	United States Climate Reference Network
USDA	United States Department of Agriculture
USGS	United States Geological Survey
UTM	Universal Transverse Mercator
VH	vertical transmit and horizontal receive
VIIRS	Visible Infrared Imaging Radiometer Suite
VNS	Volcano Notification Service
VV	vertical transmit and vertical receive
VWC	vegetation water content
WAN	wide area network
WFAS	Wildland Fire Assessment System (United States Forest Service)
WGCV	Working Group on Calibration and Validation
WWF	World Wildlife Federation

Credit: NASA/JPL-Caltech.

APPENDIX I: REFERENCES

Agnew, D. C. (2012). SPOTL: Some programs for ocean-tide loading.

Agram, P., Jolivet, R., Riel, B., Lin, Y., Simons, M., Hetland, E., et al. (2013). New radar interferometric time series analysis toolbox released. Eos, Transactions American Geophysical Union, 94(7), 69-70.

Ahlstrøm, A., Andersen, S. B., Andersen, M. L., Machguth, H., Nick, F., Joughin, I., et al. (2013). Seasonal velocities of eight major marine-terminating outlet glaciers of the Greenland ice sheet from continuous in situ GPS instruments. Earth System Science Data, 5(2), 277-287.

Ali, S., & Feigl, K. (2012). A new strategy for estimating geophysical parameters from InSAR data: Application to the Krafla central volcano in Iceland. Geochemistry, Geophysics, Geosystems, 13(6).

Alley, R. B., Clark, P. U., Huybrechts, P., & Joughin, I. (2005). Ice-sheet and sea-level changes. science, 310(5747), 456-460.

Alley, W. M., Healy, R. W., LaBaugh, J. W., & Reilly, T. E. (2002). Flow and storage in groundwater systems. science, 296(5575), 1985-1990.

Alpers, W. (1992). SAR imaging of ocean waves-A review. Paper presented at the [Proceedings] IGARSS'92 International Geoscience and Remote Sensing Symposium. IEEE, Vol. 1, 451-454.

Alsdorf, D. E., Melack, J. M., Dunne, T., Mertes, L. A., Hess, L. L., & Smith, L. C. (2000). Interferometric radar measurements of water level changes on the Amazon flood plain. Nature, 404(6774), 174-177.

Amelung, F., Galloway, D. L., Bell, J. W., Zebker, H. A., & Laczniak, R. J. (1999). Sensing the ups and downs of Las Vegas: InSAR reveals structural control of land subsidence and aquifer-system deformation. Geology, 27(6), 483-486.

Anconitano, G., Kim, S.-B., Chapman, B., Martinez, J., Siqueira, P., & Pierdicca, N. (2024). Classification of crop area using PALSAR, Sentinel-1, and planet data for the NISAR mission. Remote Sensing, 16(11), 1975.

Ansari, H., De Zan, F., & Parizzi, A. (2020). Study of systematic bias in measuring surface deformation with SAR interferometry. IEEE Transactions on Geoscience and Remote Sensing, 59(2), 1285-1301.

Arendt, A. A., Echelmeyer, K. A., Harrison, W. D., Lingle, C. S., & Valentine, V. B. (2002). Rapid wastage of Alaska glaciers and their contribution to rising sea level. science, 297(5580), 382-386.

Askne, J. I., Dammert, P. B., Ulander, L. M., & Smith, G. (1997). C-band repeat-pass interferometric SAR observations of the forest. IEEE Transactions on Geoscience and Remote Sensing, 35(1), 25-35.

Assessment, A. C. I. (2004). Impacts of a warming Arctic-Arctic climate impact assessment.

Aster, R. C., Borchers, B., & Thurber, C. H. (2018). Parameter estimation and inverse problems: Elsevier.

Attema, E., & Ulaby, F. T. (1978). Vegetation modeled as a water cloud. Radio science, 13(2), 357-364.

Baccini, A., Goetz, S. J., Walker, W., Laporte, N., Sun, M., Sulla-Menashe, D., et al. (2012). Estimated carbon dioxide emissions from tropical deforestation improved by carbon-density maps. Nature climate change, 2(3), 182-185.

Baghdadi, N., Gauthier, Y., & Bernier, M. (1997). Capability of multitemporal ERS-1 SAR data for wet-snow mapping. Remote sensing of environment, 60(2), 174-186.

Baghdadi, N., King, C., Chanzy, A. a., & Wigneron, J.-P. (2002). An empirical calibration of the integral equation model based on SAR data, soil moisture and surface roughness measurement over bare soils. International Journal of Remote Sensing, 23(20), 4325-4340.

Baker, D. J., Richards, G., Grainger, A., Gonzalez, P., Brown, S., DeFries, R., et al. (2010). Achieving forest carbon information with higher certainty: A five-part plan. Environmental science & policy, 13(3), 249-260.

Bally, P. (2012). Scientific and technical memorandum of the international forum on satellite EO and geohazards, 21–23 May 2012. Santorini, Greece. doi, 10, 5270.

Bamber, J. L., Alley, R. B., & Joughin, I. (2007). Rapid response of modern day ice sheets to external forcing. Earth and Planetary Science Letters, 257(1-2), 1-13.

Bartsch, A., Wiesmann, A., Strozzi, T., Schmullius, C., Hese, S., Duguay, C., et al. (2010). Implementation of a satellite data based permafrost information system—The DUE Permafrost Project. Paper presented at the Proceedings of the ESA Living Planet Symposium, Bergen, Norway, 28 June–2 July 2010, ESA Spec. Publ., SP686.

Bawden, G. W., Thatcher, W., Stein, R. S., Hudnut, K. W., & Peltzer, G. (2001). Tectonic contraction across Los Angeles after removal of groundwater pumping effects. Nature, 412(6849), 812-815.

Berardino, P., Fornaro, G., Lanari, R., & Sansosti, E. (2002). A new algorithm for surface deformation monitoring based on small baseline differential SAR interferograms. IEEE Transactions on Geoscience and Remote Sensing, 40(11), 2375-2383.

Bergen, K., Goetz, S., Dubayah, R., Henebry, G., Hunsaker, C., Imhoff, M., et al. (2009). Remote sensing of vegetation 3-D structure for biodiversity and habitat: Review and implications for lidar and radar spaceborne missions. Journal of Geophysical Research: Biogeosciences, 114(G2).

Bernhard, P., Zwieback, S., & Hajnsek, I. (2022). Accelerated mobilization of organic carbon from retrogressive thaw slumps on the northern Taymyr Peninsula. The Cryosphere, 16(7), 2819-2835.

Bindschadler, R. A., King, M. A., Alley, R. B., Anandakrishnan, S., & Padman, L. (2003). Tidally controlled stick-slip discharge of a West Antarctic ice. science, 301(5636), 1087-1089.

Blewitt, G. (2007). GPS and space-based geodetic methods. Geodesy, 3, 351-390.

Bonan, G. B. (2008). Forests and climate change: forcings, feedbacks, and the climate benefits of forests. science, 320(5882), 1444-1449.

Bourne, S., Maron, K., Oates, S., & Mueller, G. (2006, June 12-15). Monitoring deformation of a carbonate field in Oman: Evidence for large scale fault re-activation from microseismic, InSAR, and GPS. Paper presented at the 68th EAGE Annual Conference and Exhibition/SPE Europec, Vienna, Austria.

Bryant, R., Moran, M. S., Thoma, D., Collins, C. H., Skirvin, S., Rahman, M., et al. (2007). Measuring surface roughness height to parameterize radar backscatter models for retrieval of surface soil moisture. IEEE Geoscience and Remote Sensing Letters, 4(1), 137-141.

Burgess, E. W., Forster, R. R., & Larsen, C. F. (2013). Flow velocities of Alaskan glaciers. Nature communications, 4(1), 2146.

Bürgmann, R., Rosen, P. A., & Fielding, E. J. (2000). Synthetic aperture radar interferometry to measure Earth's surface topography and its deformation. Annual review of earth and planetary sciences, 28(1), 169-209.

Cairns, M. A., Brown, S., Helmer, E. H., & Baumgardner, G. A. (1997). Root biomass allocation in the world's upland forests. Oecologia, 111, 1-11.

Canadell, J. G., Le Quéré, C., Raupach, M. R., Field, C. B., Buitenhuis, E. T., Ciais, P., et al. (2007). Contributions to accelerating atmospheric CO2 growth from economic activity, carbon intensity, and efficiency of natural sinks. Proceedings of the national academy of sciences, 104(47), 18866-18870.

Capps, D. M., Rabus, B., Clague, J. J., & Shugar, D. H. (2010). Identification and characterization of alpine subglacial lakes using interferometric synthetic aperture radar (InSAR): Brady Glacier, Alaska, USA. Journal of Glaciology, 56(199), 861-870.

Cartus, O., Siqueira, P., & Kellndorfer, J. (2017). An error model for mapping forest cover and forest cover change using L-band SAR. IEEE Geoscience and Remote Sensing Letters, 15(1), 107-111.

Castañeda, C., Gutiérrez, F., Manunta, M., & Galve, J. P. (2009). DInSAR measurements of ground deformation by sinkholes, mining subsidence, and landslides, Ebro River, Spain. Earth Surface Processes and Landforms, 34(11), 1562-1574.

Casu, F., Buckley, S., Manzo, M., Pepe, A., & Lanari, R. (2005). Large scale InSAR deformation time series: Phoenix and Houston case studies. Paper presented at the Proceedings. 2005 IEEE International Geoscience and Remote Sensing Symposium, 2005. IGARSS'05. IEEE, Vol. 7, 5240-5243.

CEOS. (2014). Strategy for Carbon Observations from Space. The Committee on Earth Observation Satellites (CEOS) Response to the Group on Earth Observations (GEO) Carbon Strategy.(Issued Date: September, 30, 2014.

Chambers, J. Q., Negron-Juarez, R. I., Marra, D. M., Di Vittorio, A., Tews, J., Roberts, D., et al. (2013). The steady-state mosaic of disturbance and succession across an old-growth Central Amazon forest landscape. Proceedings of the national academy of sciences, 110(10), 3949-3954.

Change, I. P. O. C. (2007). Climate change 2007: the physical science basis. Agenda, 6(07), 333.

Chapman, B. D., Celi, J. E., Hamilton, S. K., & McDonald, K. C. (2014). Detection and monitoring of inundation with polarimetric L-band SAR. Paper presented at the AGU Fall Meeting Abstracts2014, G43A-0494.

Chatterjee, R., Fruneau, B., Rudant, J., Roy, P., Frison, P.-L., Lakhera, R., et al. (2006). Subsidence of Kolkata (Calcutta) City, India during the 1990s as observed from space by differential synthetic aperture radar interferometry (D-InSAR) technique. Remote sensing of environment, 102(1-2), 176-185.

Chatterjee, R. S., Roy, P., Dadhwal, V. K., Lakhera, R., Quang, T., & Saha, R. (2007). Assessment of land subsidence phenomenon in Kolkata city, India using satellite-based D-InSAR technique. Current science, 85-90.

Chatterjee, R. S., Sinha, A., Mahato, A. B., Champatiray, P. K., Lakhera, R. C., Singh, K. B., et al. (2007). Geoenvironmental Mapping of Jharia Coalfield from Multi-polarization and Interferometric Synthetic Aperture Radar Data. Paper presented at the Conference of JEP-Microwave held at Space Application Centre, Ahmedabad, India.

Chauhan, N. S., Lang, R. H., & Ranson, K. J. (1991). Radar modeling of a boreal forest. IEEE Transactions on Geoscience and Remote Sensing, 29(4), 627-638.

Chauhan, N. S., Le Vine, D. M., & Lang, R. H. (1994). Discrete scatter model for microwave radar and radiometer response to corn: comparison of theory and data. IEEE Transactions on Geoscience and Remote Sensing, 32(2), 416-426.

Chazdon, R. L., Chao, A., Colwell, R. K., Lin, S.-Y., Norden, N., Letcher, S. G., et al. (2011). A novel statistical method for classifying habitat generalists and specialists. Ecology, 92(6), 1332-1343.

Chen, C. W., & Zebker, H. A. (2002). Phase unwrapping for large SAR interferograms: Statistical segmentation and generalized network models. IEEE Transactions on Geoscience and Remote Sensing, 40(8), 1709-1719.

Chen, J. (2014). InSar Time Series Analysis of Subtle Transient Crustal Deformation Signals Associated with the 2010 Slow Slip Event at Kilauea, Hawaii: Stanford University.

Chen, J., Zebker, H. A., Segall, P., & Miklius, A. (2014). The 2010 slow slip event and secular motion at Kīlauea, Hawai'i, inferred from TerraSAR-X InSAR data. Journal of Geophysical Research: Solid Earth, 119(8), 6667-6683.

Cho, M. A., Debba, P., Mutanga, O., Dudeni-Tlhone, N., Magadla, T., & Khuluse, S. A. (2012). Potential utility of the spectral red-edge region of SumbandilaSat imagery for assessing indigenous forest structure and health. International journal of applied earth observation and Geoinformation, 16, 85-93.

Chubey, M. S., Franklin, S. E., & Wulder, M. A. (2006). Object-based analysis of Ikonos-2 imagery for extraction of forest inventory parameters. Photogrammetric Engineering & Remote Sensing, 72(4), 383-394.

Clark, D. B., Read, J. M., Clark, M. L., Cruz, A. M., Dotti, M. F., & Clark, D. A. (2004). Application of 1-M and 4-M resolution satellite data to ecological studies of tropical rain forests. Ecological Applications, 14(1), 61-74.

Cloude, S. R., Goodenough, D. G., & Chen, H. (2011). Compact decomposition theory. IEEE Geoscience and Remote Sensing Letters, 9(1), 28-32.

Coe, J. A. (2017). Landslide hazards and climate change: A perspective from the United States. In Slope safety preparedness for impact of climate change (pp. 479-523): CRC Press.

Cohen, W. B., Fiorella, M., Gray, J., Helmer, E., & Anderson, K. (1998). An efficient and accurate method for mapping forest clearcuts in the Pacific Northwest using Landsat imagery. Photogrammetric engineering and remote sensing, 64(4), 293-299.

Colony, R., & Thorndike, A. (1984). An estimate of the mean field of Arctic sea ice motion. Journal of Geophysical Research: Oceans, 89(C6), 10623-10629.

Coon, M. (1980). A review of AIDJEX modeling. Sea ice processes and models, 12, 25.

Dale, V. H., Joyce, L. A., McNulty, S., Neilson, R. P., Ayres, M. P., Flannigan, M. D., et al. (2001). Climate change and forest disturbances: climate change can affect forests by altering the frequency, intensity, duration, and timing of fire, drought, introduced species, insect and pathogen outbreaks, hurricanes, windstorms, ice storms, or landslides. BioScience, 51(9), 723-734.

Darras, S., Michou, M., & Sarrat, C. (1999). IGBP-DIS Wetland Data Initiative: a first step towards identifying a global delineation of wetlands.

Das, N. N., Entekhabi, D., Dunbar, R. S., Chaubell, M. J., Colliander, A., Yueh, S., et al. (2019). The SMAP and Copernicus Sentinel 1A/B microwave active-passive high resolution surface soil moisture product. Remote sensing of environment, 233, 111380.

Davis, J., Kellogg, L., Arrowsmith, J., Buffett, B., Constable, C., Donnellan, A., et al. (2016). Challenges and Opportunities for Research in ESI (CORE): report from the NASA Earth Surface and Interior (ESI) Focus Area Workshop, November 2–3, 2015. Arlington, Virginia.

De Zan, F., Zonno, M., & Lopez-Dekker, P. (2015). Phase inconsistencies and multiple scattering in SAR interferometry. IEEE Transactions on Geoscience and Remote Sensing, 53(12), 6608-6616.

Delbridge, B. G., Bürgmann, R., Fielding, E., Hensley, S., & Schulz, W. H. (2016). Three-dimensional surface deformation derived from airborne interferometric UAVSAR: Application to the Slumgullion Landslide. Journal of Geophysical Research: Solid Earth, 121(5), 3951-3977.

Deverel, S. J., Bachand, S., Brandenberg, S. J., Jones, C. E., Stewart, J. P., & Zimmaro, P. (2016). Factors and processes affecting delta levee system vulnerability. San Francisco Estuary and Watershed Science, 14(4).

Dixon, T. H., Amelung, F., Ferretti, A., Novali, F., Rocca, F., Dokka, R., et al. (2006). Subsidence and flooding in New Orleans. Nature, 441(7093), 587-588.

Dobson, M. C., & Ulaby, F. T. (1986). Active microwave soil moisture research. IEEE Transactions on Geoscience and Remote Sensing(1), 23-36.

Doin, M.-P., Lasserre, C., Peltzer, G., Cavalié, O., & Doubre, C. (2009). Corrections of stratified tropospheric delays in SAR interferometry: Validation with global atmospheric models. Journal of Applied Geophysics, 69(1), 35-50.

Doin, M.-P., Lodge, F., Guillaso, S., Jolivet, R., Lasserre, C., Ducret, G., et al. (2011). Presentation of the small baselin nsbas processing chain on a case example: The etan deformation monitoring from 2003 to 2010 using envisat data. Paper presented at the Fringe Symposium.

Donnellan, A., Parker, J., Heflin, M., Lyzenga, G., Moore, A., Ludwig, L. G., et al. (2018). fracture advancing step tectonics observed in the Yuha Desert and Ocotillo, CA, following the 2010 Mw7. 2 El Mayor-Cucapah Earthquake. Earth and Space Science, 5(9), 456-472.

Donnellan, A., Rosen, P., Graf, J., Loverro, A., Freeman, A., Treuhaft, R., et al. (2008). Deformation, ecosystem structure, and dynamics of ice (DESDynl). Paper presented at the 2008 IEEE Aerospace Conference. IEEE, Vol. 1-13.

Downs, B., Kettner, A. J., Chapman, B. D., Brakenridge, G. R., O'Brien, A. J., & Zuffada, C. (2023). Assessing the relative performance of GNSS-R flood extent observations: Case study in south Sudan. IEEE Transactions on Geoscience and Remote Sensing, 61, 1-13.

Dubois, P. C., Van Zyl, J., & Engman, T. (1995). Measuring soil moisture with imaging radars. IEEE Transactions on Geoscience and Remote Sensing, 33(4), 915-926.

Duputel, Z., Jiang, J., Jolivet, R., Simons, M., Rivera, L., Ampuero, J. P., et al. (2015). The Iquique earthquake sequence of April 2014: Bayesian modeling accounting for prediction uncertainty. Geophysical Research Letters, 42(19), 7949-7957.

Dzurisin, D. (2006). Volcano deformation: new geodetic monitoring techniques: Springer Science & Business Media.

Eggleston, H., Buendia, L., Miwa, K., Ngara, T., & Tanabe, K. (2006). 2006 IPCC guidelines for national greenhouse gas inventories.

Eiken, O., Ringrose, P., Hermanrud, C., Nazarian, B., Torp, T. A., & Høier, L. (2011). Lessons learned from 14 years of CCS operations: Sleipner, In Salah and Snøhvit. Energy procedia, 4, 5541-5548.

Emardson, T., Simons, M., & Webb, F. (2003). Neutral atmospheric delay in interferometric synthetic aperture radar applications: Statistical description and mitigation. Journal of Geophysical Research: Solid Earth, 108(B5).

Emery, W., Fowler, C. W., & Maslanik, J. (1997). Satellite-derived maps of Arctic and Antarctic sea ice motion: 1988 to 1994. Geophysical Research Letters, 24(8), 897-900.

Enquist, B. J., West, G. B., & Brown, J. H. (2009). Extensions and evaluations of a general quantitative theory of forest structure and dynamics. Proceedings of the national academy of sciences, 106(17), 7046-7051.

Entekhabi, D., Njoku, E. G., O'neill, P. E., Kellogg, K. H., Crow, W. T., Edelstein, W. N., et al. (2010). The soil moisture active passive (SMAP) mission. Proceedings of the IEEE, 98(5), 704-716.

Falkowski, M. J., Evans, J. S., Martinuzzi, S., Gessler, P. E., & Hudak, A. T. (2009). Characterizing forest succession with lidar data: An evaluation for the Inland Northwest, USA. Remote sensing of environment, 113(5), 946-956.

Fattahi, H., & Amelung, F. (2013). DEM error correction in InSAR time series. IEEE Transactions on Geoscience and Remote Sensing, 51(7), 4249-4259.

Fattahi, H., Simons, M., & Agram, P. (2017). InSAR time-series estimation of the ionospheric phase delay: An extension of the split range-spectrum technique. IEEE Transactions on Geoscience and Remote Sensing, 55(10), 5984-5996.

Ferretti, A., Prati, C., & Rocca, F. (2002). Permanent scatterers in SAR interferometry. IEEE Transactions on Geoscience and Remote Sensing, 39(1), 8-20.

Fielding, E. J., & Jung, J. (2024). Damage Proxy Mapping with SAR interferometric coherence change. Procedia Computer Science, 239, 2322-2328.

Fielding, E. J., Liu, Z., Stephenson, O. L., Zhong, M., Liang, C., Moore, A., et al. (2020). Surface deformation related to the 2019 Mw 7.1 and 6.4 Ridgecrest earthquakes in California from GPS, SAR interferometry, and SAR pixel offsets. Seismological Research Letters, 91(4), 2035-2046.

Fielding, E. J., Sangha, S. S., Bekaert, D. P., Samsonov, S. V., & Chang, J. C. (2017). Surface deformation of north-central Oklahoma related to the 2016 M w 5.8 Pawnee earthquake from SAR interferometry time series. Seismological Research Letters, 88(4), 971-982.

Finlayson, C., Davidson, N., Spiers, A., & Stevenson, N. (1999). Global wetland inventory–current status and future priorities. Marine and Freshwater Research, 50(8), 717-727.

Foley, J. A., DeFries, R., Asner, G. P., Barford, C., Bonan, G., Carpenter, S. R., et al. (2005). Global consequences of land use. science, 309(5734), 570-574.

Foster, J., Brooks, B., Cherubini, T., Shacat, C., Businger, S., & Werner, C. (2006). Mitigating atmospheric noise for InSAR using a high resolution weather model. Geophysical Research Letters, 33(16).

Fournier, T., Pritchard, M., & Riddick, S. (2010). Duration, magnitude, and frequency of subaerial volcano deformation events: New results from Latin America using InSAR and a global synthesis. Geochemistry, Geophysics, Geosystems, 11(1).

Freeman, A., Krieger, G., Rosen, P., Younis, M., Johnson, W. T., Huber, S., et al. (2009). SweepSAR: Beam-forming on receive using a reflector-phased array feed combination for spaceborne SAR. Paper presented at the 2009 IEEE Radar Conference. IEEE, Vol. 1-9.

Frolking, S., Palace, M. W., Clark, D., Chambers, J. Q., Shugart, H., & Hurtt, G. C. (2009). Forest disturbance and recovery: A general review in the context of spaceborne remote sensing of impacts on aboveground biomass and canopy structure. Journal of Geophysical Research: Biogeosciences, 114(G2).

Fung, A., & Eom, H. (1981). Multiple scattering and depolarization by a randomly rough Kirchhoff surface. IEEE Transactions on Antennas and Propagation, 29(3), 463-471.

Fung, A. K., Li, Z., & Chen, K.-S. (1992). Backscattering from a randomly rough dielectric surface. IEEE Transactions on Geoscience and Remote Sensing, 30(2), 356-369.

Gabriel, A. K., Goldstein, R. M., & Zebker, H. A. (1989). Mapping small elevation changes over large areas: Differential radar interferometry. Journal of Geophysical Research: Solid Earth, 94(B7), 9183-9191.

Galloway, D. L., Hudnut, K. W., Ingebritsen, S., Phillips, S. P., Peltzer, G., Rogez, F., & Rosen, P. (1998). Detection of aquifer system compaction and land subsidence using interferometric synthetic aperture radar, Antelope Valley, Mojave Desert, California. Water resources research, 34(10), 2573-2585.

Galloway, D. L., Jones, D. R., & Ingebritsen, S. E. (1999). Land subsidence in the United States (Vol. 1182): Geological Survey (USGS).

Gardner, A. S., Moholdt, G., Cogley, J. G., Wouters, B., Arendt, A. A., Wahr, J., et al. (2013). A reconciled estimate of glacier contributions to sea level rise: 2003 to 2009. science, 340(6134), 852-857.

GCOS Secretariat. (2009). Implementation plan for the global observing system for climate in support of the UNFCCC (2010 Update). Paper presented at the Proceedings of the Conference of the Parties (COP), Copenhagen, Denmark7-18.

Girard-Ardhuin, F., Mercier, G., Collard, F., & Garello, R. (2005). Operational oil-slick characterization by SAR imagery and synergistic data. IEEE Journal of Oceanic Engineering, 30(3), 487-495.

Global Carbon Project. (2025). Global Carbon Budget. Retrieved from https://globalcarbonbudget.org/

Global Forest Observations Initiative (GFOI). (2016). Integration of remote-sensing and ground-based observations for estimation of emissions and removals of greenhouse gases in forests: Methods and guidance from the Global Forest Observations Initiative, edition 2.0. UN Food and Agriculture Organization, 224.

Gomba, G., Parizzi, A., De Zan, F., Eineder, M., & Bamler, R. (2015). Toward operational compensation of ionospheric effects in SAR interferograms: The split-spectrum method. IEEE Transactions on Geoscience and Remote Sensing, 54(3), 1446-1461.

González, P. J., Tiampo, K. F., Palano, M., Cannavó, F., & Fernández, J. (2012). The 2011 Lorca earthquake slip distribution controlled by groundwater crustal unloading. Nature Geoscience, 5(11), 821-825.

Goodison, B., Waterman, S., & Langham, E. (1981). Application of synthetic aperture radar data to snow cover monitoring. Paper presented at the Canadian Symposium on Remote Sensing, 6 th, Halifax, Canada263-271.

Gov, W. Responding to the challenge of climate and environmental change: NASA's plan for a climate-centric architecture for Earth observations and applications from space. Retrieved from

Gray, A., Mattar, K., Vachon, P., Bindschadler, R., Jezek, K., Forster, R., & Crawford, J. (1998). InSAR results from the RADARSAT Antarctic Mapping Mission data: estimation of glacier motion using a simple registration procedure. Paper presented at the IGARSS'98. Sensing and Managing the Environment. 1998 IEEE International Geoscience and Remote Sensing. Symposium Proceedings.(Cat. No. 98CH36174). IEEE, Vol. 3, 1638-1640.

Grenerczy, G., & Wegmüller, U. (2011). Persistent scatterer interferometry analysis of the embankment failure of a red mud reservoir using ENVISAT ASAR data. Natural Hazards, 59, 1047-1053.

Grosse, G., Harden, J., Turetsky, M., McGuire, A. D., Camill, P., Tarnocai, C., et al. (2011). Vulnerability of high-atitude soil organic carbon in North America to disturbance. Journal of Geophysical Research: Biogeosciences, 116(G4).

Group on Earth Observations (GEO). (2005). The Global Earth Observation System of Systems (GEOSS) 10-Year Implementation Plan. Retrieved from https://www.google.com/url?sa=t&source=web&rct=j&opi=89978449&url=https://old.earthobservations.org/documents/10-Year%2520Implementation%2520Plan.pdf&ved=2ahUKEwim4qrskrqMAxWnLkQIHR0ZIx0QFnoECAoQAQ&usg=AOvVaw0bZ5oznlRbXqTN00lVg7n1

Gupta, M., Mohanty, K. K., & Majumdar, T. J. (2007). Land Subsidence Mapping in Jharia Coalfield using InSAR and DGPS Measurements. Paper presented at the Conference of JEP towards Microwave Remote Sensing Data Utilization (JEP-MW), Space Applications Center, Ahmedabad, India.

Haas, C. (2003). Dynamics versus thermodynamics: The sea ice thickness distribution. Sea ice: An introduction to its physics, chemistry, biology and geology, 82-111.

Hall, F. G., Bergen, K., Blair, J. B., Dubayah, R., Houghton, R., Hurtt, G., et al. (2011). Characterizing 3D vegetation structure from space: Mission requirements. Remote sensing of environment, 115(11), 2753-2775.

Hallikainen, M. T., Ulaby, F. T., Dobson, M. C., El-Rayes, M. A., & Wu, L.-K. (1985). Microwave dielectric behavior of wet soil-part 1: Empirical models and experimental observations. IEEE Transactions on Geoscience and Remote Sensing(1), 25-34.

Hansen, J., Sato, M., Ruedy, R., Lacis, A., & Oinas, V. (2000). Global warming in the twenty-first century: An alternative scenario. Proceedings of the national academy of sciences, 97(18), 9875-9880.

Hansen, M. C., Potapov, P. V., Moore, R., Hancher, M., Turubanova, S. A., Tyukavina, A., et al. (2013). High-resolution global maps of 21st-century forest cover change. science, 342(6160), 850-853.

Hanson, R. T. (1989). Aquifer-system compaction, Tucson Basin and Avra Valley, Arizona. Retrieved from

Hanssen, R. F. (2001). Radar interferometry: data interpretation and error analysis (Vol. 2): Springer Science & Business Media.

Harris, N. L., Brown, S., Hagen, S. C., Saatchi, S. S., Petrova, S., Salas, W., et al. (2012). Baseline map of carbon emissions from deforestation in tropical regions. science, 336(6088), 1573-1576.

Hasager, C. B., Vincent, P., Badger, J., Badger, M., Di Bella, A., Peña, A., et al. (2015). Using satellite SAR to characterize the wind flow around offshore wind farms. Energies, 8(6), 5413-5439.

He, L., Qin, Q., Panciera, R., Tanase, M., Walker, J. P., & Hong, Y. (2017). An extension of the alpha approximation method for soil moisture estimation using time-series SAR data over bare soil surfaces. IEEE Geoscience and Remote Sensing Letters, 14(8), 1328-1332.

Hensley, S., Agram, P., Buckley, S., Ghaemi, H., Gurrola, E., Harcke, L., et al. (2014). NISAR Performance Model and Error Budget. Retrieved from

Hensley, S., Chen, C., Erkmen, B., Haddad, Z., Harcke, L., Rosen, P., et al. (2010). A Performance Estimation Methodology for DESDynI. Paper presented at the 8th European Conference on Synthetic Aperture Radar. VDE, Vol. 1-4.

Hensley, S., Oveisgharan, S., Saatchi, S., Simard, M., Ahmed, R., & Haddad, Z. (2013). An error model for biomass estimates derived from polarimetric radar backscatter. IEEE Transactions on Geoscience and Remote Sensing, 52(7), 4065-4082.

Hess, L., Novo, E., Slaymaker, D., Holt, J., Steffen, C., Valeriano, D., et al. (2002). Geocoded digital videography for validation of land cover mapping in the Amazon basin. International Journal of Remote Sensing, 23(7), 1527-1555.

Hetland, E., Musé, P., Simons, M., Lin, Y., Agram, P., & DiCaprio, C. (2012). Multiscale InSAR time series (MInTS) analysis of surface deformation. Journal of Geophysical Research: Solid Earth, 117(B2).

Hibler III, W. (1979). A dynamic thermodynamic sea ice model. Journal of physical oceanography, 9(4), 815-846.

Hilley, G. E., Burgmann, R., Ferretti, A., Novali, F., & Rocca, F. (2004). Dynamics of slow-moving landslides from permanent scatterer analysis. science, 304(5679), 1952-1955.

Hinzman, L. D., Bettez, N. D., Bolton, W. R., Chapin, F. S., Dyurgerov, M. B., Fastie, C. L., et al. (2005). Evidence and implications of recent climate change in northern Alaska and other arctic regions. Climatic change, 72, 251-298.

Hock, R. (2005). Glacier melt: a review of processes and their modelling. Progress in physical geography, 29(3), 362-391.

Hock, R., & Jansson, P. (2006). Modeling glacier hydrology. Encyclopedia of hydrological sciences.

Hoffmann, J., Zebker, H. A., Galloway, D. L., & Amelung, F. (2001). Seasonal subsidence and rebound in Las Vegas Valley, Nevada, observed by synthetic aperture radar interferometry. Water resources research, 37(6), 1551-1566.

Holland, M. M., Bitz, C. M., & Tremblay, B. (2006). Future abrupt reductions in the summer Arctic sea ice. Geophysical Research Letters, 33(23).

Holt, B., Rothrock, D. A., & Kwok, R. (1992). Determination of sea ice motion from satellite images. Geophysical Monograph Series, 68, 343-354.

Hooper, A., Bekaert, D., Spaans, K., & Arıkan, M. (2012). Recent advances in SAR interferometry time series analysis for measuring crustal deformation. Tectonophysics, 514, 1-13.

Hooper, A., Zebker, H., Segall, P., & Kampes, B. (2004). A new method for measuring deformation on volcanoes and other natural terrains using InSAR persistent scatterers. Geophysical Research Letters, 31(23).

Hooper, A., & Zebker, H. A. (2007). Phase unwrapping in three dimensions with application to InSAR time series. Journal of the Optical Society of America A, 24(9), 2737-2747.

Hooper, A. J. (2006). Persistent scatter radar interferometry for crustal deformation studies and modeling of volcanic deformation: Stanford University.

Horton, D., Bringer, A., Johnson, J. T., Park, J., Al-Khaldi, M., & Bindlish, R. (2024). Modeling Soil Moisture Retrieval Errors in the Time-Series Ratio Method. IEEE Geoscience and Remote Sensing Letters, 21, 1-5.

Horton, D., Bringer, A., Johnson, J. T., Park, J., & Bindlish, R. (2022). Progress in time-series soil moisture retrieval using L-and S-band Radar Backscatter. Paper presented at the IGARSS 2022-2022 IEEE International Geoscience and Remote Sensing Symposium. IEEE, Vol. 5784-5787.

Houghton, R. (2005). Aboveground forest biomass and the global carbon balance. Global Change Biology, 11(6), 945-958.

Houghton, R., Hall, F., & Goetz, S. J. (2009). Importance of biomass in the global carbon cycle. Journal of Geophysical Research: Biogeosciences, 114(G2).

Houghton, R., Lawrence, K., Hackler, J., & Brown, S. (2001). The spatial distribution of forest biomass in the Brazilian Amazon: a comparison of estimates. Global Change Biology, 7(7), 731-746.

Houghton, R. A. (2005). Tropical deforestation as a source of greenhouse gas emissions. Tropical deforestation and climate change, 13.

Howat, I. M., Joughin, I., & Scambos, T. A. (2007). Rapid changes in ice discharge from Greenland outlet glaciers. science, 315(5818), 1559-1561.

Howat, I. M., Smith, B. E., Joughin, I., & Scambos, T. A. (2008). Rates of southeast Greenland ice volume loss from combined ICESat and ASTER observations. Geophysical Research Letters, 35(17).

Hsu, Y.-J., Simons, M., Avouac, J.-P., Galetzka, J., Sieh, K., Chlieh, M., et al. (2006). Frictional afterslip following the 2005 Nias-Simeulue earthquake, Sumatra. science, 312(5782), 1921-1926.

Huang, X., Reba, M., Coffin, A., Runkle, B. R., Huang, Y., Chapman, B., et al. (2021). Cropland mapping with L-band UAVSAR and development of NISAR products. Remote sensing of environment, 253, 112180.

Hurtt, G., Fisk, J., Thomas, R., Dubayah, R., Moorcroft, P., & Shugart, H. (2010). Linking models and data on vegetation structure. Journal of Geophysical Research: Biogeosciences, 115(G2).

Immitzer, M., Atzberger, C., & Koukal, T. (2012). Tree species classification with random forest using very high spatial resolution 8-band WorldView-2 satellite data. Remote Sensing, 4(9), 2661-2693.

Inoue, Y., Kurosu, T., Maeno, H., Uratsuka, S., Kozu, T., Dabrowska-Zielinska, K., & Qi, J. (2002). Season-long daily measurements of multifrequency (Ka, Ku, X, C, and L) and full-polarization backscatter signatures over paddy rice field and their relationship with biological variables. Remote sensing of environment, 81(2-3), 194-204.

Inter-Agency Space Debris Coordination Committee. (2007). IADC Space Debris Mitigation Guidelines. Retrieved from https://www.unoosa.org/documents/pdf/spacelaw/sd/IADC-2002-01-IADC-Space_Debris-Guidelines-Revision1.pdf

Ireland, R. L., Poland, J. F., & Riley, F. S. (1984). Land subsidence in the San Joaquin Valley, California, as of 1980: US Government Printing Office.

Ismaya, F., & Donovan, J. (2012). Applications of DInSAR for measuring mine-induced subsidence and constraining ground deformation model. In GeoCongress 2012: State of the Art and Practice in Geotechnical Engineering (pp. 3001-3010).

Iwahana, G., Uchida, M., Liu, L., Gong, W., Meyer, F. J., Guritz, R., et al. (2016). InSAR detection and field evidence for thermokarst after a tundra wildfire, using ALOS-PALSAR. Remote Sensing, 8(3), 218.

JECAM, Defourny, P., Jarvis, I., & Blaes, X. (2014). JECAM Guidelines for cropland and crop type definition and field data collection. Retrieved from http://jecam.org/documents/

Jenkins, A., & Doake, C. S. (1991). Ice-ocean interaction on Ronne Ice Shelf, Antarctica. Journal of Geophysical Research: Oceans, 96(C1), 791-813.

Jolivet, R., & Agram, P. S. (2012). Python-based atmospheric phase screen mitigation using atmospheric re-analysis. insarlab. Retrieved from https://github.com/insarlab/PyAPS

Jolivet, R., Agram, P. S., Lin, N. Y., Simons, M., Doin, M. P., Peltzer, G., & Li, Z. (2014). Improving InSAR geodesy using global atmospheric models. Journal of Geophysical Research: Solid Earth, 119(3), 2324-2341.

Jolivet, R., Duputel, Z., Riel, B., Simons, M., Rivera, L., Minson, S., et al. (2014). The 2013 M w 7.7 Balochistan earthquake: Seismic potential of an accretionary wedge. Bulletin of the Seismological Society of America, 104(2), 1020-1030.

Jolivet, R., Grandin, R., Lasserre, C., Doin, M. P., & Peltzer, G. (2011). Systematic InSAR tropospheric phase delay corrections from global meteorological reanalysis data. Geophysical Research Letters, 38(17).

Jolivet, R., Simons, M., Agram, P., Duputel, Z., & Shen, Z. K. (2015). Aseismic slip and seismogenic coupling along the central San Andreas Fault. Geophysical Research Letters, 42(2), 297-306.

Jones, C. E., & Blom, R. G. (2014). Bayou Corne, Louisiana, sinkhole: Precursory deformation measured by radar interferometry. Geology, 42(2), 111-114.

Jones, C. E., Minchew, B. B., Holt, B. B., & Hensley, S. S. (2011). Studies of the Deepwater Horizon oil spill with the UAVSAR radar. Monitoring and Modeling the Deepwater Horizon Oil Spill: A Record-Breaking Enterprise, 195, 33-50.

Jones, J., Jones, C. E., & Bekaert, D. P. (2022). Value of InSAR for monitoring land subsidence to support water management in the San Joaquin Valley, California. JAWRA Journal of the American Water Resources Association, 58(6), 995-1001.

Joughin, I. (2002). Ice-sheet velocity mapping: a combined interferometric and speckle-tracking approach. Annals of Glaciology, 34, 195-201.

Joughin, I., Abdalati, W., & Fahnestock, M. (2004). Large fluctuations in speed on Greenland's Jakobshavn Isbrae glacier. Nature, 432(7017), 608-610.

Joughin, I., & Alley, R. B. (2011). Stability of the West Antarctic ice sheet in a warming world. Nature Geoscience, 4(8), 506-513.

Joughin, I., Alley, R. B., & Holland, D. M. (2012). Ice-sheet response to oceanic forcing. science, 338(6111), 1172-1176.

Joughin, I., Kwok, R., & Fahnestock, M. (1996). Estimation of ice-sheet motion using satellite radar interferometry: method and error analysis with application to Humboldt Glacier, Greenland. Journal of Glaciology, 42(142), 564-575.

Joughin, I., MacAyeal, D. R., & Tulaczyk, S. (2004). Basal shear stress of the Ross ice streams from control method inversions. Journal of Geophysical Research: Solid Earth, 109(B9).

Joughin, I., & Padman, L. (2003). Melting and freezing beneath Filchner-Ronne Ice Shelf, Antarctica. Geophysical Research Letters, 30(9).

Joughin, I., Shean, D. E., Smith, B. E., & Dutrieux, P. (2016). Grounding line variability and subglacial lake drainage on Pine Island Glacier, Antarctica. Geophysical Research Letters, 43(17), 9093-9102.

Joughin, I., Smith, B. E., & Abdalati, W. (2010). Glaciological advances made with interferometric synthetic aperture radar. Journal of Glaciology, 56(200), 1026-1042.

Joughin, I., Smith, B. E., & Holland, D. M. (2010). Sensitivity of 21st century sea level to ocean-induced thinning of Pine Island Glacier, Antarctica. Geophysical Research Letters, 37(20).

Joughin, I., Smith, B. E., & Howat, I. (2018). Greenland Ice Mapping Project: ice flow velocity variation at sub-monthly to decadal timescales. The Cryosphere, 12(7), 2211-2227.

Joughin, I., Smith, B. E., Howat, I. M., Scambos, T., & Moon, T. (2010). Greenland flow variability from ice-sheet-wide velocity mapping. Journal of Glaciology, 56(197), 415-430.

Joughin, I. R., Kwok, R., & Fahnestock, M. A. (1998). Interferometric estimation of three-dimensional ice-flow using ascending and descending passes. IEEE Transactions on Geoscience and Remote Sensing, 36(1), 25-37.

JPL. (2018). NISAR Calibration and Validation Plan. Retrieved from https://nisar.jpl.nasa.gov/documents/27/NISAR_Mission_CalVal_Plan_20180810.pdf

Kääb, A. (2008). Remote sensing of permafrost-related problems and hazards. Permafrost and periglacial processes, 19(2), 107-136.

Kääb, A., Huggel, C., Fischer, L., Guex, S., Paul, F., Roer, I., et al. (2005). Remote sensing of glacier- and permafrost-related hazards in high mountains: an overview. Natural Hazards and Earth System Sciences, 5(4), 527-554.

Kalecinski, N. I., Skakun, S., Torbick, N., Huang, X., Franch, B., Roger, J.-C., & Vermote, E. (2024). Crop yield estimation at different growing stages using a synergy of SAR and optical remote sensing data. Science of Remote Sensing, 10, 100153.

Karam, M., Chen, K., & Fung, A. (1992). Statistics of backscatter radar return from vegetation. Paper presented at the In: IGARSS'92; Proceedings of the 12th Annual International Geoscience and Remote Sensing Symposium, Houston, TX, May 26-29, 1992. Vol. 1 (A93-47551 20-43). Institute of Electrical and Electronics Engineers, Inc., Vol.

Kaser, G., Cogley, J. G., Dyurgerov, M. B., Meier, M., & Ohmura, A. (2006). Mass balance of glaciers and ice caps: consensus estimates for 1961–2004. Geophysical Research Letters, 33(19).

Ke, Y., & Quackenbush, L. J. (2011). A review of methods for automatic individual tree-crown detection and delineation from passive remote sensing. International Journal of Remote Sensing, 32(17), 4725-4747.

Kellndorfer, J., Cartus, O., Bishop, J., Walker, W., & Holecz, F. (2014). Large scale mapping of forests and land cover with synthetic aperture radar data. Land applications of radar remote sensing, 59-94.

Kellndorfer, J., Flores-Anderson, A., Herndon, K., & Thapa, R. (2019). Using SAR data for mapping deforestation and forest degradation. The SAR Handbook. Comprehensive Methodologies for Forest Monitoring and Biomass Estimation, 65-79.

Kerr, Y. H., Waldteufel, P., Wigneron, J.-P., Delwart, S., Cabot, F., Boutin, J., et al. (2010). The SMOS mission: New tool for monitoring key elements of the global water cycle. Proceedings of the IEEE, 98(5), 666-687.

Khalil, M. A. K. (2013). Atmospheric methane: its role in the global environment: Springer Science & Business Media.

Kheshgi, H. S., Jain, A. K., Kotamarthi, V., & Wuebbles, D. J. (1999). Future atmospheric methane concentrations in the context of the stabilization of greenhouse gas concentrations. Journal of Geophysical Research: Atmospheres, 104(D16), 19183-19190.

Kienholz, C. (2010). Shrinkage of Selected South-Central Alaskan Glaciers AD 1900-2010: A Spatio-temporal Analysis Applying Photogrammetric, GIS-based and Historical Methods. Verlag nicht ermittelbar,

Kim, S.-B., & Liao, T.-H. (2021). Robust retrieval of soil moisture at field scale across wide-ranging SAR incidence angles for soybean, wheat, forage, oat and grass. Remote sensing of environment, 266, 112712.

Kim, S.-B., Moghaddam, M., Tsang, L., Burgin, M., Xu, X., & Njoku, E. G. (2013). Models of L-band radar backscattering coefficients over global terrain for soil moisture retrieval. IEEE Transactions on Geoscience and Remote Sensing, 52(2), 1381-1396.

Kim, S.-B., Tsang, L., Johnson, J. T., Huang, S., van Zyl, J. J., & Njoku, E. G. (2011). Soil moisture retrieval using time-series radar observations over bare surfaces. IEEE Transactions on Geoscience and Remote Sensing, 50(5), 1853-1863.

Kim, S.-B., Van Zyl, J. J., Johnson, J. T., Moghaddam, M., Tsang, L., Colliander, A., et al. (2017). Surface soil moisture retrieval using the L-band synthetic aperture radar onboard the soil moisture active–passive satellite and evaluation at core validation sites. IEEE Transactions on Geoscience and Remote Sensing, 55(4), 1897-1914.

Kim, Y., & Van Zyl, J. J. (2009). A time-series approach to estimate soil moisture using polarimetric radar data. IEEE Transactions on Geoscience and Remote Sensing, 47(8), 2519-2527.

Kindermann, G., McCallum, I., Fritz, S., & Obersteiner, M. (2008). A global forest growing stock, biomass and carbon map based on FAO statistics. Silva Fennica, 42(3), 387-396.

King, N., Argus, D., Langbein, J., Agnew, D., Bawden, G., Dollar, R., et al. (2007). Space geodetic observation of expansion of the San Gabriel Valley, California, aquifer system, during heavy rainfall in winter 2004–2005. Journal of Geophysical Research: Solid Earth, 112(B3).

Klein, L., & Taaheri, A. (2016). Data Model, File Format and Library. Retrieved from

Koirala, R., Kwiatek, G., Shirzaei, M., Brodsky, E., Cladouhos, T., Swyer, M., & Goebel, T. (2024). Induced seismicity and surface deformation associated with long-term and abrupt geothermal operations in Blue Mountain, Nevada. Earth and Planetary Science Letters, 643, 118883.

Kottmeier, C., Olf, J., Frieden, W., & Roth, R. (1992). Wind forcing and ice motion in the Weddell Sea region. Journal of Geophysical Research: Atmospheres, 97(D18), 20373-20383.

Kraatz, S., Lamb, B. T., Hively, W. D., Jennewein, J. S., Gao, F., Cosh, M. H., & Siqueira, P. (2023). Comparing NISAR (Using Sentinel-1), USDA/NASS CDL, and ground truth crop/Non-crop areas in an urban agricultural region. Sensors, 23(20), 8595.

Kraatz, S., Rose, S., Cosh, M., Torbick, N., Huang, X., & Siqueira, P. (2021). Performance evaluation of UAVSAR and simulated NISAR data for crop/noncrop classification over Stoneville, MS. Earth and Space Science, 8(1), e2020EA001363.

Kraatz, S., Siqueira, P., KelIndorfer, J., Torbick, N., Huang, X., & Cosh, M. (2022). Evaluating the robustness of NISAR's cropland product to time of observation, observing mode, and dithering. Earth and Space Science, 9(8), e2022EA002366.

Kraatz, S., Torbick, N., Jiao, X., Huang, X., Robertson, L. D., Davidson, A., et al. (2021). Comparison between dense l-band and c-band synthetic aperture radar (sar) time series for crop area mapping over a nisar calibration-validation site. Agronomy, 11(2), 273.

Kumar, H., Syed, T. H., Amelung, F., Mirzaee, S., Venkatesh, A., & Agrawal, R. (2025). InSAR reveals recovery of stressed aquifer systems in parts of Delhi, India: Evidence for improved groundwater management. Water resources research, 61(2), e2024WR037704.

Kurum, M., Kim, S.-B., Akbar, R., & Cosh, M. H. (2020). Surface Soil Moisture Retrievals Under Forest Canopy for $ L $-Band SAR Observations Across a Wide Range of Incidence Angles by Inverting a Physical Scattering Model. IEEE Journal of Selected Topics in Applied Earth Observations and Remote Sensing, 14, 1741-1753.

Kwok, R. (2001). Deformation of the Arctic Ocean sea ice cover between November 1996 and April 1997: a qualitative survey. Paper presented at the IUTAM Symposium on Scaling Laws in Ice Mechanics and Ice Dynamics: Proceedings of the IUTAM Symposium Held in Fairbanks, Alaska, USA, 13–16 June 2000. Springer, Vol. 315-322.

Kwok, R. (2010). Satellite remote sensing of sea-ice thickness and kinematics: a review. Journal of Glaciology, 56(200), 1129-1140.

Kwok, R., & Baltzer, T. (1995). The geophysical processor system at the Alaska SAR Facility. Photogramm. Eng. Remote Sens, 61, 1445-1453.

Kwok, R., & Cunningham, G. (2002). Seasonal ice area and volume production of the Arctic Ocean: November 1996 through April 1997. Journal of Geophysical Research: Oceans, 107(C10), SHE 12-11-SHE 12-17.

Kwok, R., Cunningham, G. F., & Hibler III, W. D. (2003). Sub-daily sea ice motion and deformation from RADARSAT observations. Geophysical Research Letters, 30(23).

Kwok, R., Curlander, J. C., McConnell, R., & Pang, S. S. (2002). An ice-motion tracking system at the Alaska SAR facility. IEEE Journal of Oceanic Engineering, 15(1), 44-54.

Kwok, R., Nghiem, S., Yueh, S., & Huynh, D. (1995). Retrieval of thin ice thickness from multifrequency polarimetric SAR data. Remote sensing of environment, 51(3), 361-374.

Lal, P., Singh, G., Das, N. N., Colliander, A., & Entekhabi, D. (2022). Assessment of ERA5-land volumetric soil water layer product using in situ and SMAP soil moisture observations. IEEE Geoscience and Remote Sensing Letters, 19, 1-5.

Lal, P., Singh, G., Das, N. N., Entekhabi, D., Lohman, R., Colliander, A., et al. (2023). A multi-scale algorithm for the NISAR mission high-resolution soil moisture product. Remote sensing of environment, 295, 113667.

Lanari, R., Lundgren, P., Manzo, M., & Casu, F. (2004). Satellite radar interferometry time series analysis of surface deformation for Los Angeles, California. Geophysical Research Letters, 31(23).

Lang, R. H. (1981). Electromagnetic backscattering from a sparse distribution of lossy dielectric scatterers. Radio science, 16(01), 15-30.

Lang, R. H., & Sighu, J. S. (1983). Electromagnetic backscattering from a layer of vegetation: A discrete approach. IEEE Transactions on Geoscience and Remote Sensing(1), 62-71.

Larour, E., Rignot, E., Joughin, I., & Aubry, D. (2005). Rheology of the Ronne Ice Shelf, Antarctica, inferred from satellite radar interferometry data using an inverse control method. Geophysical Research Letters, 32(5).

Lauknes, T. R., Zebker, H. A., & Larsen, Y. (2010). InSAR deformation time series using an $ L_ {1} $-norm small-baseline approach. IEEE Transactions on Geoscience and Remote Sensing, 49(1), 536-546.

Lavalle, M., Simard, M., & Hensley, S. (2011). A temporal decorrelation model for polarimetric radar interferometers. IEEE Transactions on Geoscience and Remote Sensing, 50(7), 2880-2888.

Lavalle, M., Telli, C., Pierdicca, N., Khati, U., Cartus, O., & KelIndorfer, J. (2023). Model-based retrieval of forest parameters from Sentinel-1 coherence and backscatter time series. IEEE Geoscience and Remote Sensing Letters, 20, 1-5.

Le Quéré, C., Andrew, R. M., Friedlingstein, P., Sitch, S., Pongratz, J., Manning, A. C., et al. (2018). Global carbon budget 2017. Earth System Science Data, 10(1), 405-448.

Le Toan, T., Quegan, S., Davidson, M., Balzter, H., Paillou, P., Papathanassiou, K., et al. (2011). The BIOMASS mission: Mapping global forest biomass to better understand the terrestrial carbon cycle. Remote sensing of environment, 115(11), 2850-2860.

Li, Z., Fielding, E. J., Cross, P., & Muller, J. P. (2006). Interferometric synthetic aperture radar atmospheric correction: GPS topography-dependent turbulence model. Journal of Geophysical Research: Solid Earth, 111(B2).

Li, Z., & Guo, H. (2000). Permafrost mapping in the Tibet plateau using polarimetric SAR. Paper presented at the IGARSS 2000. IEEE 2000 International Geoscience and Remote Sensing Symposium. Taking the Pulse of the Planet: The Role of Remote Sensing in Managing the Environment. Proceedings (Cat. No. 00CH37120). Ieee, Vol. 5, 2024-2026.

Li, Z., Muller, J. P., Cross, P., Albert, P., Fischer, J., & Bennartz, R. (2006). Assessment of the potential of MERIS near-infrared water vapour products to correct ASAR interferometric measurements. International Journal of Remote Sensing, 27(2), 349-365.

Liao, T.-H., Kim, S.-B., Handwerger, A. L., Fielding, E. J., Cosh, M. H., & Schulz, W. H. (2021). High-resolution soil-moisture maps over landslide regions in northern California grassland derived from Sar backscattering coefficients. IEEE Journal of Selected Topics in Applied Earth Observations and Remote Sensing, 14, 4547-4560.

Lin, Y. N., Yun, S.-H., Bhardwaj, A., & Hill, E. M. (2019). Urban flood detection with Sentinel-1 multi-temporal synthetic aperture radar (SAR) observations in a Bayesian framework: a case study for Hurricane Matthew. Remote Sensing, 11(15), 1778.

Lin, Y. n. N., Simons, M., Hetland, E. A., Muse, P., & DiCaprio, C. (2010). A multiscale approach to estimating topographically correlated propagation delays in radar interferograms. Geochemistry, Geophysics, Geosystems, 11(9).

Lindsay, R. W., & Stern, H. (2003). The RADARSAT geophysical processor system: Quality of sea ice trajectory and deformation estimates. Journal of Atmospheric and Oceanic Technology, 20(9), 1333-1347.

Liu, L., Jafarov, E. E., Schaefer, K. M., Jones, B. M., Zebker, H. A., Williams, C. A., et al. (2014). InSAR detects increase in surface subsidence caused by an Arctic tundra fire. Geophysical Research Letters, 41(11), 3906-3913.

Liu, L., Schaefer, K., Zhang, T., & Wahr, J. (2012). Estimating 1992–2000 average active layer thickness on the Alaskan North Slope from remotely sensed surface subsidence. Journal of Geophysical Research: Earth Surface, 117(F1).

Liu, L., Zhang, T., & Wahr, J. (2010). InSAR measurements of surface deformation over permafrost on the North Slope of Alaska. Journal of Geophysical Research: Earth Surface, 115(F3).

Liu, M., Tian, H., Yang, Q., Yang, J., Song, X., Lohrenz, S. E., & Cai, W. J. (2013). Long-term trends in evapotranspiration and runoff over the drainage basins of the Gulf of Mexico during 1901–2008. Water resources research, 49(4), 1988-2012.

Lohman, R. B., & Simons, M. (2005). Locations of selected small earthquakes in the Zagros mountains. Geochemistry, Geophysics, Geosystems, 6(3).

Lohman, R. B., Simons, M., & Savage, B. (2002). Location and mechanism of the Little Skull Mountain earthquake as constrained by satellite radar interferometry and seismic waveform modeling. Journal of Geophysical Research: Solid Earth, 107(B6), ETG 7-1-ETG 7-10.

Lu, Z., Dzurisin, D., Biggs, J., Wicks Jr, C., & McNutt, S. (2010). Ground surface deformation patterns, magma supply, and magma storage at Okmok volcano, Alaska, from InSAR analysis: 1. Intereruption deformation, 1997–2008. Journal of Geophysical Research: Solid Earth, 115(B5).

Lu, Z., Dzurisin, D., Lu, Z., & Dzurisin, D. (2014). InSAR imaging of Aleutian volcanoes: Springer.

Lu, Z., & Wicks, C. (2008). Study of the 6 August 2007 Crandall Canyon mine (Utah, USA) collapse from ALOS PALSAR InSAR. Paper presented at the AGU Fall Meeting Abstracts2008, G53A-0628.

Lucas, R., Bunting, P., Paterson, M., & Chisholm, L. (2008). Classification of Australian forest communities using aerial photography, CASI and HyMap data. Remote sensing of environment, 112(5), 2088-2103.

Lundgren, P., Casu, F., Manzo, M., Pepe, A., Berardino, P., Sansosti, E., & Lanari, R. (2004). Gravity and magma induced spreading of Mount Etna volcano revealed by satellite radar interferometry. Geophysical Research Letters, 31(4).

MacAyeal, D. R. (1993). A tutorial on the use of control methods in ice-sheet modeling. Journal of Glaciology, 39(131), 91-98.

Malinowski, R., Groom, G., Schwanghart, W., & Heckrath, G. (2015). Detection and delineation of localized flooding from WorldView-2 multispectral data. Remote Sensing, 7(11), 14853-14875.

Malvern, L. E. (1969). Introduction to the Mechanics of a Continuous Medium.

Marquardt, F., & Girvin, S. M. (2009). Optomechanics (a brief review). arXiv preprint arXiv:0905.0566.

Massonnet, D., Rossi, M., Carmona, C., Adragna, F., Peltzer, G., Feigl, K., & Rabaute, T. (1993). The displacement field of the Landers earthquake mapped by radar interferometry. Nature, 364(6433), 138-142.

Mattia, F., Balenzano, A., Satalino, G., Lovergine, F., Peng, J., Wegmuller, U., et al. (2018). Sentinel-1 & Sentinel-2 for SOIL moisture retrieval at field scale. Paper presented at the IGARSS 2018-2018 IEEE international geoscience and remote sensing symposium. IEEE, Vol. 6143-6146.

Mattia, F., Satalino, G., Pauwels, V., & Loew, A. (2009). Soil moisture retrieval through a merging of multi-temporal L-band SAR data and hydrologic modelling. Hydrology and Earth System Sciences, 13(3), 343-356.

Matzler, C. (1994). Microwave (1-100 GHz) dielectric model of leaves. IEEE Transactions on Geoscience and Remote Sensing, 32(4), 947-949.

McNairn, H., Jackson, T. J., Wiseman, G., Belair, S., Berg, A., Bullock, P., et al. (2014). The soil moisture active passive validation experiment 2012 (SMAPVEX12): Prelaunch calibration and validation of the SMAP soil moisture algorithms. IEEE Transactions on Geoscience and Remote Sensing, 53(5), 2784-2801.

Meier, M. F., Dyurgerov, M. B., Rick, U. K., O'neel, S., Pfeffer, W. T., Anderson, R. S., et al. (2007). Glaciers dominate eustatic sea-level rise in the 21st century. science, 317(5841), 1064-1067.

Meinzer, O. E. (1928). Compressibility and elasticity of artesian aquifers. Economic Geology, 23(3), 263-291.

Mermoz, S., Réjou-Méchain, M., Villard, L., Le Toan, T., Rossi, V., & Gourlet-Fleury, S. (2015). Decrease of L-band SAR backscatter with biomass of dense forests. Remote sensing of environment, 159, 307-317.

Meyer, F. (2010). A review of ionospheric effects in low-frequency SAR—Signals, correction methods, and performance requirements. Paper presented at the 2010 IEEE International Geoscience and Remote Sensing Symposium. IEEE, Vol. 29-32.

Meyer, F. J. (2011). Performance requirements for ionospheric correction of low-frequency SAR data. IEEE Transactions on Geoscience and Remote Sensing, 49(10), 3694-3702.

Meyer, F. J. (2014). Quantifying ionosphere-induced image distortions in L-band SAR data using the ionospheric scintillation model WBMOD. Paper presented at the EUSAR 2014; 10th European Conference on Synthetic Aperture Radar. VDE, Vol. 1-4.

Meyer, F. J., & Nicoll, J. B. (2008). Prediction, detection, and correction of Faraday rotation in full-polarimetric L-band SAR data. IEEE Transactions on Geoscience and Remote Sensing, 46(10), 3076-3086.

Michaelides, R. J., Zebker, H. A., & Zheng, Y. (2019). An algorithm for estimating and correcting decorrelation phase from InSAR data using closure phase triplets. IEEE Transactions on Geoscience and Remote Sensing, 57(12), 10390-10397.

Michel, R., & Rignot, E. (1999). Flow of Glaciar Moreno, Argentina, from repeat-pass Shuttle Imaging Radar images: comparison of the phase correlation method with radar interferometry. Journal of Glaciology, 45(149), 93-100.

Millennium Ecosystem Assessment (MEA). (2005). Ecosystems and human well-being (Vol. 5): Island press Washington, DC.

Mironov, V. L., Dobson, M. C., Kaupp, V. H., Komarov, S. A., & Kleshchenko, V. N. (2004). Generalized refractive mixing dielectric model for moist soils. IEEE Transactions on Geoscience and Remote Sensing, 42(4), 773-785.

Mitchard, E. T., Saatchi, S. S., Woodhouse, I. H., Nangendo, G., Ribeiro, N., Williams, M., et al. (2009). Using satellite radar backscatter to predict above-ground woody biomass: A consistent relationship across four different African landscapes. Geophysical Research Letters, 36(23).

Mohr, J. J., Reeh, N., & Madsen, S. N. (1998). Three-dimensional glacial flow and surface elevation measured with radar interferometry. Nature, 391(6664), 273-276.

Monaldo, F., Jackson, C., Li, X., & Pichel, W. G. (2016). Preliminary evaluation of Sentinel-1A wind speed retrievals. IEEE Journal of Selected Topics in Applied Earth Observations and Remote Sensing, 9(6), 2638-2642.

Monaldo, F., & Kerbaol, V. (2004). The SAR measurement of ocean surface winds: an overview for the 2nd workshop on coastal and marine applications of SAR. Paper presented at the Proc. of the 2nd workshop on SAR coastal and marine applications8-12.

Moon, T., Joughin, I., Smith, B., & Howat, I. (2012). 21st-century evolution of Greenland outlet glacier velocities. science, 336(6081), 576-578.

Moore, R. K., Claassen, J. P., & Lin, Y. (1981). Scanning spaceborne synthetic aperture radar with integrated radiometer. IEEE Transactions on Aerospace and Electronic Systems(3), 410-421.

Morlighem, M., Seroussi, H., Larour, E., & Rignot, E. (2013). Inversion of basal friction in Antarctica using exact and incomplete adjoints of a higher-order model. Journal of Geophysical Research: Earth Surface, 118(3), 1746-1753.

Mouginot, J., Rignot, E., Scheuchl, B., & Millan, R. (2017). Comprehensive annual ice sheet velocity mapping using Landsat-8, Sentinel-1, and RADARSAT-2 data. Remote Sensing, 9(4), 364.

Myneni, R. B., Dong, J., Tucker, C. J., Kaufmann, R. K., Kauppi, P. E., Liski, J., et al. (2001). A large carbon sink in the woody biomass of Northern forests. Proceedings of the national academy of sciences, 98(26), 14784-14789.

NASA. (2010). Responding to the challenge of climate and environmental change: NASA's plan for a climate-centric architecture for Earth observations and applications from space. Retrieved from

National Research Council. (1991). Mitigating losses from land subsidence in the United States.

National Research Council, Earth, D. o., Studies, L., Board, O. S., & Coasts, C. o. M. S. E. A. S. (2007). Mitigating shore erosion along sheltered coasts: National Academies Press.

National Research Council, Earth, D. o., Studies, L., Sciences, B. o. E., Resources, Seismology, C. o., et al. (2013). Induced seismicity potential in energy technologies: National Academies Press.

Neumann, M., Saatchi, S. S., Ulander, L. M., & Fransson, J. E. (2012). Assessing performance of L-and P-band polarimetric interferometric SAR data in estimating boreal forest above-ground biomass. IEEE Transactions on Geoscience and Remote Sensing, 50(3), 714-726.

Oh, Y., Sarabandi, K., & Ulaby, F. T. (2002). An empirical model and an inversion technique for radar scattering from bare soil surfaces. IEEE Transactions on Geoscience and Remote Sensing, 30(2), 370-381.

Olofsson, P., Foody, G. M., Herold, M., Stehman, S. V., Woodcock, C. E., & Wulder, M. A. (2014). Good practices for estimating area and assessing accuracy of land change. Remote sensing of environment, 148, 42-57.

Olson, D. M., Dinerstein, E., Wikramanayake, E. D., Burgess, N. D., Powell, G. V., Underwood, E. C., et al. (2001). Terrestrial Ecoregions of the World: A New Map of Life on Earth: A new global map of terrestrial ecoregions provides an innovative tool for conserving biodiversity. BioScience, 51(11), 933-938.

Onn, F., & Zebker, H. (2006). Correction for interferometric synthetic aperture radar atmospheric phase artifacts using time series of zenith wet delay observations from a GPS network. Journal of Geophysical Research: Solid Earth, 111(B9).

Onuma, T., & Ohkawa, S. (2009). Detection of surface deformation related with CO2 injection by DInSAR at In Salah, Algeria. Energy procedia, 1(1), 2177-2184.

Ouellette, J. D., Johnson, J. T., Balenzano, A., Mattia, F., Satalino, G., Kim, S.-B., et al. (2017). A time-series approach to estimating soil moisture from vegetated surfaces using L-band radar backscatter. IEEE Transactions on Geoscience and Remote Sensing, 55(6), 3186-3193.

Pachauri, R. K., & Reisinger, A. (2007). Climate change 2007: Synthesis report. Contribution of working groups I, II and III to the fourth assessment report of the Intergovernmental Panel on Climate Change: Ipcc.

Paine, J. G., Buckley, S. M., Collins, E. W., & Wilson, C. R. (2012). Assessing collapse risk in evaporite sinkhole-prone areas using microgravimetry and radar interferometry. Journal of Environmental and Engineering Geophysics, 17(2), 75-87.

Pan, Y., Birdsey, R. A., Fang, J., Houghton, R., Kauppi, P. E., Kurz, W. A., et al. (2011). A large and persistent carbon sink in the world's forests. science, 333(6045), 988-993.

Park, J., Bindlish, R., Bringer, A., Horton, D., & Johnson, J. T. (2022). Time-series ratio algorithm for nisar soil moisture retrieval. Paper presented at the IGARSS 2022-2022 IEEE International Geoscience and Remote Sensing Symposium. IEEE, Vol. 5712-5715.

Park, J., Bindlish, R., Bringer, A., Horton, D., & Johnson, J. T. (2024). NISAR Time-Series Ratio Algorithm for Soil Moisture Retrieval: Pre-Launch Evaluation With SMAPVEX12 Field Campaign Data. IEEE Journal of Selected Topics in Applied Earth Observations and Remote Sensing.

Paterson, W. S. B. (1994). The physics of glaciers. Oxford, Pergamon: Cambridge University Press.

Paulson, A., Zhong, S., & Wahr, J. (2007). Inference of mantle viscosity from GRACE and relative sea level data. Geophysical Journal International, 171(2), 497-508.

Payne, A. J., Vieli, A., Shepherd, A. P., Wingham, D. J., & Rignot, E. (2004). Recent dramatic thinning of largest West Antarctic ice stream triggered by oceans. Geophysical Research Letters, 31(23).

Peltzer, G., Hudnut, K. W., & Feigl, K. L. (1994). Analysis of coseismic surface displacement gradients using radar interferometry: New insights into the Landers earthquake. Journal of Geophysical Research: Solid Earth, 99(B11), 21971-21981.

Penman, J., Gytarsky, M., Hiraishi, T., Krug, T., Kruger, D., Pipatti, R., et al. (2003). Good practice guidance for land use, land-use change and forestry.

Peplinski, N. R., Ulaby, F. T., & Dobson, M. C. (1995). Dielectric properties of soils in the 0.3-1.3-GHz range. IEEE Transactions on Geoscience and Remote Sensing, 33(3), 803-807.

Peters, G. P., Marland, G., Le Quéré, C., Boden, T., Canadell, J. G., & Raupach, M. R. (2012). Rapid growth in CO2 emissions after the 2008–2009 global financial crisis. Nature climate change, 2(1), 2-4.

Phillips, O. (2003). Groundwater flow patterns in extensive shallow aquifers with gentle relief: Theory and application to the Galena/Locust Grove region of eastern Maryland. Water resources research, 39(6).

Piles, M., Entekhabi, D., & Camps, A. (2009). A change detection algorithm for retrieving high-resolution soil moisture from SMAP radar and radiometer observations. IEEE Transactions on Geoscience and Remote Sensing, 47(12), 4125-4131.

Poland, J. F. (1984). Guidebook to studies of land subsidence due to ground-water withdrawal.

Pritchard, M., Ji, C., & Simons, M. (2006). Distribution of slip from 11 Mw> 6 earthquakes in the northern Chile subduction zone. Journal of Geophysical Research: Solid Earth, 111(B10).

Pritchard, M., Norabuena, E., Ji, C., Boroschek, R., Comte, D., Simons, M., et al. (2007). Geodetic, teleseismic, and strong motion constraints on slip from recent southern Peru subduction zone earthquakes. Journal of Geophysical Research: Solid Earth, 112(B3).

Pritchard, M., & Simons, M. (2004). An InSAR-based survey of volcanic deformation in the central Andes. Geochemistry, Geophysics, Geosystems, 5(2).

Pritchard, M. E., & Simons, M. (2002). A satellite geodetic survey of large-scale deformation of volcanic centres in the central Andes. Nature, 418(6894), 167-171.

Pullman, E. R., Torre Jorgenson, M., & Shur, Y. (2007). Thaw settlement in soils of the Arctic Coastal Plain, Alaska. Arctic, Antarctic, and Alpine Research, 39(3), 468-476.

Ramaswamy, V., Boucher, O., Haigh, J., & Hauglustaine, D. (2001). Radiative forcing of climate. Climate Change, IPCC Scientific Assessment, 388-389.

Reiche, J., Hamunyela, E., Verbesselt, J., Hoekman, D., & Herold, M. (2018). Improving near-real time deforestation monitoring in tropical dry forests by combining dense Sentinel-1 time series with Landsat and ALOS-2 PALSAR-2. Remote sensing of environment, 204, 147-161.

Reiche, J., Lucas, R., Mitchell, A. L., Verbesselt, J., Hoekman, D. H., Haarpaintner, J., et al. (2016). Combining satellite data for better tropical forest monitoring. Nature climate change, 6(2), 120-122.

Richards, J. A. (2009). Remote sensing with imaging radar (Vol. 1): Springer.

Ridder, R. M. (2007). Global forest resources assessment 2010: options and recommendations for a global remote sensing survey of forests. FAO For. Resour. Assess. Programme Work. Pap, 141.

Rignot, E., Casassa, G., Gogineni, P., Krabill, W., Rivera, A., & Thomas, R. (2004). Accelerated ice discharge from the Antarctic Peninsula following the collapse of Larsen B ice shelf. Geophysical Research Letters, 31(18).

Rignot, E., Jacobs, S., Mouginot, J., & Scheuchl, B. (2013). Ice-shelf melting around Antarctica. science, 341(6143), 266-270.

Rignot, E., & Jacobs, S. S. (2002). Rapid bottom melting widespread near Antarctic ice sheet grounding lines. science, 296(5575), 2020-2023.

Rignot, E., & Kanagaratnam, P. (2006). Changes in the velocity structure of the Greenland Ice Sheet. science, 311(5763), 986-990.

Rignot, E., Mouginot, J., & Scheuchl, B. (2011). Ice flow of the Antarctic ice sheet. science, 333(6048), 1427-1430.

Rignot, E., Mouginot, J., & Scheuchl, B. (2011). Antarctic grounding line mapping from differential satellite radar interferometry. Geophysical Research Letters, 38(10).

Rignot, E., Velicogna, I., van den Broeke, M. R., Monaghan, A., & Lenaerts, J. T. (2011). Acceleration of the contribution of the Greenland and Antarctic ice sheets to sea level rise. Geophysical Research Letters, 38(5).

Rigor, I. G., Wallace, J. M., & Colony, R. L. (2002). Response of sea ice to the Arctic Oscillation. Journal of Climate, 15(18), 2648-2663.

Riley, F. S. (1969). Analysis of borehole extensometer data from central California.

Ringrose, P., Mansour, A., Mason, D., Espinassous, M., Myhrer, O., & Iding, M. (2008). Plume estimation around well KB-502 at the In Salah Gas Development CO2 Storage Site. Paper presented at the First EAGE CO2 Geological Storage Workshop. European Association of Geoscientists & Engineers, Vol. cp-88-00029.

Robinson, C., Saatchi, S., Neumann, M., & Gillespie, T. (2013). Impacts of spatial variability on aboveground biomass estimation from L-band radar in a temperate forest. Remote Sensing, 5(3), 1001-1023.

Romanovsky, V. E., Smith, S. L., & Christiansen, H. H. (2010). Permafrost thermal state in the polar Northern Hemisphere during the international polar year 2007–2009: a synthesis. Permafrost and periglacial processes, 21(2), 106-116.

Romeiser, R. (2013). The future of SAR-based oceanography: High-resolution current measurements by along-track interferometry. Oceanography, 26(2), 92-99.

Romijn, E., Herold, M., Kooistra, L., Murdiyarso, D., & Verchot, L. (2012). Assessing capacities of non-Annex I countries for national forest monitoring in the context of REDD+. Environmental science & policy, 19, 33-48.

Rose, S., Kraatz, S., Kellndorfer, J., Cosh, M. H., Torbick, N., Huang, X., & Siqueira, P. (2021). Evaluating NISAR's cropland mapping algorithm over the conterminous United States using Sentinel-1 data. Remote sensing of environment, 260, 112472.

Rosen, P. A., Gurrola, E., Sacco, G. F., & Zebker, H. (2012). The InSAR scientific computing environment. Paper presented at the EUSAR 2012; 9th European conference on synthetic aperture radar. VDE, Vol. 730-733.

Rosen, P. A., Hensley, S., & Chen, C. (2010). Measurement and mitigation of the ionosphere in L-band interferometric SAR data. Paper presented at the 2010 IEEE radar conference. IEEE, Vol. 1459-1463.

Rosen, P. A., Hensley, S., Joughin, I. R., Li, F. K., Madsen, S. N., Rodriguez, E., & Goldstein, R. M. (2000). Synthetic aperture radar interferometry. Proceedings of the IEEE, 88(3), 333-382.

Rosen, P. A., Hensley, S., Shaffer, S., Veilleux, L., Chakraborty, M., Misra, T., et al. (2015). The NASA-ISRO SAR mission-An international space partnership for science and societal benefit. Paper presented at the 2015 IEEE radar conference (RadarCon). IEEE, Vol. 1610-1613.

Rosenqvist, Å., Milne, A., Lucas, R., Imhoff, M., & Dobson, C. (2003). A review of remote sensing technology in support of the Kyoto Protocol. Environmental science & policy, 6(5), 441-455.

Rosenqvist, A., Shimada, M., Ito, N., & Watanabe, M. (2007). ALOS PALSAR: A pathfinder mission for global-scale monitoring of the environment. IEEE Transactions on Geoscience and Remote Sensing, 45(11), 3307-3316.

Rott, H., & Davis, R. E. (1993). Multifrequency and polarimetric SAR observations on alpine glaciers. Annals of Glaciology, 17, 98-104.

Ruiz-Ramos, J., Marino, A., Boardman, C., & Suarez, J. (2020). Continuous forest monitoring using cumulative sums of sentinel-1 timeseries. Remote Sensing, 12(18), 3061.

Rykhus, R., & Lu, Z. (2011). Monitoring a boreal wildfire using multi-temporal Radarsat-1 intensity and coherence images. Geomatics, Natural Hazards and Risk, 2(1), 15-32.

Saatchi, S., Asefi-Najafabady, S., Malhi, Y., Aragão, L. E., Anderson, L. O., Myneni, R. B., & Nemani, R. (2013). Persistent effects of a severe drought on Amazonian forest canopy. Proceedings of the national academy of sciences, 110(2), 565-570.

Saatchi, S., Halligan, K., Despain, D. G., & Crabtree, R. L. (2007). Estimation of forest fuel load from radar remote sensing. IEEE Transactions on Geoscience and Remote Sensing, 45(6), 1726-1740.

Saatchi, S., & Lang, R. (1989). Self Consistent Approach to Average Waves in a One Dimensional Discrete Random Medium. Paper presented at the PIERS: Progress in Electromagnetics Research Symposium277.

Saatchi, S., Marlier, M., Chazdon, R. L., Clark, D. B., & Russell, A. E. (2011). Impact of spatial variability of tropical forest structure on radar estimation of aboveground biomass. Remote sensing of environment, 115(11), 2836-2849.

Saatchi, S. S., Harris, N. L., Brown, S., Lefsky, M., Mitchard, E. T., Salas, W., et al. (2011). Benchmark map of forest carbon stocks in tropical regions across three continents. Proceedings of the national academy of sciences, 108(24), 9899-9904.

Saatchi, S. S., Houghton, R. A., dos Santos Alvalá, R. C., Soares, J. V., & Yu, Y. (2007). Distribution of aboveground live biomass in the Amazon basin. Global Change Biology, 13(4), 816-837.

Saatchi, S. S., Le Vine, D. M., & Lang, R. H. (1994). Microwave backscattering and emission model for grass canopies. IEEE Transactions on Geoscience and Remote Sensing, 32(1), 177-186.

Saatchi, S. S., & McDonald, K. C. (1997). Coherent effects in microwave backscattering models for forest canopies. IEEE Transactions on Geoscience and Remote Sensing, 35(4), 1032-1044.

Saatchi, S. S., & Moghaddam, M. (2002). Estimation of crown and stem water content and biomass of boreal forest using polarimetric SAR imagery. IEEE Transactions on Geoscience and Remote Sensing, 38(2), 697-709.

Sahagian, D., Melack, J., Birkett, C., Chanton, J., Dunne, T., Estes, J., et al. (1997). Global wetland distribution and functional characterizaton: Trace gases and the hydrologic cycle. Paper presented at the Joint IGBP GAIM-DIS-BAHC-IGAC-LUCC workshop, IGBP GAIM/IGBP Global Change, Santa Barbara CA, USA, 199645-45.

Sandwell, D., & Price, E. (1996). Multiple pass INSAR processing for geophysical applications: Stack phase gradient then unwrap. Eos Trans. AGU, 77, 46.

Sarabandi, K., & Lin, Y.-C. (2000). Simulation of interferometric SAR response for characterizing the scattering phase center statistics of forest canopies. IEEE Transactions on Geoscience and Remote Sensing, 38(1), 115-125.

Scambos, T. A., Bohlander, J., Shuman, C. A., & Skvarca, P. (2004). Glacier acceleration and thinning after ice shelf collapse in the Larsen B embayment, Antarctica. Geophysical Research Letters, 31(18).

Schaefer, K., Liu, L., Parsekian, A., Jafarov, E., Chen, A., Zhang, T., et al. (2015). Remotely sensed active layer thickness (ReSALT) at Barrow, Alaska using interferometric synthetic aperture radar. Remote Sensing, 7(4), 3735-3759.

Scheuchl, B., Mouginot, J., Rignot, E., Morlighem, M., & Khazendar, A. (2016). Grounding line retreat of Pope, Smith, and Kohler Glaciers, West Antarctica, measured with Sentinel-1a radar interferometry data. Geophysical Research Letters, 43(16), 8572-8579.

Schimel, D., Pavlick, R., Fisher, J. B., Asner, G. P., Saatchi, S., Townsend, P., et al. (2015). Observing terrestrial ecosystems and the carbon cycle from space. Global Change Biology, 21(5), 1762-1776.

Schweder, T. (1976). Some "optimal" methods to detect structural shift or outliers in regression. Journal of the American Statistical Association, 71(354), 491-501.

Segall, P. (2013). Volcano deformation and eruption forecasting.

Shi, J., Wang, J., Hsu, A. Y., O'Neill, P. E., & Engman, E. T. (1997). Estimation of bare surface soil moisture and surface roughness parameter using L-band SAR image data. IEEE Transactions on Geoscience and Remote Sensing, 35(5), 1254-1266.

Shimada, T., Kawamura, H., & Shimada, M. (2003). An L-band geophysical model function for SAR wind retrieval using JERS-1 SAR. IEEE Transactions on Geoscience and Remote Sensing, 41(3), 518-531.

Short, N., LeBlanc, A.-M., Sladen, W., Oldenborger, G., Mathon-Dufour, V., & Brisco, B. (2014). RADARSAT-2 D-InSAR for ground displacement in permafrost terrain, validation from Iqaluit Airport, Baffin Island, Canada. Remote sensing of environment, 141, 40-51.

Shugart, H. H., & Woodward, F. I. (2011). Global change and the terrestrial biosphere: achievements and challenges.

Simons, M., & Rosen, P. (2007). Interferometric synthetic aperture radar geodesy. Geodesy, 3, 391-446.

Smith, J. E. (2002). A model of forest floor carbon mass for United States forest types (Vol. 722): US Department of Agriculture, Forest Service, Northeastern Research Station.

Smith, S. L., Burgess, M. M., Riseborough, D., & Mark Nixon, F. (2005). Recent trends from Canadian permafrost thermal monitoring network sites. Permafrost and periglacial processes, 16(1), 19-30.

Smith, S. L., O'Neill, H. B., Isaksen, K., Noetzli, J., & Romanovsky, V. E. (2022). The changing thermal state of permafrost. Nature Reviews Earth & Environment, 3(1), 10-23.

Snedecor, G. W., & Cochran, W. G. (1989). Statistical methods, 8th Edn. Ames: Iowa State Univ. Press Iowa, 54, 71-82.

Sneed, M., Brandt, J. T., & Solt, M. (2013). Land subsidence along the Delta-Mendota Canal in the northern part of the San Joaquin Valley, California, 2003-10 (2328-0328). Retrieved from

Sneed, M., & Galloway, D. L. (2000). Aquifer-system compaction and land subsidence: measurements, analyses, and simulations: the Holly site, Edwards Air Force Base, Antelope Valley, California: US Department of the Interior, US Geological Survey.

Spreen, G., Kern, S., Stammer, D., & Hansen, E. (2009). Fram Strait sea ice volume export estimated between 2003 and 2008 from satellite data. Geophysical Research Letters, 36(19).

Stehman, S. (2005). Comparing estimators of gross change derived from complete coverage mapping versus statistical sampling of remotely sensed data. Remote sensing of environment, 96(3-4), 466-474.

Stern, H., Rothrock, D., & Kwok, R. (1995). Open water production in Arctic sea ice: Satellite measurements and model parameterizations. Journal of Geophysical Research: Oceans, 100(C10), 20601-20612.

Streletskiy, D. A., Maslakov, A., Grosse, G., Shiklomanov, N., Farquharson, L. M., Zwieback, S., et al. (2024). Thawing permafrost is subsiding in the Northern Hemisphere-review and perspectives. Environmental Research Letters.

Strozzi, T., Kouraev, A., Wiesmann, A., Wegmüller, U., Sharov, A., & Werner, C. (2008). Estimation of Arctic glacier motion with satellite L-band SAR data. Remote sensing of environment, 112(3), 636-645.

Tan, Q., Wei, Q., & Yang, S. (2010). Discussion on monitoring the subsidence of subgrade in permafrost region with satellite D-InSAR technology. Journal of Railway Engineering Society, 27(1), 4-9.

Tello, M., López-Martínez, C., & Mallorqui, J. J. (2005). A novel algorithm for ship detection in SAR imagery based on the wavelet transform. IEEE Geoscience and Remote Sensing Letters, 2(2), 201-205.

Terzaghi, K. (1925). Principles of soil mechanics. IV. Settlement and consolidation of clay. Engineering New-Record, 95, 874.

Thorndike, A., & Colony, R. (1982). Sea ice motion in response to geostrophic winds. Journal of Geophysical Research: Oceans, 87(C8), 5845-5852.

Thorndike, A. S., Rothrock, D. A., Maykut, G. A., & Colony, R. (1975). The thickness distribution of sea ice. Journal of Geophysical Research, 80(33), 4501-4513.

Toda, S., Lin, J., & Stein, R. S. (2011). Using the 2011 M w 9.0 off the Pacific coast of Tohoku Earthquake to test the Coulomb stress triggering hypothesis and to calculate faults brought closer to failure. Earth, planets and space, 63, 725-730.

Truong-Loï, M.-L., Saatchi, S., & Jaruwatanadilok, S. (2014). Soil moisture estimation under tropical forests using UHF radar polarimetry. IEEE Transactions on Geoscience and Remote Sensing, 53(4), 1718-1727.

Tsang, L., Kong, J. A., & Shin, R. T. (1985). Theory of microwave remote sensing.

Tsang, L., Kong, J. A., & Shin, R. T. (1985). Theory of microwave remote sensing.

Ulaby, F., Dobson, M. C., & Álvarez-Pérez, J. L. (2019). Handbook of radar scattering statistics for terrain: Artech House.

Ulaby, F. T., & El-Rayes, M. A. (2007). Microwave dielectric spectrum of vegetation-Part II: Dual-dispersion model. IEEE Transactions on Geoscience and Remote Sensing(5), 550-557.

Ulaby, F. T., Sarabandi, K., Mcdonald, K., Whitt, M., & Dobson, M. C. (1990). Michigan microwave canopy scattering model. International Journal of Remote Sensing, 11(7), 1223-1253.

Ulaby, F. T., Stiles, W. H., & AbdelRazik, M. (1984). Snowcover influence on backscattering from terrain. IEEE Transactions on Geoscience and Remote Sensing(2), 126-133.

UNFCCC. (2006). Climate Change: Impacts, Vulnerabilities, and Adaptation in Developing Countries. Retrieved from https://www.google.com/url?sa=t&source=web&rct=j&opi=89978449&url=https://unfccc.int/resource/docs/publications/impacts.pdf&ved=2ahUKEwjR25HTI7qMAxUFEUQIHS02BjEQFnoECBMQAQ&usg=AOvVaw0s2pyFlBQFFe4HLplpJ0Rj

Van der Werf, G. R., Morton, D. C., DeFries, R. S., Olivier, J. G., Kasibhatla, P. S., Jackson, R. B., et al. (2009). CO2 emissions from forest loss. Nature Geoscience, 2(11), 737-738.

Van Oort, P. (2006). Spatial data quality: from description to application: Wageningen University and Research.

Van Zyl, J. J. (2011). Synthetic aperture radar polarimetry: John Wiley & Sons.

Vasco, D. W., Rucci, A., Ferretti, A., Novali, F., Bissell, R. C., Ringrose, P. S., et al. (2010). Satellite-based measurements of surface deformation reveal fluid flow associated with the geological storage of carbon dioxide. Geophysical Research Letters, 37(3).

Vesecky, J. F., Samadani, R., Smith, M. P., Daida, J. M., & Bracewell, R. N. (1988). Observation of sea-ice dynamics using synthetic aperture radar images: Automated analysis. IEEE Transactions on Geoscience and Remote Sensing, 26(1), 38-48.

Wadhams, P. (2000). Ice in the ocean. (Vol. 47). Amsterdam: Gordon and Breach Science Publishers.

Walker, W. S., Stickler, C. M., Kellndorfer, J. M., Kirsch, K. M., & Nepstad, D. C. (2010). Large-area classification and mapping of forest and land cover in the Brazilian Amazon: A comparative analysis of ALOS/PALSAR and Landsat data sources. IEEE Journal of Selected Topics in Applied Earth Observations and Remote Sensing, 3(4), 594-604.

Walter, K. M., Zimov, S., Chanton, J. P., Verbyla, D., & Chapin III, F. S. (2006). Methane bubbling from Siberian thaw lakes as a positive feedback to climate warming. Nature, 443(7107), 71-75.

Watanabe, M., Koyama, C. N., Hayashi, M., Nagatani, I., & Shimada, M. (2018). Early-stage deforestation detection in the tropics with L-band SAR. IEEE Journal of Selected Topics in Applied Earth Observations and Remote Sensing, 11(6), 2127-2133.

Whelen, T., & Siqueira, P. (2017). Use of time-series L-band UAVSAR data for the classification of agricultural fields in the San Joaquin Valley. Remote sensing of environment, 193, 216-224.

Whelen, T., & Siqueira, P. (2018). Coefficient of variation for use in crop area classification across multiple climates. International journal of applied earth observation and Geoinformation, 67, 114-122.

Whelen, T., & Siqueira, P. (2018). Time-series classification of Sentinel-1 agricultural data over North Dakota. Remote sensing letters, 9(5), 411-420.

Wig, E., Michaelides, R., & Zebker, H. (2022). High-resolution measurement of soil moisture from InSAR phase closure. Paper presented at the IGARSS 2022-2022 IEEE International Geoscience and Remote Sensing Symposium. IEEE, Vol. 919-922.

Williams, S., Bock, Y., & Fang, P. (1998). Integrated satellite interferometry: Tropospheric noise, GPS estimates and implications for interferometric synthetic aperture radar products. Journal of Geophysical Research: Solid Earth, 103(B11), 27051-27067.

Woodall, C. (2010). Carbon flux of down woody materials in forests of the North Central United States. International Journal of Forestry Research, 2010(1), 413703.

Woodcock, C. E., Macomber, S. A., Pax-Lenney, M., & Cohen, W. B. (2001). Monitoring large areas for forest change using Landsat: Generalization across space, time and Landsat sensors. Remote sensing of environment, 78(1-2), 194-203.

Xu, Z.-W., Wu, J., & Wu, Z.-S. (2004). A survey of ionospheric effects on space-based radar. Waves in Random media, 14(2), S189.

Ygorra, B., Frappart, F., Wigneron, J.-P., Moisy, C., Catry, T., Baup, F., et al. (2021). Monitoring loss of tropical forest cover from Sentinel-1 time-series: A CuSum-based approach. International journal of applied earth observation and Geoinformation, 103, 102532.

Yu, Y., & Saatchi, S. (2016). Sensitivity of L-band SAR backscatter to aboveground biomass of global forests. Remote Sensing, 8(6), 522.

Yueh, S., Kong, J., & Shin, R. (1992). Extenal calibration of polarimetric radars using point and distributed targets. Journal of electromagnetic waves and applications, 6(7), 921-941.

Yun, S.-H., Hudnut, K., Owen, S., Webb, F., Simons, M., Sacco, P., et al. (2015). Rapid damage mapping for the 2015 M w 7.8 Gorkha earthquake using synthetic aperture radar data from COSMO–SkyMed and ALOS-2 Satellites. Seismological Research Letters, 86(6), 1549-1556.

Yunjun, Z., Fattahi, H., & Amelung, F. (2019). Small baseline InSAR time series analysis: Unwrapping error correction and noise reduction. Computers & Geosciences, 133, 104331.

Zebker, H. (2021). Accuracy of a model-free algorithm for temporal InSAR tropospheric correction. Remote Sensing, 13(3), 409.

Zebker, H. A., & Goldstein, R. M. (1986). Topographic mapping from interferometric synthetic aperture radar observations. Journal of Geophysical Research: Solid Earth, 91(B5), 4993-4999.

Zebker, H. A., Rosen, P. A., & Hensley, S. (1997). Atmospheric effects in interferometric synthetic aperture radar surface deformation and topographic maps. Journal of Geophysical Research: Solid Earth, 102(B4), 7547-7563.

Zebker, H. A., & Villasenor, J. (1992). Decorrelation in interferometric radar echoes. IEEE Transactions on Geoscience and Remote Sensing, 30(5), 950-959.

Zhang, J., Rothrock, D., & Steele, M. (2000). Recent changes in Arctic sea ice: The interplay between ice dynamics and thermodynamics. Journal of Climate, 13(17), 3099-3114.

Zhang, S., Sadras, V., Chen, X., & Zhang, F. (2014). Water use efficiency of dryland maize in the Loess Plateau of China in response to crop management. Field Crops Research, 163, 55-63.

Zhang, Y., Wang, C., Wu, J., Qi, J., & Salas, W. A. (2009). Mapping paddy rice with multitemporal ALOS/PALSAR imagery in southeast China. International Journal of Remote Sensing, 30(23), 6301-6315.

Zhao, W., Amelung, F., Dixon, T. H., Wdowinski, S., & Malservisi, R. (2014). A method for estimating ice mass loss from relative InSAR observations: Application to the Vatnajökull ice cap, Iceland. Geochemistry, Geophysics, Geosystems, 15(1), 108-120.

Zheng, Y., Fattahi, H., Agram, P., Simons, M., & Rosen, P. (2022). On closure phase and systematic bias in multilooked SAR interferometry. IEEE Transactions on Geoscience and Remote Sensing, 60, 1-11.

Zwieback, S., Iwahana, G., Chang, Q., & Meyer, F. (2025). InSAR estimates of excess ground ice concentrations near the permafrost table. ISPRS Journal of Photogrammetry and Remote Sensing, 223, 261-273.

Zwieback, S., Liu, L., Rouyet, L., Short, N., & Strozzi, T. (2024). Advances in InSAR Analysis of Permafrost Terrain. Permafrost and periglacial processes, 35(4), 544-556.

Zwieback, S., & Meyer, F. J. (2021). Radar interferometric phase errors induced by Faraday rotation. IEEE Transactions on Geoscience and Remote Sensing, 60, 1-11.

Zwieback, S., & Meyer, F. J. (2021). Top-of-permafrost ground ice indicated by remotely sensed late-season subsidence. The Cryosphere, 15(4), 2041-2055.

National Aeronautics and Space Administration

Jet Propulsion Laboratory
California Institute of Technology
Pasadena, California

www.nasa.gov

CL# 25-4231